

Contents

- 4A1 Numerical Techniques I
- 4A2 Induced Current in a Human Body by ELF/Intermediate Electric or Magnetic Fields
- 4A4 Microwave Materials for Functional Devices
- 4A5 UXO/Landmine Detection
- 4A6 Basic and Applied Concepts of Electromagnetic Vector Imaging: Polarimetry in Radar and SAR Remote Sensing
- 4A7 High Frequency Micromachined Circuits
- 4A8 ESD and Transients
- 4P1 Numerical Techniques II
- 4P2 Electromagnetic Modeling and Inversion and Applications
- 4P3 UWB Antennas for Radar and Telecommunication
- 4P4 Remote Sensing of Ocean/Forests
- 4P6 Electromagnetic Fields of Nanometer Electromagnetic Waves and X-ray
- 4P7 Novel Mathematical Methods in Electromagnetics III
- 4P8 Microstrip and Printed Antennas

A Low Cost Hybrid FDTD Algorithm to Compute Optical Propagation in Dispersive Media

James B. Cole and Saswatee Banerjee

University of Tsukuba, Japan

Abstract—The recursive convolution algorithm, which is widely used to solve Maxwell's equations in dispersive materials is complicated, computationally costly, and requires a model of the dispersion mechanism. We introduce a low-cost model-independent hybrid frequency / time-domain version of the Yee algorithm for which requires only the value of the complex permittivity at a single frequency for monochromatic radiation.

1. Introduction

Maxwell's equations are given by

$$\partial_t \mathbf{B}(\mathbf{x}, t) = -\nabla \times \mathbf{E}(\mathbf{x}, t), \quad (1.1)$$

$$\partial_t \mathbf{D}(\mathbf{x}, t) = \nabla \times \mathbf{H}(\mathbf{x}, t) - \mathbf{J}(\mathbf{x}, t), \quad (1.2)$$

where \mathbf{B} is the magnetic field, \mathbf{E} the electric field, \mathbf{D} the electric displacement, \mathbf{H} , the magnetic intensity, \mathbf{J} the electric current, and $\mathbf{x} = (x, y, z)$ denotes vector position. In order to simplify the discussion, let us take $\mathbf{B} = \mu \mathbf{H}$, where μ is constant. Thus (1.1) becomes

$$\mu \partial_t \mathbf{H}(\mathbf{x}, t) = -\nabla \times \mathbf{E}(\mathbf{x}, t) \quad (1.3)$$

Let us also assume a linear conducting material in which $\mathbf{J} = \sigma \mathbf{E}$, where σ is the conductivity. If the electric permittivity, ε , does not depend upon frequency, then $\mathbf{D}(\mathbf{x}, t) = \varepsilon(\mathbf{x}) \mathbf{E}(\mathbf{x}, t)$, but if ε does depend on the frequency,

$$\tilde{\mathbf{D}}(\mathbf{x}, \omega) = \tilde{\varepsilon}(\mathbf{x}, \omega) \tilde{\mathbf{E}}(\mathbf{x}, \omega) \quad (1.4)$$

in the frequency domain, where $\tilde{\mathbf{F}}$ is the Fourier transform with respect to time of \mathbf{F} .

Applying the Fourier convolution theorem to (1.4) we have

$$\mathbf{D}(\mathbf{x}, t) = \int_0^t \varepsilon(\mathbf{x}, t') \mathbf{E}(\mathbf{x}, t-t') dt' \quad (1.5)$$

in the time domain. Taking the time dependence of the fields to be $e^{i\omega t}$, eqn. (1.2) gives

$$i\omega \left(\tilde{\varepsilon}(\mathbf{x}, \omega) - i \frac{\sigma(\mathbf{x})}{\omega} \right) \tilde{\mathbf{E}}(\mathbf{x}, \omega) = \nabla \times \tilde{\mathbf{H}}(\mathbf{x}, \omega) \quad (1.6)$$

Redefining, $\tilde{\varepsilon} \rightarrow \tilde{\varepsilon} + i\sigma/\omega$, (1.6) becomes

$$i\omega \tilde{\varepsilon}(\mathbf{x}, \omega) \tilde{\mathbf{E}}(\mathbf{x}, \omega) = \nabla \times \tilde{\mathbf{H}}(\mathbf{x}, \omega). \quad (1.7)$$

Returning to the time domain we now have

$$\partial_t \int_0^t \varepsilon(\mathbf{x}, t') \mathbf{E}(\mathbf{x}, t-t') dt' = \nabla \times \mathbf{H}(\mathbf{x}, t). \quad (1.8)$$

Maxwell's equations in a conducting medium with a medium with a complex frequency-dependent conductivity are thus given by (1.3) and (1.8).

In the Yee algorithm, the derivatives of Maxwell's equations are replaced by central finite difference (FD) approximations: $\partial_t \rightarrow d_t / \Delta t$, $\nabla \rightarrow \mathbf{d}/h$, where $d_t f(\mathbf{x}, t) = f(\mathbf{x}, t + \Delta t/2) - f(\mathbf{x}, t - \Delta t/2)$, $\mathbf{d} = (d_x, d_y, d_z)$ is a vector FD operator, the d_i ($i = x, y, z$) are partial difference operators analogous to d_t , and we take $\Delta x = \Delta y = \Delta z = h$. Equation (1.3) becomes

$$d_t \mathbf{H}(\mathbf{x}, t) = -\frac{1}{\mu} \frac{\Delta t}{h} \mathbf{d} \times \mathbf{E}(\mathbf{x}, t). \quad (1.9)$$

Here the electromagnetic field components are arranged on the grid in such a way that central FDs can be taken. Solving for $\mathbf{H}(\mathbf{x}, t + \Delta t/2)$ gives

$$\mathbf{H}(\mathbf{x}, t + \Delta t/2) = \mathbf{H}(\mathbf{x}, t - \Delta t/2) - \frac{1}{\mu} \frac{\Delta t}{h} \mathbf{d} \times \mathbf{E}(\mathbf{x}, t) \quad (1.10)$$

Because of the convolution integral in (1.8) the update of \mathbf{E} is much more complicated.

In this paper we first briefly review the widely used recursive convolution algorithm, and then introduce a new algorithm that is suitable for monochromatic radiation.

2. Recursive Convolution Algorithm

Let us first decompose the permittivity, which is a complex function of frequency into constant and frequency-dependent parts in the form

$$\tilde{\varepsilon}(\mathbf{x}, \omega) = \varepsilon_1(\mathbf{x}) + \tilde{\chi}(\mathbf{x}, \omega), \quad (2.1)$$

where ε_1 is constant, and χ incorporates the frequency-dependent part of $\tilde{\varepsilon}$, including the $i\sigma/\omega$ term. Thus (1.5) becomes

$$\mathbf{D}(\mathbf{x}, t) = \varepsilon_1(\mathbf{x}) \mathbf{E}(\mathbf{x}, t) + \int_0^t \chi(\mathbf{x}, t') \mathbf{E}(\mathbf{x}, t-t') dt'. \quad (2.2)$$

Taking Δt to be small compared to the period of \mathbf{E} , we can make the approximation

$$\begin{aligned} \int_t^{t+\Delta t} \chi(\mathbf{x}, t') \mathbf{E}(\mathbf{x}, t-t') dt' &\cong \mathbf{E}(\mathbf{x}, t) \int_t^{t+\Delta t} \chi(\mathbf{x}, t') dt', \\ &= \mathbf{E}(\mathbf{x}, t) \bar{\chi}(\mathbf{x}, t), \end{aligned} \quad (2.3)$$

where $\bar{\chi}(\mathbf{x}, t)/\Delta t$ is the time average of $\chi(\mathbf{x}, t')$ on the interval $t \leq t' \leq t + \Delta t$. \mathbf{D} can thus be approximated as a sum in the form

$$\mathbf{D}(\mathbf{x}, t) \approx \epsilon_1(\mathbf{x})\mathbf{E}(\mathbf{x}, t) + \sum_{t'=0}^{t-\Delta t} \mathbf{E}(\mathbf{x}, t-t')\bar{\chi}(\mathbf{x}, t'), \quad (2.4)$$

where $t' = 0, \Delta t, 2\Delta t, \dots$. Computing $d_t \mathbf{D}(\mathbf{x}, t + \Delta t/2) = \mathbf{D}(\mathbf{x}, t + \Delta t) - \mathbf{D}(\mathbf{x}, t)$, we find

$$\begin{aligned} d_t \mathbf{D}(\mathbf{x}, t + \Delta t/2) &\approx \epsilon_1(\mathbf{x})d_t \mathbf{E}(\mathbf{x}, t + \Delta t/2) + \bar{\chi}(\mathbf{x}, 0)\mathbf{E}(\mathbf{x}, t + \Delta t) \\ &\quad + \sum_{t'=0}^{t-\Delta t} \mathbf{E}(\mathbf{x}, t-t')\Delta\bar{\chi}(\mathbf{x}, t'), \end{aligned} \quad (2.5)$$

where $\Delta\bar{\chi}(\mathbf{x}, t) = \bar{\chi}(\mathbf{x}, t + \Delta t) - \bar{\chi}(\mathbf{x}, t)$. Replacing the derivatives of (1.8) with central FD approximations and using (2.5) we have

$$\mathbf{E}(\mathbf{x}, t + \Delta t) = \frac{1}{\epsilon_1(\mathbf{x}) + \bar{\chi}(\mathbf{x}, 0)} [\epsilon_1(\mathbf{x})\mathbf{E}(\mathbf{x}, t) + \mathbf{d} \times \mathbf{H}(\mathbf{x}, t + \Delta t/2) - \Psi(\mathbf{x}, t)], \quad (2.6)$$

where Ψ , called the “accumulation field” denotes the summation in (2.5). Equations (1.10) and (2.6) constitute a modified form of the Yee algorithm, for dispersive permittivity. Because $\Psi(\mathbf{x}, t)$ is a summation over all the time steps from $0, \Delta t, 2\Delta t, \dots, t - \Delta t$ a very large amount of data must be stored to perform the update the \mathbf{E} -field using (2.6), especially in three dimensions.

If we have a model of the permittivity the computation and storage in (2.6) can be reduced. For example in the first order Debye model,

$$\tilde{\chi}(\mathbf{x}, \omega) = \frac{\epsilon_2(\mathbf{x})}{1 - i\omega\tau} + i \frac{\sigma(\mathbf{x})}{\omega}, \quad (2.6)$$

where ϵ_2 and $\tau > 0$ are constants that must be experimentally determined. Taking the inverse Fourier transform of (2.6) we find

$$\chi(\mathbf{x}, t) = \frac{\epsilon_2(\mathbf{x})}{\tau} e^{-t/\tau} + \frac{\sigma}{2} [\Theta(t) - \Theta(-t)],$$

where $\Theta(t)$ is step function. Integrating from t to $t + \Delta t$, in this model we find

$$\bar{\chi}(\mathbf{x}, t) = \epsilon_2(\mathbf{x})e^{-t/\tau} \left(1 - e^{-\Delta t/\tau}\right) + \frac{1}{2} \sigma \Delta t. \quad (2.7)$$

Thus $\Delta\bar{\chi}(\mathbf{x}, t) = -\epsilon_2(\mathbf{x}) \left(1 - e^{-\Delta t/\tau}\right)^2 e^{-t/\tau}$, and $\Delta\bar{\chi}(\mathbf{x}, t + \Delta t) = \kappa \Delta\bar{\chi}(\mathbf{x}, t)$, where $\kappa = e^{-\Delta t/\tau}$

is a constant. $\Psi(\mathbf{x}, t)$ can now be iteratively evaluated. It is easy to show that

$$\Psi(\mathbf{x}, t + \Delta t) = \Delta\chi(\mathbf{x}, 0)\mathbf{E}(\mathbf{x}, t + \Delta t) + \kappa\Psi(\mathbf{x}, t). \quad (2.8)$$

Equations (1.10), (2.6), and (2.8) are called the recursive convolution algorithm [1].

Even with this simplification, memory and computational requirements are still quite heavy, because now there are three vector fields that must be computed on the space-time grid. Moreover, experimental measurements are often difficult so is not always clear what are the

values of the model parameters. It is thus desirable to have a computational technique that does not require the additional field, Ψ , and which is model independent.

3. Hybrid Frequency/Time Domain Algorithm

In many problems we are concerned with monochromatic radiation. The \mathbf{H} -field can be updated via equation (1.10). Putting $t \rightarrow t + \Delta t$, at a fixed angular frequency, ω_0 , equation (1.6) gives

$$\mathbf{E}(\mathbf{x}, t + \Delta t) = \frac{1}{\sigma(\mathbf{x}) + i\omega_0 \tilde{\epsilon}(\mathbf{x}, \omega_0)} \nabla \times \mathbf{H}(\mathbf{x}, t + \Delta t), \quad (3.1)$$

where we use the fact that $\mathbf{F}(\mathbf{x}, t) = \tilde{\mathbf{F}}(\mathbf{x}, \omega) e^{i\omega_0 t}$. Substituting FD approximations for the derivatives we obtain

$$\mathbf{E}(\mathbf{x}, t + \Delta t) = \frac{1}{\sigma(\mathbf{x}) + i\omega_0 \tilde{\epsilon}(\mathbf{x}, \omega_0)} \frac{1}{h} \mathbf{d} \times \mathbf{H}(\mathbf{x}, t + \Delta t). \quad (3.2)$$

Now if we could estimate $\mathbf{H}(\mathbf{x}, t + \Delta t)$ from $\mathbf{H}(\mathbf{x}, t + \frac{\Delta t}{2})$ given by (1.10) we would have a Yee-like algorithm to march the electromagnetic fields forward in time. Using

$$\begin{aligned} f(t + \Delta t) &= f(t + \frac{\Delta t}{2}) + \frac{\Delta t}{2} f'(t + \frac{\Delta t}{2}) \\ &\cong \frac{3}{2} f(t + \frac{\Delta t}{2}) - \frac{1}{2} f(t - \frac{\Delta t}{2}), \end{aligned} \quad (3.3)$$

where we have used $\Delta t f'(t + \frac{\Delta t}{2}) \cong f(t + \frac{\Delta t}{2}) - f(t - \frac{\Delta t}{2})$. Using (3.3) in (3.2) we obtain

$$\mathbf{E}(\mathbf{x}, t + \Delta t) = \frac{1}{\sigma(\mathbf{x}) + i\omega_0 \tilde{\epsilon}(\mathbf{x}, \omega_0)} \frac{1}{h} \mathbf{d} \times \left[\frac{3}{2} \mathbf{H}(\mathbf{x}, t + \frac{\Delta t}{2}) - \frac{1}{2} \mathbf{H}(\mathbf{x}, t - \frac{\Delta t}{2}) \right]. \quad (3.4)$$

Thus knowing $\tilde{\epsilon}(\mathbf{x}, \omega_0)$ we can now compute the electromagnetic fields without the need to compute the Ψ -field. This algorithm is called the hybrid frequency/time domain (HFTD) algorithm was introduced in [2].

4. High Accuracy Using Nonstandard Finite Difference Approximations

In previous papers [3-4]- we have introduced a high accuracy version of the Yee algorithm for nondispersive media by replacing the usual FD approximations with what are called nonstandard finite difference (NSFD) approximations [5]. In what we now call the standard finite difference (SFD) approximation $f'(t) \cong d_t f(t)/\Delta t$. In the NSFD approximation Δt is replaced by a function of $s(\Delta t)$ which satisfies $\lim_{\Delta t \rightarrow 0} s(\Delta t) = \Delta t$, and $s'(0) = 1$. In some cases NSFD approximations can greatly increase the accuracy of FD algorithms. For $f(t) = e^{\pm at}$, where a is complex, $s(\Delta t) = d_t f(t)/f'(t)$, $f'(t) = d_t f(t)/s(\Delta t)$ exactly. For $f(t) = e^{\pm i\omega t}$ we have $s(\Delta t) = 2 \sin(\omega \Delta t / 2) / \omega$ and the time derivative in (1.10) is given by an exact FD expression. Furthermore, given that the time dependence of the electromagnetic fields is $e^{i\omega_0 t}$, we have $\mathbf{H}(\mathbf{x}, t + \Delta t) = e^{i\omega_0 \Delta t / 2} \mathbf{H}(\mathbf{x}, t + \frac{\Delta t}{2})$. NSFD methods

can be extended to the calculation of the space derivatives, but now a new FD operator for ∇ must be introduced. Let us denote the FD operator \mathbf{d} by \mathbf{d}_1 . In three dimensions there are two additional FD operators \mathbf{d}_2 , and \mathbf{d}_3 which are superposed to form a new operator \mathbf{d}_0 . For plane waves $\varphi(\mathbf{x}) = e^{i\mathbf{k} \cdot \mathbf{x}}$, where $\mathbf{k} = (k_x, k_y, k_z)$, the SFD approximation error is $(\nabla^2 - \mathbf{d}_1^2/h^2)\varphi \sim h^2\varphi$, where $\mathbf{d}_1^2 = \mathbf{d}_1 \cdot \mathbf{d}_1$. On the other hand for $\mathbf{d}_0^2 \equiv \mathbf{d}_0 \cdot \mathbf{d}_1 = \mathbf{d}_1 \cdot \mathbf{d}_0$, $(\nabla^2 - \mathbf{d}_0^2/s(h)^2)\varphi \sim h^6\varphi$, where $s(h) = 2 \sin(kh/2)/k$, and $k = |\mathbf{k}|$.

We can thus construct high accuracy versions of (1.10) and (3.4). Defining $\mathbf{H}' = (\mu h/\Delta t) \mathbf{H}$, and making the substitutions $h \rightarrow s(h)$, $\Delta t \rightarrow s(\Delta t)$, and $\mathbf{d} \rightarrow \mathbf{d}_0$ (1.10) becomes

$$\mathbf{H}'(\mathbf{x}, t + \Delta t/2) = \mathbf{H}'(\mathbf{x}, t - \Delta t/2) - \mathbf{d}_0 \times \mathbf{E}(\mathbf{x}, t), \quad (4.1)$$

and retaining $\mathbf{d} = \mathbf{d}_1$ in (3.4), we have

$$\mathbf{E}(\mathbf{x}, t + \Delta t) = \left(\frac{e^{i\omega_0 \Delta t / 2}}{\sigma(\mathbf{x}) + i\omega_0 \tilde{\epsilon}(\mathbf{x}, \omega_0)} \right) \frac{k_0^2 \sin(\omega_0 \Delta t / 2)}{\mu \omega_0 \sin^2(k_0 h \sqrt{\tilde{\epsilon}(\mathbf{x}, \omega_0)} / 2)} \mathbf{d}_1 \times \mathbf{H}'(\mathbf{x}, t + \Delta t/2), \quad (4.2)$$

where k_0 is the vacuum value of k .

5. Standard FDTD with Drude model and application

According to the first-order Drude model, $\epsilon(\omega)$ is defined as

$$\epsilon(\omega) = 1 + \frac{\omega_p^2}{\omega(i\nu_c - \omega)} = \epsilon_\infty + \chi(\omega) \quad (5.1)$$

Where ω_p is the plasma frequency, ν_c is the collision frequency, ϵ_∞ is infinite frequency dielectric constant and equal to 1. $\chi(\omega)$ is the susceptibility.

Denoting $\chi(t) = \mathbb{F}\{\chi(\omega)\}$ we find [1],

$$\chi(t) = \frac{\omega_p^2}{\nu_c} [1 - e^{-\nu_c t}] U(t), \quad (5.2)$$

where $U(t)$ is a unit step function of time.

Evaluating a convolution integral on a discrete time grid and taking E to be constant over an interval $[m\Delta t, (m+1)\Delta t]$ we get

$$\mathcal{D}^n = \epsilon_0 \epsilon_\infty \mathbf{E}^n + \epsilon_0 \sum_{m=0}^{n-1} \mathbf{E}^{n-m} \int_{m\Delta t}^{(m+1)\Delta t} \chi(\tau) d\tau \quad (5.3)$$

$$\mathcal{D}^n = \epsilon_0 \epsilon_\infty \mathbf{E}^n + \epsilon_0 \Psi^n \quad (5.4)$$

Where,

$$\begin{aligned}\Psi^n &= \sum_{m=0}^{n-1} \mathbf{E}^{n-m} \int_{m\Delta t}^{(m+1)\Delta t} \chi(\tau) d\tau \\ &= \sum_{m=0}^{n-1} \mathbf{E}^{n-m} \frac{\omega_p^2}{v_c} \left[\Delta t + \frac{e^{-v_c(m+1)\Delta t} - e^{-v_c(m)\Delta t}}{v_c} \right]\end{aligned}\quad (5.5)$$

Using the Drude model (eqns. 5.1 and 5.2) and standard finite differences the second Maxwell's equation reduce to

$$\mathbf{E}^{n+1} = \frac{\epsilon_\infty - \alpha_0 \Delta t}{\epsilon_\infty + \alpha_0 \Delta t} \mathbf{E}^n - \frac{1}{\epsilon_\infty + \alpha_0 \Delta t} (\Psi^{n+1} - \Psi^n) + \frac{\Delta t}{\epsilon_0 (\epsilon_\infty + \alpha_0 \Delta t)} \mathbf{D}_1 \times \mathbf{H}^n \quad (5.6)$$

Where $\Psi^{n+1} - \Psi^n$ is computed from a recursive relation. The other Maxwell's equation remains the same as the non-dispersive case (eqn. 1.9).

Gratings with subwavelength groove depth and period are frequently used in optics for various purposes. However, the polarization dependent diffraction characteristics of subwavelength gratings can only be computed by solving Maxwell's equations. For finite subwavelength optical structures, no analytical solutions of Maxwell's equations exist. Here, we use the SFDTD with Drude model to compute the far-field diffraction characteristics of a gold sinusoidal grating (spatial period is $1.1111 \mu\text{m}$, groove depth is $0.5 \mu\text{m}$, wavelength of light is $1.55 \mu\text{m}$). The refractive index of gold is taken to be $0.64 + i9.54$. The angle of incidence is $+60^\circ$. The simulation is done in two-dimensions. In two-dimensions, light of any arbitrary polarization can be divided into two orthogonal modes, TE (transverse electric) and TM (transverse magnetic).

Figure 1 contains the far-field diffraction properties due the above grating in TE and TM modes respectively. Each of Figs. 1a) and 1b) show two cases, e.g., case 1) width of simulated grating is equal to 11 grating periods; case 2) width of simulated grating is equal to 25 grating periods. The diffraction angles and efficiencies are specified in the figure captions. The symbols $\eta_{\pm m}$ and $\theta_{\pm m}$ are used to denote the diffraction efficiencies and angles for $\pm m$ th order respectively. The figure shows that the angles, efficiencies and the spread of the diffraction orders can be fairly different for the two cases in both modes. While results for case 1) are typical for a grating with finite width, results for case 2) actually resemble those due to an infinite grating. The example shows that the assumptions of infinite beam or infinite periodicity are not valid in case of objects of finite size.

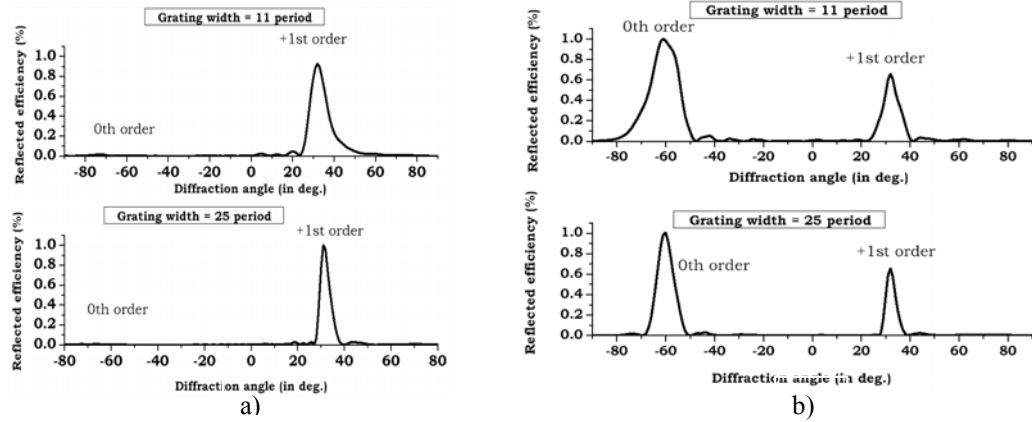


Figure 1: a) Far-field diffraction properties in TM mode. Case 1) $\eta_0 = 0.1\%$, $\theta_0 = -73^\circ$ and $\eta_{+1} = 78.5\%$, $\theta_{+1} = 30^\circ$; Case 2) $\eta_0 = 1\%$, $\theta_0 = -66^\circ$ and $\eta_{+1} = 92.5\%$, $\theta_{+1} = 30^\circ$; b) Far-field diffraction properties in TE mode. Case 1) $\eta_0 = 73.5\%$, $\theta_0 = -60^\circ$ and $\eta_{+1} = 26.6\%$, $\theta_{+1} = 30^\circ$; Case 2) $\eta_0 = 75.6\%$, $\theta_0 = -60^\circ$ and $\eta_{+1} = 24.1\%$, $\theta_{+1} = 30^\circ$

References

- [1] K. S. Kunz and R. J. Luebbers, chapter 8 in “The Finite Difference Time Domain Method for Electromagnetics,” CRC Press, New York (1993).
- [2] M. I Haftel, “FDTD Algorithms for Electromagnetic Fields with Surface Plasmons,” Chapter 4, Section 9, pp. 163-185, in *Advances in the Applications of Nonstandard Finite Difference Schemes*, R. E. Mickens, ed., Scientific (Singapore, 2005).
- [3] J.B. Cole, High Accuracy Yee Algorithm Based on Nonstandard Finite Differences: New Developments and Verifications, IEEE Trans. Antennas and Propagation, vol. 50, no. 9, pp. 1185-1191 (Sept., 2002).
- [4] J. B. Cole and S. Banerjee, Applications of Nonstandard Finite Difference Models to Computational Electromagnetics, J. of Difference Equations and Applications, vol. 9, no. 12, pp. 1099-1112 (Dec. 2003).
- [5] R.E. Mickens, “Nonstandard Finite Difference Models of Differential Equations,” World Scientific, Singapore (1984).

Analysis of Current Density Distribution Induced by ELF Magnetic Fields Utilizing Fast-Multipole Surface-Charge-Simulation Method for Voxel Data

Shoji Hamada and Tetsuo Kobayashi

Department of Electrical Engineering, Kyoto University, Japan

Abstract This paper describes an application of the FMM(fast multipole method⁽¹⁾)-SCM(surface charge simulation method) for voxel data⁽²⁾ to analyses of current density distribution in a human model induced by 50Hz magnetic fields. The performance of this method is demonstrated by calculating the induced currents in the ‘Taro’⁽³⁾ licensed by NICT (National Institute of Information and Communications Technology). Taro models a Japanese adult male and is composed of 7,977,906, 2mm×2mm×2mm voxels. The required calculation time results in about six to seven hours on a 32bit, 3GHz, 2G-RAM, single Pentium IV, Windows PC.

1. Introduction

A variety of methods are practically utilized for calculating magnetically induced electric fields and currents in realistic high-resolution human voxel models. The most popular methods, such as SPFD, FDTD, FEM, FIT, and Impedance method, require $O(D^3)$ memory-capacity and operation-cost, when the number of voxels is about D^3 . Although they are superior to $O(D^{4\sim 6})$ cost of the conventional BEM, SCM, and MoM, increasing size of D causes intolerable cost increase. In order to overcome this problem, we had proposed the FMM-SCM for voxel data⁽²⁾. This method treats a square surface of a voxel that has different inside and outside conductivities as a surface element of the SCM that calculates three-dimensional Laplacian field. The main features of the method are as follows. (I) The diagonal form FMM provides $O(D^2)$ performance in the memory-capacity and operation-cost, when the number of voxels is about D^3 . (II) The boundary equation integrated over each element strictly imposes the flux continuity, therefore the solution globally satisfies the Gauss’ law. These features make it high-speed, high-capacity, and high-stability calculation method.

2. Basic Equations and Implementation of the FMM

The basic equations of magnetically induced, low-frequency, faint current in a human body are described in a lot of previous works⁽⁴⁾. By neglecting the effect of the permittivity, the induced electric field \mathbf{E} and current density \mathbf{J} satisfy following equations.

$$\mathbf{E} = -j\omega \{\mathbf{A} + \nabla\phi\} , \quad \mathbf{J} = \sigma\mathbf{E} , \quad \nabla^2\phi = 0 \quad (1)$$

where j is the imaginary unit, ω is the angular frequency of the given field source, \mathbf{A} is the vector potential generated by the source, ϕ is an unknown scalar potential that satisfies the Laplace equation, and σ is the conductivity. The boundary equations are as follows.

$$\sigma_1 \{\mathbf{A} + \nabla\phi_1\} \cdot \mathbf{n} = \sigma_2 \{\mathbf{A} + \nabla\phi_2\} \cdot \mathbf{n} , \quad \phi_1 = \phi_2 \quad (2)$$

where subscripts 1 and 2 denote the both sides of the boundary surface, and \mathbf{n} means the unit normal vector of the surface. The SCM automatically satisfies the second equation of (2), therefore we consider only the first one of (2) in the following surface-integral form.

$$\sigma_1 \int_{S_i} \nabla\phi_1 \cdot \mathbf{n} dS - \sigma_2 \int_{S_i} \nabla\phi_2 \cdot \mathbf{n} dS = -(\sigma_1 - \sigma_2) \int_{S_i} \mathbf{A} \cdot \mathbf{n} dS , \quad i = 1 \sim N \quad (3)$$

where S means the square surface of each element, subscript i denotes the element number, and N is the number of elements. This equation describes continuity of the flux flowing through the i -th element. The SCM expresses the ϕ and $\nabla\phi$ by superposing the Laplacian fields generated by the surface elements that have equivalent surface charges. The constant charge density x_i on the i -th element can be determined as the solution of a linear system $A\mathbf{x} = \mathbf{b}$ that is equivalent to (3) by utilizing an iterative solver, such as Bi-CGSTAB2⁽⁵⁾.

In order to speed up the solver, we utilize the diagonal form FMM⁽¹⁾ by defining a cubic region composed of $4\times 4\times 4$ voxels as a leaf-cell of the three-dimensional octal-tree structure. The FMM calculates the product $A\mathbf{x}$ as the sum of the ‘near’ part and the ‘far’ part. The contribution of x_j to $\left(\int_{S_i} \nabla\phi \cdot \mathbf{n} dS\right)^{\text{near}}$ is calculated by

Table 1: No. of tissues, conductivities (Sm^{-1}), and the numbers of voxels.

No.	Tissue	σ	voxels	No.	Tissue	σ	voxels	No.	Tissue	σ	voxels
1	Cerebellum	0.1	17320	20	Duodenum	0.5	1105	39	Trachea	0.35	3563
2	CSF	2.0	54200	21	Esophagus	0.5	860	40	Urine	0.7	40055
3	Cornea	0.4	25	22	Bile	1.4	944	44	Blood	0.7	148587
5	Vitreous Humor	1.5	2124	23	Gall Bladder	0.2	548	45	Cortical Bone	0.02	456228
6	Grey Matter	0.1	73362	24	Heart	0.1	50850	46	Marrow	0.06	509507
7	Hypothalamus	0.08	77	25	Kidney	0.1	37003	47	Cartilage	0.18	33015
8	Lens	0.25	73	26	Liver	0.07	143784	48	Fat (Mean)	0.04	1962602
9	Pineal Glands	0.08	20	27	Lung	0.14	412003	49	Muscle (Mean)	0.35	3193078
10	Pituitary	0.08	39	29	Pancreas	0.35	8288	50	Nerve	0.03	11340
11	Salivary Gland	0.35	8271	30	Prostate	0.4	4053	51	Skin	0.1	422953
12	Thalamus	0.08	2967	31	Small Intestine	0.5	40280	52	Tooth	0.02	3112
13	Tongue	0.3	11896	32	Spleen	0.1	17206	53	Ligament	0.3	18268
14	White Matter	0.06	76094	33	Stomach	0.5	22925	54	Contents of 31	0.35	32270
15	Adrenals	0.35	247	34	Contents of 33	0.35	8766	55	Diaphragm	0.35	7649
16	Bladder	0.2	7701	35	Tendon	0.3	7045	56	Seminal Vesicle	0.35	2739
18	Large Intestine	0.1	43411	36	Testis	0.35	14098	57	Cavernous Body	0.35	16268
19	Contents of 18	0.35	47188	38	Thyroid, Thymus	0.5	1899		Whole body		7977906

multiplying x_j by proportional coefficients between them. The calculation of $\left(\int_{S_i} \nabla \phi \cdot \mathbf{n} dS\right)^{\text{far}}$ requires following processes. The field contribution by x_j in a leaf-cell is translated into the multipole-expansion coefficients M_n^m defined on the leaf-cell by multiplying x_j by proportional coefficients between them. The field contribution by local-expansion coefficients L_n^m defined on a leaf-cell is translated into the $\left(\int_{S_i} \nabla \phi \cdot \mathbf{n} dS\right)^{\text{far}}$ in the leaf-cell by multiplying L_n^m by proportional coefficients between them. All these coefficients can be preliminarily calculated by numerical integrations in the form of (3), therefore no integration is needed during the FMM calculation. In addition, they depend only on the relative location between two elements or between an element and the center of an expansion, therefore the memory capacity required for storing these coefficients is only several Mbytes. All required M_n^m and L_n^m are calculated by the diagonal form FMM algorithm, where the upper limit of the n is set to ten.

3. Field at the Voxel Center and Field Smoothing near Boundaries

After solving \mathbf{x} , we can calculate $\int_S \mathbf{E} \cdot \mathbf{n} dS$ on the six inner surfaces of every voxel, which are denoted by f^{x+} , f^{x-} , f^{y+} , f^{y-} , f^{z+} , and f^{z-} . They yield a representative field at the center of the voxel as follows.

$$\mathbf{E}_{\text{center}} \equiv \frac{f^{x+} + f^{x-}}{2S} \mathbf{i} + \frac{f^{y+} + f^{y-}}{2S} \mathbf{j} + \frac{f^{z+} + f^{z-}}{2S} \mathbf{k} \quad (4)$$

where S is the area of an element. It was shown that the $\mathbf{E}_{\text{center}}$ represented induced fields with good accuracy except for those in the vicinity of the boundary⁽²⁾. However, sharp fluctuation of the $\mathbf{E}_{\text{center}}$ in the vicinity of the boundary was observed owing to the lack of exact information of the boundary shape. This is a common problem shared by field calculation methods based on voxel models. Here, we add a smoothing process of the $\mathbf{E}_{\text{center}}$ near boundary region. We pay attention to both a voxel V_0 that has conductivity σ_0 and field $\mathbf{E}_0^{\text{center}}$ and its twenty-six ($3 \times 3 \times 3 - 1$) neighboring voxels $V_1 \sim V_{26}$ that have $\sigma_1 \sim \sigma_{26}$ and $\mathbf{E}_1^{\text{center}} \sim \mathbf{E}_{26}^{\text{center}}$. When all $\sigma_i (i = 1 \sim 26)$ are equal to σ_0 , which implies V_0 locates far from boundaries, no smoothing process is carried out. When more than one $\sigma_i (i = 1 \sim 26)$ is not equal to σ_0 , we replace the $\mathbf{E}_i^{\text{center}}$ by the average of the fields set $\{\mathbf{E}_i^{\text{center}}, i = 0 \sim 26 \text{ and } \sigma_i = \sigma_0\}$. We call this process as smoothing near boundaries.

4. NICT Taro Model and Applied Fields

Taro, a Japanese adult male whole body model, was developed by NICT, Kitasato Univ., Keio Univ., and Tokyo Metropolitan University⁽³⁾. He consists of 7,977,906 voxels except the air region around him, and the cubic voxel size is 2mm. Taro occupies the region of $0 \sim 516$ mm in x , $0 \sim 270$ mm in y , and $0 \sim 1732$ mm in z . The gravity center is about (251.5, 122.5, 959.5) in mm. The tissues, conductivities, and the numbers of voxels are listed in Table 1. We can determine the locations of surface elements based on these data, and the number of the surface elements becomes 3,921,953.

We apply 50Hz homogeneous fields and 50Hz magnetic dipole fields to Taro. The applied homogeneous fields are $B\mathbf{i}$ (left-to-right), $B\mathbf{j}$ (back-to-front), and $B\mathbf{k}$ (foot-to-head), where $B=1\mu\text{T}$ (peak). The magnetic dipole source fields are by $M\mathbf{i}$, $M\mathbf{j}$, and $M\mathbf{k}$, where $M=0.5\pi \mu\text{Wb} \cdot \text{m}$ (peak), which are located at (251.5, 122.5+500,

Table 2: Calculation times, iterations, current densities (μAm^{-2}), and electric field strength (μVm^{-1}) in the whole body of Taro.

Case	Time	Iterations	Before smoothing near boundaries				After smoothing near boundaries				
			J_{\max}	J_{ave}	E_{\max}	E_{ave}	J_{\max}	J_{ave}	E_{\max}	E_{ave}	
Uniform fields	B_i (left-to-right)	6h 23min.	85	74.9	1.92	199	11.2	40.6	1.91	143	11.1
	B_j (back-to-front)	5h 53min.	78	48.1	2.41	371	14.7	33.9	2.40	220	14.5
	B_k (foot-to-head)	6h 06min.	81	40.9	1.56	188	9.90	28.6	1.55	166	9.79
Dipole source fields	M_i	6h 16min.	82	43.5	1.07	209	6.46	27.3	1.06	135	6.38
	M_j	6h 42min.	88	73.4	2.22	656	14.1	47.4	2.20	315	14.0
	M_k	6h 33min.	86	43.6	1.44	295	8.98	31.3	1.43	172	8.88

1398.5). It should be noted that, when the Mk is located at $(0, 0, 0)$, it generates $1\mu\text{T}$ magnetic field at $(x, y, 0)$, where $\sqrt{x^2 + y^2}=500\text{mm}$, and it generates $2\mu\text{T}$ magnetic field at $(0, 0, z)$, where $|z|=500\text{mm}$.

5. Calculated Results

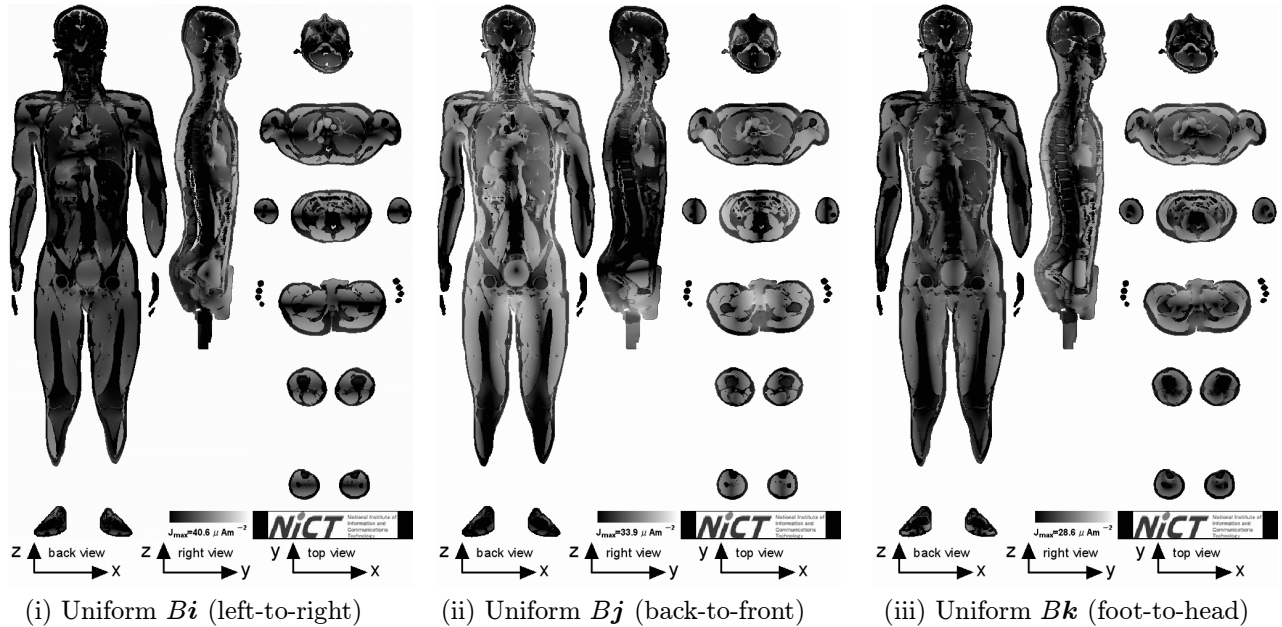
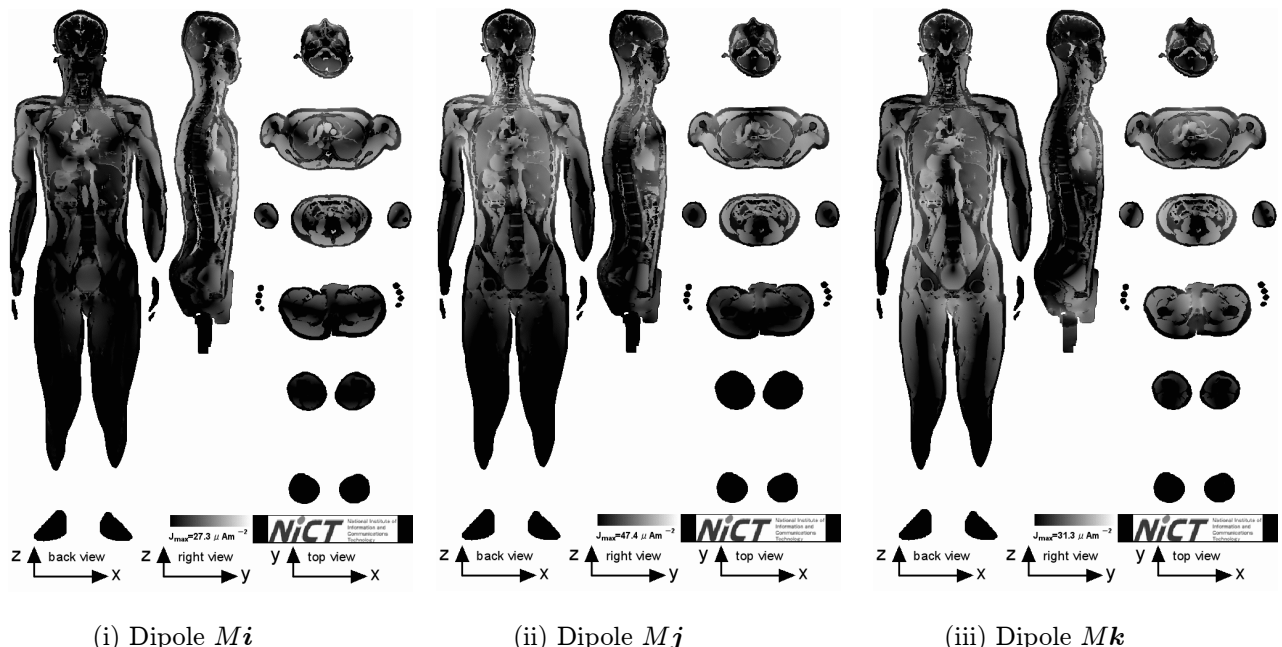
Table 2 show the calculation times, iterations, current densities J (μAm^{-2}), and electric field strength E (μVm^{-1}) in the whole body of Taro. The script ‘max’ and ‘ave’ stand for maximum and average value, respectively. It is shown that the calculation times are about six to seven hours in all cases. The significant part of the calculation time is occupied by the time required by the iterative solver. Therefore, the calculation time is almost proportional to the number of iterations, which is required to reduce the relative residual norms less than 10^{-7} . The statistical values listed in the table are qualitatively similar to those in [4]. Figs. 1 and 2 show the calculated current density distributions of these six cases, where a coronal slice is at $y=137\text{mm}$, a sagittal slice is at $x=259\text{mm}$, and horizontal slices are at $z = 1599, 1325, 1051, 777, 503$, and 229mm . The gradation from black to white corresponds to the current density from $\log_{10}(J_{\max} \times 0.01)$ to $\log_{10}(J_{\max})$. Figs. 3 and 4 show z -layer-maximum, z -layer-averaged, tissue-maximum, and tissue-averaged current densities (μAm^{-2}) before and after the smoothing near boundaries. When we compare these results, we should be aware that the field by Mj is $2\mu\text{T}$ and the others are $1\mu\text{T}$ at $(251.5, 122.5, 1398.5)$. In Figs. 3 and 4, it is clearly observed that the smoothing process almost always reduces the maximum value, and it doesn’t change the average value significantly. It is also observed that the current distributions induced by the dipole source fields are limited to the region nearby the dipole source, which explains the reduction of the whole-body-average values by the dipole source fields in the Table 2.

6. Conclusion

The performance of FMM(fast multipole method)-SCM(surface charge simulation method) for voxel data is successfully confirmed by calculating the induced currents in a Japanese adult male voxel model ‘Taro’ licensed by NICT. It is composed of 7,977,906, $2\text{mm} \times 2\text{mm} \times 2\text{mm}$ voxels, and is exposed to three kinds of homogeneous fields and three kinds of magnetic dipole source fields. It is shown that the required calculation time is about six to seven hours on a 32bit, 3GHz, 2G-RAM, single Pentium IV, Windows PC. These results demonstrate high-speed, high-capacity, and high-stability performance of the method.

REFERENCES

- (1) L. Greengard, V. Rokhlin, “A new version of the fast multipole method for the Laplace equation in three dimensions,” *Acta Numerica*, **6**, 229–269, 1997
- (2) S. Hamada, T. Kobayashi, “Analysis of electric field induced by ELF magnetic field utilizing fast-multipole surface-charge-simulation method for voxel data,” *IEEJ Trans. FM*, **126**, No. 5, 355–362, 2006
- (3) T. Nagaoka, S. Watanabe, K. Sakurai, E. Kunieda, S. Watanabe, M. Taki, and Y. Yamanaka, “Development of realistic high-resolution whole-body voxel models of Japanese adult males and females of average height and weight, and application of models to radio-frequency electromagnetic-field dosimetry,” *Phys. Med. Biol.* **49**, 1–15, 2004
- (4) T. W. Dawson, K. Caputa, and M. A. Stuchly, “Influence of human model resolution on computed currents induced in organs by 60-Hz magnetic fields,” *Bioelectromagnetics*, **18**, 478–490, 1997
- (5) M. H. Gutknecht, “Variants of Bi-CGSTAB for matrices with complex spectrum,” *SIAM J. Sci. Comput.*, **14**, 1020–1033, 1993

Figure 1: Current density distributions induced by $1\mu\text{T}(\text{peak})$, 50 Hz, uniform magnetic fields.Figure 2: Current density distributions induced by $0.5\pi \mu\text{Wb}\cdot\text{m}(\text{peak})$, 50 Hz dipole magnetic field sources.

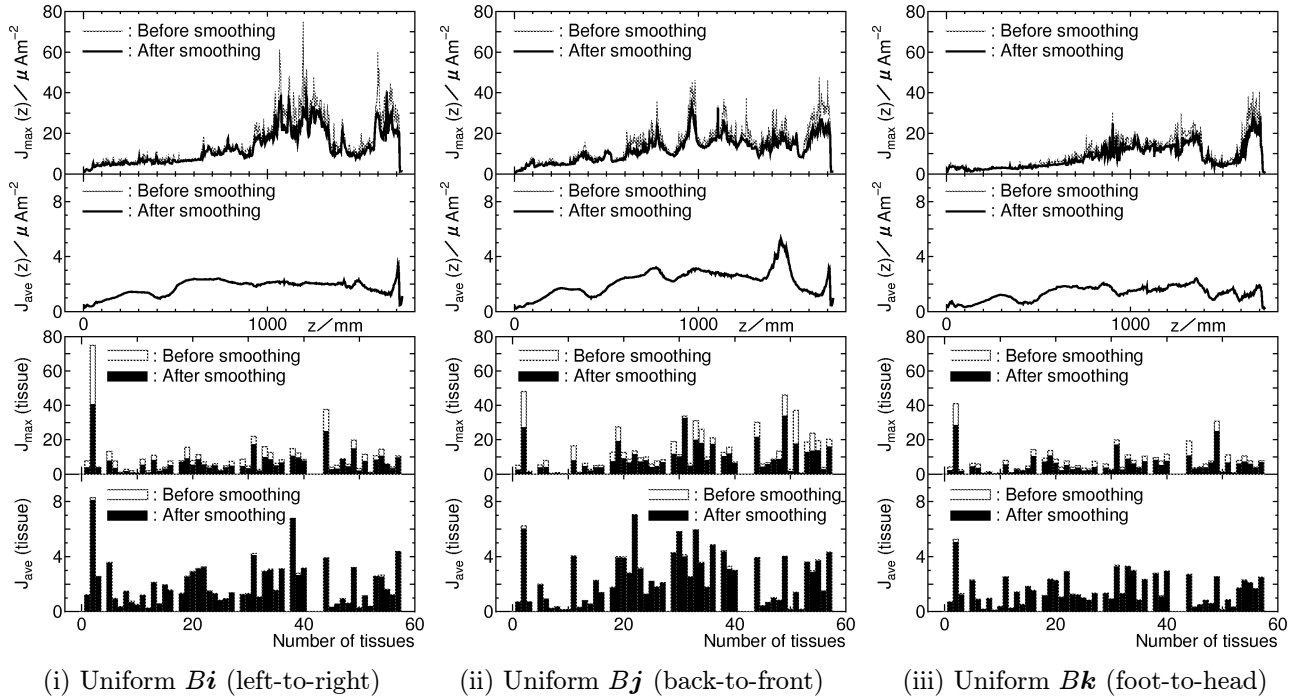


Figure 3: Layer-maximum, layer-averaged, tissue-maximum, and tissue-averaged current densities (μAm^{-2}) induced by $1\mu\text{T}(\text{peak})$, 50 Hz, uniform magnetic fields.

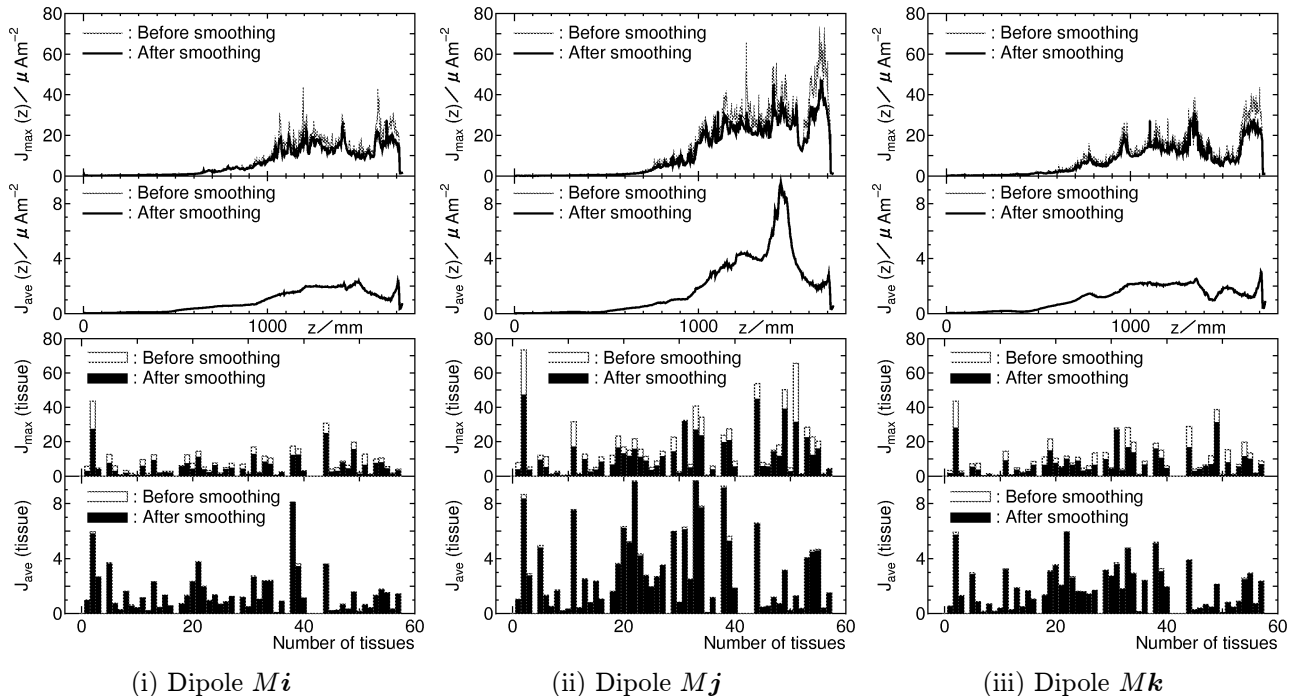


Figure 4: Layer-maximum, layer-averaged, tissue-maximum, and tissue-averaged current densities (μAm^{-2}) induced by $0.5\pi \mu\text{Wb}\cdot\text{m}(\text{peak})$, 50 Hz dipole magnetic field sources.

Electric and Magnetic Field Distributions along High Voltage Power Lines

Qing Wei Pan and Visal Kev

Manukau Institute of Technology, Department of Electrical & Computer Engineering, New Zealand

Abstract

A comprehensive measurement of electric and magnetic field distributions along 50 Hz high voltage and high current overhead transmission lines in a suburban residential area is presented. The field perturbations by different objects in the vicinity are investigated. Shielding methods are discussed.

1. Introduction

It has long been a concerning issue – that extremely-low-frequency electromagnetic-fields (ELF/EMF) generated by high voltage power transmission lines may be harmful to our health, perhaps even initiating cancer. However, solid evidence has yet to be found, although there are quite a number of weakly proven claims published. For those who are living underneath these unsightly lines, it is worthwhile to have a clear picture about the field distributions and their perturbations. The International Commission on Non-Ionized Radiation Protection (ICNIRP) advises that if exposures to the public of $E \leq 5 \text{ kV/m}$ and $B \leq 100 \mu\text{T}$ (at 50 Hz), then the basic restriction (a limit of 2 mA/m^2 on the current induced in the brain and central nervous system) will not be exceeded. However, some countries (e.g. Switzerland) have imposed, or are going to impose, more stringent limits (1 kV/m and $1 \mu\text{T}$). Effective ways for reducing EMF levels should be used in buildings located right under high voltage power lines in order to minimize residents' exposure dosage.

2. Body Fields and Currents

Electric fields close to the ground are nearly vertical. The current density in a semi-conducting medium has two components:

$$J = J_c + J_d = \mathbf{s}E + j\mathbf{w}\mathbf{e}E \quad (1)$$

where J_c is the conduction current density,
and J_d is the capacitive displacement current density.

The displacement current density outside the body (air) is approximately equal to the conduction current density inside the body (semiconductor) since the conductivity of air is virtually nil, i.e.

$$j\mathbf{w}\mathbf{e}_o E_o \gg \mathbf{s}E_i \quad (2)$$

And hence inside the body,

$$E_i \gg j\mathbf{w}\mathbf{e}_o E_o / \mathbf{s} \quad (3)$$

The internal E-field (E_i), which is very low ($< 1 \text{ V/m}$), is directly proportional to the external E-field (E_o), and inversely proportional to the conductivity (σ). Vertical E-field induces electric current flow from the head to ground, according to the conductivity of body parts, e.g. σ of human blood is 0.7 S/m . The short circuit (barefoot) current through a standing human is given approximately by [1]:

$$I_{SC} \gg (9.0 \times 10^{-11}) h^2 E_{af} \quad (4)$$

where h is the height of the human,
and f is the power frequency.

For instance, a 1.7 m tall barefoot person carries about $130 \mu\text{A}$ in a 50 Hz 10 kV/m ambient field (E_a). However, the surface field (E_o), in particular on the head, could be 30 kV/m , because a human torso and its conductivity (including footwear) perturb the field, making the human surface field (in particular, on the head) two times (when wearing $100 \text{ M}\Omega$ plastic shoes [2]) to three times ($15 \text{ k}\Omega$ leather soles) of the surrounding field level. Plastic shoes are analogous to a capacitor between the ground and the human body (a resistor). The thicker the plastic sole ($\epsilon_r \approx 4$), the smaller the capacitance, results in less current flow. Hence, the current flow through a person who wears thick plastic shoes (floating from the ground electrically) would be $2/3$ of the level in the barefoot condition, since the induced internal body field is $2/3$.

Most magnetic field components near the ground are tangential to the surface. The induced eddy current density (J_e) inside a human body is given approximately by:

$$J_e \approx \frac{1}{m_b} B_o \left(\frac{1+j}{\sqrt{2/wm_b s}} \right)^2 \quad (5)$$

Magnetic field induced current is normally less than 25 % of E-field induced current [3]. Unlike E-field, M-field is more penetrating and difficult to shield because it is not affected by non-ferrous materials. However, B (mH) lines change direction at the boundary between two media of different permeability according to the relationship:

$$\frac{\tan \alpha_1}{\tan \alpha_2} = \frac{m_{r1}}{m_{r2}} \quad (6)$$

where α_1 and m_{r1} : angle between B line and normal to boundary, and relative permeability, in medium 1
and α_2 and m_{r2} : angle between B line and normal to boundary, and relative permeability, in medium 2

Take air ($\mu_r=1$) and iron ($\mu_{r2}=7000$) boundary as an example: If α_1 is 0.1° (almost normal to the boundary) in air, α_2 becomes 85° in iron. Internal reflection will trap the M-field inside thick enough iron medium and convert it into eddy current.

3. Measuring Meters and Procedures

The E-field sensor is a square parallel-plate on FR-4 board. The voltage induced between the plates is linearly proportional to the perpendicular electric field. The calibration setup consists of two large circular metal plates which are 1 m apart. During calibration, the sensor was placed at the centre and high voltages were applied across the setup. The dimension of the sensor was set so that the digital voltmeter indicates 1 V rms when the E-field is 1 kV/m rms. The measurements of vertical E-field were made with the sensor held 1.5 m above ground by a PVC stand. The near horizontal M-fields were measured by a handheld M-field meter (Perspective Scientific) which was orientated to get a maximum level reading at every measuring point. Two double-circuit and two single-circuit 220 kV lines leading to Otahuhu sub-station traverse Otara Road where Manukau Institute of Technology is located. Measurements at 5 m intervals were conducted along the road during daytime.

4. Measurement Results

The average load of these lines is about 1 kA which is higher in the evening. It may go up to 1.5 kA during the extreme cold winter days. Figure 1 shows the top views of E and M field distributions along and perpendicular to the lines. The locations of pylons, buildings, and trees are indicated. There is a 2 m high iron fence running along the measured Area 1 and a traffic light steel post under the line. Figure 2 shows the profiles of these E and M field distributions. The line heights were measured from the lower lines to the ground. The effect of ground objects on the fields is significant. Figure 3 depicts the plane view of measured E and M fields inside a house. The house has a galvanized corrugated steel roof and wooden walls. The adjacent garage has galvanized sheet steel roof and walls. 2.5 kV/m E-field and 2.6 μ T H-field were measured under the line and 20 m away from the house. Inside the house, the E-field was reduced to 100 V/m, but the M-field was lowered to just 2 μ T. Inside the garage, the E-field stayed the same at 100 V/m and the M-field was reduced 50 % to 1.3 μ T.

5. Characteristics Summary

- Maximum E and M fields occur under the edge of a line.
- Maximum E and M fields occur at the droop of a line.
- At the base of a pylon, E and M field levels are much lower.
- A double-circuit line generates 50 % less E and M fields than single-circuit line.
- Iron objects (e.g. fence and post) reduce near ground E and M fields significantly.
- Building materials (e.g. concrete, brick and wood) and trees lower the E-field but not the M-field.
- Iron roof shields 95 % of the E-field but only a fraction of the M-field from entering the house.
- Thin iron walls shield 50 % of the M-field (the thicker the iron, the better the shielding).
- Plastic shoes or insulated floors reduce E-field induced vertical current flow through the human body.

6. Conclusion

A tall metal object (e.g. pylon) acts as an E-field umbrella which shields the space around it near the ground. An earth wire is normally hung above a power transmission line for lightning protection. It might be a good idea to have another earthed wire or wires hung below the live lines for shielding E-fields from reaching people living underneath. But, how much extra power loss would there be, and how much public reassurance would derive? Houses close to power lines should have ferrous material plated walls for M-field shielding ($< 1\mu\text{T}$).

FIGURES

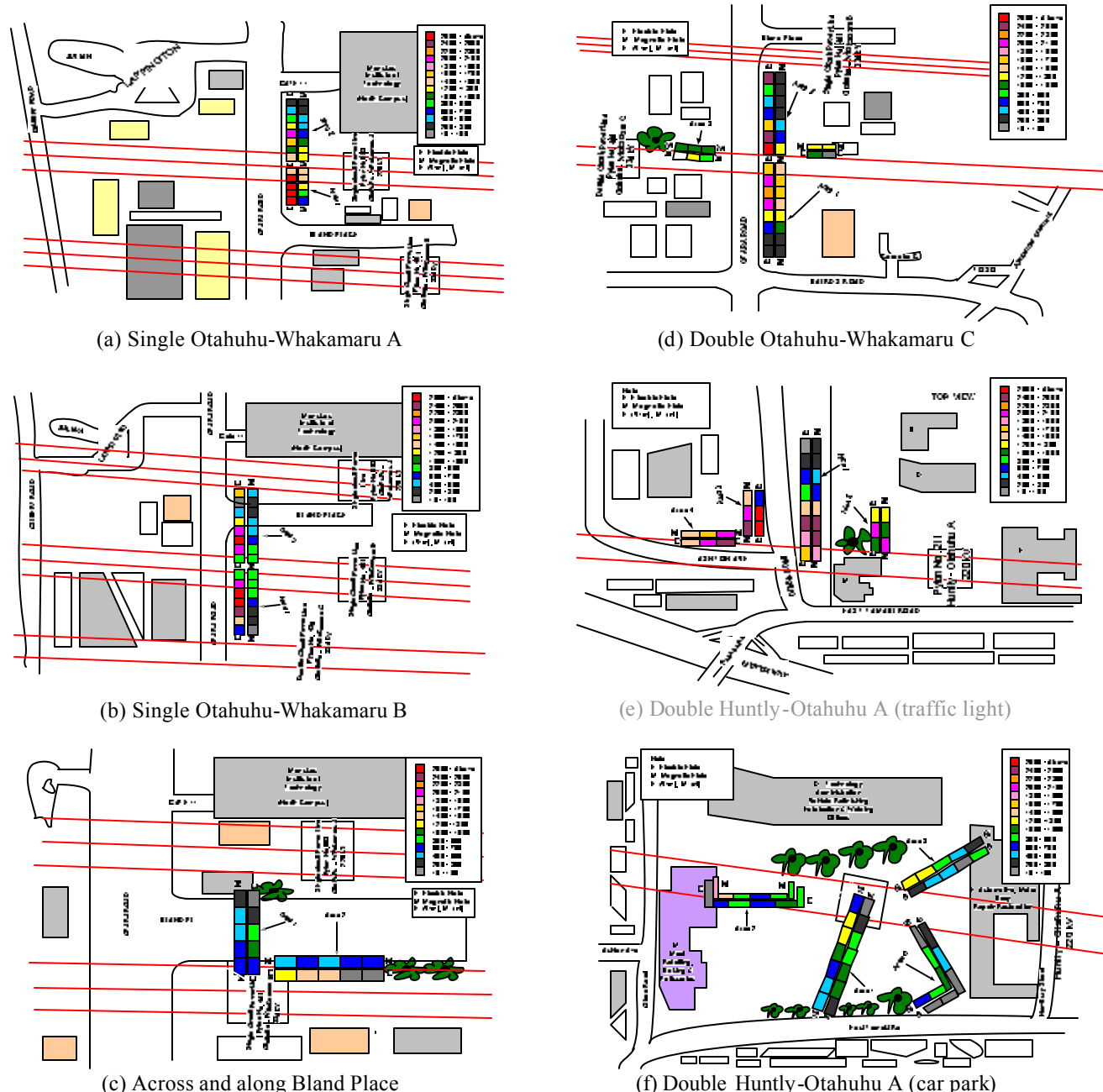
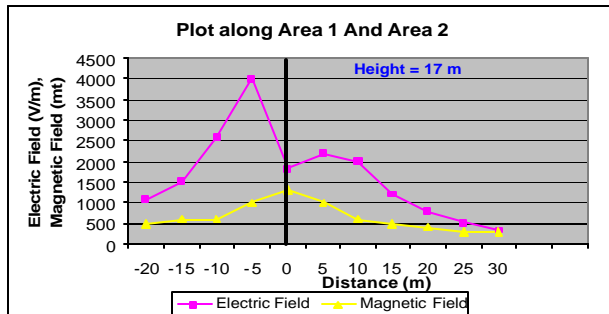
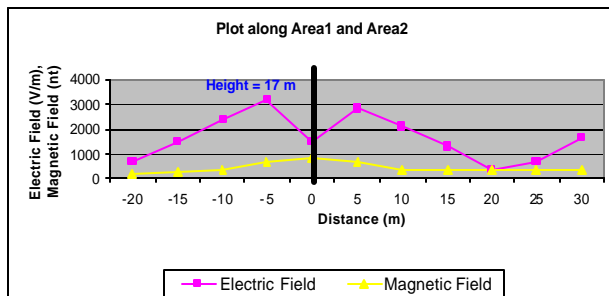


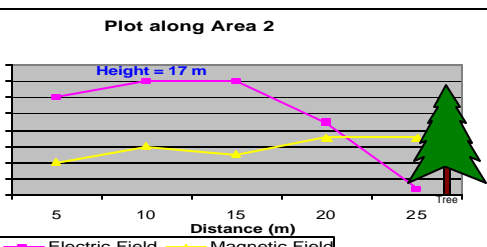
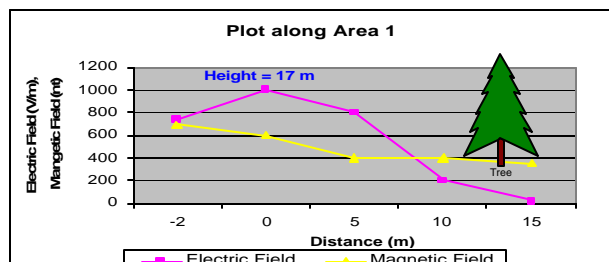
Fig. 1 Top view of E and M field distributions (scale: length of colour bar = 5 m)



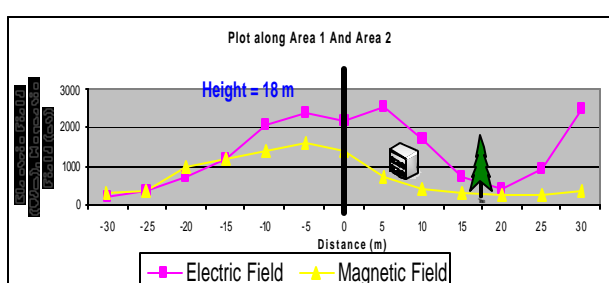
(a) Single Otahuhu-Whakamaru A



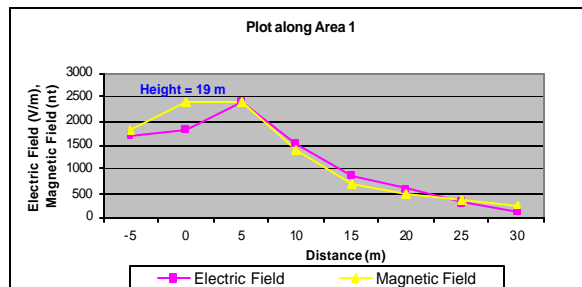
(b) Single Otahuhu-Whakamaru B



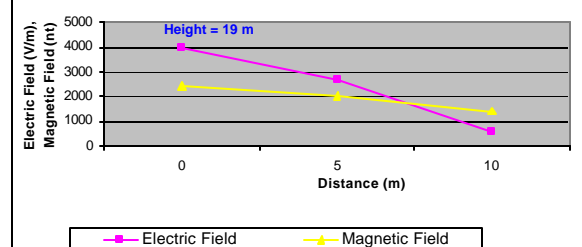
(c) Across and along Bland Place



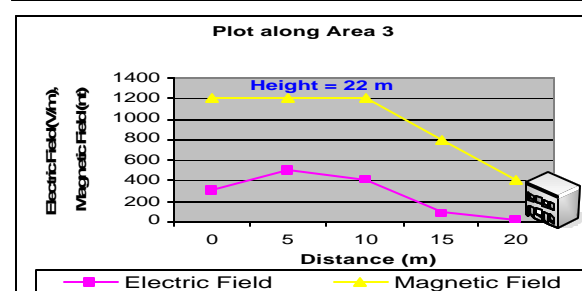
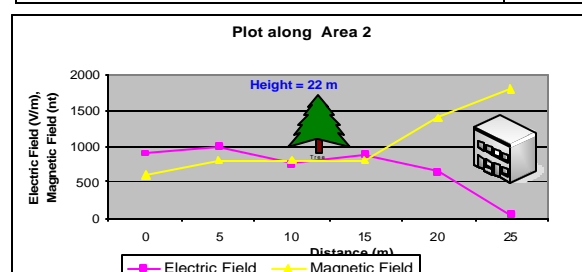
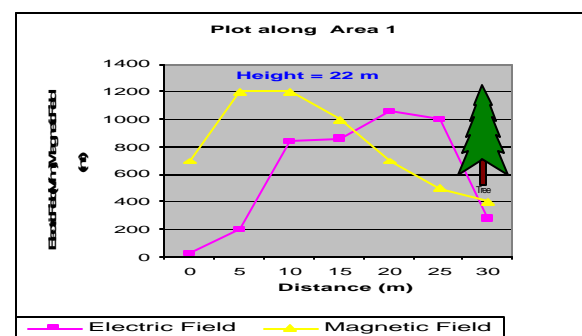
(d) Double Otahuhu-Whakamaru C



(b) Plot along Area 3



(e) Double Huntly-Otahuhu A (traffic light)



(f) Double Huntly-Otahuhu A (car park)

Fig.2 Profiles of electric and magnetic fields

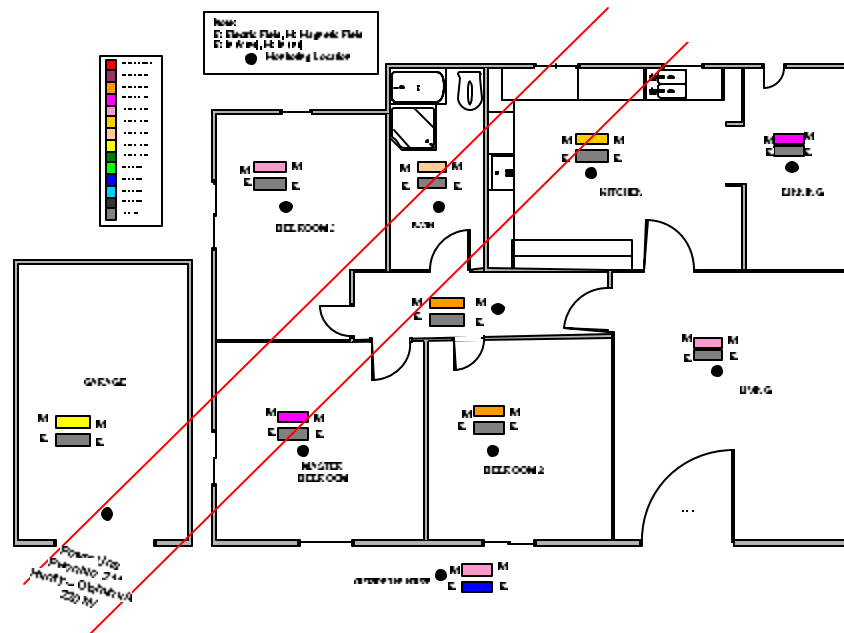


Fig.3 Electric and magnetic field levels inside a house right under a double circuit line

REFERENCES

1. Deno, D. W., "Calculating electrostatic effects of overhead transmission lines", *IEEE Trans. Power Appl. Syst.*, PAS-93, 1458-1471, 1974.
2. Deno, D. W., "Currents induced in the human body by high-voltage transmission line electric field – measurement and calculation of distribution and dose", *IEEE Trans. Power Appl. Syst.*, PAS-96, 1517-1527, 1977.
3. IPCS, *Environmental Health Criteria 35: Extremely Low Frequency (ELF) Fields*, WHO, 1992.

2-10 GHz-Range Surface Acoustic Wave Filters Using Zero-TCF • Super High Coupling Substrates

Kazuhiko Yamanouchi and Yusuke Satoh

Tohoku Institute of Technology, Sendai, Japan.

Corresponding e-mail:yamasaw@tohtech.ac.jp

Abstract — We show wide band ladder type SAW resonator filters using high coupling $\text{SiO}_2/5^\circ\text{Y-X LiNbO}_3$ with Zero Temperature Coefficients of Frequency (TCF). The experimental results showed below 1.6dB insertion loss at 2GHz range and 2dB insertion loss at 10GHz range with wide band and zero TCF. We also proposed a new single phase unidirectional transducer (UDT) with about $\lambda/4$ electrode width of the best transducer efficiency. The new UDTs are obtained by IDT on the very thin dielectric grating with $\lambda/8$ shifts. The experimental results showed the 0.9dB insertion loss at 2GHz range.

1. INTRODUCTION

The development of GHz-band surface acoustic wave (SAW) devices has become necessary because of the increasing volume of information and communication media, such as mobile telephone, satellite broadcasting, spread spectrum and UWB communications. Especially, zero TCF, low loss and, ultra wide band with an ultra-small size and high performance are required for mobile and UWB communication systems.

The resonator-type SAW filters having lattice or ladder structures similar to the ceramic or crystal filter have been reported by Tseng[1] and Sato[2]. The substrates of ladder type filters have generally used the $36^\circ\text{Y-X LiTaO}_3$ [3],[4]. The $36^\circ\text{Y-X LiTaO}_3$ substrates have some defects of small k^2 and poor TCF(-35ppm/ $^\circ\text{C}$).

We also proposed a new single phase unidirectional transducer (UDT)[5] with about $\lambda/4$ electrode width of the best transducer efficiency. The new UDTs are obtained by IDT on the very thin dielectric grating or the very thin dielectric grating with $\lambda/8$ shifts. The electromechanical couplings (k^2) of electrodes on SiO_2 films decrease rapidly for film thickness. Therefore the good properties of UDT are obtained for the very thin thickness of SiO_2 grating (about 0.03 μm at 2GHz with electrode thickness of Al of 0.07 μm).

In this paper, we showed the theoretical results of wide band ladder type SAW resonator filters using high coupling $\text{SiO}_2/5^\circ\text{Y-X LiNbO}_3$ [6][7] with Zero TCF. We show the experimental results of the ladder type filters at 2-10GHz-range.

We also describe the theoretical and experimental results of wide band and very low loss UDT filters at 2GHz-range.

2. $\text{SiO}_2/\text{Y-X LiNbO}_3$ SUBSTRATE WITH HIGH COUPLING OF k^2 AND ZERO TCF.

We developed SiO_2 /rotated Y-cut, X-propagating LiNbO_3 leaky SAW Substrates[7] with large k^2 (over 0.2) and zero TCF at a small thickness of SiO_2 compared with that of other substrates and zero propagation attenuation in the case of metallized surface. The theoretical and experimental results of TCFs are shown in Fig.1 using $\text{SiO}_2/5^\circ\text{Y-X LiNbO}_3$. The k^2 of 0.22 and zero TCF at $H/\lambda = 0.2$ are obtained.

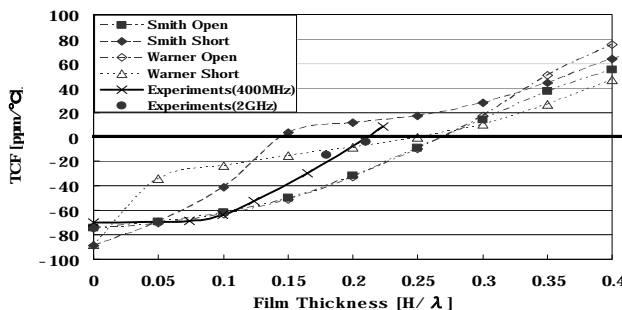


Fig.1 Theoretical and Experimental TCF vs H/λ plot of SiO_2 in the case of $\text{SiO}_2/5^\circ\text{Y-X LiNbO}_3$ ($k^2=0.22$)

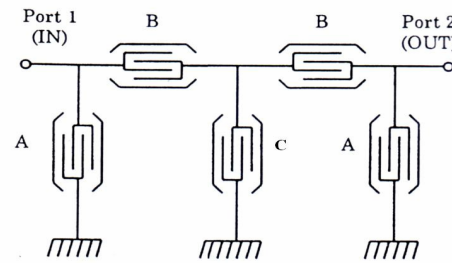


Fig.2 Configuration of a ladder-type filter

3. CALCULATION AND EXPERIMENTAL RESULTS OF LADDER TYPE SAW FILTERS USING $\text{SiO}_2/\text{Y-X LiNbO}_3$ SUBSTRATES AT 2GHZ RANGE

3.1 Calculation results

Figure 2 shows the configuration of a ladder-type filter using conventional IDT type SAW resonators without a reflector. The parameters are given in Table I . The frequency characteristics of a ladder-type filter under the consideration of velocity dispersions are shown in Fig.3. The wide band characteristics of 19 % with 0.5dB insertion loss are obtained with zero TCF.

3-2. EXPERIMENTAL RESULTS OF LADDER TYPE SAW FILTERS AT 2GHZ-RANGE

One of experimental results of resonators without reflectors using $\text{SiO}_2/5^\circ\text{Y-X LiNbO}_3$ is shown in Fig.4. The results show the frequency properties with good resonant and anti-resonant admittance with almost zero TCF (TCF=-6ppm/ $^\circ\text{C}$, SiO_2 thickness of 1.8 μm , $H/\lambda=0.22$, Al thickness=0.12 μm).

Table I Resonator filter parameter at 2GHz-range ($k^2=0.22$, $TCF=0.0ppm/^{\circ}C$)

Resonator	C type		
	①	②	③
Wavelength [μm]	2	2.313	2.313
Aperture [λ]	9.7	19.4	9.7
IDT pair number [N]	60.5	60.5	60.5

The ladder type filters with the parameter of Table I are fabricated on 5°Y-X LiNbO₃ substrates. Electrode widths are about 0.5μm and wavelengths are 2μm, respectively.

Figure 5 shows the experimental frequency characteristics of a ladder-type filter without SiO₂ thin films at 2GHz-Range. The electrode thickness is 0.07μm. Minimum insertion loss is about 2.3dB. The sharp cut-off characteristics are not obtained because of low Q-value due to the leaky attenuation. The TCF is about -75ppm/^{\circ}C. On the other hand, Fig.6 shows the frequency characteristics of a ladder-type filter with sputtered SiO₂ thin films of 0.42μm ($H/\lambda=0.21$). Minimum insertion loss is about 1.9dB (1.6dB at matching conditions). The sharp cut-off characteristics are obtained because of the high Q-value without the leaky attenuation. Almost zero TCF is obtained (the TCF= -3.5ppm/^{\circ}C).

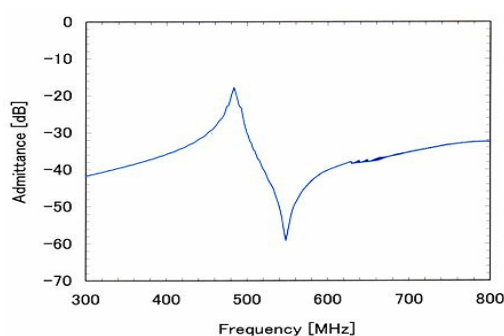


Fig.4 Experimental results of resonator without reflector
($TCF=-6ppm/^{\circ}C$, SiO_2 thickness=1.8 μ m,
 $H/\lambda=0.22$, Al thickness=0.12 μ m)

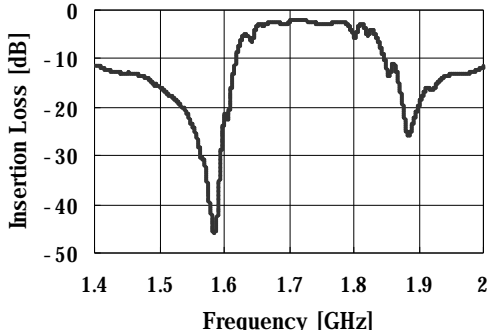


Fig.6 Experimental frequency response of a ladder-type filter with thin film of SiO_2 ($H/\lambda=0.21$, Minimum insertion loss=1.93dB, $TCF=-3ppm/^{\circ}C$)

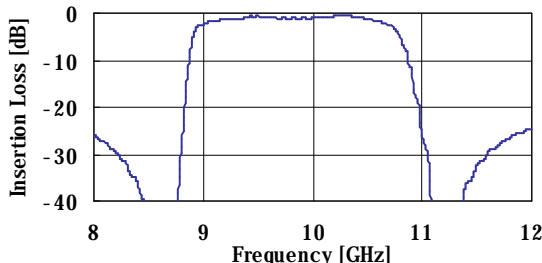


Fig.8 Calculated frequency response of a ladder type filters at 10GHz under the propagation attenuation ($0.08dB/\lambda$) and IDT resistive loss(100Ω /one electrode)

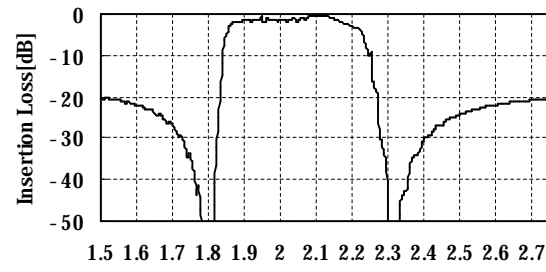


Fig.3 Calculated frequency response of a ladder-type filter under the velocity dispersion

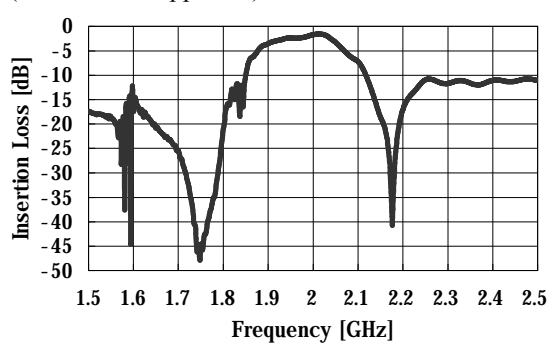


Fig.5 Experimental frequency response of a ladder-type filter without thin film of SiO_2 ($H/\lambda=0$, Minimum insertion loss=2.3dB, $TCF=-75ppm/^{\circ}C$)

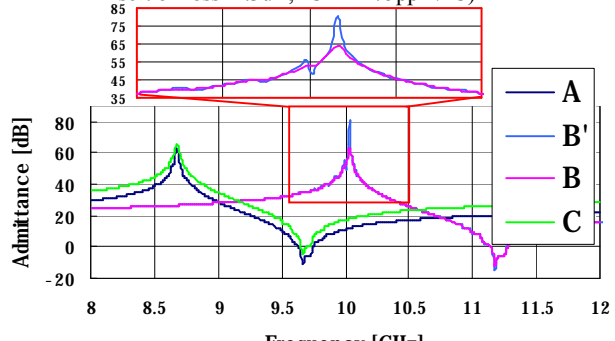


Fig.7 Calculated frequency response of a resonator at 10GHz under the propagation attenuation ($0.08dB/\lambda$) and IDT resistive loss(100Ω /one electrode) (A,B,C) and without loss and attenuation (B')

Table II Parameters of the ladder type filters in 10GHz

	Pair number	Aperture	Wavelength
Resonator A	90.5	9λ	463nm
Resonator B	90.5	9λ	400nm
Resonator C	90.5	18λ	463nm

4 Calculation and Experimental Results of Ladder Type SAW filters Using SiO₂/Y-X LiNbO₃ Substrates at 5GHz~10GHz

4.1 Calculation results

We calculate the frequency response of ladder type filter as shown in Fig.2.

Figure 7 shows the 10GHz-range SAW resonator frequency response under the consideration of resistive loss of interdigital transducers and propagation attenuation on 5°Y-X LiNbO₃ substrate. Figure 8 shows the frequency response of the filter with the parameter given in Table II. The wide band characteristics of 20 % with 0.5dB insertion loss are obtained with zero TCF.

4.2. Fabrication Technology of Nano-meter electrodes and Experimental Results of Resonators and Ladder Type SAW filters at 5 GHz and 10 GHz-Range

4.2.1. Nano-meter lithography technology

SAW device can be fabricated by applying integrated circuit fabrication techniques using lithographic processes. Many types of the fine lithography are proposed. The photo-litho graphic techniques using the Hg-sourced G-line/H-line series to I-systems (wavelength of 300 nm to 450 nm) have been developed and they are usually used in the modern SAW device fabrication. A more developed method uses shorter wavelength ray sources, such as the excimer-based KrF (248 nm), ArF (193 nm) and F₂ excimer laser (157 nm) systems. In Ultra-Large-Scale-Integration (ULSI) technology, the techniques of the 100nm or better process using ArF Laser (Step-and-repeat Scanning System, NSR-S308F, by Nikon) with a high throughput and mass-production have developed.

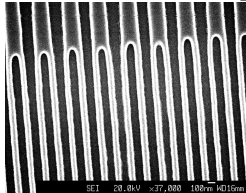


Fig.9 Fabricated resist pattern for 10GHz-range resonator
(200nm periods)

Now the next interest is below 50nm technology. Especially, in the 50nm process, there are several selections, such as electron beam lithography, X-ray lithography using Synchrotron Orbital Radiation (SOR) and F₂ excimer laser (157nm) lithography.

In this paper, the Direct Writing Electron Beam (EB) techniques using the lift-off process for fabricating the 100nm IDT electrodes are applied. The lift-off process does not cause the mechanical damage on the surface in contrast to the dry etching techniques.

The coating of positive EB resist of thickness of 30nm for 10GHz-resonator on Y-X LiNbO₃ substrate and the resistive solvent (aquaSAVE) are spincoated for avoiding charge-up by the electrons. After EB exposure, development, O₂ plasma ashing, Al evaporation (thickness: 60nm) and lift-off, Al-interdigital electrodes are obtained.

Figure 9 shows the SEM-patterns of 100nm width IDT for 10GHz-filter.

3.2. Experimental Results of 5GHz~10 GHz Range Resonators and Ladder-Type Filters

Figure 10 shows the experimental results of the resonator frequency characteristics with SiO₂ thin films (thickness H/λ=0.1) at 5GHz-Range. The electrode width is 200nm, thickness is 600nm, aperture is 20λ and electrodes pairs are N=90.5, respectively.

The good resonator characteristics without spurious signals are obtained in the case with SiO₂ thin films.

Figure 11 shows the frequency characteristics of the ladder type filters using the above resonators with SiO₂ thin films. The minimum insertion loss is about 2.9dB with matching conditions.

Figure 12 shows the electrode configuration of the ladder type filter at 5 GHz-range.

Figure 13 shows the experimental frequency characteristics of the ladder type filter without SiO₂ thin films. The spurious response is observed at the low frequency region below pass band. The minimum insertion loss is about 2.9dB with matching conditions.

Figure 14 shows the experimental frequency characteristics of the ladder type filter with SiO₂ thin films (H/λ=0.1) at 5GHz-Range. The spurious response is not observed at low frequency region below pass band. The minimum insertion loss is about 3.5dB with matching conditions.

Figure 15 shows the experimental results of the resonator frequency characteristics without SiO₂ thin films at 10GHz-Range. The electrode width is 100nm, thickness is 300nm, aperture is 20λ, N=90.5, respectively.

The good resonator characteristics without spurious signals are obtained in without SiO₂ thin films.

Figure 16 show the frequency characteristics of the ladder type filters using the above resonators without SiO₂ thin films. The minimum insertion loss is about 2.5dB with matching conditions.

Figure 17 shows the experimental results of the resonator frequency characteristics with SiO₂ thin films (thickness H/λ=0.1) at 10GHz-Range.

The good resonator characteristics without spurious signals are obtained in the case with SiO₂ thin films.

Figure 18 show the frequency characteristics of the ladder type filters using the above resonators with SiO₂ thin films. The minimum insertion loss is about 1.0dB with matching conditions.

We can obtain the lower insertion loss and better frequency characteristics filters by using the optimum

design and the interdigital transducers without defects. We can obtain the conventional RF-front end filters and wide band filters with zero-TCF using $\text{SiO}_2/5^\circ\text{Y-X LiNbO}_3$ substrates at 5GHz~10GHz ranges.

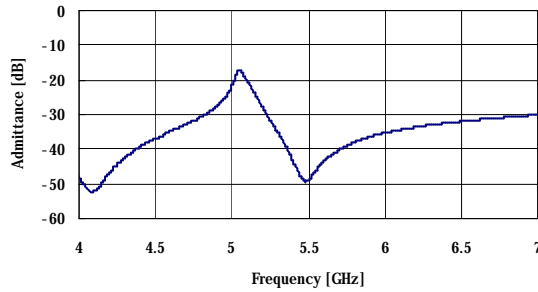


Fig.10 Experimental frequency response of resonators of $N=90.5$ at 5GHz with SiO_2 thin film

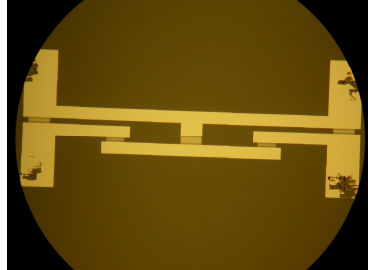


Fig.12 Electrode configuration of the ladder type filter at 5 GHz-range.

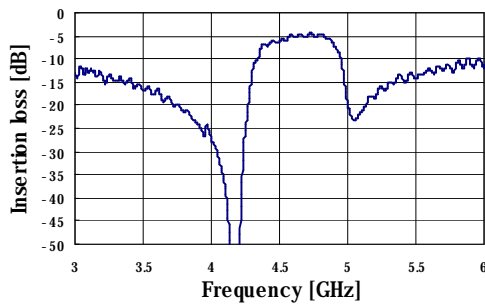


Fig.14 Experimental response of ladder type filter with SiO_2 without matching condition (insertion loss = -4.5dB)

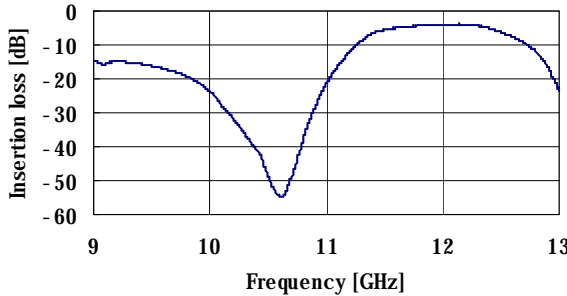


Fig.16 Experimental frequency response of ladder type filter of $N=90.5$ at 10GHz without matching condition, without SiO_2 thin film.

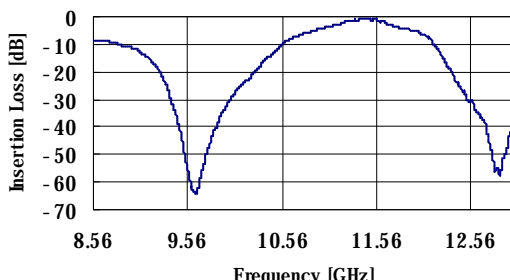


Fig.18 Experimental frequency response of ladder type filter of $N=90.5$ at 10GHz with matching condition, with SiO_2 thin film.

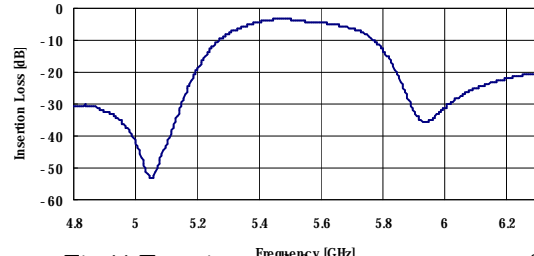


Fig.11 Experimental frequency response of ladder type filter of $N=90.5$ at 5GHz with SiO_2 thin film

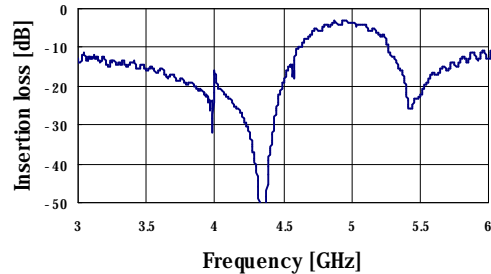


Fig.13 Experimental response of ladder type filter without SiO_2 at matching condition (insertion loss = -2.9dB)

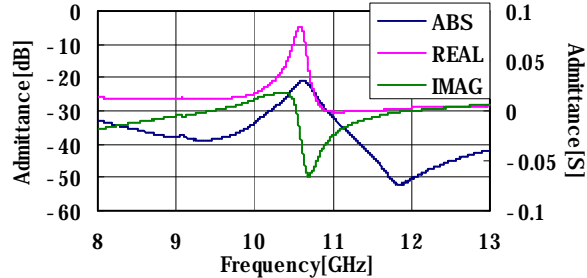


Fig.15 Experimental frequency response of resonator of $N=90.5$ at 10GHz without SiO_2 thin film.

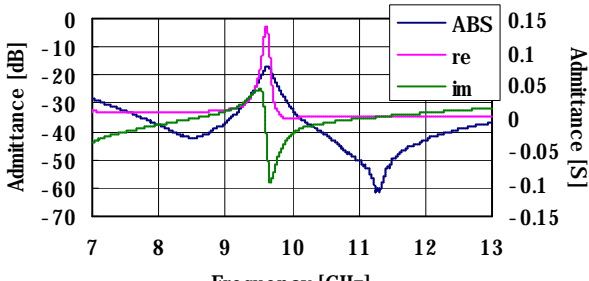


Fig.17 Experimental frequency response of resonator of $N=90.5$ at 10GHz with SiO_2 thin film.

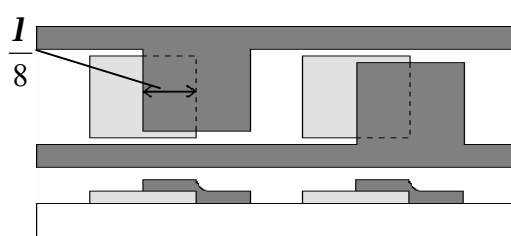


Fig.19. Configuration of UDT with IDT on thin film gratings using the difference of k^2 .

5. UNIDIRECTIONAL TRANSDUCERS WITH IDT ON THIN FILM GRATING USING DIFFERENCE OF k^2

5.1 Calculation results

Figure 19 shows the configuration of EUDT (Electro-mechanical)[5] with IDT on thin film gratings using the difference of k^2 . The very thin dielectric grating layers with $\lambda/4$ periods are fabricated on piezoelectric SAW substrates and then

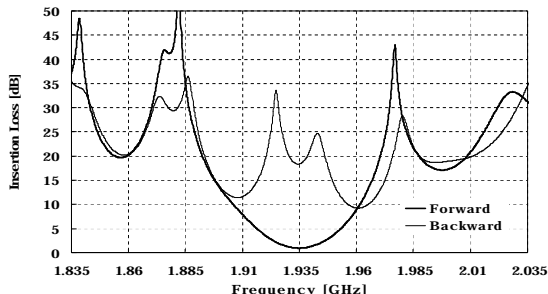


Fig.20. Experimental frequency response of UDT at 2GHz-range(After time domain process and matching condition,Minimum Insertion loss=0.9dB at 1.94GHz)

Table III Expected minimum insertion loss, band width of new UDT and grating SiO_2 thickness with experimental ones

	Insertion Loss [dB]	Grating SiO_2 Thickness [μm]	Maximum Band Width [%]
10MHz	0.2	4	30
100MHz	0.3	0.4	25
500MHz	0.5(Exp 0.7)	0.06	20
1GHz	0.7	0.04	15
2GHz	1.2(Exp 0.9)	0.02	10
5GHz	2	0.008	8
10GHz	3	0.004	6

conventional IDTs are fabricated on grating SAW substrates with the off-set by about $\lambda/8$. The k^2 on SiO_2 are less than that of the electrodes on LiNbO_3 . For example, k^2 is almost 1/2 at $H/\lambda=0.01$ (λ : wavelength of SAW, H: SiO_2 film thickness) on 128°Y-X LiNbO_3 . The difference of k^2 produces the reflected waves on the electrodes. Furthermore, the SiO_2 and Al electrode strips operate as a reflector owing to the mass-loading effects. A larger directivity is obtained due to the reflection coefficients of the differences of k^2 and mass loading effects.

5.2. EXPERIMENTAL RESULTS OF EUDT

The experimental UDT filter configuration is shown in Fig19, using IDT parameters of SiO_2 thickness $H/\lambda=0.01$, $k^2=0.055$, $N=40.5$, 6dB Band width 3% on substrate of 128 °Y-X LiNbO_3 . The electrode width is $0.5\mu\text{m}$, thickness is $0.07\mu\text{m}$, SiO_2 thickness is $0.03\mu\text{m}$, respectively. The stepper with reduction ratio of 1:5 (alignment accuracy of below $0.04\mu\text{m}$) is used for the distance difference of $\lambda/8$ ($0.25\mu\text{m}$) between SiO_2 and IDT electrode.

Figure 20 shows the experimental results at 2GHz-range filters after time domain process and matching. The results show the minimum insertion loss of 0.9dB at 1.94GHz with matching. These values are better than those of ladder type SAW filters. The theoretical and experimental ones are also in good agreement.

5.3. DISCUSSION

The thickness of SiO_2 are about $H/\lambda=0.01 \sim 0.02$ in the above UDTs. Therefore, the values of H show about $0.4\mu\text{m}$ at 100MHz and $0.04\mu\text{m}$ at 1GHz, respectively. These values are almost the same or thinner than those of the IDT electrode thickness. Also, the mask alignment accuracies of the stepper with minimum line width of $0.1\mu\text{m}$ have the $0.016\mu\text{m}$ precision or better. The 5GHz UDT filters and devices of the above UDT can be obtained. Also thick thickness of electrode can use for UDT because a mass-loading reflection contributes to the unidirectionality. Therefore, the electrode resistive loss is reduced at GHz-range. Table III shows the expected insertion loss, band width of new UDT and grating thickness of SiO_2 with experimental ones. The extremely low loss and wide band SAW devices with the wide band range of 10MHz~10GHz can be obtained using the above UDT.

6. CONCLUSION

We show ladder type SAW resonator filters using $\text{SiO}_2/5^\circ\text{Y-X LiNbO}_3$ with Zero TCF. The experimental results showed below 1.6dB insertion loss at 2GHz range and 2dB insertion loss at 10GHz range with a wide band and zero TCF. We are now investigating the ladder-type filters at 5-10GHz-range with lower insertion loss.

We also proposed new types of UDT. The thickness of SiO_2 for the above UDT are almost the same or thinner than those of the IDT electrodes. Also, the mask alignment techniques have the $0.016\mu\text{m}$ precision or better. We have performed the experiments of UDT filters at 2 GHz-range and obtained 0.9dB insertion loss. We are now investigating the UDT filter at 5GHz-range and wide band filters.

REFERENCES

- [1]S. C. Tseng, and G. W. Lynch, "SAW Planar Network," Proc. IEEE Ultrason. Symp., 1974, pp. 282-285
- [2]Y. Satoh, O. Ikata, T. Matsuda, T. Nishihara and T. Miyashita, "Resonator-Type Low-Loss Filters", Proc. Int. Symp. SAW Devices for Mobile Comm. ", Edited by K. Shibayama and K. Yamanouchi, Dec. 1992, pp. 179-185 (ISSN:0914-5621)
- [3]K. Iwahashi, K. Yamanouchi and K. Shibayama, "Temperature dependence of leaky surface wave velocity in $\text{SiO}_2/\text{LiTaO}_3$ structure with high coupling", Proc. Ultrason. Comm. in Inst. Electron. Comm. Eng. Japn. US77-43, (Sept. 1977), pp.37-42, and K. Yamanouchi, K. Iwahashi, and K. Shibayama, "Temperature dependence of Rayleigh waves and piezoelectric leaky surface wave velocity in rotated Y-cut LiTaO_3 and $\text{SiO}_2/\text{LiTaO}_3$ structure", Wave Electronics, 3 (March, 1979), pp.319-333
- [4]K.Nakamura, F. Kazumi and H. Shimizu, "SH-type and Rayleigh-type surface wave in rotated Y-cut LiTaO_3 ", Proc. Ultrason. Comm, in Inst. Electron. Comm. Eng. Japan., US77-42, (Sept. 1977), pp. 31-36, and K. Nakamura, F. Kazumi and H. Shimizu, "SH-type and Rayleigh-type surface wave in rotated Y-cut LiTaO_3 ", 1977 IEEE Ultrason. Symp. Proc. (Oct., 1977), pp. 819-822
- [5] K. Yamanouchi and Y.Sato,"Unidirectional Interdigital Tramsducers Using Grating SAW Substrate and Application to Low Loss Wide Band Filters",Proc.IEEE Ultrason.Symp., 2003,Sept .,Vol.2,pp.2069-2072
- [6]K.Yamanouchi and K. Shibayama, "Propagation and amplification of Rayleigh waves and piezoelectric leaky surface waves in LiNbO_3 ", J. Appl. Phys. 43, Vol. 3, (March, 1972), pp. 856-862
- [7] K.Yamanouchi and T.Ishii, "High Temperature Stable High Electromechanical Coupling Substrates and Application for Surface Acoustic Wave Devices", Proc.IEEE Ultrason.Symp.,Oct.2001, Vol.1, pp.189-192

Plastic Landmine Imaging with Integrated Walled LTSA Handset

Soichi Masuyama and Akira Hirose

Department of Electronic Engineering, The University of Tokyo

7-3-1 Hongo, Bunkyo-ku, Tokyo 113-8656, Japan

soichi@eis.t.u-tokyo.ac.jp , ahirose@ee.t.u-tokyo.ac.jp

Abstract — We proposed, designed and fabricated a handset for plastic landmine imaging. First we designed a narrow width antenna element named a "walled linearly tapered slot antenna" (Walled-LTSA) and integrated them(12×12). The antenna has small aperture size($14\text{mm} \times 28\text{mm}$) and it operates at the wideband frequency range 8-12GHz. The handset is composed of integrated Walled-LTSA elements and RF mechanical switches, which are used to select transmitting and/or receiving antenna(s). We report that regions of metal can and plastic mines are clearly classified by the handset as well as the adaptive nonlinear signal processing performed by the complex-valued self-organizing map (CSOM).

1 Introduction

Ground penetrating radar (GPR) technology is expected to become a powerful technique in detecting nonmetallic landmines [1] [2] [3]. However, it is still difficult to detect plastic landmines. This is due to the small size of the plastic mines, low reflectance of plastics and the influence of ground surface. We previously proposed a multiple-frequency radar imaging system using a complex-valued self-organizing map (CSOM) to visualize plastic mines[4][5][6]. It observes complex amplitude (amplitude and phase) of the reflection in both the spatial and frequency domains. The three dimensional data (two spatial and one frequency dimensions) are fed to a CSOM[7][8] so that we obtain a segmented image to indicate landmines. However, our previous system takes long time for observation because a pair of transmitting and receiving antennas is mechanically scanned over the ground surface. In this paper, we propose and design a wideband and compact walled linearly tapered slot antenna (Walled LTSA) and integrate them. In addition, the RF mechanical switches are used to select one or two antennas from 144 elemental array of antennas as the transmitting and/or receiving antenna. We report that we can find plastic landmines using this handset with a reduced observation time.

2 Handset for landmine detection

The handset for mine detection comprises two parts, namely, the integrated antenna and the switching circuit. The integrated antenna is composed of 144 Walled-LTSA elements (12×12 in space) which are newly designed. The switching circuit is to select one or two antennas as transmitting and/or receiving antenna(s). We fabricated the integrated antenna and the handset.

2.1 Design and Integration of Walled LTSA

Our radar system needs small aperture-sized antennas for integration. Furthermore, antennas should be wideband and compact. We proposed and designed Walled LTSAAs. LTSA is a wideband, compact microstrip antenna[9]. However, we found in numerical analysis that when the width of LTSA gets narrower, return loss increases to around -5dB at 8-12GHz. To realize less return loss with narrow width of LTSA, we introduced a metal-walled structure.

Fig.1 shows the structure of a Walled LTSA element. It is an LTSA surrounded on its four sides by aluminium plates. Intervals of the aluminium plate is determined such as to realize a single-mode (TE_{10}) operation in the 8-12GHz frequency band. The aperture size of the Walled LTSA is determined to be $14\text{mm} \times 28\text{mm}$, resulting in the whole aperture size of approximately $18\text{cm} \times 36\text{cm}$ for the 12×12 elements.

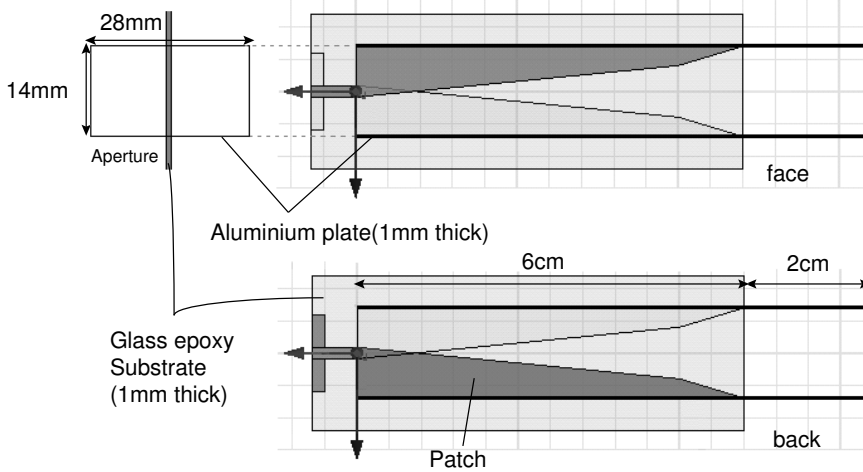


Figure 1: Structure of Walled LTSA

We measured return loss characteristics of two of the 144 Walled-LTSA elements and compared them with the results in numerical analysis(Fig2). Directivity of the Walled-LTSA element was also analyzed. From the figure, return loss of the Walled LTSA is found to be less than -10dB in the 8-18GHz frequency band. The -3dB beamwidth was 100deg(E-plane), 50deg(H-plane) at 8GHz.

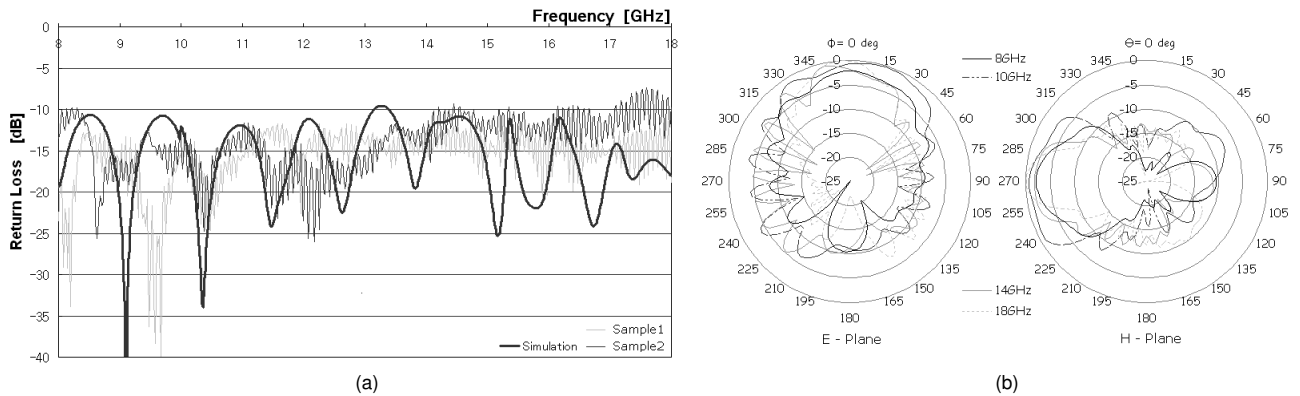


Figure 2: (a)Measured and simulated return loss and (b)Calculated E-plane, H-plane beam pattern of Walled LTSA

2.2 Switching circuit

Switching circuit is composed of three types of RF mechanical switches (12pin-type \times 12, 6pin-type \times 2, transfer-type \times 6), i.e., 20 switches in total. Switching circuit selects one or two of the 144 Walled-LTSA elements to be connected to ports of a vector network analyzer (VNA) which measures complex amplitude. Furthermore, we used two digital input/output boards to control RF switches by note PC. Fig.3 shows the construction of the fabricated handset. The whole size is about 20 \times 40 \times 90 cm.

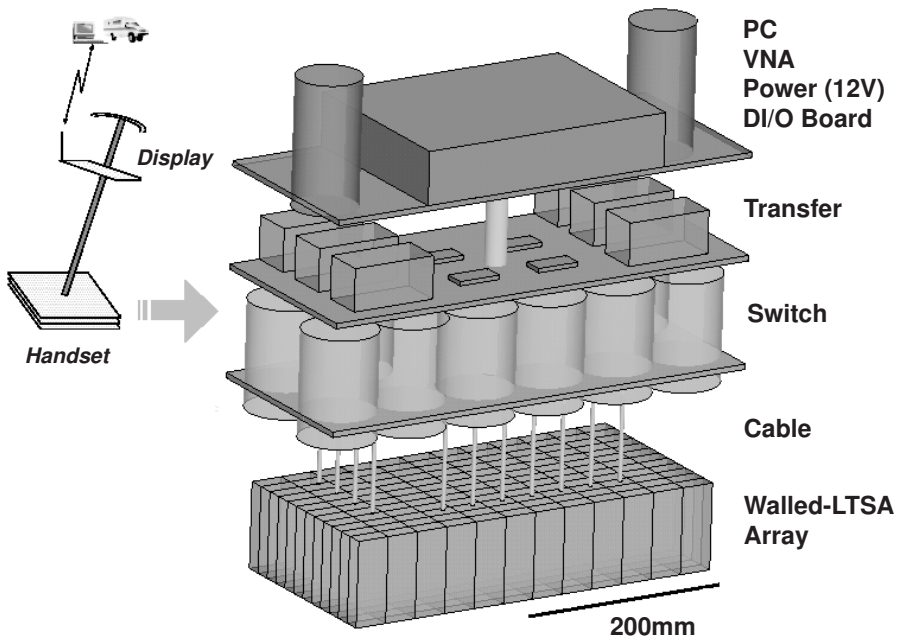


Figure 3: Handset construction

3 Buried objects visualization

We observed a metal can and a plastic mock landmine using the fabricated handset. The object was placed at approximately 1cm below the ground surface. Table 1 shows the features of objects. A metal can is supposed to simulate a metallic landmine. A plastic mock mine has almost the same dielectric constant as that of a real landmine.

In this experiment, we used a double-ridged horn antenna for transmission while the switched Walled LTSA elements are used for reception. Through observations, the transmitting antenna is fixed, and the receiving antenna is switched electrically one by one to collect data at 144 spatial points. The handset and the transmitting antenna are faced to the ground at the height of approximately 30cm. A VNA measures the transmitting coefficient S_{21} from 8 to 12GHz, 51 sample points.

Since the distances between the transmitting and receiving antennas are not constant, the obtained complex amplitude was compensated. Only the phase was compensated because the differences in the distance influences the value of the phase to a large extent. We measured metal plate placed on the ground beforehand, and we subtracted the values from obtained phases. Then, the obtained multiple-frequency complex amplitude image is segmented by a CSOM, which we previously proposed.

Table 1: Feature of objects: Metal can and plastic mock mine

	Metal can	Plastic mock mine (TYPE 72)
Diameter	100mm	78mm
Height	45mm	40mm
Material	Metal	Rubber, small amount of metal, resin, filling having the same dielectric constant as that of explosive powder

3.1 Metal can visualization

Fig.4 shows the amplitude, phase and CSOM output images of the metal can. The amplitude and phase images show the values obtained at a certain frequency data, whereas a CSOM image is calculated from the data of multiple frequency points. Since the object was metallic, we can recognize the metal can only from the amplitude image. From the phase image, we can recognize the flat surface of the can as a constant phase region. Also, after CSOM processing, the metal can part is clearly classified into a single class.

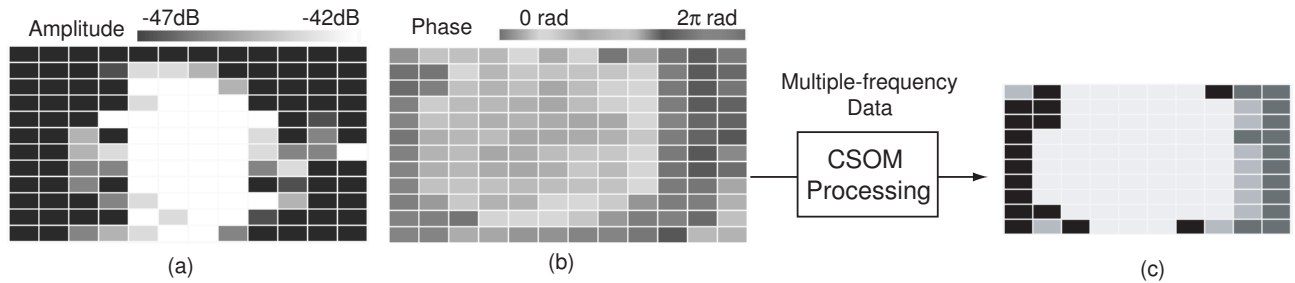


Figure 4: (a)Amplitude, (b)phase, and (c)classification result for the metal can buried in the ground.

3.2 Plastic mock mine visualization

Fig.5 shows the amplitude, phase and CSOM output images of the plastic mock landmine. Since the object is plastic, it is difficult to recognize the landmine only from the amplitude image. However, after CSOM processing, the mock mine part is clearly classified into a single class.

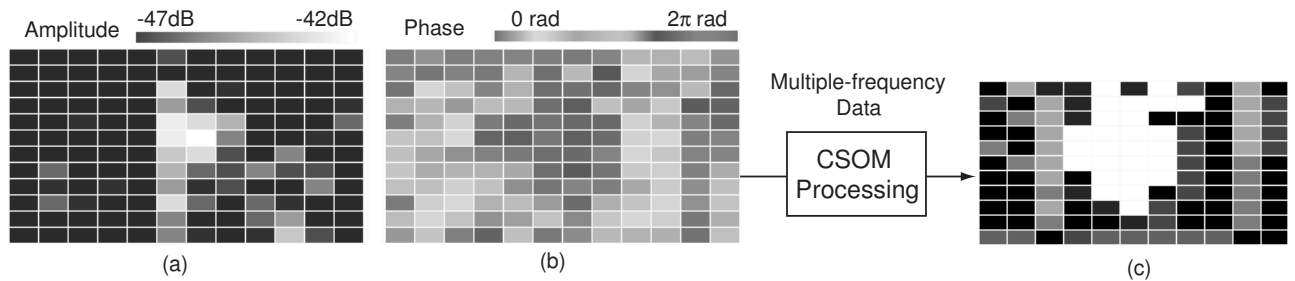


Figure 5: (a)Amplitude, (b)phase, and (c)classification result for the plastic landmine buried in the ground.

3.3 Measurement time

Measurement time has been reduced to 62s for 144 sampling points in space at 51 frequency points. It is approximately 1/10 of the observation time in the previous system in which we scanned a pair of antennas mechanically.

4 Summary

We proposed, designed and fabricated an integrated Walled-LTSA handset for subsurface imaging. We observed a metal can and a plastic mock mine buried in the ground suface. We have succeeded in visualization of both of the objects. The measuring time is reduced to 62s, which is 1/10 of the time required in our previous moving-antenna system.

Acknowledgement

This work was partially supported by the grant from the Ministry of Education, Science, Sports and Culture under Grant-in-Aid for Scientific Research (A) 15206047 to A.Hirose.

REFERENCES

1. J.M. Bourgeois and G.S. Smith, "A complete electromagnetic simulation of the separated-aperture sensor for detecting buried land mines," *IEEE Trans. Antenna and Propagation*, vol.46, no.10, pp.1419–1426, October 1998.
2. T.P. Montoya and G.S. Smith, "Land mine detection using a ground-penetrating radar based on resistively loaded vee dipoles," *IEEE Trans. Antenna and Propagation*, vol.47, no.12, pp.1795–1806, December 1999.
3. L. Peters Jr. and J.J. Daniels, "Ground penetrationg radar as a surface environmental sensing tool," *Proceedings of the IEEE*, pp.1802–1822, December 1994.
4. T. Hara and A. Hirose, "Plastic mine detecting radar system using complex-valued self-organizing map that deals with multiple-frequency interferometric images," *Neural Networks*, vol.17, no.8-9, pp.1201–1210, 2004.
5. A. Hirose, A. Toh Jiayun, and T. Hara, "Plastic landmine identification by multistage association," *IEICE Tech. Rep.*, no.NC2004-156, 2005.
6. T. Hara and A. Hirose, "Adaptive plastic-landmine visualizing radar system: effects of aperture synthesis and feature-vector dimension reduction," *IEICE Transactions on Electronics*, vol.E88-C, no.12, pp.2282–2288, 2005.
7. A.B. Suksmono and A. Hirose, "Adaptive complex-amplitude texture classifier that deals with both height and reflectance for interferometric sar images," *IEICE Transaction on Electronics*, vol.E83-C, no.12, pp.1905–1911, December 2000.
8. A. Hirose, *Complex-Valued Neural Network, Studies in Computational Intelligence*, Springer-Verlag, Heidelberg, 2006.
9. K.S. Yngvesson, D.H. Schaubert, T.L. Korzeniowski, E.L. Kollberg, T. Thungren, and J.F. Johansson, "Endfire tapered slot antennas on dielectric substrates," *IEEE Trans. on Antennas and Propagation*, vol.AP-33, no.12, pp.1392–1400, 1985.

Test and Evaluation of Japanese GPR-EMI dual sensor systems at Benkovac Test Site in Croatia

Jun Ishikawa and Mitsuru Kiyota
Japan Science and Technology Agency (JST), Japan

Nikola Pavković

Katsuhisa Furuta
Tokyo Denki University (TDU), Japan

Abstract – This article presents an experimental design and evaluation results of trials that were carried out from 1 February to 9 March 2006 at Benkovac test site in Croatia. The objective of the Croatia-Japan joint trials is to confirm performance of dual sensor systems, which use both ground penetrating radar (GPR) and electromagnetic inductive (EMI) sensor, in comparison with existing EMI sensors, i.e., metal detectors (MDs) and to provide reliable data as a basis for future work. Increasing probability of detection (PD) and decreasing false alarm rate (FAR) will contribute to improve working efficiency in humanitarian demining. Therefore, by analyzing the data from which general principles can be established on the relative value of the different technologies, the trials aim at evaluating differences in performance between dual sensors and MDs, especially in terms of discrimination of landmines from metal fragments and extension of detectable range in the depth direction. Devices to be evaluated here are four prototypes of anti-personnel landmine detection systems developed under a project of the Japan Science and Technology Agency (JST), the supervising authority of which is the Ministry of Education, Culture, Sports, Science and Technology (MEXT). The prototypes that provide operators with subsurface images make no explicit alarm and final decision whether or not a shadow in the image is a real landmine is left to the operator. This is similar to the way that medical doctors find cancer by reading CT images. Since operators' pre-knowledge of the locations of buried targets significantly influences the test results in these kinds of systems, three test lanes have been designed to be suitable for blind tests. The results showed that the dual sensor systems have a potential to discriminate landmines from metal fragments and that reducing operation time is the most important problem to be solved for practical use.

1. Introduction

Japanese Research teams from universities and industries, which are funded by the Japan Science and Technology Agency (JST), have been developed the GPR+EMI dual sensor systems since October 2002 under the program of “Research and Development of Sensing Technology, Access and Control Technology to Support Humanitarian Demining of Anti-personnel Mines.” To evaluate the prototypes, a series of trials were carried out from 8 February to 11 March 2005 in Sakaide City, Japan^{1,2}. The concept of the developed systems is to make no explicit alarm and to dedicate itself to provide operators with clear subsurface images (Figure 1). Therefore, decision-making using the subsurface images is entirely left to operators’ subjectivity. Since operators’ pre-knowledge of the locations of buried targets significantly influences the detection results for these kinds of systems, all the test lanes in Japan were designed to be suitable for blind tests. Evaluation results of the trial showed that probability of detection for targets in deeper levels than 10cm can be improved by combining GPR with an EMI sensor.

After the trials in Japan, the prototypes have been improved to be more robust, simple and cost-effective, and the next step of the project has been to take field tests to evaluate these features in Croatia, which is a well-experienced country in test and evaluation for humanitarian demining equipment. This article shows evaluation results of the Croatia-Japan joint test and evaluation for anti-personnel landmine detection systems using GPR+EMI dual sensors at the test site Benkovac of Croatian Mine Action Centre - Center for Testing, Development and Training (HCR-CTRO) in Croatia.

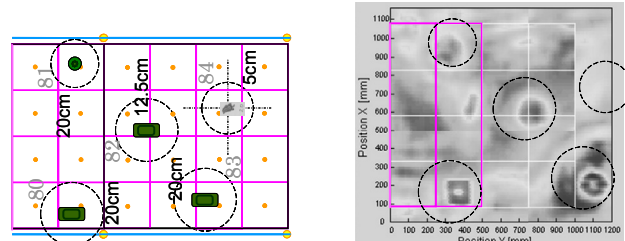


Figure 1: Examples of detection image acquired by a stepped-frequency SAR-GPR⁶ mounted on MHV⁵ during the Croatia trials. The left figure shows locations of targets with depth (one PMA-2s, three PMA-A1s and one metal fragment) and the right image is a wrapped image composed of several slices of different depth.

2. Design of Test and Evaluation

The objective of the test and evaluation is to confirm performance of GPR+EMI dual sensor systems in comparison with existing metal detectors (MDs) and to provide reliable data as a basis for future work. By using the data from which general principles can be established on the relative value of different equipment and techniques, the trial aims at clearing differences of performance between dual sensors and MDs, especially in terms of discriminating landmines from fragments and expanding detectable range in the depth direction. Improvement of the performance will contribute to increasing probability of detection (PD) and decreasing false alarm rate (FAR).

2.1. Test site Benkovac

The trials were conducted from 1 February to 9 March 2006 at the test site Benkovac in Croatia. The test site is well-known to have been used in the International Test and Evaluation Programme (ITEP) project 2.1.1.2 "Reliability Model for Test and Evaluation of Metal Detectors³" in accordance with the CEN workshop agreement (CWA) 14747⁴. Three types of soils available in the Benkovac test site, that is, (a) red bauxite with neutral stones in lane #7, (b) red bauxite in lane #1, and (c) neutral clay in lane #3⁵. In the later half of the trials, the weather was harsh, raining and snowing. Measurements of the soil moisture sometimes reached more than 40% (Figure 2).

2.2. Four devices to be evaluated

Four sensor systems were evaluated in the trials. One of those is Mine Hunter Vehicle (MHV), the vehicle and manipulator part of which have been developed by a research team of Prof. Nonami, Chiba University⁵. MHV can interchangeably mount 2 GPR sensors in addition to a commercial-off-the-shelf MD. One is a stepped frequency SAR-GPR developed by Prof. Sato's team of Tohoku University⁶ referred as **MHV#1** in the following part (Figure 3, left). Stepped frequency radar determines distance to a target by constructing a synthetic range profile, which is a time domain approximation derived from the frequency response of a combination of stepped frequency signals via inverse fast Fourier transform (IFFT). The major advantage of stepped frequency methods is that the spectrum bandwidth can be easily tuned to set the parameters to be optimum according to environment conditions such soil moisture. The other is an impulse GPR, LAMDAR-III, developed by Prof. Arai's project of University of Electro-Communications⁷ referred as **MHV#2** in the following part (Figure 3, right). This kind of GPR operates by transmitting a very narrow pulse of electromagnetic wave (less than 1 nanosecond), the advantage of which is that the measurement time required to generate one range profile is very short.



Figure 3: MHV#1 (left) and MHV#2 (right).

Figure 4: Gryphon (left) and ALIS (right).

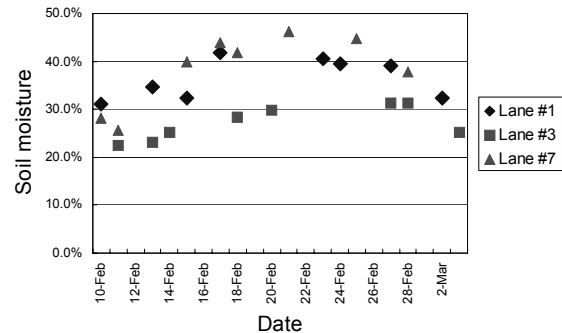


Figure 2: Soil moisture measurements through trials.

The 3rd system to be evaluated is **Gryphon** (Figure 4, left), which can be remotely controlled to access to minefields. The robotic buggy has been developed by Prof. Hirose's team of Tokyo Institute of Technology⁸. The manipulator that is mounted on the buggy has been designed so as to cancel reaction force induced by sensor scanning. The sensor part of Gryphon is a GPR+EMI dual sensor named Advanced Landmine Imaging System (**ALIS**), which can be also used as a hand-held detector⁹. ALIS has been developed by the above mentioned Prof. Sato's team and took a field trial in Afghanistan in December 2004. The hand-held type ALIS is the 4th system to be tested here (Figure 4, right).

2.3. Experimental design

Through the trials, influences of 3 factors on probability of detection (PD) are evaluated by analysis of variance (ANOVA), that is, target types that consist of landmines and metal fragments, target depth and soil types as follows:

- Target type: PMA-1A, PMA-2, ITOP I₀ and Free-formed metal fragment (Figure 5),
- Target depth: 5.0cm, 12.5cm and 20.0cm, and
- Soil type: uncooperative and heterogeneous (Lane #7), uncooperative and homogeneous (Lane #1) and cooperative and homogeneous (Lane #3).

Due to the limitation of time for the trials and the number of landmines that can be used, it is impossible to test all the combinations of levels (4 levels of target type, 3 levels of target depths and 3 levels of soil conditions). To impartially collect unbiased data for statistical analysis under this limitation, an orthogonal experimental design based on L₁₈(2¹×3⁷) is used. According to the L₁₈ array, a combination of levels in every factor is derived as listed in Table 1. The number of target in each level is 7. Burying targets has done on 8-9 December 2005 so that the targets could be left as it is for 2 months.

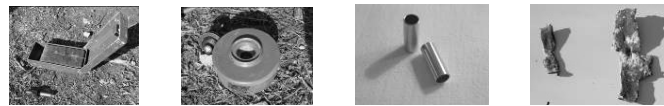


Figure 5: PMA-1A, PMA-2, ITOP I₀ and metal fragment.

Table 1: Combination results of levels of each factor via L₁₈(2¹×3⁷) experimental design.

No.	Target type	Target depth	Lane # (Soil type)
1	PMA-1A	5.0cm	7
2	PMA-1A	12.5cm	1
3	PMA-1A	20.0cm	3
4	PMA-2	5.0cm	7
5	PMA-2	12.5cm	1
6	PMA-2	20.0cm	3
7	ITOP-I0	5.0cm	1
8	ITOP-I0	12.5cm	3
9	ITOP-I0	20.0cm	7
10	Fragment	5.0cm	3
11	Fragment	12.5cm	7
12	Fragment	20.0cm	1
13	PMA-1A	5.0cm	1
14	PMA-1A	12.5cm	3
15	PMA-1A	20.0cm	7
16	PMA-2	5.0cm	3
17	PMA-2	12.5cm	7
18	PMA-2	20.0cm	1

3. Experimental Results

3.1. Trial procedures

Two testees of each system took blind tests of 3 lanes, i.e., #1, #3 and #7. All the testees declared detected anomalies by putting tags on the ground where the targets are considered to be buried. As described in Table 2, the tags show confidence rating of the testee and the final decision whether the declared anomaly is a target (landmine/fragment) or clutter.

Table 2: Definition of confidence rating and tag that indicates declared location.

Definition of confidence rating	I'm 100% sure that there is nothing here.	It seems that there might be something here.	I'm almost sure that there is something here.	I would classify the detected object as a landmine or fragments.	I confidently classify the detected object as a landmine or fragments.	
Final decision	I declare that it is a clutter.		I declare that it is a landmine.			
Confidence rating and tag color	N/A	25 Yellow	50 Pink	75 Orange	100 Red	
Final decision	I declare that it is a clutter.		I declare that it is a fragment.			
Confidence rating and tag color	N/A	25 White/Black	50 White	75 Green	100 Blue	

To compare the performance of GPR+EMI dual sensors with that of existing MDs, a benchmarking was conducted by two Croatian deminers, who do not know the target positions. The design of the experiment, the training of deminers and the monitoring has been organized by the Federal Institute for Materials Research and Testing (BAM). The deminers claimed that they cannot distinguish a metal fragment from a landmine only based on the audio signal of the MD. Therefore, only two levels of confidence were used in this trial. When the deminers heard an audio signal, they marked its location with 100% confidence if they would investigate that location with a prodder. If they would not investigate it, believing it comes from the soil or other source of noise, they marked the location with 25% confidence. In the following section, when results of Japanese testees are compared with those of Croatian deminers, tags with higher or equal to 50% confidence were counted as declaration, and the color of tags was not taken into consideration. For example, both a red tag on a metal fragment and a blue tag on a landmine were considered to be true positives, and this is hereinafter referred to as the normal detection criterion.

3.2. Experimental results

This section shows some experimental results. Figure 6 shows probability of detection (PD) of 5 testees for 18 experimental runs with the normal detection criterion, where ITOP I₀ and metal fragments treated as targets intended to be detected. One testee from each system, who attained higher PD than the other, has been chosen. GPR+EMI systems attained higher PD than a deminer (Deminer 1) for deeply-buried PMA-2 in mineralized uncooperative soil. On the other hand, the deminer can very precisely determine the location of ITOP I₀, which is very small and has no recognizable shape by GPR.

A testee of ALIS (ALIS 1) attained 81.7% of average PD, which matches those of two deminers, who attained 84.0% and 81.0%. Figure 7 shows average PD for each level of factor. The detail should be discussed after ANOVA, but superiority of ALIS to deminers was observed in the levels of PMA-2 and Lane #1 (uncooperative and homogeneous soil). On the other hand, ALIS took 30-40min. for 1m² detection while deminers took about 5min., the other 3 vehicle-mounted systems 15-20min.. Figure 8 shows false alarm ratio (FAR) separately calculated from each soil type (i.e., each lane) for the same 5 testees as those in Figure 6. Compared with the deminer's results, the GPR+EMI sensors tended to have less influence of soil type on FAR, especially for Gryphon and MHV#2.

Data of ALIS have been analyzed by the colored tags explained in Table 2 to see if the dual sensor can tell landmines from metal fragment. In this case, declarations by wrong-colored tags were treated as false positives. For example, a declaration for a landmine with a blue tag means having missed the landmine. Lines with diamonds in Figure 9 show this strict criterion case for ALIS. Compared with the case where the PD was calculated by the normal detection

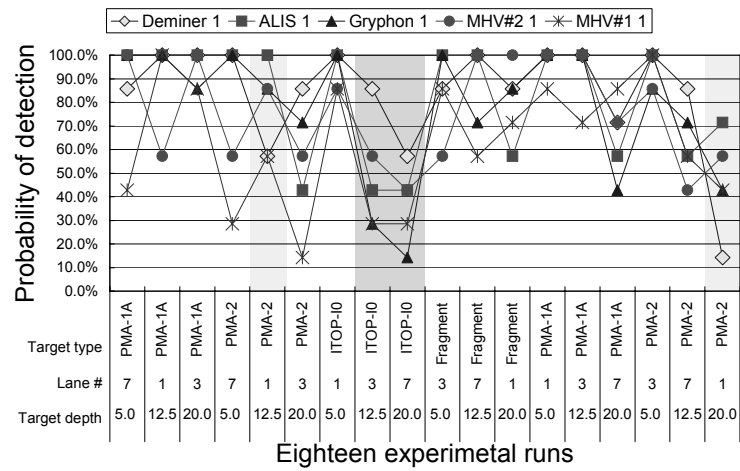


Figure 6: PD for 18 experimental runs: one testee from each system has been selected.

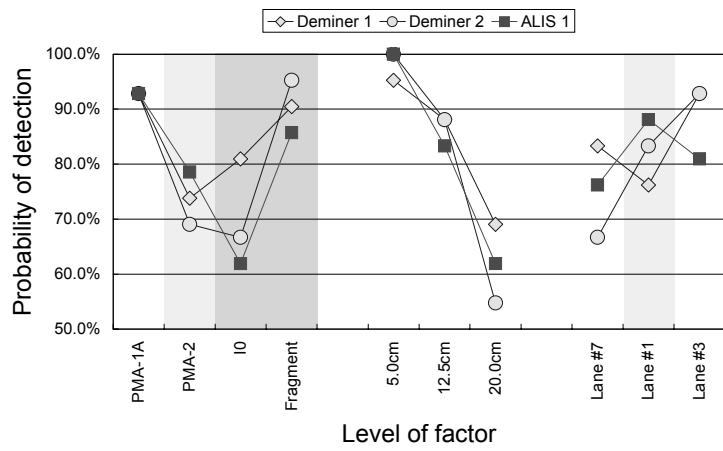


Figure 7: Average PD for each level of factors.

criterion (line with squares in Figure 9) , it was shown that ALIS found 50% of metal fragments as metal fragments discriminating from landmines although a small degradation in PD for landmines was observed. This means that dual sensors have a possibility of discrimination of landmines from metal fragments.

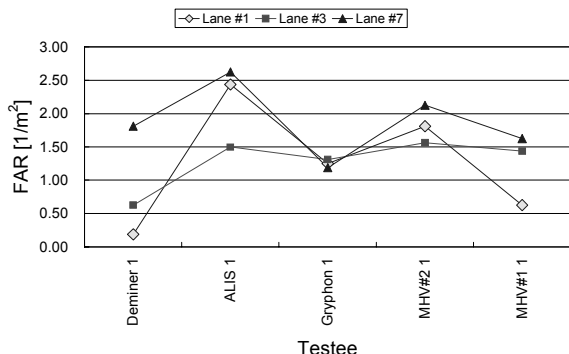


Figure 8: FAR for 5 testees: the same testee from each system has been selected.

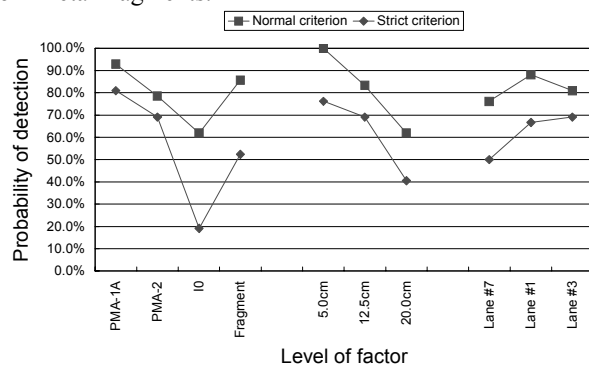


Figure 9: Comparison of average PD of ALIS to see an ability of metal fragment discrimination.

4. Conclusions

Through the trials, many lessons have been learned such that PD for small targets in mineralized (uncooperative) soil can be improved by using GPR. These results were fed back to the testees for further improvement. The next step is to put one or two promising system(s) into practical field trials that will be conducted by a third party after the modification.

Acknowledgement

The authors would like to thank all the project members especially for the trial participants from Tohoku University, Chiba University, Tokyo Institute of Technology, University of Electro-Communications, Fuji Heavy Industries Ltd., TAU GIKEN Co. Ltd., Yamate Corporation, HiBot Corporation.

The authors also would like to thank Dr. Christina Müller and her colleagues of the Federal Institute for Materials Research and Testing (BAM) for their comments in statistical analysis and coordination of blind-tests by deminers.

REFERENCES

- Ishikawa, J., Kiyota, M. and Furuta, K., "Experimental design for test and evaluation of anti-personnel landmine detection based on vehicle-mounted GPR systems," *Proc. of SPIE Vol. 5794, Detection and Remediation Technologies for Mines and Minelike Targets X*, pp. 929-940, 2005.
- Ishikawa, J., Kiyota, M. and Furuta, K., "Evaluation of Test Results of GPR-based Anti-personnel Landmine Detection Systems Mounted on Robotic Vehicles," *Proc. of the IARP International workshop on Robotics and Mechanical Assistance in Humanitarian Demining (HUDEM2005)*, pp. 39-44, 2005.
- Mueller, C., et al., "Reliability Model for Test and Evaluation of Metal Detectors," *ITEP Project 2.1.1.2 Final Report*, http://www.itep.ws/pdf/Itep_no2.1.1.2_reliability_model.pdf, 2004.
- CEN Workshop Agreement, *Humanitarian Mine Action - Test and Evaluation- Metal Detectors*, CWA 14747, http://www.itep.ws/pdf/CWA_metal_detectors.pdf, 2003.
- Nonami, K. and Aoyama, H., "Research and Development of Mine Hunter Vehicle for Humanitarian Demining," *Proc. of the HUDEM2005*, pp.76-81, 2005.
- Sato, M., Hamada, Y., Feng, X., Kong, F., Zeng, Z. and Fang, G., "GPR using an array antenna for landmine detection," *Near Surface Geophysics*, Vol. 2, pp. 3-9, February, 2004.
- Shrestha, S. M. and Arai, I., "High Resolution Image Reconstruction by GPR using MUSIC and SAR Processing Method for Landmine Detection," *Proc. of the 2003 IEEE International Geoscience and Remote Sensing Symposium (IGRASS2003)*, pp. 505-508, 2003.
- Fukushima, E. F., et al., "Teleoperated Buggy Vehicle and Weight Balanced Arm for Mechanization of Mine Detection and Clearance Tasks," *Proc. of the HUDEM2005*, pp. 58-63, 2005.
- Sato, M., Fujiwara, J., Feng, X., Zhou, Z. and Kobayashi, T., "Development of a hand-held GPR MD sensor system (ALIS)," *Proc. of SPIE Vol. 5794, Detection and Remediation Technologies for Mines and Minelike Targets X*, pp. 1000-1007, 2005.

Remote sensing of explosives in a landmine by Nuclear Quadrupole Resonance

G. Ota¹, H. Itozaki^{1,2}, J. Barras¹, K. Sakuta¹, and M. Tachiki²

1. Osaka University, Japan

2. National Institute for Materials Science, Japan

Abstract

We investigated the sensitivity of NQR for explosives such as trinitrotoluene (TNT) and cyclotrimethylenetrinitramine (RDX), the main constituent of explosives of landmines. We succeeded in the remote detection of RDX from 8 cm away using NQR.

We have developed a prototype of an NQR landmine detector.

1. Introduction

Although removing all the abandoned landmines in the world is currently a big issue, it will take some time when using conventional metal detectors because of their high false alarm rate. A highly sensitive metal detector to find an antipersonnel landmine with as little as 10 g of metallic content gives an alarm every time it encounters few grams of trash and this results in a bad performance of the detection. A nuclear quadrupole resonance detector, on the contrary, identifies the explosive material itself based on its resonant frequency and can reduce drastically the false alarm rate. [1,2,3]

NQR detects a resonant signal from a spin with separated eigenstates after irradiation by RF wave. If the irradiating RF wave has a specific frequency equivalent to the difference between the spin's eigenstates, the RF wave is adsorbed by the spins which are then excited to the upper state. Finally, the RF wave is re-emitted. The uniqueness of the resonant frequency allows us to identify the material with the detection of the RF wave emitted from the spin.

2. NQR detection of explosives

Fig. 1 shows the NQR signal from TNT and RDX, both of which are widely used for landmine explosives. The signal was detected by a loop coil antenna winded around 400g of the sample enclosed in an electromagnetic shield. The NQR signal of TNT at 872 kHz (Fig. 1(a)) and RDX at 3.410 MHz (Fig.1 (b)) was clearly detected. The clear resonant signal in Fig.1 shows the ability of NQR landmine detection determining the existence of a dangerous explosive instead of depending on indirect clues as the subsidiary metal or object outline. The NQR frequencies of major explosives are shown in Fig. 2.

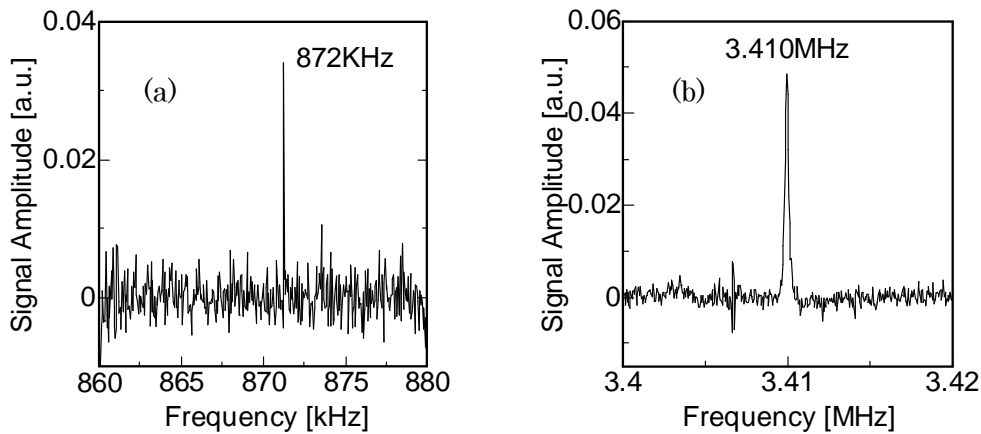


Fig. 1 NQR signal from explosives

(a) TNT, (b) RDX. Both signal is detected from 400g of the sample inserted in the detection coil inside an electromagnetic shield.

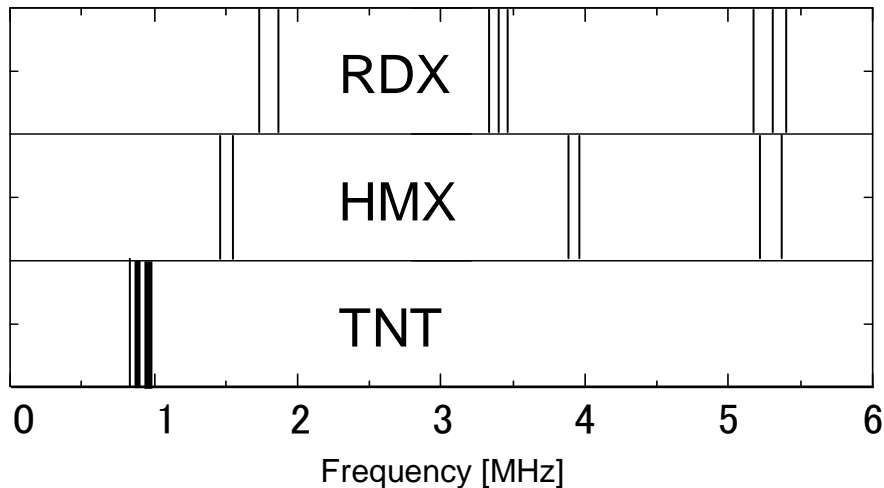


Fig. 2 NQR frequency of major explosives, TNT, HMX, and RDX.

We can identify the explosive content of the mine by the comparison of the frequency of resonant signal with this frequency map.

3. Remote sensing by NQR

We succeeded in detecting a sample distant from the antenna. A block diagram of our antenna unit is shown in Fig.3. A four-turn loop coil 200 mm in diameter is used in this experiment. The coil is tuned and matched at 50Ω through a matching circuit at the

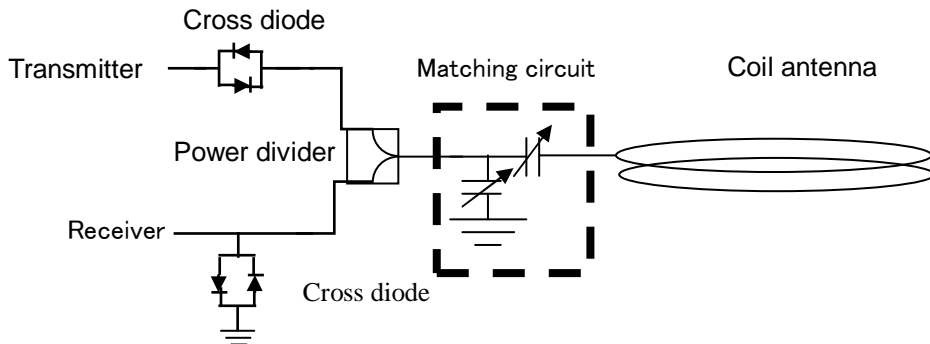


Fig. 3 Block diagram of the antenna unit for NQR remote detection

NQR frequency to catch a weak signal. The set of a power divider and cross diodes allows the coil to act as both the transmitter and receiver by allowing only a strong signal current to flow from a transmitting circuit and weak signal to the receiving circuit.

Fig. 4 shows the result of remote sensing of 500 g of RDX enclosed in an electromagnetic shield and 1,000 scans were accumulated to improve the signal-to-noise (S/N) ratio. As shown in Fig. 4, we can detect RDX 80 mm away from the antenna with S/N~2. This result shows the capability of NQR remote sensing.

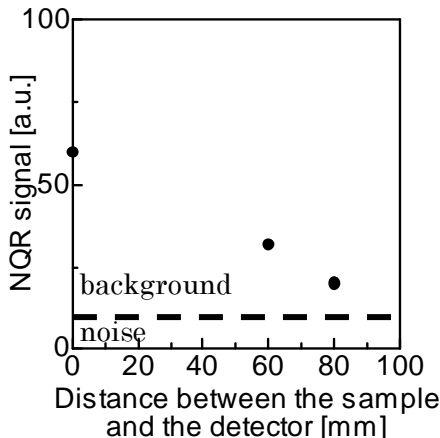


Fig. 4 Remote sensing of 500 g of RDX.

We also observed the two-dimensional NQR image of a sample. This experiment was done in our laboratory and we cannot use a real explosive for safety reasons. So hexamethylenetetramine (HMT), an ingredient for RDX is used for the target. 500 g of HMT in a bottle with 80 mm of diameter and 140 mm of height is laid down in the scanning area and 4 turn coil 60 mm in width and 55 mm in depth scanned 10 mm

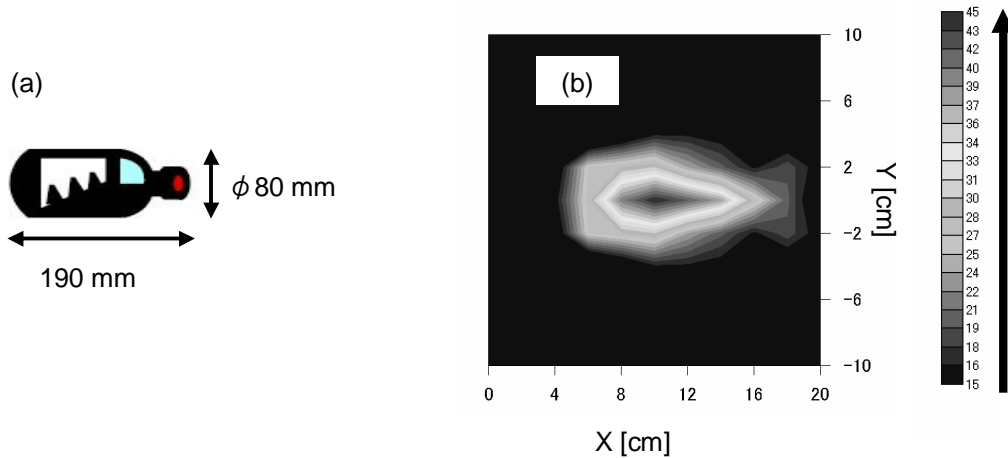


Fig. 5 two-dimensional scanning by NQR.

(a) Outline of the sample (500 g of HMT) and (b) Output of the scan.

above the scanning area every 20 mm. The result is shown in Fig. 5. The output in Fig. 5 shows a result of 100 times accumulation at each detection point. As shown in Fig. 5(b), the outline of the HMT inside the bottle is well observed including the local amount of the sample by NQR detection. This result reveals that NQR can draw a two-dimensional mapping of the amount of a faraway sample.



Fig. 6 The prototype landmine detector we exploited.

We integrated a prototype of an NQR landmine detector shown in Fig. 6. This prototype consists of a power supply unit, electronic circuit unit, and probe unit and probe unit is attached to a handheld rod in Fig. 6. We exploited a small NQR transceiver for the electronic circuit. The size and weight of this transceiver is H 550 mm X W 250 mm X D 400 mm and 20 kg, respectively, which allows us to bring one easily by a small vehicle even off-road. Electric power consumption is also cut down to 35 W full-time and 50 W on detection. This value means that even a commercially available gasoline-driven generator can supply enough power for 8 hours. So there is no problem about power supply. The probe unit consists of a detection coil, a matching box, a pre-amplifier, and a

portable electromagnetic shield. The total weight is as light as 3 kg. It means that one can carry it easily. We are improving this prototype landmine detector to pursue the realization of a practical NQR landmine detector.

4. Conclusion

We detected the NQR signal of TNT and RDX and succeeded in detecting the NQR signal from RDX located 80 mm away from the detection coil. We also scan the detector above the sample and draw a two-dimensional NQR image of it. Based on these achievements, we have developed the prototype of the NQR landmine detector and are improving it to realize a practical system.

Acknowledgement

This research is partly supported by the Japan Science and Technology Agency.

References

1. Grechishkin, V. S. and Sinyavskii, N. A. , "nuclear quadrupole resonance as an explosive and narcotic detection technique", *Phys. Usp.*, vol.40, 393-406 ,1997.
2. Suits, B. H., Garraway, A. N., Miller, J. B. and Sauer, K. L., "¹⁴N magnetic resonance for materials detection in the field", *Solid State NMR*, vol.24, 123-136, 2004.
3. Hirshfeld, T., and Klainer, S. M., "short range remote NQR measurement", *J. Molec. Struct.*, vol.58, 63-77, 1980.

Hand-Held GPR MD Sensor System (ALIS) and its Evaluation Test in Croatia

Xuan Feng^{1,2}, Qi Lu^{1,3}, Takao Kobayashi^{1,3}, Kazunori Takahashi¹ and Motoyuki Sato¹

¹Center for Northeast Asian Studies, Tohoku University, Japan

² College of GeoExploration Science and Technology, Jilin University, China

³Japan Science and Technology Agency, Japan

Abstract - Currently for landmine detection, metal detector (MD) and ground penetrating radar (GPR) are the most popular sensor. Both of the sensors are based on the electromagnetic field. ALIS (Advanced Landmine Imaging System) is a novel hand-held sensor system combined with MD and GPR and can offer subsurface visualization information, and can show the MD sensor output in real time. The system has a sensor position tracking system that needs only one CCD camera attached on the sensor handle. The GPR of the system is a stepped frequency radar system whose RF component is a newly developed compact vector network analyzer. Based on the diffraction electromagnetic waves of subsurface targets, we combined migration algorithm into GPR system that can improve signal-clutter ratio and can image buried objects clearly. Considering the effects of ground surface and inhomogeneous soil to diffraction field, we optimize the migration aperture based on the comparison between migration trajectory and diffraction surface of the electromagnetic waves. Some field test for landmine detection sensors including ALIS had been carried out in 2006 from February to March at Benkovac test site in Croatia. The evaluation tests are organized by the Japan Science and Technology Agency (JST) and the Croatian Mine Action Center - Center for Testing, Development and Training (HCR-CTRO). In the test, ALIS can detect 100% shallow landmines.

1. Introduction

Because of good compatibility with the usually used MD, the ground penetrating radar (GPR) is commonly expected to be integrated to a multi-sensor system. The use of GPR for the detection of landmines is still recent but significant improvements. But the GPR normally suffers from very strong clutter. We are developing a novel hand-held sensor fusion system combined with MD and GPR, ALIS (advanced landmine imaging system). The GPR of the ALIS combines with the migration processing to improve the signal-clutter ratio.

Some field test for landmine detection sensors, including ALIS (Advanced Landmine Imaging System), had been carried out in 2006 from February to March at Benkovac test site in Croatia. The evaluation tests are organized by the Japan Science and Technology Agency (JST), the competent authority of which is the Ministry of Education, Culture, Sports, Science and Technology (MEXT) and the Croatian Mine Action Center - Center for Testing, Development and Training (HCR-CTRO).

In this paper, we will introduce the ALIS system, the evaluation tests, and show some test results including some images and ROC curve analysis.

2. ALIS

We developed ALIS (Advanced Landmine Imaging System), shown in Fig.1, which is a novel hand-held sensor system combined with MD and GPR and can offer subsurface visualization information, and can show the MD sensor output in real time. The system has a sensor position tracking system that needs only one CCD camera attached on the sensor handle. The GPR of the system is a stepped frequency radar system whose RF component is a newly developed compact vector network analyzer with an operational frequency range of

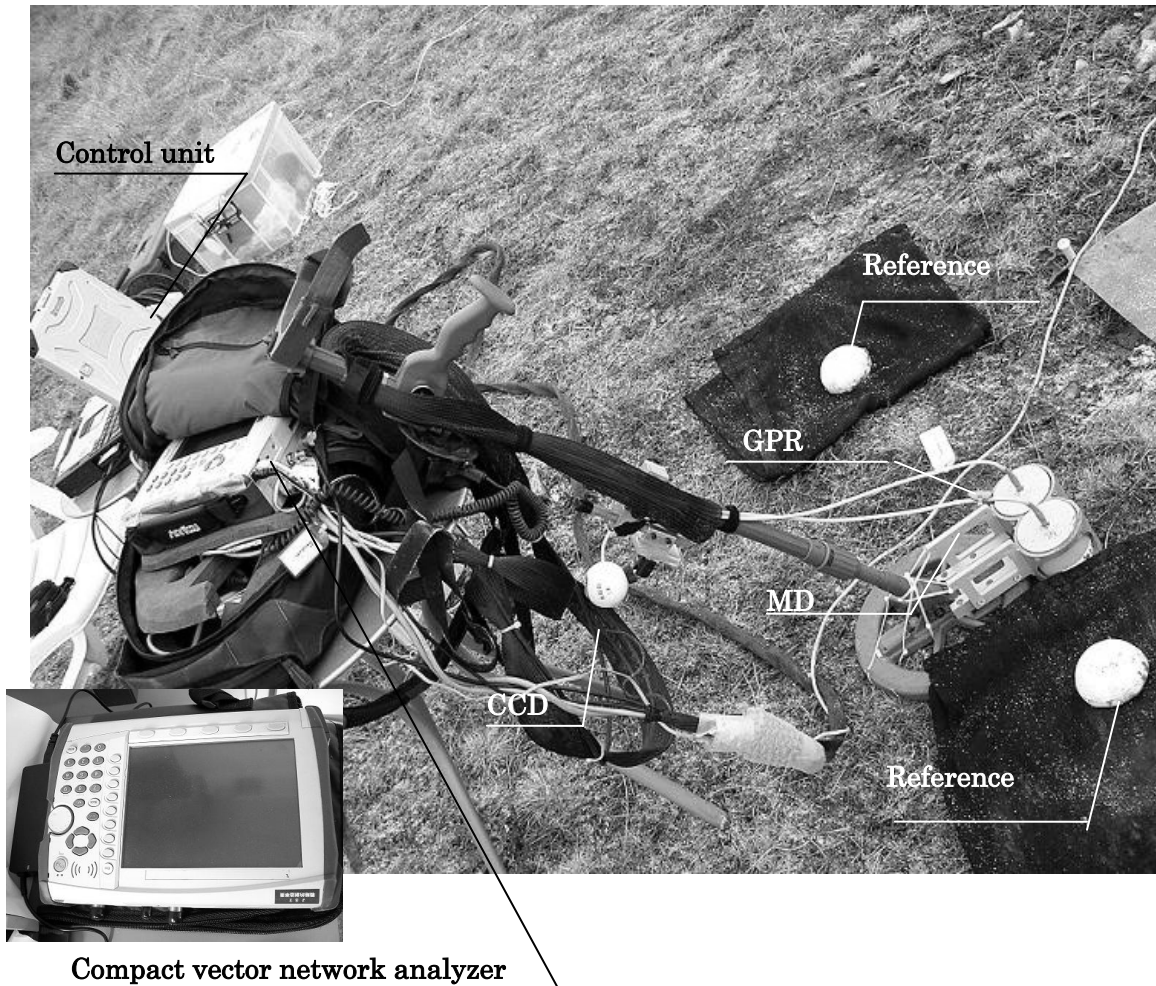


Figure 1: ALIS system.

500 MHz to 4 GHz. The MD of the system is CEIA metal detector MIL-D1 that is a portable, high-sensitivity Metal Detector designed to detect magnetic and non-magnetic metals in conductive and nonconductive soils and is widely used for landmine detection in Afghanistan. The MIL-D1 provides overall superior performance in the areas of detection distance, soil compensation capability and immunity to external interference.

The CCD camera is used to track two reference points and sensors when operating. Then the sensor position can be defined relative to reference points in real time. The scanning by ALIS follows the same procedure that normal hand-held metal detector is using. Generally the operator is asked to control sensors to slowly scan the measurement area in X-Y plane and to keep the sensor at same height as much as possible. After the operator finishes the scanning, the control computer will process the data set and display the MD image and GPR image. Because of human being operator the system it is impossible to scan field with grid x-y position and the sensor position is practically random.

We designed a processing procedure to process GPR data set, shown in Fig.2. The procedure includes preprocessing procedures that subtracting antenna coupling, bandpass filtering, and inverse discrete Fourier transform (IFFT). Considering the effect of antenna

coupling, which is measured by pointing the antennas upward without any target, we subtract it in frequency domain, because the relatively large fluctuations of antenna coupling might mask a signal of interest. Then a band pass filter and inverse discrete Fourier transform (IFFT) are used to transform the signal from frequency domain to time domain. For the old type GPR system, pulse radar system (X. Feng etc., 2005), we just need substitute DC filtering for the preprocessing procedures. Then we build continuous variation root-mean-square (CV-RMS) velocity (X. Feng and M. Sato, 2004). The velocity is computed from two layers model including air layer and soil layer by Dix equation. The propagation velocity of electromagnetic wave in air is well known. The propagation velocity of electromagnetic wave in soil is calculated from the moisture, which can be measured by TDR, by Topp's equation. Then the CV-RMS velocity will be used in the migration processing. Before migration we used common interpolation method to produce the grid data set.

3. Evaluation Tests in Croatia

In the Croatia evaluation tests, there have three test lanes of 1m x 16m. They are referred 3 types of soils respectively, uncooperative and heterogeneous soil, uncooperative and homogeneous soil, and cooperative and homogeneous soil. In these lanes 4 types targets, PMA-1A, PMA-2, ITOP I₀, and free-formed metal fragment were buried at 3 kinds of depth, 5cm, 12.5cm, and 20cm. Fig.3 show the photos of PMA-1A and PMA-2. Because we met the heavy rain when the ALIS gone into the evaluation test, the moisture of the soil was change from 15% to 30%. Fig.4 shows one calibration measurement result. In the calibration measurement, both PMA-1A and PMA-2 were buried at 8cm in the cooperative and homogeneous soil and the moisture was about 20%. From the MD image, we can find the PMA-1A clearly and from the GPR image, we can find both PMA-1A and PMA-2 clearly.

All tests were blind test for each lane. The testee declared all the detected targets every 1m x 1m area by putting tags at the positions where the targets were considered to be buried. The tags showed confidence rating of the testee and his final decision whether the declared target was a landmine, metal fragment, or clutter. After testee finished detection, the tester determined whether the declared locations can be considered to be from the intended targets. Fig. 5 shows the one evaluation result of ALIS. From the figure, we can find that the ALIS can detect 100% shallow targets.

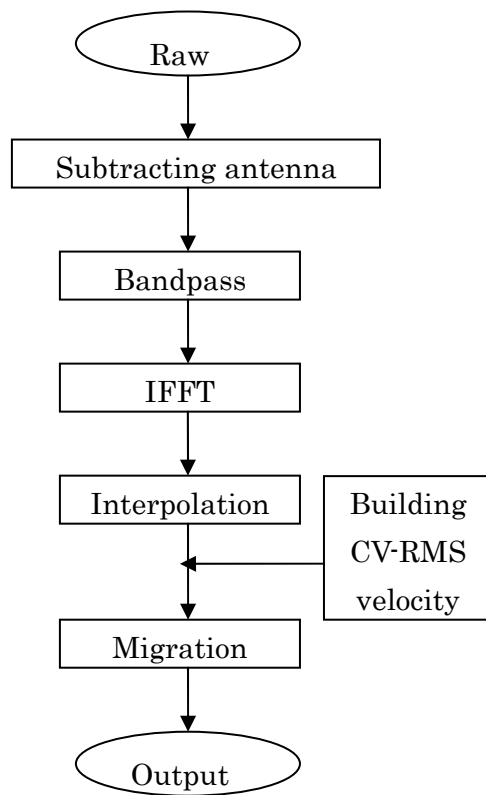
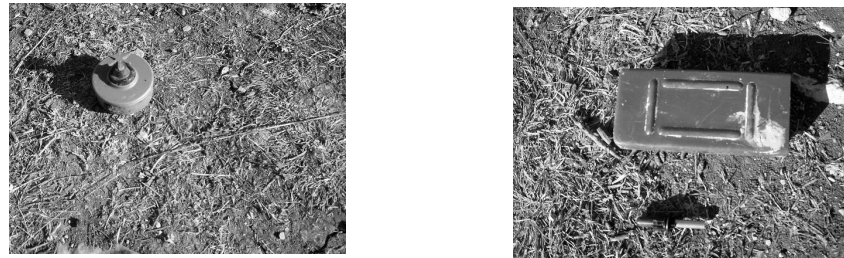


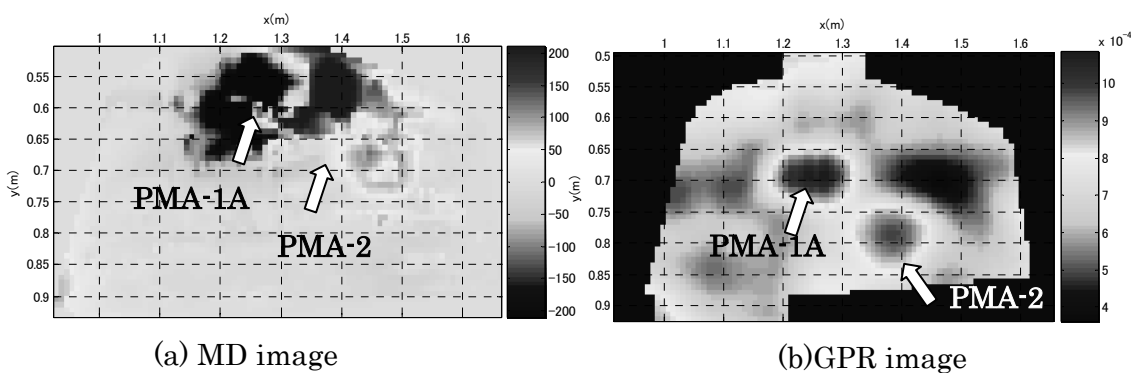
Figure 2: GPR processing flowchart.



(a) PMA-2

(b) PMA-1A

Figure 3: AP landmines used in the evaluation test.



(a) MD image

(b) GPR image

Figure 4: A result of ALIS in Croatia evaluation test.

4. Conclusions

New type ALIS with stepped frequency GPR can acquire good subsurface GPR image and can show the MD image in real time. In the evaluation tests in Croatia, the ALIS can detect 100% shallow landmines and can possibly identify metal fragments from landmines.

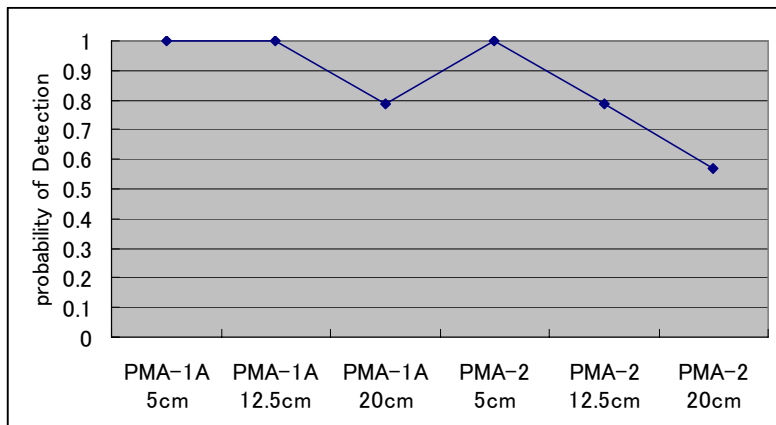


Figure 5: Detection probability of ALIS in Croatia evaluation test.

Acknowledgements

Part of this work was supported by JSPS Grant-in-Aid for Scientific Research (S)14102024 and by JST (Japan Science and Technology Agency).

REFERENCES

1. Ö. YILMAZ, *seismic data processing*, Stephen M. Doherty, ed., Society of Exploration Geophysicists, Tulsa, 1987.
2. K. C. Ho, Leslie M. Collins, Lisa G. Huettel, and Paul D. Gader, "Discrimination Mode Processing for EMI and GPR Sensors for Hand-Held Land Mine Detection", *IEEE Transactions on Geoscience and Remote Sensing*, Vol.42, 249-263, 2004.
3. M. Sato, X. Feng, T. Kobayashi, Z. S. Zhou, T. G. Savelyev and J. Fujiwara, "Preparation of GPR+MD sensors evaluation tests in Japan and Afghanistan", in *Detection and Remediation Technologies for Mines and Minelike Targets X, Proceedings of SPIE*, Orlando, USA, April, Vol.5794, 919-928, 2005.
4. M. Sato, J. Fujiwara, X. Feng, Z. S. Zhou and T. Kobayashi, "Development of a hand-held GPR MD sensor system (ALIS)", in *Detection and Remediation Technologies for Mines and Minelike Targets X, Proceedings of SPIE*, Orlando, USA, April, Vol.5794, 1000-1007, 2005.
5. X. Feng and M. Sato, "Pre-stack migration applied to GPR for landmine detection", *Inverse Problems*, Vol.20, S99-S115, 2004.
6. X. Feng and M. Sato, "Estimation of 3D velocity model by SAR-GPR and its application to landmine detection", *Proceedings of the 7th SEGJ international symposium-imaging technology*, Sendai Japan, November, 108-113, 2004.
7. X. Feng, J. Fujiwara, Z. S. Zhou, T. Kobayashi and M. Sato, "Imaging algorithm of a Hand-held GPR MD sensor (ALIS)", in *Detection and Remediation Technologies for Mines and Minelike Targets X, Proceedings of SPIE*, Orlando, USA, April, Vol.5794, 1192-1199, 2005.

Polarimetric Analysis of Radar Signature of a Manmade Structure

Jong-Sen Lee¹, Ernst Krogager², Thomas L. Ainsworth¹, Wolfgang-Martin Boerner³

¹Naval Research Laboratory, Washington DC, USA

²Danish Defence Research Establishment, Copenhagen O, Denmark

³University of Illinois at Chicago, , Chicago, USA

Abstract: Identification of manmade structures from radar images has always been a difficult task, especially for single-polarization radar. Fully polarimetric radar, however, can provide detailed information on scattering mechanisms that could enable the target or the structure to be identified. Complexity remains stemming from overlaps of single bounce scattering, double bounce scattering and triple and higher order bounce scattering from various components of manmade structure that makes physical interpretation a challenge. In this paper, we will present an interesting example using polarimetric SAR data of the Great Belt Bridge, Denmark, to illustrate the capability of polarimetric SAR in analyzing radar signatures. Polarimetric target decomposition is used to differentiate the multiple bounce scattering contributions contained in the polarimetric SAR images. Two C-band Danish EMISAR data takes, the first obtained during the bridge's construction and the second after its completion, are used to extract the scattering characteristics of the bridge deck, bridge cables and supporting structures.

1. Introduction

Interpreting radar images of manmade structures or targets has always been a challenge, especially for single polarization radar. Recent advance in the high-resolution synthetic aperture radar (SAR) technology provide the capability of obtaining detailed target signatures, but multiple bounce scattering contributions from various parts of the target made the interpretation and classification difficult. Fully polarimetric radar can provide detailed information on scattering mechanisms to separate odd bounces from even bounces that enable the target or the structure to be identified. In this paper, we will present an interesting example using polarimetric SAR images of the Great Belt Bridge, Denmark, to illustrate the capability of polarimetric SAR in analyzing radar signatures. Polarimetric target decomposition [1, 2] is used to differentiate the multiple bounce scattering components. The first of two C-band EMISAR data takes shows the bridge during construction; the scattering characteristics are relatively simple and straightforward. However, the SAR imagery collected after construction displays more complicated scattering characteristics of the bridge deck, bridge cables and supporting structures, and complex interactions between the individual scatterers.

Polarimetric SAR measures the reflectivity of a medium with quad-polarizations and the scattering matrix (for single-look complex data) is

$$S = \begin{bmatrix} S_{HH} & S_{HV} \\ S_{VH} & S_{VV} \end{bmatrix} \quad (1)$$

For backscattering from reciprocal media, $S_{HV} = S_{VH}$ which is assumed here. The tilt of an object from its vertical or horizontal position induces polarization orientation angle shifts that increase the HV returns and modify the scattering matrix [3]. For manmade structures, backscattered signals in general are from single bounce, double bounce and mulitple bounce returns of various parts of the structure, and they are not likely to come from defused scattering of random media, such as vegetation. Therefore, the dominant contribution to the cross-polarization, HV and VH, arises from orientation angle effects. The Great Belt Bridge PolSAR signature to be discussed in the next two sections shows combinations of single and multiple bounce returns, ideally suited for polarimetric interpretation.

2. Polarimetric signature of the bridge during construction

During the construction of this suspension bridge, EMISAR imaged the site with its C-band polarimetric SAR. The radar look angle is between 28° and 64°, and the range and the azimuth resolution are about 3 meters. The bridge deck was not installed during that time as shown in an aerial photo in Fig. 1A.

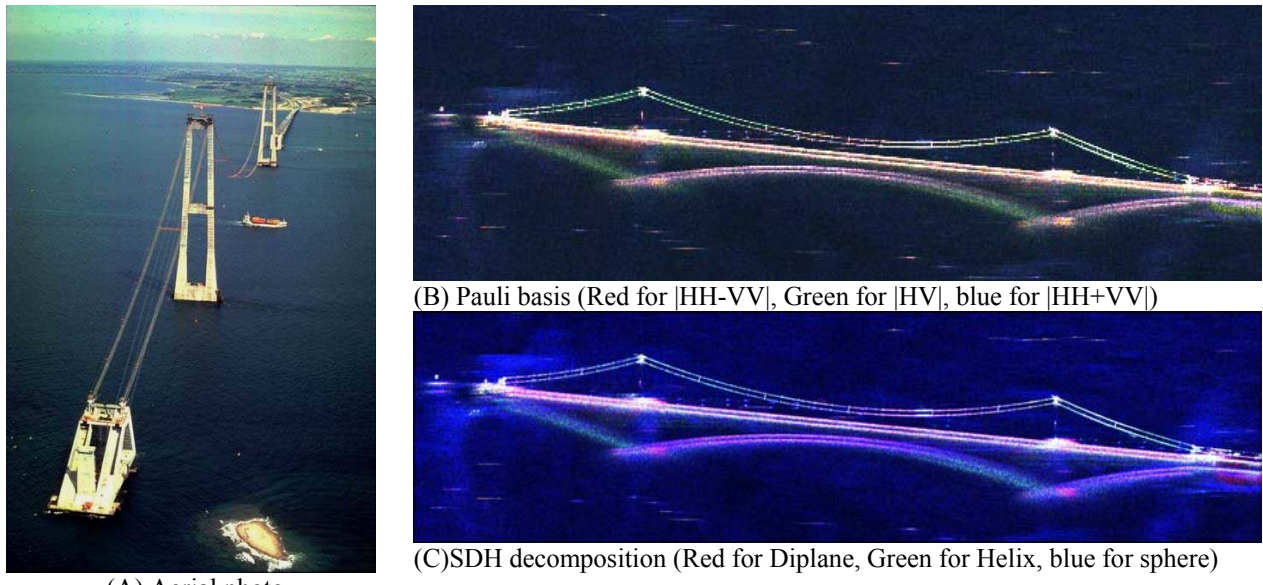


Fig. 1 Bridge signature during construction. The deck was not installed.

Pauli and Surface-Diplane-Helix Decompositions

Detailed analysis based on polarimetric decomposition reveals that the two bright lines in the middle are double bounce returns from the cables, and the lower arcs are triple bounce returns from the cables. The two giant cables were assembled from several hundred of small cables, and they were not tightened together by wrapping wires. The Pauli vector display (Fig. 1B) of the POLSAR data, using $|\text{HH}-\text{VV}|$, $|\text{HV}|$ and $|\text{HH}+\text{VV}|$ as red, green, and blue, respectively, separates the dihedral, cross-pol and surface scattering. In addition, the Surface-Diplane-Helix (SDH) decomposition [1] is shown in Fig. 1C with surface scattering in blue, diplane in red, and helix in green. It reveals similar scattering characteristics for this case as that from the Pauli decomposition.

Single Bounce Returns

The single bounce returns are expected from the ocean surface and the water surface is predominately blue in both the Pauli and the SDH representations, see Figs. 1B and 1C. The single bounce returns from the cables, in Fig. 1B, are green because the tilted cables induce higher returns in $|\text{HV}|$ due to the polarization orientation angle effect. We also notice that the color changes along the cables match the changing orientation angle.

Double Bounce Returns

Two middle straight lines in Fig. 1B are from strong double-bounce returns. The radar roundtrip distance for double bounce returns is equal to the roundtrip distance from the point vertically projected on the ocean surface in this case. Since the ocean surface is horizontal and flat, the double bounces from the cables are straight lines. We also observe from Fig. 1B and 1C that the double bounce returns from the two supporting towers are extremely strong, because double bounce returns from all parts of the towers are projected down to the ocean surface. The summation of these returns increases the overall power at the receiving end.

Triple Bounce Returns

The triple bounce returns in Fig. 1B show a rainbow of colors caused by the tilts of the cables. The triple bounces near horizontal possessed higher returns from HH and VV, but HV is higher for the other parts of the triple bounce returns because of the polarization orientation angle effect from the tilted cables [3]. We also notice the blurring effect of the triple bounce signatures caused by the capillary waves of the ocean surface.

3. Polarimetric signature of the bridge after construction

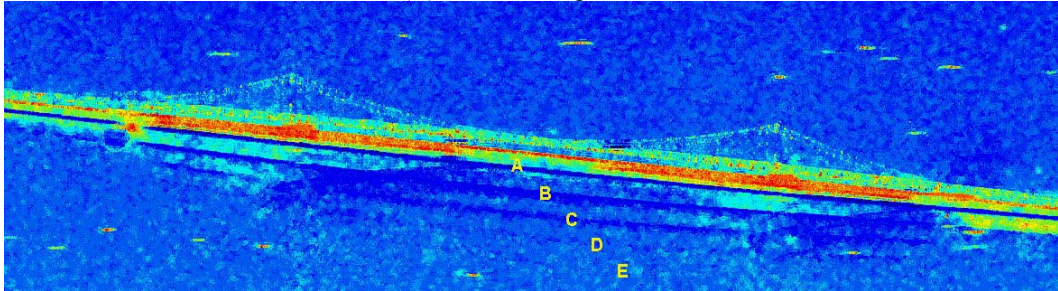
The polarimetric signature of the bridge becomes much more complicated after completion of construction. The deck has been installed, and the cables have been wrapped reducing their radar cross sections. The addition of the deck makes multiple bounces from the deck overlap with those from the cables. A photo of the completed bridge is shown in Fig. 2A for reference. We observe in the photo that the deck is not horizontal but has a slight upgrading toward the middle of the span where the cables meet the deck.



(A) An aerial photo of the bride after completion



(B) Pauli decomposition



(C) Average alpha angle

Fig. 2 Images after the completion of bridge construction. An aerial photo is shown in (A). The Pauli decomposed image (B) shows the bridge signatures very different from those during construction. The alpha angle image obtained by the Cloude-Pottier decomposition is shown in (C). The triple bounce from the deck is denoted as "A" in figure (C). The other parallel signatures denoted by "B", "C", "D" and "E" are induced by higher order of multiple odd bounces from the deck and the ocean surface.

Single, Double, and Triple Bounce Scatterings

The Pauli decomposed image (Fig.2B) shows the bridge signatures very different from those during construction. The single bounce returns from the cables are much weaker than that in Fig. 1B due to smaller radar cross-sections of the wrapped cables. The single bounce returns from the deck are not a straight line, but have a slight curvature as expected, and the returns are very strong because of the massive structure of the deck. The double bounce returns from the cables and the deck appear as two straight lines and are totally overlapped as they are all projected down to the ocean surface. The triple bounce returns from the cables are weaker and partially obscured by the strong returns from the deck. The triple bounce returns from the deck have an inverted curvature from that of the direct single bounce return. The alpha angle image obtained by the Cloude-Pottier decomposition is shown in Fig. 2C. It reveals multi-bounce scattering mechanisms of the cables and the deck much better than the display based on the Pauli vector (Fig. 2B). The signatures of the cables are weaker due to wrapped cable and the triple bounce

are obscured by multiple bounce returns from the deck. The strong double bounce in red from the deck is exactly overlaid on that from the cables. The triple bounce from the deck (denoted as “A” for a curvi-linear line in Fig. 2C) in blue has the alpha angles between 0° and 30° , indicative of odd bounce. The triple bounce signature is extended beyond the suspension bridge to the approaching bridges, because the deck is continuous beyond the suspension bridge.

Higher Order Multi-Bounce Scatterings

The two curvi-linear lines (marked as “B” and “C” in Fig. 2C) below the triple bounce signature (marked as “A”) from the deck also show blue color, indicative of odd bounce, in the alpha angle image, but the number of bounces must be higher than three, because their slant ranges are longer than that from the triple bounce. The “B” curvi-linear line below the triple bounce are produced by the path: from the radar \rightarrow ocean surface \rightarrow the bottom of the bridge deck \rightarrow ocean surface (vertically down) \rightarrow the bottom of the bridge deck (vertically up) \rightarrow ocean surface \rightarrow the radar. The total number of bounces is five and could be as high as seven if the bounces from the bottom of the bridge deck were double bounces. We have no detailed information about the structure of the deck, especially its supporting structure under the deck. The vertically downward bounce from the bottom of the deck probably involves a local double bounce, and the same from the ocean surface back to the deck before out to the ocean surface and return to the radar. The total number of bounce becomes seven. From Fig. 2C, this interpretation seems logical judging from the slant range distances among the double bounce signatures, the triple bounce, and the five-bounce signature that we just analyzed. The “C” curvi-linear line below this line involves an additional two bounces from the deck to ocean surface and back to the deck. The distances between these curvi-linear signatures in the alpha angle image support this interpretation. We can also observed two more curvi-linear lines (marked as “D” and “E” in Fig. 2C) below these two, somewhat broken up, but still visible in this alpha angle image. We believe additional bounces between the deck and ocean surface is the cause. Each bounce from the ocean surface weakens the intensity of returns due to scattering from the rough ocean surface. This combination of ocean surface and the understructure of the bridge deck almost forms a “resonant cavity”. The radar returns are delayed by their total path length in this cavity (the number of vertical bounces between bridge and water).

4. Conclusion

In this paper, we presented an example showing the advantage of polarimetric SAR data and polarimetric analysis techniques in interpreting radar signatures of manmade structures. We have demonstrated the importance of multi-bounce scatterings mechanisms that contribute toward the overall complexity of target signatures. We hope that this paper contributes toward understanding and analyzing target signatures by showing how different polarimetric decompositions can be jointly analyzed to more accurately describe detailed scattering characteristics of manmade objects. In this Letter we have concentrated solely on the Store Belt bridge, both during and after construction; however, we hope that this example is indicative of the capabilities of polarimetric SAR and polarimetric decompositions for the analysis of manmade structures. Clearly, the advantages of polarimetric SAR over single polarization SAR have been demonstrated.

References

- [1] E. Krogager, “A new decomposition of radar target scattering matrix,” *Electronic Letter*, Vol. 26, no. 18, pp. 1525-1526, 1990.
- [2] S.R. Cloude and E. Pottier, “A review of target decomposition theorems in radar polarimetry,” *IEEE Trans. on Geoscience and Remote Sensing*, Vol. 34, No. 2, pp. 498-518, March 1996.
- [3] J.S. Lee, D. Schuler, T.L. Ainsworth, E. Krogager, D. Kasilingam, and W.M. Boerner, “On the estimation of radar polarization orientation shifts induced by terrain slopes,” *IEEE Transactions on Geoscience and Remote Sensing*, vol. 40, no.1, 30-41, January 2002.

Implementation of differential repeat-pass SAR interferometry for (i) the search for earthquake precursory land-cover deformation in Taiwan in coordination with the integrated Search for Taiwanese Earthquake Precursors iSTEP' Taiwanese program for promoting research excellence; and (ii) the assessment of land-cover subsidence by ground-water withdrawal and/or sea-water infusion by coastal erosion

Chih-Tien WANG

Center for Space & Remote Sensing Research
National Central University, Jhung-Li, Tao-yuan, Taiwan

Wolfgang-Martin Boerner

Department of Electrical and Computer Engineering
University of Illinois at Chicago, Chicago, USA

Abstract—Worldwide, medium- to short-term earthquake prediction is becoming ever more essential for safeguarding man due to an un-abating population increase, but hitherto there have been no verifiable methods of reliable earthquake prediction developed - except for a few isolated examples of earthquake prediction in China and in Greece. This dilemma is a result of previous and still current approaches to earthquake prediction which are squarely based on the measurement of crustal movements, observable only after a tectonic stress-change discharge (earthquake) has occurred. The prediction models were derived from past histories of measurements, mainly carried out during the past 30 – 40 years, although initiated soon after the San Francisco Earthquake of 1906. During the past decade it was proved and shown that it is not possible to derive reliable models for earthquake predictions from crustal movement measurements alone, and that an entirely new approach must be taken and rigorously pursued over years and decades to come. In support of this conclusion, there have been reported throughout the history of man anecdotal historical up to scientifically verifiable earthquake precursor or “*seismo-genic*” signatures of various kind – biological, geological, geo-chemical and especially a rather large plethora of diverse electromagnetic ones on ground, in air and space, denoted as “*seismo-electromagnetic*” signatures. The existence of all of these signatures can no longer be denied even by the fiercest seismological expert opponents; and it is absolutely high noon that those signatures be more rigorously assessed in order to develop a strategy for designing and carrying out controlled “*seismo-genic*” and “*seismo-electromagnetic*” studies on how to set up world-wide a network of measurement sites for conducting a holistic set of measurements for providing an improved understanding on why and how such precursor signatures are generated, and how and where those may best be observed subject to the rather poor signal-to-noise ratio (SNR), requiring much improved digital instrumentation as time goes on due to the ever increasing man-made electromagnetic noise generation. A number of pilot studies had been initiated, had been supported for a few years, and then aborted because of the high operating costs involved, the poor SNR making signal detection tedious if not impossible with the current state of the art in instrumentation, and because earthquakes don’t appear upon demand. For example such major studies as the USGS/NSF NEHER Program of the early 1990’s after the Loma Prieta M 7 earthquake of 1987; in Japan the ERSFP after the Kobe Earthquake of 1995; in Greece the ongoing electro-potential methods of Varatsov; in China, and in various regions as well as independent states of the former Soviet Union. There exists a rather large number of fiercely competing groups in Russia coming up with their own diversified yet highly incomplete modeling approaches seeking support from the West for unfortunately all too low-cost scientific mercenary services. No clear picture has evolved and should not be expected; and a much wider internationally coordinated investigation is required, which may well last for several decades before a unified approach and with it a solution to this vital problem may be found – if ever. In this overview a systematic analysis of main historical records, a summary of pertinent “*seimo-genic*” as well as observed “*seismo-electromagnetic*” effects and modern ground-based to air- and space-borne metrological signature investigations are presented. Specifically, remote sensing techniques not yet conceived but in urgent need - such as the remote sensing of the groundwater table - for advancing our understanding of this highly interdisciplinary complicated geophysical problem are being identified, and input is sought from participants for possible active future involvement.

Keywords-SAR Interferometry, Repeat-Pass Differential SAR Interferometry, Tectonic Stress Analysis, Earthquake Electromagnetic Precursor Signal Analysis

1. INTRODUCTION

In fact, we need to discover the true intrinsic forces including electrodynamic stress that cause the tectonic plates to move and to undergo continuous gradual as well as abrupt seismic changes, and which are active long to close before the tectonic stress-changes occur. Implementation of novel high-altitude drone (UAV) and space borne satellite RP-Diff-POL-In-SAR will add most essential tools for advancement as will be demonstrated. In support of this conclusion, there have been reported throughout the history of man anecdotal historical up to scientifically verifiable earthquake precursor or “*seismo-genic*” signatures of various kinds – first biological, geological, geo-chemical and then a rather large plethora of diverse electromagnetic ones - on ground, in air and space, denoted as “*seismo-electromagnetic*” signatures. The existence of all of these signatures can no longer be denied even by the fiercest seismological expert opponents – residing especially deep within the hinterland of USA like “*bush*” among trees! Indeed, it is absolutely high noon that those past signatures be more rigorously assessed in order to develop a strategy for designing and

carrying out controlled “*seismo-genic*” and “*seismo-electromagnetic*” studies on how **to set up world-wide a network of measurement sites for collecting a holistic set of measurables**. This is necessary in order to provide an improved understanding on why and how such precursor signatures are generated, and how and where those may best be observed - either in the ground or on the surface through the atmosphere into the ionosphere - subject to the rather poor signal-to-noise ratio (SNR) - requiring much improved digital instrumentation. Again, the addition of implementing novel high-altitude drone (UAV) and space borne satellite RP-Diff-POL-In-SAR imaging technology will become most essential.

2. PREVIOUS AND ONGOING PILOT STUDIES

A number of pilot studies had been initiated in this direction during the past two decades, had been supported for a few years, and then aborted for several reasons. Those are the high operating costs involved, the poor SNR that makes signal detection very tedious if not impossible with the existing state of the art in instrumentation, and the fact that earthquakes just don't appear upon demand, requiring many years and decades until “*they*” happen. One needs to keep at all times in focus the ever persistent opposition of the scientific establishment against us “*radio-seismo-genic-alchemists*”. Several major studies were initiated: the USGS/NSF NEHER Program of the early 1990's after the Loma Prieta M 7.1 Earthquake of 1989 October 19; in Japan, the ERSFP after the 1995 January 17 Hyogo-Ken Nanbu M 7.2 Earthquake near Hanshin, Awaki Island; in Greece, due to continuously reoccurring earthquakes of M 4.5 – 6.0, the ongoing electro-potential methods of Varatsov et al; in China, already before the devastating Yanshin M 8.1 Earthquake [1]; and now also in Taiwan as a result of the Chi-Chi M 7.4 & Chia-yi M 6.8 Earthquakes on 1999 September 21 & October 22/23 in Central-Southwest Taiwan [2]. From the USSR conversion process of the 1990s to present time, many rather un-coordinated group efforts have developed in various regions as well as in some independent states of the former Soviet Union. These efforts have been initiated due to the Spitak M 8.0 Earthquake of March/April 1989 which has been incorrectly considered as the first time that ground-based “*seismo-electromagnetic*” precursors had been observed. This honor goes to Professor Takeo Yoshino of UEC in Chofu-Shi, Tokyo, Japan who observed such “*seismo-electromagnetic*” precursors since the very late 1970-ies at ground and in space. Unpleasant reasons for these misplaced statements are manifold, and will be highlighted in a major forthcoming paper. It is noteworthy and must be reported here that there exists indeed a rather large number of fiercely competing groups within the former USSR. Each group is developing their own diversified, yet highly incomplete modeling approaches while seeking support from the West for “*unfortunately all too low-cost scientific mercenary services*”, which in the current globalization craze result in cutting resources elsewhere. In addition to the research being carried out within the Russian Federation and neighboring independent states like Georgia, Armenia, Kazakhstan, Mongolia, and so on, there also exist several competing teams in China and Japan, and teams in Taiwan and Sumatra which are collaborating more harmoniously. Outranking among all previous multi-year assessment studies was the very productive international outreach oriented one in Japan after the Hanshin Awaji Earthquake of 1995 January 15. This study coordinated by Professor Masashi Hayakawa resulted in four books [1] that may be considered the best collection of scientifically evaluated precursor records; this work should be taken more seriously worldwide. Yet, no clear picture has evolved and should also not be expected to because existing measurement studies are still too sparse, and a much wider internationally harmonious coordinated investigation is required. It may take several decades before a unified approach and solution to this vital problem may be found – if ever.

3. ADVANCEMENTS OF GROUND-BASED TO SPACE-BORNE SEISMO ELECTROMAGNETIC MEASUREMENTS

In order to obtain a much better insight into the worldwide appearance of “*seismo-electromagnetic precursors*”, it would seem most essential to upgrade the existing INTER-MAG magnetometer network (only records up to frequencies of 0.1 mHz are collected and stored on venerable magnetic tapes) by adding 3-axis flux-gate magnetometers (able to operate up to several Hertz) at each of the INTER-MAG stations worldwide. This was already proposed more than fifteen years ago by the late Dr. Arthur William (Bill) Green, the colleague of Dr. Wallace Campbell and former director of USGS-GRF in Golden, CO. Such an upgrade is costly but highly desirable also for various other reasons, and now feasible with the highly improved ELF/ULF digital signal recording plus centralized telemetric collection, storage, analysis and processing systems, which did not exist only fifteen years ago, when Bill Green strongly recommended such studies. With it several sub-oceanic recording INTER-MAG recording stations require also to be upgraded. In order to assess any lithospheric to mesospheric to ionospheric precursor interaction effects such vital important continuous 3-axis magneto-metric records up to several Hertz must be obtained and the frequency bands of measurement and data storage must be extended to about 20 Hz. Note that Bill Green did not observe any seismo-electromagnetic signatures below 10 mHz but above 100 mHz, which appears to apply to all earthquakes; and since very few or no measurements were conducted on a standardized continuous manner with only a very few exceptions and then only for short periods of time within this ELF/ULF frequency band of 10 mHz to about 20 Hz as is here desired, these vital “*seismo-electromagnetic precursors*” signatures were inadvertently not or only very incompletely and rarely being observed [2]. Prime emphasis must also be given to ionospheric precursor observations, which are summarized well in the various book-reports by Hayakawa et al [1]. There exist a few pertinent newly discovered types of observations, which need to be further explored such as the flare-up of ionosphere-bound lightning discharges, the “*sprites (or Spritzer – according to Schumann)*”, in addition to the observable earth-bound lightning- strokes “*Blitz*” located above highly ionized clouds generated during the early phases of final localized tectonic stress culmination close to epicenter regions. These phenomena require subtle additional studies and coordinated coincident ground to space recordings as proposed in several papers by Hayakawa, Yoshino in Japan, and others in China and Taiwan.

More so, remote sensing techniques - not yet conceived but in urgent need – are much sought for. An example is the remote sensing of the groundwater table with the tracking of sub-surface fluid flow [3]. The implementation of existing well established historical records collected by utilities worldwide is in desperate need. They are required for advancing our understanding of this highly interdisciplinary, complicated geophysical problem. Input is sought for highly expanded international collaboration and possible involvement for a major long-lasting global pilot study to be carried out simultaneously at several “*seismic hot spots*.” The common saying of “*Detecting Groundwater from Satellite Platforms*” is highly misleading in that the referenced satellite SAR and/or GRACE techniques only permit the very coarse recognition of the top layers of sub-surface surface water – at most down to a meter, and not much deeper. Entirely novel techniques for identifying and tracking the fluid flow at depths down to several hundreds of meters are desired. This remains to be a very essential research task of the twenty-first century, and of paramount relevance to these kinds of “*seismo-genic and seismo-electromagnetic precursor*” investigations. Closely related to the detection of sub-surface fluid-flow is the bulging and subsidence of surfaces before, during and after tectonic stress change events which need not necessarily be catastrophic. This can now be achieved with implementation of air/high-altitude/space-borne RP-Diff-POL-In-SAR imaging. As regards the acquisition of satellite SAR measurement data sets, the space-launched ALOS PALSAR, the forthcoming RADARSAT-II and TERRASAT-1&2 fully polarimetric sensors will play an essential role, and ought to be fully integrated in all of the forthcoming studies [4].

4. DEVELOPMENT OF MULTI-MODAL SYNTHETIC APERTURE RADAR (SAR) IMAGING TECHNOLOGY IN AIR AND SPACE

Decisive progress was made in advancing fundamental POL-IN-SAR theory and algorithm development during the past decade, which was based on the underlying accomplishments of fully polarimetric SAR and differential SAR interferometry and its current merger. This was accomplished with the aid of airborne & shuttle platforms supporting single-to-multi-band multi-modal POL-SAR and also some POL-IN-SAR sensor systems, which will be compared and assessed with the aim of establishing the hitherto incomplete but required missions such as tomographic and holographic imaging. Because the operation of airborne test-beds is extremely expensive, aircraft platforms are not suited for routine monitoring campaigns. These are better accomplished with the use of drones (UAV). Such unmanned aerial vehicles (drones), hitherto developed mainly for defense applications, are currently lacking the sophistication for implementing advanced forefront POL-IN-SAR technology. This shortcoming will be thoroughly scrutinized resulting in the finding that we do now need to develop most rapidly also POL-IN-SAR drone-platform technology because low to medium altitude aircraft platforms cannot be deployed in severe weather conditions. Thus, drones are required in order to develop algorithms for RP-Diff-POL-IN-SAR environmental stress change monitoring. High altitude drones are necessary for a great variance of applications beginning with flood, bush/forest-fire to tectonic-stress (earthquake to volcanic eruptions) for real-short-time hazard mitigation. For routine global monitoring purposes of the terrestrial covers neither airborne sensor implementation - aircraft and/or drones - are sufficient; and therefore multi-modal and multi-band space-borne POL-IN-SAR space-shuttle and satellite sensor technology needs to be further advanced at a much more rapid pace. The existing ENVISAT and most recently launched ALOS-PALSAR will be compared with the forthcoming RADARSAT-2 and the TERRASAT-1&2, demonstrating that at this phase of development the fully polarimetric and polarimetric-interferometric SAR modes of operation must be treated as preliminary algorithm verification support, and not to be viewed as routine modes. The same considerations apply to the near future implementation of any satellite-cluster bi/multi-static space-borne tomographic imaging modes, which must however be developed concurrently in collaboration with all major national or joint continental efforts in order to reduce spending and the proliferation of space-platforms. Prioritization of developmental stages will be assessed according to applications, and will differ for air-borne to space-borne sensors with the aim of developing a permanently orbiting fleet of equidistantly space-distributed satellites similar to the GPS configuration, and each being equipped with the identical set of multi-band POL-IN-SAR sensors [4 - 7].

5. IMPLEMENTATION OF RP-DIFF-POL-IN-SAR ENVIRONMENTAL STRESS-CHANGE MONITORING FOR THE ANALYSES OF EARTHQUAKE EPISODES IN TAIWAN WITH SUBSEQUENT LAND-COVER SUBLIMATION AND BULGING

Taiwan is an island located in the ‘Circum-Pacific Seismic Belt’ subjected to the ongoing collision of the Philippine-Sea and the Eurasian Plates, and it experienced disastrous earthquakes in the past. The electromagnetically inter-related Chi-Chi (990921: M = 7.6) - Chia-Yi (991022/23: M = 6.8) earthquakes, which caused a total loss of more than 2500 lives, the collapse of more than 100,000 household dwelling-units, several bridges and major highways, hydro-electric dams and electric power-line distribution systems along the affected Chelungpu fault [1 – 3]. The incessant plate collision implies that Taiwan will inevitably face earthquake hazards in the future and for a very long time to come. Earthquakes unfortunately cannot be forecasted today for various reasons, one being the past lack of integrated wide-area ground-based, air- and space-borne sensing and imaging. Taiwan and its environs to the East have, are, and will be experiencing seismic activity on a very wide scale from millions of small to several truly large earthquakes a year, Taiwan is ideally suited for embarking on a long-lasting major Earthquake Hazard investigation program. In comparison with other similar seismically active regions of the two major terrestrial seismic belts, Taiwan is relatively small, compact in shape, sits on top of two violently colliding plates. In comparison to other highly populated earthquake regions, it is still rather virgin as regards electromagnetic background noise. Therefore, it was decided appropriate to initiate a National Taiwanese Program for Excellence in University Research on the subject of “Research on Seismo-Electromagnet Precursors of Earthquakes” entitled ‘*Integrated Search for Taiwanese Earthquake Precursors – iSTEP*’ at the National Central University (NCU) in Chung-Li,

Tao-Yuan, Taiwan [3]. In support of the well developing iSTEP ground-based magneto-metric seismo-genic signature measurements [2], the SAR Image processing and analysis group of the NCU CSRSR (Center for Space & Remote Sensing Research) have embarked on a rigorous program for producing a large set of RP-Diff-In-SAR overlay interferometric images that show the temporal stress-change history of up to six months in advance of the Chi-Chi (990921; M = 7.6), during the electromagnetically exceedingly active time-period until the two major aftershocks of the Chia-yi (991022/23; M = 6.8) earthquakes occurred, and thereafter for several months [3]. Every effort is now being made for correlating the time-sequential ground-based "seismo-electromagnetic" signatures with the corresponding set of RP-Diff-In-SAR overlay interferometric images. In addition, associated land-cover subsidence and bulging episodes plus resulting mud-avalanches will be scrutinized and interpreted. In addition, the assessment of land-cover subsidence by ground-water withdrawal and/or sea-water infusion by coastal erosion as it pertains to the Taiwan West coast will also be investigated.

6. CONCLUSION

It was shown that several electromagnetic precursors associated with earthquakes provide essential information on tectonic stress change events which when correlated with high resolution RP-Diff-POL-IN-SAR imaging of crustal deformation will bring us closer to developing more reliable earthquake prediction methods. Specifically, the application of repeat-pass SAR interferometry proves to provide a useful high resolution tool for monitoring different types of crustal deformation in spite of the difficulties encountered from the dense subtropical vegetation in an area such as Taiwan. The results obtained come with unprecedented spatial density and compare favorably with other approaches including geodetic DEM variations derived from GPS networks [3, 4]. The knowledge gained from the Chi-Chi and Chia-Yi earthquake duplet has opened new approaches to combine electromagnetic and seismic earthquake analyses of the future.

ACKNOWLEDGMENT

The outstanding contributions by members of the National Central University (NCU), iSTEP (integrated Search for Taiwanese Electromagnetic Earthquake Precursors) team of Jhonli Taoyuan, Taiwan; and especially of Professors Kun-Shan Chen, Jann-Yenq (tiger), Chung-Pai Chan, and especially of Dipl. Ing. Chie-Tien Wang is gratefully acknowledged. We are grateful for the continuing interest in our research of Professors Masashi Hayakawa of the University of Electro-Communications at Chofu-Shi, Tokyo, Japan as well as of Professor Katsumi Hattori of the Chiba University, Kanto District, Japan.

REFERENCES

- [1] M.Hayakawa, (Ed.), 2006, Proceedings of IWSE-05 (International Workshop on Seismo-Electromagnetics), University of Electro-Communications, UEC Chofu-Shi, Tokyo, Japan, 2005 March 15 – 17, TERRAPUB, Tokyo, (in final printing)
- [2] Tsai, Y.-B. and J.-Y. Liu, (Eds.), 2004 Special Issue on Earthquake Precursors, TAO (Terrestrial, Atmospheric and Oceanic Sciences), Vol. 15, No. 3, I-IV, publ. by Meteorol. Society of Taiwan (ROC), Taipei, 564p.
- [3] Chang, C.-P., Chen, K.-S., Wang, C.-T., Yen, J.-Y., Chang, T.-Y., and Lin, C.-W., 2004, Application of space-borne radar interferometry to crustal deformations in Taiwan: A Perspective from the Nature of Events, TAO, Vol. 15 (3), Sept. 2004, pp. 523 – 543.
- [4] Boerner, W-M, 2003, "Recent Advances in Extra-wide-band Polarimetry, Interferometry and Polarimetric Interferometry in Synthetic Aperture Remote Sensing, and its Applications, *IEE Proc.- Radar Sonar Navigation, Special Issue of the EUSAR-02*, vol. 150, no. 3, June 2003, pp. 113-125
- [5] Boerner, W-M., H. Mott, E. Lüneburg, et al., 1998, "Polarimetry in Radar Remote Sensing: Basic and Applied Concepts", Ch. 5 (pp. 271-357) in F.M. Henderson & A.J. Lewis, (eds.), Principles and Applications of Imaging Radar, vol. 2 of Manual of Remote Sensing, (ed. R.A. Reyerson), 3rd Ed., John Wiley & Sons, New York, 940 p, ISBN: 0-471-29406-3.
- [6] Massonet D. and K.L. Feigl, 1998, "Radar Interferometry and its Application to Displaying Stress-Changes in the Earth's Crust", *Review of Geophysics*, vol. 36(4), 1998 Nov, pp. 441-500.
- [7] Cloude, S. and K. Papathanassiou, 1998, "Polarimetric SAR Interferometry", *IEEE Trans. Geosci. Remote Sensing*, vol. 36 (4), pp. 1551-1565 (also see: Papathanassiou, K.P., "Polarimetric SAR Interferometry", 1999, Ph. D. Thesis, Tech. Univ. Graz (ISSN 1434-8485 ISRN DLR-FB-99-07), Graz, Austria).

How Infrasonic Imaging, HF-Surface radar & HF-OTHR and GPS Technology can favorably be implemented for detecting the On-set of Tsunamis and the real-time imaging of its spreading

Wolfgang-Martin Boerner

Department of Electrical and Computer Engineering
University of Illinois at Chicago, Chicago, USA

Abstract: Worldwide, medium to short term tsunami prediction is becoming ever more essential for safeguarding man due to an un-abating population increase within low-lying coastal regions of all of the affected oceans. But hitherto there have been no verifiable methods of reliable tsunami prediction developed - except for a few isolated examples of placing arrays of costly short-lived sensors along the ocean bottom requiring monthly re-calibration efforts. This dilemma is a result of not yet having identified the proper approaches to tsunami prediction. The question on whether there do exist reliable prediction methods was answered long ago by fauna living within the coastal littoral zone that is affected by tsunamis. Especially during the last devastating "Boxing Day 050426 Tsunami" caused by the Sumatra-Andaman "Super-Earthquake" of $M = 9.3$ with epicenter near Simeulue Island, there were many verifiable episodes on how fish escaped the affected coastal region in time; the elephants, water-buffalos and other non-domesticated animals rushed for higher ground locations well in time before the tsunami crest and subsequent swells approached, and so on. These observations provide proof that some electromagnetic or, more likely, infrasonic local warning signatures are received by these creatures relatively long before the approaching tsunami strikes. We presume that the signatures could be infrasonic waves traveling at high speeds as under-water surface waves that could be detected by marine fauna as well as coastal animals and birds. Tsunamis have existed for millions of years and fauna of the affected coastal region has developed instinctive warning mechanisms that we need to explore. Another promising natural sensor may utilize electromagnetic precursor signatures that yet need to be fully discovered. Both, the role electromagnetic phenomena and the role infrasonic signatures will be scrutinized. The results of successful post-event model reconstructions of viable electromagnetic and infrasonic precursor signatures will be presented.

1. Introduction

The two largest super-earthquakes along the Indo-Australian and southeastern Eurasian plates of the past forty years provided invaluable rich precision measurement data – seismic, electromagnetic and infrasonic in nature – as well as satellite altimeter recordings which are here being scrutinized for developing a viable hazard mitigation approach for the inevitable reoccurring tsunami hazards [1]. The first of these devastating candidate earthquakes occurred at the southern extension of the Nicobar – Andaman island chain on "Boxing-Day 2004" ($M = 9.3$, 00:58:53 UT, 3.3° N, 96° E) near Simeulue Island causing a rupture of about 1300 km with a 10 m vertical subduction slip at the depth of 30 km along the Andaman Microplate of the East Indian Ocean all the way up to Myanmar (Burma). It resulted in more than 290,000 deaths and over 3,000 coastal villages being almost completely destroyed along the shores of the Eastern Indian Ocean. The second earthquake episode occurred on 2005 March 23 ($M = 8.7$ (+ 8.6), 16:09:36 UT, 21° N, 97.8° E) at the slightly more southern island of Nias as the main aftershocks of the main shock, which were not vertical but a lateral slips, thus generating only minor tsunamis. The total energy released by these two electromagnetically related earthquakes exceeded 4.3×10^{18} Joules (equivalent to a 100+ Giga-ton nuclear explosion), being equivalent to energy consumed within 10 months in the extended EU. The vertical slipping finally reached after several months a cumulative slip of 16 m near Banda Aceh at the northern tip of Sumatra. This super-earthquake episode displaced more than 30 km^3 of sea-water, raising the global ocean sea level by .2 mm, and enlarging the average earth radius by 2.3 cm [1, 2].

The main shock caused a generation of vertical tsunami waves traveling in all directions from its origin at Simeulue Island into the Indian Ocean with average ocean wave height of about 1 m; reaching into the mouth of the Malacca Strait, into the northern reaches of the Bay of Bengal, into the western Indian Ocean up to Somalia and into the Arctic Ocean, finally reaching the Pacific as well as the Atlantic oceans. It was recorded that the tsunami crest heights exceeded 10 m, and subsequent swells reached 15 m at a few shore locations, whereas the receding anti-swells were dipping down by more than 12 m at some large coves with 10 m dip in average.

2. Other recent terrestrial tsunami in comparison to the 2004 Simeulue $M = 9.3$ and the 2005 Nias $M = 8.7$

During the past fifty years there were other major devastating tsunamis of comparable sizes to the candidate super-earthquakes such as those, for example, in 1952 at the Kamchatka, $M = 9.1$; in 1957 at Andreanov Island $M = 9.2$ in

the Aleutian islands; the most devastating 1960 Southern Chile $M = 9.4$; the 1964 Prince William Sound $M = 9.1$ near Anchorage, Alaska. These super-earthquakes ruptured mega thrust plate boundaries similar to the Sumatra-Andaman event along the Andaman micro-belt subduction zones. These and previous and/or future giant earthquakes occur where large oceanic plates under-thrust continental margins involve fault zone areas, typically 200km wide and by +/- 1000 km long with 10 + m vertical slips. Past history shows that one of the most active subduction megathrust plate boundaries is along the Indo-Australian Plate along the Andaman Microplate extending from southwestern Sumatra via the Andaman Miniplate to north of Myanmar (Burma) into the Himalayan eastern frontal thrust with giant earthquakes of $M > 8.7$ at 20 – 60 year repetition rates [1, 2]. Commonly, these major main shocks – causing the tsunami due to the vertical slip - are followed by duplets of lateral shift aftershocks rarely generating additional major tsunamis. Only most recently was it discovered that there exist major geo-electromagnetic forces creating abnormally super-high variations of the local geo-magnetic fields which appear as if they were caused by equivalent subsurface current sources, below 10 – 30 km, exceeding 10^6 Amperes. These findings need to be explored in greatest detail during forthcoming giant megathrust plate earthquake episodes subject to improving the global geomagnetic measurement network.

However, not all earthquakes generate tsunami and those that do must satisfy certain characteristics [3]:

- the epicenter must lie underneath or near an ocean subduction zone
- fault vertical movement of the sea floor must be of several meters (6 – 10 m) over a large area ($\sim 30,000 \text{ km}^2$ to over $100,000 \text{ km}^2$) and of great length (300 – 1000 km and more)
- the main-shock magnitude must be high (above 7.5) and of shallow focus (less than 40 km)

A tsunami consists of a series of acoustic ocean waves of extremely long wavelength generated mainly by earthquakes occurring below or near the ocean floor causing vertical slip deformation. The associated wave motions are of three major types [3]:

- *Sound waves*
 - Longitudinal compressional waves
 - Compression-rarefaction waves
 - Common acoustic water waves
- *Vertically transverse waves*
 - Light waves
 - Gravity waves
- *Horizontally transverse waves*
 - Rossby waves

Ocean waves need to be distinguished by their wavelength: extremely long (tsunami) versus very short (capillary) waves:

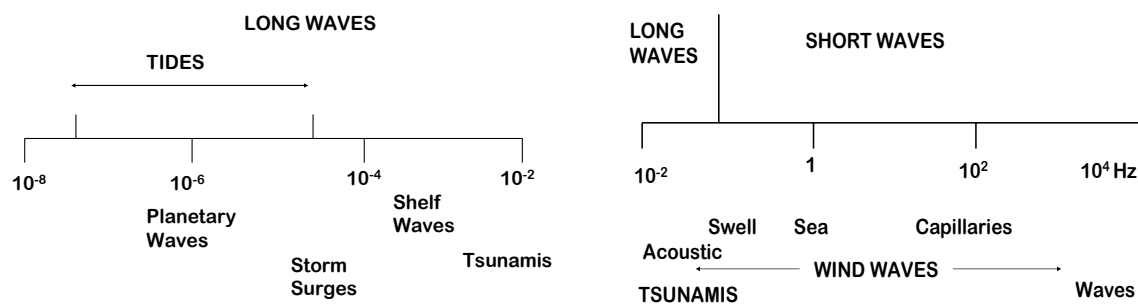


Fig 1, Spectra of short and long waves (in Hz)

For the vertical transverse tsunami waves the velocity is given approximately by $v_t \sim (g D)^{1/2}$ with g denoting acceleration due to gravity (gravitational constant), and D the averaged local ocean depth, respectively. Thus, the deeper the ocean, the faster the tsunami wave will travel. At a depth of 7 km the velocity reaches about 950 km/hr with a wavelength of about 290 km, whereas at a depth of 2 km the velocity reduces to 500 km/hr with a wavelength of 150 km. As the tsunami travels across the ocean, the velocity and the wavelength change proportional to ocean depth – at times slow and then also very rapidly depending on the ocean bottom topography – and once it reaches shallower inclined, slowly sloping coastal transition zones at about 10 m depth, the velocity reduces to about 36 km/hr with a wavelength of about 10 km. Meanwhile the wave height increases sharply from less than a meter at

depths of about 5 km to several meters, reaching heights of 15 to 20 m [4]. In summary, the tsunami on a wide open ocean consists of a series of traveling waves that may last for hours. The enormous outflow of coastal water, succeeding the approaching tsunami crest and that of subsequent tsunami waves, usually cause more damage than the incoming wave fronts; and the first crest reaching several meter height is not always the largest and is commonly superceded by the second and third approaching tsunami waves depending on the local coastal ocean bottom slope characteristics. Thus an approaching tsunami displays three general appearances [1 - 4]

- a sudden fast rising tide
- a subsequent withdrawal of coastal ocean sea water
- a cresting wave of steep and almost vertical slope of several meters height
- a series of bores with step-like changes in water level rises that advance rapidly and with slow intermittent withdrawals at times of several minutes up to 20 minutes of the coastal inundating water in between that can last for several hours.

3. Continental Drift and Plate Theory – expansion of terrestrial planet caused by continuing successive super-earthquakes and tsunami

Both large earthquakes and tsunami make themselves felt around, through and across the entire terrestrial sphere, deep down into the mantle and high up through the atmosphere, mesosphere and beyond the ionosphere. It was Alfred Wegner who first explored and introduced the Continental Drift concept in 1912 also discovering most of the boundaries between plate zones, assuming a constant earth radius. It was then Ottmar C. Hilgenberg in 1932 questioned the constant earth radius postulate, demonstrating that an early “*crustal earth model*” of one third of the current earth-radius could be assumed and that all continental blocks could be adjusted in a puzzle-fit manner on the assumed model surface. The model of an expanding earth with coincident creation of the oceans was revived in the 1960’s together with the modern tectonic plate theory including plate subduction, lateral shifts, rotations, and so on [5].

In the meantime, seismological metrology and instrumentation technology have advanced to almost the physical limits of perfection, and a global seismic network with digital equipment is in place. The existence of such an enormous global network of seismic instrumentation on ground and also on the ocean sea bottom came very handy for collecting extremely precise and exhaustive seismic signatures for the two great earthquakes at Simeulue of 2004 December 26 and the aftershock duplet at Nias of 2005 March 28 plus all the intermittent and post-event earthquake swarms. The observed seismic signatures assisted in obtaining a highly improved solid earth model of the earth’s interior; and the observed earth’s free oscillations, lasting for a very long time (over one year), allowed the precise determination of the earth’ surface height increase by about 0.1 mm, the ocean sea surface increase by about 0.2mm, and that of the earth’s mean radius by slightly more than 2.3 cm [1]. So we may conclude that with every giant earthquake and resulting tsunami the earth is expanding in surface area, ocean water volume and radius which require further analyses. However, the state of perfection of geo-electromagnetic instrumentation and of a global geo-electromagnetic measurement network, which allows precise polarimetric 3-axis geomagnetic flux-gate measurements from at least 10 mHz up to about 20 Hz is unfortunately in a very poor and imperfect state. The existing INTER-MAG (enabling total power measurements of the quasi-static geo-magnetic field below 0.1 mHz) is of little use because seismo-geoelectromagnetic signatures do not exist at frequencies below 10 mHz. The desirable global geo-electromagnetic metrology network (10 mHz up to about 20 Hz) does not exist, must be added and created in order to obtain a complete understanding of the intricate tectonic stress-change events which are directly coupled to geo-electromagnetic phenomena - still to be explored throughout this twenty-first century.

4. Geo-electromagnetic Ground to Ionospheric Disturbances due to Earthquakes and Tsunami

In a companion paper it was deliberated that there exist undoubtedly verifiable geo-electromagnetic phenomena at the lithospheric to ionospheric levels that can be related to earthquakes. The underlying phenomena are not at all understood and require extensive local to global research investigations and with it highly improved geo-electromagnetic instrumentation.

It is well known that the ionosphere can be affected by a great variety of external disturbances such as the solar wind and the inter-galactic magnetic field variations with subsequent solar-magnetic storms, and so on, as well by internal (to ionosphere) earth generated phenomena such severe weather with mega-volt lightning discharges to ground (*Blitz*) and to the ionosphere (*Spritzer – sprites*); including cyclones (*hurricanes or typhoons*), activating and active volcanoes, and so also due to major tectonic stress-changes like earthquakes with at times subsequent tsunamis [6, 7]. Although the ionosphere is primarily affected by solar and magnetic disturbances, while solid earth phenomena are

generally minimal in comparison; there now exists increasing verifiable evidence observed by ionosondes and high frequency (HF) Doppler radar sounding systems that at times strong transient disturbances occurred in the ionosphere as a result of various tectonic stress-changes and especially the greater and in particular the giant earthquakes such as the Simeulue of 2004 December 26 and the aftershock duplet at Nias of 2005 March 28 plus all the intermittent and post-event earthquake swarms [1, 2, 8].

More recently, aeronomists analyzing high precision data recorded at numerous ground-based cartographic mapping stations of the Global Satellite Positioning Systems (GPS (USA), GLONASS (RF), GNSS (EU)) have observed ionospheric disturbances of the electron content of the ionospheric E & F layers, and the total electron content (TEC) triggered by various tectonic stress-changes including earthquakes and volcanic activation phenomena as well as the vertical transverse acoustic/gravitation tsunami waves [6 - 9]. As regards the tsunami waves, acoustic gravity waves generated at the ocean sea surface travel vertically through the atmosphere, mesosphere and interact with the E & F-layers causing ionospheric disturbances. The time varying TEC along the slant range from the HF Surface Radar (HFSR) as well as Over-The-Horizon HF-Radar (OTHR) toward the affected ionosphere and from GPS-Satellite to a ground-based receiver station can be employed to detect far-distant ionospheric variations above the locally activated tectonic stress-change (earthquake) or tsunami region, denoted as the Tsunami Ionospheric Disturbances (TID). Approximating the ionosphere shell height as 350 km in the equatorial region, then the intercept of the slant path on the ionospheric shell surface can serve as a monitoring station floating at an ionospheric point above the tsunami wave peak location [8]. As regards the transient tsunami description, it is then possible not only to determine the local tsunami wave-peak-point along its outward traveling route but at the same time the associated velocity of travel, except that the TID peak lags the tsunami by several minutes when the GPS approach is implemented due to a time lag in charging up the E & F layers.

5. Comparison of results implying the GPS and the HF-Radar approaches

Several independent research teams, first in Japan (Masashi Hayakawa et al.) [6] and in Taiwan (Jann-Yenq (*Tiger*) Liu et al.) [7, 8], then in Indonesia [9] and in India (A. DasGupta et al. [10] and A. K. Gwal et al. [11]) and now also elsewhere [3], analyzed the GPS signature variations due to the “*Boxing Day 2004 Tsunami*” and calculated the resulting TID from which they determined its travel history including travel speed and the time-dependent local tsunami wave peak location. Here the results obtained by the first four research groups will be compared and analyzed using “*Tiger Liu’s*” method [8] as base standard; and it was found that all of the major approaches provide similar results. Although the HF Surface Radar and OTHR systems provided real time imaging, only qualitative results can be shown here due to the ‘*closed nature*’ of the imaging systems and the real measurement data not being made available for open distribution [12].

In addition, there exist several other proposals for space borne satellite constellations of altimeters utilizing various orbiting satellite navigation and altimeter systems for mapping tsunami fronts across the oceans. One such proposal is the PARIS concept of ESA based on a passive reflectometry and interferometry approach (ESA Journal, 1993 December) implementing a constellation of 10 PARIS altimeters with the use of GPS, GNSS, Egnos, Galileo and GLONASS which deserves further attention [13].

6. Infrasonic surface wave detection of traveling tsunami wave peaks

The highly efficient infrasonic method for detecting close (several km) to far distant (several 1000 km) impulsive and turbulent disturbances for implementation in peaceful applications was long overlooked [14].

Infrasound is the range of acoustic frequencies below the audible range - typically below 25 Hz [lowest frequency on a piano keyboard is A¹ 27.5 Hz, and an acoustic frequency of 1 Hz is 8 octaves below middle C⁴ of 261.63 Hz (according to the American scale)] - where the thresholds of human hearing and feeling cross over. Large animals like elephants, rhinoceros, moose, water buffalo, and so on, may be able to detect and recognize frequencies well below the human audible threshold, down to several Hertz within the near infrasound range. There exists a rational analog between sound and the relationship of infrasound to light. Thus, one may call the frequency range 1 (3) – 20 (30) Hz near infrasound – similar to near infrared - and the range from about 0.05 (0.03) – 1 (3) Hz infrasound; and below 0.03 Hz, where gravity becomes important for propagation, and atmospheric waves are commonly denoted as acoustic/gravity waves, and so on [14]. A critical breakthrough for being able to measure infrasound was the development of effective noise and turbulence reduction methods which was achieved in the early 1960’s by introducing noise-reducing pneumatic line-microphones consisting of impedance-matched resonant pipes along a pneumatic hose. An infrasonic noise reducer and signal receiver looks very much like an octopus with the center

head section containing the electronic signal reception and pre-processing electronics from which up to twelve black porous hoses up to 30 m (50 m) in length are protruding straight outwards with equisectorial radial spacing of 30°, and resonant pipes of differing height (like organ pipes) and ports spaced along this acoustic transmission line about 20 cm apart and covering a planar radial area of 60 – 100 m diameter. Several of these basic noise reducers are laid out in linear or circular patterned arrays depending on application, and a rather complex signal collection and processing system was developed in order to detect minute acoustic disturbances over a semi-spherical observation space with highest directional (a few grade-seconds) and very large radial distances (n1000 km) and high detection accuracy (several meters). Great efforts have been and are currently further expended by Professor Dr. Alfred J. Bedard of the University of Colorado, Center for Interdisciplinary Research in Environmental Sciences (UC-CIRES) – formerly with NOAA-ETL Infrasonic & Acoustic Sensing Laboratory - for further advancing these infrasonic high resolution imaging techniques for detecting severe down-bursts, avalanches, tornadoes, explosions, moving vehicles at close to far distant ranges including meteor impacts with the ionosphere, and so on [14 – 16]. By combining Polarimetric Meteorological Radar & Infrasonic Array sensor technology, severe storm analyses including the early detection of tornadoes were advanced [17]. In particular, the far distant detection of earthquake episodes, of activating volcanoes, and also of tsunami frontal movements - from shore side sensor locations - was demonstrated [14 – 16].

Extensive high precision Infrasonic Arrays have also been deployed in all of the major oceans – the Atlantic, the Pacific, the Indian, the Arctic and the Antarctic Oceans – as part of the International Monitoring System (IMS) of the Comprehensive Nuclear-Test-Ban Treaty (CTBT), and have been in use for the past thirty or more years. It turned out from long-term uninterrupted continuous around-the-clock monitoring operations that these rather humongous instrumentation facilities are very well suited for detecting close to far distant earth & sea quakes, volcano activation and also tsunami events. There also exist several of these Infrasonic Arrays in the Indian Ocean and down to the adjacent Antarctic Ocean [18] which were able to detect infrasonic signatures created by the candidate tsunami – (i) the arrival of seismic P, S, T waves of the earthquakes at Simeulue on 2004 December 26 and the swarm of immediate mini-aftershocks as well as those of the Nias main aftershocks of 2005 March 28, and so on; (ii) the direct incoming responses from the outward radiating front of the tsunami wave peaks, across the Indian into the Ant-arctic Ocean; (iii) secondary and tertiary arrivals of ducted acoustic gravity waves through the atmosphere, in the ocean, coupled into ocean bottom and re-appearing again, and so on. Although it was found that there exist subtle differences of the observed candidate signals between the low infrasonic range of 0.02 (0.03) Hz – 0.1 (0.3) Hz, the medium range of 0.3 (0.5) – 3 (5) Hz, and the upper range or near infrared range of 3 – 20 Hz, responses were received for all of the candidate Simeulue and Nias events, respectively, with signal strength of the much smaller Nias tsunami being far less than that of the mighty Simeulue tsunami [18].

The tsunami source location near the earthquake epicenters, in conjunction with the unique signatures observed at the various Infrasonic Array stations of the Indian and Antarctic Oceans, strongly suggest that Infrasound combined with other HF-radar, OTHR and GPS techniques such as the PARIS concept [13], may provide an essential discriminator for tsunami genesis and tsunami wavefront propagation.

7. Conclusions and Recommendations

We have introduced for consideration various viable geo-electromagnetic ionospheric HF-Radar, OTHR, and GPS dynamic monitoring techniques for determining the outward radiating front of the ocean sea surface tsunami wave peak, complimented by the novel Infrasonic Imaging technique for disturbances that may be related to tsunamis. Indeed, extensive fundamental research is now in desperate need for advancing our understanding of these promising techniques which at the same time will require the dedicated advances of instrumentation, real time in situ processing and interpretation techniques. In addition, there exist various novel ground-based electromagnetic precursor signature recording techniques within the ULF/ELF electromagnetic frequency ranges as well as the RP-Diff-POL-IN SAR high-altitude drone and space borne satellite methods – discussed in another companion review paper – which need to be integrated for ultimately discerning the proper hazard mitigation inputs. Thus, we do not at all agree with the common view adopted by venerable seismologists that earthquake and tsunami prediction can never be done and is out of reach - albeit based on their seismological approaches only. Yes, we agree that “*Natural hazards are inevitable*”, but we are confident to state that also in the case of earthquake and tsunami hazards we can reduce the impact of natural disasters which are not inevitable subject to implementation of alternative electromagnetic and infrasonic sensor modalities in order to utilize hitherto neglected seismo- electromagnetic, GPS, HF radar and infrasonic signatures which were scrutinized in this and the companion overview papers.

8. Acknowledgements

This research pursuit was initiated over the past two decades during close interactions with Alfred (Al) J. Bedard, a pioneer of infrasonic imaging technology, and with Eugene (Gene) A. Mueller, a pioneer of POL-METEO-RAD investigations. By combining Polarimetric Meteorological Radar and Infrasonic Array sensor technology, severe storm analyses including the early detection of tornadoes were advanced. Based on this close collaboration, WMB's interest in pursuing other applications of combined Infrasonic and Polarimetric Transient Doppler Radar including co-registration with HF-Radars resulted in collaboration with Dr. Stuart J. Anderson at DSTO of Australia. In addition, during repeated and extended research interaction tenures since 1970 in various East-Asian research centers, WMB got deeply involved in seismo-electromagnetic research studies on earthquake precursor signatures which for the past ten years included tsunami research in Japan, Taiwan and now also in Indonesia, and India. The continuing strong interaction with his East and South Asian collaborators is gratefully appreciated.

9. References

- [1] Hanson, B. (Inv. Ed.), 2005, Special Issue on « *The Great Sumatra-Andaman Earthquake – Learning from Natural Disasters* », Science, Vol. 308, No. 5725, pp.1125 – 1146, 2005 May 2005: see separate papers
- [2] Widarto, D. S., 2006, Lithospheric Seismo-electromagnetic phenomena in the Great Sumatran Fault Zone, Indonesia, in preparation (Report of LIPI, Geophysical Institute of Indonesia, Bandung, Indonesia).
- [3] Murty, T. et al., 2006, Vertically transverse long gravity waves in the ocean as a natural hazard, Overview presented at the IGU Annual Convention, Bhopal, India, 2005 December 06 – 09 (to be included in the proceedings).
- [4] Chadha, R. K., 2006, Vulnerability of the Indian coast to Tsunami Threat, Overview presented at the IGU Annual Convention, Bhopal, India, 2005 December 06 – 09 (to be included in the proceedings).
- [5] Sen, S., 2006, EARTH – the planet extraordinary, Overview presented at the IGU Annual Convention, Bhopal, India, 2005 December 06 – 09 Overview presented at IGU Annual Convention, Bhopal, India, 2005
- [6] M.Hayakawa, (Ed.), 2006, Proceedings of IWSE-05 (International Workshop on Seismo-Electromagnetics), University of Electro-Communications, UEC Chofu-Shi, Tokyo, Japan, 2005 March 15 – 17, TERRAPUB, Tokyo,
- [7] Tsai, Y.-B. and J.-Y. Liu, (Eds.), 2004, Special Issue on Earthquake Precursors, TAO (Terrestrial, Atmospheric and Oceanic Sciences), Vol. 15, No. 3, I-IV, Meteorol. Society of Taiwan (ROC), Taipei, 564p.
- [8] Liu, J-Y. (Tiger), et al., 2006, Ionospheric GPS TEC disturbances triggered by the December 26 2004 Indian Ocean tsunami, Proceedings of IWSE-05 (International Workshop on Seismo-Electromagnetics), UEC Chofu-Shi, Tokyo, Japan, 2005 March 15 – 17, TERRAPUB, Tokyo, (in final printing), 8 p.
- [9] Widarto, D. S. et al, 2006, Seismo-Electromagnetic Signatures Associated with the Earthquakes During the Period of 1997-2000 in the Southern Part of Sumatra Island, Indonesia, Proceedings of IWSE-05 (International Workshop on Seismo-Electromagnetics), University of Electro-Communications, UEC Chofu-Shi, Tokyo, Japan, 2005 March 15 – 17, TERRAPUB, Tokyo, (in final printing), 6p.
- [10] DasGupta, A., A. Das, D. Hui, 2006, Ionospheric disturbances observed by the Indian East Coast GPS stations following the 2006 December 26 Sumatra-Andaman Earthquake, Overview presented at the IGU Annual Convention, Bhopal, India, 2005 December 06 – 09 (to appear in its Proceedings – in completion).
- [11] Gwal, A. K., S. Sarkar, Sh. Bhattacharya and M. Parrot, 2006, Ionospheric responses to the Sumatra Earthquake observed by the DEMETER Satellite, Overview presented at the IGU Annual Convention, Bhopal, India, 2005 December 06 – 09 (to appear in its Proceedings – in completion).
- [12] Anderson, S. J., 2005, Prospects for tsunami detection, mapping, and characterization using the Surface and OTHR HF Radar systems, DSTO Internal Report, DATO, Salisbury , SA, Australia.
- [13] Martin-Neira, M. et al., 2005, Detecting tsunamis using the PARIS concept. Proceedings URSI-B, SMRS-05 (Microwave Remote Sensing of the Earth, Oceans, Ice and Atmosphere), ESA-JRC, 2005 April 20-21.
- [14] Bedard, A. J., 2005, Low-Frequency Atmospheric Acoustic Energy associated with Vortices produced by Thunderstorms, Monthly Weather Review, Vol. 133, No. 1, pp. 241 – 263, January 2005
- [15] Bedard, A. J., 1971, Seismic response of infrasonic microphones, J. Res. NBS. Vol 75C, pp. 41 – 45, 1971.
- [16] Bedard, A. J., T. M. Georges and G. E. Greene, 1975, Infrasound from Convective Storms, Part IV: Is it useful for warning?, J. Appl. Meteor. Vol 14, 1303 – 1316, 1975.
- [17] Hubbert, J. V., V. N. Bringi, L. D. Cary, and S. Bolen, 1998, CSU-CHILL polarimetric meteorological radar measurements from a severe hailstorm in Eastern Colorado (including simultaneous Near-infrasonic measurements by A. J. Bedard in collaboration with E. A. Mueller), J. Appl. Meteor. Vol 37, pp. 749 – 775, 1998.
- [18] Garces, M., P. Caron and Claus Hertz, Infrasound from the 2004 – 2005 earthquakes and tsunami near Sumatra, Echoes – the newsletter of The Acoustical Society of America, Vol. 15, No. 4, p. , Fall 2005.

Recent Developments of Radar Remote Sensing

Air- and Space-borne Multimodal SAR Remote Sensing in Forestry & Agriculture, Geology, Geophysics (Volcanology and Tectonology): Advances in POL-SAR, IN-SAR, POLinSAR and POL-DIFF-IN-SAR Sensing and Imaging with Applications to Environmental and Geodynamic Stress-change Monitoring

Wolfgang-Martin Boerner

Department of Electrical and Computer Engineering
University of Illinois at Chicago, Chicago, USA

Abstract—Radar Polarimetry Radar Interferometry and Polarimetric SAR Interferometry represent the current culmination in ‘Microwave Remote Sensing’ technology, but we still need to progress very considerably in order to reach the limits of physical realizability. Whereas with *radar polarimetry* the textural fine-structure, target orientation, symmetries and material constituents can be recovered with considerable improvement above that of standard ‘amplitude-only’ radar; by implementing ‘radar interferometry’ the spatial (in depth) structure can be explored. With Polarimetric Interferometric Synthetic Aperture Radar (POL-IN-SAR) imaging, it is possible to recover such co-registered textural and spatial information from POL-IN-SAR digital image data sets simultaneously, including the extraction of Digital Elevation Maps (DEM) from either Polarimetric (scattering matrix) or Interferometric (dual antenna) SAR systems. Simultaneous Polarimetric-plus-Interferometric SAR Imaging offers the additional benefit of obtaining co-registered textural-plus-spatial three-dimensional POL-IN-DEM information, which when applied to *Repeat-Pass Image-Overlay Interferometry* provides differential background validation and environmental stress-change information with highly improved accuracy. Then, by either designing multiple dual polarization antenna POL-IN-SAR systems or by applying advanced POL-IN-SAR image compression techniques, will result in ‘POL-arimetric TOMO-graphic’ (Multi-Interferometric) SAR or POL-TOMO-SAR imaging. By advancing these EWB-D-POL-IN/TOMO-SAR Imaging modes, we are slowly but steadily approaching the ultimate goal of eventually realizing air-borne and space-borne ‘Geo-Environmental Background Validation, Stress Assessment, and Stress-Change Monitoring and Wide-area Military Surveillance of the Terrestrial and Planetary Covers’.

Keywords-Radar Polarimetry, SAR Polarimetry, Polarimetric and Interferometric SAR, Polarimetric SAR Interferometry.

1. INTRODUCTION

Very decisive progress was made in advancing fundamental POL-IN-SAR theory and algorithm development during the past decade [1], which was based on the underlying accomplishments of fully polarimetric SAR [2] and differential SAR interferometry [3] and its current merger [4]. This was accomplished with the aid of airborne & shuttle platforms supporting single-to-multi-band multi-modal POL-SAR and also some POL-IN-SAR sensor systems, which will be compared and assessed with the aim of establishing the hitherto not completed but required missions such as tomographic and holographic imaging. Because the operation of airborne test-beds is extremely expensive, aircraft platforms are not suited for routine monitoring missions; those are better accomplished with the use of drones (UAV). Such unmanned aerial vehicles (drones) were hitherto developed for defense applications, however currently lacking the sophistication for implementing advanced forefront POL-IN-SAR technology. This shortcoming will be thoroughly scrutinized resulting in the finding that we do now need to develop most rapidly also POL-IN-SAR drone-platform technology especially for environmental stress-change monitoring subject to severe operational constraints due to adverse unsafe flight conditions with a great variance of applications beginning with flood, bush/forest-fire to tectonic-stress (earthquake to volcanic eruptions) for real-short-time hazard mitigation. However, for routine global monitoring purposes of the terrestrial covers neither airborne sensor implementation - aircraft and/or drones - are sufficient; and there-fore multi-modal and multi-band space-borne POL-IN-SAR space-shuttle and satellite sensor technology needs to be further advanced at a much more rapid pace. The existing ENVISAT and ALOS-PALSAR with the forthcoming RADARSAT-2, and the TERRASAR 1 & 2 will be compared, demonstrating that at this phase of development the fully polarimetric and polarimetric-interferometric SAR modes of operation must be treated as preliminary algorithm verification support, and at this phase of development are still not to be viewed as routine modes. The same considerations apply to the near future implementation of any satellite-cluster bi/multi-static space-borne tomographic imaging modes, which must however be developed concurrently in collaboration of all major national or joint continental efforts in order to reduce proliferation of space-platforms and for cost-cutting reasons. Prioritization of developmental stages will be assessed according to applications, and will differ for air-borne to space-borne sensors with the aim of developing a permanently orbiting fleet of equidistantly space-distributed satellites – similar to the GPS configuration, however each equipped with the identical set of multi-band POL-IN-SAR sensors.

2. ADVANCES IN THE DEVELOPMENT OF SAR POLARIMETRY AND POL-IN-SAR TECHNOLOGY

Radar polarimetry and polarimetric SAR theory, algorithm development and technology have developed to a highly matured state although not yet fully driven to the limits of physical realizability [1]. It has been clearly demonstrated beyond an iota of doubt that fully polarimetric (scattering matrix) SAR image data take acquisition – as complicated as it is regarding calibration and validation – provides input for highly improved environmental image feature interpretation although lacking depth information [2]. Similarly, non-polarimetric (single amplitude) SAR interferometry has provided reasonable Digital Elevation Maps (DEM) however lacking the ability of differentiating the origin of the backscattering returns from which the interferograms are being

constructed [5]. This deficiency was overcome with the implementation [6] of the POL-IN-SAR “*polarimetric-interferometric contrast phase optimization methods*” for delineating the canopy, from the under-store versus ground returns so enabling three-dimensional SAR-Imaging. This 3-dim imaging method was further enhanced with the implementation of multiple bistatic (repeat-pass) fully polarimetric “*tomographic*” TOMO-SAR image data take acquisition, which in the limit results in polarimetric SAR holography, from which three-dimensional voluminous imagery of vegetation structures can be reconstructed subject to the sensor frequency and bandwidth [7]. However, what has not yet been demonstrated is how “*fully polarimetric Differential SAR interferometry*”— based on multiple repeat-pass POL-IN-SAR imagery - will improve the three-dimensional depiction of lateral, sheared and torsionally skewed surface and volumetric underburden deformations, which is one of the major unresolved research topic to be addressed in the forthcoming decade [8].

3. COMPARISON OF AIRBORNE MULTI-BAND POL-SAR & POL-IN-SAR TEST PLATFORMS

There by now exist about 15 or more aircraft-platforms for supporting POL-SAR and some also POL-IN-SAR imaging capabilities, but not a single one of them was designed to satisfy the ideal performance conditions for conducting Multi-band POL-IN-SAR Imaging. This is truly a very sore dilemma and ought to be removed by realizing the design of the ideally designed *POL-IN-SAR Aircraft Imaging Platforms*. From a thorough comparison it seems that currently the DLR ESAR, the CRL PISAR and the ONERA RAMSES multi-band POL-(IN)-SAR are leading in advancing this vital remote sensing technology, and also have integrated high-precision repeat-pass GPS co-registration capabilities. In order for realizing fully Polarimetric (scattering matrix) Differential SAR Interferometry both the ideal platform design for sustaining on-board POL-IN-SAR imaging and highest possible precision of GPS co-registration become paramount [8]. Definitely, for the testing of novel multi-modal imaging algorithms aircraft platforms will be required for a long time to come, and therefore design of aircraft dedicated for SAR-imaging missions is fully justified.

4. THE NEED FOR DEVELOPING DRONES (UAV) MONITORING PLATFORMS WITH MULTI-BAND POL-SAR AND POL-IN-SAR REPEAT-PASS IMAGING CAPABILITIES

The maintenance and operation of any sophisticated imaging test-aircraft platform requiring crews of three to twelve pilots including the sensor operators such as for Multi-band POL-IN-SAR is extremely costly; and therefore it is justified and necessary to develop rapidly mission dedicated drones (UAV) for carrying out regional routine remote sensing and environmental stress-change monitoring missions. However, the design of such multi-purpose drones must accommodate the most advanced Multi-band POL-SAR and POL-IN-SAR operational modes that had been tested and performance-hardened previously with the aid of the aircraft test-platforms, and also with the aid of the highly successful shuttle SIR-C/X-SAR mission. Under no circumstance must we regress to a ‘venerable Landsat technology of the 1970-ies’ as impressive as those products truly are; and the remote sensing SAR user’s community must wake up and be challenged to utilize the immense additional novel monitoring capabilities *Multi-band POL-IN-SAR* sensors have to offer, and especially with the aid of less costly drones. Indeed, we do now need to develop most rapidly the most advanced POL-IN-SAR drone-platform technology especially for environmental stress-change monitoring subject to severe operational constraints due to adverse unsafe flight conditions with a great variance of applications beginning with flood, bush/forest-fire to tectonic-stress (earthquake to volcanic eruptions) for real-short-time hazard mitigation.

5. ACCELERATION OF ADVANCEMENT OF MULTI-BAND POL-SAR AND POL-IN-SAR SPACE –BORNE SENSOR-TECHNOLOGY FOR SHUTTLE AND SATELLITE DEPLOYMENT

One of the most successful and ingenious space-borne remote sensing accomplishments was that of the two SIR-C/X-SAR missions of April and September/October 1994 demonstrating at C-Band & L-Band how useful and irreplaceable fully polarimetric SAR image acquisition also from space truly is. More so, its well co-registered sets of repeat-pass C&L-Band POL-SAR image data takes along the Baikal rift zone of Inner Asia made possible the testing and verification of the novel POL-IN-SAR algorithms developed by Cloude and Papathanassiou [6] at DLR. In hindsight, some of us be-mourn (*or are still weeping bitterly about*) the fact that it was not possible to make the otherwise rather successful SRTM mission also fully polarimetric because so much more could have been gained on properly determining global vegetation cover and in highly improved soil parameter acquisition [9]. Therefore, we desire to have that SRTM mission concept be enlarged and extended to include a fully polarimetric X/C/L/P-multi-band POL-IN-SAR performance capability and to have it redone at the earliest possible date. In fact, all of the brilliantly designed and *executed “SAR Remote Sensing Shuttle Missions”* were so successful and irreplaceable for the rapid advancement of satellite-borne SAR technology so that those must not be abandoned but continued. As regards the advancement of Space-SAR technology a crucial milestone was achieved during the recent ESA POLinSAR-03 Workshop [8] during which the implementation of fully polarimetric (scattering matrix) SAR modes for all future satellite-born SAR systems of ESA, DLR, NASA and also NASDA was in essence decided, and the first step in this direction was achieved with the successful launches of ENVISAT (ASAR) and of ALOS (PAL-SAR), and then towards Fall 2006 RADARSAT-2 and of TERRASAR following soon thereafter. Here, it needs to be emphasized that to consider the implementation of the fully polarimetric POL-SAR and the POL-IN-SAR capabilities to be just another “*technology push*” is absolutely unacceptable in that it has been demonstrated beyond any further doubt that proper and more correct biomass and soil estimation parameters [9, 10, 11] can only be obtained with multi-band POL-IN-SAR imagery; and similarly it will be shown shortly that more correct and complete lateral, sheared and torsion-twisted surface and volumetric

underburden deformations can only be recovered with onboard POL-IN-SAR satellite sensors operated in contiguous repeat-pass orbital modes – both of which provide most essential and basic inputs at arriving at more reliable global change predictors.

6. BI-STATIC MULTI-BAND POL-IN-SAR SATELLITE CLUSTERS & DEVELOPMENT OF PERMANENT FLEET OF MULTI-BAND POL-IN-SAR SATELLITES

In order to improve the detection capability of objects occluded under vegetation cover from space, it is necessary to implement tomographic and holographic imaging principles – next to frequency diversity – and for space-SAR satellite implementation that asks for the design of orbiting clusters of equidistantly gyrating satellites as proposed with the ESA Cartwheel and the USAF High-Tech Space-SAR concepts. Although somewhat more sophisticated, the implementation of fully polarimetric POL-SAR sensors for each of the symbiotic cluster sub-satellites must also be developed and it is feasible. The space SAR cartwheel concept can only be viewed as the a partial forerunner of developing the orbiting fleet of equidistantly grid-distributed multi-modal multi-band POL-IN-SAR satellites very similar to the configuration of equidistantly grid-distributed GPS satellites; however in the imaging case replacing each of the orbiting individual satellites by a cluster of three to eight parasitic satellites gyrating around a central POL-IN-SAR Transceiver Satellite and each one carrying a set of multi-modal multi-band POL-IN-SAR sensors. Another mode of operation includes the use of existing communications satellites as sources with orbiting clusters of passive satellite sensors, and so on.

7. CONCLUSION

By means of placing such an orbiting fleet of satellites into space - *in the long run* - will reduce the exorbitant cost for establishing a viable “*home-globe security protection*” technology. It will provide rather accurate global change data eventually on an hourly basis accessible to all who need to know. The pertinent National and International airborne and space borne multi-modal, multi-band SAR remote sensing and security conflict surveillance support agencies are herewith invited for co-sponsoring our proposal as time proceeds, in that it is timely and POLinSAR platforms are urgently required to be placed into space [8].

REFERENCES

- [1] Boerner, W-M, “Recent Advances in Extra-wideband Polarimetry, Interferometry and Polarimetric Interferometry in Synthetic Aperture Remote Sensing and its Applications”, IEE Proceedings, Radar Sonar and Navigation, Special Issue EUSAR-02, June 2003
- [2] Boerner, W-M., H. Mott, E. Lüneburg, C. Livingston, B. Brisco, R. J. Brown and J. S. Paterson with contributions by S.R. Cloude, E. Krogager, J.S. Lee, D.L. Schuler, J. J. van Zyl, D. Randall P. Budkevitsch and E. Pottier, 1998, “*Polarimetry in Radar Remote Sensing: Basic and Applied Concepts*”, Chapter 5 (pp. 271-357, + 12 image plates) in F.M. Henderson, and A.J. Lewis, (eds.), *Principles and Applications of Imaging Radar*, vol. 2 of *Manual of Remote Sensing*, (ed. R.A. Reyerson), Third Edition, John Wiley & Sons, New York, 940 p, ISBN: 0-471-29406-3.
- [3] Massonet D. and K.L. Feigl, 1998, “Radar Interferometry and its Application to Displaying Stress-Changes in the Earth’s Crust”, *Review of Geophysics*, vol. 36(4), 1998 Nov, pp. 441-500.
- [4] Pottier, E., S. R. Cloude and W-M. Boerner, Recent development of data processing in Polarimetric and Interferometric SAR, Proc, URSI-GA-02, Maastricht, NL, pp. , (edited by R. W. Stone); Also see: ibid, Invited Paper, Radio Science Bulletin N0. 304, March 2003, pp. 48-59, ISSN 1024-4530.
- [5] Bamler, R. and P. Hartl, 1998, “Synthetic Aperture Radar Interferometry”, State of the Art Review, *Inverse Problems*, vol. 14, pp. R1-R54, IOC Publications, Bristol, UK.
- [6] Cloude, S. and K. Papathanassiou, 1998, “Polarimetric SAR Interferometry”, *IEEE Trans. Geosci. Remote Sensing*, vol. 36 (4), pp. 1551-1565 (also see: Papathanassiou, K.P., “*Polarimetric SAR Interferometry*”, 1999, Ph. D. Thesis, Tech. Univ. Graz (ISSN 1434-8485 ISRN DLR-FB-99-07), Graz, Austria).
- [7] Reigber, A., A. Moreira, “First Demonstration of Airborne SAR Tomography Using Multi-Baseline L Band Data”, *IEEE Transactions on Geoscience and Remote Sensing*, Vol. 38, No 5, pp 2142-2152, September 2000 (see: Reigber, A., 2001, “*Polarimetric SAR Tomography*”, Dissertation, University of Stuttgart, 2001 October 15 (ISSN 1434-8454, ISRN DLR-FB-2002-02)
- [8] Boerner, W-M, Why we do Need to Place Multi-Band Single and Multiple Pass POLinSAR Monitoring Platforms into Space, Proceedings POLinSAR Workshop at ESA-ESRIN, Frascati, Italy, 2003 January 14-16, 24 pages, in print.
- [9] Hajnsek, J., 2001, “*Inversion of Surface Parameters (soil moisture & roughness) Using Polarimetric SAR*”, Doctoral Thesis, FSU, Jena, Germany, 2001 October 17 (ISSN 1434-8485 ISRN DLR-FB-2001-30). (see: Hajnsek I., E. Pottier and S.R. Cloude, 2002, “Inversion of Surface Parameters from Polarimetric SAR”, *IEEE Transactions in Geoscience and Remote Sensing*, vol. 41, (4), pp. xx-yy, April 2003)
- [10] Chen, K.S., T. D. Wu, L. Tsang, Qin Li, J. C. Shi and A. K. Fung, “The Emission of Rough Surfaces Calculated by the Integral Equation Method with a Comparison to a Three-Dimensional Moment Method Simulations,” *IEEE Trans. Geoscience and Remote Sensing (SCI)* , vol.41 no.1, pp.1-12, 2003.
- [11] Lee, J.S., W-M Boerner, D. L. Schuler, T. L. Ainsworth, I. Hajnsek, K. P. Papathanassiou, E. Lüneburg, A Review of Polarimetric SAR Algorithms and Their Applications, *Journal of Photogrammetry and Remote Sensing*, Volume 9, No. 3, September 2004, pp. 31-80

Microwave Radiometry Technology for the Nature-Society System Biocomplexity Assessment

Vladimir F. Krapivin, Ferdinand A. Mkrtchyan

Institute of Radioengineering and Electronics, Russian Academy of Sciences, Moscow, Russia

Abstract

The problem of biocomplexity in global Nature/Society System (NSS) is considered in the framework of complex hierarchical systems theory. The interactions between the NSS elements having different spatial and temporal scales are modelled in the terms of information value, diversity of elements, dynamical stability of biogeochemical cycles, and relations between the spaces of elements. Simulation-methodical model of biocomplexity dynamics founded on the correlations between basic elements of the NSS is synthesized. Mechanisms of living processes regulation and presence of restriction by the environment quality are taken into consideration. Principal aspects of the NSS model are formulated, and analysis of corresponding knowledge base is given. Interconnection between the criteria of the NSS biocomplexity, stability and survivability is analysed.

This report is oriented on the development of biocomplexity indices basing on the remotely measured environmental characteristics. Microwave radiometry is used as effective technique to assess the land cover parameters. Other ranges help to form input information for the NSS Biocomplexity Model that will be developed in the framework of this work.

Keywords: biocomplexity, nature-society system, remote observations, microwave radiometry

Introduction

Biocomplexity refers to phenomena that result from dynamic interactions between the physical, biological and social components of the *Nature/Society System* (NSS). The investigations of the processes of interaction between the *Society* and *Biosphere* are, as a rule, targeted at understanding and estimating the consequences of such interactions. The reliability and precision of these estimations depend on criteria founded on conclusions, expertise and recommendations. At present, there is no unified methodology for selection between the set of criteria due to the absence of a common science-based approach to the ecological standardization of anthropogenic impacts on the natural environment. After all, the precision of the ecological expertise for the functioning and planning of anthropogenic systems, as well as the quality of the global geoinformation monitoring data, depend on these criteria.

The processes that have their origin in the environment can be presented as a combination of interactions between its subsystems. The human subsystem is a part of the environment and it is impossible to divide the environment into separate subsystems such as Biosphere and Society. The problem is to search for methodologies to describe existing feedbacks between Nature and Humanity and to simulate reliably the dynamic tendencies in the NSS. Unfortunately the part of the NSS that is responsible for the quality of modelling the climatic processes introduces instability in the modelling results. That is why it is supposed below that the NSS climatic component is replaced by a scenario describing stable climatic trends during the time interval of investigation. What is actually studied is the NSS.

We are introducing the scale of biocomplexity ranging from the state where all interactions between the environmental subsystems are broken to the state where they correspond to natural evolution. In this case, we have an integrated indicator of the environmental state including bioavailability, biodiversity and survivability. It reflects the level of all types of interactions among the environmental subsystems. In reality, specific conditions exist where these interactions are changed and transformed. For example, under the biological interaction of the type *consumer/producer* or *competition-for-energy-resources* there exists some minimal level of food concentration where contacts between interacting components cease. In the common case, physical, chemical and other types of interactions in the environment depend upon specific critical parameters. Environmental dynamics is regulated by these parameters and the main task is in the parametrical description of it. Biocomplexity reflects these dynamics.

Biocomplexity model

The NSS consists of subsystems $B_i (i = 1, \dots, m)$ the interactions of which are formed during time as functions of many factors. The NSS biocomplexity reflects the structural and dynamic complexity of its components. In other words, the NSS biocomplexity is formed under the interaction of its subsystems $\{B_i\}$. In due course the subsystems B_i can change their state and, consequently, change the topology of the relations between them. The evolutionary mechanism of adaptation of the subsystem B_i to the environment allows the hypothesis that each subsystem B_i , independently from its type, has the structure $B_{i,S}$, behaviour $B_{i,B}$ and goal $B_{i,G}$, so that $B_i = \{B_{i,S}, B_{i,B}, B_{i,G}\}$. The strivings of subsystem B_i to achieve certain preferable conditions are represented by its goal $\hat{A}_{i,G}$. The expedience of the structure $B_{i,S}$ and the purposefulness of the behaviour $B_{i,B}$ for subsystem B_i are estimated by the effectiveness with which the goal $B_{i,G}$ is achieved.

As an example, we consider the process of fish migration. The investigations of many authors revealed that this process is accompanied by an external appearance of purposeful behaviour. From these investigations it follows that fish

migrations are subordinated to the principle of complex maximization of effective nutritive ration, given preservation of favourable environmental conditions (temperature, salinity, dissolved oxygen, pollution level, depth). In other words, the travel of migrating species takes place at characteristic velocities in the direction of the maximum gradient of effective food, given adherence to ecological restrictions. That is why we can formulate that the goal $B_{i,G}$ of the fish subsystem is toward the increase of their ration, the behaviour $B_{i,B}$ consists in the definition of the moving trajectory securing the attainability of the goal $B_{i,G}$.

Since the interactions of the subsystems B_i ($i = 1, \dots, m$) are connected with chemical and energetic cycles, it is natural to suppose that each subsystem B_i realizes the geochemical and geophysical transformation of matter and energy to remain in a stable state. The formalism of approach to this process consists in the supposition that the interactions between the NSS subsystems are represented as a process whereby the systems exchange a certain quantity V of resources spent in exchange for a certain quantity W of resources consumed. Represent this process by the name (V,W) -exchange.

The goal of the subsystem is the most advantageous (V,W) -exchange, i.e. it tries to get maximum W in exchange for minimum V . The quantity W is a complex function of the structure and behaviour of interacting subsystems, $W = W(V, B_i, \{B_k, k \in K\})$, where K is the space of subsystem numbers interacting with the subsystem B_i .

Designate $B_K = \{B_k, k \in K\}$. Then the following (V,W) -exchange is the result of interactions between the subsystem B_i and its environment B_K

$$W_{i,0} = \max_{B_{ii}} \min_{B_K} W_i(V_i, B_{i,opt}, B_{K,opt}); W_{K,0} = \max_{B_K} \min_{B_i} W_k(V_K, B_{i,opt}, B_{K,opt})$$

Hence it follows that some range of the goal of the subsystem B_i exists which defines the levels of V_i and V_K . Since the limiting factors are in force in nature then in this case it is natural to suppose that some level $V_{i,min}$ exists when the subsystem B_i ceases to spend its energetic resource for obtaining the external resource, i.e. if $V_i \leq V_{i,min}$ the subsystem B_i transfers to the regeneration of its internal resource. In other words, when $V_i \leq V_{i,min}$ the decrease of the biocomplexity indicator $\xi_{\alpha}(t)$ is realized at the expense of breaking off interactions of the subsystem B_i with other subsystems. Commonly, the structure of $V_{i,min}$ is a checkered function, i.e. the change-over of x_{ij} from state $x_{ij} = 1$ to state $x_{ij} = 0$ is not realized for all j at the same time. Actually, in any trophical pyramid of living subsystems the relationships of "producer/consumer" type cease under the decrease of the consumer biomass concentration below some critical level. In other cases the interactions of the subsystems $\{B_i\}$ can be stopped at the expense of various combinations of its parameters. The parametrical description of possible situations of interactions of subsystems $\{B_i\}$ can be realized in the framework of the NSS simulation model.

Figure 1 represents a block-scheme for the global model of the NSS (GMNSS). The synthesis of the GMNSS is based on its consideration as a self-organizing and self-structuring system, in which the elements are coordinated in time and space by the process of natural evolution. The anthropogenic constituent in this process breaks this integrity. Attempts to parameterize, on a formal level, the process of co-evolution of nature and humans, as elements of the biosphere, are connected with the search of a single description of all processes in the NSS, which would combine all spheres of knowledge in perceiving the laws of the environment. Such a synergistic approach forms the basis of numerous studies in the field of global modelling [1,2].

We introduce the scale Ξ of biocomplexity ranging from the state when all interactions between the environmental subsystems are broken to the state when they correspond to natural evolution. In this case, we have an integrated indicator of the environmental state including bioavailability, biodiversity and survivability. It reflects the level of all types of interactions among the environmental subsystems. In reality, specific conditions exist when these interactions are changed and transformed. For example, under the biological interaction of "consumer/producer" or "competition for energy resources" type there exists some minimal level of food concentration when contacts between interacting components cease. In the common case, physical, chemical and other types of interactions in the environment depend upon specific critical parameters. Environmental dynamics is regulated by these parameters and the main task is in the parametrical description of it. Biocomplexity reflects this dynamics.

All of this corroborates the fact that biocomplexity is related to categories which are difficult to measure empirically and to express by quantitative values. However, we will try to transfer the truly verbal tautological reasoning to formalized quantitative definitions. For the transition to gradations of the scale Ξ with quantitative positions it is necessary to postulate that relationships between two values of Ξ are of the type $\Xi_1 < \Xi_2$, $\Xi_1 > \Xi_2$ or $\Xi_1 \equiv \Xi_2$. In other words, always there exists a value of the scale ρ that defines a biocomplexity level $\Xi \rightarrow \rho = f(\Xi)$, where f is a certain transformation of the biocomplexity concept to a number. Let us attempt to search for a satisfactory model with which to reflect the verbal biocomplexity image onto the field of conceptions and signs, subordinating to the formal description and transformation. With this purpose m subsystems of the NSS are selected. The correlations between these subsystems are defined by the binary matrix function: $X = ||x_{ij}||$, where $x_{ij} = 0$, if subsystems B_i and B_j do not interact and $x_{ij} = 1$, if subsystems B_i and B_j are interacting. Then any one point $\xi \in \Xi$ is defined as the sum

$$\xi = \sum_{i=1}^m \sum_{j=i}^m x_{ij}. \quad \text{Certainly there arises the need to overcome uncertainty for which it is necessary to complicate the scale } \Xi; \text{ for example, to introduce weight coefficients for all NSS subsystems. The origin of these coefficients depends}$$

on the type of subsystem. That is why three basic subsystem types are selected: living and nonliving subsystems and vegetation. Living subsystems are characterized by their density, estimating by numbers of elements or by biomass value per unit area or volume. Vegetation is characterized by the type and portion of occupied territory. Nonliving subsystems are measured by their concentration per unit square or volume of the environment. In the common case, certain characteristics $\{k_i\}$, corresponding to the significance of the subsystems $\{B_i\}$, are assigned to every subsystem B_i ($i = 1, \dots, m$). As a result we obtain more closely the definition of the formula to move from the biocomplexity concept to the scale Ξ of its indicator:

$$\xi = \sum_{i=1}^m \sum_{j>i}^m k_j x_{ij}.$$

It is clear that $\xi = \xi(\varphi, \lambda, t)$, where φ and λ are geographical latitude and longitude, respectively, and t is the current time. For the territory Ω the biocomplexity indicator is defined as mean value:

$$\xi_\Omega(t) = (1/\sigma) \int_{(\varphi, \lambda) \in \Omega} \xi(\varphi, \lambda, t) d\varphi d\lambda,$$

where σ is the area of Ω .

Thus the indicator $\xi_\Omega(t)$ is the integrated NSS complexity characterization reflecting the individuality of its structure and the behaviour at each time t in the space Ω . According to the natural evolution laws a decrease (increase) in ξ_Ω will correspond to an increase (decrease) of biocomplexity and the survivability of the nature-anthropogenic systems. Since a decrease of biocomplexity disturbs the exclusiveness of the biogeochemical cycles and leads to a decrease of stress on the nonrenewal of resources, then the binary structure of the matrix X is changed in the direction to intensify the resource-improvement technologies. The vector of energetic exchange between the NSS subsystems is moved to the position where the survivability level of the NSS is reduced.

$$\xi = \sum_{i=1}^m \sum_{j>i}^m k_j x_{ij}.$$

It is clear that $\xi = \xi(\varphi, \lambda, t)$, where φ and λ are geographical latitude and longitude, respectively, and t is the current time. For the territory Ω the biocomplexity indicator is defined as mean value:

$$\xi_\Omega(t) = (1/\sigma) \int_{(\varphi, \lambda) \in \Omega} \xi(\varphi, \lambda, t) d\varphi d\lambda, \quad (1)$$

where σ is the area of Ω .

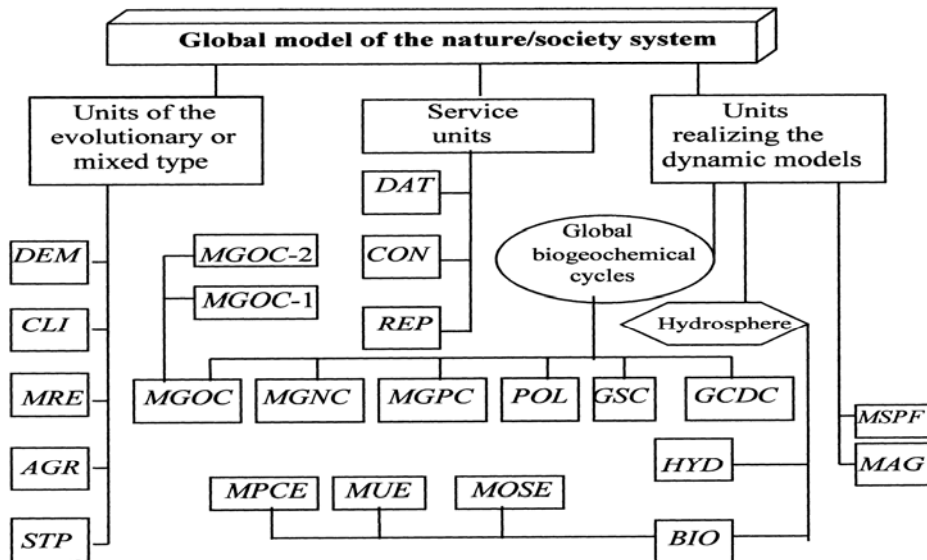
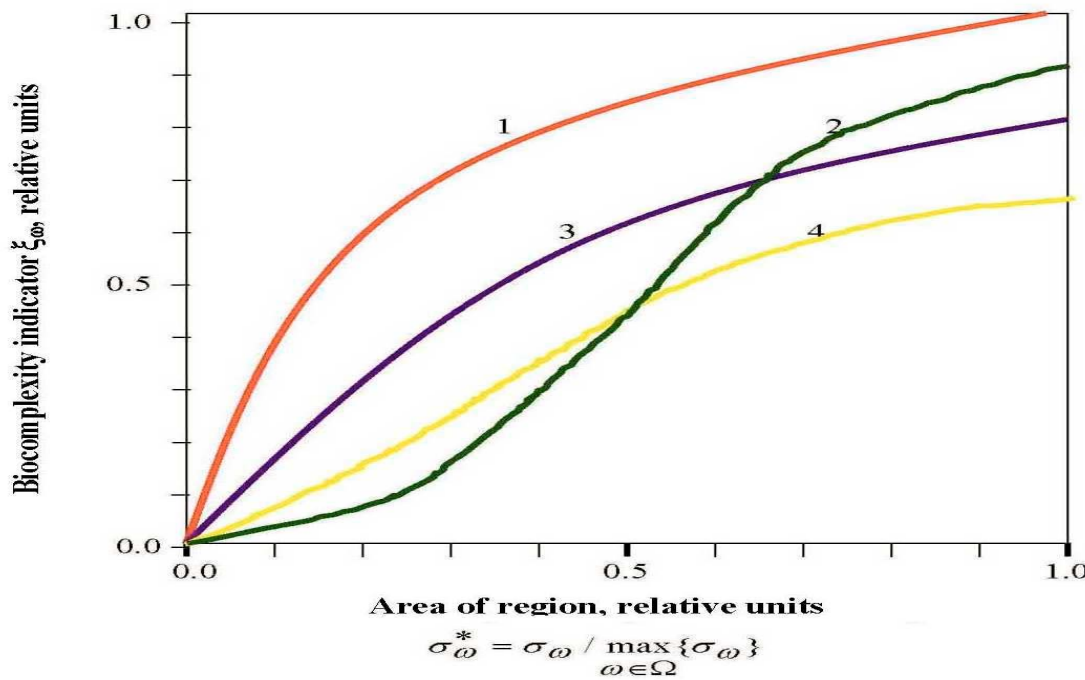


Figure 1. Structure and items of the GMNSS. List of items is given in Table 1.

Table 1. A description of the items in Figure 1.

Item	An item description
DEM	A set of demographic models that parametrize the population dynamics with the consideration of age structure.
CLI	A set of climate models with various spatial resolution.
MRE	Model for the control of mineral resources.
AGR	Model of agriculture production.
STP	Model of science-technical progress.
DAT	Controlling procedure of interface between the MGNSS items and database.
CON	Informational procedure for the MGNSS items adaptation to the simulation experiment conditions and its control.
REP	Reporting and visualization procedure.
GCDC	Model of global carbon dioxide cycle.
GSC	Model of global sulphur cycle.
MGOC	Model of global oxygen (MGOC-1) and ozone (MGOC-2) cycles.
MGNC	Model of global nitrogen cycle.
MGPC	Model of global phosphorus cycle.
POL	A set of models parametrizing the pollutant kinetics within different medias.
BIO	A set of models parametrizing the aquatic ecosystems in different climatic zones.
HYD	Model of global hydrodynamic processes and the biosphere water balance.
MSPF	A set of biocenotic models describing different classification of soil-plant formations.
MAG	Model of the magnetosphere processes related to the global biogeochemical cycles.
MUE	Typical model of the upwelling ecosystem of the World Ocean.
MOSE	Model of the Okhotsk Sea Ecosystem.
MPCE	Model of Peruvian Current Ecosystem.

**Figure 2.** Designation: 1- developed countries with agricultural lands no more 20%; 2 - regions with investments no more 20%; 2 - regions with agricultural lands more 20%; and 4 - regions with investments more 20%.

Biocomplexity of the Okhotsk Sea

Trophic pyramid Of the Okhotsk Sea ecosystem is described by the matrix $X = ||x_{ij}||$, where x_{ij} is binary value equaled to «1» or «0» under existence or absence of nutritive correlation between the i th and j th components, respectively. Define the biocomplexity as function:

$$\xi(\varphi, \lambda, z, t) = \sum_{i=1}^{20} \sum_{j=1}^{19} x_{ij} C_{ij}; \quad x_{ij} = \begin{cases} 1, & \text{if } B_m \geq B_{m,\min}; \\ 0, & \text{if } B_m < B_{m,\min}; \end{cases}$$

where φ and λ are geographical latitude and longitude; t is current time; z is the depth; $B_{m,\min}$ is the minimal biomass of the m th component consumed by other trophic levels; $C_{ij} = k_{ji} B_{i,*} / \Sigma_{j+}$ is the nutritive pressure of the j th component upon the i th component; $\Sigma_{j+} = \sum_{m \in S_i} k_{im} B_m$ is real food storage which is available to the i th component; $B_{i,*} = \max\{0, B_m - B_{m,\min}\}$; $k_{i,m} = k_{i,m}(t, T_W, S_W)$ ($i = 1, \dots, 17$) is the index of the satisfaction of nutritive requirements of the i th component at the expense of the m th component biomass; $k_{i,m}$ ($i = 18, 19$) is the transformation coefficient from m th component to the i th component; $k_{i,20}$ is the characteristic of anthropogenic influence on the i th component; $S_i = \{i : x_{ij}=1, j=1, \dots, 19\}$ is the food spectrum of the i th component; T_W is water temperature; S_W is water salinity.

Maximal value of $\xi = \xi_{\max}$ (≈ 20) is reached during spring-summer time when nutritive relations into the Okhotsk Sea ecosystem are extended, the intensity of energetic exchanges is increased, horizontal and vertical migration processes are stimulated. In the winter time value of ξ is changed near ξ_{\min} (≈ 8). Spatial distribution of ξ reflects a local variability of food spectrum for the components. Calculations show that basic variability into the $\xi^* = \xi/\xi_{\max}$ is caused by migration processes. Under this the quick redistribution of interior structure of matrixes X and $\|C_{ij}\|$ are occurred.

Many fishes during spring time migrate to the shelf zone, and during winter time they move to the central aquatories of sea. Therefore value $\xi^* \rightarrow 1$ during spring and $\xi^* \rightarrow 0.6$ during winter for the shelf zone, respectively. It means that biocomplexity of Okhotsk sea ecosystem in the shelf decreases by 40% in winter in comparison with spring. For the central aquatories the ξ^* is changed near 0.7 during year. Such stability of biocomplexity indicator is explained by the balance between nutritive correlations and productivity during spring, summer and winter times.

It can be established that variability in the ξ^* reflects the changes of fish congestions which are controlled by environmental conditions. Specifically, during spring time *Clupea pallasii* occupies the area with the $T_W < 5^\circ\text{C}$. Other fishes have the elective depth for their feeding and spawning. All these processes influence on variability of the ξ^* . A more detail investigation of correlations between value ξ^* and structural and behavioral dynamics of Okhotsk Sea ecosystem demands additional studies.

Conclusion

Biocomplexity is clearly important characteristic of the NSS dynamics. It has importance for complex study of interactions between living and non-living elements of environment and, more significantly, it is can use make valuable contributions to the understanding and solution key socio-economic and environmental problems. It is reasonable to expect that over the nearest time the biocomplexity will be to use as informative indicator analogous to such indicators as normalized difference vegetation index (NDVI), leaf area index (LAI) etc. [3]. It appears that the only satisfactory way to develop an appropriate definition of biocomplexity indicator is to summarize the many structural ideas in the forms of a series of global biospheric models. The synthesis of these models requires not only their coexistence with global databases, but also the interconnections between different sources of data. This paper proposes global model and biocomplexity indicator only one category in which biospheric processes are considered as predominating. Further study is to be oriented on the expansion of information taking into account in the global model and it is necessary the correlation dependencies between socio-economic and biospheric components make more precise.

REFERENCES

1. Kondratyev K.Ya., Krapivin V.F., and Phillips G.W. *Global environmental change: Modelling and Monitoring*, Springer, Berlin, 2002, 319 pp.
2. Kondratyev K.Ya., Krapivin V.F., Savinikh V.P., and Varotsos C.A. *Global Ecodynamics: A Multidimensional Analysis*. Springer/PRAXIS, Chichester U.K., 2004, 658 pp.
3. Krapivin V.F., Shutko A.M., Chukhlantsev A.A., Golovachev S.P., and Phillips G.W. (2006). GIMS-based method vegetation microwave monitoring. *Environmental Modelling and Software*, **21**(3), 330-345.

An Adaptive Polarization Optics Technology for Ecological Monitoring of the Aquatic Environment

F. A. Mkrtchyan, V. F. Krapivin, V.I. Kovalev, V.V. Klimov, S.P. Golovachev
 Institute of Radioengineering and Electronics, Russian Academy of Sciences (IRE RAS)
 E-mail: ferd@ms.ire.rssi.ru

Abstract - Spectroellipsometry is a peak of polarization optics. The creation of multichannel polarization optical instrumentation and use of spectroellipsometric technology are very important for the real-time ecological control of aquatic environment. Spectroellipsometric devices give us high precision of measurements. Spectroellipsometric multichannel measurements in an aquatic environment provide an information basis for the application of modern algorithms for the recognition and identification of pollutants. New original elements (coaxial polarization switchers and achromatic compensators), developed in IRE RAS, allow to design cheap polarization systems (for example, spectroscopic ellipsometers, polarization spectrometers, polarimeters, dichrometers, polarization microscopes and interferometers, sensitive photometers, differential reflectometers) without expensive standard polarization elements.

1. Introduction

The creation of multichannel polarization optical instrumentation and use of spectroellipsometric technology are very important for the real-time ecological control of aquatic environment. It should be mentioned that efficient solution of this multiparametric problem greatly depends on the precision and simplicity of ellipsometric devices.

This report is aimed to describe

- A technology of combined use of spectroellipsometry and algorithms of identification and recognition that allowed the creation of a standard integral complex of instrumental, algorithmic, modular and software tools for the collection and processing of data on the aquatic environment quality with forecasting and decision-making functions
- A compact measuring - information multichannel spectroellipsometric system (device) for monitoring the quality of aquatic environment, that is based on the combined use of spectroellipsometry and training, classification, and identification algorithms

This spectroellipsometric system will differ from modern foreign analogues by the use of a new and very promising method of ellipsometric measurements, an original element base of polarization optics and a complex mathematical approach to estimating the quality of a water object subjected to anthropogenic influence.

Unlike foreign analogues, the system has no rotating polarization elements. This allows one to increase the signal-to-noise ratio and the long-term stability of measurements, to simplify and reduce the price of multichannel spectroellipsometers.

The system will be trainable to the recognition of the pollutants of aquatic environment.

2. Measuring Complexes

A spectroellipsometer in laboratories of IRE RAS is designed for in-situ real time measurements of spectra of ellipsometric parameters Psi and Delta with consequent change-over to spectra of transmitted and reflected signal from water media in frames of used physical model of water environment

A compact measuring - information multichannel spectroellipsometric system (device) is applied for monitoring the quality of natural and waste water, that is based on the combined use of spectroellipsometry and training, classification, and identification algorithms

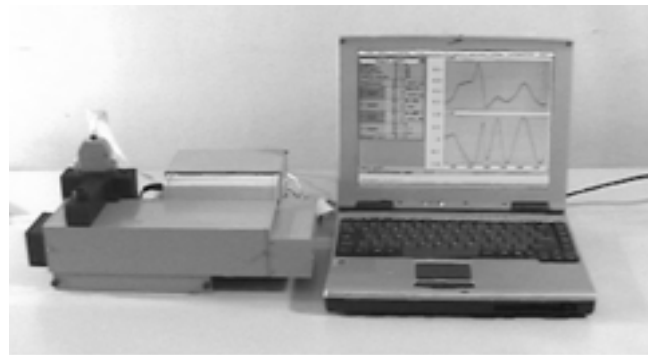


Figure 1: High precision real-time multi-wavelengths spectroscopic ellipsometer with binary polarization modulation (one of modifications) with registration and recognition system at the base of notebook

2.1. Device composition:

- Polarizer block;
- Analyzer block;
- Power supply unit;
- Illuminator;
- Fiber-optic cable;
- Notebook with interface unit;
- Wide-band filters/

2.2. Features of high precision real time multi-wavelengths spectroscopic ellipsometers created for monitoring the quality of natural and waste waters

- New approach in ellipsometry, based on binary polarization modulation;
- New low cost effective polarization elements;
- No rotating polarization elements;
- Excellent signal-to-noise ratio and the long-term stability of measurements makes possible to simplify and reduce the price of the multichannel spectroellipsometers;
- One of the key element of the systems is a polarization switch which transforms unpolarized light from a source into highly linearly polarized light with alternate (up to KHz or more) and orthogonal polarizations;
- Sets of silicon photodiodes with arbitrary access to them;
- Flexibility, simple design, low cost, high precision, long term stability.

2.3. Specifications of some spectroellipsometers used:

a) Specification of portable 35-channel spectroellipsometer:

- Spectral range 280-600 nm
- Minimal measurement time 0.5 sec
- Precision and stability 0.01 and 0.02 degree in Psi and Delta, respectively, polarization rotation angle – 0,001 degree
- Sources: miniature pulsed xenon lamp PX-2 with high resource and laser diode
- Micro spot focus 300 μ m with PX-2 and 30 μ m with laser diode
- Acromatic compensator
- User-friendly software
- A weight of measuring device – about 4 kg.

b) Specification of compact 35-channel spectroellipsometer with halogen lamp.

- Spectral ranges-380-740 nm and 650-930 nm.
- Minimal measurement time- 0.6 sec.
- Precision to 0.003 and 0.01 degree in Psi and Delta, respectively, polarization rotation angle – 0,001 degree.
- Sources: halogen lamp KGM-9-70
- Long-term stability 0,01 degree
- Use of acromatic compensator on the basis of Fresnel rhomb made of fused quartz enhances precision of measurements.
- A weight of measuring device – about 4 kg.
- Polarization block-2 kg. Analyzer block-2 kg

3. Adaptive Identifier

For the first time the combined use of real - time spectroellipsometry measurements and data processing methods has been realized in an **Adaptive Identifier**.

3.1. Structure of the Adaptive Identifier:

- The algorithmic support of the Adaptive Identifier is based on a complex application of recognition and classification algorithms on the basis of 35 spectra images registered during a fixed period of time.
- A time interval of 1 second is usually established and provides about 30 value of brightness for each of the 35 optical channels.
- The spectra obtained are sources of set of statistical parameters and different characteristics united into vector spaces for their comparison with the standard samples of famous pollutants stored on the computer.
- The technology of this comparison depends on the diversity of identification methods.

3.2. Learning procedure description

The system is trainable to the recognition of the pollutants of aquatic environment.

Learning procedure includes:

- The Adaptive Identifier is designed to learn from the measurements of spectral characteristics and the simultaneous independent measurement of the content of chemical elements in the aquatic environment.
- As a result, a standard data bank is created in the knowledge base, comparison with which provides the solution of the identification problem. The software of the Adaptive Identifier provides different algorithms for the solution of this problem, and cluster analysis is among them.

4. Measuring Technique Features

There are some specific features of measurements of the quality of natural and waste water using spectroellipsometric technology:

1. Measurements of natural and waste water quality may be performed using
 - a) **transmission** scheme when quality of sample is measured during inserting the fused quartz cuvette with water analyzed into spectroelipsometer device.
 - b). **reflection** scheme when quality of water is measured by inserting of spectroellipsometer sensor into water media examined.
- 2 Because of high accuracy of measurements with the spectroellipsometers it is not possible to use whole potential of method for remote measurements of natural and waste water quality (Even small waves, ripples, foam can influence on quality of measurements)

5. Application

The Adaptive Identifier can be used in different fields where the quality of water should be estimated or the presence of a particular set of chemical elements should be revealed. The Adaptive Identifier solves these problems by real-time monitoring of the aquatic environment. In the stationary version it allows the tracking of the dynamics of water quality in a stream, and when placed on a ship, it allows the measurement of water parameters along the route.

The functionality of the Adaptive Identifier can be extended by increasing the volume of standards in the knowledge base. The use of a natural light source allows the examination of soils, the indication of oil products on a water surface, the determination of the degree of the pollution of atmospheric air and the estimation of the conditions of other objects of the environment, whose spectral images may change.

An adaptive spectroellipsometric technology may be applied to following areas:

- Estimation of natural and wastewater quality;
- Analysis of liquids in medicine, biochemistry, food industry.
- Measurement of the mineralization level and chemical pollution of reservoir depending on the pollution type
- Estimation of water salinity variations
- Ellipsometrically based biosensor and gas sensor systems
- Testing the organic pollution clots in water environment

6. Experience

The Adaptive Identifier was tested under expeditionary conditions on board of the research vessel "Dmitry Mendeleev" in the Japanese Sea and in central areas of the Pacific Ocean and also during the investigation of aqueous systems of South Vietnam and Siberia (lake Baikal, Angara and Yenisey river) within the framework of the Russian - American and Russian - Vietnamese ecological expeditions.

A Russian - Vietnamese scientific and engineering laboratory has been created to create a standards base and to prepare the Adaptive Identifier for full - scale production.

7. Perspectives and Objectives

The main objective of work is to create in future the compact information systems for monitoring the quality of aquatic environment and to investigate their potential efficiency. These systems are based on the combined application of methods of the spectroellipsometry, and algorithms of training, classification, and identification.

The realization of this objective will require the combined use of engineering and the algorithmic tools providing real - time measurements and data processing..

The technology of combined use of spectroellipsometry and the algorithms of detection and classification will allow the creation of an original system of instrumental, algorithmic, modular and software tools for the collection and processing of data on the aquatic environment with forecasting and decision-making functions.

The theoretical part of the work will include the use of methods of polarization optics, mathematical statistics, the theory of pattern recognition and mathematical modelling.

- creation of a new element base for polarization optics with simple and efficient switches of the polarization state (SPS), that successfully substitutes for the conventional expensive polarizer – modulators of polarization state with rotating polarization elements
- optimization of the spectrum of the ellipsometric method concerning the change of the amplitudes and phases of mutually orthogonal components of electromagnetic radiation for measuring the thickness of thin films on a water surface. Determination of sensitivity and precision limits of adaptive spectroellipsometers in different operating regime
- creation of methods for investigating the water surface, determination of statistical characteristics of "spottiness" as informative signs for solving detection, classification, and identification problems
- elaboration and optimization of algorithms for the detection, classification, and identification of the characteristics of the aquatic environment for adaptive spectroellipsometers. Creation of a bank of standards on the basis of the measurement of the pollution level of the aquatic environment for training the adaptive spectroellipsometer.

The experimental part of the work described in report will include description:

- the laboratory and on-site measurements of absorption, scattering, and reflection of electromagnetic waves from aquatic objects under local and structural adaptation of the model estimation of the efficiency of the technique, algorithms and models for specific aquatic objects

REFERENCES

1. Klimov, V.V., Kovalev, V.V., Krapivin, V.F., Mkrtchyan, F.A., Nitu, C., "An expert system to diagnose pollutant spills on the water surface", - Proceedings of Int. Confer. on Control Systems and Computer Sci., Bucharest, May, 277-283, 1999.
2. Armand, N.A., Krapivin, V.F., Mkrtchyan, F.A., Methods of Processing Radiophysical Exploration of Environment. Moscow, Nauka, 1987(in Russian).
3. Mkrtchyan, F.A., Krapivin, V.F., Kovalev, V.I., Klimov, V.V., Rukovichnikov, A.I., Golovachev, S.P., "An adaptive spectroellipsometric technology for the ecological monitoring of the aquatic environment", Proceeding of 25-th ACRS, Chiang-Mai, Thailand, 7-13, 2004.

Amplitude Modulation Using Injection Locking Oscillator Under Strong Envelop Variation Injection

Chanchai Thongsopa¹, Apichart Intarapanich² and Charinsak Saetiarw¹

(1) School of Telecommunication Engineering, Suranaree University of Technoligly,
Nakorn Ratchasima, 30000 Thailand.

Email:chan@sut.ac.th

(2) National Electronics and Computer Technology Center, Pathumthani ,12120
Thailand.

Email:apichart.intarapanich@nectec.or.th

Abstract: In this paper, an analysis of injection locking oscillator with amplitude modulation injecting signal is presented. The derivation is based on strong amplitude variation of injecting signal. We show that the amplitude and frequency of oscillator output vary with the amplitude of the injecting signal. The oscillator output variations can be controlled by modulation index, modulation frequency and frequency of the injected signal. To validate the result, an active antenna with injection locking oscillator is design and built with a dual-gate FET and various AM signals are injected into the oscillator.

Keywords: Strong injection locking, Active antenna, AM modulation

1. Introduction

Active antennas have been developed for low cost and low complexity applications. Some important applications of active antenna are power combining [1] and beam forming [2]. These applications utilize phase variation of active antenna operating in injection locking condition.

The injection locking phenomena has been well studied in [3, 4] which provided the relationship between the phase variation and injecting signal with small amplitude variation. In this research, we give the analysis of the injection locking phenomena with strong amplitude variation of the injecting signal. We derive a relationship between the amplitude variation of the oscillator output and the injecting signal. We show that the injecting signal with strong amplitude variation can alter amplitude variation of the oscillator output. Hence, the amplitude modulation (AM) can be obtained by injecting strong amplitude modulation to the oscillator. To verify the derivation, an active antenna with injection locking oscillator is built using a dual gate FET NE 25139 with free running frequency of 1.6 GHz. The active antenna is injected with various signals.

The paper is organized as follows. The analysis and design of injection locking oscillator are given in Section 2. In Section 3, the experiment validation of the injection locking oscillator is given. We summarize the paper and draw conclusions in Section 4.

2. Analysis and Design

2.1 Analysis of the strong injection oscillator

To analyze the amplitude variation of the oscillator output, an equivalent circuit of the oscillator is represented in term of negative resistance and series of lumped R , L , C resonant circuit as shown in Figure 1. The negative resistance, $-R_d$ is assumed to be frequency dependent.

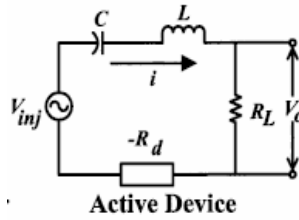


Figure 1. The equivalent circuit of injection locking oscillator.

By applying Kirchoff's Voltage Law and expressing in term of quality factor and resonance frequency, after some manipulations the output signal can be written as a function of time as

$$\frac{dV_0}{dt} = V_0 \left[\frac{\mu\omega_0}{2Q} (\alpha_0^2 - |V_0|^2) + j\omega_0 \right] + \frac{\omega_0}{2Q} V_{inj} \quad (1)$$

where V_{inj} is the injection signal and it can be written in a phasor form of $V_{inj} = A_{inj}e^{j\theta_{inj}}$ where A_{inj} and θ_{inj} are amplitude and phase of the injection signal respectively. The output voltage V_0 is a complex signal and it can also be written in phasor form of $V_0 = A_0e^{j\theta(t)}$ where A_0 and $\theta(t)$ are amplitude and phase of the output signal respectively. Q and ω_0 are quality factor and resonant angular frequency, respectively. α_0 is the oscillator magnitude and μ is non-linearity of the oscillator. By decomposing (1) into real and imaginary part, the amplitude and phase variation can be written as follows.

$$\frac{dA_0(t)}{dt} = \frac{\mu\omega_0 A_0(t)}{2Q} (\alpha_0^2 - A_0^2(t)) + \frac{\omega_0}{2Q} A_{inj}(t) (\cos(\theta_{inj} - \theta)) \quad (2)$$

$$\frac{d\theta}{dt} = \omega_0 + \frac{\omega_0}{2Q} \frac{A_{inj}(t)}{A_0(t)} \sin(\theta_{inj} - \theta) \quad (3)$$

To investigate the effect of the amplitude variation of the output signal, both (2) and (3) will be considered. By writing (2) and (3) in the form of the difference in output phase θ and injecting phase θ_{inj} :

$$\cos(\theta_{inj} - \theta) = \frac{2Q}{\omega_0 A_{inj}(t)} \left[\frac{dA_0(t)}{dt} - \frac{\mu\omega_0 A_0(t)}{2Q} (\alpha_0^2 - A_0^2(t)) \right] \quad (4)$$

$$\sin(\theta_{inj} - \theta) = \frac{2Q A_0(t)}{\omega_0 A_{inj}(t)} \left[\frac{d\theta}{dt} - \omega_0 \right] \quad (5)$$

When the system is in steady-state and locking condition, the change in magnitude of output signal will be equal to the initial magnitude of oscillator i.e. $A_0(t) = \alpha_0$ [5]. By using the relationship between phase and instantaneous frequency, $d\theta/dt = \omega_{inj}$, the identity $\cos^2(\theta_{inj} - \theta) + \sin^2(\theta_{inj} - \theta) = 1$ and the locking condition $\omega_{inj} = \omega_0$, the magnitude of output signal can be written in term of injecting signal as

$$\frac{dA_0(t)}{dt} = \frac{\omega_0 A_{inj}(t)}{2Q} \quad (6)$$

Equation (6) shows that the amplitude variation of the output signal is directly proportional to the magnitude of injecting signal. It can be also seen that (6) resembles the amplitude modulation.

To obtain the amplitude modulation at the output, the injecting signal is chosen so that the output is

$$A_0(t) = A_{EN} + A_{EN} m \sin(\omega_s t + \alpha) \quad (7)$$

where

$$m = \frac{A_{EN}(\max) - A_{EN}(\min)}{A_{EN}(\max) + A_{EN}(\min)} \quad (8)$$

m is the modulation index. A_{EN} is a magnitude of the output signal. ω_s and α are frequency and phase of the envelop of the output signal respectively, as shown in Figure 2. Therefore, the magnitude of the output signal, as a function of time, can be written as

$$\frac{dA_0(t)}{dt} = A_{EN} m \omega_s \cos(\omega_s t + \alpha) \quad (9)$$

From (6) and (9), the injecting signal can be written in term of the output signal as

$$A_{inj}(t) = \frac{2Qm\omega_s A_{EN} \cos(\omega_s t + \alpha)}{\omega_0} \quad (10)$$

It can be seen from (10) that the magnitude of the output signal can be controlled by modulation index, frequency and phase of the injecting signal.

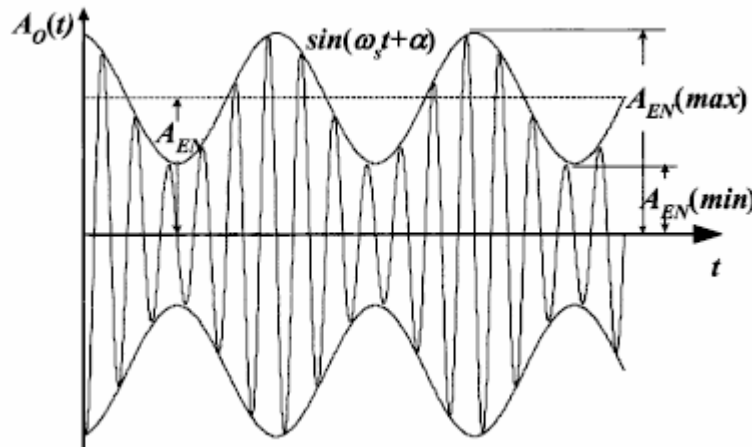


Figure 2. The output signal with sine wave modulation

2.2 The design of active antenna

The dual gate FET is equivalent to stack of two FETs. The first FET is used as an active device in the oscillator while the external signal is injected to the second FET to obtain locking condition. This injection technique offers stronger injecting signal than coupling injection method. The injecting frequency is 1.5 GHz. A short circuit stub is connected to the gate terminal of the first FET as a resonator. A short circuit stub is connected to source terminal to provide a positive feed back network. A rectangular patch antenna is connected to the drain terminal.

A rectangular patch antenna is designed with resonant frequency at 1.5GHz. The antenna is fabricated on 1.5 mm thick FR4 substrate with relative dielectric constant of 4.5. With $V_{ds} = 5V$, $V_{g1s} = -0.2 V$ and $V_{g2s} = 0 V$, S-parameter for this bias point are $S_{11} = 1.939 \angle -29.362^\circ$, $S_{12} = 0.876 \angle 59.031^\circ$, $S_{21} = 3.037 \angle -145.186^\circ$ and $S_{22} = 2.206 \angle -53.808^\circ$. The corresponding Rollet

stability factor is -0.936 which is less than one. Thus, the circuit is in unstable condition. The complete oscillator with a patch antenna is shown in Figure 3.

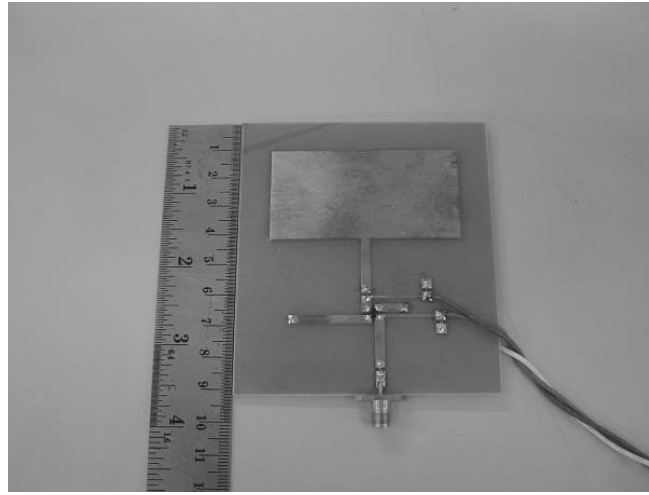


Figure 3. The active antenna with an injection locking oscillator.

3. Experiment Results

We first investigate injection locking phenomena of the active antenna. Free running frequency of the oscillator is observed to be about 1.6 GHz. Then, the second gate of the oscillator is injected by a sine wave with frequency of 1.5 GHz and power of -5 dBm. The output frequency is measured by a spectrum analyzer and it is exactly equal to the injecting frequency i.e. 1.5 GHz. Further more, the phase noise at 10 kHz offset is -89 dBc/Hz.

Once, the injection locking phenomena is verified. The oscillator is then injected by strong AM signal and its effect to the oscillator output is observed. The carrier of 1.5 GHz is modulated with a 10 KHz sine wave and the modulation index of 50% and 80%. The AM output spectrum can be clearly seen for both 50% and 80% modulation index as shown in Figure 4.

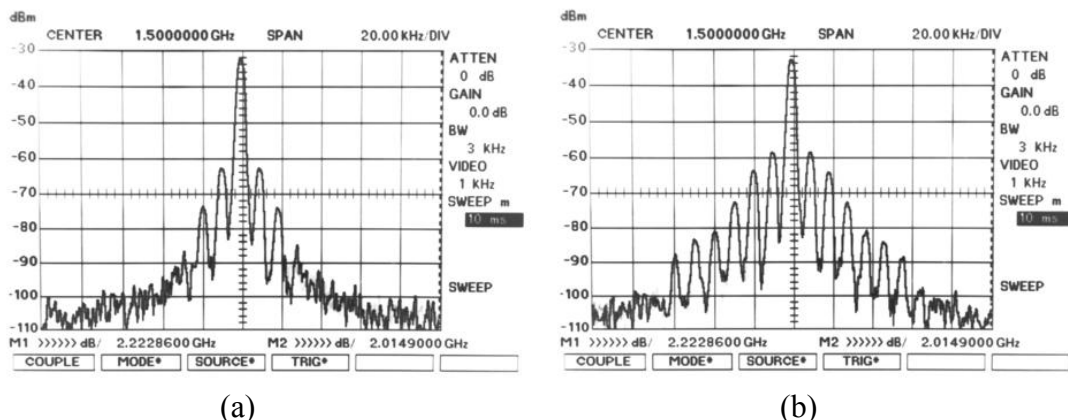


Figure 4 . The output spectrum with 10 KHz sine wave (a) 50% modulation index and (b) 80% modulation index.

Next, the same carrier is modulated with a 20 kHz sine wave and modulation index of 50% and 80%. It can be seen from Figure 5 that the sine wave clearly appears at 20 kHz from 1.5 GHz carrier. Thus the output AM

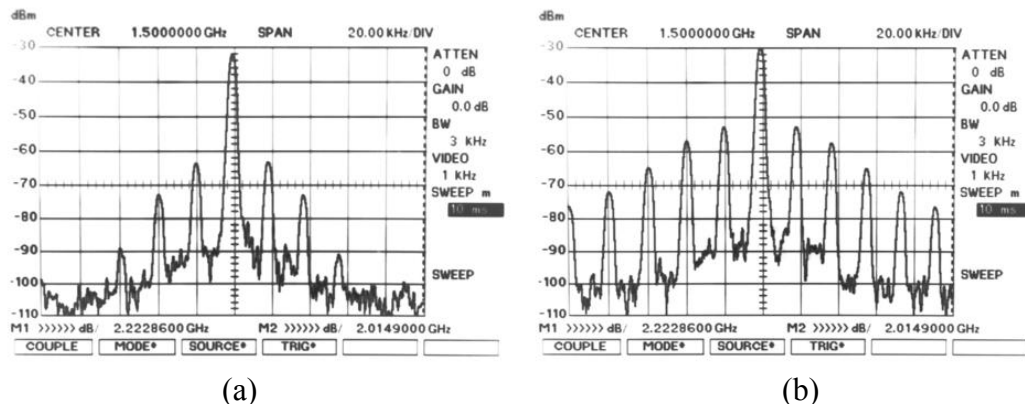


Figure 5. The output spectrum with 20 KHz sine wave (a) 50% modulation index and (b) 80% modulation index.

The experiments show that the amplitude modulation at the oscillator output can be obtained by injecting the signal with condition in (10). The AM output can be controlled by varying the frequency (ω_s) and modulation index (m). It can also observe that the oscillator maintains locking condition regardless of envelop variation of the injecting signal.

4. Conclusion

In this paper, we present the analysis of strong amplitude injection oscillator. We derive a condition on the injecting signal to obtain AM output signal. The active antenna is built utilizing the injection locking oscillator to verify the result. The dual gate FET is used as the active device in the active antenna. The experiments show that the AM output can be controlled by two parameters. i.e. the modulating frequency and modulation index.

References

- [1] J. Harvey, E. R. Brown, D. B. Rutledge, and R. A. York, "Spatial Power Combining for High-power transmitters", *IEEE Microwave Mag.*, Vol 1, No. 4, pp 48-59, Dec., 2000
- [2] P. Liao and R. A. York, "A New Phase-shifterless Beam Scanning Technique Using Arrays of Coupled Oscillators", *IEEE Trans. Microwave Theory and Tech.*, Vol 41, No. 10, pp 1810-1815, Oct., 1993
- [3] B. Van Der Pol. " The nonlinear theory of electric oscillation," *Proc.IRE*, vol 22,no.9,pp.1051-1085,Sept.1934.
- [4] R.Adler, "A study of locking phenomena in oscillators," *Proc.IRE*, vol. 34, pp.351-357, June 1946.
- [5] R.A. York, "Nonlinear analysis of phase relationships in quasi-optical oscillator arrays." *IEEE Trans. Microwave Theory & Tech.*,vol.41,no.10,pp.1799-1809,Oct.1993.

Wideband Measurement of Voltage and Current Rise Time Due to Micro Gap Discharge as Low Voltage ESD Using the 12 GHz Experimental System

Ken Kawamata*, Shigeki Minegishi**, Akira Haga** and Osamu Fujiwara***

* Hachinohe Institute of Technology, JAPAN

**Faculty of Engineering, Tohoku Gakuin University, JAPAN

*** Nagoya Institute of Technology, JAPAN

Abstract: The voltage and current transition durations due to small gap discharge as the low voltage ESD was investigated in time domain. The measurement system was set up a very wide band experimental system using the distributed constant line and coaxial electrode. The insertion loss of the experimental system was within -3dB in frequency range below 12GHz. It was confirmed that the distributed constant experimental system enables to measure the very fast transients of about 40 ps in 12GHz bandwidth. As a consequence of the experiment using the system, voltage and current rise time of transition duration were shown 40 ps or less. Besides, the rise times were changed in configuration of electrodes, source polarity and discharging voltage.

Keywords: ESD, transition durations, time domain, distributed constant line

1. Introduction

It is well known that the very fast transients of electromagnetic field are arisen from gap discharges of ESD (electrostatic discharge) and electrical contacts. The transient due to gap discharge is a very wide band (high frequency) electromagnetic noise source. Over the past few years a considerable number of studies have been made on electromagnetic noises of the ESD and contacts from the point of view of the electromagnetic compatibility. The electromagnetic noise characteristics of gap discharge are gradually becoming clearer [1]-[7].

However, there has been only a little amount of information about measured voltage or current waveforms of the transition duration (voltage rise time and current rise time) due to a starting of the discharge in very wide band time domain [8]-[11]. Very little is known about characteristics of the transition duration at voltage rise part and current rise part due to the ESD and the gap discharge.

The main purpose of our research is to illuminate a relation between the electromagnetic noise characteristics and the discharge phenomenon as the EMI source. Up to now we were set up an experimental system using the distributed constant lines to observe the transition durations due to low voltage gap discharge, because the transients are very rapid. It was possible to observe the voltage waveform and the frequency distribution of transition durations in 6GHz [12]-[13].

In this paper, the experimental system was improved to observe the voltage and current waveform due to discharging in 12GHz real time measurement. The voltage waveform, and the current waveform was measured by an electric field sensor (infinitesimal monopole antenna), and a magnetic field sensor (infinitesimal loop antenna) respectively. The insertion loss of the coaxial electrode system was within about -3dB in frequency range below 12GHz.

It was confirmed that the distributed constant experimental system enables to measure the very fast transients of about 40 ps in 12GHz bandwidth. As a consequence of the experiment using the system, voltage and current rise time of transition duration were shown 40 ps or less. Besides, the rise time was changed in configuration of electrodes, source polarity and discharging voltage.

2. 12GHz Distributed Constant Experimental System

The experimental system using distributed constant line system shown in Fig.1 was set up. The system consists of a power supply, coaxial cables, semi rigid cables, needle to plan electrodes, an electric field probe and magnetic field probe. The probes were used to observe the very fast transition durations due to discharging. The electrode setup and the probes disposition were shown in Fig.2. The needle electrode was made from a sharpening the inner conductor of source side semi-rigid coaxial cable. The radius of curvature

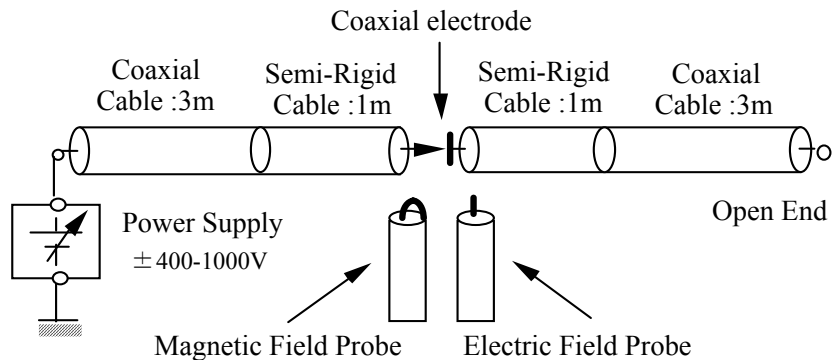


Fig.1 Composition of the 12GHz experimental system using the distributed constant

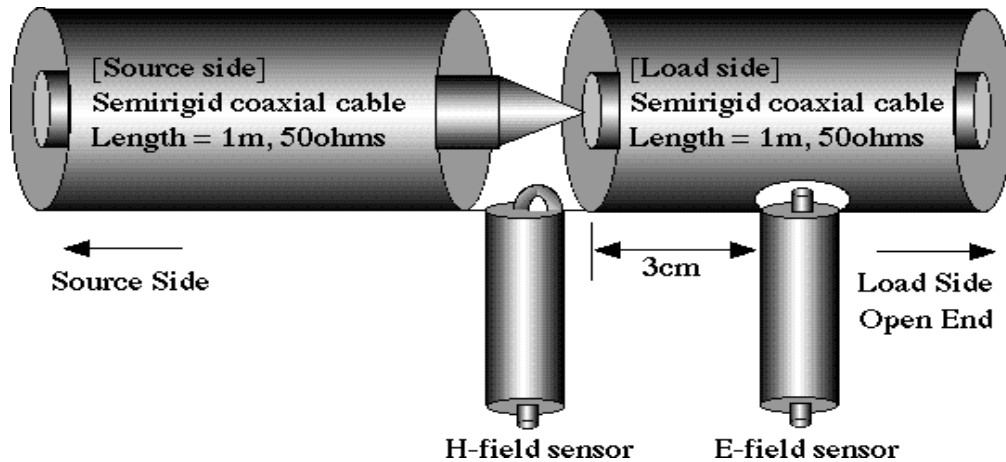


Fig.2 Disposition of the coaxial electrodes and E-field probe and H-field probe.

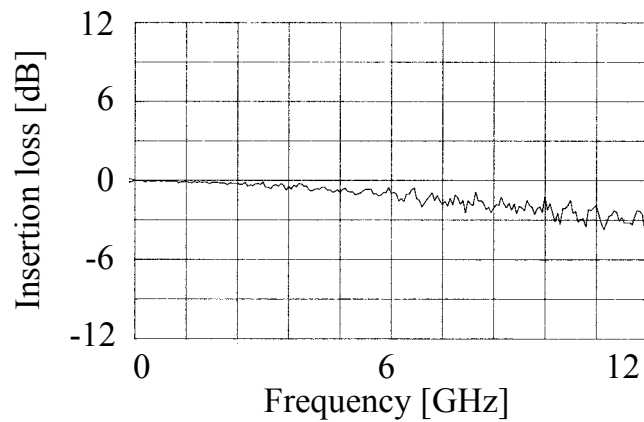


Fig.3 Insertion loss of the distributed constant experimental system with the coaxial electrodes.

of the needle electrode is $r=0.1$ mm, and $r=0.5$ mm, respectively. The plan electrode was made at inner conductor of load side semi-rigid coaxial cable. The electric field sensor was used by infinitesimal monopole antenna, and the magnetic field sensor was used by infinitesimal loop antenna.

Fig.3 shows the insertion loss of the distributed constant experimental system with coaxial electrodes. The insertion loss of the system was measured by a network analyzer (HP8720C, 20GHz). The gap of electrodes was made by mechanical connection. The insertion loss of the coaxial electrode system was within about

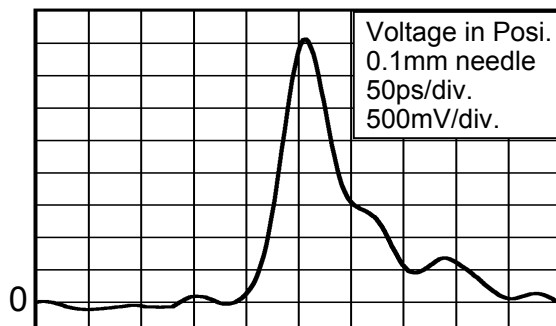
-3dB in frequency range below 12GHz. The time domain response of the E-field sensor and H-field sensor was confirmed by a sampling oscilloscope (HP54750A, 18GHz). The distributed constant line system in connected the coaxial electrode was driven by 35 ps rise time step waves. The time response of E-field probe was about 37 ps rise time. Also, H-field probe was 35 ps rise time.

The factors of E-field sensor and H-field sensor were examining into transform the real electric field and magnetic field values. However, the transform factors were complicated in the time domain, because the ingredient of the frequency spectra was disagreed due to the rise time of voltage transients. In this time, the results were shown by relative voltage value of the E-field sensor and the H-field sensor, respectively. Measured value of a gain at the E-field sensor is about -29dB, and H-field sensor is about -28.6dB, in 34ps rise time step wave.

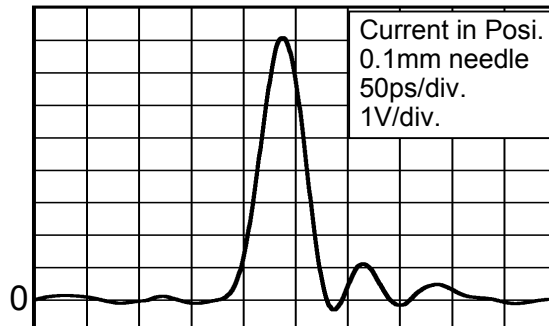
In the experiment, the semi-rigid cable with the needle electrode is moved slowly by hand. The gap space was reduced gradually. A shingle-shot real time waveform of voltage transients at the instance of discharge was observed with the wide band digitizing oscilloscope (Tektronix TDS6124C, 12GHz) when the source voltage were 400V, 600V, 800V, and 1000V in positive polarity and negative polarity. The voltage and current rise time of the transition durations was determined by average value of five to ten measurements.

3. Experimental Results

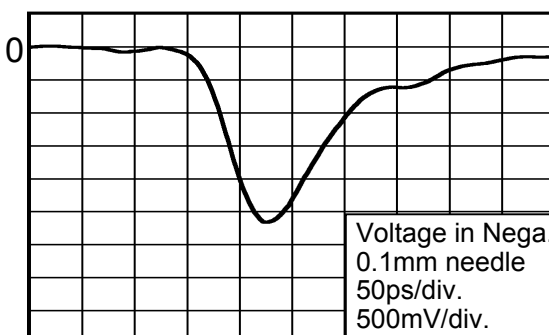
The example voltage waveform and current waveform of transition duration are shown in Fig.4 and Fig.5 respectively. In the both waveforms, the radius of curvature of needle electrode is 0.1 mm, and discharge voltage is 800V. In figures, (a) is the rising part of transition duration in positive polarity and (b) is in negative polarity. The horizontal axis is 50 ps/div., respectively. The voltage on a distributed constant line at the load side should rise to a half amplitude of the source voltage. However, the peak value of the waveforms was lower because of the influence of the coupling characteristics of the E-field probe and H-field probe. Especially, in Fig.5 (b), the peak value was low, because the high frequency components of transition duration were decreased due to slowdown of rise time. In this report, the study was limited only to the relative duration time of the voltage transients. In Fig.4, the voltage rise time of (a), and (b) is about 38 ps,



(a) 800V in positive polarity.

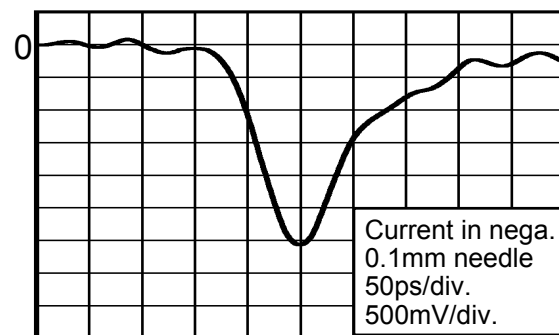


(a) 800V in positive polarity.



(b) 800V in negative polarity.

Fig.4 Measured waveforms of voltage transition duration using the E-field probe.



(b) 800V in negative polarity.

Fig.5 Measured waveforms of current transition duration using the H-field probe.

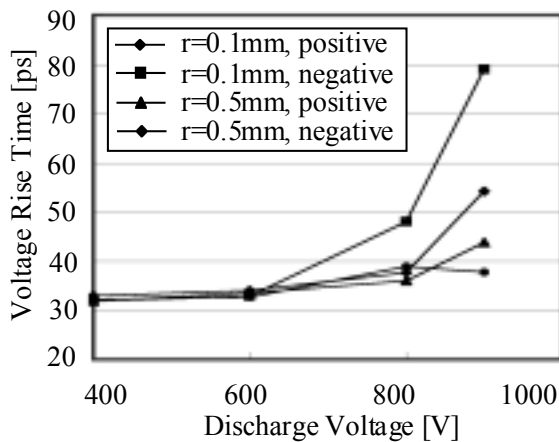


Fig.6 Relationship between the discharge voltage and voltage rise time.

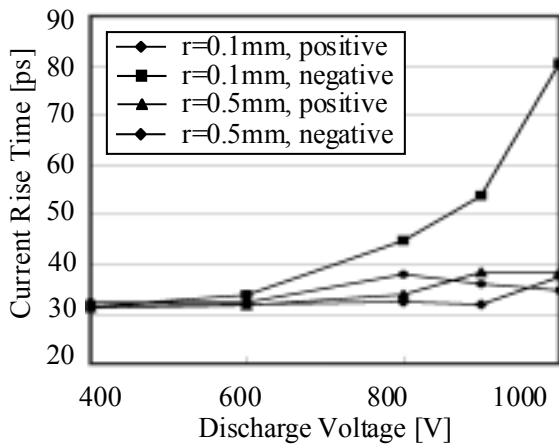


Fig.7 Relationship between the discharge voltage and current rise time.

and 50 ps respectively. In Fig.5, the current rise time of (a), and (b) is about 32 ps, and 53 ps respectively.

The relationship between the discharge voltage and the rise time of transition duration were confirmed. The relation of voltage rise time and current rise time was shown in Fig.6 and in Fig.7. The voltage rise time was somewhat slowed down in positive polarity, while the voltage rise time was slowed down remarkably from about 32 ps to about 80 ps in negative polarity of the r=0.1 mm needle. Also, the current rise time was slowed down remarkably in same condition. It can be considered that the cause of the difference in transition duration influenced the distribution of the electric field in the gap electrode.

4. Conclusions

The very fast transition duration due to the micro gap discharge was investigated in time domain using the distributed constant line experimental system.

In the first, the experimental system was improved to more wideband measurement. It enabled to measure the transition duration in frequency range of 12GHz band width. As a consequence of the experiment using this system, the voltage and current rise time showed very fast transition duration of about 40 ps or less. The voltage and current rise time were slowed down from about 30 ps to about 80 ps for an increasing of the discharge voltage from 400 V to 1000 V when experiment was performed in negative polarity for the 0.1 mm needle electrode.

REFERENCES

- [1] P.F.Wilson and M.T.Ma, "Field radiated by electrostatic discharges", IEEE Trans. on EMC, EMC-33, no.1, pp.10-18, Feb. 1991.
- [2] M.Honda, "Indirect ESD measurement using a short monopole antenna", 1990 IEEE Int'l. Symp. on Electromagn. Compat., pp.641-645, Aug. 1990.
- [3] L.M.MacLeod and K.G.Balmain,"Compact Traveling-Wave Physical Simulator for Human ESD", IEEE Trans. on Electromagn. Compat., vol. 39, no. 2, pp. 89-99, May 1997.
- [4] D.Pommerenke:"ESD:transient fields, arc simulation and rise time limit", Journal of ELECTROSTATICS, vol.36, pp.31-54, 1995.
- [5] R.Zaridze, D.Karkashadze, R.G.Djobava, D.Pommerenke, and M.Aidam, "Numerical Calculation and Measurement of Transient Fields from Electrostatic Discharge", IEEE Trans. on Components, Packaging, and Manufa. Tech., Part C, vol.19, no.3, July 1996.
- [6] O.Fujiwara, "An Analytical Approach to Model Indirect Effect Caused by Electrostatic Discharge", IEICE Trans. on Commun., vol.E-79-B, no.4, April 1996.
- [7] S.Ishigami, R.Gokita, Y.Nishiyama, I.Yokoshima and T.Iwasaki:"Measurements of fast transient fields in the vicinity of short gap discharges", IEICE Trans. on Commun., vol.E78-B, no.2, pp.199-206, Feb. 1995.
- [8] K.Arai, W.Janischewskyj and N.Miguchi , "Microgap Discharge Phenomena and Television Interference ", IEEE Trans.Power Appar.&Syst.,PAS-104,No.1, 1985.

- [9] D.Pommerenke:"ESD:waveform calculation, field and current of human and simulator ESD", Journal of ELECTROSTATICS, vol.38, pp.31-54, 1996.
- [10] B.Daout and H. Ryser, "The reproducibility of the rising slope in ESD testing", Proc. of 1986 IEEE Int'l Symp. on Electromagn. Compat., pp.467-474, Aug.1986.
- [11] R.Wallace, "6GHz time Domain Measurement of Fast Transient Events", Proc. of 1992 IEEE Int'l Symp. On Electromagn. Compat., pp.460-463, Aug.1992.
- [12] K.Kawamata, S.Minegishi,A.Haga and R.Sato, "A Measurement of Very Fast Transition Durations Due to Gap Discharge in Air Using Distributed Constant Line System", IEEE Trans. On EMC., vol.41, no.2, pp.137-141,May 1999
- [13] K. Kawamata, S. Minegishi and A. Haga, "Wideband Measurement of transition duration and frequency spectra due to small gap discharge as low-voltage ESD", Journal of ELECTROSTATICS, 62, pp.185-193, 2004

Effects of the non-linear heating of the ionosphere due to lightning discharges

S. S. De, S. K. Adhikari, M. De, A. Guha

Centre of Advanced Study in Radiophysics & Electronics, University of Calcutta,
Kolkata 700 009, India

and

B. K. De

Tripura University, Suryamaninagar 799 130, West Tripura, India

E-mail: de_syam_sundar@yahoo.co.in

Abstract The non-linear heating of the ionosphere due to incidence of electromagnetic pulses coming from lightning discharges has been investigated theoretically in this presentation. The electromagnetic radiation from lightning discharges introduces variation in electron temperature, ionising frequency and effective collision frequency of electrons. The energy gained by the free electrons from the incident electric fields of wide-band electromagnetic pulses from lightning strokes is not instantaneously transferred to the heavy particles in the medium due to which the electron temperature is raised. Variation of temperature increase has been estimated.

1. INTRODUCTION

Above the thunderstorm cloud, the presence of luminous flashes at high altitudes is due to lightning. The peak luminosity is found in the vicinity of 60 km [1, 2]. The non-linear effects in the ionosphere produced by electromagnetic radiations from lightning are well-known [3, 4]. Wide-band electromagnetic pulses radiated from lightning strokes initiate the process of heating [5]. In this presentation, the heating effect at the lower edge of the ionosphere (D-region) due to incidence of electromagnetic pulses coming from lightning discharges has been investigated theoretically. The influence of horizontal lightning strokes causing the variation of temperature increase is discussed.

The electromagnetic radiation from lightning discharges introduces variation in electron temperature, ionising frequency and the effective collision frequency of electrons. The magnitude of temperature changes of electrons has been estimated through some model calculations.

2. MATHEMATICAL FORMULATION

The physical situation may be represented by the following energy balance expression, the momentum transport equation and continuity equation:

$$\frac{3}{2} \frac{\partial}{\partial t} (NkT_e) + eN\vec{v} \cdot (\vec{E} + \vec{v} \times \vec{H}) + G_{eff}(T_e) \mathbf{n}_e(T_e) + \frac{3}{2} \mathbf{d}\mathbf{n}_e(T_e) Nk(T_e - T) - \nabla \cdot \vec{q} - \mathbf{c} \nabla^2 T + Q_i \frac{\partial N}{\partial T} = 0 \quad (1)$$

$$\frac{\partial \vec{v}}{\partial t} + (\vec{v} \cdot \nabla) \vec{v} = -\frac{e}{m} \vec{E}(t) - \frac{e}{m} (\vec{v} \times \vec{H}) - \frac{\nabla p}{m} + \frac{\mathbf{h}}{m} \nabla^2 \vec{v} \quad (2)$$

$$\frac{\partial N}{\partial t} = (\mathbf{n}_i - \mathbf{n}_a) N - \mathbf{a} N^2 \quad (3)$$

where, $\vec{E}(t)$ is the radiated horizontal electric field; \vec{H} , the geomagnetic field; \mathbf{n}_i , the ionizing frequency; \mathbf{n}_e , the effective electron collision frequency; \mathbf{n}_a , the electron-neutral molecule attachment frequency; \vec{v} , the average electron velocity; Q_i , the ionizing energy of the medium; N , the electron number density; $\mathbf{d} = \frac{2m}{m'}$, m' is the mass of the heavy particle; T , the equilibrium temperature; T_e , the electron temperature; \mathbf{h} , the coefficient of viscosity of the medium; \mathbf{c} , the thermal conductivity; G_{eff} , the fraction of energy transfer per collision; \mathbf{a} , the electron-ion recombination coefficient and \vec{q} is the heat flow vector.

$$\vec{q} = -\mathbf{I}(T_e)\nabla T_e$$

where, $\mathbf{I}(T_e)$ is the effective coefficient of electron energy conduction.

$$\mathbf{I} = k_T(1 - \mathbf{m}\mathbf{t}' / \mathbf{s}_0 k_T)$$

k_T is the coefficient of electron energy conduction at constant electron velocity; \mathbf{m} , the coefficient of electron energy conduction due to dc electric field; \mathbf{t}' , the current flow coefficient due to thermal gradients at constant electron pressure, $p = NkT_e$; \mathbf{s}_0 , the dc electrical conductivity and k is the Boltzmann constant. The other symbols have their usual significance.

Due to incidence of lightning pulses in the weakly ionized D-region of the ionosphere, the effective electron collision frequency (\mathbf{n}_e) and the ionizing frequency (\mathbf{n}_i) vary with electron temperature (T_e) because of their dependence on the average electron velocity. The ionisation frequency \mathbf{n}_i represents the production and loss processes and can be expressed as [6]

$$\mathbf{n}_i(T_e) = n \left(\frac{8kT_e}{pm} \right)^{1/2} (pa_0^2) \exp\left(\frac{Q_i}{kT_e}\right) \quad (4)$$

n is the neutral particle number density, a_0 is the Bohr radius. The effective collision frequency has been taken as $\mathbf{n}_e = nvS_m(v)$. (5)

S_m is the velocity dependent momentum transport cross-section.

For wide energy range of electrons, the collisions frequency would be averaged over the Maxwellian distribution of electron velocities. Within the lower ionosphere, the collision between N₂, O₂ and A_r are important for the determination of effective collision frequency. Electron-neutral particle collisions are strongly dependent on T_e . S_m values for O₂, N₂ and A_r are expressed as [7]

$$S_m = a + bT_e^{1/2} + cT_e + dT_e^{3/2} \quad (6)$$

a, b, c, d are listed in Table-1.

Table-1: Values of a, b, c, d of expression (6)

Species	a	b	c	d
O ₂	0.51468 (-16)	0.14597 (-16)	-0.12554 (-18)	0.35801 (-21)
N ₂	0.85924 (-16)	0.12275 (-16)	0.12679 (-18)	-0.16887 (-20)
A _r	0.78638 (-15)	-0.39515 (-16)	0.65673 (-18)	-0.35480 (-20)

From (2), the expression of \bar{v} can be obtained as

$$\bar{v} = \exp(-A) \frac{e}{m} \int_0^t \vec{E}(t') \exp \left\{ A + \int_t^{t'} M dt'' \right\} dt' \quad (7)$$

$$A = \int_0^t \left\{ (\bar{v} \cdot \nabla) + \mathbf{n}_e(T_e) + \frac{\hbar k^2}{m} + \frac{C}{m} \right\} dt' \quad (8)$$

and $M = \begin{pmatrix} 0 & H_z & -H_y \\ -H_z & 0 & H_x \\ H_y & -H_x & 0 \end{pmatrix}$, $C = \text{Reynold number}$

Substituting $\frac{\partial N}{\partial t}$ from (3) in (1) and making some algebraic simplifications, one can get the expression of normalized electron temperature as

$$y = \frac{T_e - T}{T} = \frac{2}{3NkT \mathbf{d}\mathbf{n}_e(T_e)} \left[k_T \left(1 - \frac{\mathbf{m}\mathbf{t}'}{\mathbf{s}_0 k_T} \right) k^2 T_e - \mathbf{c} k^2 T - G_{eff} \mathbf{n}_e(T_e) - Q_i \{ (\mathbf{n}_i - \mathbf{n}_a) N - \mathbf{a} N^2 \} \right] - \frac{ie}{3\mathbf{p}e c^2 [\exp \{ \mathbf{d}\mathbf{n}_e(T_e) t \} - 1] kT} \int_0^t \left[-\exp(-A) \frac{e}{m} \int_0^{t'} E(t'') \exp \left\{ A + \int_{t'}^{t''} M dt''' \right\} dt'' \right] \frac{\mathbf{w} I dS(\mathbf{w}) W(x)}{h} \times \exp \{ -ikD + \mathbf{d}\mathbf{n}_e(T_e) t \} dt \quad (9)$$

where $W(x) = \frac{x}{(x^2 + 1)^{3/2}}$, $x = \frac{R}{h}$

h is the height of the lower edge of the ionosphere; $W(x)$, the space dependent part of the incident field; R , the horizontal distance from the source; \mathbf{w} , the angular wave frequency; $I dS$, the current moment of the source and D is the distance from the source to a point at the edge of the ionosphere.

3. RESULTS

Following the model of Jones [8], the heating effects have been considered by horizontal lightning strokes with specific temporal and spatial variations of temperature increases. The median peak current of 24 KA is assumed to reach after some **ms** later from the start [5, 8]. The radiated spectra cover a wide-frequency range from few Hz to several kHz. Numerical analysis reveals that the waves are in the temporal domain with a short intense pulse having a peak around 4.6 **ms** (Fig.1). After that, it decays exponentially thus giving a broad weak negative pulse with the maximum around tens of **ms**. The first positive pulse provides the heating of the lower ionospheric electrons. The nature agrees with the previous work [5].

For the day-time model, the ionospheric plasma is taken to be sharply bounded at a height $h=50$ km, where the ambient temperature $T = 272$ K [9]. The peak velocity of the streamer is assumed as 9×10^7 msec⁻¹. 50 km height is chosen as the height of the lower edge of the ionosphere where the heating effects occur due to the incidence of electromagnetic pulses from lightning discharges. The frequencies used in the present calculations are 5.88×10^5 Hz, 3.03×10^4 Hz, 2.0×10^3 Hz and some other lower values. The calculation shows substantial heating from a single median stroke of cloud-to-ground discharge. The position of the lightning discharge is taken at a height of 4 km from the ground. The direct and ground reflected pulses have been considered. For horizontal discharge, the temporal variation of electron temperature above the stroke produced by the same source has been evaluated using equation (9).

The results are shown in Fig.1. Thus due to lightning discharges, the value of electron temperature at the lower ionosphere may be even 115 K higher than its undisturbed value. The trend of this result is in agreement with earlier works with horizontal discharge [5, 8]. Moreover, the enhancement of temperature due to lightning discharge field maintains correspondence with effective collision frequency growth[10].

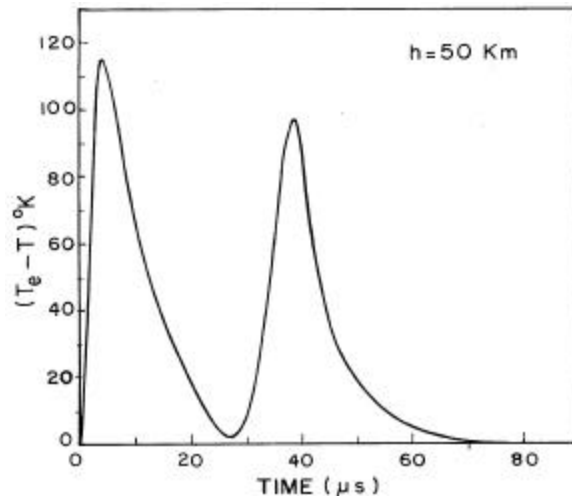


Figure 1: Increase of electron temperature over the ambient value just after the lightning discharge. The intense pulse gives the peak around 4.6 **ms**. At this instant after the start, the value of electron temperature may be even 115 K higher than its undisturbed value. Lightning discharge height = 4 km, $h = 50$ km.

4. DISCUSSION

When the incident electric field in the lower ionosphere is very high, the energy gained by the free electrons from such fields cannot be readily transferred to the heavy particles of the medium. Hence the average energy of the electrons or the electron temperature is raised by the incident field. Then the velocity distribution functions of the electrons will differ from Maxwellian function. The deviation of distribution

function from Maxwellian form may be of importance in the interpretation of cross-modulation data. Similar situation prevails in the case of weakly ionized auroral ionosphere which appears rapidly to reach non-Maxwellian stationary states under the effect of large convective electric fields [11]. For such interpretation, it has been generally assumed that the energy absorbed from the discharging field appears as a change in the temperature of the electrons and this change is simply given by 2/3 K times the absorbed energy. Actual conditions in the lower ionosphere, however, deserve a non-Maxwellian distribution. Value of the number of electrons obtained from Maxwellian distribution is higher than that obtained from non-Maxwellian distribution. This is prominent for lower values of discharging fields and decreases with increasing magnitude of the field.

In the D-region of the ionosphere, the ratio of the change in conductivity for the non-Maxwellian distribution and for the Maxwellian distribution would decrease in magnitude for non-elastic collisions within the medium. Hence, the error due to Maxwellian distribution will be reduced substantially for non-elastic or partly non-elastic collisions [12, 13]. Thus, for brevity, the Maxwellian distribution functions have been used for this problem as the field due to the lightning discharge is very high.

Acknowledgement

This work is funded by Indian Space Research Organization (ISRO) through S. K. Mitra Centre for Research in Space Environment, University of Calcutta, Kolkata 700 009, India.

REFERENCES

1. Velinov, I. I. Y. and Tonev, P. T., "Thundercloud electric field modeling for the ionosphere-Earth region. 1. Dependence on cloud charge distribution," *J. Geophys. Res.*, Vol. 100, 1477-1485, 1995.
2. Lyons, W. A., "Characteristics of luminous structures in the stratosphere above thunderstorm as imaged by low-light video," *Geophys. Res. Lett.*, Vol. 21, 875-878, 1994.
3. Taranenko, Y. N., Inan, U. S. and Bell, T. F., "Interaction with the lower ionosphere of electromagnetic pulses from lightning: heating, attachment and ionization," *Geophys. Res. Lett.*, Vol. 20, 1539-1542, 1993a.
4. Milikh, G. M., Papadopoulos, K. and Chang, C. L., "On the physics of high latitude lightning," *Geophys. Res. Lett.*, Vol. 22, 85-88, 1995.
5. Nickolaenko, A. P. and Hayakawa, M., "Heating of the lower ionosphere electrons by electromagnetic radiation of lightning discharges," *Geophys. Res. Lett.*, Vol. 22, 3015-3018, 1995.
6. Papa, R. J., "The nonlinear interaction of an electromagnetic wave with a time-dependent plasma medium," *Can. J. Phys.*, Vol. 43, 38-56, 1965.
7. Aggarwal, K. M., and Setty, C. S. G. K., "Collisions and transport of electrons in the ionosphere," *Indian J. Radio Space Phys.*, Vol. 9, 105-111, 1980.
8. Jones, D. L., "Electromagnetic radiation from multiple return strokes of lightning," *J Atmos. Terr. Phys.*, Vol. 32, 1077-1093, 1970.
9. Cospar International Reference Atmosphere (CIRA) ed. A. C. Stickland, Akademie-Verlag, Berlin, 1972.
10. Inan, U. S., "VLF heating of the lower ionosphere," *Geophys. Res. Lett.*, Vol. 17, 729-732, 1990.
11. Hubert, D. J., "Non-Maxwellian velocity distribution functions and incoherent scattering of radar waves in the auroral ionosphere," *J. Atmos. Terr. Phys.*, Vol. 46, 601-611, 1984.
12. Huxley, L. G. H., "A discussion of the motion in nitrogen of free electrons with small energies with reference to the ionosphere," *J. Atmos. Terr. Phys.*, Vol. 16, 46-58, 1959.
13. Frost, L. S. and Phelps A. V., "Rotational excitation and momentum transfer cross sections for electrons in H₂ and N₂ from transport coefficients," *Phys. Rev.*, Vol. 127, 1621-1633, 1962.

Combined RWG-Orthogonal Polynomial Expansion for MoM Analysis of Printed Antenna on Finite Dielectric Substrate

Amin Saeedfar, Hiroyasu Sato, and Kunio Sawaya
Tohoku University, Japan

Abstract—An integral equation approach with a new MoM solution method is used to obtain current on the surface of a printed dipole antenna on a dielectric finite substrate, which is required for computation of antenna characteristic. For this purpose, a coupled tensor-volume/surface integral equations(TVSIE)is employed. To solve the tensor-volume integral equation, a mixed-domain MoM expansion using modified Legendre polynomial basis function and cubic modeling are adopted. For current modeling on the printed structure, Rao-Wilton-Glisson (RWG) basis function is used. The accuracy of the proposed approach is verified through comparison with the MoM solution based on the spectral domain Green's function for infinitely large substrate, the results of FDTD method, and experimental data.

1. Introduction

The study of the electromagnetic wave scattering from arbitrarily shaped three-dimensional dielectric bodies has been of considerable current interest owing to the wide range of applications such as analysis of printed antennas on dielectric substrate with finite size. Analytical and full-wave numerical methods have been widely used in analysis and design of many types of printed and patch antennas. Typical numerical methods for a printed structure analysis include the method of moments(MoM), the finite-difference time-domain(FDTD) method, the finite elements method(FEM), and the transmission line method(TLM). The techniques that are based on integral equation approaches, usually rely on the layered Green's function using Sommerfeld formulation, and hence are limited to infinitely large and flat dielectric substrates. By using this method in practical applications, accurate results can be achieved when the substrate size is much larger than that of the printed structure. However, it is generally accepted that when the substrate edge is close to that of printed patch, the input impedance will not be accurate if the integral equation approach with Green's function of infinitely large dielectric substrate is utilized.

In this paper, a coupled tensor-volume/surface integral equations system is adopted and solved by the Galerkin's based MoM using a hybrid-domain polynomial expansion for three-dimensional dielectric substrate and the RWG basis function for a printed antenna. There are different reports of similar studies for modeling printed structures with finite size substrate by MoM using different basis and testing functions, numerical integration and also different geometric modeling [1]-[3]. Nevertheless, there are some main differences between this work and previous studies. The first difference is the extreme care, which has been exercised in calculation of the principle value integrals for singularity extractions of self coupling of volume-volume, surface-volume and surface-surface impedance matrix elements through the Galerkin's method computation. The second difference of this paper with the previous ones is use of three-dimensional modified Legendre polynomials [4] with various degrees for field estimation inside the dielectric body applying a combined sub-domain and entire-domain expansion method so-called mixed-domain moment method. These two tasks cause to obtain more accurate and stable solutions of MoM including dielectric bodies of finite sizes. In fact, this approach in MoM using two types of polynomials has been previously introduced and well applied in [5]-[8] for solutions of single tensor-volume integral equation and coupled tensor-volume/line integral equations. In this paper, it is applied for the TVSIE solution and its accuracy is compared with the results of MoM solution based on the spectral domain Green's function for infinitely large substrate and the results of FDTD method.

2. Sub-domain Surface and Mixed-Domain Volume Expansions in MoM

An important issue affecting the accuracy and convergence of MoM solutions is the choice of expansion functions used to represent the unknown currents or fields in formulation of a radiation or scattering problem.

In this work, for current estimation on the surface of the conducting printed structure, RWG basis function [9] is applied. It has been used and verified by many articles that it gives high level of accuracy for current distribution on conducting surfaces.

Furthermore, a mixture of three-dimensional polynomials with various degrees is applied for field expansion inside the dielectric body. In mixed-domain expansion method, polynomials with higher degrees are used for some macro-blocks located in the internal part of the dielectric object and polynomials with lower degrees (pulse function as a special case), which behave as sub-domain basis function are used for smaller blocks at corners and boundaries of the dielectric body to provide a suitable estimation of dielectric shape. In other words, since the main profile of the modal field is well represented by the entire-domain basis function, fewer sub-domain basis functions are required for further refinement of the field representation to get the same accuracy compared to formulation using only sub-domain basis function. In fact, this hybrid expansion bridges the limitations of entire-domain and sub-domain expansions in some problems and combines the geometric flexibility inherent in sub-domain expansion with computational efficiency of entire-domain formulation. The analytic property of polynomial function is especially useful in field expansion procedure for the near field problems and complex materials because of the non-uniform behavior of fields in these circumstances.

Two types of three-dimensional polynomials may be utilized as the basis function in MoM procedure, i.e., power polynomials and modified Legendre polynomial. Both have polynomial characteristics over the proposed MoM but modified Legendre polynomial, which has been introduced in [4] can enhance the accuracy and stability of the solutions at the expense of more complicated computations. It is given by the following relations

$$\mathbf{J}_p = \sum_{n=1}^N \sum_{c=1}^3 \sum_{i=0}^{N_{nx}} \sum_{j=0}^{N_{ny}} \sum_{k=0}^{N_{nz}} a_{ijk}^{(nc)} \mathbf{g}_{ijk}^{(nc)}, \quad u_n(\mathbf{r}) = \begin{cases} 1 & \text{if } \mathbf{r} \in V_n \\ 0 & \text{Otherwise} \end{cases} \quad (1)$$

$$\mathbf{g}_{ijk}^{(nc)} = \hat{P}_i^{(c)}(x_1) \hat{P}_j^{(c)}(x_2) \hat{P}_k^{(c)}(x_3) u_n(\mathbf{r}) \hat{c} \quad (2)$$

$$(\hat{1}, \hat{2}, \hat{3}) = (\hat{x}, \hat{y}, \hat{z}), (x_1, x_2, x_3) = (x, y, z) \quad (3)$$

$$\hat{P}_i^{(c)}(x_\alpha) = \begin{cases} C_i P_i(x_\alpha) & , \alpha \neq c \\ \tilde{C}_i \tilde{P}_i(x_\alpha) & , \alpha = c \end{cases}, \quad \tilde{P}_i(x_\alpha) = \begin{cases} 1 - x_\alpha & , i = 0 \\ 1 + x_\alpha & , i = 1 \\ P_i(x_\alpha) - P_{i-2}(x_\alpha) & , i \geq 2 \end{cases} \quad (4)$$

$$P_i(x) = \frac{1}{2^i i!} \frac{d^i}{dx^i} (x^2 - 1)^i, \quad \int_{-1}^1 P_i(x) P_j(x) dx = \frac{2}{2i+1} \delta_{ij} \quad (5)$$

This basis function is derived from orthogonal Legendre polynomial, which is modified to impose the current continuity condition of the currents between neighboring elements. This allows the use of high-order basis functions without introducing ill-conditioning of the resulting MoM matrix and improves the accuracy at the same time [4], [6].

3. MoM Formulation of TVSIE

The basic idea of tensor-volume/surface integral equation method is to use the surface equivalent theorem and volume equivalent principle to replace the conducting patch with a surface current, and the dielectric volume with a polarization current. Coupling between the dielectric object and the antenna is considered by forcing the incident field in the body to be that radiated by the antenna, and the total tangential electric field on the surface of the perfectly conducting antenna to be zero. This results in a set of coupled integral equations to be solved simultaneously, which yields the total field setup by the radiator/dielectric system, and the circuit characteristics of the radiator itself. It is given by

$$\begin{pmatrix} \frac{1}{j\omega\Delta\epsilon} + L_d & L_a \\ (\hat{n} \times L_d) & (\hat{n} \times L_a) \end{pmatrix} \begin{pmatrix} \mathbf{J}_d \\ \mathbf{J}_a \end{pmatrix} = \begin{pmatrix} \mathbf{E}^{inc} \rightarrow \mathbf{r} \in V \\ \hat{n} \times \mathbf{E}^{inc} \rightarrow \mathbf{r} \in S \end{pmatrix} \quad (6)$$

where

$$L_d = j\omega\mu_0 \int_V \overline{\mathbf{G}}_0(\mathbf{r}, \mathbf{r}') \cdot (*) dv', \quad L_a = j\omega\mu_0 \int_S \overline{\mathbf{G}}_0(\mathbf{r}, \mathbf{r}') \cdot (*) ds', \quad \Delta\epsilon = \epsilon(\mathbf{r}) - \epsilon_0 \quad (7)$$

Now, by substitution of basis functions into the system of integral equations and applying the inner product procedure in the case of mixed-domain expansion for dielectric volume, the following simultaneous algebraic

equations system is achieved

$$\sum_{n:V_n \cap V_m \neq \emptyset} \left(j\omega\mu_0 \langle \mathbf{w}_{pqr}^{(md)}, \mathbf{I}_2^{(n)} \rangle + \frac{1}{j\omega\epsilon_0} \langle \mathbf{w}_{pqr}^{(md)}, \left(\frac{1}{3} + \frac{1}{(\epsilon_r^* - 1)} \right) \mathbf{f}_n \rangle \right) + j\omega\mu_0 \sum_{n:V_n \cap V_m = \emptyset} \langle \mathbf{w}_{pqr}^{(md)}, \mathbf{I}_1^{(n)} \rangle + \sum_{t=1}^{N_A} b_t \langle \mathbf{w}_{pqr}^{(md)}, L_a(h_t(\mathbf{r})) \rangle = \langle \mathbf{w}_{pqr}^{(md)}, \mathbf{E}^{inc} \rangle \quad (8)$$

$$\sum_{n=1}^N \langle h_t(\mathbf{r}), \hat{n} \times L_d(\mathbf{f}_n u_n(\mathbf{r})) \rangle + \sum_{t=1}^{N_A} b_t \langle h_t(\mathbf{r}), \hat{n} \times L_a(h_t(\mathbf{r})) \rangle = \langle h_t(\mathbf{r}), \hat{n} \times \mathbf{E}^{inc} \rangle \quad (9)$$

where

$$\mathbf{I}_1^{(n)} = \int_{V_n} \overline{\mathbf{G}}_0(\mathbf{r}, \mathbf{r}') \cdot \mathbf{f}_n(\mathbf{r}') dv', \quad \mathbf{I}_2^{(n)} = \lim_{V_\delta \rightarrow 0} \int_{V_n - V_\delta} \overline{\mathbf{G}}_0(\mathbf{r}, \mathbf{r}') \cdot \mathbf{f}_n(\mathbf{r}') dv', \quad \epsilon_r^* = \epsilon_r + \frac{\sigma}{j\omega} \quad (10)$$

and

$$\mathbf{f}_n = \sum_{c=1}^3 \sum_{i=0}^{N_{nx}} \sum_{j=0}^{N_{ny}} \sum_{k=0}^{N_{nz}} a_{ijk}^{(nc)} \hat{P}_i^{(c)}(x_1) \hat{P}_j^{(c)}(x_2) \hat{P}_k^{(c)}(x_3) \hat{c}, \quad \mathbf{J}_a = \sum_{t=1}^{N_A} b_t h_t(\mathbf{r}) \quad (11)$$

In the above relations, $h_t(\mathbf{r})$ denotes the RWG basis function and two sets of unknowns represented by $\{b_t\}$ and $\{a_{ijk}^{(nc)}\}$ are obtained by solving the generalized matrix equation derived from (8) and (9).

As it was mentioned before, there are three types of singularity through the calculation of inner product integrals in Galerkin's method. During the calculation of volume-volume elements of impedance matrix of mixed-domain MoM, singularity happens not only in the calculation of generalized self-impedance terms, but also in the calculation of some generalized mutual-impedance elements between two blocks in which their integration regions overlap improving the current continuity condition. Detail analysis for removing these kind of singularities is presented in [8], [10]. In the case of surface-surface elements, the singular integrals are evaluated using the classical method of RWG basis function mention in [9]. Finally, in the case of volume-surface terms, when the surface of the printed structure coincides with the surface of a volume cell, singularity occurs in the corresponding inner product integral, which is treated differently. The Duffy method [3], [11], [12] is applied for this singular treatment. In Duffy's approach, the domain, which includes a singular point is first subdivided into certain sub-regions that share a common vertex at the singular point. Then, each sub-region is mapped to a unit domain via a change of variable. It can be shown that the integrand in the new domain is not singular and regular Gaussian quadrature rules can be applied to evaluate the integral [11].

3. Numerical Results

In this section, we present some numerical examples to demonstrate the application of the proposed solution of TVSIE in impedance calculation of a printed dipole antenna with a three-dimensional substrate. The analysis model is shown in Figure 1. The following parameters have been adopted in this analysis model for numerical calculations: $L_z = L_x = 200mm$, $L_y = 2.4mm$, $w = 3mm$, $2H = 100mm$. In MoM procedure, the dielectric material is first divided into $20 \times 3 \times 20$ where the size of blocks is $10mm \times 0.8mm \times 10mm$. After that, for mixed-domain computation the whole dielectric body is considered as an entire-domain region and only the sub-domain blocks on the sides of the entire-domain region are used for overlapping regions [8].

In FDTD calculations, number of cells is $881 \times 107 \times 441$ and the number of time steps is taken as 30,000. Also, the cell sizes are $\Delta x = 0.25mm$, $\Delta y = 0.4mm$ and $\Delta z = 0.5mm$. It should be mentioned the applied cell size is quite small compared with the effective wavelength of used frequency band. This was done to get results as accurate as possible by FDTD technique. FDTD calculations were performed by supercomputer of Tohoku University SX-7.

Figures 2 and 3 indicate the input impedance of the applied model for $\epsilon_r = 10.2$ and Figures 4 and 5 show it for $\epsilon_r = 20$. The presented results have been obtained using proposed MoM, FDTD method, infinite substrate MoM with corresponding Green's function and experimental data [13]. It can be observed that in the case of higher-permittivity, the difference between MoM results and FDTD results is larger than that of lower-permittivity case. Figure 6 shows the return loss of the printed dipole antenna. It is seen that the center frequencies obtained from proposed MoM and infinite large substrate MoM are more close compared with that of FDTD method.

4. Conclusion

A hybrid TVSIE approach was applied to calculate the input impedance of the printed structure with a finite dielectric substrate. A mixed-domain Galerkin-based MoM was used for an accurate and efficient solution of the tensor-volume integral equation (TVIE) using three-dimensional modified Legendre polynomial expansion in combination with a sub-domain MoM expansion using RWG basis function. The accuracy of the proposed method was confirmed by comparing with FDTD method, MoM solution based on Green's function for infinitely large substrate, and experimental data for two relatively high values of permittivities.

REFERENCES

1. Sarkar, T. K., Arvas, E.“An integral equation approach to the analysis of finite microstrip antennas:volume/surface formulation,” *IEEE Trans. Antennas Propag.*, Vol. 38, No. 3,pp.305-312, March 1990.
2. Sarkar, T. K., Rao, S. M., Djordjevic, R.“Electromagnetic scattering and radiation from finite microstrip structures,” *IEEE Trans. Antennas Propag.*, Vol. 38, No. 11,pp.1568-1575, Nov.1990.
3. Lu, C. C., Yu, C.“Computation of input impedance of printed antennas with finite size and arbitrarily shaped dielectric substrate and ground plane,” *IEEE Trans. Antennas Propag.*, Vol. 52, No. 2,pp.615-619, Feb.2004.
4. Jorgensen, E., et al. “Higher order hierarchical Legendre basis functions for electromagnetic modeling,” *IEEE Trans. Antennas Propag.*, Vol. 52, No. 11,pp.2985-2995, Nov.2004.
5. Saeedfar, A., Sawaya, K.“Mixed-domain moment method solution of the tensor-volume integral equation for three-dimensional dielectric scatterers,” *proceedings of the International Conference on Electromagnetics in Advanced Applications (ICEAA05)*, pp.271-274, September2005, Torino, Italy.
6. Saeedfar, A., Sawaya, K.“Mixed-domain Galerkin’s method for tensor-volume integral equation using Legendre polynomial expansion and efficient numerical integration,” *accepted by the 2006 IEEE AP-S /URSI Symposium*.
7. Saeedfar, A., Sato, H., Sawaya, K.“Numerical and experimental impedance analyses of a thin-wire antenna in the presence of a high-permittivity 3D dielectric body,” *accepted by the 2006 IEEE AP-S /URSI Symposium*.
8. Saeedfar, A., Sawaya, K.“Improved solution of tensor-volume integral equation using mixed-domain MoM with polynomial expansion,” *submitted to the IEICE Transactions on Communications*.
9. Rao, S. M., Wilton, D. R., Glisson, A. W.“Electromagnetic scattering by surfaces of arbitrary shape,” *IEEE Trans. Antennas Propag.*, Vol. 30, No. 3,pp.409-418, May 1982.
10. Kottmann, J. P., Martin, O. J. F.“Accurate solution of the volume integral equation for high-permittivity scatterers,” *IEEE Trans. Antennas Propag.*, Vol. 48, No. 11,pp.1719-1726, Nov.2000.
11. Duffy, M. G.“Quadrature over a pyramid or cube of integrands with a singularity at a vertex,” *SIAM J. Num. Anal.*, Vol. 19, No. 6,pp.1260-1262, Dec.1982.
12. Sertel, K., Volakis, J. L.“Method of moments solution of volume integral equations using parametric geometry,” *Radio Sci.*, Vol. 37, No. 1,pp.1-7, Jan.-Feb.2002.
13. Hwang, J. H., *Study on Analysis of Antennas on High-Permittivity Dielectric Substrates*, Ph.D. Dissertation, Tohoku Univ., 1998.

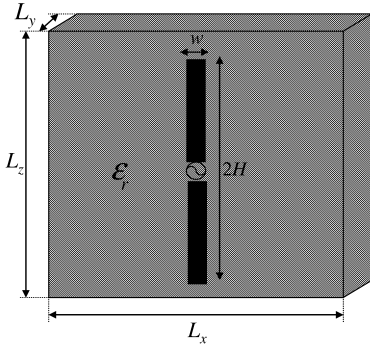


Figure 1: Analysis Model.

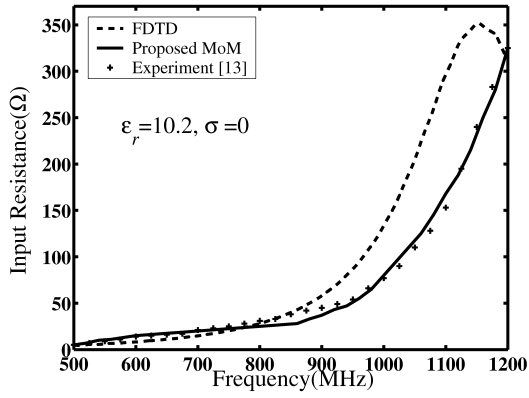
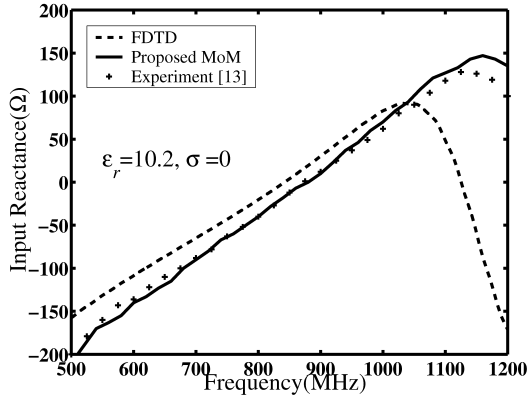
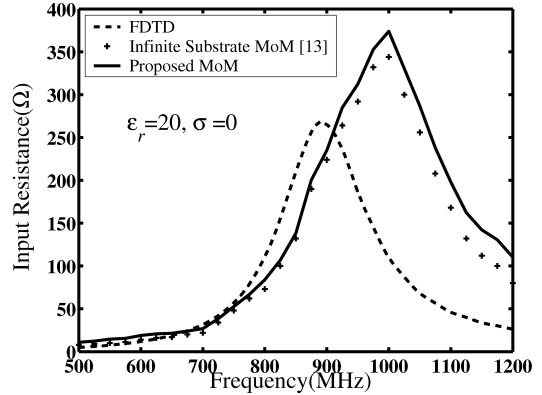
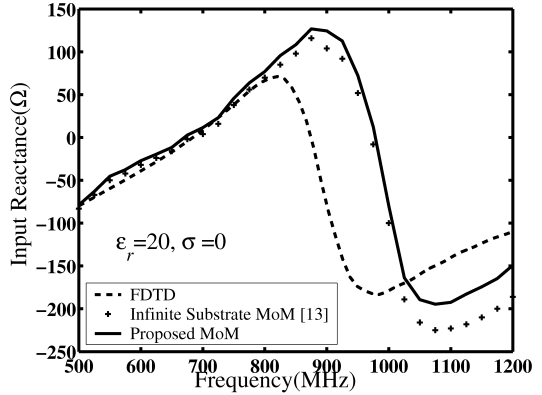
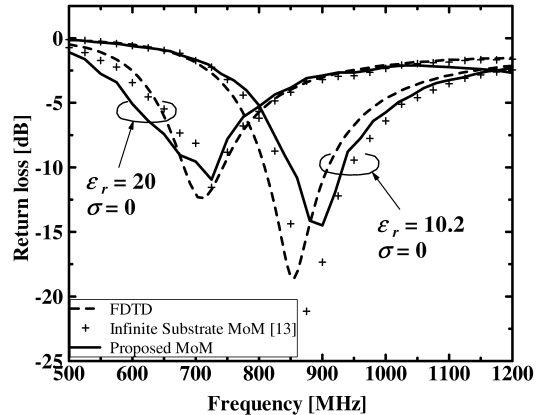
Figure 2: Input resistance for $\epsilon_r=10.2$.Figure 3: Input reactance for $\epsilon_r=10.2$.Figure 4: Input resistance for $\epsilon_r=20$.Figure 5: Input reactance for $\epsilon_r=20$.

Figure 6: Return loss.

Hybrid Numerical Simulation of Electrostatic Force Microscopes in 3D

U. B. Bala, M. Greiff , W. Mathis
University of Hanover, Germany

Abstract—In this paper a hybrid numerical approach for the simulation of electrostatic force microscopes(EMF) is presented. In the simulation model electrical part is considered. In this paper a detailed description is given on the 3D coupling methods together with several simulation results of the EFM.

1. Introduction

Due to the rapid miniaturization of integrated devices into the mesoscopic regime and the increasing interest in very small structures, high resolution measurement instruments have become very important within the last years. An example of such measuring instrument is the atomic force microscope (AFM). Its ability to scan surfaces with nearly atomic resolution and its versatility make it one of the most important measurement devices in nanotechnics. If the sample under investigation holds a charge distribution and the distance between the AFM tip and the sample is kept large then all other interaction forces except electrostatic force can be neglected. This special working mode of AFM is known as electrostatic force microscope (EFM) which can be used for scanning samples with nearly atomic resolution. In this paper a 3D model of the EFM is presented and several numerical methods are applied to calculate the electric field more efficiently.

2. 3D Model of the EFM

For modeling and simulating the EFM, multi physics aspects must be taken into consideration. From the numerical point of view additional problems arise since frequently we are confronted with multi-scale problems. Therefore advanced numerical methods have to be applied. At the same time the coupled mechanical and electrical behavior have to be taken into account. This can be achieved by dividing the model into an electrical part and a mechanical part [2] as shown in Fig. 1. The interaction between them can conveniently be realized by using a staggered simulation approach.

For developing a model of the EFM different effects have to be considered. For example long distance interaction, charge distribution and non-linearity of the material properties, singularity etc. In order to take into consideration these effects the simulation region is divided into three regions as shown in Fig. 2. As high value of the electric field will occur at the pick of the tip, a special numerical method is needed to calculate this electric field more effectively. For this reason an augmented FEM will be applied to region Ω_M . Since charge distribution and nonlinearities of the dielectric properties may have to be considered, a versatile numerical method such as finite element method (FEM) should be applied to region Ω_F . As boundary element method (BEM) works well when the boundary is infinite or semi-infinite, the large distance interaction between the tip and the cantilever can be conveniently treated by using BEM in the region Ω_B . Later all these three numerical methods will be coupled with each other.

Since the scanning process of an EFM is dynamic, the FEM mesh has to be updated at each time step which is achieved by implementing arbitrary Lagrangian Eulerian (ALE) algorithm in 3D. In this algorithm the mesh is modeled as a massless elastic which is deformed by the changing position of the cantilever and the sample (Fig. 3). Here it is obtained by solving the vector Laplace equation in 3D.

2. Formulation of the Problem

The energy-related functional in the electrostatic calculation domain Ω (Fig. 2) can be written as

$$W = \int_{\Omega} (\nabla u)^2 d\Omega \quad u \in H_D^1(\Omega) : \left\{ u \in H^1 | u|_{\Gamma_D} = u_0 \right\} \quad (1)$$

where $u(a_1, a_2, \dots, a_m, x, y)$ is an approximation of the potential $u(x, y)$. It is well known that the solution of

$$\frac{\partial W}{\partial a_i} = 2 \int_{\Omega} \nabla u \frac{\partial \nabla u}{\partial a_i} d\Omega = 0 \quad (2)$$

yields an approximative solution for the Laplace equation in Ω where only Dirichlet boundary conditions are taken into account. The electrostatic potential u in the spherical region Ω_M of radius R can be approximated by [11]

$$u(x, y, z) = \sum_{j=1}^n u_j \psi_j(x, y, z) + M(r) \sum_{l=0}^{\infty} \sum_{m=-l}^l \left(A_{lm} r^l + B_{lm} r^{-(l+1)} \right) Y_{lm}(\theta, \phi), \quad (3)$$

where

$$M(r) = \begin{cases} 1, & 0 \leq r \leq \frac{R}{2} \\ \frac{1}{2} (1 + \cos(\frac{2}{R}r - 1)\pi), & \frac{R}{2} < r < R \\ 0, & R \leq r \end{cases} \quad (4)$$

and $Y_{lm}(\theta, \phi)$ can be expressed by the Legendre functions $P_{lm}(\cos \theta)$ [7]

$$Y_{lm}(\theta, \phi) = \sqrt{\frac{2l+1}{4\pi} \frac{(l-m)!}{(l+m)!}} P_l^m(\cos \theta) e^{jm\phi}. \quad (5)$$

This leads to the stiffness matrix

$$\frac{\partial W}{\partial u_i} = 2 \int_{\Omega} \nabla u \frac{\partial \nabla u}{\partial u_i} d\Omega, \quad \frac{\partial W}{\partial A_{ik}} = 2 \int_{\Omega} \nabla u \frac{\partial \nabla u}{\partial A_{ik}} d\Omega, \quad \frac{\partial W}{\partial B_{ik}} = 2 \int_{\Omega} \nabla u \frac{\partial \nabla u}{\partial B_{ik}} d\Omega. \quad (6)$$

The integrals that include the FEM shape functions $\psi_j(x, y, z)$ are solved numerically on the FEM mesh while the integrals only including the spherical functions $Y_{lm}(r, \theta, \phi)$ are calculated by Gauss integration on a spherical grid.

On the FEM-BEM transmission interface [2] $\Gamma_T = \Gamma_B \cap \Gamma_F$, $u_B = u_F$ and $\frac{\partial u_B}{\partial n} + \frac{\partial u_F}{\partial n} = 0$. Using the Gauss theorem on $\Omega_{FM} = \Omega_F \cup \Omega_M$ one obtains [3]

$$\int_{\Gamma_F} \frac{\partial u_{FM}}{\partial n} v d\Gamma = \int_{\Omega_{FM}} \operatorname{div}(\nabla u_{FM} \cdot v) d\Omega = \int_{\Omega_{FM}} \Delta u_{FM} \cdot v d\Omega + \int_{\Omega_{FM}} \nabla u_{FM} \cdot \nabla v d\Omega \quad (7)$$

i.e., for all $v \in H_{D,0}^1(\Omega_{FM}) := \{v \in H^1(\Omega_{FM}) : v|_{\Gamma_D \cap \Gamma_F} = 0\}$

$$a(u_{FM}, v) := \int_{\Omega_{FM}} \nabla u_{FM} \cdot \nabla v d\Omega = \int_{\Omega_{FM}} f \cdot v d\Omega + \int_{\Gamma_F} \frac{\partial u_{FM}}{\partial n} v d\Gamma =: (f, v)_{\Omega_{FM}} + \left\langle \frac{\partial u_{FM}}{\partial n}, v \right\rangle_{\Gamma_F} \quad (8)$$

where u_{FM} includes u_j , A_{lm} and B_{lm} . The representation formula of the Laplace equation for the solution of u_B inside Ω_B

$$u_B(x) = \int_{\Gamma_B} \left\{ \frac{\partial}{\partial n(y)} G(x, y) u_B(y) - G(x, y) \frac{\partial u_B}{\partial n(y)} \right\} d\Gamma, \quad x \in \Omega_B \quad (9)$$

with the fundamental solution of the Laplacian in 3D given by

$$G(x, y) = \frac{1}{4\pi} |x - y|^{-1} \quad (10)$$

If one computes the Cauchy data [10] u_B and $\partial u_B / \partial n$ of $u_B(x)$, one will get two boundary integral equations on $\partial\Omega_B$,

$$V \frac{\partial u_B}{\partial n} = (I + K) u_B \quad (11) \quad W u_B = (I - K') \frac{\partial u_B}{\partial n} \quad (12)$$

where the boundary integral operators are defined as

$$V\psi(x) := 2 \int_{\Gamma_B} G(x, y) \psi(y) d\Gamma_y, \quad K\psi(x) := 2 \int_{\Gamma_B} \frac{\partial}{\partial n_y} G(x, y) \psi(y) d\Gamma_y, \quad x \in \Gamma_B \quad (13)$$

$$K'\psi(x) := 2 \frac{\partial}{\partial n_x} \int_{\Gamma_B} G(x, y) \psi(y) d\Gamma_y, \quad W\psi(x) := -2 \frac{\partial}{\partial n_x} \int_{\Gamma_B} \frac{\partial}{\partial n_y} G(x, y) \psi(y) d\Gamma_y, \quad x \in \Gamma_B \quad (14)$$

where the single layer potential V and the hypersingular operator W are symmetric and the double layer potential K has the dual K' [1].

Using (12) one can eliminate $\partial u_B / \partial n$ with (11). This leads to

$$Wu_B = (I - K') \frac{\partial u_B}{\partial n} = 2 \frac{\partial u_B}{\partial n} - (I + K') \frac{\partial u_B}{\partial n} = 2 \frac{\partial u_B}{\partial n} - (I + K')V^{-1}(I + K)u_B \quad (15)$$

with the Poincaré-Steklov-Operator S applied to u_B

$$Su_B := (W + (I + K')V^{-1}(I + K))u_B = 2 \frac{\partial u_B}{\partial n} \quad (16)$$

which can be used for symmetric coupling. In variational form for all $w \in \tilde{H}^{1/2} := \{w \in H^{1/2}(\Gamma_B) : w|_{\Gamma_D \cap \Gamma_B} = 0\}$ holds

$$\langle Su_B, w \rangle_{\Gamma_B} = 2 \langle \frac{\partial u_B}{\partial n}, w \rangle_{\Gamma_B}. \quad (17)$$

With (8) and (17) one can obtain the variational formulation

$$2a(u_{FM}, v) + \langle Su_B, v \rangle_{\Gamma_T} = 2(f, v)_{\Omega_{FM}} + 2 \langle t_0, v \rangle_{\Gamma_N \cap \Gamma_F} \quad (18)$$

$$\langle Su_B, w \rangle_{\Gamma_B \cap \Gamma_N} = 2 \langle t_0, w \rangle \quad (19)$$

for all $(w, v) \in \tilde{H}^{1/2} \times H_{D,0}^1(\Omega_F)$ with f being the charge distribution inside Ω_F and t_0 are the Neumann boundary conditions.

The Poincaré-Steklov-Operator S cannot discretize directly because the inverse single layer potential V cannot be descretized in the usual way. For this reason without Poincaré-Steklov-Operator the problem can be rewritten as saddle point formulation. The saddle point formulation of the problem for all $(w, v, \psi) \in \tilde{H}^{1/2} \times H_{D,0}^1(\Omega_{FM}) \times \tilde{H}^{-1/2}(\Gamma_B)$

$$2a(u_{FM}, v) + \langle Wu_B, v \rangle_{\Gamma_T} + \langle (I + K')\varphi, v \rangle_{\Gamma_T} = 2(f, v)_{\Omega_{FM}} + 2 \langle t_0, v \rangle_{\Gamma_N \cap \Gamma_F} \quad (20)$$

$$\langle Wu_B, w \rangle_{\Gamma_B \cap \Gamma_N} + \langle (I + K')\varphi, w \rangle_{\Gamma_B \cap \Gamma_N} = 2 \langle t_0, w \rangle_{\Gamma_B \cap \Gamma_N} \quad (21)$$

$$\langle (I + K)u_B, \psi \rangle_{\Gamma_B} - \langle V\varphi, \psi \rangle_{\Gamma_B} = 0 \quad (22)$$

If the bases are introduced as $\text{span}\{v_1, \dots, v_F\} = X_F$, $\text{span}\{w_1, \dots, w_B\} = X_B$ and $\text{span}\{\psi_1, \dots, \psi_F\} = Y_B$, the basis functions of X_F and X_B are supposed to be ordered such that

$$\text{span}\{v_1, \dots, v_F\} = X_F \cap H_{D,0}^1(\Omega_F)$$

$$\text{span}\{w_1, \dots, w_B\} = X_B \cap H^{1/2}(\Gamma_B).$$

If the coefficients of u_{FM} and u_B are denoted by u and the coefficients of φ are denoted by φ again then this system is equivalent to the original differential equation that can be used for descretization. This system corresponds to a matrix formulation which can be written as

$$\begin{pmatrix} M & B^T & 0 & 0 & 0 \\ B & F_{NN} & F_{NC} & 0 & 0 \\ 0 & F_{CN} & F_{CC} + W_{CC} & W_{CN} & (K^T + I)_C \\ 0 & 0 & W_{NC} & W_{NN} & (K^T + I)_N \\ 0 & 0 & (K + I)_C & (K + I)_N & -V \end{pmatrix} \begin{pmatrix} u_m \\ u_F \\ u_T \\ u_B \\ \varphi \end{pmatrix} = \begin{pmatrix} b_m \\ b_F \\ b_T \\ b_B \\ b_\varphi \end{pmatrix} \quad (23)$$

where the subscript C means contribution from the coupling nodes and N means contribution from the non-coupling nodes. Finally the blocks $W, V, K + I$, and $K^T + I$ provide the coupling between the two ansatz spaces X_F and X_B . Here u_m includes the coefficients A_{lm} and B_{lm} (3), u_F and u_B are the nodal potentials inside the FE domain and on the boundary of the BE domain respectively, u_T are the nodal potentials on the FE-BE coupling interface and φ are the normal components of the electric field distribution on the boundary of the BE

domain. The vector b includes the corresponding boundary conditions. As the matrix in (23) is not positive definite, a specific algorithm such as the MINRES algorithm is required for the solution.

A typical simulation of potential distribution and electric field distribution are shown in Fig. 4 and 6 respectively. The result of a typical simulation of potential distribution and electric field distribution considering a moving sample using FEMBEM coupling in the cut plane through the middle of the cantilever is shown in Fig. 5 and 7 respectively. Here ALE is implemented to fit the mesh with the moving boundaries. The mesh deformation considering moving boundaries are shown in Fig. 3. In Fig. 7 a high value of electric field can be observed near the pick of the tip which reaches its maximum when the moving object is exactly below the bottom of the tip. By utilizing this high value of electric field EFM will scan the surface of the moving object.

3. Figures

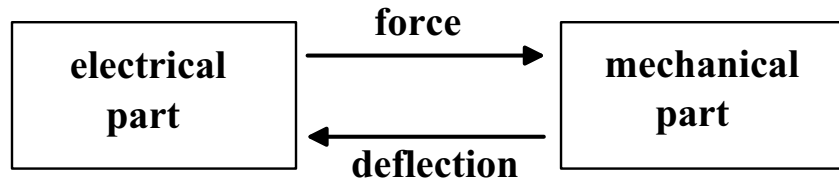


Figure 1: Mechanical and Electrical Part

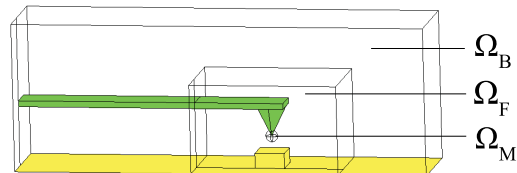


Figure 2: 3D EFM model

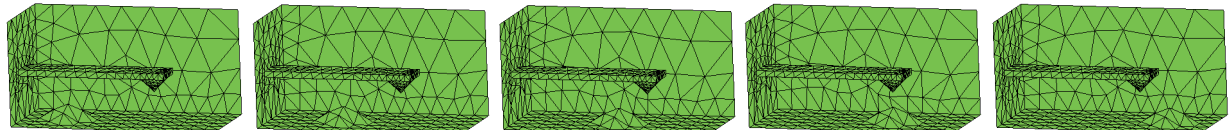


Figure 3: 3D ALE Mesh Deformation

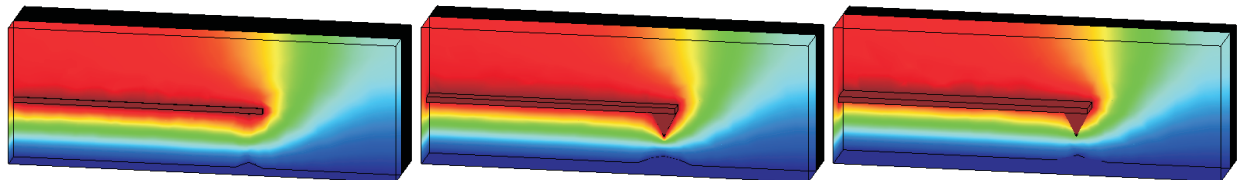


Figure 4: Potential distribution on different places of an EFM

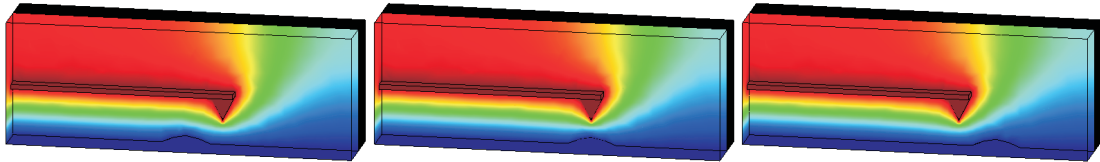


Figure 5: Potential distribution on the middle position of EFM with moving object

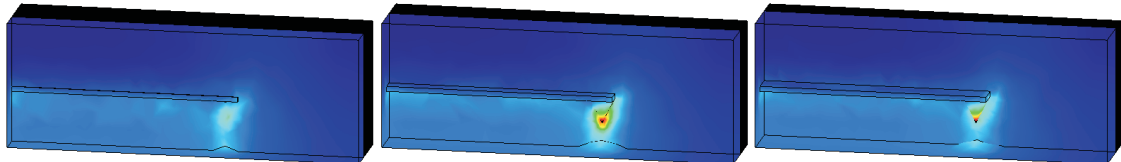


Figure 6: Electric field distribution on different places of an EFM

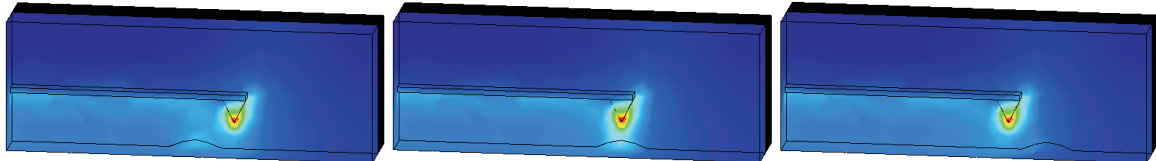


Figure 7: Electric field distribution on the middle position of EFM with moving object

4. Conclusion

A hybrid numerical approach for the simulation of electrostatic force microscope is presented here. In order to fulfill the different requirements various numerical methods are applied to different regions. Here the simulation is implemented using FEMBEM coupling. As a high value of electric field is observed near the pick of the tip, implementing augmented FEM near the tip will obviously calculate this field more efficiently. In this model ALE is implemented to update the FEM mesh to fit with the moving boundaries in 3D.

Acknowledgment

The authors would like to thank PD Dr. rer. nat. M. Maischak (Institute of Applied Mathematics, Hanover University) for his contribution and valuable discussions on numerical coupling. This work has been supported by the German Research Foundation (DFG), GRK 615.

REFERENCES

1. Stephan, E. P., "Coupling of Boundary Element Methods and Finite Element Methods," *Encyclopedia of Computational Mechanic*, Vol. 01, Chapter 13, 375–412, 2004.
2. Greiff, M., Bala, U. B., Mathis, W., "Hybrid Numerical Simulation of Micro Electro Mechanical Systems," *Progress In Electromagnetic Research Symposium (PIERS)*, 270–274, 2006.
3. Reddy, J.N., *Finite Element Method*, McGraw-Hill International Editions, Singapore, 1993.
4. Bhushan B., *Handbook of Nano-technology*, Springer, Berlin, 2004.
5. Zi Cai Li, *Numerical Methods for Elliptic Problems with Singularities*, World Scientific, 1990.
6. Jackson, J.D., *Classical Electrodynamics*, Wiley, 1975.
7. Jacobs, H. O., Leuchtmann P., Homan O.J., Stemmer A., "Resolution and contrast in Kelvin probe force microscopy," *Journal of Applied Physics*, Vol. 84, No. 3, 1998.
8. Morita, S., Wiesendanger, R., Meyer, E., *Noncontract Atomic Force Microscopy*, Springer, 2002.
9. Belytschko, T., Kam Liu, W., Moran, B., *Nonlinear Finite Elements for Continua and Structures*, Wiley, Sussex, 2004.
10. Costabel, M., "A symmetric Method for the Coupling of Finite Elements and Boundary Elements," *The Mathematics of Finite Elements and Applications*, Vol. VI, 281–288, 1988.
11. Strang, G., Fix, G. J., "An Analysis of the Finite Element Method", Prentice-Hall (1973)

Ray-tracing acceleration techniques to compute diffraction and double and triple effects in RCS prediction methods based on physical optics

L. Lozano, F. Sáez de Adana, M.F. Cátedra
 Dpto. de Ciencias de la Computación, Universidad de Alcalá
 28806 Alcalá de Henares. Madrid. Spain
 Fax: +34 91 885 66 46 E-mail: kiko.saez@uah.es

Abstract—A combination of acceleration techniques to compute the RCS (Radar Cross Section) of complex targets is presented. The approach is based on the application of the Angular Z-Buffer (AZB) algorithm together with the Space Volumetric Partitioning (SVP) algorithm, for electrically large and complex bodies modelled by a high number of flat and/or curved surfaces. The technique is suitable for RCS prediction methods based on PO (Physical Optics). The contributions of simple reflection, diffraction and double and triple reflection are considered in the approach.

I. INTRODUCTION

Nowadays, tools for the RCS prediction of complex targets modelled by flat or curved facets using physical optics (PO) are quite efficient. An example of such tools is FASCRO [1]. A desirable new feature is that these tools will be as fast as possible, without losing accuracy in the numerical predictions. The application of the AZB algorithm together with the SVP algorithm is proposed to achieve this aim. The main objective is to reduce the number of surfaces that should be checked as possible contributor to the RCS and to reduce the number of surfaces to be tested as possible candidates to shadow the RCS contributor surfaces.

In the past, the AZB algorithm has been used together with the Geometric Theory of Diffraction (GTD) to compute the radiation pattern of on board antennas [2] and for the planning of picocellular systems in outdoor and indoor environments [3]. These two problems have in common that their sources are antennas that illuminate the surfaces by means of spherical waves. But, in the case of RCS a new problem appears, now the source is in the far field and illuminate the target by means of a plane wave. In order to solve this problem, a new version of the AZB algorithm has been developed in combination with the SVP algorithm to reduce the CPU-time in the RCS computations.

II. AZB AND SVP ALGORITHMS

A. AZB Algorithm

The AZB algorithm is based on the Light Buffer [4] technique that was developed for graphical design applications. Here, its application for the analysis of the contribution of diffraction, simple, double and triple reflection is outlined. The application of higher order mechanisms that contribute to the RCS can be derived from the present description and those of [2, 3].

In this case, the space seen from the origin of the absolute coordinate system of reference is divided into angular regions called anxels (angular elements), considering the angles (θ, ϕ) of the spherical coordinates system. The anxel size ($\Delta\theta, \Delta\phi$) is defined by the number of anxels considered in the angular space, figure 1.

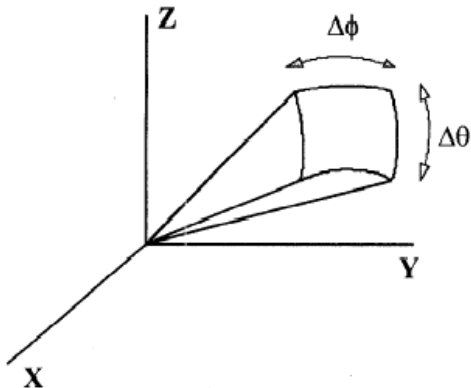


Figure 1. Anxel

A matrix AZB for each one of the effects that contribute to the RCS is obtained. The surfaces storage in the AZB matrix for simple, double and triple reflection and diffraction effects is explained below.

- 1) *Simple Reflection Effect:* the surfaces that define the geometry of the targets are located in the appropriated anxel according to its normal vector. If a surface is flat, then it is stored in the anxel according to the spherical angular coordinates of its normal vector plus a given margin. On the other hand, if the surface is curved, then it is stored in the anxels that extend over the values of the spherical angular coordinates of all the normal vectors to the surface, figures 2 and 3.
- 2) *Diffraction Effect:* the edges of the targets that form a convex dihedral. These edges are located in the appropriated anxel according to its edge vector.
- 3) *Double Reflection Effect:* the pairs of surfaces of the targets that form a concave dihedral, are quasi-perpendicular, the surfaces are close. These dihedrals are stored based on the line of intersection between the planes that contain the surfaces.
- 4) *Triple Reflection Effect:* the dihedrals formed in the double reflection are taken and they are checked if they form a concave trihedral. These trihedrals are located in the appropriated anxel according if the triple reflection is possible.

In any case, the AZB algorithm is used to reduce the time by avoiding the computation of the scattering of surfaces that do not contribute significantly to the RCS. For each direction to evaluate, only the surfaces that are located in the anxel that contains that direction are tested, reduction in that way the number of surfaces to evaluate. The reduction of the computation time increases with the number of regions considered and is only limited by the memory size available.

B. SVP Algorithm

The SVP is based on splitting a parallelepiped that encloses the target in small volumetric cells called voxels. A matrix is associated to each voxel. This matrix contains information about all the surfaces of the target that are contained or have some of their points in that voxels. Therefore, when it is necessary to test if a line is intersected by any surface in the volume of a voxel we need to check only the surfaces contained in the matrix associated with the voxel. The SVP algorithm is used to reduce the time in the shadowing test, because only the surfaces that are located in certain voxels are checked as potential occluding surfaces.

Also, when the target is excessively complex, and double reflection or higher order reflection and diffraction effects are considered, the AZB algorithm requires a large amount of computer memory for problems whose geometry is modelled by a high number of surfaces. To overcome this difficulty the original complex body is divided in a set of bodies with a less number of surfaces and the SVP algorithm is applied to these simpler bodies. The main objective is to obtain that these tools are as fast as possible and than they can be run in a PC, without losing accuracy in the numerical predictions.

III. METHODOLOGY

This method is based on the combination of the AZB and SVP algorithms. Once the surfaces have been stored in the appropriated AZB and SVP matrices, the process to obtain the RCS is as follows:

- 1) Consider a voxel of SVP matrix of the geometric model.
- 2) Given a direction of RCS analysis, the surfaces candidates to contribute to each effect are selected. The selection is made considering the matrices associated to the anxel where is located of the direction under study. These surfaces are called active surfaces.
- 3) For each one of the active surfaces it is found the potential surfaces that can shadow in the observation direction the active surface. The surfaces that potentially can shadow the active surface are all those that are contained in the SVP matrices of the voxels that are cut by the incident ray.
- 4) The process will be end when the active surface is shadowed; in other case its contribution to the RCS is computed.
- 5) The steps 2-4 are performed for all the active surfaces.
- 6) The steps 1-6 are repeated for all directions in which the RCS should be computed.

The methodology explained previously is repeated for each voxel in which the total space has been divided.

The new technique developed presents a great advance computing the RCS o complex targets modelled using parametric surfaces. The CPU-time is reduced with this approach because the AZB algorithm selects the potential contributor surfaces, and the computer memory required is reduced because the SVP algorithm splits “the great” problem in smaller problems.

IV. VALIDATION AND COMPUTE TIME

To validate this method, the RCS of the model of the T72 tank indicated in figure 4 has been considered. Two models have been considered, one with 33154 flat facets and another one with 6827 flat facets. The frequency in the analysis is 10 GHz. The angular sleeping is from $\phi=0.0^\circ$ to $\phi=360.0^\circ$, in a $\theta=72.0$ cut (the z axis is vertical to the horizontal plane that supports the tank).



Figure 4. Geometric Model f the T72 Tank

Figure 5 shows the comparison of the results obtained using both versions of FASCRO, previous version of FASCRO code and new FASCRO code that includes the accelerating technique based on AZB and SVP algorithms previously outlined.

As can be seen, there is a good agreement between both results.

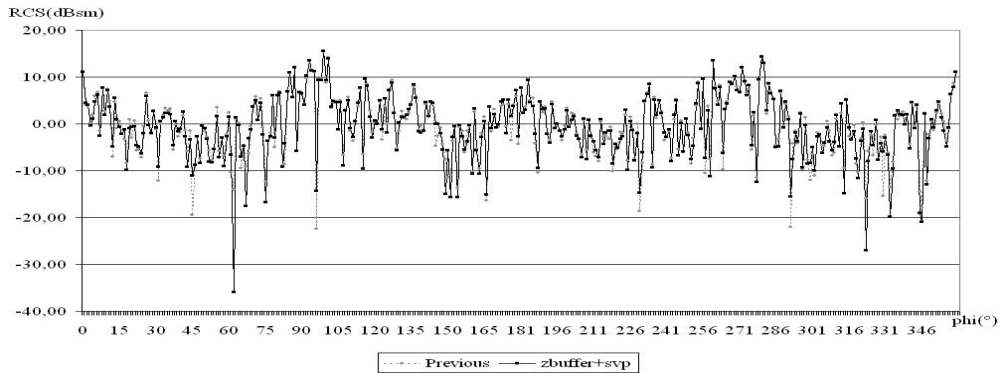


Figure 5. RCS numerical results of the T72 tank.

Table I, II, III, IV and V compare the CPU-times using different versions of code FASCRO. The computer was a PENTIUM IV, it has a processor with 2.4 GHz and 1 Gbyte of RAM memory.

Software	CPU-Time
FASCRO code without ray-tracing acceleration techniques	8h. 52 min. 32 sec.
FASCRO code with ray-tracing acceleration technique (without division of target) (10 regions in theta and 20 regions in phi)	1 h. 1 min. 11 sec.
FASCRO code with ray-tracing acceleration technique (without division of target) (50 regions in theta and 100 regions in phi)	44 min. 59 sec.

Table I. Comparison of CPU-time to compute the simple reflection effect to RCS (33154 flat facets). 1000 directions

Software	CPU-Time
FASCRO code without ray-tracing acceleration techniques	14 h. 16 min. 5 sec.
FASCRO code with ray-tracing acceleration technique (without division of target) (10 regions in theta and 20 regions in phi)	58 min. 49 sec.

Table II. Comparison of CPU-time to compute simple reflection and diffraction effects to RCS (33154 flat facets). 100 directions.

In order to, verify that the time reduction depends on the complexity of the model. A new T72 tank modelled with 6827 flat facets is used to run the previous cases. Tables III and IV present a comparison of the CPU-time to compute the previous cases with the new model.

Software	CPU-Time
FASCRO code without ray-tracing acceleration technique	1 h. 6 min. 48 sec.
FASCRO code with ray-tracing acceleration technique (without division of target) (10 regions in theta and 20 regions in phi)	31 min. 23 sec.

Table III. Comparison of CPU-time to compute the simple reflection effect to RCS (6827 flat facets). 1000 directions.

Software	CPU-Time
FASCRO code without ray-tracing acceleration technique	1 h. 22 min. 56 sec.
FASCRO code with ray-tracing acceleration technique (without division of target) (10 regions in theta and 20 regions in phi)	4 min. 33 sec.

Table IV. Comparison of CPU-time to compute the simple reflection and diffraction effects to RCS (6827 flat facets). 100 directions.

Finally, table V shows a comparison of the CPU-time to compute simple and double effects. The T72 tank is modelled with 33154 flat facets. In such a case, it is important to highlight that a previous division using the SVP algorithm is necessary to compute the simple and double reflection effects with this model.

Software	CPU-Time
FASCRO code without ray-tracing acceleration technique	6 h. 6 min. 40 sec.
FASCRO code with ray-tracing acceleration technique (without division of target)	Not Enough Memory
FASCRO code with ray-tracing acceleration technique (with division of target)	2h. 57 min. 16 sec.

Table V. Comparison of CPU-time to compute the simple and double reflection effects to RCS (33154 flat facets). 50 directions.

The same numerical results are obtained with and without ray-tracing acceleration techniques but with a less computational cost when ray-tracing is included because the numbers of the surfaces or combination of surfaces to analyze is substantially smaller.

V. CONCLUSIONS.

The ray-tracing acceleration technique presents a great advance in the compute of the RCS of complex geometric structures modelled by parametric surfaces NURBS. The memory load is reduced because the surfaces to analyze are reduced. Also, the same results that the old version of the software tool are obtained with less CPU-time.

The future lines of work, the application of AZB and SVP algorithms to compute diffraction-reflection, reflection-diffraction and high order effects are being developed.

ACKNOWLEDGMENT

This work has been support by the Spanish Defense Department, Project: EUCLID JP 1.18. "Joint Programme concerning Target and Target Background Modelling and Validation for High Resolution Radar" and by Comunidad de Madrid and Universidad de Alcalá, projects PI2005/069 and CAM-UAH 2005/005.

REFERENCES

- [1] M. Domingo, F. Rivas, J. Pérez, R. P. Torres, M. F. Cátedra, "Computation of the RCS of Complex Bodies Modelled Using NURBS Surfaces", IEEE Antennas and Propagation Magazine, vol. 37, No. 6, pag. 36-47, December 1995.
- [2] M. F. Cátedra, J. Pérez Arriaga, "Cell Planning for wireless communications", Artech House, 1999.
- [3] M. F. Cátedra, J. Pérez, F. Sáez de Adana, O. Gutiérrez, "Efficient Ray-Tracing Techniques for 3D Analyses of Propagation in Mobile Communications: Application to Picocell and Microcell Scenarios", IEEE Antennas and Propagation Magazine, vol. 40, No. 2, pag. 15-28, April 1998.
- [4] E. A. Hines, D. P. Greenberg, "The Light Buffer: A Shadow-Testing Accelerator", IEEE Computer Graphics and Applications, vol. 6, No. 9, pag. 6-16, September 1986.

Microwave Surface Impedance of a Nearly Ferroelectric Superconductor

Chien-Jang Wu¹, Chao-Ming Fu¹, and Tzong-Jer Yang²

¹ Department of Applied Physics, National University of Kaohsiung, Kaohsiung 811,
Taiwan, R.O.C.

² Department of Electrophysics, National Chiao-Tung University, Hsinchu 300, Taiwan,
R.O.C.

Abstract

The intrinsic microwave surface impedance for a nearly ferroelectric superconducting film of finite thickness in the dielectric-like response is theoretically investigated. It is based on the electrodynamics of a nearly ferroelectric superconductor that incorporates the Maxwell's equations, the lattice equations for an ionic lattice, and the superconducting London equation as well. It is found that the surface resistance will be enhanced with decreasing the film thickness when the thickness is less than the London penetration depth. However it will begin to resonate as a function of film thickness at the thickness being more than one London penetration depth. The anomalous resonance peaks occur when the thickness equals the even multiple of the London penetration depth. In the frequency-dependent surface resistance, the number of the resonance peaks is strongly dependent on the film thickness, increasing with increasing the thickness. In addition, these peaks are not regularly spaced at a fixed interval. Discussion on this anomaly in the surface resistance will be given.

Introduction

Microwave measurements have played a useful and important role in the study of fundamental physics of superconductivity for a superconductor. The most common quantity to be measured in the microwave experiments is the surface impedance, $Z_s = R_s + jX_s$, where the real part, R_s , is called the surface resistance, whereas the imaginary part, X_s , is known as the surface reactance. R_s quantifies the power dissipation in a superconductor and X_s is related to the magnetic penetration depth. Both can be, in general, well described on the basis of the two-fluid model of superconductor [1].

There have been lots of reports on the microwave surface impedances since the discovery of high- T_c superconductors. The reports are mainly focused on the cuprate superconductors, especially on the Y-123 and Bi-2212 systems [2-3]. On the other hand, there exists another special class of superconductor called nearly ferroelectric superconductor (NFE-SC). A NFE-SC could be a high- T_c one such as Na-doped WO_3 (Na_xWO_3 , $x \sim 0.05$, $T_c \sim 90$ K) [4]. It could be also a superconductor with very low T_c like the n -doped SrTiO_3 (STO) having a $T_c \sim 1-3$ K [5]. A NFE-SC material means that it can be in the superconducting state and in the nearly ferroelectric state as well. Nearly ferroelectric state means that a material is a soft-mode ionic system with relatively high

permittivity. For example, the host STO is a familiar nearly ferroelectric with $\epsilon_r \sim 10^4$ in the temperature range at which superconductivity occurs [6]. The electrodynamics of a NFE-SC material has recently been proposed by Birman and Zimbovskaya [7]. It is indicated that the response to an electromagnetic wave can be divided into two types. In some frequency regime one has the so-called Meissner response where the NFE-SC materials behave as the usual superconductors. In some other frequency regime, one will have the dielectric-like response where the electromagnetic field can be allowed to propagate as in a usual dielectric. Using the material parameters of *n*-STO it is found that the dielectric-like response occurs at frequency ranging from 14.3 GHz to 25.4 GHz which falls in the microwave regime [7]. The study of microwave surface impedance for this material will thus be of great interest and use. However, this has been lacking thus far to our knowledge.

In this paper, we shall give a theoretical study on the microwave properties for a NFE-SC thin film. We calculate the intrinsic film surface impedance as a function of the film thickness and radiation frequency. We then make some numerical analyses on the surface resistance and then the interesting anomalous resonance behavior can be explored. The results are expected to trigger some related microwave measurements which would be helpful in testing the validity of the electrodynamical theory of NFE-SC.

Basic equations

The microwave surface impedance can be determined by the relevant theory of a superconductor. For a NFE-SC material, the electrodynamics can be described by the combination of Maxwell's equations, London equations of superconductors, and lattice equations for the host ionic lattice of a ferroelectric. The governing field equation for a NFE-SC can be expressed as [7]

$$\nabla \times \nabla \times \mathbf{E} = -\mu_0 \epsilon(\omega) \frac{\partial^2 \mathbf{E}}{\partial t^2} - \frac{1}{\lambda_L^2}, \quad (1)$$

where the London penetration length is given by

$$\lambda_L = \left(\frac{m^*}{\mu_0 n_s e^2} \right)^{1/2}, \quad (2)$$

where m^* is the electron effective mass, e the electronic charge, and n_s the carrier density of the superelectrons. The dielectric function in Eq. (1) is given by

$$\epsilon(\omega) = \epsilon'_\infty \frac{\omega_{LO}^2 - \omega^2}{\omega_{TO}^2 - \omega^2}, \quad (3)$$

where ω_{TO} and ω_{LO} are the transverse and longitudinal soft-mode lattice frequencies, respectively. For a time-harmonic electromagnetic wave propagation in the z -direction, Eq. (1) reduces to Helmholtz equation from which the wavenumber can be defined by

$$k = \tilde{\lambda}^{-1} = (\omega \mu_0 \epsilon(\omega) - \lambda_L^{-2})^{1/2}. \quad (4)$$

It follows from Eq. (4) that the electromagnetic response depends on the value of k . If $k > 0$, an electromagnetic wave is allowed to propagate in the material and it is referred to as the dielectric-like response. If k is an imaginary, then the wave cannot propagate and only exponentially decay into the material characterized by the field penetration depth. In this case, the NFE-SC would behave like a simple superconductor and we thus

have a Meissner response. If $k = 0$, the corresponding frequencies calculated from Eq. (4) are called the cutoff frequencies which are determined by the following expression

$$\omega_{c1,c2} = \omega_{TO} \left(\frac{\omega_{LO}^2}{2\omega_{TO}^2} \left(1 + \frac{1}{a^2} \right) \pm \frac{\omega_{LO}}{2\omega_{TO}} \left(\left(1 + \frac{1}{a^2} \right)^2 \frac{\omega_{LO}^2}{\omega_{TO}^2} - \frac{4}{a^2} \right)^{1/2} \right)^{1/2}, \quad (5)$$

where the smaller one is the lower cutoff frequency ω_{c1} and the larger the upper cutoff frequency ω_{c2} and $a^2 = \mu_0 \epsilon'_\infty \omega_{LO}^2 \lambda_L^2$. For n -STO, $\omega_{TO} = 1.6 \times 10^{11}$ rad/s, $\omega_{LO} = 5.2 \times 10^{12}$ rad/s, and $a^2 = 2.1$ [7], one has $\omega_{c1} = 9 \times 10^{10}$ rad/s, $\omega_{c2} = 6.32 \times 10^{12}$ rad/s. Thus, the low frequency region of dielectric-like response is $\omega_{c1}/2\pi = 14.3$ GHz $\sim \omega_{TO}/2\pi = 25.4$ GHz, falling in the microwave regime.

For a superconductor occupying the half space $z \geq 0$, surface impedance at $z = 0$ is given by

$$Z_s = \frac{\omega \mu_0}{k} = \frac{\omega \mu_0}{\sqrt{\omega^2 \mu_0 \epsilon(\omega) - \lambda_L^{-2}}}, \quad (6)$$

This one is called the intrinsic surface impedance (intrinsic to a bulk material). In the dielectric-like response, surface impedance is real, i.e., $Z_s = R_s$. As for a superconducting thin film of thickness d ($0 \leq z \leq d$), the intrinsic film surface impedance $Z_{s,int} = R_{s,int} + jX_{s,int}$ can be calculated by the impedance transformation, with the result

$$R_{s,int} = \frac{R_s^2}{Z_0} \frac{1}{\sin^2(d/\tilde{\lambda}) + (R_s^2/Z_0^2) \cos^2(d/\tilde{\lambda})}, \quad (7)$$

$$X_{s,int} = \frac{1}{2} \left(\frac{R_s^3}{Z_0^2} - R_s \right) \frac{\sin(2d/\tilde{\lambda})}{\sin^2(d/\tilde{\lambda}) + (R_s^2/Z_0^2) \cos^2(d/\tilde{\lambda})}. \quad (8)$$

where $Z_0 = 120\pi \Omega$ is the intrinsic impedance of free space. In the limit of $d \rightarrow 0$, Eqs. (7) and (8) then reduce to the intrinsic bulk surface impedance given in Eq. (6). In the case where the superconducting film is deposited on the dielectric substrate with relative permittivity ϵ_d . Equations (7) and (8) will still hold with the replacement of $Z_0 \rightarrow Z_0 / \sqrt{\epsilon_d}$. In this case the impedance is generally referred to as the effective microwave surface impedance that is related to the material parameters and the thicknesses of both superconductor and dielectric substrate.

Numerical results and discussion

In what follows we will present the numerical results for the intrinsic film surface resistance for the system, n -STO. This is the only NFE-SC with the all related material parameters being available thus far [7]. Figure 1 shows the calculated $R_{s,int}$ as a function of the film thickness. It is interesting to find that there are two much different regimes for the thickness-dependent $R_{s,int}$. In the first regime, it is seen that the resistance decreases with increasing film thickness for d being small than the London penetration length λ_L . In the second one where $d > \lambda_L$, $R_{s,int}$ will start to resonate as a function of the film thickness. The first one consists with the result of the high- T_c cuprate system, Y-123 [8, 9]. In the cuprate material the microwave surface impedance can be well described only

by the two-fluid model. The result here indicates that a NFE-SC in this region behaves like a pure superconductor and the ferroelectric effect is smeared out due to the size effect. The second resonant part shown in Fig. 1 is replotted in Fig. 2, where the horizontal axis is in linear scale for the purpose of observing the resonant position. The resonant peaks of $R_{s,int}$ are regularly spaced and resonant positions occur at the condition where $d = 2\lambda_L, 4\lambda_L, \dots$

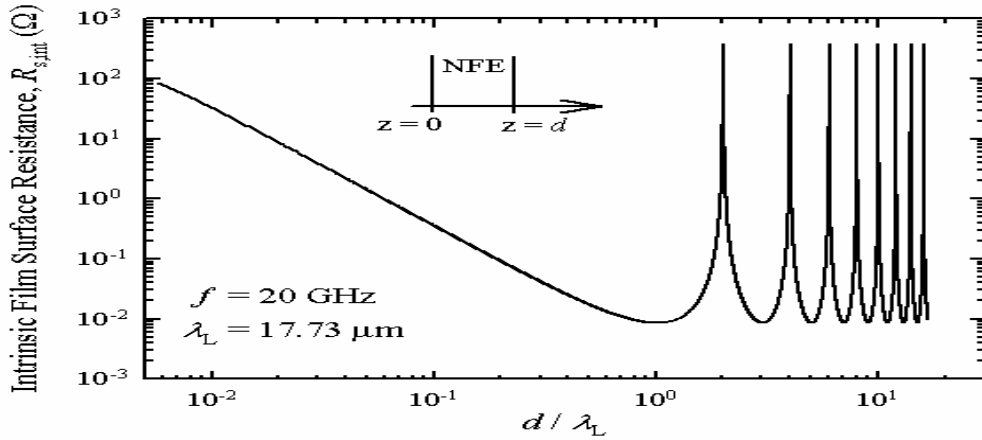


FIG. 1 Calculated intrinsic film surface resistance versus the thickness of superconducting film. The radiation microwave frequency is taken to be 20 GHz and the calculated London penetration depth is 17.73 μm .

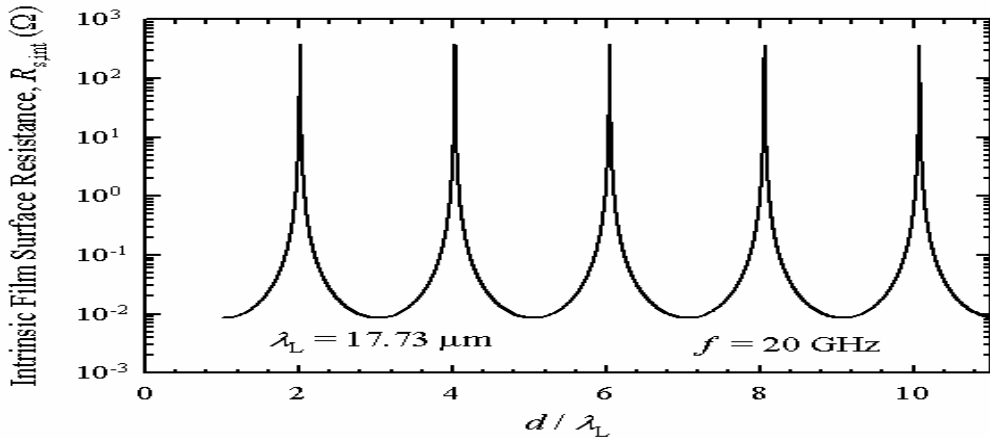


FIG. 2 Resonant intrinsic film surface resistance extracted from Fig. 1 for $d > \lambda_L$. The horizontal axis is in the linear scale while in Fig. 1 is in log scale.

In Fig. 3 we plot the frequency dependence of the intrinsic film surface resistance at film thickness, $d = \lambda_L, 2\lambda_L$, and $8\lambda_L$, respectively. It can be seen that $R_{s,int}$ exhibits anomalous sharp peaks and the number of peaks increases with increasing film thickness. A comb-like distribution is seen for $d = 8\lambda_L$ and these peaks are not regularly spaced as in Fig. 2. At resonance, $R_{s,int} = Z_0$, indicating the film is totally transparent to the incident microwave radiation. In addition, the resonant position can be determined as follows: Based on Eq. (7), the resonance condition is $\sin(d/\tilde{\lambda}) = 0 \rightarrow \tilde{\lambda} = d/(n\pi)$, $n = 1, 2, 3, \dots$ This together with Eq. (4) then explicitly determines the resonance frequency as shown in Fig. 3. In addition, it should be noted that the most left peak for each film thickness is not a

real resonant peak. It is the one that occurs at $\omega = \omega_{cl}$ which in turn leads to $\lambda_L \rightarrow \infty$ and thus $\sin(d/\tilde{\lambda}) = 0$ is automatically satisfied.

In summary, the intrinsic microwave surface impedance of a NFE-SC thin film has been theoretically investigated. It is found that the surface resistance will resonant as a function of film thickness as the thickness is larger than the London penetration depth. The resonant peaks are regularly spaced and occur at the even multiple of the London penetration length. The frequency-dependent surface resistance shows an anomalous comb-like resonant peak. The peak number is strongly dependent on the film thickness. These peaks however are not regularly spaced in the frequency domain.

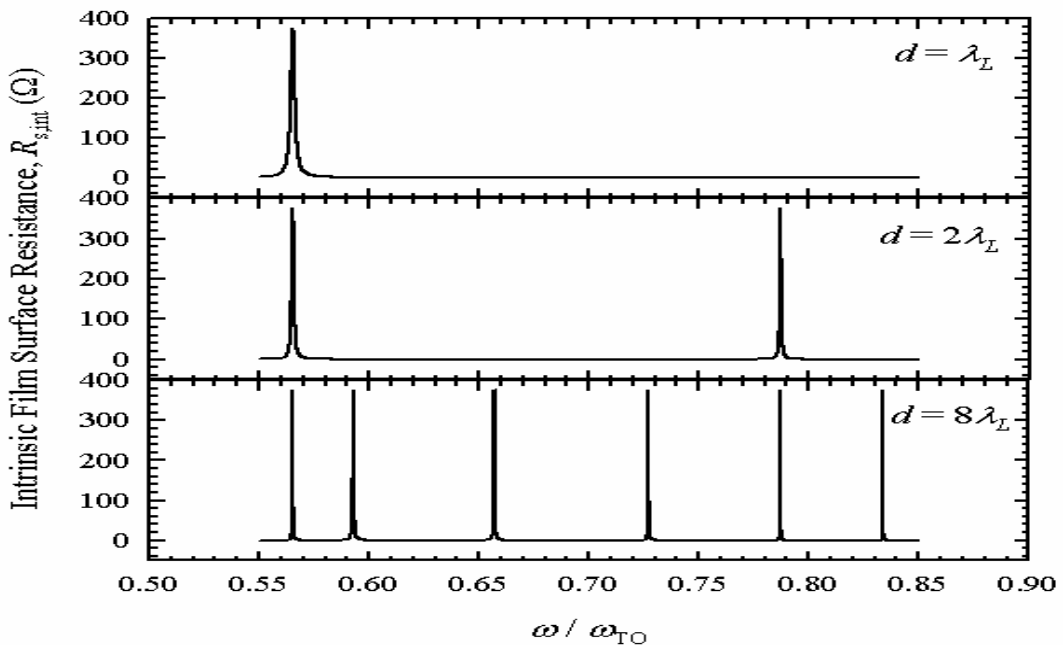


FIG. 3. Calculated intrinsic film surface resistance as a function of the frequency at different thicknesses of film.

Acknowledgments

The author CJW is indebted to the financial support by the National Science Council of the Republic of China under grant No. NSC-94-2112-M-390-004.

References

- [1] Z.-Y. Shen, *High-Temperature Superconducting Microwave Circuits*, Artech House, Norwood, 1994.
- [2] V. M. Pan *et al.*, *Low Temp. Phys.*, **31**, 254 (2005), and references therein.
- [3] M. R. Trunin, *J. Supercond.*, **11**, 381 (1998).
- [4] Y. Levi *et al.*, *Europhys. Lett.*, **51**, 564 (2000).
- [5] C. S. Koonce *et al.*, *Phys. Rev.*, **163**, 380 (1968).
- [6] E. Savaguchi *et al.*, *J. Phys. Soc. Jpn.*, **17**, 1666(1962).
- [7] J. L. Birman and N. A. Zimbovskaya, *Phys. Rev. B*, **64**, 144506 (2001).
- [8] N. Klein *et al.*, *J. Appl. Phys.*, **67**, 6940(1990).
- [9] C.-J. Wu and T.-Y. Tesng, *IEEE Trans. Magnetics*, **33**, 2348 (1997).

Calculations of Optical Properties of an Annular Dielectric Mirror

Chien-Jang Wu¹ and Shangjr Gwo²

¹ Department of Applied Physics, National University of Kaohsiung, Kaohsiung, Taiwan 811, R.O.C.

² Department of Physics, National Tsinghua University, Hsinchu, Taiwan 300, R.O.C.

Abstract

Optical reflectance spectra of an annular dielectric mirror have been theoretically calculated and investigated based on the transfer matrix method for the cylindrical wave. The numerical results reveal some fundamental features about the annular mirror. It is found that the reflection response at azimuthal mode $m = 0$ for an annular mirror is almost identical to that of a planar mirror with the same material parameters. The dependence of reflectance spectrum on the starting radius in an annular mirror is shown to be very weak. In addition, for a higher azimuthal mode such as $m = 1$, the difference between the E -polarization and H -polarization can be seen. The upper wavelength bandedge will be lowered down in the H -polarization.

Introduction

A distributed dielectric mirror also called distributed Bragg reflector (DBR) has been playing an important role in the modern semiconductor laser systems such as DFB (distributed feedback) laser, DBR laser, and VCSEL (vertical cavity surface-emitting laser) as well [1]. A DBR shown in Fig. 1 is a periodic multilayer structure consisting of many bilayers with high and low indices of refraction. Traditional planar DBRs (the right in Fig. 1) have been a must in the optical and electromagnetic textbooks [2, 3]. The applications of the planar DBRs include the optical filters, resonators, waveguides and mirrors in semiconductor lasers. It could further act as a photonic crystal if the number of periods becomes very large.

With the advance of modern fabrication techniques, the annular DBR depicted in the left of Fig. 1 has become possible. By introducing a ring defect into the annular periodic structure, an annular type resonator or laser has been recently reported [4, 5]. Annular type laser has a very important feature of vertical emission which makes it of particular use in the optical electronics and communication.

In this paper, we shall theoretically investigate the basic features for an annular DBR. These features can be seen from the optical reflection spectrum calculated on the basis of the transfer matrix method in cylindrical waves [6]. With the field solutions of the cylindrical waves being related to the azimuthal mode number, m , we first demonstrate that reflection response at $m = 0$ will almost be identical to that of the planar DBR. And with formulation being closely dependent on the starting radius, it is necessary to explore its role on the reflection spectrum. The distinction in the reflection responses between the E - and H -polarization will also be illustrated.

Transfer matrix theory

The reflection response calculated from transfer matrix theory for a planar DBR has been available in the textbook [2,3] and thus will not be addressed here. For an annular DBR shown in the left of Fig. 1 transfer matrix theory in cylindrical wave has been recently developed by Kaliteevski *et al* [6]. This theory essentially could be regarded as an analogous version to the planar one. The cylindrical wave is diverging radially from the axis of symmetry, $\rho = 0$, and is normally incident on the circular interface, $\rho = \rho_0$, where it is referred to as the starting radius. Due to the geometric factor, the cylindrical wave can be classified as the E -polarization and H -polarization as well. For E -polarization the nonzero fields are E_z , H_ϕ , and H_ρ . As for H -polarization we have H_z , E_ϕ , and E_ρ . We here assume an $e^{j\omega t}$ time dependence for all nonzero fields. The field solution includes the radial part related to Bessel function with azimuthal mode number, m , and the angular part, $e^{jm\phi}$ also described by this azimuthal mode number.

In the E -polarization the tangential electric and magnetic fields in the first and final interfaces can be related by the system matrix

$$\mathbf{M} = \begin{bmatrix} m_{11} & m_{12} \\ m_{21} & m_{22} \end{bmatrix} = \mathbf{M}_1 \mathbf{M}_2 \cdots \mathbf{M}_{2N+1}, \quad (1)$$

where \mathbf{M}_i denotes the characteristic matrix for the individual layer- i . For a typical DBR, the layer with n_1 is a high-index material, while with n_2 the low-index one. Thus for an N -period structure, we will have, in total, $2N + 1$ layers. Each layer matrix is dependent on the radii of two interfaces there. An analytical expression for the matrix elements of \mathbf{M}_i can be obtained [6]. However, it can not be obtained for the system matrix \mathbf{M} . The matrix elements of the system matrix can only be numerically determined. Once the matrix elements are found, one can then calculate the reflectance for an annular DBR. The result for H -polarization can be obtained by simply replacing $\mu \leftrightarrow \epsilon$, and $j \leftrightarrow -j$ in the formulas of E -polarization.

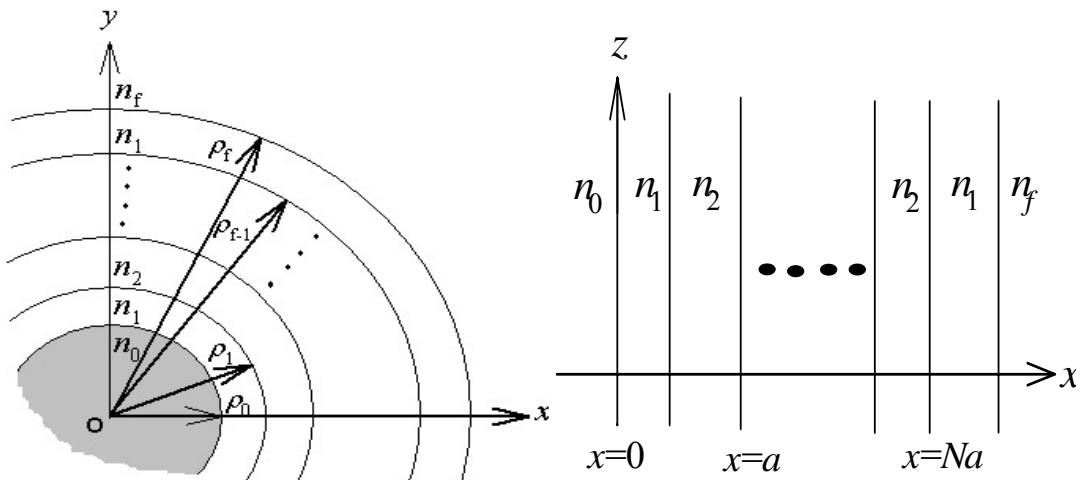


FIG. 1 A portion of the top view of an annular DBR (left) and a plot for the planar DBR (right). In general, the high-index material is n_1 -layer while n_2 -layer the low-index. For annular type each interface is denoted by the radius ρ_i , $i = 0, 1, \dots, f$.

Numerical results and discussion

In what follows we will present the numerical results for the reflectance response. We shall consider the GaN/Air DBR. The index of refraction of GaN is $n_1 = 2.4$ and the design wavelength is taken to be $\lambda_0 = 480$ nm (blue light) [7]. And other layers are airs, i.e., $n_0 = n_2 = n_f = 1$. The DBR bilayer is made of quarter-wavelength each, i.e., $n_1 l_1 = n_2 l_2 = \lambda_0/4$. Figure 2 shows the calculated reflectance versus wavelength for 8-period DBR. The starting radius is $\rho_0 = 2\lambda_0 = 960$ nm. The solid line is for the annular DBR at azimuthal mode $m = 0$ and in the E -polarization, and the gray dash line is for the planar DBR. It is interesting to find that both reflection spectra almost coincide. This means at $m = 0$ the effect arising from geometric curved interfaces in an annular DRB can be neglected and its optical properties can be studied equivalently by the planar DBR. This can be ascribed to the fact that at zero azimuthal number the field solution has only radial part and it thus behaves much like a plane wave as in planar geometry. In this case, the bandedges in Fig. 2 can be calculated according to the planar DBR theory, namely $\lambda_2 = 657.7$ nm and $\lambda_1 = 377.9$ nm, giving a bandwidth of $\Delta\lambda = \lambda_2 - \lambda_1 = 279.8$ nm. The reflection band covers all visible light.

In Fig. 3, we plot the annular DBR reflectance spectra (the E -polarization) at higher mode $m = 1$ for three different starting radii. It is seen that the dependence of spectrum on the starting radius is very weak. The bandwidth is not pronouncedly affected. Only the side lobes are raised up at small starting radius. In fact, at $m = 0$, the variation in the spectrum due to the starting radius is hardly seen. For $m \neq 0$, a change in spectrum may be seen at very small starting radius (compared to the design wavelength). However, small starting radius in annular mirror might not be feasible in reality. Therefore, we believe that the reflection response is much weakly dependent on the starting radius.

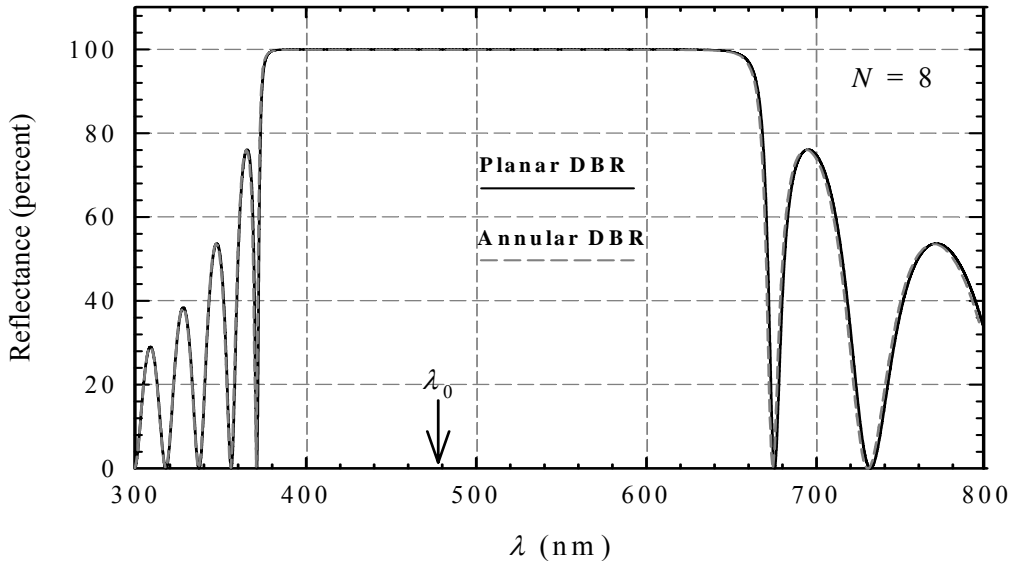


FIG. 2. Calculated reflectance versus the wavelength for DBR made of GaN/Air bilayers. The solid is the for the planar DBR while the dashed the annular DBR. The number of period is $N = 8$ for both cases.

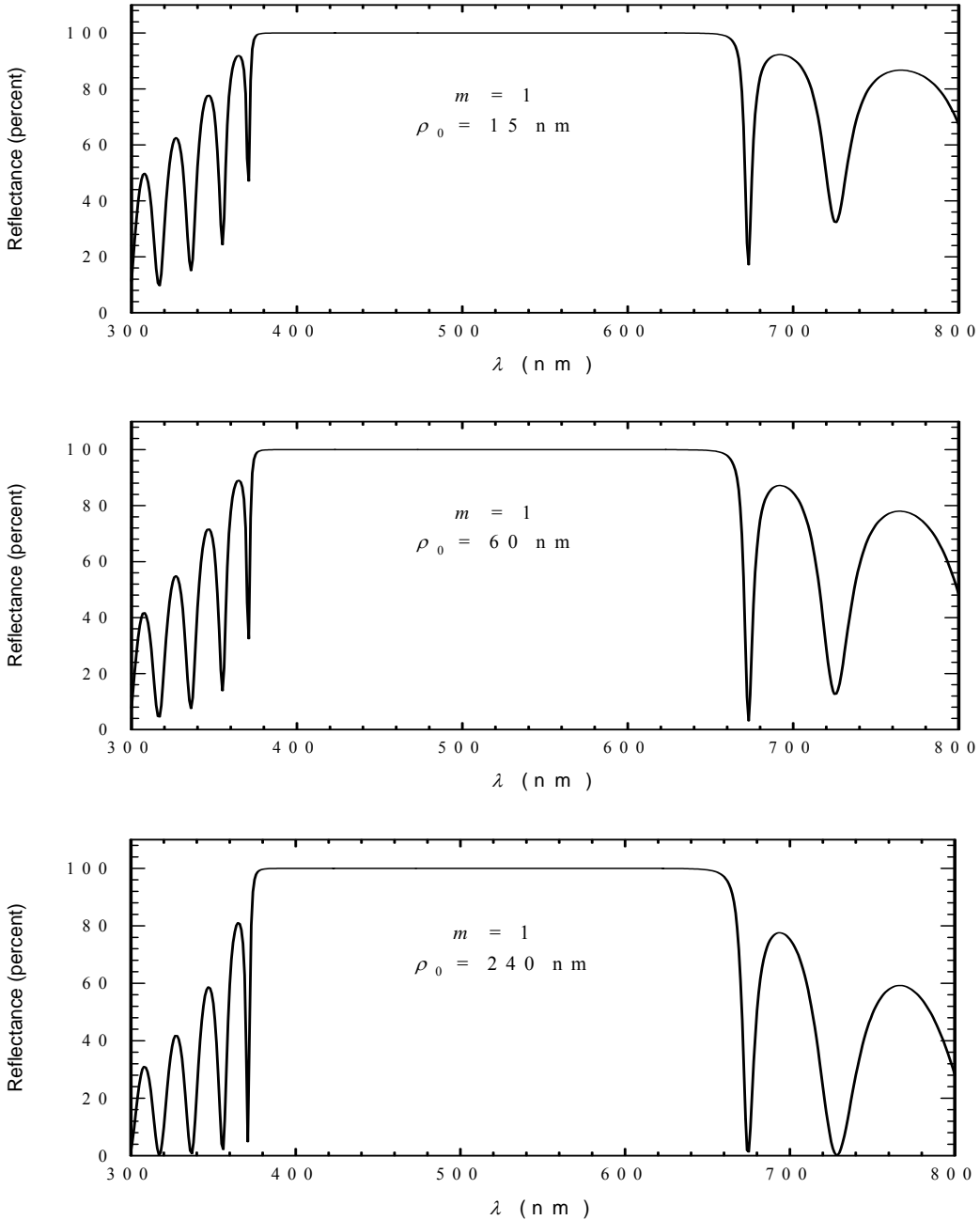


FIG. 3. Calculated reflectance spectra for an annular DBR at azimuthal mode $m = 1$ for three different starting radii.

In Fig. 4, we plot the reflection spectra for both E -polarization and H -polarization at the conditions of $N = 8$, $\rho_0 = \lambda_0/4 = 120$ nm, and azimuthal number $m = 1$. It follows from the figure that the overlapping covers almost the whole bandwidth. In addition, the upper bandedge in the H -polarization is smaller than that of E -polarization, indicating that the bandwidth will be lowered down appreciably in the case of H -polarization.

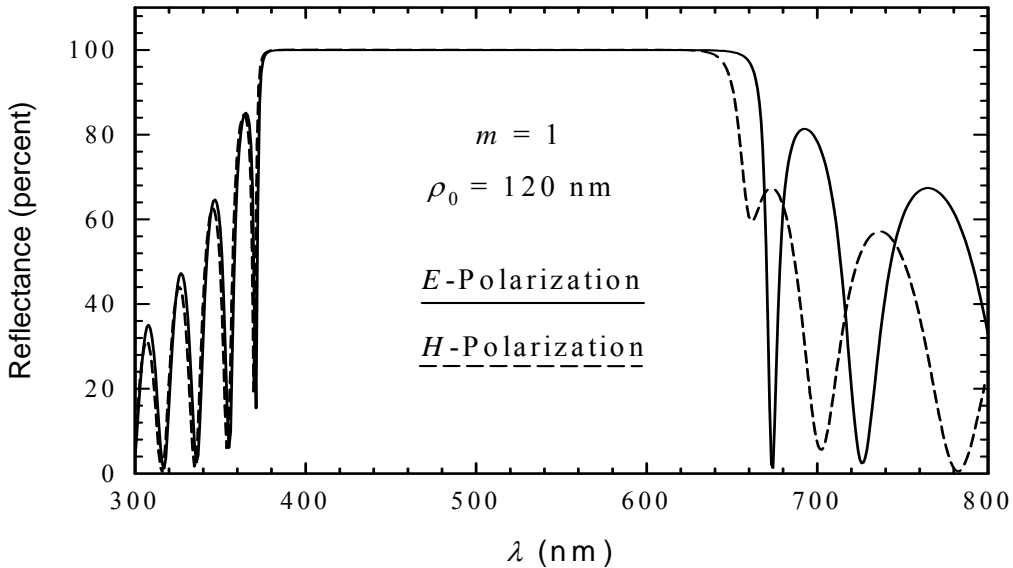


FIG. 4. Calculated reflectance spectra for an annular DBR at azimuthal mode $m = 1$ for three different starting radii.

Conclusions

In summary, we have numerically demonstrated some basic optical information for the annular dielectric mirror. The annular mirror can be equivalently replaced by the planar one when the azimuthal number is zero. In the annular mirror, the dependence of starting radius can be generally omitted. Due to the curved interfaces the optical wave has two possible polarizations, E - and H -polarizations, even in the normal incidence. The bandwidth is coincident in most region for both polarizations. However, the bandwidth of H -polarization is appreciably small than E -polarization.

Acknowledgment

The author C.-J. Wu is indebted to the financial support by from the National Science Council of the Republic of China under grant No. NSC-94-2112-M-390-004.

References

- [1] D. Meschede, *Optics, Light and Lasers*, Wiley-VCH, Weinheim, 2004.
- [2] M. Born and E. Wolf, *Principles of Optics*, Cambridge, London, 1999.
- [3] P. Yeh, *Optical Waves in Layered Media*, John Wiley & Sons, Singapore, 1991.
- [4] J. Scheuer, W. M. J. Green, and Y. Yariv, *Opt. Lett.*, **29**, 2641 (2004).
- [5] J. Scheuer *et al.*, *Appl. Phys. Lett.*, **84**, 3669 (2004).
- [6] M. A. Kaliteevski *et al.*, *J. Mod. Opt.*, **46**, 875 (1999).
- [7] M. E. Levinshtein *et al.*, *Properties of Advanced Semiconductor Materials*, John Wiley & Sons, New York, 2001.

A MODEL OF POROUS MEDIUM MAGNETO-HYDRO-DYNAMICS AND ITS INVERSE PROBLEM

YOUZHONG GUO and ZI GUO

Chinese Academy of Science and Wuhan Institute for Industrial and Applied Mathematics

ABSTRACT

In this paper, we propose a new model for dynamics of porous solid medium saturated with compressible magneto-fluid, directly coupled the stress, flow and electromagnetic fields, studied their interactions and propagation regularity of waves and proved that there exist various P and S waves, and also their mixture, which generally possess damping and frequency scattering effects. In magnetic (geomagnetic and bio-magnetic etc) field, conductive fluid (seawater, oil and blood etc) flows to induce electric current thus changes the magnetic field; whereas electric current flows in magnetic field producing mechanical force, which influences the deformation of solid skeleton and the fluid, the deformation of solid skeliton and Darcy osmosis in the interstitial passage in true changing the flow of the fluid. After the linearization of the model, the general decompositions of the displacement vectors on solid and flow fields as well as magnetic field are given. In the diphase medium, we have theoretically shown the existence of six types of various forms of waves and their behaviors. The difficulties and abundant anticipated contents of the new model come right from the complicated interactions.

In this paper, some mistakes on magneto-hydrodynamics have been corrected, the (Micro-)Bermuda Effect, the possible mechanism of the luminescence in earthquake and a iterative method for solving its inverse problem of Xie Ganquan Type are presented. Various inverse problems, mathematical research on conservation laws, similarities of the Transmission Wire Theory, concentrations of dynamical stress, nonlinear waves, variational principles and many other inverse problems related to the model will be presented later.

Further study of this model is undoubtedly important in geophysics, oceanography, life science and the science of energy resources.

An Omnidirectional UWB Printed Dipole Antenna with Small Waveform Distortion

Michitaka AMEYA, Manabu YAMAMOTO, Toshio NOJIMA

Graduate School of Information Science and Technology, Hokkaido University, Japan

Abstract—In this paper, we propose a novel UWB printed dipole antenna which has omnidirectional radiation patterns over the frequency range of 3.0 to 11.5 GHz. The realized gain of the antenna is between 1 dBi and 3 dBi. From calculations of cross-correlation between source pulse and received pulse waveforms, it is observed that the waveform distortion caused by this antenna is very small.

1. Introduction

Ultra-wideband (UWB) communication systems have attracted considerable attention in recent years. In impulse-based UWB communications, if correlation detection is used as the demodulation scheme, waveform distortions of transmitted and received pulses caused by antennas induce degradations of the communication performance[1]. In order to avoid these degradations, it is necessary that radiation characteristics of the antenna be constant over the wide frequency range.

Since the FCC announced that it would allow the unlicensed use of the bandwidth of 3.1 to 10.6 GHz[2], many UWB antennas have been studied[3]–[6]. Schantz proposes various new designs such as magnetic slot antennas[3] and planar elliptical dipole antennas[4]. Chen et al. investigated the characteristics of a few types of square dipole antennas[5] and also proposed the bi-arm rolled monopole[6]. However, there exists little information on waveform distortions caused by antennas. In this paper, we focus on the waveform distortions and propose a novel UWB printed dipole antenna with small waveform distortions.

In Section 2, the antenna geometry and design guideline are first introduced. The antenna characteristics are investigated by comparing the experimental results with the numerical results using the electromagnetic simulator SEMCAD[7] based on the FDTD method, and then the results and discussion are described in Section 3. Finally, the conclusions of this work are given in Section 4.

2. Antenna Configuration

In order to achieve wideband characteristics, the antenna is required to have constant input impedance over the wide frequency range. The principle of self-complementarity[8] is a method for realizing constant impedance characteristics. Hence, we use the element based on the theory of self-complementarity as the radiation elements of the printed dipole antennas. The ideal self-complementary antenna presupposes an infinite structure. Therefore, we need to truncate the infinite structure for designing practical radiating elements. As long as self-complementarity is maintained around the feeding point of the radiating elements, various kinds of

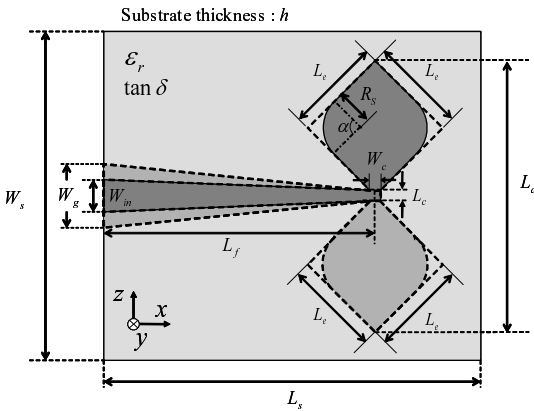


Table 1: Antenna parameters.

W_s [mm]	L_s [mm]	h [mm]	ε_r	\tan
40	55	0.762	2.17	0.0009
R_s [mm]	[deg]	L_e [mm]	W_c [mm]	L_c [mm]
7.1	90	12	0.2	0.2
W_{in} [mm]	W_g [mm]	L_f [mm]	L_a	
2.4	12	45	$2\sqrt{2}L_e$	

Figure 1: Geometry and coordinate system.

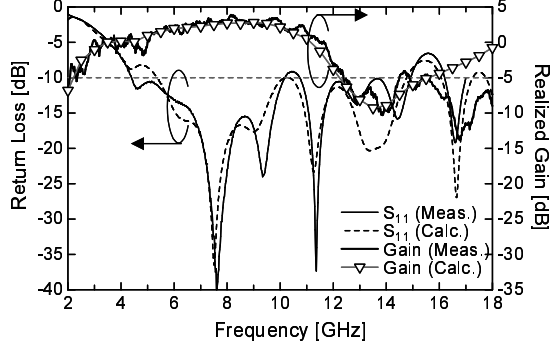
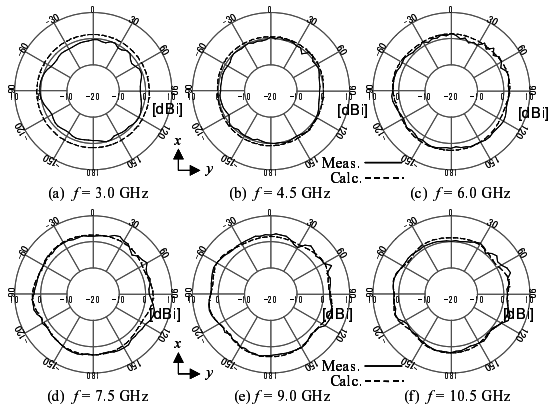


Figure 2: Return loss and realized gain versus frequency.

Figure 3: Radiation patterns in xy plane.

shapes can be adopted for the truncated part of the radiating element. In this paper, leaf-shaped elements are employed as shown in Fig. 1. Two leaf-shaped radiating elements are arranged on upper and lower surfaces of a dielectric substrate. These elements are excited by a 45mm tapered microstrip line.

The parameter of the proposed antenna is shown in Table 1. The proposed antenna was fabricated on a Te on substrate with thickness $h = 0.762$ mm, dielectric constant $\varepsilon_r = 2.17$, and $\tan \delta = 0.0009@10$ GHz. The width L_c of the feeding line at the center is set to 0.2 mm because the input impedance at the center of both radiating elements, which is calculated by using FDTD delta-gap feeding model, is about 150Ω . This value is close to the input impedance of the self-complementary planar structure (120 Ω /2). The width W_{in} of the feeding line at the input port is 2.4 mm for connecting to a 50Ω SMA connector. The length and width of the substrate W_s and L_s are set to 40 mm and 50 mm in such a way that the substrate encloses the whole antenna element with some margin. The leaf-shape is designed by rounding the corner of the square shape, and then the curvature radius of the rounded corner is set to 7.1 mm.

3. Results and Discussion

3.1 Return Loss, Realized Gain, and Radiation Patterns

The frequency responses of the measured and calculated return loss (S_{11}) are illustrated in Fig.2. As shown in this figure, the measurement and calculated results are in good agreement. The frequency range for which $S_{11} < -10$ dB is from 4.5 GHz to 15.0 GHz in the measured results.

The realized gain in the y direction as a function of frequency is also plotted in Fig.2. The fluctuation in the measurements is due to the reflection noise from the wall. The measurement results generally agree with the calculated results. The realized gain is -1 through 3 dBi over the frequency range of 3.0 to 11.5 GHz. This bandwidth fulfills the UWB bandwidth approved by FCC. The -1 dBi gain can be obtained although the return loss is about -5 dB at 3 GHz. Therefore, it is observed that smaller antenna can be designed by focusing on not only the return loss but also the realized gain.

The radiation patterns in the azimuthal plane (xy plane) are measured at every 500MHz from 2.0 GHz to 18 GHz in an anechoic chamber. Some of these results are shown in Fig.3. For each frequency, an omnidirectional pattern is achieved in both measured and calculated results.

3.2 Transmission Characteristics

In order to investigate the transmission characteristics of the proposed antenna, the measurements of the transmission loss and group delay characteristics were conducted. We investigated the transmitting and receiving system using a pair of the proposed antennas, which are arranged with a separation of $d = 2$ m. To clarify variation of the transmission characteristics due to changing azimuthal angle, the measurements were performed at every 45° from $\theta = 0^\circ$ to 315° . For comparison purpose, the measurements of the MSL thin dipole, which is 1.2 mm in width and 24 mm in length, were also performed.

The measured transmission loss and group delay at $\theta = 0^\circ, 45^\circ, 90^\circ$ are plotted in Figs.4 and 5. These figures show the results of the proposed antenna and those of the MSL thin dipole antenna, respectively. In the case of the proposed antenna, the transmission loss is from -55 up to -50 dB in 2.5–10 GHz. It is observed that the fluctuation due to the frequency is small. The group delay is within a band of 7.2–7.5 ns over the frequency range of 3.0 to 11.0 GHz. On the other hand, for the MSL thin dipole antenna, two peaks of the transmission

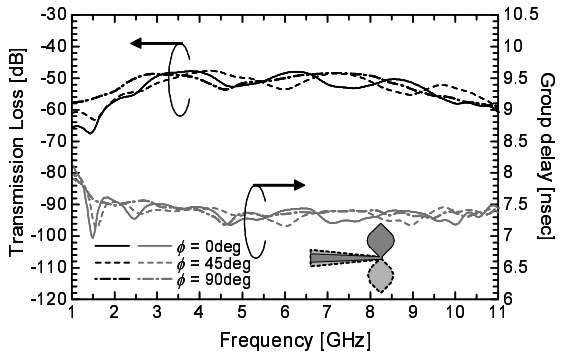


Figure 4: Measured transmission loss and group delay of the proposed UWB antenna.

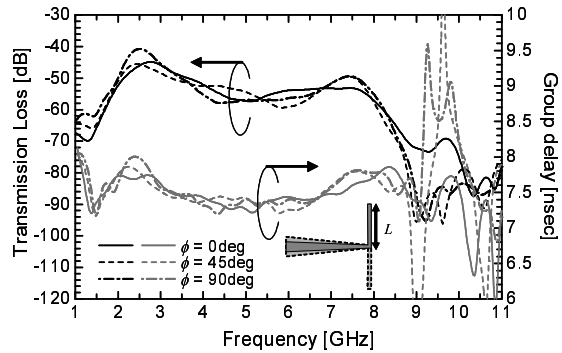


Figure 5: Measured transmission loss and group delay of the thin dipole antenna ($L = 24$ mm).

loss are observed at 2.5 and 7.5 GHz. These frequencies of the peaks are the frequencies that the element length of thin dipole are $\lambda/2$ and $3\lambda/2$, respectively. Consequently, they operate as a $1/2$ and $3/2$ wavelength dipole antennas and have good impedance matching at the frequencies. The group delay of the thin dipole is within a band of 7.2–7.9 ns in 3.0–8.5 GHz. Above 8.5 GHz, we couldn't measure the correct value of group delay because the amplitude is quite small. As a result, the group delay of the proposed antenna has less frequency variation than that of the thin dipole antenna.

3.3 Waveform Distortions

In this section, we explain the evaluation method of waveform distortions using cross-correlation. For evaluating waveform distortions, we need to examine the degree of similarity between source pulse and received pulse waveforms. The degree of similarity between both waveforms can be obtained by calculating the cross-correlation coefficient between source and received pulses. The cross-correlation coefficient (CC_{sync}) can be expressed as follows:

$$CC_{sync} = \int_{-\infty}^{+\infty} \hat{s}(t) \hat{r}(t + \tau_{sync}) dt \quad (1)$$

where τ_{sync} is synchronization time, $\hat{r}(t)$ is the normalized received pulse, and $\hat{s}(t)$ is the normalized source pulse. Note that the source pulse and received pulse were assumed to be synchronized in this calculation. The normalized received pulse and the source pulse are defined as:

$$\hat{r}(t) = \frac{r(t)}{\sqrt{E_r}} = \frac{r(t)}{\sqrt{\int_{-\infty}^{+\infty} r(t)^2 dt}} \quad (2)$$

$$\hat{s}(t) = \frac{s(t)}{\sqrt{E_s}} = \frac{s(t)}{\sqrt{\int_{-\infty}^{+\infty} s(t)^2 dt}} \quad (3)$$

where $r(t)$ is the received pulse, $s(t)$ is the source pulse, E_r is the total energy of the received pulse, and E_s is the total energy of the source pulse. The received pulse $r(t)$ is also calculated as:

$$r(t) = \int_{-\infty}^{+\infty} h(\tau) s(t - \tau) d\tau \quad (4)$$

where $h(\tau)$ is the impulse response of the propagation channel, which includes the effects of transmitted and received antennas. $h(\tau)$ is obtained by calculating the inverse Fourier transformation of the transmission characteristics measured in the previous section. Therefore, by substituting (2), (3), and (4) into (1), the cross-correlation coefficient (CC_{sync}) can be obtained.

The correlation coefficient (CC_{sync}) and the received energy (E_r) are shown in Fig.6. These results are obtained by using the transmission characteristics measured at each azimuthal angle. We employed a modulated cosine roll-off pulse[9] as a source pulse $s(t)$, which is defined as:

$$s(t) = \frac{\sin(Bt)}{Bt} \frac{\cos(Bt)}{1 - (2/Bt)^2} \cos(2\pi f_c t) \quad (5)$$

where α is the roll-off factor, B is the pulse bandwidth, and f_c is the frequency of the modulating wave. In this report, we select the values of $\alpha = 1.0$, $B = 5.8$ GHz, and $f_c = 6.85$ GHz. The total energy of the source pulse is normalized to 1 J ($E_s = 1$ J). For comparison purposes, the results when using the MSL thin dipole antenna used in the previous section are also shown in this figure. The proposed antenna has high correlation coefficients of 0.92–0.96 at any direction in the xy plane. The received energies of the proposed antenna are greater than those of the thin dipole antenna because the thin dipole antenna cannot transmit the energy above 8.5 GHz although the source pulse spectrum spreads over the bandwidth of 3.1 to 10.6 GHz. The waveforms of the source pulse and the received pulses are shown in Fig.7. It is clear that the waveform distortion of the received pulse caused by the proposed antenna is very small.

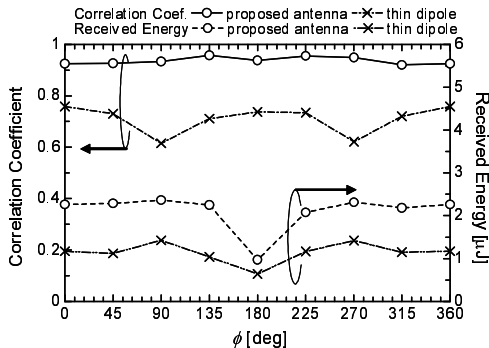


Figure 6: Correlation coefficient and received energy versus azimuthal angle.

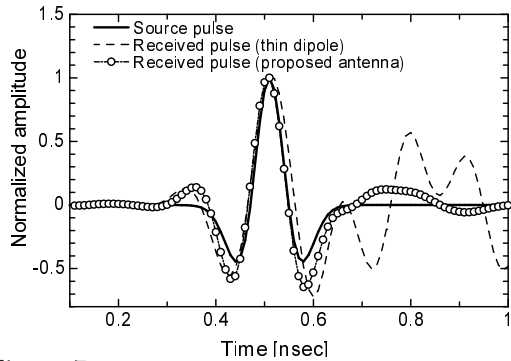


Figure 7: Source pulse waveform and received pulse waveform at $\phi = 135^\circ$.

4. Conclusion

In this paper, a novel UWB printed dipole antenna has been proposed and investigated. The proposed antenna has the realized gain between 1 to 3 dBi in the frequency bandwidth of 3.0 to 11.5 GHz. The radiation patterns in the xy plane of the proposed antenna are omnidirectional in the UWB band. In addition, from the results of transmission characteristics measurements, the fluctuations of the proposed antenna in transmission loss and group delay are less than those of thin dipole antenna. The correlation coefficient, which is a measure of the degree of the waveform distortions, is between 0.92 and 0.96. Therefore, the waveform distortion caused by this antenna is very small. Based on these results, the proposed antenna can be a suitable candidate for impulse-based UWB communication systems using correlation detection.

Acknowledgment

This work was supported in part by a grant from Japan Society for the Promotion of Science 16760284 and Hokkaido University Clark Memorial Foundation.

REFERENCES

1. Taylor, J. D., *Introduction to Ultra-Wideband Radar Systems*, CRC PRESS, Boca Raton, 1995.
2. FCC, "First Report and Order, Revision of Part 15 of the Commission's Rules Regarding Ultra-Wideband Transmission System," , FCCO2-48, Apr. 2002.
3. Schantz, H. G. et al., "The COTAB UWB magnetic slot antenna," *IEEE AP-S Int. Symp. Dig.*, vol. 4, 104–107, Boston, 2001.
4. Schantz, H. G., "Planar elliptical element ultra-wideband dipole antennas," *IEEE AP-S Int. Symp. Dig.*, vol. 3, 44–47, San Antonio, 2002.
5. Chen, Z. N. et al., "Comparison of Planar Dipoles in UWB Applications," *IEEE Trans. Antennas Propag.*, vol. 53, no. 6, 1973–1983, 2005.
6. Chen, Z. N., "Novel bi-arm rolled monopole for UWB applications," *IEEE Trans. Antennas Propag.*, vol. 53, no. 2, 672–677, 2005.
7. <http://www.semcad.com/main.html>
8. Mushiake, Y., *Self-Complementary Antennas: Principle of Self-Complementarity for Constant Impedance*, Springer, 1996.
9. Proakis, J. G., *Digital Communications*, 4th ed., McGraw-Hill, New York, 2000.

Time Domain Characterization of 1-2 GHz Circular End Bowtie Antenna with Coaxial Balun Using Normalized Impulse Response

Joko Suryana AB Suksmono Sugihartono A Kurniawan Kenji Tanaka K Igarashi Mitsuyoshi Iida
 STEI ITB, Indonesia NiCT Japan ARIB Japan
 e-mail: joko@ltrgm.ee.itb.ac.id

Abstract—Frequency domain analysis is a powerful and compact tool for characterizing the antenna parameters such as gain, radiation pattern and the impedance as a function of frequency. However, if time or space as a major concern, such as in the GPR application, the time domain analysis would be a very important tool due to their unique capability for determining the echo delay and range profile of target image. In this paper, we will describe the classical theory of system characterization in time domain, and then also propose the mathematical model for characterizing the 1 – 2 GHz circular-ended Bowtie antenna. From the measurement results, we concluded that the implemented Bowtie antenna with coaxial balun has good normalized impulse response with very small ringing, so it is suitable for GPR applications.

1. Introduction

When antenna is excited with simple waveforms, frequency dependence on antenna parameters is often analysed in frequency domain at its working bandwidth. Frequency domain analysis provides compact antenna characteristics such as : gain, beam pattern and input impedance [1]. In the meanwhile, in applications where time or space is the main concern, time domain analysis is important.

For example, in GPR applications, reflection time setting and range profile from target imaging needs time/space domain analysis [2][3]. So, in GPR applications, antenna parameters such as gain, or radiation pattern are less important than antenna ringing characteristics, maximum amplitude which can be received by antenna or impulse response duration. Because of this reason, in its development, time domain analysis on antenna characteristics is becoming a serious study to improve performance of imaging using microwave.

In this paper, we will describe classical theory of time domain system characterization, then mathematical modelling for application in characterizing circular ended bowtie antenna with coaxial balun which is working in 1 – 2 GHz frequency.

2. Impulse Response and Transfer Function of Antenna

Antenna can be categorized as a linear system, where its characteristics can be described in impulse response (time domain) or transfer function (frequency domain). Mathematically, relationship between antenna output and input follows this convolution integral equation [4]:

$$y(t) = \int_{-\infty}^{+\infty} h(t).x(t-t)dt \quad (1)$$

with :
 $x(t)$ is antenna input signal
 $y(t)$ is antenna output signal
 $h(t)$ is impulse response of antenna

The above formula can also be written in convolutional operator notation ‘*’ :

$$y(t) = h(t) * x(t)$$

While in frequency domain, above equation can be written as :

$$Y(\mathbf{w}) = H(\mathbf{w}).X(\mathbf{w})$$

With $Y(\mathbf{w})$ dan $X(\mathbf{w})$ is Fourier Transform from output $y(t)$ and input $x(t)$. While $H(\mathbf{w})$ is transfer function of antenna where its equation is from Fourier Transform of impulse response $h(t)$.

$$H(\mathbf{w}) = \frac{1}{2\pi} \int_{-\infty}^{+\infty} h(t).e^{-j\mathbf{w}t} dt \quad (2)$$

Representation of antenna characterization in time domain and frequency domain can be described in figure 1 :

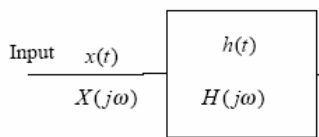


Figure 1 Linear System Representation

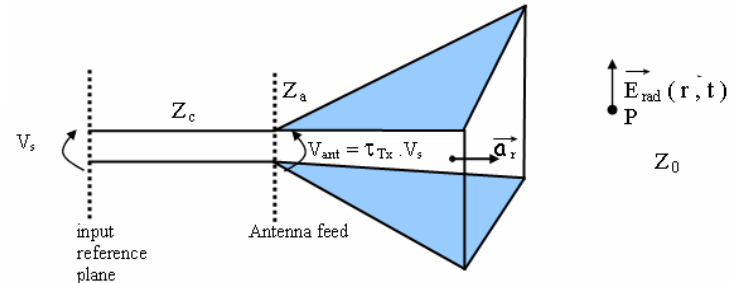


Figure 2 Transmitting Antenna Model as a Linear System

3. Time Domain Equations of Transmitting Antenna

Figure 2 is model of transmitting antenna as a linear system [2] with initial coordinate $r = 0$. Voltage V_s is fed to antenna as an input. Radiated field $E_{rad}(r, t)$ at point P in far field can be written as :

$$E_{rad}(r, t) = \frac{1}{2\pi r c f_g} \cdot \frac{dh_{tx}(a_r, t)}{dt} * V_{ant} * \delta(t - t_{d,tx}) \quad (3)$$

with :

$$V_{ant} = t_{tx} \cdot V_s$$

$$t_{tx} = \frac{2Za}{Zc + Za}$$

$$f_g = \frac{Za}{Z_0}$$

Where $h_{tx}(a_r, t)$ is defined as impulse response from transmitting antenna in a_r direction, V_{ant} is excited voltage to antenna, t_{tx} is voltage transmission coefficient from cable to antenna, Za is antenna input impedance and Zc is line impedance. Equation convolution on dirac function $\delta(t - t_{d,tx})$ is delay caused by propagation time from antenna to point P, where E_{rad} value is evaluated. If we only consider linear polarization, then the equation can be simplified into :

$$E_{rad}(r, t) = \frac{t_{tx}}{2\pi r c f_g} h_{tx}(a_r, t) * \frac{dV_s(t)}{dt} * \delta(t - t_{d,tx}) \quad (4)$$

4. Time Domain Equations of Receiving Antenna

In the meanwhile, for the receiving antenna [2], the antenna model used to get the receiving signal equations is :

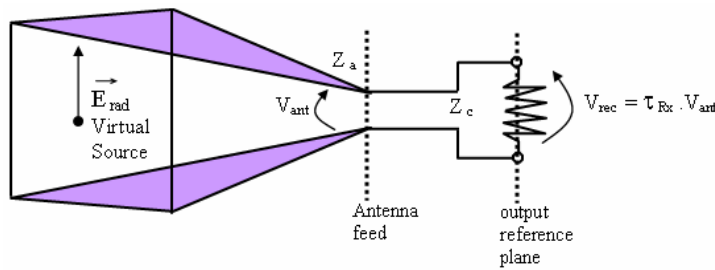


Figure 3. Receiving Antenna Model as a Linear System

In conditions where polarization is dominated by linear polarization, then output voltage $V_{rec}(t)$ recorded by oscilloscope by an incident field is :

$$V_{rec}(t) = t_{rx} \cdot h_{rx}(-a_r, t) * E_{inc,vs}(t) * \delta(t - t_{d,rx}) \quad (5)$$

with :

$$t_{rx} = \frac{2Zc}{Zc + Za}$$

In this case, $h_{rx}(-a_r, t)$ is impulse response of a receiving antenna in $-a_r$ direction and $t_{d,rx}$ represents propagation time between source and receiving reference point, that is position where $V_{rec}(t)$ is recorded. If transmitting and receiving antennas are identical pair, then $h_{tx} = h_{rx}$.

5. Normalized Impulse Response of Antenna

The problem of using the above transmitting and receiving antennas' impulse response equations (equation 4 and 5) is that in reality Z_a value depends on frequency, so \mathbf{t}_{tx} , \mathbf{t}_{rx} and f_g is not constant. To solve this problem we need normalized impulse response equation. Normalizing impulse response equations on transmitting and receiving antennas is done by dividing former equations by local characteristic impedances, that the equations become :

$$\frac{E_{rad}(r,t)}{\sqrt{Z_o}} = \frac{1}{2\mathbf{p}rc} h_{N,tx}(a_r, t) * \frac{1}{\sqrt{Zc}} \frac{dVs(t)}{dt} * \delta(t - t_{d,tx}) \quad (6)$$

$$\frac{V_{rec}(t)}{\sqrt{Zc}} = h_{N,rx}(-a_r, t) * \frac{E_{inc,vs}(t)}{\sqrt{Zo}} * \delta(t - t_{d,rx}) \quad (7)$$

With $h_{N,tx}$ and $h_{N,rx}$ are normalized impulse responses of transmitting and receiving antennas as described as follows :

$$\frac{E_{rad}(r,t)}{\sqrt{Zo}} = \frac{1}{2\mathbf{p}rc} \cdot h_{N,tx}(a_r, t) * \frac{1}{\sqrt{Zc}} \frac{dVs(t)}{dt} * \delta(t - t_{d,tx}) \quad (8)$$

$$V_{rec}(t) = \frac{1}{2\mathbf{p}Rc} h_{N,tx}(a_r, t) * h_{N,rx}(-a_r, t) * \frac{dVs(t)}{dt} * \delta(t - t_{d,tx} - t_{d,rx}) \quad (9)$$

$$h_{N,tx} = \sqrt{\frac{Zc}{Za}} \frac{\mathbf{t}_{tx}}{\sqrt{f_g}} h_{tx}$$

$$h_{N,rx} = \sqrt{\frac{Za}{Zc}} \frac{\mathbf{t}_{rx}}{\sqrt{f_g}} h_{rx}$$

If both antennas are identical, then combination of the above equations become :

$$\frac{V_{rec}(t)}{\sqrt{Zc}} = h_{N,rx}(-a_r, t) * \frac{E_{inc,vs}(t)}{\sqrt{Zo}} * \delta(t - t_{d,rx}) \quad (10)$$

6. Measurement of Normalized Antenna Impulse Response in Boresight Direction

6.1. Measurement Method using VNA

In this research, we use Vector Network Analyzer to measure normalized antenna impulse response. Because VNA measurement is in frequency domain, then the above equations has to be also formulated in time domain by using inverse Fourier Transform. For some cases where both antennas are identical, the transfer function of the antenna is :

$$H_N(\mathbf{w}) = \sqrt{\frac{2\mathbf{p}RcV_{rec}(\mathbf{w})}{j\mathbf{w}Vs(\mathbf{w})}} e^{j\mathbf{w}(t_{d,tx} + t_{d,rx})} \quad (11)$$

Total delay $t_{d,tx} + t_{d,rx}$ can be replaced with R/c , while parameter $V_{rec}(?) / Vs(?)$ is S_{21} parameter between port 1 and port 2 of VNA. The above equation can be re-written in more compact form :

$$H_N(\mathbf{w}) = \sqrt{\frac{2\mathbf{p}Rc}{j\mathbf{w}}} S_{21} e^{j\mathbf{w}\frac{R}{c}} \quad (12)$$

When S_{21} is measured, we will have the normalized transfer function of the antenna, and after applying the Inverse Fourier Transform, we will have the normalized impulse response of the antenna.

6.2. Implementation of Circular Ended Bowtie Antenna

In this experiment, we will implement a circular ended bowtie antenna with 70° flare angle, as shown in figure 4.

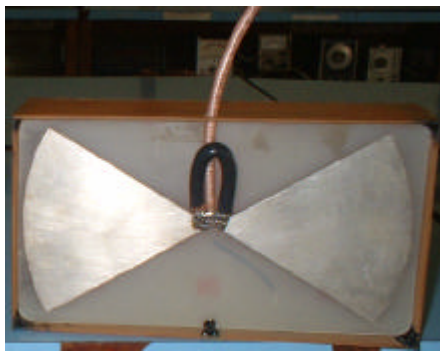


Figure 4. Photograph of the Implemented Circular Ended Bowtie Antenna with coaxial balun

6.3. Measuring Forward Transmission Coefficient (S21)

The objective of $S21$ measurement is to know the transmission characteristics of a system. In this case, two identical circular ended bowtie antennas are used for transmitter and receiver, as shown in this block diagram as illustrated in figure 5.

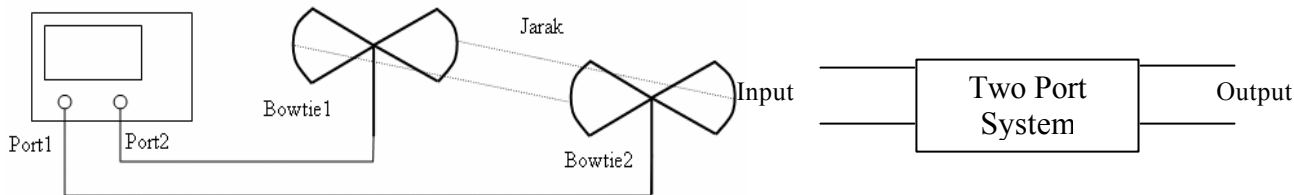


Figure 5. $S21$ Measurement Scheme using VNA

Figure 6. Model of two port network

The parameter measured is actually a comparison between transmitted power to the output and power coming to the input of the system. Antenna system in this measurement can be modeled as a two port network as shown in figure 6. Since this antenna is designed for GPR application in 1 – 2 GHz frequency range, then $S21$ parameter is also measured in the same working frequency, that is 1 – 2 GHz, with 511 point samples for antenna distances : 4 cm, 10 cm and 16 cm.

7. Measurement Results

This part will show the result of $s21$ parameter measurement in time domain and the normalized impulse response of circular ended bowtie antenna for antenna distances : 4 cm, 10 cm and 16 cm, as shown in figure 7.

The graphs of normalized impulse response measurement can also be compared with 9 – 10 samples different impulse position for 6 cm antenna distance. This result is closed with theoretical measurement that for 1 GHz bandwidth, λ length in free space is 30 cm, where one monocyte is 46 samples [5], so for 6 cm distance = 0.2 λ is equivalent with 9 samples.

To compare the three normalized impulse responses, we can use some important parameters: impulse width at half voltage, under impulse area and impulse tail fluctuation. Table 1 shows comparison between the three normalized impulse response characteristics at 4cm, 10cm, and 16cm. In measuring the normalized impulse response, distances between both antennas influence the waveforms, since at 4, 10 and 16 cm distances, both antennas are still the near-field [1], where interactions between both antennas (coupling, continuous reflections) still exist.

Table 1. Comparison between Normalized Impulse Response Characteristics for Antenna Distances : 4cm, 10cm, and 16cm

Distance	Impulse width (sample)	Under Impulse area	Tail Fluctuation
4 cm	20	0.7	20%
10cm	20	0.65	30%
16cm	17	0.65	40%

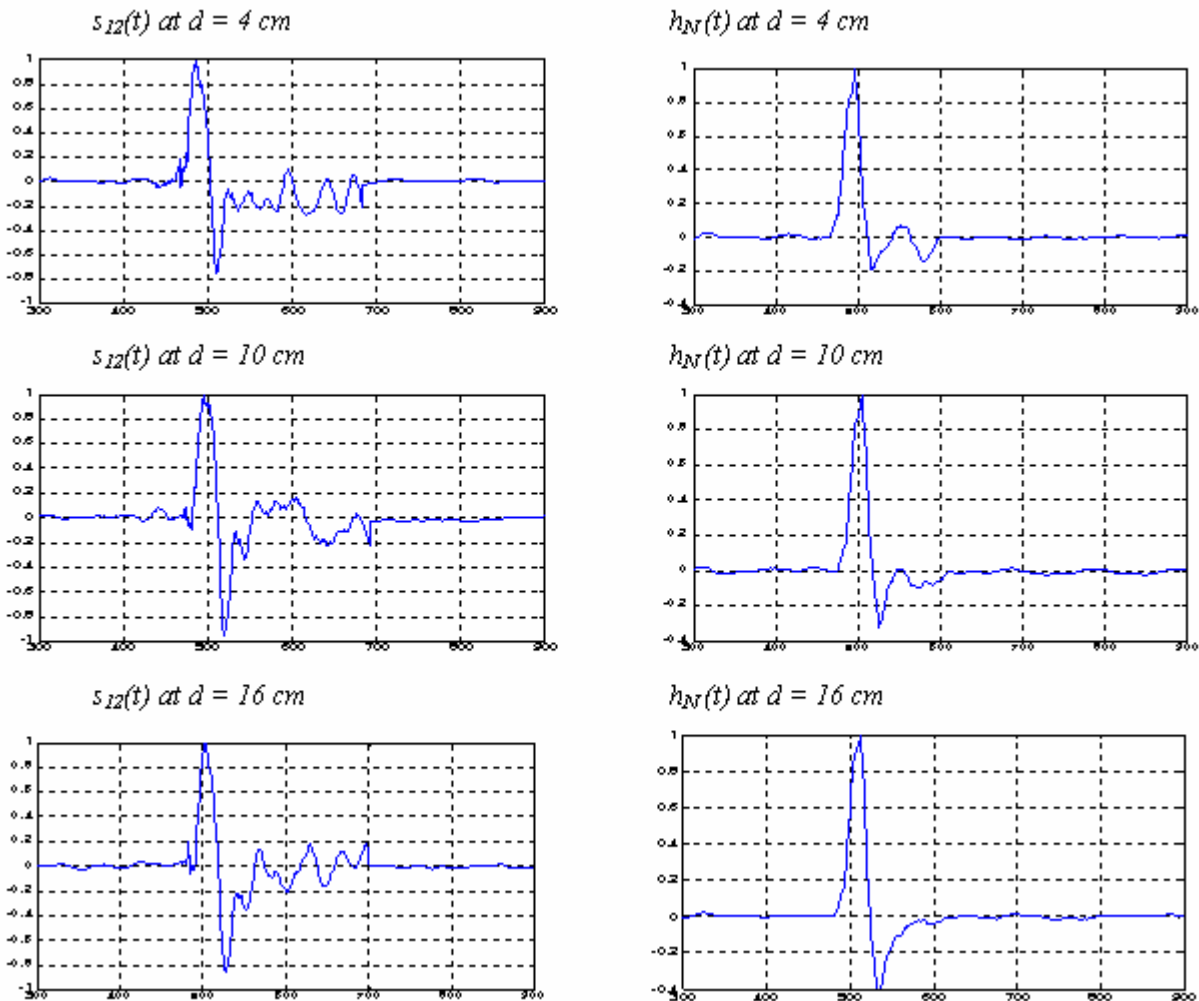


Figure 7. Measurement Results on $s_{12}(t)$ parameter and normalized impulse response $h_N(t)$ for antenna distances 4cm, 10cm and 16cm

8. Conclusion

From the normalized impulse response measurement of 1 – 2 GHz circular ended bowtie antenna, we can conclude that this antenna has relatively small ringing, so it is suitable for GPR applications.

This type of bowtie antenna does not contribute to waveform degradation of transmitting signal and GPR echo, but only functioned as delay unit type convolver from signal transmitted by GPR and also functions as delay unit when receiving echo signals.

REFERENCES

- [1]. Balanis C A, "Antenna Theory: Analysis and Design", John Wiley & Sons, New York), 1997 950 pp
- [2]. Bart Scheers, "Ultra-Wideband Ground Penetrating Radar, with Application to the Detection of Anti Personnel Landmines" , PhD Dissertation, Universite Catholique De Louvain Laboratoire D'Hyperfrequencies, Belgia, March 2001
- [3]. Daniels D J, "Surface penetrating radar", The Inst. Electrical Eng., London, 1996 320 pp.
- [4]. J.G. Proakis & D.G. Manolakis: Digital Signal Processing, New Jersey: Prentice Hall, 3rd edition, 1996.
- [5]. J.Suryana et.al,"Desain dan Realisasi Stepped Frequency GPR 1-2GHz untuk Aplikasi Deteksi Logam", Laporan Penelitian Awal Doktoral, Departemen Teknik Elektro ITB, 2005

A Modified UWB Bow-Tie Antenna for Impulse Radio

A.A. Lestari, A.G. Yarovoy, L.P. Ligthart

International Research Centre for Telecom and Radar
Delft University of Technology
Delft, The Netherlands
a.lestari@ircr.tudelft.nl

E.T. Rahardjo

Department of Electrical Engineering
University of Indonesia
Depok, Indonesia
eko@ee.ui.ac.id

Abstract – A UWB antenna, which is adopted from a Ground Penetrating Radar (GPR) antenna, is proposed for impulse radio applications. The proposed antenna has dimensions of 7 cm by 1.5 cm and is based on a modified bow-tie structure. It employs improved resistive loading for transmission of 0.2-ns monocytes with minimal ringing. The antenna radiation efficiency is enhanced by some discontinuities in the antenna that serve as secondary sources of radiation. Theoretically, it has been found that antenna ringing is adequately suppressed after less than 3 times the pulse duration. This will set the potential limit of data rate at more than 1 Gbit/s. Furthermore, the antenna is omni-directional, has stable radiation patterns, and shows a relatively flat gain in the 3 – 10 GHz frequency range. Experimentally, it has been found that within this bandwidth its input impedance is relatively flat and assumes values of around 100 Ohms.

1. Introduction

The 3.1 – 10.6 GHz frequency range allocated for UWB radio applications by the FCC in 2002 has stimulated research and development activities in UWB communication by the industry and academia. UWB communication is very attractive due to its advantages which include large channel capacity, low spectral density of transmitted power, high immunity against EMI, and fading robustness. One of the realizations of UWB telecommunication is the so-called impulse radio, in which information is sent by transmitting very short electromagnetic pulses. Transmission of such pulses requires specially-designed UWB antennas. In general, within the 3 – 10 GHz range an antenna for this application should be non-dispersive for stable pulse duration, has flat input impedance for minimal late-time ringing, has flat gain and stable radiation patterns for minimal variation of transmit waveform, and has a small planar (2-D) structure to simplify its implementation in small devices. For some applications in (tele-) communication it is also desired that the antenna be omni-directional.

A variety of antennas for impulse radio have been proposed [1] – [4], which include various designs of slotted, monopole and horn antennas. However, only few have the preferred small planar structure. In this paper, we propose an antenna which we adopted from the impulse Ground Penetrating Radar (GPR) antenna developed in our previous work [5]. That antenna was designed for transmission of 5-ns monocyte pulses and scaled down in this work to be suitable for impulse radio using 0.2-ns monocytes. The waveform and spectrum of that monocyte are shown in Figure 1 where can be seen that at the -5 dB level it occupies the 2 – 10 GHz range with center frequency of around 5.5 GHz.

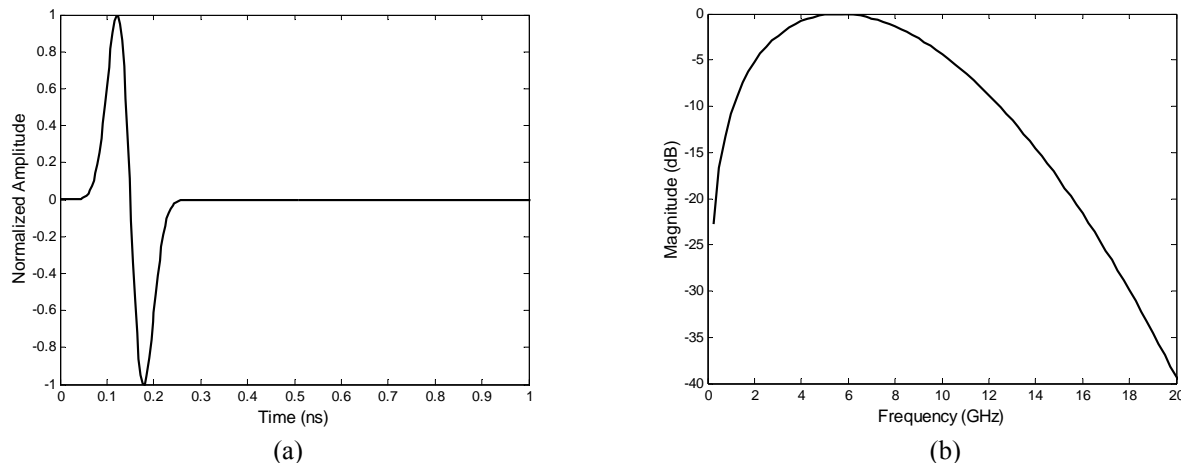


Figure 1: A monocyte with 0.2-ns duration for impulse radio, (a) waveform and (b) spectrum.

2. Design of the Antenna

The original antenna design was made to transmit 0.8-ns monocycle pulses for a high-resolution GPR and firstly introduced in [6]. The design was later on adopted to transmit 5-ns monocycle pulses for a low-resolution GPR and the loading profile was improved for better ringing suppression [5]. In this work the antenna dimensions in [5], except for its thickness, were reduced by a factor of 20 to make it well-suited for impulse radio applications, for which generally compactness of the antenna is important.

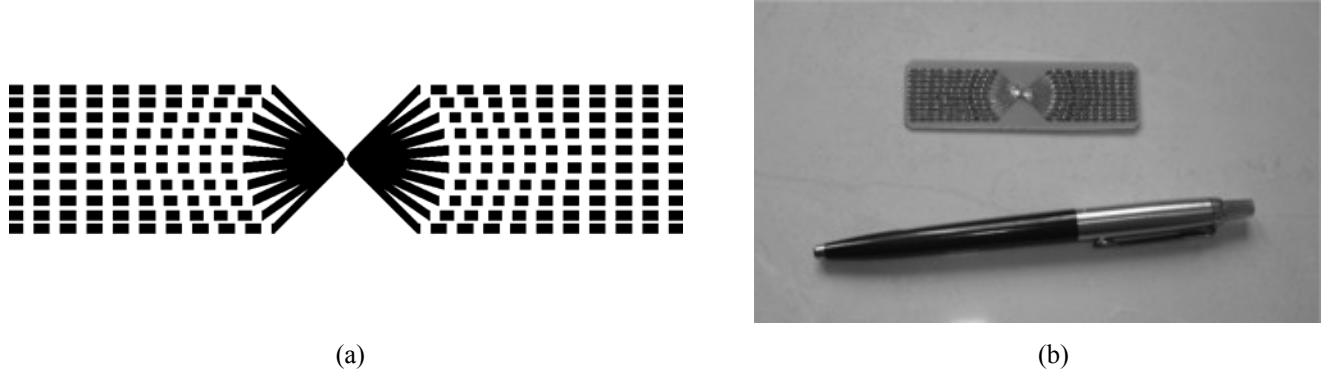


Figure 2: (a) Geometry of the antenna: length = 7 cm, width = 1.5 cm, strip width = 1 mm, flare angle = 90°, distance from feed point to bends = 1 cm. Chip resistors for antenna loading are soldered across the gaps. The resistor values are given in Table 1. Each strip has the same loading profile. (b) Realization of the antenna on a dielectric substrate.

The proposed antenna has a small planar structure with dimensions of 7 by 1.5 cm which should make it suitable for small devices, as shown in Figure 2. This antenna works according to the same principle as the ones discussed in [5] and [6]. Resistive loading for ringing suppression is applied along the antenna from the bends to the antenna ends (see Figure 2). The bends and the beginning of the loading together form discontinuities in the antenna, from which secondary radiations occur. In the broadside direction of the antenna these secondary radiations combine constructively with the primary radiation from the feedpoint when the feedpoint – bends distance is chosen to be $\lambda_c/4$ where λ_c is the wavelength corresponding to the central frequency of the pulse [7]. As a result, the amplitude of the transmit waveform in the broadside direction increases and one practically improves the radiation efficiency of the antenna.

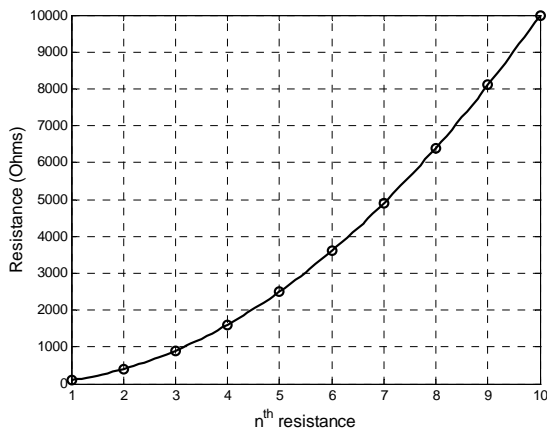


Figure 3: The employed resistive loading profile with 10 resistors. The resistor values are given in Table 1.

Table 1: Values of the resistors in Figure 3. R_1 and R_{10} are the resistors located at the bends and nearest to the ends, respectively.

R_1	R_2	R_3	R_4	R_5	R_6	R_7	R_8	R_9	R_{10}
100	400	900	1k6	2k5	3k6	4k9	6k4	8k1	10k

It was shown in previous works [5]-[6] that a series of resistors can be used successfully as resistive loading for suppression of late-time ringing. In this work we employ the improved loading profile reported in [5]. This loading profile allows better ringing suppression with only a small number of resistors. Due to the small size of the antenna, only 10 resistors can be used along each strip in the antenna. For such a small number of resistors, the famous Wu-King profile will not be properly approximated by the resistors. The employed loading profile was found by means of the FDTD method and plotted in Figure 3 with its values listed in Table 1.

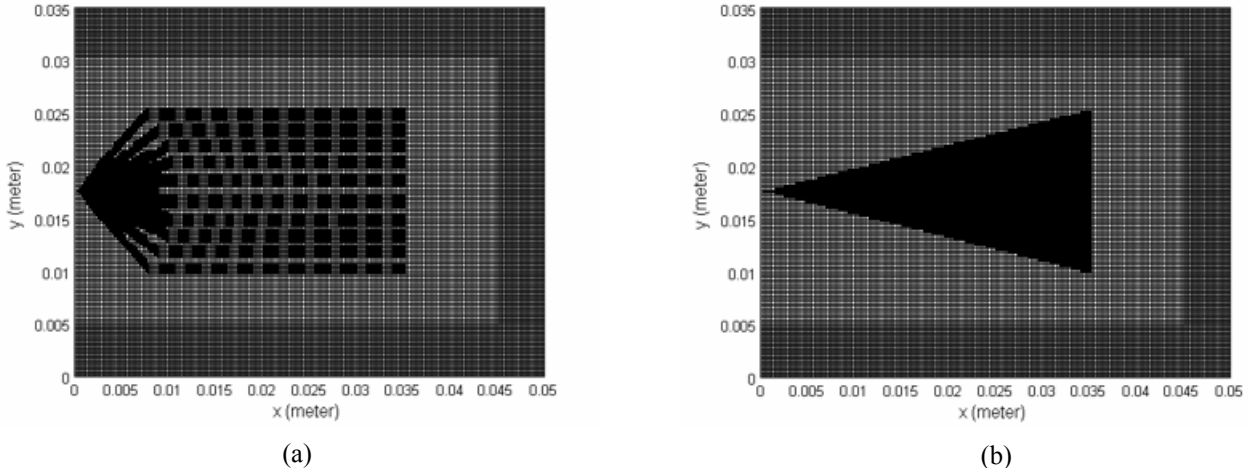


Figure 4: FDTD model for the antenna. The antenna's metallic parts are given in black. The light-colored rectangle around the antenna represents a dielectric substrate. An electric wall is defined on the $x = 0$ plane to include the antenna's left arm. (a) The model for the antenna in Figure 2, and (b) the model for a conventional bow-tie antenna as comparison. The chip resistors are given by the grey cells along the strips in (a).

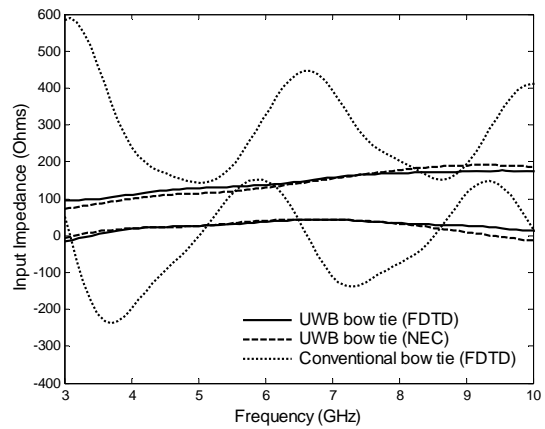


Figure 5: Computed input impedance of the proposed antenna. The computed input impedance of the conventional bow-tie antenna in Figure 4(b) is included for comparison.

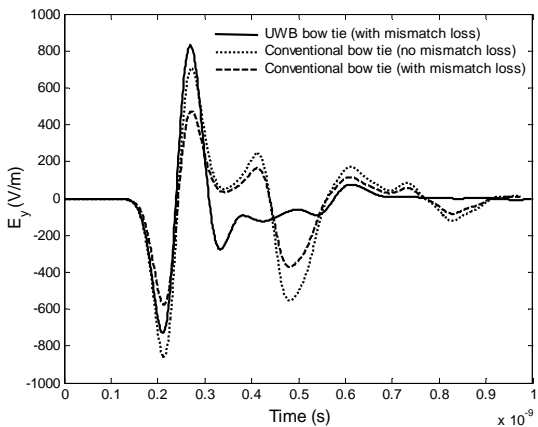


Figure 6: Computed transmit waveforms at a distance of 2.5 cm in the broadside direction of the antenna with and without mismatch loss. Transmit waveform of the conventional bow-tie antenna in Figure 4(b) is included for comparison.

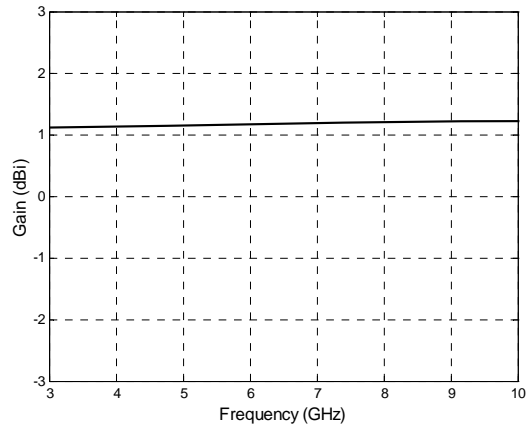


Figure 7: Computed gain of the proposed antenna.

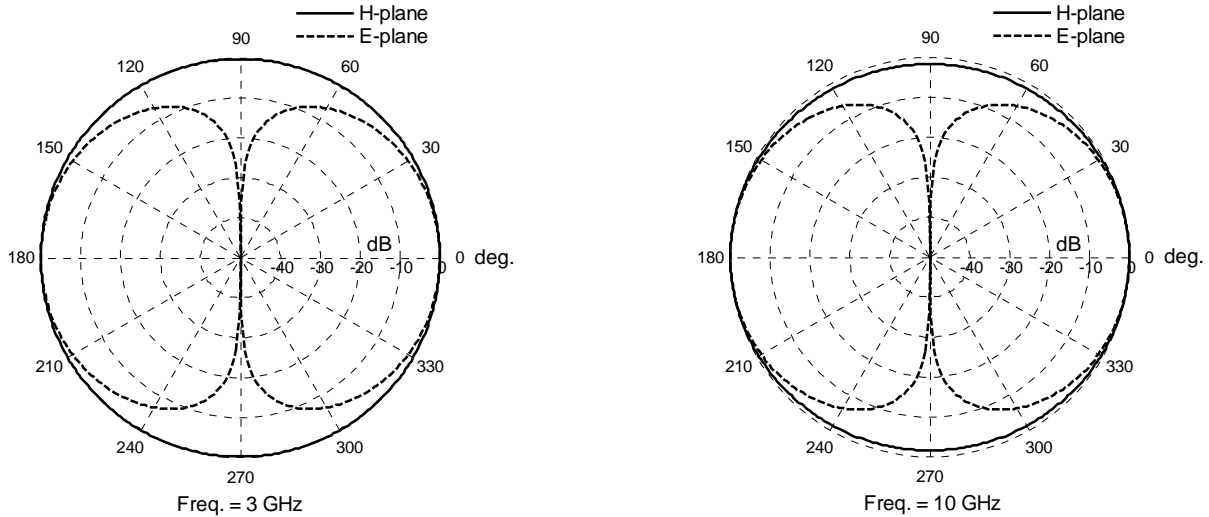


Figure 8: Computed radiation patterns of the proposed antenna at 3 and 10 GHz.

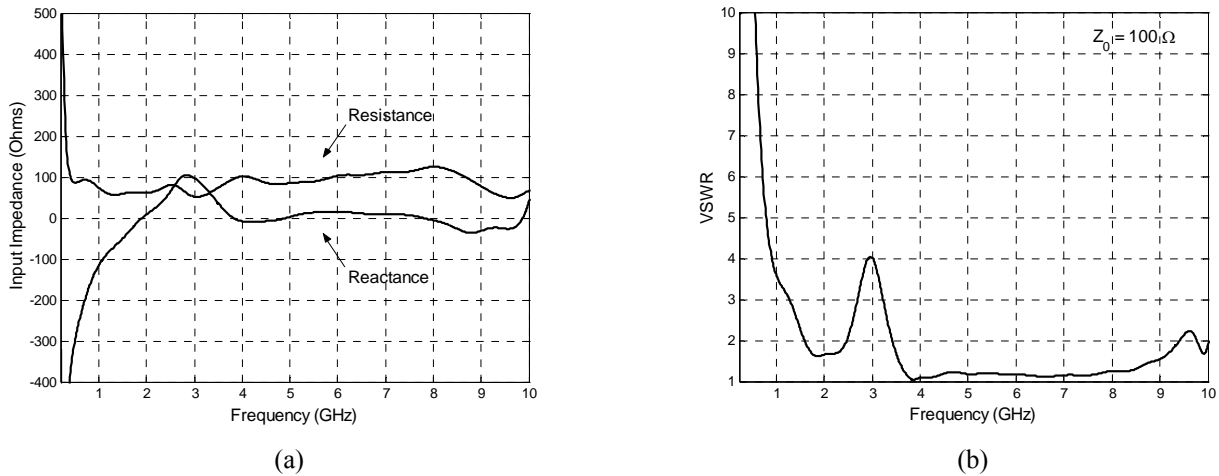


Figure 9: (a) Measured input impedance of the proposed antenna, and (b) the corresponding VSWR for a 100-Ohm feedline.

3. Theoretical Analysis

We employed a homemade FDTD code [8] and the well-known Numerical Electromagnetics Code (NEC) to analyze the antenna theoretically. The FDTD code was used to analyze the transmit waveforms and the input impedance of the antenna while NEC was used to analyze the antenna's radiation pattern and gain. In NEC the tape-like strips of the antenna were approximated by thin wires using the equivalent radius formula [9].

The FDTD model for the proposed antenna is illustrated in Figure 4(a). We made use of standard Yee cells of $0.25 \times 0.25 \times 0.25 \text{ mm}^3$, which should be sufficiently small for accurate computation of the antenna's input impedance and transmit waveforms. Furthermore, Figure 4(b) shows the FDTD model for a conventional bow-tie antenna used as comparison. This antenna is not loaded and of a comparable size with the proposed antenna.

It has been found that the computed input impedances by FDTD and NEC are in agreement as indicated in Figure 5. This result demonstrates that in the 3 – 10 GHz range the antenna exhibits relatively flat input impedance with no resonance behavior which on the contrary is obvious in the input impedance of the conventional bow-tie antenna due to the absence of loading.

The transmit waveforms of the antenna have been computed with and without accounting for mismatch loss. The results are plotted in Figure 6 where the result for the conventional bow-tie antenna is also included as comparison. It is apparent that when mismatch loss is taken into account the waveform peak of the proposed antenna is substantially higher, indicating improved antenna efficiency. Moreover, we observe that late-time ringing is adequately suppressed after less than 3 times the pulse duration and this will set the potential limit of data rate at more than 1 Gbit/s.

In addition, within the 3 – 10 GHz range the gain of the antenna is found to be adequately flat, as indicated in Figure 7, and the antenna is omni-directional. The radiation pattern is stable within this frequency range as indicated by the patterns at 3 and 10 GHz plotted in Figure 8.

4. Experiment

The experimental antenna is displayed in Figure 2(b). In this paper only the results of input impedance measurements are reported. By the time this paper was written, measurement results of other antenna parameters were not available yet.

The antenna's input impedance was measured using the technique introduced in [10] and the result is given in Figure 9(a). The measured input impedance is found to be relatively flat within the 3 – 10 GHz range and assumes values of around 100Ω with small reactance, as can be seen in the Figure.

In Figure 9(b) the VSWR of the antenna with respect to a 100Ω feedline is plotted. It is demonstrated that the values of VSWR are smaller than 2 between 3.4 – 9.4 GHz, indicating a bandwidth of 6 GHz.

Finally, it is worth mentioning that for proper operation of the antenna one may need a UWB balun transformer that should work efficiently in the 3 – 10 GHz range and provide a smooth impedance transition from 50Ω to 100Ω . Preferably it should also have a planar structure for its practical implementation with the antenna. Development of such a balun transformer for the proposed antenna is in progress and will be reported in a future paper.

5. Conclusions

A UWB antenna for impulse radio applications has been proposed. The antenna is optimized for transmission of 0.2-ns monocycles. The antenna ringing is adequately suppressed after less than 0.6 ns (3 times the pulse duration). This will set the potential limit of data rate at more than 1 Gbit/s.

Within the 3 – 10 GHz range the antenna shows stable radiation patterns and gain, and relatively flat input impedance. Its VSWR is smaller than 2 between 3.4 and 9.4 GHz (6 GHz bandwidth) when fed with a 100Ω feedline.

The antenna has a planar structure with dimensions of 7×1.5 cm, making it suitable for implementation in small devices. A UWB balun transformer giving a smooth impedance transition from 50Ω to 100Ω may be needed to properly feed the antenna.

REFERENCES

- [1] X. Qing, M. Y. W. Chia, and X. Wu, "Wide-slot antenna for UWB applications," *2003 IEEE Int. Antennas Propagat. Symp. Dig.*, vol. 41, pp. 834 - 837, June 2003.
- [2] M. Manteghi and Y. Rahmat-Samii, "Tilted inverted triangular pulse antenna for impulse radio applications," *2003 IEEE Int. Antennas Propagat. Symp. Dig.*, vol. 41, pp. 596 - 599, June 2003.
- [3] S.-Y. Suh, W. L. Stutzman, and W. A. Davis, "Multi-broadband monopole disc antennas," *2003 IEEE Int. Antennas Propagat. Symp. Dig.*, vol. 41, pp. 616 - 619, June 2003.
- [4] X. Li, S. C. Hagness, M. K. Choi, and D. W. van der Weide, "Numerical and experimental investigation of an ultrawideband ridged pyramidal horn antenna with curved launching plane for pulse radiation," *Antennas Wireless Propagat. Lett.* 2, pp. 259 - 262, 2003.
- [5] A. A. Lestari, et al., "Design and Realization of a GPR Antenna for Hydrological Application," *Proc. 11th Int. Conf. Ground Penetrating Radar (GPR 2006)*, Columbus, Ohio, June 2006.
- [6] A.A. Lestari, Y.A. Kirana, A.B. Suksmono, A. Kurniawan, E. Bharata, A.G. Yarovoy, L.P. Ligthart, "Compact UWB Radiator for Short-Range GPR Applications," *Proc. 10th Int. Conf. Ground Penetrating Radar (GPR 2004)*, vol. 1, pp. 141-144, Delft, The Netherlands, June 2004.
- [7] A.A. Lestari, A.G. Yarovoy, L.P. Ligthart, "RC loaded bow-tie antenna for improved pulse radiation," *IEEE Trans. Antennas Propagat.*, vol. 52, no. 10, pp. 2555-2563, Oct. 2004.
- [8] G. Mur, *User's Guide for FDTD3D: The C++ Finite-Difference Code for Electromagnetic Fields in Three Dimensions and Time*, IRCTR and Laboratory for Electromagnetic Research, Delft University of Technology, Delft, The Netherlands, May 2000.
- [9] C. M. Butler, "The equivalent radius of a narrow conducting strip," *IEEE Trans. Antennas Propagat.*, vol. 30, no. 4, pp. 755-758, Jul. 1982.
- [10] A. A. Lestari, A. G. Yarovoy, and L. P. Ligthart, "Ground influence on the input impedance of transient dipole and bow-tie antennas," *IEEE Trans. Antennas Propagat.*, vol. 52, no. 8, pp. 1970-1975, Aug. 2004.

Array Geometry for Real-time Ultra Wideband Systems

N. Yahya Soltani †, M. Asgari*, F. Hodjat Kashani**

†, ** Department of electrical engineering, Iran University of Science and Technology, Tehran, Iran

*IRIB Faculty, Tehran, Iran

Abstract- In this paper we want to focus on finding appropriate array geometry for DOA of wideband sources. Although there are many wideband DF algorithms for wideband systems, we cannot rely on this kind of algorithms. This is because they are not real-time and therefore applicable, especially when the number of sources increases. That's why; we prefer to concentrate on using a narrowband DF algorithm and try to eliminate the errors of these algorithms for DOA of wideband sources, by determining the array configuration constraints. In fact, we will prove that frequency independent array geometry can help us avoid of using a complex wideband algorithm. Here, a typical circular array is introduced to show the problem of using narrowband DOA for a wideband signal, so array pattern and algorithm behavior to this array configuration will be compared. Then to solve the problem, frequency independent array geometry will be investigated and some typical results are shown.

1. Introduction

Up to now several DOA algorithms for different kind of sources have been proposed. But to define the DOA of a wide-band signal arriving from a definite direction, the processes should be performed using a wide-band algorithm which consists of complex operations and consequently, this will lead to a procedure which is not fast and therefore real-time and applicable. On the other hand, if we use a narrow-band algorithm, which is much faster, to estimate the direction of arrival of a wide-band signal, different results for different frequencies in the frequency band of the wideband signal will be obtained which are not acceptable ,since the algorithm is designed for a single frequency .

In this paper we want to find a frequency independent antenna array configuration to use a narrowband DF algorithm for detecting the azimuth angle of a wideband signal.

An important and popular class of narrow-band DOA algorithms is based on subspace. These algorithms structure such as MUSIC algorithm arises from a zero-bandwidth signal assumption. For non-zero bandwidth, DOA errors will arise (see [1, 2] for the effect of bandwidth). On the other hand the use of narrow band algorithms is much more preferable. This is because they are less complex and much faster.

To show how frequency independent array pattern can help us to solve this problem, we use spiral array (see [3]) and for an angle we see the algorithm behavior. An outline of this paper is as follows: In section 2 we present MUSIC algorithm and circular array DOA results using MUSIC. Spiral model as a configuration to solve this problem is presented in section 3 and in section 4 the measurement results are shown.

2. Problem Formulation

Consider an array of N identical sensors located in the space at locations r_i for $i \in [1, N]$. As we may consider both linear and planar arrays, for planar array we have $r_i = [r_{xi}, r_{yi}]^T$.

Assume a single far-field source $s(t)$, which is in general wideband, impinges on the array from direction $\theta = [\varphi, \psi]$, φ denoting the azimuth angle measured counterclockwise from the x -axis on the x - y plane, and ψ denoting the elevation angle measured counterclockwise from the x -axis on the x - z plane. The noise at the sensors is independent, zero mean Gaussian noise, and independent of the source signal. Then,

$$x = A(\theta, \varphi) s(t) + n(t) \quad (1)$$

Where $A(\theta, \varphi)$ for two dimensional sensor locations are $\exp(j\pi(r_x \cos(\theta) \cos(\varphi) + r_y \sin(\theta) \cos(\varphi)))$. $s(t)$ depends on the number of arriving wave. If M signals impinge on the array from M different directions according to the number of the sensors $x(t), n(t)$ are $N \times 1$ vectors and $A(\theta, \varphi)$ will be $N \times M$.

2.1 MUSIC Algorithm

In brief, in MUSIC algorithm, by finding the zeros of the function $f(\theta)$, DOAs of the signal can be found.

$$f(\theta) = \frac{a^*(\theta)E_n E_n^* a(\theta)}{a^*(\theta)a(\theta)} = \text{Tr}(P_\theta E_n E_n^*) \quad (2)$$

Where P_θ is defined as the projection matrix $P_\theta = a(\theta)[a(\theta)^* a(\theta)]^{-1} a^*(\theta)$, $a(\theta)$ is the complex array response for a source with direction of arrival θ and $E_s = [e_1, \dots, e_d]$, $E_n = [e_{d+1}, \dots, e_m]$, and $\lambda_1 \geq \dots \geq \lambda_d > \lambda_{d+1} = \dots = \lambda_m = \sigma^2$ which are achieved by performing an eigen decomposition on covariance matrix R of the received data. Assuming the noise and signals are uncorrelated, and for the moment that the noise is spatially white, we have

$$R = E\{x(t)x^*(t)\} = ASA^* + \sigma^2 I \quad (3)$$

In this work we will use MUSIC algorithm as one of the most popular ones to estimate the azimuth angle of a wideband signal. Where S is the covariance matrix of the emitter signals and σ^2 is the noise power in each channel.

$$\underline{a}(\theta) \underline{a}^H(\theta) = [I_i I_k \exp(j\beta \cos \varphi (Dx_{ih} \cos \theta + Dy_{ih} \sin \theta))]$$

2.2 Array Geometry Effects on the Performance of the Algorithm

In this part, to define how differently the narrowband MUSIC algorithm results in direction of arrival of a wideband signal, it will be shown that ([3]) to have the algorithm perform for a wideband system properly; the sensor array should be wideband. To introduce a wideband array we introduce a frequency factor, which shows how frequency changes in a typical frequency band comparing the main frequency f_r of the system. There are many different definitions depending on the applications for wideband, for example in this paper we introduce wideband for bandwidth changes of 1 to 10.

$$F = \frac{f_i}{f_r} \quad 1 \leq F \leq 10 \quad (4)$$

Where f_i is one of the frequencies in the frequency band for which the calculations are performed.

In other words, the frequency factor shows the relationship of the frequencies of a wideband signal spectrum, with the normalized frequency of the system. For an array of N similar sensors in locations

d_1, d_2, \dots, d_N , where $d_k = (dx_k, dy_k)$ we have,

$$\begin{bmatrix} x_1(t) \\ x_2(t) \\ \vdots \\ x_N(t) \end{bmatrix} = \begin{bmatrix} I_1 \exp(-j\beta dx_1 \cos \theta_1 - j\beta dy_1 \sin \theta_1) \cos \varphi_1 \\ I_2 \exp(-j\beta dx_2 \cos \theta_1 - j\beta dy_2 \sin \theta_1) \cos \varphi_1 \\ \vdots \\ I_N \exp(-j\beta dx_N \cos \theta_1 - j\beta dy_N \sin \theta_1) \cos \varphi_1 \end{bmatrix} S_1(t) + n \quad (5)$$

As described before, to find the DF results, the zeros of $f(\theta)$ or minimums of it must be found. Therefore we try to find a formula in a closed form to estimate the array geometry effects on this algorithm. First of all, by considering the excitation magnitudes as I_1, I_2, \dots, I_N , we have

$$\underline{a}^H(\theta) \underline{a}(\theta) = |I_1|^2 + |I_2|^2 + \dots + |I_N|^2 = Q \quad (6)$$

$$\underline{a}(\theta) \underline{a}^H(\theta) = \begin{bmatrix} |I_1|^2 & \dots & I_1 I_N \exp(j\beta \cos \varphi (j\beta \cos \varphi ((dx_N - dx_1) \cos \theta + (dy_N - dy_1) \sin \theta))) \\ \vdots & \ddots & I_2 I_N \exp(j\beta \cos \varphi (j\beta \cos \varphi ((dx_N - dx_2) \cos \theta + (dy_N - dy_2) \sin \theta))) \\ \dots & \dots & \vdots \\ & & |I_N|^2 \end{bmatrix}$$

$$= \begin{bmatrix} |I_1|^2 & I_1 I_2 \exp(j\beta \cos \varphi (Dx_{21} \cos \theta + Dy_{21} \sin \theta)) & \dots & I_1 I_2 \exp(j\beta \cos \varphi (Dx_{N1} \cos \theta + Dy_{N1} \sin \theta)) \\ \vdots & \vdots & \ddots & \vdots \\ & & \dots & |I_N|^2 \end{bmatrix} \quad (7)$$

where $Dx_{ih} = dx_i - dx_h$ and $Dy_{ih} = dy_i - dy_h$, $1 \leq i, h \leq N$

Now we should find $E_n E_n^*$,

$$E_n E_n^H = \begin{bmatrix} e_{11} & e_{12} & \dots & e_{1N-1} \\ e_{21} & e_{22} & \dots & e_{2N-1} \\ \vdots & \vdots & \ddots & \vdots \\ e_{N1} & e_{N2} & \dots & e_{NN-1} \end{bmatrix} \begin{bmatrix} e_{11}^* & e_{21}^* & \dots & e_{N1}^* \\ e_{12}^* & e_{22}^* & \dots & e_{N2}^* \\ \vdots & \vdots & \ddots & \vdots \\ e_{N1}^* & e_{N2}^* & \dots & e_{NN-1}^* \end{bmatrix} = \begin{bmatrix} \sum_{i=1}^{N-1} |e_{1i}|^2 & \sum_{i=1}^{N-1} e_{1i} e_{2i}^* & \dots & \sum_{i=1}^{N-1} e_{1i} e_{Ni}^* \\ \sum_{i=1}^{N-1} e_{2i} e_{1i}^* & \sum_{i=1}^{N-1} |e_{2i}|^2 & \dots & \sum_{i=1}^{N-1} e_{2i} e_{Ni}^* \\ \vdots & \vdots & \ddots & \vdots \\ \sum_{i=1}^{N-1} e_{Ni} e_{1i}^* & \sum_{i=1}^{N-1} e_{Ni} e_{2i}^* & \dots & \sum_{i=1}^{N-1} e_{Ni} e_{Ni}^* \end{bmatrix} \quad (8)$$

Assuming that C_h 's are diagonal elements of the product of these two matrixes, the trace function of this algorithm will be reformed to these equations:

$$\begin{aligned} \text{tr}(Q^{-1} \underline{a}(\theta) \underline{a}^H(\theta) E_n E_n^H) &= \sum_{h=1}^N C_h \left(\sum_{h=1}^N |I_h|^2 \left(\sum_{i=1}^{N-1} |e_{hi}|^2 \right) \right) + \sum_{h=2}^N e^{j\beta \cos \varphi (Dx_{h-1h} \cos \theta + Dy_{h-1h} \sin \theta)} (I_{h-1} I_h^* \sum_{i=1}^{N-1} e_{hi} e_{h-1i}^*) \\ &+ \sum_{h=3}^N e^{j\beta \cos \varphi (Dx_{h-2h} \cos \theta + Dy_{h-2h} \sin \theta)} (I_{h-2} I_h^* \sum_{i=1}^{N-1} e_{hi} e_{h-2i}^*) + \sum_{h=4}^N e^{j\beta \cos \varphi (Dx_{h-3h} \cos \theta + Dy_{h-3h} \sin \theta)} (I_{h-3} I_h^* \sum_{i=1}^{N-1} e_{hi} e_{h-3i}^*) \\ &+ \dots + \sum_{h=N}^N e^{j\beta \cos \varphi (Dx_{h-N+1h} \cos \theta + Dy_{h-N+1h} \sin \theta)} (I_{h-N+1} I_h^* \sum_{i=1}^{N-1} e_{hi} e_{h-N+1i}^*) + \sum_{h=2}^N e^{-j\beta \cos \varphi (Dx_{h-1h} \cos \theta + Dy_{h-1h} \sin \theta)} (I_{h-1}^* I_h \sum_{i=1}^{N-1} e_{hi}^* e_{h-1i}) \\ &+ \sum_{h=3}^N e^{-j\beta \cos \varphi (Dx_{h-2h} \cos \theta + Dy_{h-2h} \sin \theta)} (I_{h-2}^* I_h \sum_{i=1}^{N-1} e_{hi}^* e_{h-2i}) + \dots + \sum_{h=N}^N e^{-j\beta \cos \varphi (Dx_{h-N+1h} \cos \theta + Dy_{h-N+1h} \sin \theta)} (I_{h-N+1}^* I_h \sum_{i=1}^{N-1} e_{hi}^* e_{h-N+1i}) \end{aligned} \quad (9)$$

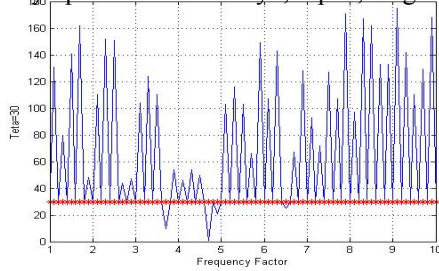
Comparing the equation above to a general formula $AF = \sum_{n=0}^{N-1} I_n e^{(j\beta \psi_n)}$, it can be easily seen that these

summations are like different array factors of several arrays. The whole number of summations is $2N-1$ and the parameters in the parentheses are considered as the coefficients (magnitude and phase) of the AF's. We can easily conclude that designing all these array factors wideband can help the MUSIC algorithm to detect the correct results. That is, when these AF's do not change very much by the frequency, the function $f(\theta)$ doesn't change versus frequency. In other words, the minimums of it remain unchanged. On the other hand, the coefficients depend on SNR, signals correlations, the angle of detection, etc. It will be easily seen that each summation can be divided into two different parts,

$X(e^{i\beta(Dx \cos \theta + Dy \sin \theta)})Y(\theta, \text{SNR}, \text{samples}, \dots)$, where X is the similar part of each summation with the main array factor and Y is considered as magnitude and phase coefficients of each summation. Here we conclude that if the main array is frequency independent or in other words if βd_k is frequency independent, it means that βd_k is a constant. Therefore, as all the summations have a form similar to array factor equations and they are quite similar to the main array factor in X, it can be concluded that if the main array doesn't change by frequency, each of the trace components does not change by frequency.

Now we examine some array configurations to show it better. We can easily find the whole array pattern or $f(\theta)$ scheme for specific angles. For example, the simulation results of a circular array of 8 equally

spaced elements for $\theta = \frac{\pi}{6}$ are shown in figure below.

Figure1: MUSIC algorithm results for circular array and $\theta = \pi / 6$

According to the figure above, the DOA results which show big errors in the frequency band seem to be wrong.

What is clear in here is that, as the frequency changes the array pattern and therefore the algorithm result changes so that algorithm error increases [2]. Now, we want to understand if the array configuration can affect the algorithm results or not. In other words, we want to know if the array geometry for a wideband array pattern, can lead to better results in DF algorithm.

Let's consider Ref. [2], in which the writer introduces a parameter β_k which shows the effects of non-zero bandwidth on narrowband DF algorithms. β_k itself, is a function of many parameters such as the array configuration. This means the better the array configuration, the less the error of DF algorithm. Using these results we conclude that finding the appropriate array geometry can help us to solve the problem shown above.

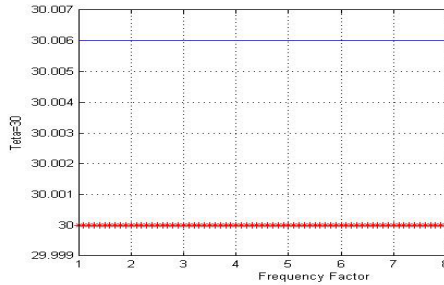
3. Problem Solution

As described in section 2.2, a frequency independent array configuration would be the best choice to solve the problem. Here, we show that by using an appropriate array configuration the direction of arrival of a wideband signal will be obtained correctly. In fact spiral [4] array configuration shows frequency independent characteristics. This model is introduced and compared with circular array (for similar conditions), so that the algorithm behavior to these arrays in different frequencies will be investigated.

For $[f_l, f_u] = [314.81 \sim 2500 \text{MHz}]$ the spiral array parameters as the Ref.[4] introduces are given as:

$$r_i = \frac{\lambda_{N-i}}{4} \Rightarrow \frac{r_i}{r_0} = \frac{\lambda_{N-i}}{\lambda_u} = e^{a\varphi_i}, \quad \varphi_i = \frac{1}{a} \ln \frac{\lambda_{N-i}}{\lambda_u} \quad (10)$$

The number of sensors is 8 for $\varphi = 3\pi$ and the most practical value of a according to the references is considered 0.221. The simulation result of MUSIC algorithm for one angle is shown in figure below.

Figure2: MUSIC algorithm results for spiral array and $\theta = \pi / 6$

The simulation results show that spiral array DOA results are much closer to the correct angles than circular array's.

3. Measurements Results

We used 8 microphones (AKG, C417) to test what has been gained in theory. The measurement results can be seen in tables below. It can be seen that spiral array works much better than circular array.

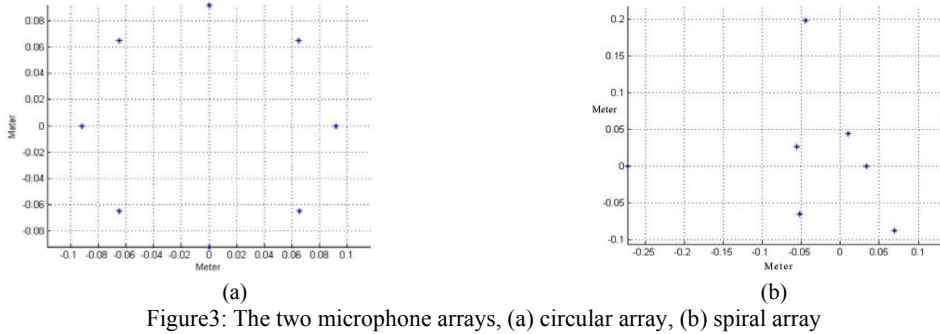


Figure3: The two microphone arrays, (a) circular array, (b) spiral array

Table1: Circular array measurement results

Angle	$f = 1837 \text{ Hz}$	$1.9f$	$3.45f$
26.56°	23.3°	111.6°	17.1°
73°	71.6°	95°	95°
135°	132°	61.3°	124°

Table2: Spiral array measurement results

Angle	$f = 1837 \text{ Hz}$	$1.9f$	$3.45f$
26.56°	22.6°	26.9°	28.2°
73°	73.6°	73.2°	70.1°
135°	130°	132.1°	135.2°

4. Conclusions

In this paper we have presented the behavior of MUSIC algorithm on wideband systems. That is, the azimuth angle of a wideband arriving wave, estimated by MUSIC algorithm was investigated. First of all, we obtained a formula which showed the algorithm results relations to array configuration and it was proved that if the array pattern is frequency independent, the algorithm behaves independently.

Then to show the problem better, a circular array was investigated. The simulation results of this array seemed to be changing in different frequencies. Then we introduced spiral array in section 3, as a frequency independent array model which could work for a narrowband DF algorithm. It was shown that the results seemed to be much better than the former.

In other words, we showed that wideband array geometry can help us to solve the problem of finding the DOA of a broadband signal. That is, once finding the appropriate array geometry; we can avoid complex operations of a wideband DF algorithm.

References:

- [1] U. Nickel," On the influence of channel errors on array signal processing methods," *International Journal of Electronics and Communications*, vol. AEU, No. 4, pp. 209-219, 1993.
- [2] Joakim Sorelius, Randolph L Moses, Torsten Söderström and A LEE Swindlehurst," Effects of Non-zero bandwidth on direction of arrival estimators in array signal processing," *IEEE Digital Signal Processing Workshop*, (Loen, Norway), Sept. 1-4, 1996.
- [3] Nasim Yahya Soltani, "Optimised array geometry for DOA of a wideband signal using narrowband DF algorithms," *MS.c thesis, Iran University of Science and Technology*, 2005.
- [4] Stutzman, W. G. and G. A. Thiele, *Antenna Theory and Design*, New York: John Wiley & Sons, 1981.

Transmit and Receive Timing Control in LOS MIMO-UWB Environments

Masaki Takanashi, Toshihiko Nishimura, Yasutaka Ogawa, and Takeo Ohgane

Graduate School of Information Science and Technology, Hokkaido University, Japan

Abstract—The UWB-IR(Ultra Wideband-Impulse Radio) technology and MIMO system have attracted interest for next generation high speed radio communications. We have researched multiple-input multiple-output ultra wideband(MIMO-UWB) systems for higher speed radio communications. The UWB system will be used in a range of less than 10 meters. Then, we usually have line-of-sight(LOS) environments in the MIMO-UWB systems. We can consider that the direct waves have high power and cause high correlations between antennas in this environment. Thus, it is conjectured that the direct waves affect the performance of signal detection by spatial filtering and equalization techniques. In order to examine the feasibility of MIMO-UWB systems, we conducted propagation measurement of MIMO-UWB systems in LOS environments, and evaluated bit error rate(BER) performance using the measured data. Considering the measurement results, we noticed that the arrival time of direct waves from different transmit antennas differs for MIMO configurations, and affects the BER performance. In this paper, we show the measurement results, and propose performance improvement with the transmit(Tx) and receive(Rx) timing control.

1. Introduction

The UWB-IR(Ultra Wideband-Impulse Radio) technology[1][2] and MIMO system[3] have attracted interest for next generation high speed radio communications. The multiple-input multiple-output ultra wideband(MIMO-UWB) systems for higher speed radio communications have been researched in [4],[5]. We have researched MIMO-UWB systems using the FDE(Frequency Domain Equalization) technique[6] with the MMSE spatial filtering technique. These researches have been conducted using computer simulations with multipath model such as S-V model[7] or 802.15.3a model[8]. The UWB system will be used in a range of less than 10 meters. Then, we usually have line-of-sight(LOS) environments in the MIMO-UWB systems. We can consider that the direct waves have high power and cause high correlations between antennas in this environment. Thus, it is conjectured that the direct waves affect the performance of signal detection using spatial filtering and equalization techniques. However, these models are not necessarily applicable to the MIMO environment. In this paper, to examine the feasibility of MIMO-UWB systems, we conducted propagation measurement of MIMO-UWB systems in LOS environments, and evaluated bit error rate(BER) performance using the measured data. Considering the measurement results, we noticed that the arrival time of direct waves from different transmit antennas differs for MIMO configurations, and affects the BER performance. In this paper, we show the measurement results, and propose performance improvement with the transmit(Tx) and receive(Rx) timing control.

2. Wideband Propagation Measurement

In this measurement, we obtained MIMO propagation data in a frequency domain with a vector network analyzer. We used broadband printed dipole antennas employing self-complementary radiating element and microstrip line feed[9] as Tx and Rx antennas. We show the experimental environment in Fig.1. We measured transmission coefficients of each Tx and Rx antenna pair from 50[MHz] to 12.05[GHz] with a frequency interval 7.5[MHz]. We examined three types of MIMO configuration as shown in Fig.2 and obtained 2100 data changing the position of Tx and Rx antenna array pair along x-axis and y-axis for each configuration. We moved antenna system by every 1[cm] along the x-axis or y-axis. Then, the Tx and Rx arrays were fixed 1[m] apart each time. The moving ranges along the x-axis and y-axis were 70[cm] and 30[cm], respectively. Because there were no objects between

transmit and receive antennas, the direct waves arrived at each Rx antenna, that is, it was a LOS environment. Because the measurement was conducted in a shield room, we did not have interference from other radio systems, and did not interfere with other radio systems. Also, there were no moving objects that change the propagation environment.

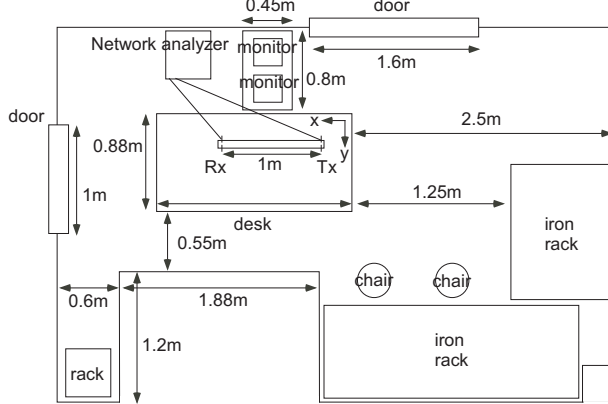


Fig. 1: Measurement environment (top view).

We assumed a Tx monocycle pulse given by $p(t) = [1 - 4\pi(t/\tau)^2] \exp[-2\pi(t/\tau)^2]$ ($\tau = 0.2877[\text{ns}]$). In Figs.3, 4, and 5, we show examples of received pulses for “pos1”, “pos2” and “pos3” in the MIMO environments, respectively. They were calculated using the measured transmission data. We indicate pulses that are considered to be the direct waves by the arrows in the figures. In Fig.3, we can see that all the direct waves arrive at the receive antennas at about 4.2 nsec for “pos1”. In Fig.4, we can see that the direct waves from the first transmit antenna arrive at the receive antennas at about 4.2 nsec. On the other hand, the direct waves from the second transmit antenna arrive at the receive antennas at about 4.5 nsec for “pos2”. This is because the second transmit antenna is 8[cm] farther than the first transmit antenna from the receive antenna system. In Fig.5, we can also see that the direct wave from each transmit antenna arrives at receive antennas at different time. From these results, we can see that the arrival time of the direct waves differs for MIMO configurations because of the difference of propagation distance.

In Fig.6, we show the power decay for each MIMO configuration. From this result, we can see that the average received power is high and different for the MIMO configurations in the shorter delay region, and it is almost the same in the longer delay region. In Figs.7 and 8, we also show correlations at transmitter and receiver sides for each MIMO configuration. From these results, we can see that the correlations are low in the longer delay region. On the other hand, in the shorter delay region, the correlations are very high. The high correlations are conjectured to be due to the direct waves. Then, we can refer the difference of the arrival time of direct waves to the difference of MIMO configurations.

3. Transmit and Receive Timing Control and the BER performance

We have shown that the arrival time of the direct waves differed for the MIMO configurations in the previous section. In this section, we evaluate the BER performance for each MIMO configuration at first. We show the parameters for evaluating BER performance in Tab.1. In Fig.9, we show the BER performance versus normalized TX power. Here, the normalized

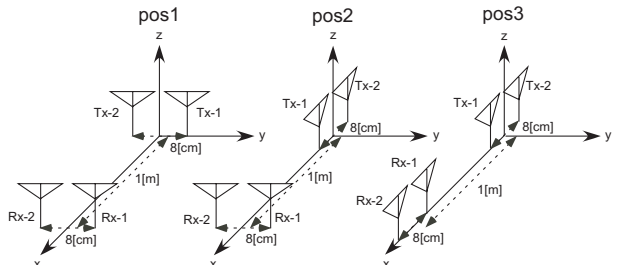


Fig. 2: MIMO configuration.

Table 1: Simulation Parameters

Symbol interval	0.667 nsec
Sampling interval	0.667 nsec
Modulation	BPSK
Transmit and receive antenna	(Tx,Rx)=(2,2)
Spatial filtering and equalization	MMSE-FDE
Channel state information	known
FFT window size	1024 sample
CP length	256 sample

TX power denotes total transmitted power normalized by the transmit power giving $E_b/N_0 = 0[\text{dB}]$ when the signal is transmitted from a single transmit antenna. This transmit power is calculated

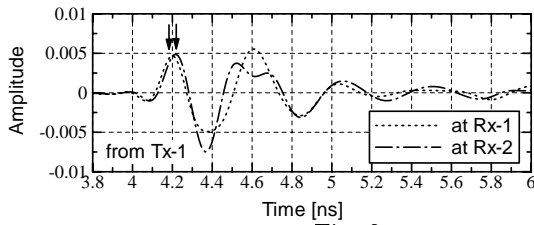


Fig. 3: Examples of received pulse shape ("pos1").

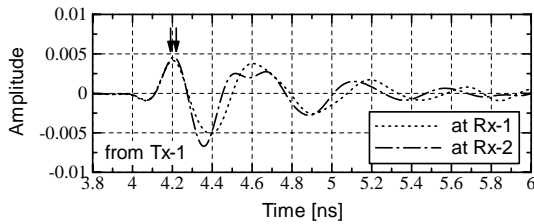
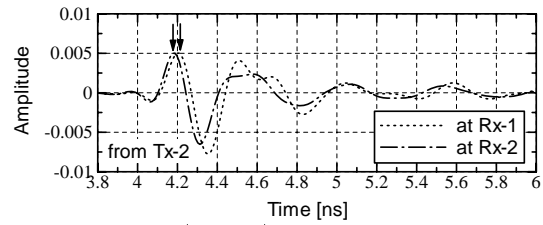


Fig. 4: Examples of received pulse shape ("pos2").

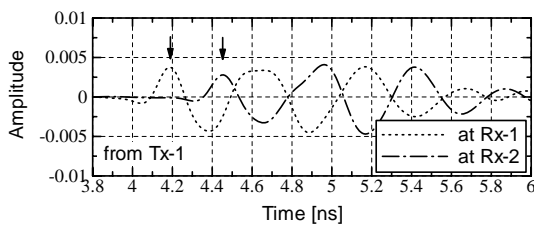
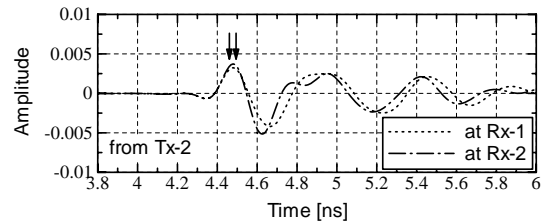


Fig. 5: Examples of received pulse shape ("pos3").

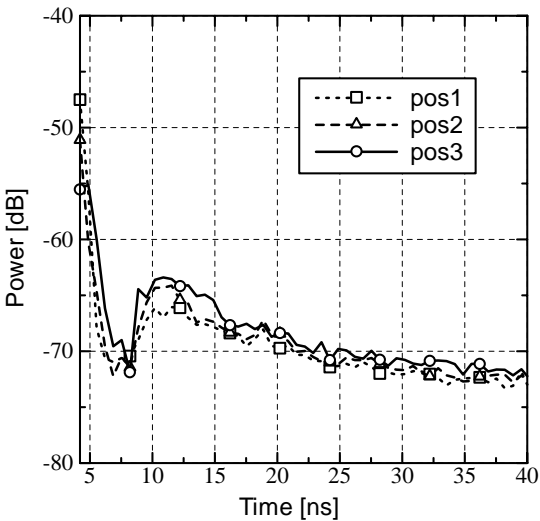
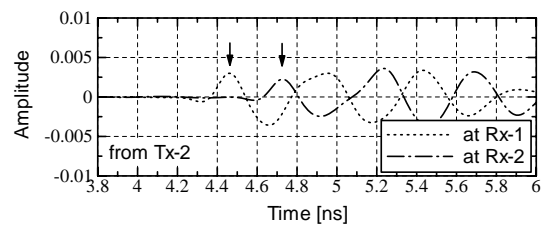


Fig. 6: Power decay.

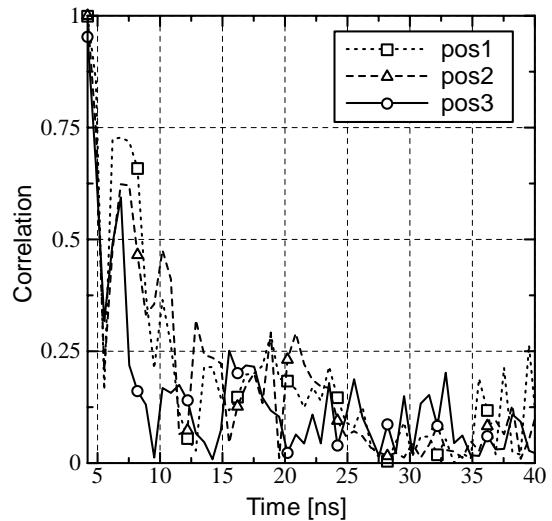


Fig. 7: Correlation between receive antennas.

using the theoretical equation of propagation loss($L[dB] = -20 \log_{10}(\frac{4\pi d}{\lambda})$, d : distance between transmit and receive antennas, λ : wave length) for 1[m]. Also, we assume that isotropic antennas at the transmitter and receiver are used in a free space. Using this scale, we have also considered directional characteristics of the antennas that we actually used. In this figure, the BER performance for "pos1" is the best. It is conjectured that the received power is higher than the other configurations. However, "pos1" is not actually the best receiving timing because of high correlation of the direct waves. In this case, because the amplitude of the direct waves in "pos2" and "pos3" is decreased by the antenna directivity, the BER performance in "pos1" is best. From this result, we can see that the BER performance differs for MIMO configurations. From the propagation result mentioned in the previous section, we can say that the BER performance depends on the arrival time of direct waves. Then, from this fact, we propose timing control scheme in order to improve the performance.

Now, we analyze the receiving condition at a receiver for MIMO configurations in detail. We show

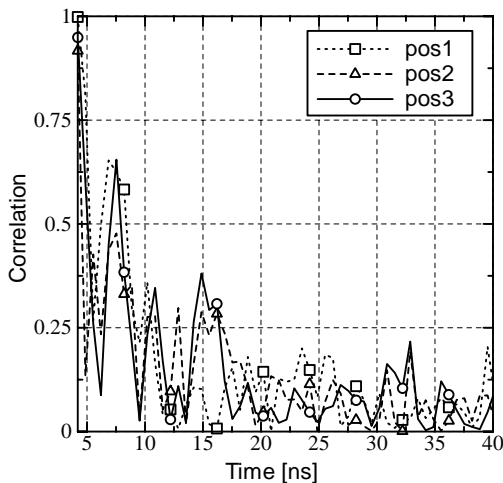


Fig. 8: Correlation between transmit antennas.

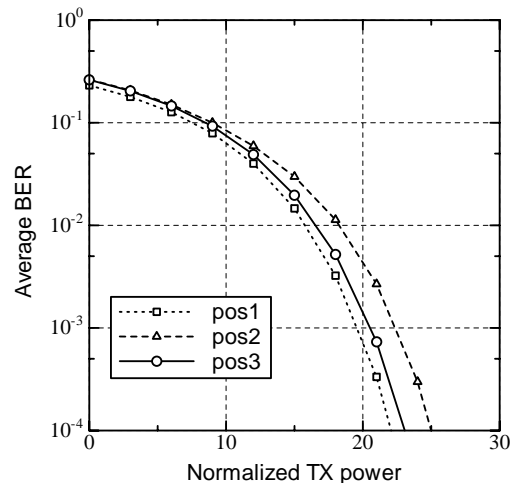


Fig. 9: The BER performance for 3 types of MIMO configuration.

the conditions of three cases in Fig.10. We receive both the transmitted direct waves at the first sampling time for “type1”. It is equal to the case of “pos1”. We receive only one transmitted wave at the first sampling time for “type2”. It is equal to the case of “pos2”. We receive one transmitted wave by a Rx antenna at the first sampling time, and another transmitted wave by the other Rx antenna at the second sampling time for “type3”. It is equal to the case of “pos3”. In each case, the timing of direct waves is different. This can be realized by not only adjusting the MIMO antenna configuration but also controlling the Tx and Rx timing. The Tx timing is controlled by adjusting the transmitting instant. The Rx timing is controlled by adjusting the sampling instant.

We show BER performance with timing control in Figs.11, 12 and 13. In Fig.11, we show the BER performance for “pos1”. In this case, “type1” is equal to not using timing control. From this figure, we can see that the timing control scheme of “type3” is the best for performance improvement. On the other hand, “type2” is the worst for the performance. In Fig.12, we show the BER performance for “pos2”. In this case, “type2” is equal to not using timing control. From this figure, we can also see that “type3” is the best scheme of timing control, and “type2” is the worst one for performance improvement. In Fig.13, we show the BER performance for “pos3”. In this case, “type3” is equal to not using timing control. From this figure, we can see that the BER performance for “type1” is almost the same as that for “type3”, and that the performance for “type2” is the worst. From these results, we can say that “type3” is the best timing control scheme. It is conjectured that the correlation is the lowest for “type3”, and that co-channel interference suppression is best in this case. For a case of “type1”, the received power is very high because we can obtain direct wave’s components. However, the correlation is also very high. It is conjectured that the high correlation degrades the spatial filtering performance.

4. Summary

We have shown the MIMO-UWB measurement, and proposed transmit and receive timing control for performance improvement. In the MIMO-UWB measurement, we have shown the effect of direct waves in LOS environments. In this case, the arrival time was different for MIMO configurations, and the arrival conditions with the longer delay region did not depend on the configuration. Then, we have evaluated the BER performance, and shown that the performance differs by the configuration. From these results, we have noticed that the BER performance depends on the configuration. Also, we have proposed the transmit and receive timing control. We have shown that we can obtain better BER performance using the scheme of “type3” mentioned in this paper.

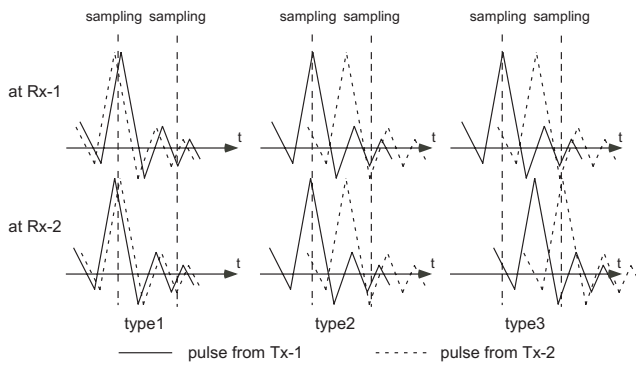


Fig. 10: Reception of direct waves.

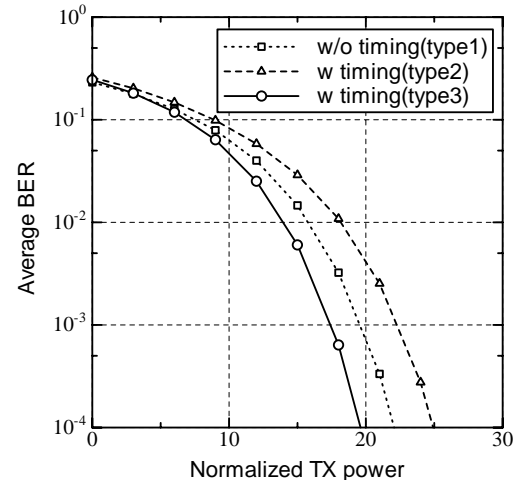


Fig. 11: The BER performance for “pos1” with timing control.

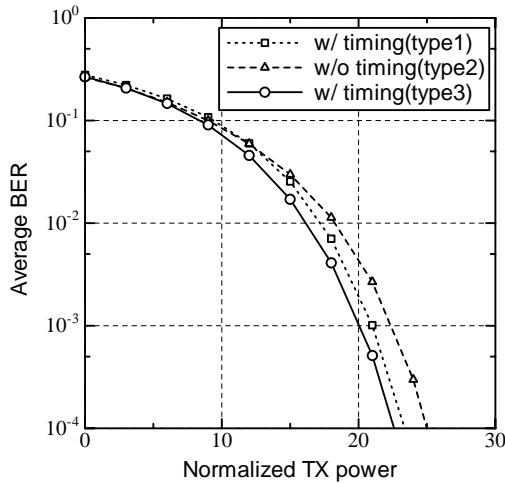
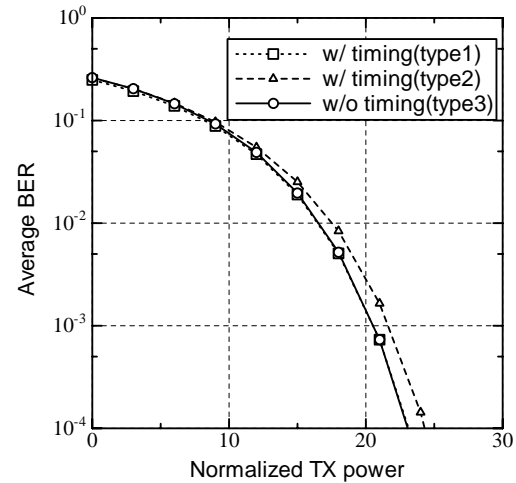


Fig. 12: The BER performance for “pos2” with timing control. Fig. 13: The BER performance for “pos3” with timing control.



REFERENCES

1. M. Z. Win and R. A. Scholtz, “Ultra-Wide Bandwidth Time-Hopping Spread-Spectrum Impulse Radio for Wireless Multi-Access Communications”, IEEE Trans. Commun., vol.48, no.4, pp.679-691, April 2000.
2. S. Roy, J. R. Foerster, V. S. Somayazulu, and D. G. Leeper, “Ultrawideband Radio Design: The Promise of High-Speed, Short-Range Wireless Connectivity”, Proc. IEEE, vol.92, no.2, pp.295-311, Feb. 2004.
3. G. J. Foschini and M. J. Gans, “On Limits of Wirelss Communications in a Fading Environment When Using Multiple Antennas”, Wireless Personal Communications, vol.6, no.3, pp.311-335, 1998.
4. L. Zhiwei, B. Premkumar, and A. S. Madhukumar, “MMSE Detection for High Data Rate UWB MIMO Systems”, in Proceedings IEEE Vehicular Technology Conference. IEEE VTC Sept. 2004.
5. W. Siriwongpairat, M. Olfat, and K. J. Ray Liu, “On the Performance Evaluation of TH and DS UWB MIMO Systems”, WCNC2004-Fall, vol.3, pp.1800-1805, March 2004.
6. D. Falconer, S. L. Ariyavitsakul, A. B. Seeyar and B. Eidson, “Frequency Domain Equalization for Single-Carrier Broadband Wireless Systems”, IEEE Commun. Mag., vol.40, pp.58-66, April 2002.
7. A. A. M. Saleh and R. A. Valenzuela, “A Statistical Model for Indoor Multipath Propagation”, IEEE J. Sel. Areas. Commun., vol.5, no.2, pp.128-137, Feb 1987.
8. J. Foerster, “P802.15-02/490r1-SG3a-Channel-Modeling-Subcommittee-Report-Final.doc”, <http://grouper.ieee.org/groups/802/15/pub/>.
9. M. Ameya, M. Yamamoto, T. Nojima, and K. Ito, “Broadband Printed Dipole Antenna Employing Self-Complementary Radiating Element and Microstrip Line Feed”, IEICE Trans. Commun. (Japanese Edition), vol.J88-B, no.9, pp.1662-1673, Sep. 2005.

A Generic Multi-Agent System for Analyzing Spatial–Temporal Geographic Information

I. R. FARAH, K. SAHEB ETTABA, I. HAMDI, and M. B. AHMED

Laboratoire de Recherche en Informatique Arabisée et Documentique Intégrée, ENSI, Tunisia

Abstract—In a lot of theoretical and practical applications of different geographical disciplines, the use of Geographical Information Systems (GIS) is by now a more or less common issue. Visualization, presentation, administration and analysis of geographical relevant data are the main feature of scientific research and teaching. Furthermore, in commercial contexts like advertisement, marketing, navigation, administration, project management and planning becomes crucial. The retrieval and location of geographic information will require a significant amount of time and effort. In addition, different users usually have different views and interests in the same information. In order to resolve such problems, this paper proposes a generic geographic information model system based on multi-Agent (MA) architecture. By paralyzing tasks and offering more efficiency and flexibility, this approach seems to be fruitful in order to construct flexible and extensible system improving more capability and efficiency of GIS services. We further illustrate the design and implementation of the multi-agent system that uses image analysis agents for generating and processing parallel programs by calling the available method. Firstly, we validated our approach on satellite images of SPOT4 representing the north Tunisian region for different dates in order to detect changes for a possible prediction and a better decision making. Secondly, we represent how to model and represent geographic data.

1. Introduction

Over the past, GISs have been widely adopted in support of planning, agriculture, forestry, infrastructure maintenance and many other fields. Geographical Information (GI) includes maps, images, data sets, analysis operations and reports. Nowadays, this tool contains a huge source of geographical information and offers already many different services. The advantages of using such technology are obvious to most users of geodata and geoprocessing resources. However, effective use of information is becoming increasingly difficult because of their sheer size and diversity, thus intelligent GIS needs to be developed. In contrast to this, the use of tools provided by Artificial Intelligence is marginal in spatial analysis.

Application of intelligent agents in the GIS environment is actively being explored. Thus, some projects have been reported in which different types of agents are being employed to improve usability of GIS software as well as users access to geospatial data and services. Geospatial information retrieval and filter, intelligent geospatial search, knowledge discovery, decision model and assessment are typical applications based on using agents in GIS.

2. Agent technology

Geographic Information that includes digital, literal, graphic and image information which directly or indirectly relates to various quantity, quality, distribution features, spatial relation and rule in the geographical field[3]. GI has three basic functions of describing, recording the spatial location and reflecting the transformation process of the phenomenon, and is basically the relating of all kinds of information in the real world and forming a synthesis information entity that is continually distributed in time and space.

The concept of Agent originated from Distributed Artificial Intelligent (DAI) [7], and is a basic term of DAI. In the context of spatial reasoning, the term agent is mostly used to describe a system that performs a specific task as route advice. The Agent is a computer system which locates in dynamic and complex environment, can astronomically sense the environment and act accordingly to complete its tasks or goals. Agent is a computing entity with four features of autonomy, reactivity, interaction and initiative. In the research on Agent, different researchers endowed Agent with different construction, context and capability in their own system so that they can conveniently work deep in a specific field [1]. In the context of spatial reasoning, the term agent is mostly used to perform specific task as route advice [6].

Multi-agent systems can be identified by several rationales for distributing an AI system, such as adaptability, cost-effectiveness, and improvements in the development and management process [2]. Further more, they argue

that the distribution facilitates specialization, and may increase the reliability, robustness, and/or efficiency of the entire system [8].

Accounted for these features of Agent, it is natural to introduce Agent into the GIS system where it can be applied to such aspects as gathering of geographic information, downloading and transformation of geographic data, cooperation of geographic information service, system integration and individuation style design[5]. Agent offers a new method for computation and problem solution, which has many advantages such us autonomy, reactivity, interaction, intelligence, distributing and reusability.

3. The proposed Architecture

The proposed architecture handled by the Geographic information system and based on Multi-Agent System as shown in figure1, contains a set of software agents like the interface agent, the information gathering agent, the GIS agent. These agents may run on one computer, and may be distributed on different computers in the network. To complete the GIS task, Agent needs to communicate and cooperate with other participants (such as users, other Agents or data sources).

3.1. Interface Agent

The interface Agent is designed to achieve the interaction between system and users. This interface include the describing user's searching request in some kind of fixed format, the vague-searching through communication with KDB (Knowledge Base) and the communicating with information gathering Agent and GIS Agent, submitting the searching request and returning the resulting data to user.

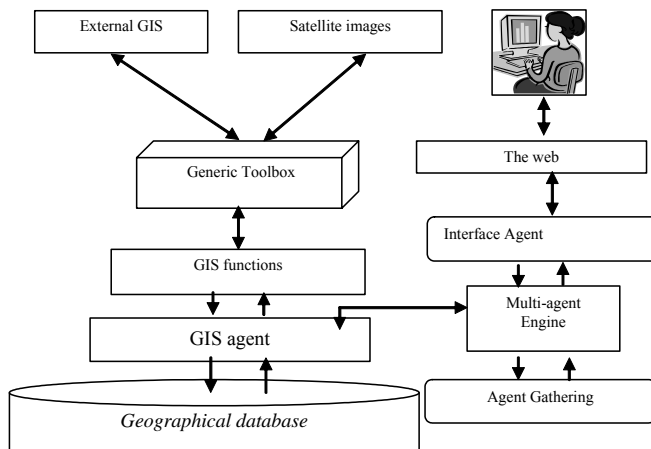


Figure1. Multi-Agent System Architecture

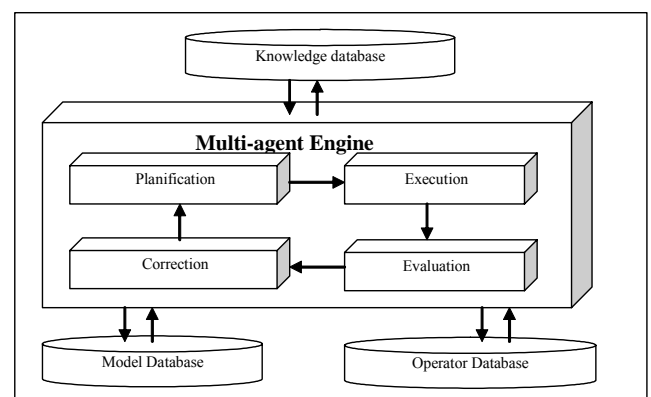


Figure2. Multi-Agent Engine

3.2 Multi-Agent Engine

The Multi-agent Engine as shown in figure2 manages the whole system, processing the complex communication between the inside and outside of the system, coordinating all the Agents in the system, and distributes controls in the system. It is unique in the system [9].

The Multi agent Engine performs the different reasoning phases. An initial planning phase determines the best strategy to reach the goal of the end user which is provided by a request. An execution phase launches the agents. During this execution, the Engine determines goals and initializes some parameters. An evaluation phase assesses the quality and the contents of the resulting data at the end of each agent execution. If results are correct, planning can continue. If not, the result judged incorrect, a repair phase decides what is the following action to undertake depending on the evaluation judgments. The Multi agent Engine carries out reasoning, it operates in a loop. The reasoning loop switches between execution and deliberation. At each time-step the agent both considers the actions to undertake next and also executes any plans that have been previously added to the intention stack. Reasoning happens in four main steps : Starting with the goal library, at any time there will be a series of pending, unachieved goals and a set of beliefs that describe the agent's state or world view.

3.3 Gathering Agent

Information gathering Agent is the Agent that searches and filters the geographic information, acting as an important part of the system. Information gathering Agent receives the client request from the interface Agent, and then searches. After getting the searching result, information gathering Agent is going to filtrate the information according to the user's interests and strategies stored in KDB. In addition, it is going to modify the personal interests of users and individualize them for later searching to be referenced. Other work, such as the downloading of geographic information, is in the charge of GIS Agent.

3.4 GIS Agent

The GIS Agent is the Agent with some specific function in the system, such as displaying Agent, analyzing Agent and downloading Agent. The creating process of GIS Agent is:

- The Interface Agent transfers the user's request to Multi-Agent engine.
- Multi-Agent engine searches the Agent that needs to be created according to the description of the request.
- Multi-Agent engine creates the instance of GIS Agent.

3.5 Knowledge Base

The knowledge database stores the embedded knowledge in the system and the rules defined by an expert. The different types of knowledge, such as data, programs and criteria are described in the knowledge base, structured by different concepts. The engine uses the information in order to build a solution to give a goal. The knowledge is described by:

- Goals: represent an image processing functionality (Figure3).
- Operators: describe actions that can be performed. They contain the information to satisfy goals.
- Arguments: list an input and output data.
- Requests: is a goal to be reached.
- Data description: information about an image like the size.
- Context: General information concerning the application.

3.6 The Generic Toolbox

This generic toolbox gathers the common functionalities to all real toolbox which makes it possible to include all data formats as shown in figure4 [4]. The architecture of the generic toolbox for our proposed platform contains the following modules [4]:

- Format Conversion: This module can translate all heterogenous data format to a unified format like XML (eXtensible Markup Language).
- Model : This module allows modeling a geographic data to be represented in the XML format. The UML language (Unified Modeling Language) is used also for the spatial and temporal modeling.

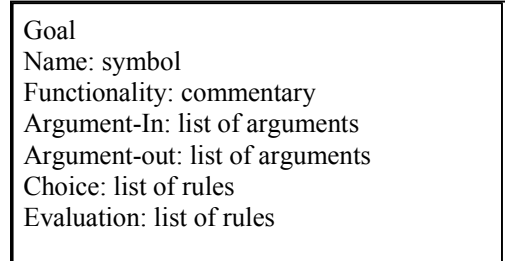


Figure3. Goal compound

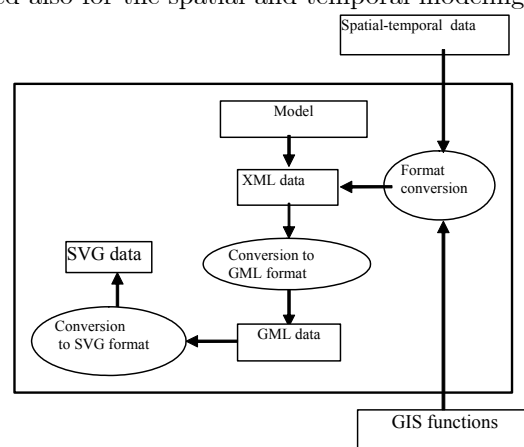


Figure4. Generic toolbox architecture

- Conversion to GML format : Among the tasks of this module is the translation of the XML file in GML file. The resulted file can be visualised using GIS interface or the SVG (Scalable Vector Graphics) representation.
- Conversion to SVG : The conversion from GML data to SVG data will be carried out by language XSLT (Extended SteelSheets Language Transformation). The GML file can be requested with the Gquery language (GML query)[4].

3.7. The Geographical database

The database of the proposed system contains a set of spatial-temporal data. Spatial-temporal object can be defined like spatial object whose form and/or position vary with the time.

4. Implementation and validation

The validation of our approach concerns the processing and extracting the separate class of different types of land use. The study area is situated in northern Tunisia (North Africa). The satellite images were used in this study:

- Two images (XS1) of SPOT3 captured on 1987 and 1999, having a space resolution of 20m.
- An image (XS1) of SPOT4 captured on 2001, having a space resolution of 10m.



Figure5. Zone of interest 1987

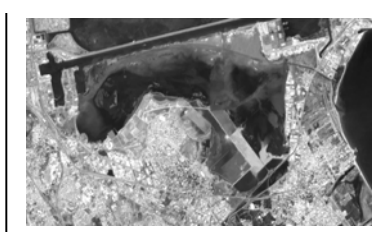


Figure6. Zone of interest 1999

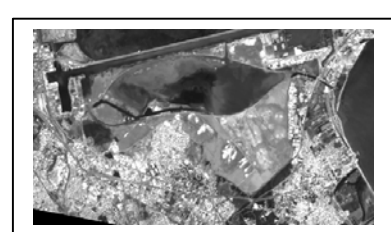


Figure7. Zone of interest 2001

In order to use these extracted images, we are carrying out the pre-processing of SPOT images with different filters. The basic system implemented by a multi-agent system, each agent was associated to an operator located in the operator base and provided by the engine. As an input, the satellite images (as shown in figure5, 6 and 7) used in our application are provided from the XS1 sensor. The first agent was an Agent classifier using unsupervised operators for classification provided by the operator base and evaluated by an Multi-agent Engine which combine facts and rules provided from knowledge base [10]. The output classified images (as shown in figure8, 9 and 10) were given as an input to the Agent change Detection in order to detect the change occurred since 1987 in our zone of interest as shown in figure11.

5. Conclusion

There still remains considerable work in developing the framework described here. Agent communication, agent roles, agent cooperation and competition for resources, spatial dependencies all need further work. Model validation, transparency and the how the results will be used by decision makers are other issues requiring further exploration. These issues are the subjects of current research.

Agent technology gives us a brand new method to solve the problem. After analyzing geographic information and Agent, this paper proposed a model of geographic information gathering based on multi-Agent (MA) architecture and discussed the system construction. The prototype system with this architecture has the following features and advantages:

- System construction is flexible and extensible. Agent with different functions can be customized.
- Users can retrieve geographic information.
- Agent provides different searching strategies according to user's interests, and keeps the personal characteristics of the user.
- Improving the capability and efficiency of GIS service. Because of the limitation of system design and implementing method, the prototype system still needs to be improved. What is more, it needs further research for MA (Multi-Agent) system to be applied in practice. In addition, MA system lack of a standard of system architecture and organization, and efficient methods to construct and to evaluate MA system.

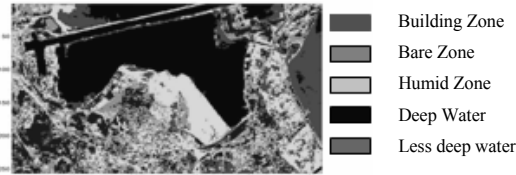


Figure 8. Zone of interest 1987 (XS1) classified

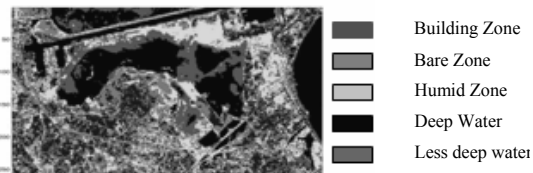


Figure 9. Zone of interest 1999 (XS1) classified

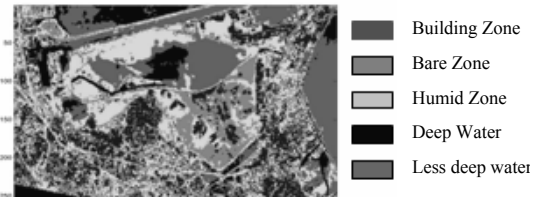


Figure 10. Zone of interest 2001 (XS1) classified

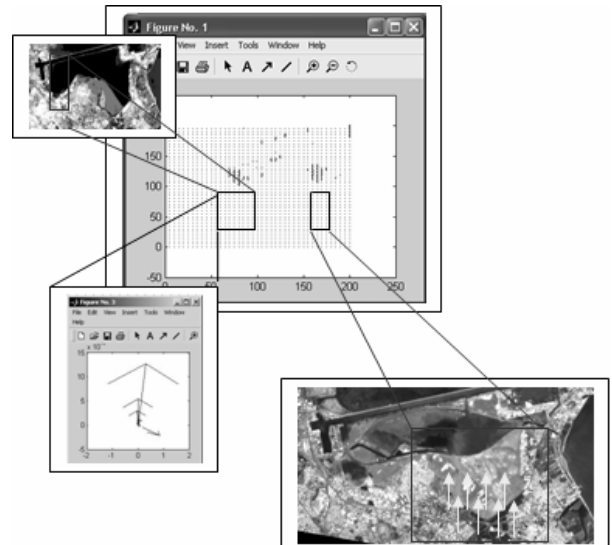


Figure 11. Change detection using the optical flow operator

REFERENCES

1. BUSETTA, P., RONNQUIST, R., HODGSON., A., LUCAS A., 1998, JACK Intelligent Agents - Components for Intelligent Agents in Java. Technical report, Agent Oriented Software Pty. Ltd, Melbourne, Australia, 1998.
2. DEAN, J., GUNNERMAN, G., EPSTEIN, J., AXTELL L., SWEDLUND A. C., PARKET M. T. and MCCARROLLV S., 2000 Understanding Anasazi Culture Change Through Agent-Based Modelling, Pages 179-206 in T. A. Kohler and G. J. Gumerman, eds. Dynamics in Human and Primate Societies. Oxford University Press.
3. GANG-yi, G., 2003, A multi-Agent system architecture for geographic, Journal of Zhejiang University SCIENCE 2003 - ISSN 1009-3095.
4. HAMDI, I., FARAH, I. R. and AHMED, M. B., 2004, System design for management of the temporal data and the spatial data based on a generic toolbox. IEEE, The first International conference on information and communication technologies: From theory to application, ICTTA04, Syria, 2004.
5. LUCAS A. and GOSS, S., 1999, The Potential for Agents in Defence Simulation Information, Decision and Control. pp579-583. October 1999.
6. MAAB, W., 1995, Visual grounding of route description in dynamic environments. In AAAI Fall Symposium of computational models of integrating language and vision. Mit Cambridge, 1995 MA:AAAI
7. MOSS, S., and DAVIDSON, P., 2000, Multi-Agent Systems and Agent-Based Simulation, Lecture Notes in Artificial Intelligence, 2000.
8. PRAK, S. and WU, C., 2001, Intelligent Search Agent for Software Components. IEEE Computer, p.154-161. OpenGIS Consortium, 2001.
9. SAHEB, E. K., FARAH, I. R. and AHMED, M. B., 2004, Multi-Agent system for detecting and analysing changes on satellite image sequence. IEEE, International Conference on Industrial Technology, Hammamet, December 2004. ISBN:0-7803-8663-9, IEEE Catalogue Number:04TH8771C.
10. SAHEB, E. K., FARAH, I. R. and AHMED, M. B., 2005. Analyse Intelligente d'une Séquence d'Images Satellitaires pour le Suivi des Masses Nuageuses. IEEE, SETIT, Sousse, Tunisie, Mars 2005. ISBN:0-7803-8663-9, IEEE Catalogue Number:04TH8771C.

Potential Estimation of Heat Flux through Sea Ice and Cover Snow by Remote Sensing

Y. Sasaki, S. Iwasaki

National Defense Academy, Japan

S. Kakuta

Japan Marine-Earth Science and Technology Organization, Japan

V. K. Pavlov

Norwegian Polar Institute, Norway

T. J. Weingartner

University of Alaska, U.S.A

Abstract-Authors discuss the potential estimation of the heat flux through sea ice and cover snow by remote sensing. Among several parameters involved in this process, *a-priro*i data or seasonal data may be useful for some parameters which show a limited range of variability, however, the surface temperature and thickness of the cover snow have much higher variabilities. Also, the ice concentration must be monitored for accurate estimation of these two parameters. Authors discuss the estimation of these parameters by microwave, visible and infrared remote sensing technologies.

1. Introduction

More than 10% of the earth surface is covered with ice/snow through the year. The Arctic Ocean is covered with ice accompanied by cover snow, however, the ice coverage is highly variable. Today it is evident that the development of some arctic events like AO (Arctic Oscillation) is closely correlated with the heat exchange processes between the Arctic Ocean and atmosphere. The sea ice is a thermal insulator against the heat transfer from the Arctic Ocean to atmosphere with cover snow, but a large amount of heat flux still flows through ice and snow layers. The cover snow has only one tenth of thermal conductivity compared with that of sea ice, but its thickness is very variable. We discuss how to estimate the heat flux using *a-priori* data and remote sensing.

2. Parametric Analyses of Heat Flux in Sea Ice and Cover Snow.

Several parameters are involved in the heat transfer processes in the sea ice and cover snow layers. The typical parameters are the thickness, thermal conductivity and surface and bottom temperatures of ice and snow layers. The parameters except the thickness and surface temperature of snow are less variable and *a-priori* data (e.g., seasonal data) will be helpful, but other two parameters must always be monitored with ice concentration because of their high variabilities.

2.1 *A-priori* data

Figure 1 shows the sites where a series of observations were made [1]. Figures 2 through 11 show the results [1]. Figures 2 through 4 show that the thermal conditions in ice and snow layers well correspond to the change in atmospheric temperature [1]. Figure 5 is the results from Ono's report and Sasaki's observations and shows that the heat flux through ice layer is inversely proportional to ice thickness [1]. Figure 6 shows the dependence of thermal conductivity of sea ice on ice density and depth from ice surface [1]. Figure 7 is the temperature gradient model in shallower cover snow and shows that the boundary temperature between ice and snow can be

estimated with this model [1]. The ice thickness has a seasonal and spatial mean for many years. After all, these *a-priori* idea and data will enable us to estimate the six parameters, i.e., thickness (ice), thermal conductivity (ice and snow), and surface (ice) and bottom temperatures (ice and snow) within an error of 10%.

2.2 Parameters with higher variabilities

Unlike six parameters mentioned above, the surface temperature and thickness of cover snow are most important in the flux estimation, however, neither *a-priori data* nor seasonal data is useful. These two parameters must be sensed remotely as discussed in the following section.



Figure 1 Observation sites

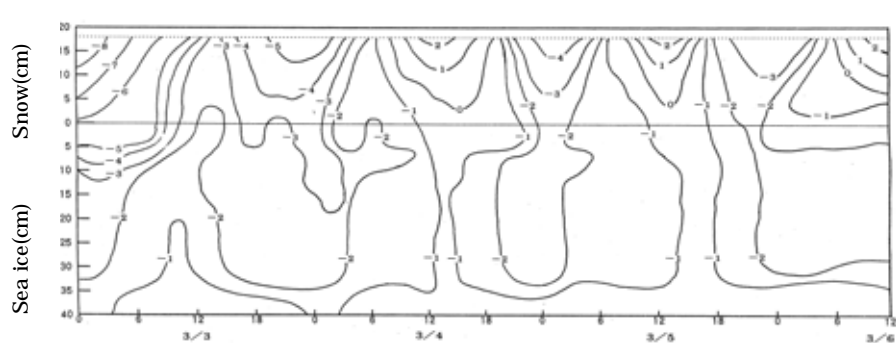


Figure 2 Temperature variability in ice and snow layers in the Sea of Okhotsk (, 1987) [1].

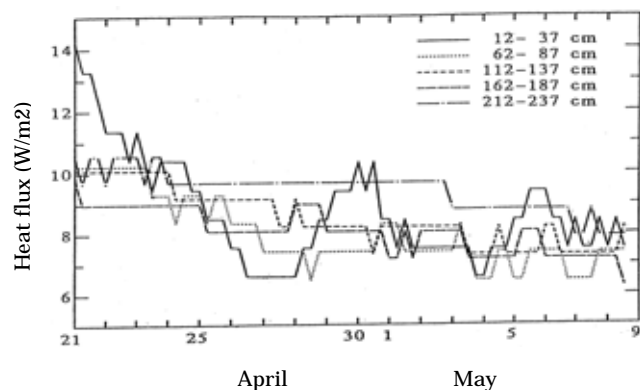
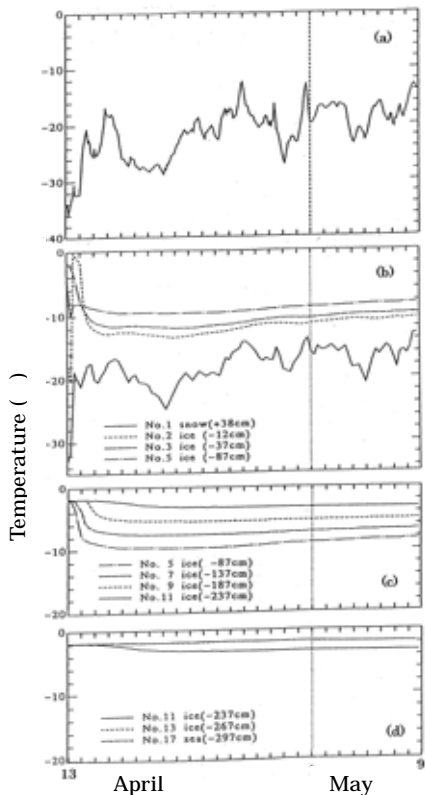


Figure 4 Heat flux at five levels in sea ice in the Arctic Ocean(1992)[1].

Figure 3 Observed temperature variability in ice and snow layers in the Arctic Ocean (1992) [1].

3. Remote sensing of surface temperature and thickness of cover snow

Figure 8 compares the surface radiation of cover snow in infrared region derived from observed

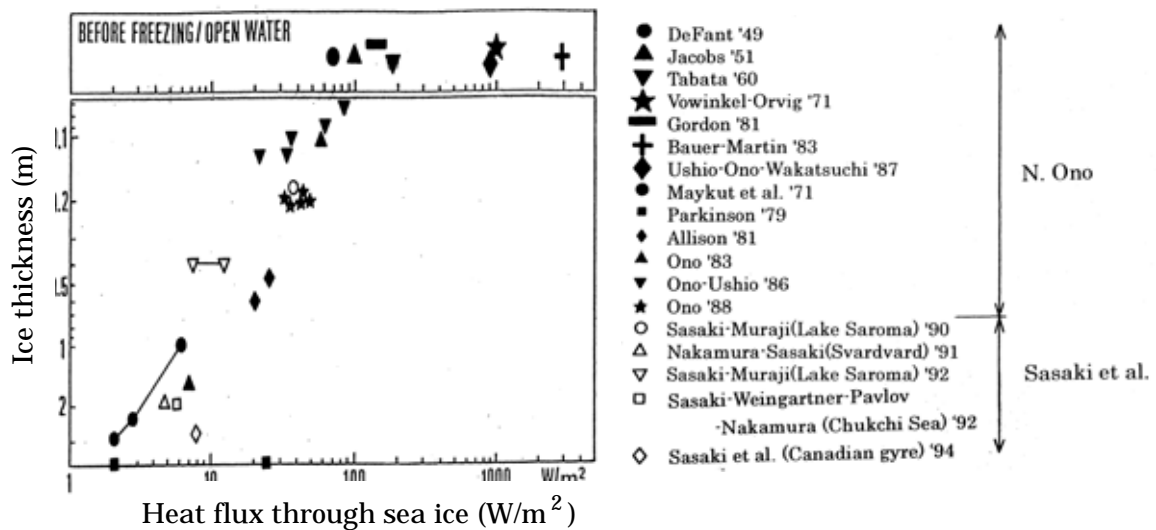


Figure 5 Ice thickness dependence of heat flux through sea ice [1].

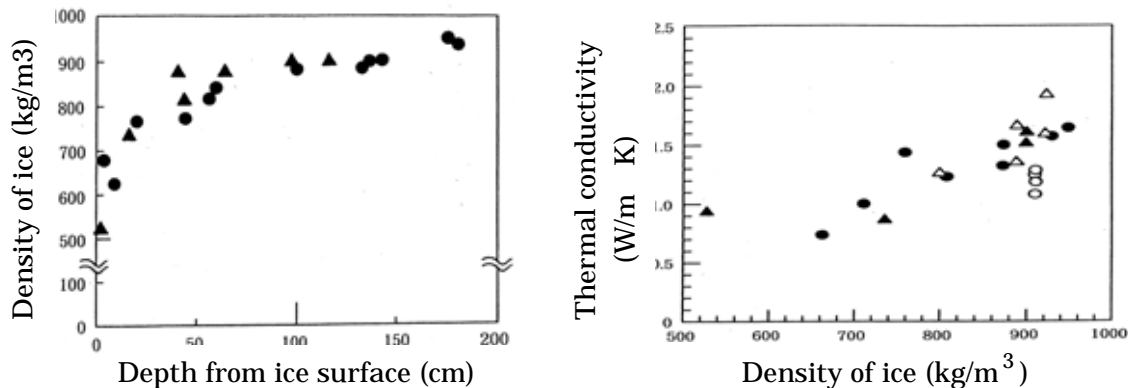


Figure 6 relationships among thermal conductivity, ice density and depth in ice layer.

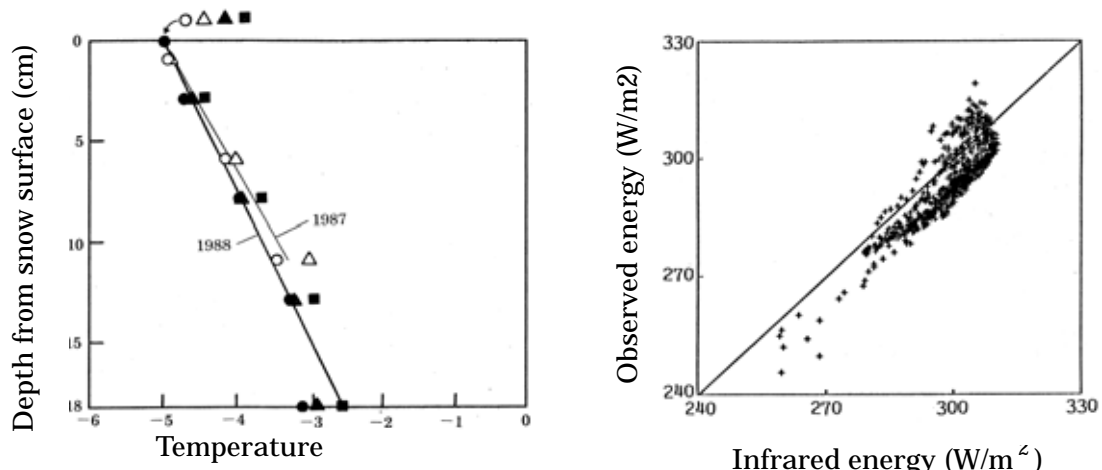


Figure 7 Observed temperature gradient in snow layer.

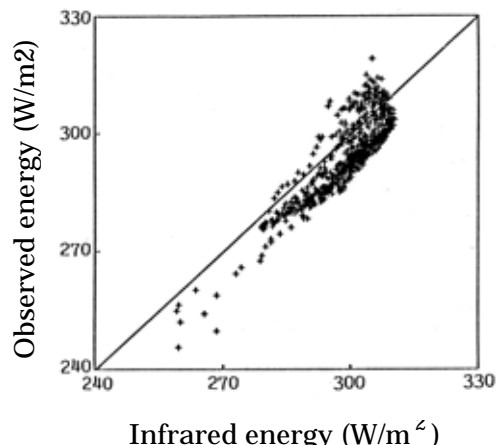


Figure 8 Comparison of surface radiation of snow, estimated from observed and infrared temperatures

and infrared temperatures [1]. At higher intensities, in other words, at higher temperatures, both measurements agree within an error range of ± 2 K in temperature, however, the infrared estimation is 3 K lower than observation at lower temperatures. The infrared technique can be employed to measure the surface temperature of cover snow, but we must take this consideration.

Snow is usually one tenth of sea ice in thermal conductivity, in other words, snow is a ten times larger thermal insulator. The 30 cm thick snow layer is equivalent to the 3 m thick sea ice in terms of heat flux. Figure 9 shows the occurrence of cover snow depth in the marginal seas of the Arctic Ocean, observed by Sasaki et al. in summer season. Sasaki et al. [1] reported from this observation that the heat flux in sea ice with this snow depth occurrence was estimated 16 % larger than that with cover snow with 20 cm uniform thickness. Considering this effect of variability in thickness of cover snow, the thickness is one of the most important parameters affecting the heat flux. Microwave radiometry has been said useful for snow observation.

Figure 10 shows the dependence of surface-brightness temperature of snow on sea ice on incidence angle, polarization and snow depth. Left and right figures correspond to 6.7 and 18.6 GHz, respectively. In each figure, a pair of curves (open and solid circles ; i.e., H- and V-polarizations) at the lowest brightness temperatures correspond to snow-free ice surface. Other upper pairs of curves correspond to the thicker cover snow. The largest thickness is 44 cm [2-3]. Fig.10 depicts that the microwave emission from background sea ice and cover snow shows neither marked incidence angle dependence nor polarizability at smaller incidence angles. After all it would be very reasonable to introduce an assumption that the microwave radiation in the snow layer is fully diffused and isotropic at any level (including the snow surface). If this is the case we

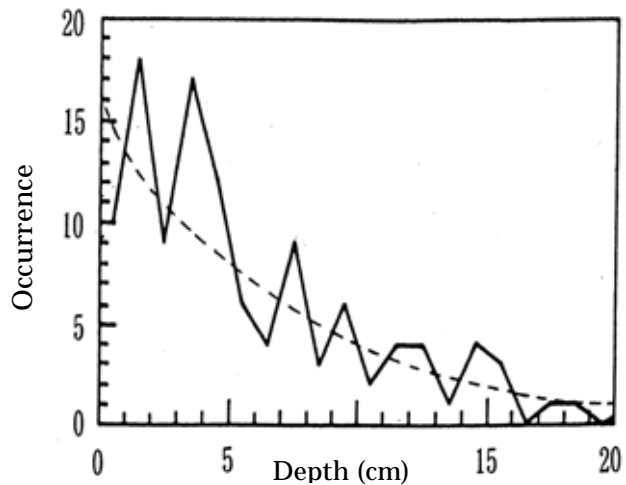


Figure 9 Occurrence of cover snow depth in the Arctic Ocean

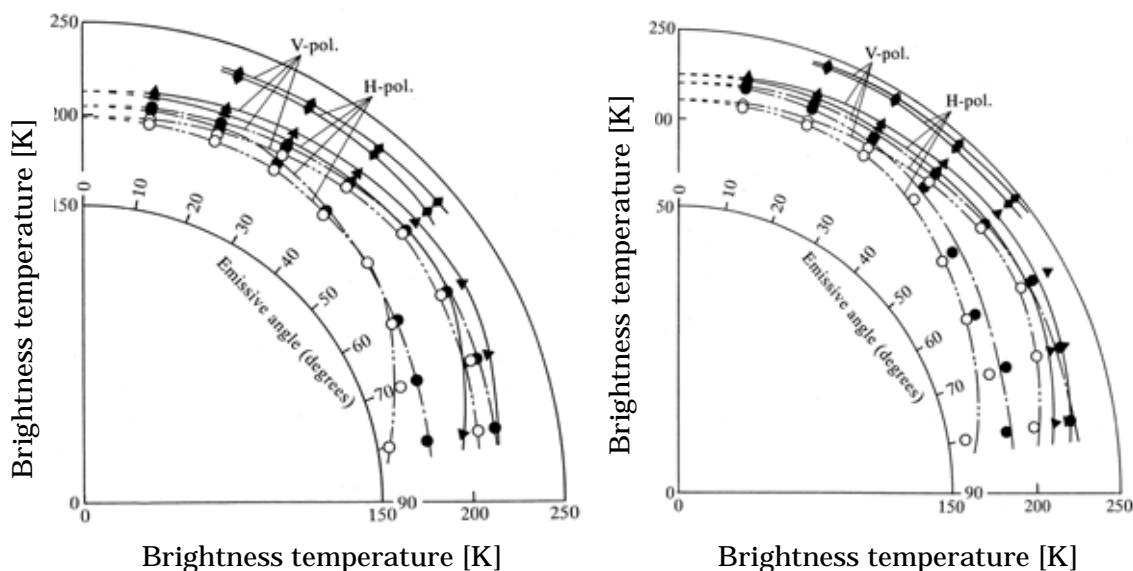


Figure 10 Dependence of surface brightness temperature of snow on incidence angle and snow thickness (left:6.7GHz, right:18.6GHz)

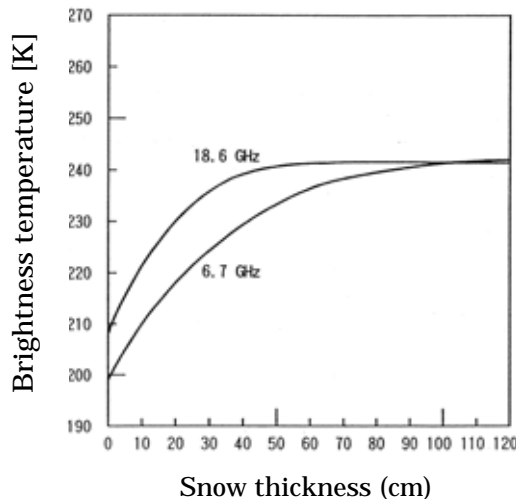


Figure 11 Thickness dependence of surface brightness temperature of snow on sea ice

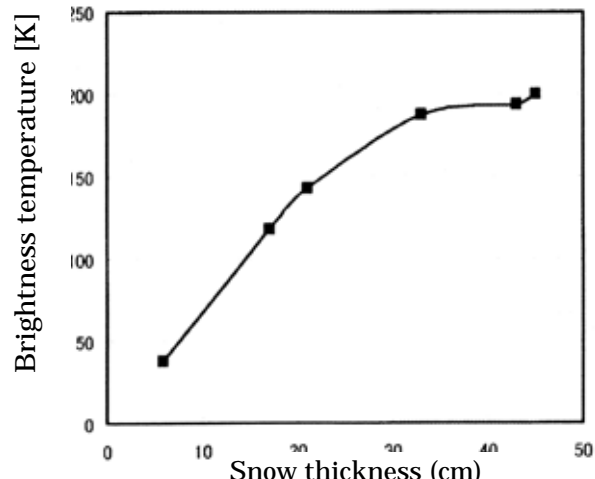


Figure 12 Thickness dependence of surface brightness temperature of land snow in Alaska (Effect of snow only.)

can apply the “Two-Flow” theory to correlate the surface brightness temperature with snow thickness [2-3]. Figure 11 compares the thickness dependence of surface brightness temperature of cover snow on sea ice at normal incidence between 6.7 and 18.6GHz, applying the “Two-Flow” theory to the data in Fig.10 [2-3]. It is noticeable from Figure 11 that the longer wave (6.7GHz) is less sensitive to increase in snow thickness than the shorter wave (18.6GHz), therefore, the longer wave would be more useful for thicker cover snow and vice versa. Figure 12 shows the thickness dependence of surface brightness temperature of land snow in mid-Alaska (19GHz of SSM/I) for reference. Figures 11 and 12 show quite similar pattern [3].

In microwave radiometric estimation of cover snow thickness, ice concentration is very significant, because the microwave radiometry is very poor in ground resolution. Fortunately, visible and infrared techniques can provide higher ground resolution, i.e., higher accuracy in ice concentration.

4 . Conclusion

Microwave and infrared radiometries are the key technology to observe the surface temperature and thickness of cover snow on sea ice that have the highest temporal and spatial variabilities among several glaciological parameters involved in the heat transfer processes in sea ice and cover snow on sea ice. We can use *a-priori* data or seasonal data for other glaciological parameters. When we can estimate the surface temperature and thickness of cover snow within an error of $\pm 10\%$, the error in estimation of the heat flux in sea ice would be at most 20%.

REFERENCES

1. Sasaki, Y., Muraji, Y., Nakata, K., Weingartner, T. J., and Pavlov, V., “Relationships between Glaciological Parameters of Snow Cover and Sea-ice,” *J. Adv. Marine Sci. Tech. Soc. Japan*, Vol.8, No.2, 77-88, 2003 (in Japanese).
2. Sasaki, Y., Iwasaki, S., Nakamura, T., Kakuta, S., and Nakata, K., “Analysis of the Microwave Radiative Transfer Process in a Snow Layer on Sea Ice Using the “Two-Flow” Theory,” *ibid.*, Vol.10, No.2, 1-18, 2004.
3. Sasaki, Y., Iwasaki, S., Nakajima, K., Hayakawa, M., and Koyama, N., “Multiple Scattering Effect of Microwave in a Land Snow Layer in Satellite Brightness Temperature,” *Proc. 27th Symp. Remote Sens. Environ. Sci.*, Aug. 27-29, 2005, Hayama. Kanagawa, Japan, 31-36.

Directional characteristics of wind-wave development under high-resolution wind fields

Teruhisa Shimada and Hiroshi Kawamura

Center for Atmospheric and Oceanic Studies,

Graduate School of Science, Tohoku University, Sendai, Japan

shimada@ocean.caos.tohoku.ac.jp

Abstract—We investigate fetch-limited wind-wave development under alternating coastal wind jets and wakes induced by orographic effects. Synthetic Aperture Radar and scatterometer resolve wind jets and wakes with widths of 10–40 km. Using the wind field and a third-generation wave model, we simulate the nearshore wave field. As a result, broader directional wave spectra are seen in wakes while we can find evolution of the directional wave spectrum with offshore distance in both wind jets and wakes. Especially within the offshore distance of 40 km, directional wave spectra have two peaks. These characteristics are well reflected in the overall directional spreading field. The overall directional spreading closely corresponds to the wind speed distribution, and is small/large in wind jet/wake region. The results mean that wave energies that come from neighboring wind jet regions cross in wake regions and combine with wave energy generated by local wind in wake regions.

I. INTRODUCTION

A large number of studies have investigated one-dimensional fetch-limited wave growth [e.g., Hasselmann et al., 1973]. The conditions have a beneficial effect on the intrinsic examination of wind-wave development. However, winds and waves are sampled along the defined fetches on the assumption that the wind is uniform in a direction transverse to the fetches all over the study area. Therefore, discussions have been restricted only to downwind characteristics of wind-wave development.

Recently, Shimada and Kawamura [2004] have presented alternating surface wind jets and wakes and demonstrated that in a direction transverse to the wind jets and wakes, significant wave heights (SWHs) vary along with the wind speeds. It is quite new to discuss fetch-limited wind-wave development under the two-dimensional wind configuration of alternating wind jets and wakes. We here raise questions about any modification of the wind-wave development by such a wind configuration. Standing on the case study of Shimada and Kawamura [2004], we investigate fetch-limited wind-wave development under alternating wind jets and wakes in term of directional characteristics of wind waves by using a state-of-the-art wave model. In this study, wind jets and wakes are defined by relative wind speed differences.

II. DATA AND WAVE MODEL

We carry out a pilot simulation of wind-wave development in a domain (241×151 pixels) with grid size of 0.01° (Figure 1). We here focus on how a wind configuration is reflected in a wave field and discuss time-independent characteristics of wave directionality. In fact, near-equilibrium wave conditions can be expected around the wind observation times [Shimada and Kawamura, 2004].

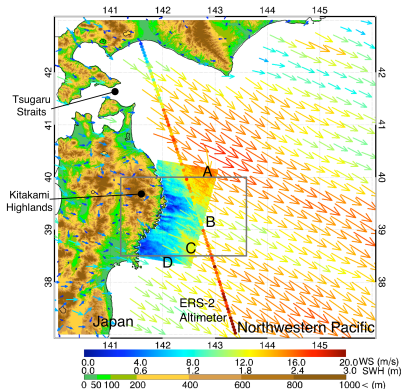


Figure 1 Ocean surface winds measured by QuikSCAT and ERS-2 SAR. Vectors over the land are from AMeDAS. Winds are measured by QuikSCAT, ERS-2 SAR, and AMeDAS at 0906, 0115, and 0100 UT on 25 February 2000, respectively. SWHs measured by ERS-2 altimeter (1252 UT on 25 February 2000) are also plotted. The square indicates a model domain. Color scales indicate the magnitude of wind speed (WS), SWH and elevation. Geographical names are also shown. Alphabetical symbols (A-D) indicate the wind jets and wakes discussed in the text.

We construct a wind field with grid size of 0.01° from the European Remote sensing Satellite (ERS)-2 SAR-derived winds. The offshore side of the model domain is covered with QuikSCAT winds at 0.25° resolution by averaging their wind measurements. Despite the simple merging way, wind jets and wakes are well reproduced continuously from nearshore to offshore. The SAR images with a nominal spatial resolution of 30 m can be converted into wind speed maps by applying SAR wind retrieval

[e.g., Scoon et al. 1996] using the CMOD IFR2 scatterometer model function [Quilfen et al., 1998] and wind direction data from the 6-hourly forecast of the JWA (Japan Weather Association) Local Wave Model. The typical accuracies in wind speed are 1 m/s for QuikSCAT [e.g., Ebuchi et al. 2002] and about 2 m/s for SAR [e.g., Shimada and Kawamura, 2004]. We use wind measurements over the land at stations called Automated Meteorological Data Acquisition System (AMeDAS) operated by Japan Meteorological Agency.

We use a third generation wave model SWAN (Simulating WAves Nearshore) developed for shallow waters [Booij et al. 1999; Ris et al. 1999]. Directional wave spectra (DWS) are computed at 180 equally spaced propagation directions (θ) and 41 logarithmically spaced frequencies (f) between $f_{\min} = 0.04$ and $f_{\max} = 1.00$ Hz. For main energy source terms, the following default expressions are adopted. For wind input and whitecapping, the expressions of Komen et al. [1984] are used. The quadruplet nonlinear wave-wave interactions are computed with the Discrete Interaction Approximation [Hasselmann et al., 1985]. Bathymetric effects are not significant in this experiment. We focus on only wind-generated waves. Thus incoming waves at the open boundaries of the model domain are assumed to be zero. The SWAN model is run in stationary mode to identify an equilibrium state under the wind input. SWHs measured by ERS-2 altimeter are used to compare with the simulated SWHs.

III. WIND FIELD AND WIND WAVE DEVELOPMENT

Figure 1 shows the wind field off the Pacific coast of northern Japan on 25 February 2000 from the case study of Shimada and Kawamura [2004] with a focus on the present study area. Wind jets and wakes with typical width of 40 km are indicated in Figure 1 by the alphabetical symbols (A-D). To put it briefly, QuikSCAT wind vectors manifest two separate wind jets (A and C) with speeds above 12 m/s. They extend from the proximity of the Tsugaru Straits and the south of the Kitakami Highlands. Between these two jets, we can see a wake (B) extending downwind from the lee of the Kitakami Highlands. The SAR-derived wind map captures a part of the northern wind jet (A). Wind speeds are lower than 8 m/s in the nearshore region within 50 km from the coastline. We can see smaller-scale alternating high/low wind regions with 5-10 km widths, which correspond to indentations of the ria coast (Figure 1 and 4 (a)). We can identify another wake (D) on the south of the wind jet (C) with wind speeds less than 6 m/s. It is verified that variation of SWH along the altimeter ground track well correlated with wind speed variation. The QuikSCAT and forecast wind fields prove that wind directions are almost in the same direction over the study area and that wind convergences in the transverse direction of the axes of the wind jets and wakes are insignificant (Figure 4 (a)). This fact allows us to distinguish fetch-limited wind-wave development under the two-dimensional wind configuration of alternating wind jets and wakes from conventional one-dimensional fetch-limited wind-wave development.

Using the wind field and SWAN, we compute the fetch-limited wind-wave development. The model domain contains two pairs of wind jets and wakes (A-D) as shown in Figure 1. First, we investigate differences of evolution of DWS in wind jet and wake regions (Figure 2). We define two lines in the wind jet (C) and wake (B) along the wind direction, i.e. fetch, as shown in Figure 4 (a), and choose representative grid points with offshore distances of 20, 40, and 70 km for each line. Polar plots in Figure 2 represent the DWS together with the local wind directions at the grid points.

Figure 2 (a)-(c) show the evolution of DWS in the wind jet regions with the offshore distance. With increasing offshore distance, the peak energy increases and the peak frequency downshifts. They all have one primary spectrum peak, and the spectral shapes do not change significantly with the offshore distance. The directions of the spectrum peaks coincide with local wind directions all over the offshore distances. The above-mentioned characteristics are typical aspects of one-dimensional fetch-limited wind wave growth. On the other hand, the DWS in the wake region show different spectrum evolution (Figure 2 (d)-(f)). The spectrum energy evolves with the offshore distance, but they are lower than those in the wind jet region. The spreading of DWS at lower frequencies is much broader than those in the wind jet region. In particular, bimodal DWS are shown at the distance of 20 and 40 km. The directions of the two peaks are 30° and 260° , deviating more than 40° from the local wind direction. At the distance of 70 km, the DWS (Figure 2 (f)) is unimodal and the spectrum shape is similar to the DWS in the wind jet region (Figure 2 (c)).

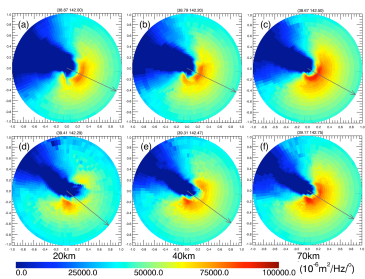


Figure 2 Directional wave spectra along (a-c) wind jet (C) and (d-f) wake (B). Logarithmic color scale is used. Top (bottom) figures are obtained at the points along the line 1 (2) shown in Figure 4 (a).

We can comprehensively examine the differences of spectrum directionality between wind jet and wake regions by taking notice of the overall directional spreading (DSPR) field. The overall DSPR can be considered as a weighted average of the DSPR

(the one-sided directional width of the spectrum) per frequency, and defined as [Kuik et al., 1988]:

$$DSPR^2 = \left(\frac{180}{\pi} \right)^2 \cdot \left[2 - 2 \frac{\left\{ \left(\int_{f_{min}}^{f_{max}} \int_0^{2\pi} \cos\theta E(f, \theta) d\theta df \right)^2 + \left(\int_{f_{min}}^{f_{max}} \int_0^{2\pi} \sin\theta E(f, \theta) d\theta df \right)^2 \right\}^{1/2}}{\int_{f_{min}}^{f_{max}} \int_0^{2\pi} E(f, \theta) d\theta df} \right], \quad (1)$$

where $E(f, \theta)$ is DWS.

The effects of alternating wind jets and wakes are remarkably reflected in the overall DSPR field (Figure 3). To put it into perspective, we can find that the regions of the wind jets (A and C) correspond to lower overall DSPR ($< 30^\circ$ for A and $< 40^\circ$ for C) and the regions of the wakes (B and D) correspond to higher overall DSPR ($> 40^\circ$ for B and D). Then, we take a close look at smaller-scale wind variations in the nearshore region (Figure 4 (a)). We can also see the same relation between wind speed and the overall DSPR (Figure 4 (b)). Namely, the overall DSPR is large ($> 50^\circ$) in the nearshore wake regions and small ($< 45^\circ$) in the nearshore wind jet regions.

Figure 3 (b) shows variation of wind energy (square of wind speed), the overall DSPR, and the computed SWH along the solid line indicated in Figure 3 (a). The line intersects the axes of the nearshore wind jets and wakes. For intercomparison of their fluctuations, the following parameter is defined as:

$$\delta I/I_0 = (I - I_0)/I_0, \quad (2)$$

where I is wind energy and SWH along the line and I_0 is average over the line. SWH variation coincides with wind energy variation. However, the SWH fluctuations are much smaller than those of wind energy. On the other hand, it is also ascertainable from Figure 3 (b) that the overall DSPR is negatively correlated with wind energy.

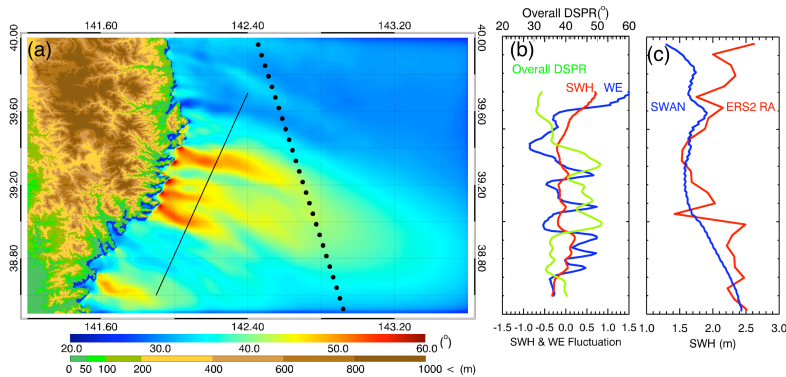


Figure 3 (a) Overall DSPR field. (b) SWH fluctuation (red), wind energy (WE) fluctuation (blue) and the overall DSPR (green) are plotted along the solid line in (a). (c) Comparison between the simulated and altimeter observed SWHs along the altimeter ground track indicated by the dotted line in (a).

The computed SWHs are compared with SWHs from ERS-2 altimeter along the ground track (Figure 3 (c)). It can be concluded that SWH variations are generally well reproduced by SWAN. This result supports the reasonableness of the simulation with a focus on nearshore regions. At higher latitudes ($> 39.7^\circ\text{N}$), SWHs are underestimated because the model domain does not completely contain the wind jet (A) or because incoming wave energy is assumed to be zero. However, the fact has no relation to the essence of the study.

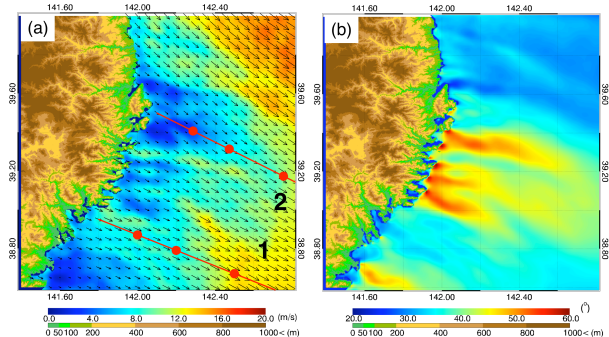


Figure 4 Close-up views of (a) the wind field and (b) the overall DSPR with a focus on the nearshore region. As to the two red lines in (a), see the caption of Figure 2.

IV. DISCUSSION

From the results above, we can propose a conceptual model for the different directionalities of DWS in wind jet and wake regions as below. One wind jet/wake promotes the formation of relatively weak/strong wind on both sides, inducing alternating wind jets and wakes. Wind waves are generated and developed downwind by local wind both in regions of wind jets and wakes. More energy is transferred to wind waves from local wind in wind jet regions than in wake regions. On the other hand, in all wind conditions, wave components propagate at a range of angles beyond the range of variation of local wind direction. This directional spreading, associated with wave energy transfer processes, is frequency dependent [e.g., Young et al., 1995]. However, energies that spread from wind jet regions are much larger than those from wake regions. Thus, the dominant wave energies outflowing from wind jet regions cross each other in neighboring wake regions, and combine with wave energy developed by local wind in wake regions. That is to say, wave energies incoming from neighboring wind jet regions induce broader DWS in wake regions. In cases where the wind speed contrast between wind jets and wakes is large, bimodal DWS are seen in wake regions. Departing at a certain distance from the coast, higher spectrum energy aligns along the local wind direction, and bimodal peaks in the DWS disappear. This is because the wind speed contrast between wind jets and wakes decreases with offshore distance and because wave spectrum energy in wake regions grows in equal measure with spectrum energy inflowing from the neighboring wind jet regions. Such directional characteristics of wind waves are not reflected in the computed SWH field because SWH is an integrated parameter of wave spectrum over the direction. This conceptual model casts the orographic modification of wind as the ultimate cause of the directionality of wave spectra in coastal seas. Observational studies are required to make sure of the sequence of the processes. Further studies are required to investigate the dependence of spectrum width on characteristics of wind fields such as wind speeds, wind speed differences between wind jets and wakes, widths of wind jets and wakes and time variation.

In the case of addressing fetch-limited wave growth in deep water, the following source terms in the action balance equation of SWAN can play a significant role in directional spreading: the generation by wind, dissipation by whitecapping, and nonlinear wave-wave interactions. Because high-frequency wave components respond relatively quickly to wind direction [e.g., van Vledder and Holthuijsen, 1993], wind variability is successful in generating broader DWS [Ponce and Ocampo-Torres, 1998]. Directional distribution functions incorporated in wind input source term are conducive to broader DWS [e.g., the first power of cosine by Komen et al. 1984]. A reduced directional spreading has been observed when dissipation is relatively high [Banner and Young, 1994]. Above all, many studies stress that nonlinear wave-wave interactions dominantly induce spreading of the wave directional structure [e.g., Young and van Vledder, 1993]. In the present case, the input wind energy distribution is complex due to the wind speed differences between wind jets and wakes. Such energy imbalance induced by the wind input should be compensated by the nonlinear wave-wave interactions. Consequentially, spectrum shapes in wake regions come close to those in wind jet regions with offshore distance. It remains as a future challenge to examine the directional distributions of the source terms, and their balance. To consider these points, full representation of nonlinear wave-wave interactions should be adopted [e.g., Young et al., 1995].

V. SUMMARY

We simulate wind-wave development under alternating wind jets and wakes with typical widths of 5-40 km by using SWAN wave model and the high-resolution wind field resolved by SAR and scatterometer. The following conclusions are obtained.

- 1) Broader directional wave spectra are seen in the wake region than in the wind jet region. Moreover, bimodal directional wave spectra are distinguished with offshore distances of less than 40 km. The directions of the two peaks are at angles of more than 40° from the local wind direction.
- 2) The spatial distribution of the overall directional spreading corresponds to the wind speed variation associated with the wind jets and wakes. The overall directional spreading is large in the wake regions and small in the wind jet regions.

This study demonstrates that wind configuration of alternating wind jets and wakes has a great impact not only on difference of wind energy input but also on energy transfer between waves. Namely, such a wind configuration induces different directionality in wave field. This study can be also characterized as a counterpart of the swell sheltering effect of islands, inducing complex spectrum directionality in the lee of the islands [Ponce and Soares, 2005]. The characteristic directionality of ocean surface wave fields brings better understanding of high individual wave occurrences, spectrum shapes, sea surface slopes, and wave energy transfer.

ACKNOWLEDGMENT

ERS-2 SAR data were provided from Japan Aerospace Exploration Agency. QuikSCAT data were obtained from NASA Physical Oceanography Distributed Active Archive Center at the Jet Propulsion Laboratory. AMeDAS data were provided by the Japan Meteorological Agency. The authors thank the SWAN team for making SWAN available. Outputs of Local Wave Forecast Model are purchased from Japan Weather Association. Bathymetric data from Japan Oceanographic Data Center were used for wave simulation. The SWAN simulations are carried out using the supercomputer system SX-7 of Information Synergy Center, Tohoku University. We thank two anonymous reviewers for their careful reading of the manuscript and constructive suggestions for improvement.

- Banner, M. L. and I. R. Young (1994), Modeling spectral dissipation in the evolution of wind waves. Part I: Assessment of existing model performance, *J. Phys. Oceanogr.*, 24, 1550-1571.
- Booij, N., R. C. Ris and L. H. Holthuijsen, (1999), A third-generation wave model for coastal regions, Part I, Model description and validation, *J. Geophys. Res.* C4, 104, 7649-7666.
- Ebuchi, N., H.C.Grabek, and M.J.Caruso (2002), Evaluation of wind vectors observed by QuikSCAT/SeaWinds using ocean buoy data, *J. Atmos. Oceanic Technol.*, 19, 2049-2062.
- Hasselmann, K., T. P. Barnett, E. Bous, H. Carlson, D. E. Cartwright, K. Enke, J. A. Ewing, H. Gienapp, D. E. Hasselmann, P. Kruseman, A. Meerburg, P. Mullar, D. J. Olbers, K. Richter, W. Sell, and H. Walden (1973), Measurement of wind-wave growth and swell decay during the Joing North Sea Wave Project (JONSWAP), *Dtsch. Hydrogr. Z.*, 8 (12), suppl. A, 95.
- Hasselmann, S., K. Hasselmann, J. H. Allender, and T. P. Barnett (1985), Computations and parameterizations of the nonlinear energy transfer in a gravity-wave spectrum. Part II: Parameterization of the nonlinear energy transfer for application in wave models, *J. Phys. Oceanogr.*, 15, 1378-1391.
- Komen, G. J., S. Hasselmann, and K. Hasselmann (1984), On the existence of a fully developed wind-sea spectrum, *J. Phys. Oceanogr.*, 14, 1271-1285.
- Kuik, A. J., G. P. van Vledder and L. H. Holthuijsen (1988), A method for the routine analysis of pitch-and-roll buoy wave data, *J. Phys. Oceanogr.*, 18, 1020-1034.
- Ponce, S. and F. J. Ocampo-Torres (1998), Sensitibity of a wave model to wind variability, *J. Geophys. Res.*, 103, 3179-3201.
- Ponce de León, S. and C. Guedes Soares (2005), On the sheltering effect of islands in ocean wave models, *J. Geophys. Res.*, 110, C09020, doi:10.1029/2004JC002682.
- Quilfen, Y., B. Chapron, T. Elfouhaily, K. Katsaros and J. Tournadre (1998), Observation of tropical cyclones by high-resolution scatterometry, *J. Geophys. Res.*, 103, 7767-7786.
- Ris, R. C., N. Booij and L. H. Holthuijsen, 1999, A third-generation wave model for coastal regions, Part II, Verification, *J. Geophys. Res.* C4, 104, 7667-7681.
- Scoon, A., I. S. Robinson, and P. J. Meadow (1996), Demonstration of an improved calibration scheme for ERS-1 SAR imagery using scatterometer wind model, *Int. J. Remote Sens.*, 17(2), 413-418.
- Shimada, T. and H. Kawamura (2004), Wind jets and wind waves off the Pacific coast of northern Japan under winter monsoon captured by combined use of scatterometer, SAR and altimeter, *J. Geophys. Res.*, 109, C12027, doi:10.1029/2004JC002450.
- van Vledder, G. P. and L. H. Holthuijsen (1993), The directional response of ocean waves to turning winds, *J. Phys. Oceanogr.*, 23, 177-192.
- Young, I. R., and G. P. van Vledder (1993), A review of the central role of the nonlinear interactions in wind-wave evolution, *Philos. Trans. R. Soc. Lond. A* 342, 505-524.
- Young, I. R., L. A. Verhagen, and M. L. Banner (1995), A note on the bi-modal directional spreading of fetch-limited wind waves, *J. Geophys. Res.*, 100, 773-778.

Automatic Detection Approach of Ship using RADARSAT-1 Synthetic Aperture Radar

*Chan-Su Yang**, *Kazuo Ouchi***

**Ocean Satellite Research Group, Korea Ocean Research & Development Institute(KORDI)*

1270 Sa2-dong Sangrokgu Ansan, Seoul 426-744 Korea

yangcs@kordi.ac.kr

***Department of Environmental Systems Engineering, Kochi University of Technology (KUT)*

Tosayamada-cho, Kochi , 782-8502, Japan

ouchi.kazuo@kochi-tech.ac.jp

Abstract- Ship detection is a crucial application for global monitoring for environment and security. It permits to monitor traffic, fisheries, and to associate ships with oil discharge. An automatic ship detection approach for RADARSAT Fine Synthetic Aperture Radar (SAR) image is described and assessed using *in situ* ship validation information collected during field experiments conducted on August 6, 2004. Ship detection algorithms consist of five stages: calibration, land masking, prescreening, point positioning, and discrimination. The fine image was acquired of Ulsan Port, located in southeast Korea, and during the acquisition, wind speeds between 0 m/s and 0.4 m/s were reported. The detection approach is applied to anchoring ships in the anchorage area of the port and its results are compared with validation data based on Vessel Traffic Service (VTS) radar. Our analysis for anchoring ships, above 62 m in length, indicates a 100 % ship detection rate for the RADARSAT single beam mode.

1. Introduction

With the increasing importance in monitoring ship traffic in both coastal and ocean waters, an automatic detection of ships, wakes, and ship velocity is very desirable. By using land-based radar, Vessel Traffic Service (VTS) has been developed and applied in waterways around ports. The control of ships near coasts is currently supported by VTS radar but it is restricted because of available information limitations. In addition to that, the coverage of monitoring ships by the traditional VTS is limited to the bay area or the approach from the sea to a harbour. There is a requirement for improving the VTS to be able to cover areas where radar coverage is almost impossible to achieve.

Yang and Park (2003) suggested an approach merging of satellite remote sensing and environmental stress model to ensure marine safety for the navigational waters off the radar range. RADARSAT has the capability to detect both stationary and moving ships on the ocean. Ships are good microwave reflectors, or hard targets, in a sense acting as radar corner reflectors. They return a large portion of the incident energy back to the SAR sensor and may appear in the SAR imagery as relatively bright points or elongated bright blobs. Due to this strong hard target behavior, the location of fishing fleets can be easily determined using SAR imagery. Successful SAR detection of ships depends, nevertheless, on the size and type of vessel, the prevailing wind speed conditions, the SAR resolution used and the viewing angle [Vachon et al. (1997), Morse and Protheroe (1997), Wackerman (1996)].

The work presented in this paper focuses on a procedure of detecting ship target in a fully automatic way for Radarsat-1 Fine SAR imagery. In this paper, the proposed method is to utilize a difference of pixels intensity between ships and sea clutter. Ship detection algorithms consist of five stages: calibration, land masking, prescreening, point positioning, and discrimination including the labeling technique and morphological filtering.

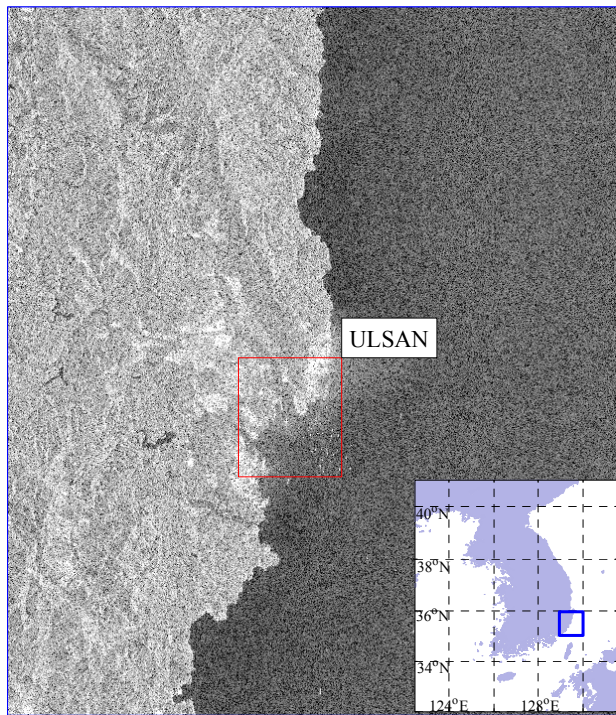


Fig. 1. RADARSAT image, Ulsan Port-centered East Coast of South Korea, on August 6, 2004. The image of 17716 lines by 20544 pixels was acquired in fine mode and descending passage.

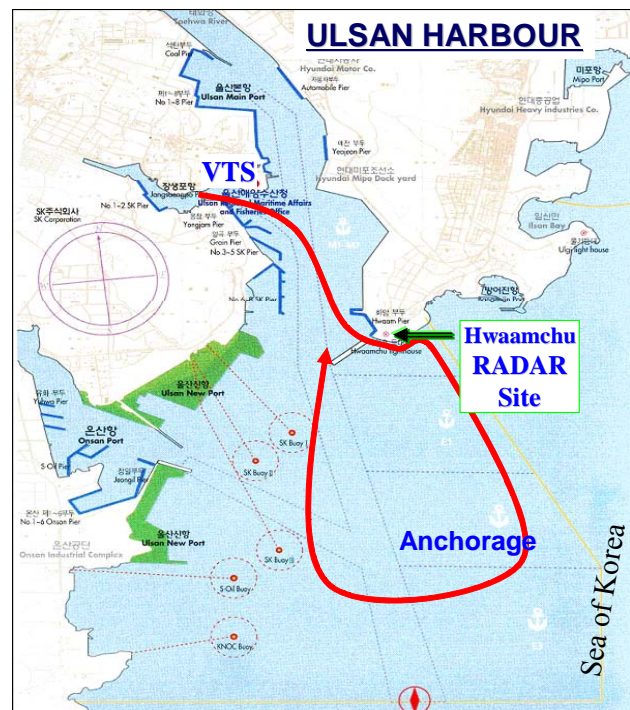


Fig. 2. Map of Ulsan Bay. Radar and weather data were measured at Hwaamchu site. The bold line represents a trajectory of ship used here.

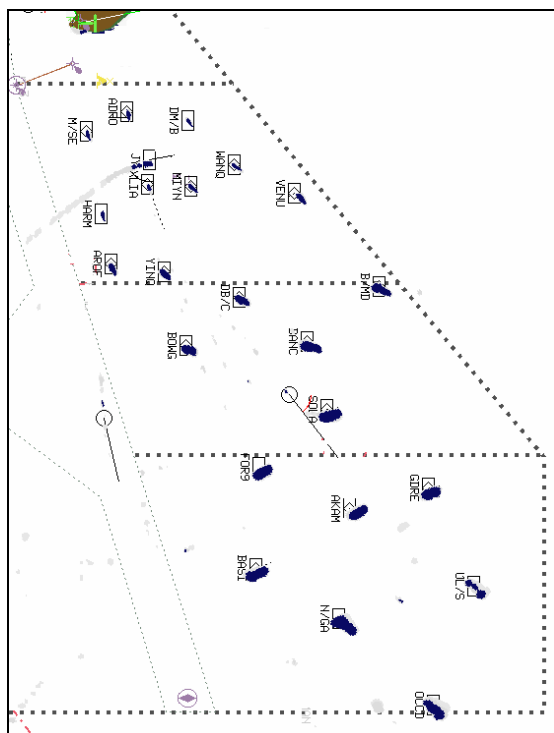


Fig. 4. VTS-Radar based ship locations and codes: June 19, 2004



Fig. 3. Ship used during the field experiment.

2. Data

2.1 SAR Image Data: Fine Mode

RADARSAT-1 satellite SAR data were acquired on August 6, 2004 and processed at the Korea Earth Observation Center (KEOC) as shown in Fig. 1. SAR image is calibrated to geophysical (sigma naught) values of radar cross section (RCS) even if data numbers (DN) on these detected images can be viewed as indicating relative radar backscatter intensities.

2.2 Wind and Validation Data

During the SAR data acquisition, wind data was acquired from Hwaamchu station (Fig. 2) and northwest winds, with speeds from 0 m/s to 0.4 m/s were recorded. The line in Fig. 2 shows a trajectory moved aboard a pilot ship as shown in Fig. 3.

Validation data includes ship name, call sign, latitude/longitude position, ship size and type, and ship photographs from the scene.

- Automatic Identification System (AIS) GPS ship position
- Vessel Traffic Service (VTS) data: vessel code, radar image
- Ship photographs from the scene

The vessels tracked by the Ulsan-VTS during the SAR acquisition are shown in Fig. 4, and listed in Table 1.

Table 1. Ship Information: Aug 6, 2004

Ship Name	Ship Code	Length (LOA, m)	Breadth (m)	Depth (m)	Type of ship
Morning Sea	M/SE	79	14	6.7	Chemical Tanker
Harmony	HARM	68	11.6	5.7	General Cargo
Adoracion	ADRO	78	12.8	5.8	Chemical Gas
Aro Forest	AROF	93	15.8	7.8	Chemical Tanker
Xin Liang	XLIA	85	16.2	7.2	General Cargo
Ju Yeon	JY	98	15.2	7.5	Petroleum Product
Dongmyung B.	DM/B	73	13.6	7.7	General Cargo
Yinquan	YINQ	105	16.4	7.8	Petroleum Product
Mi Yeon	MIYN	92	14.6	7.4	Petroleum Product
Bow Giovanni	BOWG	127	20.5	10	Chemical Tanker
Wanquanhai	WANQ	96	15.2	8.4	Petroleum Product
DB Coral	DB/C	111	19.5	10.2	Chemical Tanker
Venus Gas	VENU	84	15	7	Liquefied Gas(LPG)
Formosa Nine	FOR9	167	30	14.2	Chemical Tanker
Basic Arron	BASI	182	32.2	16.5	General Cargo
Danchi	DANC	171	32	14	Petroleum Product
Solar Oceania	SOLA	162	27.2	13.4	General Cargo Ship
Bunga Melati Dua	B/MD	168	30	15	Petroleum Product
Akama	AKAM	174	32.2	19.1	Petroleum Product
Navios Galaxy	N/GA	216	32.2	19.3	General Cargo
Global Dream	GDRE	154	26	11	General Cargo Ship
Ocean Concord	OCCD	237	42	19.5	Petroleum Product
Ulsan Spirit	UL/S	244	42.7	21.5	Petroleum Product

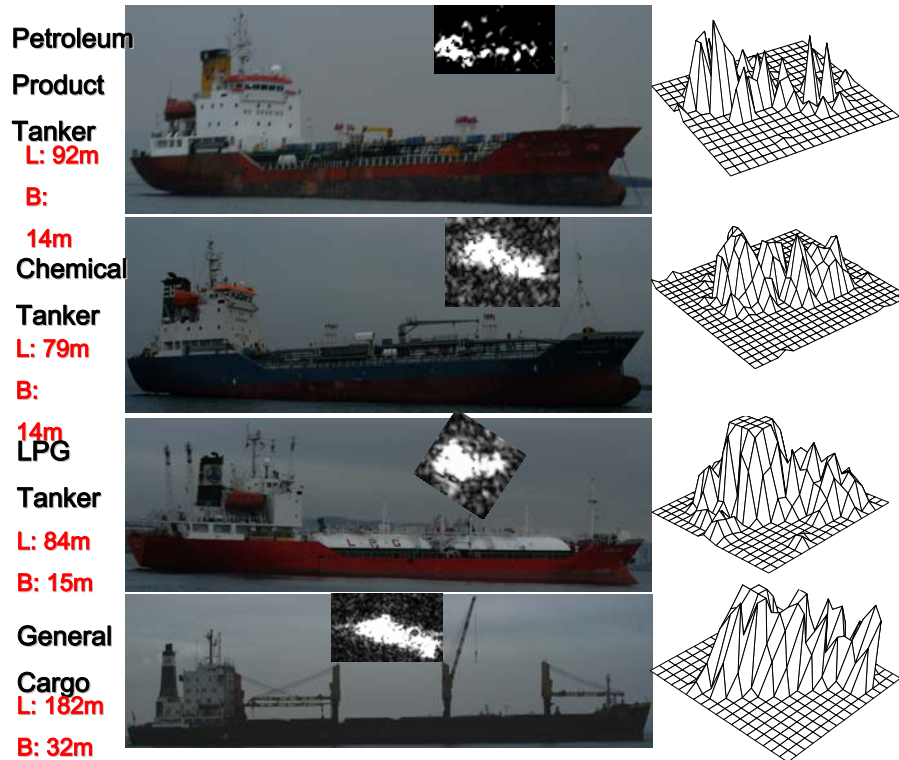


Fig. 5. Vessel classification by RADARSAT Fine mode image (August 6, 2004): from left vessel information, photo, scattering locations of the vessel, and 3d intensity values.

3. Ship Detection Algorithm

The proposed structure of the detection algorithm is illustrated in Fig. 5. The principle of the detection algorithm is based on the theoretical considerations and practical experience, and the algorithm uses a processing chain consisting of calibration, land masking, thresholding, point positioning, labeling technique, morphological erosion, morphological dilation, morphological bridging, and attribute-extraction.

Vessels at anchorage No. 1 and No.2 as shown in Fig. 3 are identified in SAR image. Breakwater (B.W. in Fig. 3) is also not seen in the image, but the two light-houses at each end of the breakwater appear as a bright dot.

4. Validation Results

The validation process is straightforward, requiring comparison of ship validation positions with RADAR-SAT candidate target positions. As a validation data, 23 vessels in anchorage were selected, because their positions show hardly variation with time and are reported to VTS center using AIS. Figure 6 represents the locations of 23 vessels and RADARSAT-detected ship targets. Figure 7 is the superposition of the ship targets transmitted by AIS to VTS center (Fig. 6 left image) and the potential ship targets identified by SAR imagery. The SAR data detected all targets that were reported to VTS. In a portion of ships, a large discrepancy in position appears, but that is why the SAR-ship position is calculated as a centroid of potential ship area, and an AIS transmitter is installed on bridge.

5. CONCLUSIONS

In this paper, we introduced a ship detection technique and its validation result. The main advantage of the method is that the difference of light intensities between a ship and the sea can be obtained quickly and automatically without human intervention.

Two fine imagery of Ulsan Port under calm condition were used to detect stationary ships at anchorage and reveals 100% accuracy for merchant vessels with a variety of types.

ACKNOWLEDGEMENTS

This work was supported by the Basic Research Project, “Development of Management and Restoration Technologies for Estuaries” of KORDI and the Public Benefit Project of Remote Sensing, “Satellite Remote Sensing for Marine Environment” of Korea Aerospace Research Institute.

REFERENCES

- [1] Yang, C.S. and Park, Y.S., Merging of satellite re-mote sensing and environmental stress model for ensur-ing marine safety. *Intl. J. Navigation and Port Research*, 27(6), pp. 645-652, 2003.
- [2] Morse, A.J. and Protheroe, M.A., Vessel classifica-tion as part of an automated vessel traffic monitoring system using SAR data. *Intl. J. Rem. Sensing*, 18(13), pp. 2709-2712, 1997.
- [3] Vachon, P., Campbell, J., Bjerkelund, C., Dobson, F., and Rey, M., Validation of Ship detection by the RADARSAT SAR, Proceedings PORSEC'96, Victoria, Canada, 1996.
- [4] Vachon, P.W., Campbell, J., Bjerkelund, C., Dob-son, F., and Rey, M., Ship Detection by the RADAR-SAT SAR: Validation of Detection Model Predictions, *Canadian Journal of Remote Sensing*, 23(1), pp. 48-59, 1997.
- [5] Wackerman, C., An algorithm for automatically de-tecting and characterizing Kelvin wakes in SAR imagery. ERIM Report 606131-1-X, August 1996, Ann Arbor, 1996.

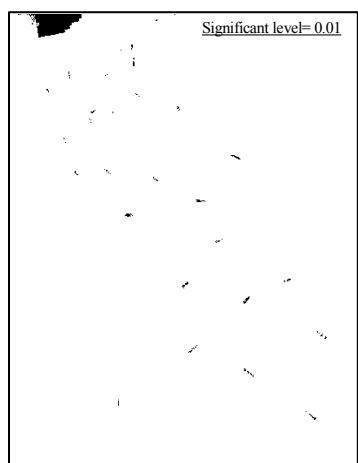


Fig. 6. 23 vessels in anchorage from AIS positions (left) and RADARSAT candidate target positions (right): Aug 6, 2004.

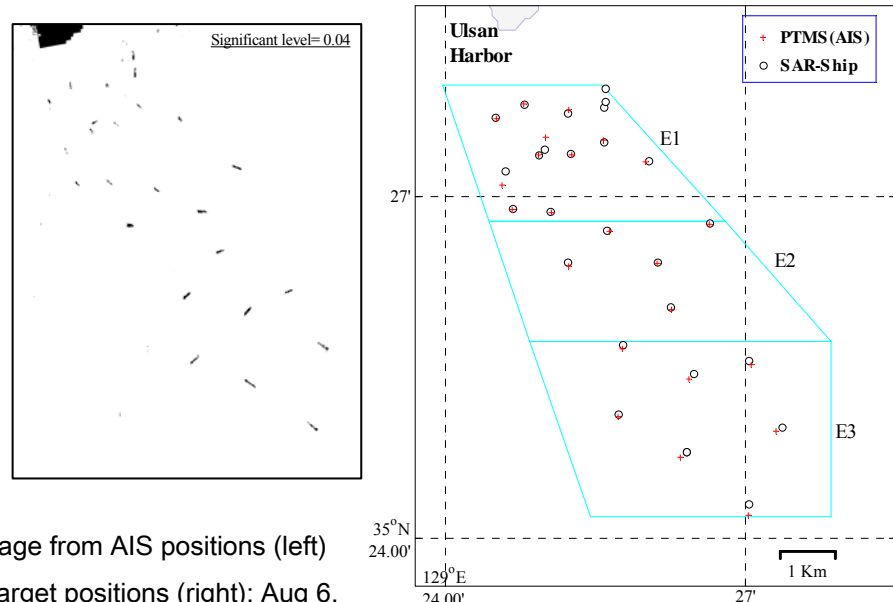


Fig. 7. Collocated RADARSAT and AIS(VTS) targets.

GIMS - Technology for the Classification and Qualitative Interpretation of the Data of Remote Sensing for Water Surface

Mkrtyan F.A.⁽¹⁾, Krapivin V.F.⁽¹⁾, Shapovalov S.M.⁽²⁾

⁽¹⁾ *Institute of Radioengineering & Electronics RAS
1 Vvedensky Sq., Fryazino, Moscow reg., 141190 Russia
Tel.: 7+095+5269276, Fax: 7+096+5649060, Email: ferd@ms.ire.rssi.ru*

⁽²⁾ *Institute of Oceanology RAS
36 Nakhimovskii st., Moscow, 117856 Russia
Tel.: 7+095+1245981
Email: smshap@ocean.ru*

Abstract - One of the basic tasks of geoinformation monitoring of an environment is automation of data processing of measurements with the principal goal of the task decision for phenomena detection and classification on a water surface. The methods and algorithms of cluster and discriminant analysis for the classification and qualitative interpretation of remote sensing data characterizing the water surface are considered. The problem of classification of aquatories using the remote sensing measurements is one of important among them. Various algorithms of the theory of images recognition, statistical decisions and cluster analysis are used to solve this problem. The mathematical model describing the background characteristics of water surface spottiness is proposed. Operative software for this model is realized. The results of the software application to the satellite data processing for the Atlantic and Pacific regions are given.

1. Introduction

The basic scheme of collection and processing of the information in geoinformation monitoring system recognizes that effective monitoring of investigated object is possible under complex use of methods of simulation modeling, collection and processing of the information [1].

From the position of system analysis, the system of collection and processing of the information in geoinformation monitoring represents the structure uniting the computers of various classes, databases and the advanced problem-oriented software. Creation of such system demands the development of formalized description of the information flows and unique methodology of its processing.

Development of geoinformation monitoring systems requires the decision of a set of problems related to the formation of data measurements flows to be solved. The problem of classification of aquatories using the remote sensing measurements is one of important among them. Various algorithms of the theory of images recognition, statistical decisions[2,3,4,5,6] and cluster analysis[7] are used to solve this problem.

2. About Methods of Classification

At present time there are many methods of recognition which are caused appreciably by variety of statements of concrete tasks. The problem of recognition consists in the division of some group of objects into the classes at the base of certain requirements. The objects having general properties are related to one class. An initial data for the solution of a recognition problem are results of some observations or the direct measurements, that are named initial attributes.

Method of taxonomy (clustering) is one of the important methods of recognition and classification of images. Let's assume set of M it is required to divide by not crossed subsets (clusters), and the elements included in the same clusters should be close to each other enough from the point of view of the chosen criterion of nearness, and elements from different clusters should be far enough from each other. In one of many possible statements of this task two numbers a and b ($0 < a < b$) are given. It is considered, that two elements x and y are close to each other enough, if $p(x,y) < a$, and are far enough from each other, if $p(x,y) > b$.

Kings method is one of well-known methods of taxonomy, which gives good results in those cases, when the quantity of the available information in assumed clusters is moderate. According to this method the distance between groups of points in space of attributes is defined as distance between centers of masses of these groups. Clustering in this case is based on the assumption that sites of the increased density in space of attributes correspond to similar situations.

3. Model of Spottiness

The feature of remote measurements is information acquisition, when the data of measurements, acquired during tracing of flying system along routes of survey, are directed to input of the processing system. As result the twodimensional image of investigated object is registered. Statistical model of spottiness for investigated space is one of models for this image.

In real conditions, the study of spots, the acquiring of their statistical characteristics and their using in a problem of detection is enough a complex problem. It is necessary to develop the criteria allowing the distinguishing the spots from other phenomena. For example, it is necessary to determine such threshold the exceeding of which is the spot indicator. Also it is necessary to develop model presentation of processes of spots detection.

The method of the thresholds determination in the most obvious and simple way for spots definition. In this case that part of space belongs to area of spots, on which the parameter of environment measured within the chosen channel exceeds value (\bar{I}^+) or, on the contrary, does not exceed value (\bar{I}) a threshold. Let $y = y(x_1, x_2)$ is function of coordinates (x_1, x_2) of points within considered region. If "level surface" $y=const$ is outlined at the region surface, then the closed curves of level y that bound the spots are projected on it.

Algorithms for simulation of spottiness are based on the numerical solution of the algebraic inequalities determining coordinates of internal points of spots. It is impossible to write the equation of spots contours in a general.

Therefore contours of spots are described by system of the simple algebraic equations connected among themselves by equation $\sum \varphi_i(x, y) = 0$, where $\varphi_i(x, y)$ is the equation of an elementary curve. For simplification of software realization of simulation of spottiness image as the equations $\varphi_i(x, y)$ the equation of a circle with varied coordinates of the centre and radius is accepted. Complex forms of spots are formed by overlapping on a plane of the drawing of several circles with different parameters that is defined by system of inequalities of a kind:

$$\sum \{(x-a_i)^2 + (y-b_i)^2 - r_i^2\} \leq 0$$

Where x, y are the cartesian coordinates of internal points of spots, a_i, b_i, r_i are coordinates of the centre and radius i -th circle, respectively, n is quantity of the circles composing the modeled image. To simulate the randomness of background distribution for spottiness the spottiness model parameters a_i, b_i, r_i are set by means of random-number generators. By changing laws of distribution of random numbers and their statistical parameters, it is possible to receive statistically different spottiness images.

4. Software

The list of software items of the simulation system of classification of the phenomena on a terrestrial surface is given in Table1. An important point of algorithms and the software of system is the possibility of spatial interpolation and data restoration using remote and in-situ measurements.

One of main aspects of the practical importance of developed system is qualitative interpretation and visualization of results of remote measurements. For primary processing of remote measurements it is useful to apply an overage-connecting method of cluster analysis to detect the specific informational zones [1,7]. That method is effective under small volumes of sampling. Two variants of this approach are realized to be distinguished by the organization form of algorithms and indeu spaces.

Table 1. Structure of the Software.

Software name	The functional characteristic an software
REICM	Reduction of the experimental information in a computer memory.
DRHIM	Data reconstruction by means of the harmonics interpolation method
SIDSM	Spatial interpolation of the data by means of a spline method
DRMOT	A method of optimal interpolation.
CASRS	Cluster analysis focused on singe space of remote sensors.
CALRS	Cluster analysis focused on the account of local reading of sensors.
RSC	Research of spottiness. characteristics.
RRADA	Realization of recognition algorithm by a method of the discriminant analysis.
CSAIRM	Sorting and accumulation of the in-situ and remote measurements.
CMS	Computer mapping of the spots.

5. Application

Analysis of statistical characteristics of "spottiness" for three types of areas of Atlantic and Pacific oceans was conducted. These statistical characteristics were determined for the most informative thresholds. At that time statistical characteristics of "spottiness" for the same areas, selected using criteria of minimal value of coefficient of correlation for joint sample of positive and negative spots. Analyzis of these characteristics showed, that the statistical characteristics of "spottiness" coincide for areas with temperate sea roughness and storm zones. Minimum for the coefficient of correlation ρ_{\min} is run down for a case of most informative thresholds. But for quiet area the situation is different.

In Table 2 results of statistical data processing spottiness brightness temperatures on a wave of $\lambda_1 = 0,8$ sm received by a method of the transect-analysis for area with a high pressure (1025 B) and speed of wind $V < 5$ m / sec (quiet area) (Data Space Satellite « Cosmos - 1500 » for 8-9 February, 1984) are submitted. The maximal value brightness temperatures $T_{\text{я}, \text{max}} = 162,3$ K, the minimal value brightness temperatures $T_{\text{я}, \text{min}} = 144,2$ K. The most informative are thresholds which values get in an interval from 149K up to 152 K.

For these thresholds the greatest rapprochement of the average sizes of positive and negative spots is marked. For a threshold $X = 151,4$ difference of average values of the sizes of spots makes $\Delta M = 1,18$. The minimal value of factor of correlation is fixed also for the most informative thresholds. So, for a threshold $X = 149,6$, $\rho_{\min} = 0,074$. In this case with a high probability it is possible to approve, that distribution of positive and negative spots are independent.

It is possible to be limited to research one-dimensional histogram (I^+, I^-) - characteristics. The analysis of theoretical and empirical distribution of negative spots also has shown their independence for the most informative thresholds. So, average of theoretical and empirical distribution for value of a threshold $X = 149,6$ has made $\Delta = 0,048$, and for $X = 151,4$, $\Delta = 0,016$.

Table 2. Statistical characteristics "spottiness" (I^+ , I^-) - characteristics) area of Pacific ocean on data Space Satellite « Cosmos - 1500 »(the channel $\lambda_1 = 0,8$ cm, pressure 1025, speed of wind $V < 5$ m / sec)

Threshold	The size of sample		M	σ^2	MIN	MAX	RAZ	A	Θ	ρ
147,8	13	+	11	326	1	69	68	2,53	5,27	-0,101
		-	1,08	0,08	1	2	1	3,02	7,09	
149,6	18	+	6,72	162,31	1	54	53	2,99	7,84	0,074
		-	2,06	3,7	1	9	8	2,74	7,07	
151,4	19	+	4,79	116,9	1	48	47	3,4	10,52	-0,234
		-	3,61	7,9	1	13	12	1,87	4,17	
153,2	9	+	6,56	205,36	1	47	46	2,45	4,07	-0,266
		-	12,13	107,61	3	34	31	1,16	-0,16	

In Table 3 statistical characteristics "spottiness" are submitted to water area of Pacific ocean for area with normal pressure 1010 and speed of a wind of 6 m / sec $\leq V \leq 10$ m / sec (moderate excitement). For this area extreme values brightness temperatures the following: $T_{\text{я}, \text{min}} = 156,8$ K, $T_{\text{я}, \text{max}} = 175,8$ K.

The most informative thresholds are in a range from 161K up to 164K. For the same thresholds the least sharpness of the average sizes of positive and negative spots is observed also. For $X = 161,8$ difference $\Delta M = 1,88$. The factor of correlation reaches(achieves) the minimal value $\rho = -0,02$ for a threshold $X = 163,7$, that testifies to independence of distribution of positive and negative spots. The average deviation(rejection) of theoretical and empirical joint distribution makes $\Delta = 0,01$, that also confirms it. For this threshold, and also for a threshold $X = 161,8$ ($\rho = -0,198$) it is possible to be limited to research one-dimensional histograms, and for the others research bi-dimensional histograms is desirable.

Table 3. Statistical characteristics "spottiness" ((l+, l-) - characteristics) area of Pacific Ocean on data Space Satellite «Cosmos - 1500 » (the channel $\lambda_1 = 0,8$ cm, pressure 1010, speed of a wind of 6 m /sec $\leq V \leq 10$ m / sec)

Threshold	The size of sample	M	σ^2	MIN	MAX	RAZ	A	\mathcal{E}	ρ
159,9	16	+	12,31	257,09	1	61	60	1,82	2,66
		-	1,4	0,37	1	3	2	1,26	0,51
161,8	35	+	4,09	23,79	1	22	21	2,45	5,66
		-	2,21	5,28	1	13	12	3,31	11,99
163,7	37	+	1,81	3,5	1	11	10	3,46	13,23
		-	4,08	35,16	1	34	33	3,67	14,95
165,6	8	+	2,57	3,10	1	6	5	0,82	-0,61
		-	25	1268,5	1	117	116	2,06	2,63

In Table 4 statistical characteristics "spottiness" water areas of Pacific ocean with low pressure (< 1005 Б) and speed of wind $V \approx 16$ m /sec (a storm zone) for the channel $\lambda_1 = 0,8$ cm. Extreme values brightness temperatures the following: $T_{\min} = 160,6$ K, $T_{\max} = 220,1$ K.

The most informative thresholds located in a range from $163K$ up to $164K$. However, the average sizes of positive and negative spots are closest for a threshold $X = 166,5$ and $\Delta M = 0$, whereas for $X = 163,5$ $\Delta M = 3,5$. The factor of correlation reaches(achieves) the minimum $\rho_{\min} = 0,034$ for a threshold $X = 163,5$, that testifies to independence of distributions positive (t^+) and negative (t^-) spots. For the same threshold the minimal deviation(rejection) of joint theoretical and empirical distribution $\Delta = 0,007$ is received, that confirms this independence.

Analyzing statistical characteristics "spottiness" three types of areas of Pacific ocean, received for the most informative thresholds, with statistical characteristics "spottiness" the same areas, selected on the minimal value of factor of correlation of joint sample of positive and negative spots it is possible to notice, that for areas with moderate excitement and storm zones statistical characteristics "spottiness" coincide, that is the minimum of factor of correlation ρ_{\min} is reached(achieved) for the most informative thresholds. And for quiet area it not so.

From the aforesaid follows, that statistical characteristics "spottiness" brightness temperatures can be used at recognitions and classifications of the phenomena on a surface of the ocean, distinguished by a degree of excitement.

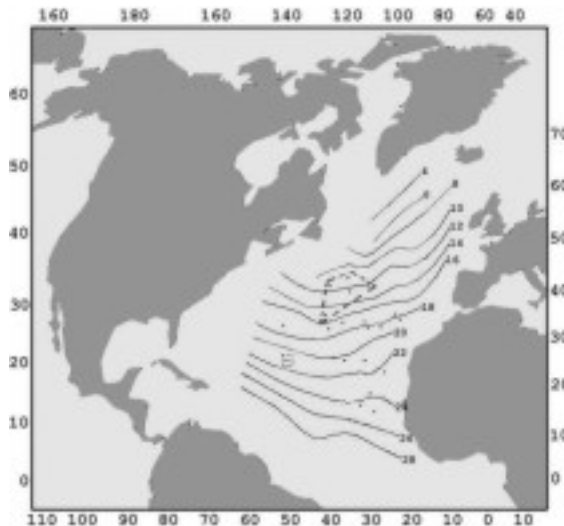
Table 4. Statistical characteristics "spottiness" ((l+, l-) - characteristics)
area of Pacific Ocean on data Space Satellite « Cosmos - 1500 »
(the channel $\lambda_1 = 0,8$ cm, pressure ≤ 1005 , speed of wind $V \approx 16$ m / sec).

Threshold	The size of sample	M	σ^2	MIN	MAX	RAZ	A	\mathcal{E}	ρ
162	6	+	13,5	333,25	1	52	51	1,42	0,39
		-	1,5	1,25	1	4	3	1,79	1,2
163,5	12	+	5,5	157,25	1	47	46	2,99	7,01
		-	2	1	1	4	3	0,5	-1
166,5	7	+	7,5	96,58	1	29	28	1,63	0,89
		-	7,5	86,58	1	23	22	0,78	-1,29

On fig. 1. the example of work of the automated system in a mode of monitoring of temperature of a surface of Northern Atlantic on data Space Satellite « Cosmos- 1151 » (8 - April, 14, 1980) is given. The system allows to receive maps of temperatures on enough rarefied grid of trajectory SS. Points on a map designate areas of realization of ship measurements. The analysis of satellite and contact measurements shows, that there is an

appreciable regular understating satellite estimations of temperature of ocean concerning ship which on the average makes 1,6 K.

The root-mean-square deviation(rejection) of satellite estimations T from ship measuring on all given sample makes 3,3K. The dotted line on a map designates areas where the difference between ship and satellite measurements exceeds 4 K. It is typical, that high overcast is registered in all these points (on the data weather forecasters). The root-mean-square deviation of satellite measurements of temperature from ship, designed without taking into account the allocated points, makes 1,4 K.



Present Status and Future Prospect of Saga Synchrotron Light Project

Masao Kamada, Kazutoshi Takahashi, Jyunpei Azuma, Tooru Tanaka, and Hiroshi Ogawa

Synchrotron Light Application Center, Saga University, Honjo 1, Saga 840-8502, Japan

Abstract. The first synchrotron in Kyushu Island has been constructed in Saga. The accelerator complexes consisting of a 250 MeV linac and a 1.4 GeV accelerator/storage ring have passed the inspection by the government on December 15, 2005 and now they are operational, providing Synchrotron Light (SL). Three prefecture open beam lines and one university's beam line are ready for uses after recent efforts in construction. The Synchrotron Light Application Center of Saga University has been carrying out academic researches using advantage of SL. The center is interested in the new frontier fields such as non-thermal process and photo-CVD, advanced analyses, creation of combination system between semiconductors and bio-specimens, basic and application in environmental and material science, and so on. The center is also interested in the industrial application with SL as well. It is expected that the useful and powerful SL may produce wide variety of applications.

INTRODUCTION

Since the first observation of Synchrotron Light (SL) in 1947, the science and technology using SL have been grown up to the present. SL has many useful characteristics (wide photon energy range from far-infrared to x-rays, high flux, high brilliance, small divergence, cleanliness, polarization, short pulse, and so on), and is powerful and promising tool for nano-technology, bio-technology, material engineering, environmental applications, and so on.

Saga Light Source (Saga-LS), which is the first synchrotron light facility in Kyushu Island, has been constructed at Tosu city in Saga prefecture, and it has become operational in February of 2006, after the governmental inspection on December 15, 2005. The Saga-ring has the circumstance of 75.6 m, the storage electron energy of 1.4 GeV and the emittance of 25.5 nm-rad. The critical photon energy from bending magnets is about 1.9 KeV, while a wiggler of 5 T can provide the critical energy of about 6.5 KeV. From the comparison with the spectral distribution of Spring-8 that is the biggest storage ring for SL in the world, the photon flux of Saga-LS is comparable with that of Spring-8 in the soft x-ray regions, as seen in Figure 1. The Saga-LS is therefore expected to be used for wide variety of industry applications as well as the academic studies in the Kyushu area.

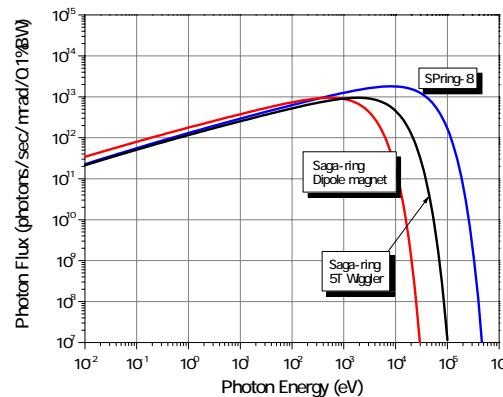


FIGURE 1. The spectral distribution of Saga-LS

SAGA SYNCHROTRON LIGHT PROJECT

The Saga synchrotron light project has been planned and promoted by the close relation between Saga University and Saga Prefecture Government with supports from the Japanese National Government. There are several purposes of the Saga synchrotron light project. The first is the industrial application of SL. The second is to create a key station for collaboration of industry, academia and government. We expect to enhance and create new regional industries from the excellent center in Asia for advanced science and technology. The third aim is to congregation of excellent talent and brains for world-class research and education. We expect to grow up many young persons' capability for future science and technology. We will also educate many public persons to have essential understanding of science and technology. Our intelligent synchrotron light center is based on the collaboration of many universities and Saga Prefecture Government, and the close collaboration between the Kyushu Synchrotron Light Research Center belonging to the Saga Prefecture Government and the Synchrotron Light Application Center of Saga University plays an important role. We have also good collaborations with domestic and foreign universities, and also partnerships with synchrotron light facilities in the world. We hope to create venture companies from the partnership with facilities in Saga university such as Venture Business Laboratory.

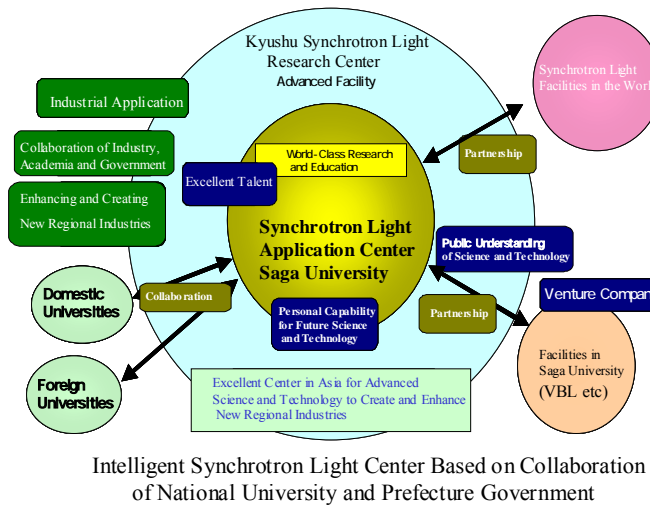


FIGURE 2. Schematic picture showing Saga synchrotron light project

BEAM LINES AND SYNCHROTRON LIGHT APPLICATION

There are two application fields of SL. One is the application for material developments. Using Lithography, CVD and LIGA technologies, we can develop the LSI, 3D-electronic devices, and micro-machine, respectively. Another application is to use SL for advanced analyses. Using SL for surface and interface analyses, protein crystallography, and trace analyses, we can know important information for nano-technology, bio-technology, and environment and intelligent function materials, respectively.

Table I shows the list of the beamlines that have been constructed in Saga. There are 3 prefecture beamlines for industry applications, and one university beamline for academic use. The BL9 aims applications for material development. The BL9 can cover the VUV region and a white light region for irradiation and fabrication of materials. The BL12 is used for soft x-rays applications to precise analyses. The BL12 can provide soft x-rays for photoelectron spectroscopy and EXAFS analyses. The BL15 aims hard x-rays applications, and then BL15 covers the hard X-rays for XAFS, Diffraction, Scattering and Imaging. These beamlines are ready for uses after recent efforts in construction. Many users from Industries, Universities, and Institutes are welcome to activate and encourage the economics and young persons in the Saga/Kyushu areas.

Besides these open beamlines, the Synchrotron Light Application Center of Saga University has also constructed a soft x-rays beamline BL13 for advanced researches on nano-surface and interface of semiconductors as well as education. The center has been carrying out academic subjects using advantage of SL. The center is interested in the new frontier fields such as non-thermal process and photo-CVD, advanced analyses, creation of combination system between semiconductors and bio-specimens, basic and application in environmental and material science, and so on as well as the industrial application with SL. The useful and powerful SL may produce wide variety of applications.

TABLE 1. List of beamlines

	Beamline No.	Energy Range	Main Methods
Industry Application	BL9(Saga Pref.)	10 ~ 50 eV White Light	Irradiation for thin film growth Fabrication using Etching
	BL12(Saga Pref.)	40 ~ 1000 eV	Photoelectron Spectroscopy XAFS
	BL15(Saga Pref.)	2.1 ~ 10 keV	XAFS Diffraction, Scattering Imaging
Academic Use	BL13 (Saga-Univ.)	30 ~ 800 eV	High resolution Photoelectron Spectroscopy, Combination of SL and Laser

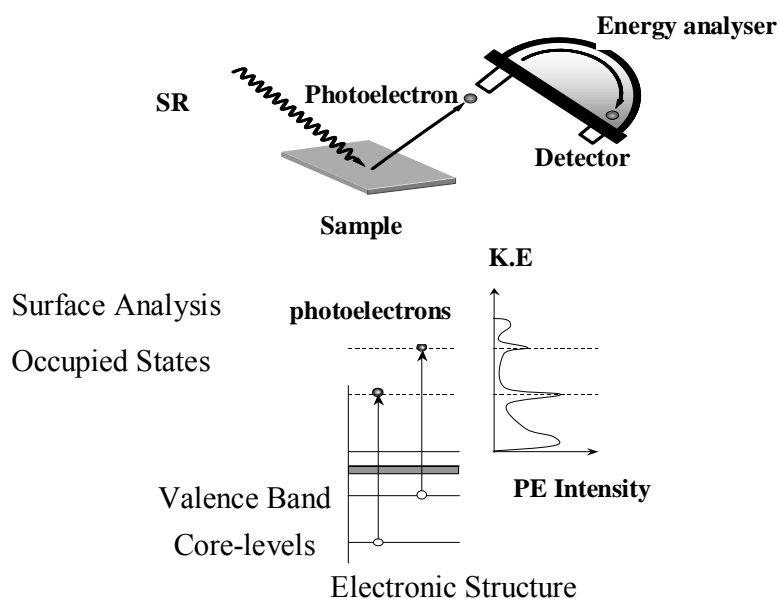


FIGURE 3. Application of synchrotron light for photoelectron spectroscopy.

Figure 3 shows the application for precise analyses by using soft X-rays. Using SL and energy analyzer, we can get useful information of surface and occupied states from the photoelectron spectroscopy. The photoelectron spectroscopy is very powerful to know the electronic states of various materials used in industries and is a necessary method to promote nano-technology. Figure 4 shows scheme of university beamline BL13. This consists of two branches. Both of them consist of several mirrors and gratings. SL from a dipole magnet is introduced to the photoelectron and luminescence spectroscopy station, while undulator radiation is used at high-resolution photoelectron spectroscopy station. We will conduct the study for dynamics on nano-scale surface and interfaces using SL and laser.

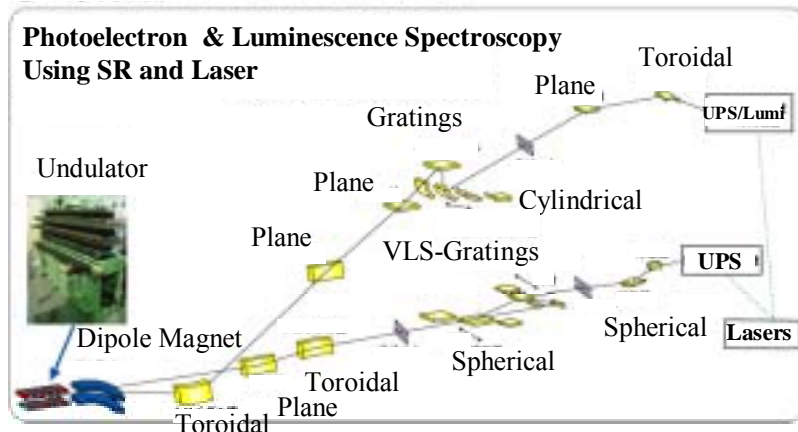


FIGURE 4. The scheme of university beamline BL13.

PRESENT PICTURES AND FUTURE PROSPECT

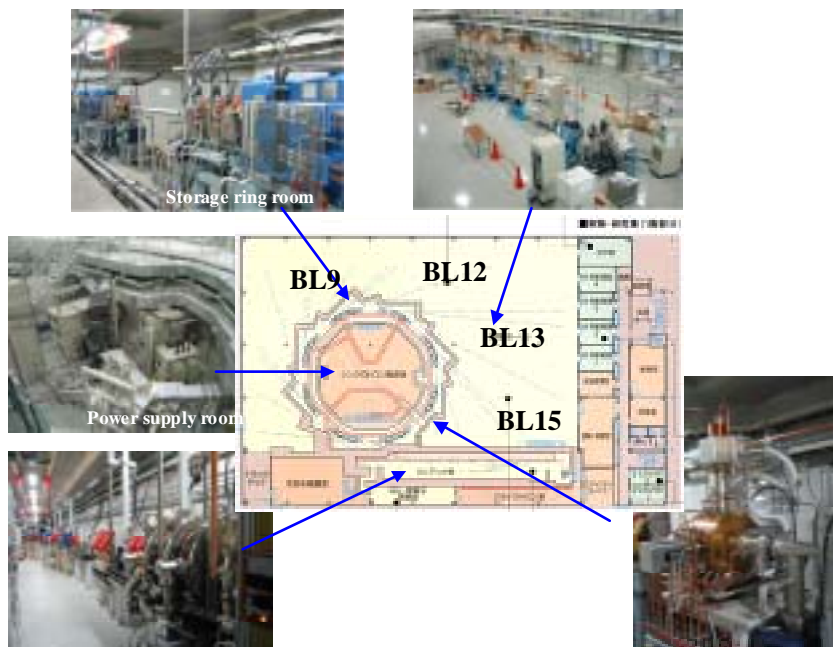


FIGURE 5. Recent pictures of LINAC, Synchrotron, and BL13.

The recent pictures are shown in Figure 5. There are the injector LINAC that has 250 MeV in energy, the power supply for RF cavity in the center of the Saga-ring, the RF cavity located in the storage-ring room. In the storage ring, there are straight sections for insertion devices. Outside the storage-ring room, the university beamline BL13 is seen, the distance of which is about 36 m, indicating capability of the high-resolution spectroscopy.

In summary, Saga-LS has been constructed under the collaboration of Saga University and Saga Prefecture Government with many supports in Kyushu Island and becomes operational. Three beamlines for industrial application and one beamline for academic researches are ready for users. Saga is expected to be a good place for SL applications to create new industry, advanced researches and educations as well as international collaborations in Asian countries. The promotion of new industries and local developments in the Saga/Kyushu area are strongly expected.

ACKNOWLEDGMENTS

We would like to thank the Saga Prefecture Government for its effort to construction of accelerators, and also thank many scientists and engineers working in the existing synchrotron radiation facilities, universities, and companies for their kind and useful information about recent SL-related technologies.

Electromagnetic Characteristics of Grid Structures for Scattering Fields of Nano-meter Electromagnetic Waves and X-rays

Yasumitsu Miyazaki

Department of Electronics and Information Engineering, Aichi University of Technology
50-2 Manori, Nishihazama-cho, Gamagori, 443-0047 Japan

Abstract

Medical image diagnosis using X-rays is very important technical tools for physiological examination of human body. Image responses of X-ray projection include X-ray scattering characteristics that disturb X-ray transmission properties through biological structures. In this paper, technical methods of spatial filtering for X-ray scattering are discussed to improve image diagnosis. Statistical theory of X-ray is described for X-ray propagation, attenuation and scattering in random inhomogeneous biological media. Spatial filtering characteristics of grid structure are shown for exact image X-ray projection excluding scattering effects through physiological media.

Introduction

X-ray, that is, nano-meter electromagnetic wave is very important physical tool for medical diagnosis and recently automatic image diagnosis using X-ray is rapidly developed^[1]. However, image processing for medical diagnosis, based on photo-electric absorption, interactions between electrons and photons of X-ray, Thomson scatterings and Compton scatterings that are physiological and physical phenomena of X-rays in biomedical media are not so much studied^[2-4]. The spatial characteristic in the received X-ray image is determined by the intensity of transmitted waves with scattered waves. The characteristics of transmitted waves depend on both the absorption and scattering characteristics. Therefore, for the identification of the characteristics of biomedical media by X-ray transmission, signal to noise ratio of primitive X-ray diagnosis is not so high. Although the use of the grid is efficient to remove the scattering wave from the transmitting wave, the grid has not been studied sufficiently. Also, by using spatial grid filter and the characteristics of scattering, absorption, dispersion and spectroscopy properly, it may be possible to find more accurate new method of X-ray image diagnosis. In this paper, the electromagnetic wave characteristics, primarily, the scattering filter characteristics of X-ray beam using the grid are studied. Based on this analysis, the optimum scattering wave filter may be found.

Statistical theory of X-ray propagation in random media is discussed by integral equations with Green's function, using correlation functions of random media. Scattering characteristics of incident Gaussian beam in random physiological media consisting of biological materials such as proteins. Electromagnetic filtering properties by X-ray waveguides with lossy wall for off-axial scattered fields are discussed using impedance characteristics of waveguides consisting of lossy metal walls.

Electromagnetic X-Ray Fields in Biological Random Media

X-rays, nanometer electromagnetic waves are incident on random media (I) ($0 \leq z \leq \ell$). Incident X-ray has y-direction linearly polarization $\mathbf{E} = \phi(x, z)\mathbf{i}_y$. Biological random media have dielectric constants as

$$\varepsilon_t = \varepsilon + \varepsilon\Delta\eta(\mathbf{r}_t) \quad (1)$$

where $\Delta\eta$ is random function and $\varepsilon = \varepsilon' - j\varepsilon''$. Here, $\mathbf{r}_t = x\mathbf{i}_x + z\mathbf{i}_z$, and we consider two dimensional scattering fields. The field function $E(x, z)$ concerned with electric field satisfies the following wave equations, using $k^2 = \omega^2\varepsilon\mu = (k_r - jk_i)^2$

$$\nabla_{xy}^2 E(\mathbf{r}_t) + k^2 E(\mathbf{r}_t) = -\omega^2 \varepsilon \Delta\eta E(\mathbf{r}_t) \quad (2)$$

Incident Gaussian X-ray of $\mathbf{E}^{inc} = E_{inc}(\mathbf{r}_t)\mathbf{i}_y$

$$\mathbf{E}_{inc}(\mathbf{r}_t) = \mathbf{i}_y \frac{A}{\sqrt{1-j\varsigma}} e^{-jk(z+z_0)} e^{-\frac{x^2}{x_0^2(1-j\varsigma)}} \quad (3)$$

where beam parameters are $\varsigma = \frac{2(z+z_0)}{kx_0^2}$, beam waist is $z = -z_0$, and beam spot size is x_0 .

Green's function $G(\mathbf{r}_t, \mathbf{r}'_t)$ for free space is

$$G(\mathbf{r}_t, \mathbf{r}'_t) = -\frac{j}{4} H_0^{(2)}(k|\mathbf{r}_t - \mathbf{r}'_t|) \quad (4)$$

G satisfies the following wave equation

$$\nabla_t^2 G + k^2 G = -\delta(\mathbf{r}_t - \mathbf{r}'_t) \quad (5)$$

Applying Green's formula in random biological media (I) for $E_{tot} = E_{scatt} + E_{inc}$ and G ,

$$\int (G\nabla_i^2 E - E\nabla_i^2 G) dS = \oint \left\{ G \frac{\partial E}{\partial n} - E \frac{\partial G}{\partial n} \right\} dS \quad (6)$$

We have when $\underline{\Gamma} = G\underline{I}$, using unit dyad \underline{I} ,

$$E_{tot} = E_{inc} - \frac{j}{4} \int_{S_I} dS' (\omega^2 \epsilon \Delta \eta) E_{tot}(\mathbf{r}_t, \mathbf{r}'_t) H_0^{(2)}(k|\mathbf{r}_t - \mathbf{r}'_t|) \quad (7)$$

$$\mathbf{E}_{tot} = \mathbf{E}_{inc} + \int k^2 \Delta \eta \underline{\Gamma}(\mathbf{r}_t, \mathbf{r}'_t) \cdot \mathbf{E}(\mathbf{r}'_t) dS' \quad (8)$$

$$\text{From Maxwell's equation } \mathbf{H} = \frac{1}{(-j\omega\mu)} \nabla \times \mathbf{E},$$

magnetic field is derived as, $\mathbf{H}_{inc} = \frac{j}{\omega\mu} \nabla \times \mathbf{E}_{inc}$

$$\mathbf{H}_{tot} = \mathbf{H}_{inc} - \frac{1}{j\omega\mu} \int k^2 \Delta \eta \nabla \times \underline{\Gamma} \cdot \mathbf{E} dS' \quad (9)$$

when $\mathbf{E} = E \mathbf{i}_y$, $\mathbf{H} = \frac{1}{j\omega\mu} \mathbf{i}_y \times \nabla \mathbf{E}_y$, we have

$$\frac{1}{-j\omega\mu} \nabla \times \underline{\Gamma} = \frac{1}{j\omega\mu} (\mathbf{i}_y \times \nabla G) \mathbf{i}_y$$

Scattered Fields in Random Media

Based on the fundamental equations (8) and (9) in the previous section, we calculate the scattered field by iterative method in this section. Employing the representation of functional analysis, we can solve the integral equations (8) and (9) in operator forms. If we define vectors \mathbf{E}_0 and \mathbf{E} in functional space for the vectors \mathbf{E}_{inc} and \mathbf{E} , and integral operator K_E for the integral $\int k^2 \Delta \eta \underline{\Gamma} \cdot dS'$, we obtain the field as follows:

$$\mathbf{E} = (\mathbf{I} - K_E)^{-1} \mathbf{E}_0 = \mathbf{E}_0 + K_E \mathbf{E}_0 + K_E K_E \mathbf{E}_0 + \dots \quad (10)$$

Using the similar definition for the magnetic field and eq. (9), we have

$$\mathbf{H} = \mathbf{H}_0 + K_H \mathbf{E} = \mathbf{H}_0 + K_H \mathbf{E}_0 + K_H K_E \mathbf{E}_0 + K_H K_E K_E \mathbf{E}_0 + \dots \quad (11)$$

Equations (10) and (11) express the total electromagnetic field. The optical intensity, which is the most important quantity in the optical range, *i.e.*, the mean intensity of the energy flow in the harmonic electromagnetic field is given by the real part of the complex Poynting vector $\bar{\mathbf{S}} = \frac{1}{2} \mathbf{E} \times \mathbf{H}^*$.

$$\mathbf{I} = \operatorname{Re} \bar{\mathbf{S}} = \frac{1}{2} \operatorname{Re} (\mathbf{E} \times \mathbf{H}^*) \quad (12)$$

The conjugate of the vector \mathbf{H} is indicated by the sign \mathbf{H}^* .

Consequently, the optical intensity as shown as

$$\mathbf{I} = \frac{1}{2} \operatorname{Re} \left\{ (\mathbf{E}_0 \times \mathbf{H}_0^*) + \mathbf{E}_0 \times (K_H \mathbf{E}_0)^* + (K_E \mathbf{E}_0) \times \mathbf{H}_0^* + K_E \mathbf{E}_0 \times (K_H \mathbf{E}_0)^* + (K_E K_E \mathbf{E}_0) \times \mathbf{H}^* + \mathbf{E}_0 \times (K_H K_E \mathbf{E}_0)^* + \dots \right\} \quad (13)$$

The first term of the right hand side in eq. (13) means the optical intensity of the incident wave. The succeeding terms show the light scattering. Particularly, the terms containing multiple K_s' such as $(K_H K_E \mathbf{E}_0)^*$ and $(K_E K_E \mathbf{E}_0)$ imply the multiple scattering due to inhomogeneities.

First order scattered fields corresponding to $K_E \mathbf{E}_0$ in eq. (10) and $K_H \mathbf{E}_0$ in eq. (11) are

$$\mathbf{E}_{scatt} = -\frac{j}{4} k^2 \int \Delta \eta(\mathbf{r}_t') H_0^{(2)}(k|\mathbf{r}_t - \mathbf{r}'_t|) E_{inc}(\mathbf{r}'_t) \mathbf{i}_y dS', \quad \mathbf{H}_{scatt} = -\frac{j}{4} \frac{k^3}{\omega\mu} \int \Delta \eta(\mathbf{r}'_t) H_0^{(2)}(k|\mathbf{r}_t - \mathbf{r}'_t|) (\mathbf{n}(\mathbf{r}'_t) \times E_{inc}(\mathbf{r}'_t)) \mathbf{i}_y dS' \quad (14)$$

The second order scattered fields corresponding to $K_E K_E \mathbf{E}_0$, and $K_H K_E \mathbf{E}_0$ are

$$\begin{aligned} \mathbf{E}_{scatt} &= \left(-\frac{j}{4} k^2 \right)^2 \mathbf{i}_y \iint \Delta \eta(\mathbf{r}'') \Delta \eta(\mathbf{r}'') H_0^{(2)}(k|\mathbf{r}'_t - \mathbf{r}''_t|) H_0^{(2)}(k|\mathbf{r}_t - \mathbf{r}'_t|) E_{inc}(\mathbf{r}'') dS' dS'' \\ \mathbf{H}_{scatt} &= \left(-\frac{j}{4} \frac{k^3}{\omega\mu} \right) \left(-\frac{j}{4} k^2 \right) \iint \Delta \eta(\mathbf{r}'') H_0^{(2)}(k|\mathbf{r}'_t - \mathbf{r}''_t|) (\mathbf{n}(\mathbf{r}'') \times \mathbf{i}_y) \Delta \eta(\mathbf{r}'') H_0^{(2)}(k|\mathbf{r}_t - \mathbf{r}''_t|) E_{inc}(\mathbf{r}'') dS' dS'' \end{aligned} \quad (15)$$

In case the distance $|\mathbf{r}_t - \mathbf{r}'_t|$ of the observation point from the sample is large compared with the wavelength, *i.e.*, $k|\mathbf{r}_t - \mathbf{r}'_t| \gg 1$, the Green's dyadic $\underline{\Gamma}$ can be asymptotically evaluated,

$$\underline{\Gamma} = G\underline{I} = \sqrt{\frac{2}{\pi k |\mathbf{r}_t - \mathbf{r}'_t|}} e^{-j(k|\mathbf{r}_t - \mathbf{r}'_t| \frac{\pi}{4})} \quad (16)$$

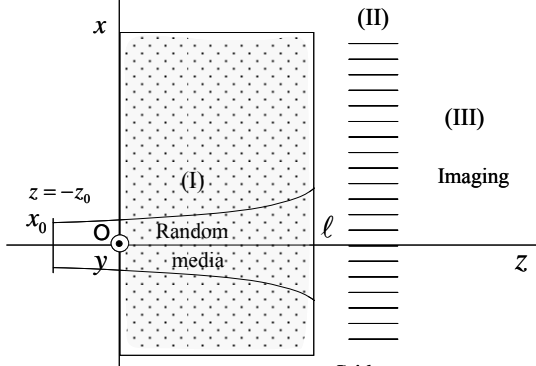


Fig.1: X-ray scattering and X-ray grid arrays

The unit vector \mathbf{n}' are directed from the point in the sample toward the point of observation and given by $\mathbf{n}' = \mathbf{n}(\mathbf{r}_t') = (\mathbf{r}_t - \mathbf{r}_t')/|\mathbf{r}_t - \mathbf{r}_t'|$. With the help of eq. (14), the integral operation K_E of $K_E \mathbf{E}_0$ in eqs. (10), (11) and (13) is described as asymptotic fields,

$$K_E \mathbf{E}_0 \approx -\left(\frac{j}{4}\right) \int k^2 \Delta \eta \sqrt{\frac{2}{\pi k |\mathbf{r}_t - \mathbf{r}_t'|}} e^{-j(k|\mathbf{r}_t - \mathbf{r}_t'| - \frac{\pi}{4})} (E_{inc} \mathbf{i}_y) dS' \quad (17)$$

Similarly, the integral operation K_H of $K_H \mathbf{E}_0$ is given by

$$K_H \mathbf{E}_0 \approx -\frac{k}{\omega \mu} k^2 \left(\frac{j}{4}\right) \int \Delta \eta \sqrt{\frac{2}{\pi k |\mathbf{r}_t - \mathbf{r}_t'|}} e^{-j(k|\mathbf{r}_t - \mathbf{r}_t'| - \frac{\pi}{4})} (\mathbf{n}' \times E_{inc} \mathbf{i}_y) dS' \quad (18)$$

Hence, the dominant term of the scattered field in the inhomogeneous medium, $\frac{1}{2} \operatorname{Re}(K_E \mathbf{E}_0 \times (K_H \mathbf{E}_0)^*)$, can be written as

$$\frac{1}{2} \operatorname{Re}(K_E \mathbf{E}_0 \times (K_H \mathbf{E}_0)^*) = \frac{k}{\omega \mu} \left(\frac{k^2}{4}\right)^2 \frac{2}{\pi k} \operatorname{Re} \iint \frac{e^{-jk_r |\mathbf{r}_t - \mathbf{r}_t'| + jk_r |\mathbf{r}_t - \mathbf{r}_t''|}}{\sqrt{|\mathbf{r}_t - \mathbf{r}_t'| |\mathbf{r}_t - \mathbf{r}_t''|}} e^{-k_t |\mathbf{r}_t - \mathbf{r}_t'|} e^{-k_t |\mathbf{r}_t - \mathbf{r}_t''|} \Delta \eta(\mathbf{r}') \Delta \eta^*(\mathbf{r}'') \mathbf{n}'' E'_{inc} E''_{inc} dS' dS'' \quad (19)$$

where we define $\mathbf{E}'_0 = \mathbf{E}_0(\mathbf{r}')$, $\mathbf{E}''_0 = \mathbf{E}_0(\mathbf{r}'')$ and $\mathbf{n}'' = \mathbf{n}(\mathbf{r}_t, \mathbf{r}_t'') = (\mathbf{r}_t - \mathbf{r}_t'')/|\mathbf{r}_t - \mathbf{r}_t''|$. These equations are the fundamental formulae for the scattered field. In the next section the statistical properties of these equations are discussed.

Statistical Properties of Scattered Field in Random Media

The scattered field intensity of the incident wave \mathbf{E}_0 due to inhomogeneities $\Delta \eta$ in the medium is obtained from eq. (13). If the statistical average $\langle \Delta \eta \rangle$ of fluctuations in the sample is equal to zero, the first order terms $\langle \mathbf{E}_0 \times (K_H \mathbf{E}_0)^* \rangle$ and $\langle (K_E \mathbf{E}_0) \times \mathbf{H}_0^* \rangle$ in eq. (13) vanish. The symbol $\langle \rangle$ indicates an ensemble average.

In order to be able to perform the integration of the second order terms we have to know the average value of the product $\Delta \eta(\mathbf{r}') \Delta \eta(\mathbf{r}'')$ in which the first fluctuation is measured in a point \mathbf{r}' and the second in another point \mathbf{r}'' . In the case of stationary fluctuations we shall obtain this average by letting the measuring stick $(\mathbf{r}', \mathbf{r}'')$ take up all possible positions and orientations within the scattering medium. We shall here consider only the isotropic case. In this case the product in question will be a function of the distance $|\mathbf{r}' - \mathbf{r}_t''|$ only. For $|\mathbf{r}' - \mathbf{r}_t''| = 0$, this product takes the value

$$\langle \Delta \eta \Delta \eta \rangle = \overline{\Delta \eta^2} \quad (20)$$

For large values of the distance $|\mathbf{r}' - \mathbf{r}_t''|$ the product obviously tends to zero. We now introduce the correlation function by the definition

$$\langle \Delta \eta(\mathbf{r}') \Delta \eta(\mathbf{r}'') \rangle = B_\eta(\mathbf{r}' - \mathbf{r}'') \quad (21)$$

Consequently, from eq. (13) the statistical average of the total field is expressed as

$$\langle \mathbf{I} \rangle = \mathbf{I}_0 + \frac{1}{2} \operatorname{Re} \langle K_E \mathbf{E}_0 \times (K_H \mathbf{E}_0)^* + \mathbf{E}_0 \times (K_H K_E \mathbf{E}_0)^* + (K_E K_H \mathbf{E}_0) \times \mathbf{H}_0^* + \dots \rangle + \dots \quad (22)$$

where $\mathbf{I}_0 = \frac{1}{2} \operatorname{Re}(\mathbf{E}_0 \times \mathbf{H}_0^*)$ is the intensity of the incident wave and the second term indicates the scattering intensity. For weakly fluctuated medium the second order term $\langle K_E \mathbf{E}_0 \times (K_H \mathbf{E}_0)^* \rangle$ provides the dominant contribution to the total scattering and higher order terms of the multiple scattering concerned with higher order correlations of the inhomogeneities can be neglected. The multiple scattering, which in strongly fluctuated medium contributes to the total scattering, will be evaluated in the subsequent paper. In this paper we study the dominant term of the X-ray scattering, which leads to the following total intensity $\langle \mathbf{I} \rangle$

$$\langle \mathbf{I} \rangle \approx \mathbf{I}_0 + \frac{1}{2} \operatorname{Re} \langle K_E \mathbf{E}_0 \times (K_H \mathbf{E}_0)^* \rangle \quad (23)$$

If the observation point is far from the sample and the condition $|\mathbf{r}_t - \mathbf{r}_t'| \gg \rho_t = |\mathbf{r}_t - \mathbf{r}_t''|$ is satisfied it is then convenient to use a Taylor expansion of $\mathbf{n}'' - \mathbf{n}'$ in the terms of the distance vector between two different points \mathbf{r}' and \mathbf{r}'' in the sample. In this case we can write approximately the scattered field in eq. (19) as follows:

$$\langle \mathbf{I}_s \rangle \approx \frac{k}{\omega \mu} \left(\frac{k^2}{4}\right)^2 \frac{2}{\pi k} \operatorname{Re} \iint \frac{e^{-jk_r |\mathbf{r}_t - \mathbf{r}_t'| + jk_r |\mathbf{r}_t - \mathbf{r}_t''|}}{\sqrt{|\mathbf{r}_t - \mathbf{r}_t'| |\mathbf{r}_t - \mathbf{r}_t''|}} e^{-k_t |\mathbf{r}_t - \mathbf{r}_t'|} e^{-k_t |\mathbf{r}_t - \mathbf{r}_t''|} B_\eta(\mathbf{r}', \mathbf{r}'') \mathbf{n}'' E'_{inc} E''_{inc} dS' dS'' \quad (24)$$

This gives the scattered field derived, with the help of the Green's dyadic, for the autocorrelation function $B_\eta(\mathbf{r}', \mathbf{r}'')$ of random inhomogeneities and an arbitrary incident wave \mathbf{E}_{inc} .

Statistical Average of X-ray Beam Scattering

The X-ray beam is assumed to be the Gaussian TEM₀₀ mode. TEM₀₀ mode decays rapidly with increasing the trans-

verse distance from the beam center. If beam has a beam width x_0 and a plane phase front at the beam waist $z = -z_0$, and is linearly polarized in the transverse direction of \mathbf{i}_y , the field at any given point can be written in coordinates (x,z) as

$$\mathbf{E}_{inc}(\mathbf{r}) = \mathbf{i}_y \frac{A}{\sqrt{1 - j \frac{2(z + z_0)}{kr_0}}} e^{-jk(z+z_0)} \exp \left\{ -\frac{j2x^2(z + z_0)}{kx_0^4 \left\{ 1 + \frac{4(z + z_0)^2}{(kx_0^2)^2} \right\}} \right\} \exp \left\{ -\frac{r^2}{x_0^2 \left\{ 1 + \frac{4(z + z_0)^2}{(kx_0^2)^2} \right\}} \right\} \quad (25)$$

The first exponential factor describes the phase of a plane wave and the second exponential factor is responsible for phase front curvature. The last exponential factor determines the intensity in the transverse direction.

Taylor expansions as $|\mathbf{r}_t - \mathbf{r}'_t| = |\mathbf{r}_t - \mathbf{r}'_t| + \mathbf{n}' \cdot \mathbf{p}_t + \frac{1}{2|\mathbf{r}_t - \mathbf{r}'_t|} \{\mathbf{p}'_t - (\mathbf{p}_t \cdot \mathbf{n}')^2\} + \dots$, $\mathbf{r}'^2 = \mathbf{r}'^2 + \mathbf{p}_t \cdot \mathbf{i}_z (2\mathbf{r}' - \mathbf{p}_t) \cdot \mathbf{i}_t - 2\mathbf{r}' \cdot \mathbf{p}_t + \mathbf{p}_t^2$,

$\mathbf{n}' = \mathbf{n}_0 + \{\mathbf{n}_0(\mathbf{n}_0 \cdot \mathbf{r}') - \mathbf{r}'\}/|\mathbf{r}'|$ and $\mathbf{p}_t = \mathbf{r}' - \mathbf{r}''$, $\mathbf{n}(o) = \mathbf{n}_0$. We have scattered field intensities in random media, as

$$\langle \mathbf{I}_s \rangle \equiv \frac{k}{\omega\mu} \left(\frac{k^2}{4} \right)^2 \frac{2}{\pi k} \operatorname{Re} \iint \frac{e^{jk_r(\mathbf{n}' \cdot \mathbf{i}_z)\mathbf{p}_t}}{|\mathbf{r}_t - \mathbf{r}'_t|} e^{-k_r(\mathbf{n}' \cdot \mathbf{i}_z)\mathbf{p}_t} B_\eta(\mathbf{p}) \mathbf{n}' A^2 g(k_i |\mathbf{r}_t - \mathbf{r}'_t|) e^{-2k_i(z'+z_0)} \frac{e^{-\frac{2x^2}{x_0^2(1+\zeta_0^2)}}}{\{1 + \zeta_0^2\}^{1/2}} f(\mathbf{p}_t, \mathbf{r}'_t) d^2 \mathbf{r}' d^2 \mathbf{p}_t \quad (26)$$

where $g(k_i |\mathbf{r}_t - \mathbf{r}'_t|) = e^{-2k_i |\mathbf{r}_t - \mathbf{r}'_t|}$, inside random media of \mathbf{r}_t , $= 1$, outside

$f(\mathbf{p}_t) = \exp[-\{\mathbf{p}_t^2 - 2\mathbf{r}'_t \cdot \mathbf{p}_t + \mathbf{p}_t \cdot \mathbf{i}_z (2\mathbf{r}'_t - \mathbf{p}_t)\} \mathbf{i}_z]/x_0^2 \{1 + j(2z_0/(kx_0^2))\}$, and $\zeta_0 = 2z_0/kx_0^2$. When the correlation function is $B_\eta(\mathbf{p}_t) = \overline{\Delta \eta^2} e^{-\rho^2/\rho_0^2}$, where parameters $\overline{\Delta \eta^2}$ and ρ_0 give the variances and correlation lengths of fluctuations,

$$\int B_\eta(\mathbf{p}_t) e^{jk_r(\mathbf{n}' \cdot \mathbf{i}_z)\mathbf{p}_t} d^2 \mathbf{p}_t = \overline{\Delta \eta^2} \rho_0^2 \pi e^{-\frac{-k_r^2 \rho_0^2 (\frac{1-\mathbf{n}' \cdot \mathbf{i}_z}{2})}{2}} \quad (27)$$

$$(1 - \mathbf{n}' \cdot \mathbf{i}_z) = (1 - (z - z')/|\mathbf{r}'_t|) - (z - z')(rr' \cos(\theta - \theta') + zz')/|\mathbf{r}'_t|^3 + (z - z')(r'^2 + z'^2)/2|\mathbf{r}'_t|^3 + \dots$$

From eq. (26), (27), when $\rho_0 < x_0$, length of random media ℓ , we have for the cylindrical coordinate (r, θ) assuming $g(k_i |\mathbf{r}_t - \mathbf{r}'_t|) = e^{-2k_i |z_t - z'|}$ in random media of $0 \leq z \leq z_t$,

$$\langle \mathbf{I}_s \rangle = \mathbf{i}_r \frac{k}{\omega\mu} \left(\frac{k^2}{4} \right)^2 \frac{\sqrt{2\pi}}{k} A^2 \overline{\Delta \eta^2} x_0 \rho_0^2 \frac{\ell}{|\mathbf{r}|} e^{-k_r^2 \rho_0^2 \sin^2 \frac{\theta}{2}} = \mathbf{i}_r \frac{k}{\omega\mu} \frac{\sqrt{2\pi}}{16} \overline{\Delta \eta^2} A^2 k^3 x_0 \rho_0^2 \frac{1}{|\mathbf{r}|} e^{-k_r^2 \rho_0^2 \sin^2 \frac{\theta}{2}} e^{-2k_i(z_t + z_0)} z_\ell \quad (28)$$

Electromagnetic Characteristics in Grid Waveguides

Electromagnetic characteristics of X-ray and nano-meter electromagnetic waves in waveguide arrays consisting of grid structures are expressed by mode expansions of lossy modes. In the region (II) of grid arrays, propagation spaces are

$$z_{g1} \leq z \leq z_{g2}, \quad -\frac{a}{2} + s(a+d) \leq x \leq \frac{a}{2} + s(a+d), \quad s = -m, -(m-1), \dots, -1, 0, 1, \dots, m-1, m \quad (29)$$

and lossy metal materials for X-rays are

$$z_{g1} \leq z \leq z_{g2}, \quad \frac{a}{2} + s(a+d) \leq x \leq \frac{a}{2} + d + s(a+d) \quad (30)$$

when $\psi_n = A \cos \left(\frac{n\pi}{a} \left(x + \frac{a}{2} \right) \right)$ for, $-a/2 + s(a+d) \leq x \leq a/2 + s(a+d)$,

0 for $a/2 + s(a+d) \leq x \leq a/2 + d + s(a+d)$, $A = \sqrt{2/a}$, and $h_n = n\pi/a$, fields in waveguide are

$$H_z = \sum B_n h_n^2(x) e^{j\omega t - \gamma_n z} \quad (31)$$

$$E_y = j\omega \mathbf{i}_z \times \sum_{n=1}^{\infty} B_n \nabla_z \psi_n e^{j\omega t - \gamma_n z} = j\omega \mu \sum_{n=1}^{\infty} B_n \left(-\frac{n\pi}{a} \right) A \sin \frac{n\pi}{a} \left(x + \frac{a}{2} \right) e^{j\omega t - \gamma_n z}$$

$$H_x = -\sum_{n=1}^{\infty} B_n \gamma_n \nabla_z \psi_n e^{j\omega t - \gamma_n z} = -\sum_{n=1}^{\infty} B_n \gamma_n \left(-\frac{n\pi}{a} \right) \sin \frac{n\pi}{a} \left(x + \frac{a}{2} \right) e^{j\omega t - \gamma_n z}$$

X-ray intensity can be expressed as mode expansions

$$P = \frac{1}{2} \operatorname{Re} \int \mathbf{i}_z \cdot \mathbf{E}_t \times \mathbf{H}_t^* dS$$

In case of lossy waveguide walls of conductivity σ , impedance boundary condition is $\mathbf{n} \times \mathbf{E} = \frac{1}{2} \delta \mu \omega (1+j) \mathbf{H}$,

$\delta = \sqrt{2/\omega\mu\sigma}$, propagation constant $\beta_n = \beta_n^{(r)} - j\beta_n^{(i)}$ are derived as perturbations from waveguide modes for perfect conductivity, when $R_s = \sqrt{\frac{\omega\mu}{2\sigma}}$, $\varsigma = \sqrt{\frac{\mu}{\epsilon}}$,

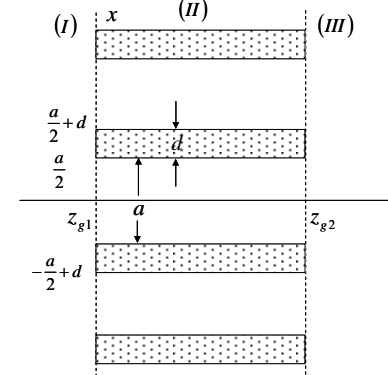


Fig. 2: Grid structure for scattering filtering

$$\beta_n^{(r)} = \sqrt{k^2 - \left(\frac{n\pi}{a}\right)^2}, \quad \beta_n^{(i)} = \frac{R_s}{\varsigma a} \frac{2k(h_n/k)^2}{\sqrt{k^2 - h_n^2}} \quad (32)$$

Hence, we have

$$\gamma_n = j\beta_n^{(r)} + \beta_n^{(i)}, \quad P = \frac{1}{2} \omega \mu \sum_{n=1}^{\infty} |B_n| \beta_n^{(r)} \left(\frac{n\pi}{a}\right)^2 e^{-\beta_n^{(i)} z} \quad (33)$$

Using large attenuation constants of higher modes, spatial filtering of incident off-axis scattered fields can be estimated.

Scattered Field Filtering by Grid Waveguides

When scattered fields in random media expressed by eq. (8),(9), and (14) are incident to grid waveguides, off-axis scattered fields with large scattering angles excite higher modes in grid waveguides and attenuate rapidly in grid waveguides with lossy walls. Spatial filtering corresponding to higher mode attenuation in lossy grid waveguides can be evaluated by mode coefficients in grid waveguides.

Incident waves at the input of the grid waveguide are described by mode coefficients as, from eq. (8), at surface $S_{g1}^{(s)}$

$$B_n^{(s)} = B_n^{(s),inc} + B_n^{(s),scatt}, \quad B_n^{(s),inc} = \frac{1}{C_n} \int_{S_{g1}^{(s)}} [E_{inc}(\mathbf{r}'')] \sin \frac{n\pi}{a} \left(x_s''' + \frac{a}{2}\right) dS''' \quad (34)$$

$$B_n^{(s),scatt} = \frac{1}{C_n} \int_{S_{g1}^{(s)}} \left[-\frac{j}{4} k^2 \int \Delta \eta(\mathbf{r}') H_0^{(2)}(k|\mathbf{r}''' - \mathbf{r}'|) E_{inc}(\mathbf{r}') dS' \right] \sin \frac{n\pi}{a} \left(x_s''' + \frac{a}{2}\right) dS'''$$

where $C_n = j\omega\mu \left(-\frac{n\pi}{a}\right) A \frac{a}{2}$, surface $S_{g1}^{(s)}$ is $z = z_{g1}$, $-a/2 + s(a+d) \leq x \leq a/2 + s(a+d)$, $x_s''' = x''' + s(a+d)$.

Mode power characteristics are shown as statistical coefficients as, from eq. (33), $\langle |B_n^{(s)}|^2 \rangle = |B_n^{(s),inc}|^2 + \langle |B_n^{(s),scatt}|^2 \rangle$,

$$\text{where } \langle |B_n^{(s),scatt}|^2 \rangle = \frac{1}{|C_n|^2} \iint_{S_{g1}^{(s)}} \iint \langle E_{scatt}(\mathbf{r}'', \mathbf{r}') E_{scatt}^*(\mathbf{r}''', \mathbf{r}') \rangle dS' dS'' \sin \frac{n\pi}{a} \left(x_s''' + \frac{a}{2}\right) \sin \frac{n\pi}{a} \left(x_s''' + \frac{a}{2}\right) dS''' dS'''$$

Spectral Method of Grid Filtering

To obtain the electromagnetic filtered and transmitting fields with X-rays incident on the grid, the electromagnetic boundary value problem is considered using filter grid shown in fig. 3. The grid structure consists of atoms arranged periodically in x- and z-directions in the inner region II with grid material region $II^{(1)}$ and grid space region $II^{(2)}$. In fig. 3, the X-ray incidents on the grid input boundary $z = z_{g1}$ in exterior region I and the characteristics of filtered and transmitting waves in exterior region III are investigated for the nano-meter electromagnetic waves, the grid material $II^{(1)}$ has complex dielectric constant due to the periodic structure of the atoms. In this case, the complex dielectric constant is considered to be periodic in x- and z-directions.

In case of y-polarized nano-meter electromagnetic wave, the electromagnetic fields in the grid region $II^{(1)}$ are analyzed by using periodic Fourier expansions in x- and z-directions. The y-polarized plane wave propagating toward z-direction is considered as an incident wave. In each region, the electromagnetic fields are expressed as integral representation with respect to the spectrum α of z-direction using spectral functions. Hence, all the electromagnetic fields can be derived from the spectral functions determined by boundary conditions. The component unit of grid ($d \times \ell_z$) is arranged along x-direction with a period $T=a+d$. The transmitted and filtered field in region III are determined using the boundary condition at the boundary of the grid $z = z_{g2}$. The tangential component of the electromagnetic fields should be continuous at the boundaries $z = z_{g1}, z_{g2}$ and $x = \pm a/2 + sT$, $z_{g1} \leq z \leq z_{g2}$. Using the periodicity of the grid in x-direction, the spectral function is assumed to be periodic in x-direction. The transmitted and filtered fields can be given by Wiener-Hopf method, as a method of spectral resolution.

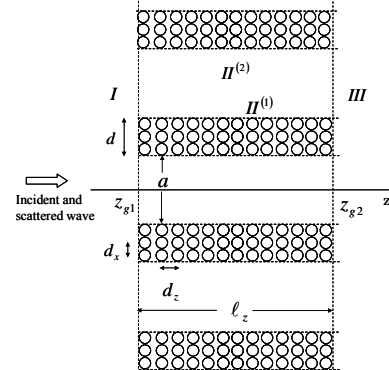


Fig.3 Lossy grid waveguide filter

Conclusion

The electromagnetic scattering and transmitted characteristics through X-ray grids are shown. X-ray grids have the spatial filter characteristics necessary to signal processing of the receiving characteristics in X-ray diagnosis. Based on this theory, the identification method of transmitting and absorption characteristics may be improved, and also it may be possible to utilize the scattering and spectroscopic characteristics effective for developing more accurate X-ray image diagnosis.

References

- [1] H. Aichinger, et al, Radiation Exposure and Image Quality in X-Ray Diagnostic Radiology (2003).
- [2] Y. Miyazaki, Trans. IEE Japan, Vol.83, No.2, pp.132-136 (2000).
- [3] Y. Miyazaki, The Papers of Technical Meeting on Electromagnetic Theory, IEE Japan, EMT05-77 (2005).
- [4] Y. Miyazaki, Jpn. Jour. Appl. Phys., Vol.13, No.8, pp.1238-1248 (1974).

FDTD Parallel Computing of Fundamental Scattering and Attenuation Characteristics of X-ray for Medical Image Diagnosis

Koichi Takahashi and Yasumitsu Miyazaki

Department of Electronics and Information Engineering, Aichi University of Technology
50-2 Manori, Nishihazama-cho, Gamagori, 443-0047 Japan

Nobuo Goto

Department of Information and Computer Sciences, Toyohashi University of Technology
1-1 Hibarigaoka, Tempaku-cho, Toyohashi, 441-8580 Japan

Abstract

X-ray diagnosis depends on the intensity of transmitting and scattering waves in X-ray propagation in biomedical media. X-ray is scattered and absorbed by tissues, such as fat, bone and internal organs. However, image processing for medical diagnosis, based on the scattering and absorption characteristics of these tissues in X-ray spectrum is not so much studied. In this paper, X-ray scattering and absorption in biomedical media are studied using FDTD method. As a result of computer simulation, the statistical properties of transmitted and scattered electric fields are presented numerically. The FDTD parallel computing for the analysis of big area is also shown.

Introduction

X-ray is indispensably important for medical image diagnosis as a tool to obtain information on the internal part of human body. Recently, automatic X-ray image diagnosis based on digital signal processing technique has been developing rapidly. X-ray diagnosis depends on the intensity of transmitted and scattered waves in X-ray propagation in biomedical media. To obtain precise information on tissues, such as fat, bone and internal organs in biomedical media, the characteristics evaluation of refractive index and absorption depending on X-ray wavelength are indispensable. Particularly, scattering characteristics are important to decrease scattered wave and to improve the accuracy of X-ray image diagnosis.

In this paper, X-ray scattering and absorption in biomedical media are studied using two-dimensional FDTD method. In case of X-ray scattering, the analysis space becomes much larger than the wavelength and long calculation time is required. We consider parallel computing of FDTD method to make possible the analysis of big area in reasonable calculation time.

When the wavelength of X-ray is shorter than 0.5 nm, the structure of a material is considered to be discrete. In this study, electromagnetic scattering of X-ray Gaussian beam with 0.05-0.2 nm wavelength by random media is analyzed by 2-D FDTD method.

Scattering Analysis using FDTD method

FDTD analysis is demonstrated to show the characteristics of wave propagation, scattering, absorption in X-ray region. 2-D analysis space is shown in Fig. 1. In the material region, Maxwell's equations are

$$\nabla \times \mathbf{E} = -\mu_0 \frac{\partial \mathbf{H}}{\partial t}, \quad \nabla \times \mathbf{H} = \epsilon(\mathbf{r}) \frac{\partial \mathbf{E}}{\partial t} + \sigma(\mathbf{r}) \mathbf{E} \quad (1)$$

where, $\epsilon(\mathbf{r})$ and $\sigma(\mathbf{r})$ are the dielectric constant and conductivity of the material. The incident wave is x-polarized Gaussian beam with angular frequency $\omega = 2\pi f$, beam spot r_0 and beam waist at $z=z_0$. Since the wavelength of X-ray is very short, successive segmented FDTD analysis based on the division of the analysis space is implemented as shown in Fig. 2.

In this method, total analysis space is divided into the small subregion D_m ($m=1, 2, \dots, M$) and z coordinate in each region is $z_{m-1} \leq z \leq z_m$. Here, backscattering of X-ray from atoms is very weak, we consider the effects on the forward propagating wave due to the scattering and absorption.

In the first subregion D_1 , the electromagnetic fields at point (i,j) at time $n \Delta t$ are calculated by difference equations,

$$\begin{aligned}
E_x^n(i, j) &= C_1 E_x^{n-1}(i, j) - C_2 J_x^{n-1}(i, j) + C_3 \{H_z^{n-1}(i-1, j) - H_z^{n-1}(i-1, j) - H_y^{n-1}(i, j) + H_y^{n-1}(i, j-1)\} \\
H_y^n(i, j) &= H_y^{n-1}(i, j) - C_4 \{E_x^n(i, j+1) - E_x^n(i, j)\}, \quad H_z^n(i, j) = H_z^{n-1}(i, j) + C_4 \{E_x^n(i+1, j) - E_x^n(i, j)\} \\
J_x^{n-1}(i, j) &\begin{cases} \neq 0 & (j=1) \\ = 0 & (j \neq 1) \end{cases}, \quad C_1 = \frac{1 - \sigma \Delta t / (2\varepsilon)}{1 + \sigma \Delta t / (2\varepsilon)}, \quad C_2 = \frac{\Delta t / \varepsilon}{1 + \sigma \Delta t / (2\varepsilon)}, \quad C_3 = \frac{\Delta t / \varepsilon}{1 + \sigma \Delta t / (2\varepsilon)} \frac{1}{\Delta s}, \quad C_4 = \frac{\Delta t}{\mu_0 \Delta s}
\end{aligned} \tag{2}$$

Here, y , z and t are discretized by $y=i \Delta s$, $z=j \Delta s$ and $t=n \Delta t$.

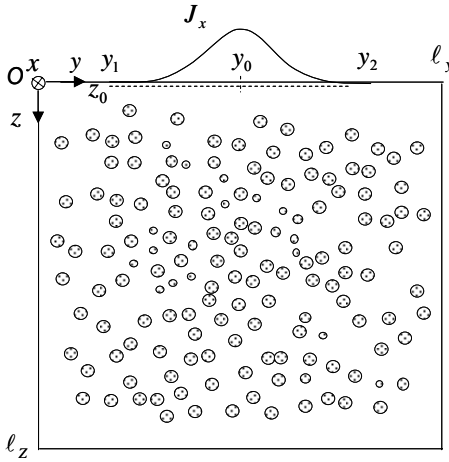


Fig. 1 Analysis space of the first subregion D_1

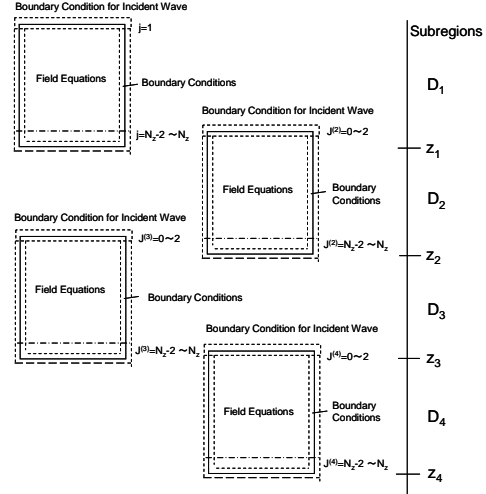


Fig. 2 Successive segmented calculation based on the division of the analysis space

In the atom region of the material, complex

$$\text{dielectric constant } \varepsilon^* \text{ and } n_a^* \text{ are given by } \varepsilon^* = \varepsilon + \frac{\sigma}{j\omega} = n_a^* \varepsilon_0,$$

$n_a^* = n_1 - jn_2$. By using complex refractive index, the dielectric constant and conductivity of the atom are $\varepsilon = \varepsilon_0(n_1^2 - n_2^2)$ and $\sigma = 2\varepsilon_0 \omega n_1 n_2$. Here, relative dielectric constant $\varepsilon_r = \varepsilon / \varepsilon_0$ is given by $\varepsilon_r = (n_1^2 - n_2^2)$. The dielectric constant of background medium is ε_0 . In this analysis, the shape of an atom is assumed to be square. Random scatterers are generated by giving the length of a side of squares $a(i,j)$, positions of one apex (y_i, z_i), and dielectric constants $\varepsilon_r(i,j)$.

In the first subregion D_1 , the incident wave is generated by current density

$$J_x^n(i, 1) = J_0 \exp \left\{ - \left(\frac{(i - i_0) \Delta s}{r_0} \right)^2 \right\} H(n \Delta t) \sin(2\pi f n \Delta t) \quad H(n \Delta t) = \begin{cases} 1, & 0 \leq n \Delta t \leq \tau \\ 0, & n \Delta t < 0, n \Delta t > \tau \end{cases} \tag{3}$$

where f is the frequency of the incident wave, k_0 is the wave number, $f = 1/\lambda_0 \sqrt{\varepsilon_0 \mu_0} = k_0 / 2\pi \sqrt{\varepsilon_0 \mu_0}$, $y_0 = i_0 \Delta s$ is the center point of the incident beam, r_0 is the beam waist at $z=z=z_0(j=1)$, τ is the transmission time. In subregion D_1 , the calculation is conducted during the time $t < T + \tau$, where T is the time the incident wave reaches at $z=z_1=N_s \Delta s$. In the first region, the electric fields at $z=z=z_1, z_1+\Delta s, z_1+2\Delta s$ ($j=N_s, N_s+1, N_s+2$) are stored in memory for the initial value of calculation in next subregion D_2 . In subregion D_m ($m \geq 2$), the stored electric field data is read as initial value for the calculation.

Statistical properties of electromagnetic scattering and absorption are discussed by using statistical parameters, such as average and variance of $a(i,j)$ and $\varepsilon_r(i,j)$.

Also, the correlation length of fluctuation is evaluated. Here,

$$\begin{aligned}
E[a^{(s)}] &= \frac{1}{N} \sum_{i=0}^{N_x-1} \sum_{j=0}^{N_z-1} a^{(s)}(i, j), & Va[a^{(s)}] &= \frac{1}{N} \sum_{i=0}^{N_x-1} \sum_{j=0}^{N_z-1} (a^{(s)}(i, j) - E[a^{(s)}])^2 \\
E[\varepsilon_r^{(s)}] &= \frac{1}{N_y N_z} \sum_{i=0}^{N_y-1} \sum_{j=0}^{N_z-1} \varepsilon_r^{(s)}(i, j), & Va[\varepsilon_r^{(s)}] &= \frac{1}{N_y N_z} \sum_{i=0}^{N_y-1} \sum_{j=0}^{N_z-1} (\varepsilon_r^{(s)}(i, j) - E[\varepsilon_r^{(s)}])^2
\end{aligned} \tag{4}$$

where, N is the number of atoms in the analysis space and s ($s=1, 2, \dots, S$) is the realization's number.

The correlation length of fluctuation $\rho_0^{(s)}$ is defined by $\rho_0^{(s)} = \left\{ \text{Max } \rho \left| \frac{B_\eta^{(s)}(m, n : \rho)}{B_\eta^{(s)}(0, 0 : \rho)} \right| = e^{-1} \right\} \cdot B_\eta^{(s)}(m, n : \rho)$ is

the auto correlation function of the fluctuation $\Delta\eta^{(s)}$ given by $\varepsilon^{(s)}(\mathbf{r}) = \varepsilon^{(s)}(1 + \Delta\eta^{(s)}(\mathbf{r}))$, where $\varepsilon^{(s)}$ is the average dielectric constant of random media.

FDTD parallel processing using the grid computer

We develop a new approach to perform FDTD parallel processing using grid computer network. In FDTD analysis, the electromagnetic fields are calculated by difference equations derived from Maxwell's equations. We transform the difference equations to discrete linear equations. By the definition of the incident wave or electromagnetic field generated by antenna source as $\phi_s(i, j) = (\phi_1, \phi_2, \phi_3)_{r=(i\Delta y, j\Delta z)}$ and vector \mathbf{X} for electromagnetic fields as $\mathbf{X}(i, j) = (E_x, H_y, H_z)_{r=(i\Delta y, j\Delta z)}$, discrete equations for FDTD can be rewritten using coefficient matrix $\mathbf{A}_{u,v}$, as $\mathbf{X}^n(i, j) = \sum_{u=-1}^1 \sum_{v=-1}^1 \mathbf{A}_{u,v} \mathbf{X}^{n-1}(i+u, j+v) + \Phi^n(i, j)$.

Here, the matrix $\mathbf{A}_{u,v}$ is determined by eq. (2). For instance, $\mathbf{A}_{0,0}$ is given by eq. (5). Fig. 3 shows the lattice point of FDTD computation. To calculate the value of \mathbf{X} at point (i, j) , the values at "●" points, are necessary. In the matrix equation, n is the time step and when $n=1, 2, \dots, T$, we have eq. (6).

$$\mathbf{A}_{0,0} = \begin{bmatrix} C_1 & -C_3 & C_3 \\ C_1 C_4 & 1 - 2C_3 C_4 & C_3 C_4 \\ -C_1 C_4 & C_3 C_4 & 1 - 2C_3 C_4 \end{bmatrix} \quad (5)$$

$$\begin{bmatrix} I & 0 & 0 & \dots & 0 & 0 \\ -A & I & 0 & \dots & 0 & 0 \\ 0 & -A & I & \dots & 0 & 0 \\ \vdots & \vdots & \vdots & -A & I & 0 \\ 0 & 0 & 0 & 0 & \dots & -A & I \end{bmatrix} \begin{bmatrix} X^1 \\ X^2 \\ \vdots \\ X^{T-1} \\ X^T \end{bmatrix} = \begin{bmatrix} \phi^1 \\ \phi^2 \\ \vdots \\ \phi^{T-1} \\ \phi^T \end{bmatrix} \quad (6)$$

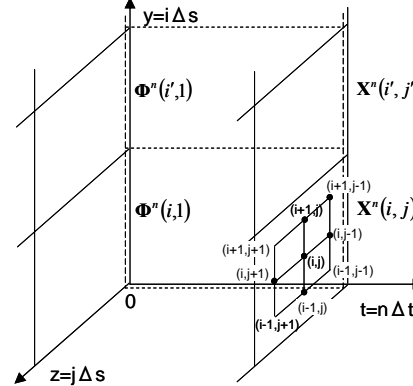


Fig.3 Lattice point for FDTD parallel Computation

By using backward substitution, \mathbf{X}^T is obtained by the initial value of the fields, where T is the final time step of the calculation. The advantages of this algorithm are relatively efficient. Relatively, small memory is required comparing with conventional FDTD and no concurrent data communication is occurred.

Statistical properties of scattering and absorption of X-ray Gaussian beam

Scattering and absorption characteristics of incident X-ray Gaussian beam are evaluated using FDTD method. Numerical parameters are shown in Table 1. For the incident wave, $f=1.5 \times 10^{18} \text{ Hz}$ ($\lambda_0=0.2 \text{ nm}$), $r_0=15 \lambda_0=3 \text{ nm}$, $J_0=10^9 \text{ A/m}^2$ and $\tau=2 \times 10^{-17} \text{ s}$, are used. The size of a subregion is 30 nm along y-direction and 20 nm along z-direction. Here, the number of cells Ny and Nz are 3000 and 2000, respectively. As shown in Table 1, four random media models Case 1-4 with different complex refractive index of atoms are considered. To evaluate statistical properties of X-ray scattering and absorption, five realizations of random media are analyzed in each case and the average amplitude of transmitted and scattered electric fields averaged over five realizations are presented. The distribution of dielectric constant of D_1 of the first realization $\varepsilon_r^{(1)}$ is shown in Fig. 4. In Case 1-4, the distribution of atoms is same and only refractive index of atom is different. Fig. 5 and 6 show the average amplitudes of transmitted and scattered electric fields $|E_x^{(t)}|$ and $|E_x^{(t)}| - |E_0^{(inc)}|$ at $z=\ell_z=20 \text{ nm}$. Here,

$$|E_0^{(inc)}| = \text{Max}_{t \in [t', t'+T]} |E_0^{(inc)}(y, \ell_z, t)|, \quad |E_x^{(t)}|_{\max} = \frac{1}{S} \sum_{s=1}^S \text{Max}_{t \in [t', t'+T]} |E_x^{(s)}(y, \ell_z, t)| \quad (7)$$

t' is the time when the fields assumed to be steady state. FDTD simulation is conducted by five models in each case and the results of electric field amplitudes are averaged to obtain the statistical properties. Table 2 shows the statistical average and variance of a length of a side of atoms $a^{(s)}(i, j)$ and Table 3 shows the average and variance of the dielectric constant of random media. These tables show that each realization

$z(\text{nm})$

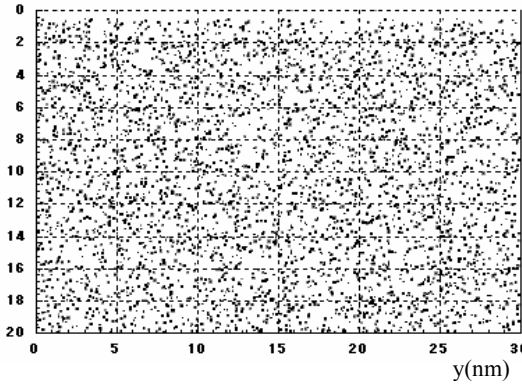


Fig. 4 Distribution of dielectric constant of random media $\epsilon_r^{(1)}(N=3800, a=0.1 \sim 0.2\text{nm}, n_a^* = n_1 - jn_2)$

Table 1 Parameters for the simulation of X-ray scattering and attenuation characteristics

Parameters	Values				
f : Frequency of incident wave	$1.5 \times 10^{18}\text{Hz}$				
λ_0 : Wavelength of incident wave	$0.2\text{nm} (c/f)$				
ℓ_y : Length of an analysis space (y-direction)	$30\text{nm} (150\lambda_0)$				
ℓ_z : Length of an analysis space (z-direction)	$20\text{nm} (100\lambda_0)$				
y_0 : Center point of incident beam	$15\text{nm} (\ell_y/2=75\lambda_0)$				
r_0 : Beam spot at $z=z_0$	$3\text{nm} (r_0/\lambda_0=15)$				
Δs : Length of a cell	$0.01\text{nm} (\Delta s/\lambda_0=1/20)$				
Δt : Time increment	$2.25 \times 10^{-20}\text{s}$				
N : A number of atoms	3800				
a : Length of a side of atoms	$0.1 \sim 0.2\text{nm} (a/\lambda_0=0.5 \sim 1.0)$				
n_a^* : Complex refractive index of atoms	<table border="1"> <tr> <td>0.99 -j0.005 (Case 1)</td> </tr> <tr> <td>0.995 -j0.002 (Case 2)</td> </tr> <tr> <td>0.999 -j0.001 (Case 3)</td> </tr> <tr> <td>0.9995 -j0.0005 (Case 4)</td> </tr> </table>	0.99 -j0.005 (Case 1)	0.995 -j0.002 (Case 2)	0.999 -j0.001 (Case 3)	0.9995 -j0.0005 (Case 4)
0.99 -j0.005 (Case 1)					
0.995 -j0.002 (Case 2)					
0.999 -j0.001 (Case 3)					
0.9995 -j0.0005 (Case 4)					

Table 2 Statistical parameters for atom size

s	$E[a^{(s)}]$ (nm)	$Va[a^{(s)}]$
1	0.144	8.2×10^{-4}
2	0.145	8.0×10^{-4}
3	0.144	8.3×10^{-4}
4	0.144	8.2×10^{-4}
5	0.144	8.3×10^{-4}

Table 3 Statistical parameters for dielectric constant

(a) Case 1					(b) Case 2				
Model	s	$E[\epsilon_r^{(s)}]$	$Va[\epsilon_r^{(s)}]$	$\rho_0^{(s)}$ (nm)	Model	s	$E[\epsilon_r^{(s)}]$	$Va[\epsilon_r^{(s)}]$	$\rho_0^{(s)}$ (nm)
Case1	1	0.9974	4.47×10^{-5}	0.1	Case2	1	0.9987	1.12×10^{-5}	0.1
	2		4.51×10^{-5}			2		1.13×10^{-5}	
	3		4.47×10^{-5}			3		1.12×10^{-5}	
	4		4.47×10^{-5}			4		1.12×10^{-5}	
	5		4.51×10^{-5}			5		1.13×10^{-5}	
(c) Case 3					(d) Case 4				
Case3	1	0.9997	4.50×10^{-7}	0.1	Case4	1	0.9974	1.13×10^{-7}	0.1
	2		4.54×10^{-7}			2		1.14×10^{-7}	
	3		4.50×10^{-7}			3		1.13×10^{-7}	
	4		4.51×10^{-7}			4		1.13×10^{-7}	
	5		4.54×10^{-7}			5		1.14×10^{-7}	

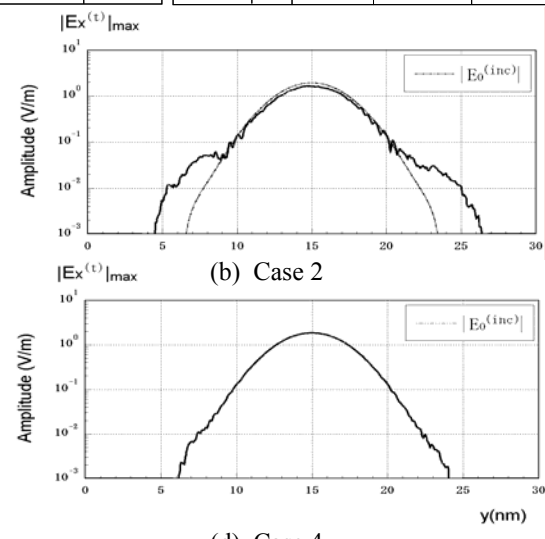
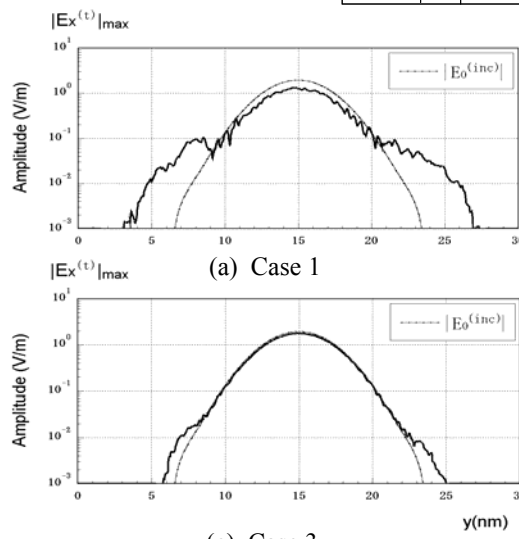
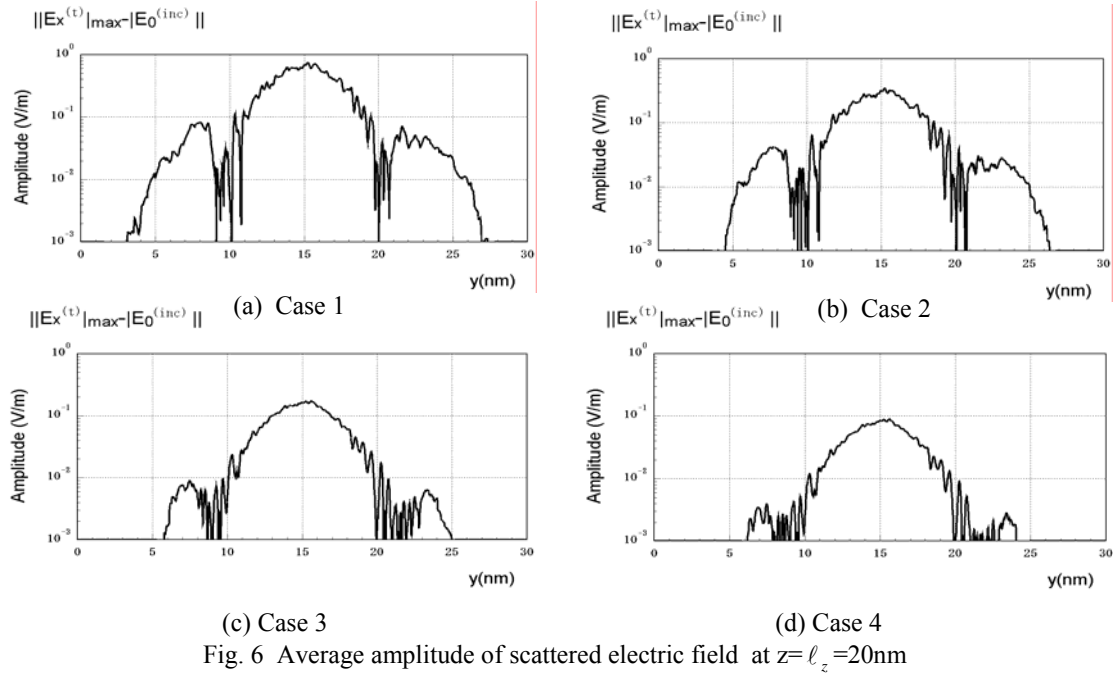


Fig. 5 Average amplitude of transmitted electric field at $z=\ell_z=20\text{nm}$



has similar statistical properties. Simulation results show that qualitatively, as n_a^* becomes smaller than 1.0, the attenuation of the electric field amplitude at the center point of the beam becomes large and the intensity of scattering field becomes relatively strong at the foot of the beam.

Fig. 7 shows the average attenuation characteristics of the electric field along propagation direction. $|E_x|_{\max}(y_0, z)$ is the mean amplitude of electric field at the center point $y=y_0=15\text{nm}$. In each case, five models with same statistical conditions are generated. In Fig. 7, the tendency that the attenuation of the electric field is slow as the refractive index of the atoms becomes far from 1.0. Also, strong fluctuation of the amplitude due to the effect from multiple scattering in random media is observed in Case 1 and 2.

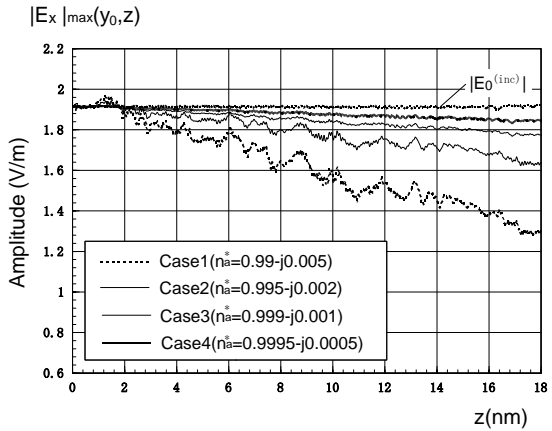


Fig. 7 Attenuation characteristics at $y = y_0 = 15\text{nm}$
averaged over five realizations

Conclusion

In this paper, the fundamental X-ray scattering and absorption characteristics are evaluated using FDTD method. In future, evaluating the characteristics of scattering, absorption, dispersion and spectroscopy, it may be possible to find more accurate new method for X-ray image diagnosis. Also, FDTD parallel processing using grid computer is considered to simulate more big area to obtain more realistic accurate results.

References

- [1] Y. Miyazaki, Jour. of IEICE, Vol.83, No.2, pp.132-136, 2000.
- [2] H. Aichinger et al., Radiation Exposure and Image Quality in X-Ray Diagnosis Radiology, 2003.
- [3] Y. Miyazaki, J. Sonoda and Y. Jyonori, Trans. IEE Japan, Vol.117-C, No.1, pp.35-41, 1997.
- [4] K. Takahashi and Y. Miyazaki, Trans. IEE Japan, Vol.120-C, No.12, pp.1905-1912, 2000.
- [5] K. Takahashi, H. Xinmin and Y. Miyazaki, Digest of ISMOT-2005, Fukuoka, Japan, B-16,p.109,2005.
- [6] G. Rodriguez, Y. Miyazaki and N. Goto, IEEE Trans. Antennas and Propagation, Vol.54, No.3, pp.785-796, 2006.

“STRUCTURE DEPENDENT MAGNETIC AND ELECTRICAL PROPERTIES OF SOME NANO FERRITES”

Priya. P. Kulkarni, Vaishali. R. Bote, Sandeep. A. Mane and R. B. Pujar

S. S. Arts & T. P. Science Institute, Sankeshwar – 591 313, India

Abstract: Ferrites are iron oxide based ceramic materials, which behave as ferrimagnets. There is a growing need for nano sized ferrites for advanced technological applications. Chemical synthesis routes play a crucial role in designing final products. Chemical process minimizes the problem of diffusion, impurities and agglomeration. The solution was composed of metal nitrates with polymer PVA and Sucrose. Thermolysis of the precursor mass, at an external temperature around 500°C, resulted in the oxide phase. The exothermic decomposition of precursors helps the material to disintegrate and to dissipate heat of decomposition, inhibiting the sintering of the fine particle. Sucrose, being excess to metal ions, works not only as chelating agent but also serves as an efficient fuel for the combustion reaction. The oxide system investigated through this process includes Ni – Zn – Cu, Ni – Zn – Mg and Ni – Zn nano ferrites.

X-ray diffraction patterns confirm the formation of single phase ferrites. All the samples show face centred cubic structure. IR absorption bands γ_1 and γ_2 are assigned to the vibrations of tetrahedral and octahedral complexes respectively.

The presence of Fe²⁺ at octahedral sites results in the splitting of γ_2 band. SEM micrographs indicate the development of porosity at the base of the neck. Metal ion vacancies produce large pores at the boundaries of the crystallites. Hysterisis studies show the small values of M_r/M_s. This suggest that MD particles are present in all the samples. The variation of resistivity with temperature indicates the break at Curie temperature. It is due to the transition of the sample from ferrimagnet to paramagnetic region. The electrical conductivity follows VerWey de Bore mechanism.

Keywords: Nano, ferrites, sucrose, PVA, SEM and MD.

1. Introduction

Ferrites are iron oxide based ceramic materials. Because of their high resistivity they find wide applications from microwave to radio frequencies. The quantities such as magnetization, coercivity, conductivity etc. are greatly influenced by porosity, grain size and microstructure of the samples. Recently considerable interest has been developed in nano crystalline material because of their unique optical, electronic, mechanical and catalytical properties. Because of their high potential, nano materials find wide applications on areas such as composites, optics and electronics. The unique properties and improved performances of nano materials are determined by their size, surface structure and inter particle interactions. Recently novel chemical route has been developed to obtain nano sized uniform particles of high purity. Hence an attempt has been made to synthesize Ni – Zn – Cu, Ni – Zn – Mg and Ni – Zn ferrites by chemical route to characterize for undertaking the studies on magnetic and electrical properties.

2. Experimental

Ferrites with the general chemical formula $N_{1-x} Cu_x Zn_{0.5} Fe_2O_4$, $Ni_{1-x} Mg_x Zn_{0.5} Fe_2O_4$ and $Ni_{1-x} Zn_x Fe_2O_4$ with $x = 0.1$ to 0.5 were prepared by chemical route by using metal nitrates, sucrose and PVA. The powders were pre sintered at $600^{\circ}C$ for 6 hours in air medium. Then the powders were pressed into pellets by applying a pressure of about 5 tones per square inch for 5 minutes by putting a powder of about 1gram in a die of 1cm in diameter. The pellets were subjected to final sintering at $800^{\circ}C$ for 8 hours and furnace cooled in air medium. This helps to obtain homogeneous composition of raw materials. The densification and grain growth occurs simultaneously during the final sintering.

X-ray diffraction, IR absorption bands and VSM analysis were obtained from Indian Institute of Science, Bangalore where as SEM micrographs were obtained from Shivaji University, Kolhapur and are shown in Fig.1.

Saturation magnetization was noted from the graphs of magnetization Vs magnetizing field (Fig.2.) Magnetic moment of each sample was calculated by the relation.

$$\mu_B = \left(\frac{M}{5585} \right) M_s \quad (1)$$

where M = molecular weight, M_s = Saturation Magnetization.

The d. c. conductivity was measured by two probe method from room temperature to $700^{\circ}C$. The silver paste was applied on either side of pellets to provide good ohmic contact. Resistivity was calculated by the relation

$$\rho = \rho_0 e^{\frac{\Delta E}{KT}} \quad (2)$$

where ρ_0 = constant depending on temperature

ΔE = activation energy

T = absolute temperature.

K = Boltzmann constant

From the graphs of $\log \rho$ vs. $1/T$, activation energies and Curie temperature were calculated. The activation energy is given by the relation

$$\Delta E = 1.982 \times 10^{-4} \times m \quad (3)$$

where m = slope of graph $\log \rho$ Vs $1/T$

3. Figures and Tables

3.1 Figures

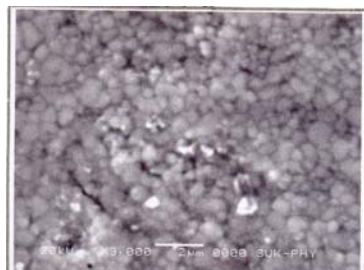
 $x = 0.5$  $x = 0.3$ 

Fig 1

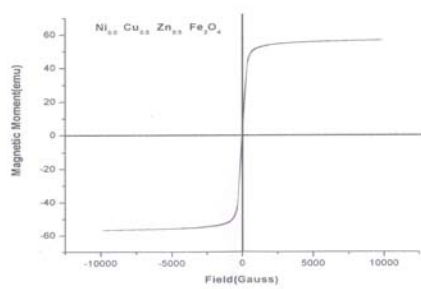


Fig 2. V. S.M. Analysis

3.2 Tables

Table 1. Data on Porosity

Content (x)	Porosity
0.1	25%
0.2	36%
0.3	13%
0.4	13%
0.5	10%

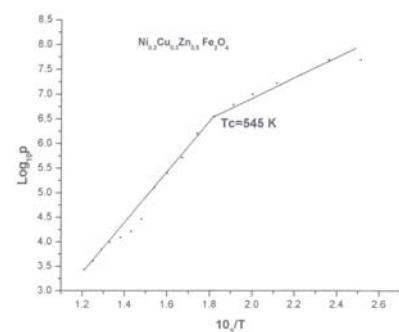


Fig 3. D. C. Conductivity

Table 2. Average grain diameter

Content (x)	Average grain diameter (μm)
0.1	0.75
0.2	0.23
0.3	0.58
0.4	0.63
0.5	0.52

Table 3. V.S.M.Analysis

Table 4. Activation energy & Curie temperature

Content (x)	M_s (emu)	μ_B	$\frac{M_r}{M_s}$	H_c (Gauss)
0.1	4.3	0.19	0.14	43
0.2	1.95	0.08	0.39	92
0.3	3.8	0.16	0.3	102
0.4	1.27	0.06	0.33	101
0.5	56.5 emu/gr	2.42	0.43	98

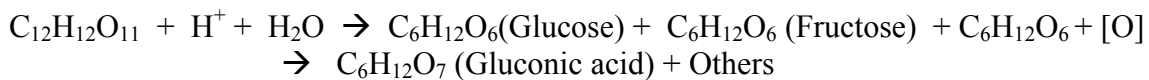
Content (x)	Activation Energy		Curie temperature T_c °K
	Para region ΔE_1 (e _V)	Ferri region ΔE_2 (e _V)	
0.1	1.23	0.19	550
0.2	1.25	0.14	498
0.3	1.20	0.40	545
0.4	2.60	0.16	535
0.5	0.86	0.30	534

4. Results and Discussions

Sucrose in the solution form provides a wrapping through co-ordination for the cations in solution and circumvents their selective precipitation from the solution during the evaporation process. The overall reaction can be represented as



Sucrose also serves as an efficient fuel for the combustion reaction due to oxidation of nitric ions. The aqueous solution of sucrose in presence of dilute nitric acid gets hydrolyzed to fructose and glucose, which get further oxidized to a gluconic acid or polyhydroxy acid. The reaction is given by



PVA provides polymeric matrix structure for the cations and helps in the polycondensation reaction in presence of oxidized saccharides and gives rise to the branched chain polymeric network structure where the metal ions (M^{2+}) are held in the hydroxylic pockets of the branched chain through complex formation¹. During the pyrolysis various gases are released from the pockets making the structure highly porous and fluffy.

The absence of extra line in the diffractogram confirms the formation of single phase of ferrites. All the samples exhibit face centred cubic structure. IR spectra exhibit three prominent absorption bands, attributed to vibrations of tetrahedral and octahedral complexes.

The magnetic moment of $Cu^{2+}(1.2\mu_B)$ is smaller than that of Ni ($2.3\mu_B$). Both Cu and Ni prefer B site as per their preference energies. Hence the addition of Cu decreases the amount of Ni at B site. As a result, the magnetic moment of B site decreases. This leads to the decrease in magnetic moment with increase in Cu content². However the variation of M_s with composition is attributed to the density of sample (Table 1 and Table 3).

According to site preference energies, Zn occupies A-site, and both Cu and Ni occupy B-site. While Fe^{3+} occupies both A and B sites. The presence of Zn causes for the sub division of lattice leading to the formation of y-k angle types of spins. When Zn is constant and Ni and Cu being non y-k, it is expected that y-k angles should remain constant with an increase in Cu content. Therefore it can be concluded that magnetization in all samples obey y-k model. The small values of M_r/M_s suggest the existence of MD particles in the samples³.

Another important factor that influences the magnetization of ferrites is microstructure. Each grain has certain magnetic moment. The presence of pores breaks the magnetic circuits among the grains. This leads to the net decrease in the magnetic moment with increase in pore concentration. At higher sintering temperature small number of large grains are produced and consequently porosity is reduced. Hence magnetization increases with an increase in sintering temperature (Table 2).

The variation of $\log p$ vs $1/T$ is shown in Fig.3. While the variation of activation energy and Curie temperature with content is tabulated in Table 4.

The conduction in ferrites is due to the hopping of electrons from Fe^{2+} to Fe^{3+} . The discontinuity is caused by the ordering of Fe^{2+} and Fe^{3+} ions on the octahedral sites, followed by a small change in crystal structure. The decrease in activation energy is due to ordering of spins

of electrons at Curie temperature. The electrical conductivity in ferrites can also be explained on the basis of Verwey de Boer mechanism i.e. exchange of electrons between the ions of same element that are present in more than two valence states and distributed randomly over equivalent crystallographic lattice sites. The expression for Curie temperature is given by

$$T_c = \frac{2S(S+1). Z. J}{3K} \quad (4)$$

where S = Spin angular momentum
 J = Total angular momentum
 Z = number of nearest ions
 K = Boltzmann constant

The addition of Ni decreases Cu and increases A-B interactions due to more magnetic moment of Ni than that of Cu. This in turn increases Curie temperature. The Ni ions occupy B site by forcing Fe^{3+} ions to A site. As a result A-B interaction increases and thereby Curie temperature increases⁴.

Electrical properties are mainly governed by heat treatment during preparation. At elevated temperature dissociation of oxygen takes place forming small amount of divalent metal ions and this results in the increase of conductivity in ferrites⁵.

The presence of air gaps between the grains form inhomogeneous structure. This largely affects d.c. conductivity and hence conduction mechanism in ferrites is largely dependent on porosity and microstructure. Hence it can be emphasized that the higher conductivity in ferrites is due to the increase in grain size and decrease in pore concentration.

Acknowledgement

I express my sincere thanks to U G C for providing the financial assistance to carry out the research work.

REFERENCES

1. Lessing. P. A., "Ceram. Bull". 68, 1002, 1989.
2. Heiks. R. R and Johnson. W. D., "J. Chem. Phys"., 26, 582, 1957.
3. Pujar. R. B., "Ph.D. Thesis", 1995, Shivaji University, Kolhapur (India).
4. Tatsuya. Nakamura., "J. Appl. Phys". Vol. 88 No.1, 348, 2000.
5. Ghodake. S. A, "Ph.D. Thesis", 2001, 243, Shivaji University, Kolhapur (India).

Innovation use of Nano Technology in Magnetic Storage Devices

D. Bajalan

Corresponding author: Diyar Bajalan, E-Mail: diyar.bajalan@austromail.at

Abstract: The fluence of ion irradiation on polycrystalline thin films affects both anisotropy and spontaneous magnetisation M_s . The dependence of coercivity and initial susceptibility on M_s is predicted by a hysteresis model considering the balance of energy with good qualitative agreement.

Keywords: magnetic thin films; anisotropy; hysteresis modelling; magnetic nanostructures

1 Introduction

Demands for the continuous increase in the data storage density bring the challenge to overcome physical limits for currently used magnetic recording media [1, 2]. Ferromagnetic nano-particles of different polycrystalline thin films have been formed by heavy or light ion irradiation [2, 3, 4]. Although this modification technique may be a way to produce nano-magnetic particles, there are some critical size limits of nanomagnetic structures like the superparamagnetic limit (SPML) which faces magnetic nano-technology. The magnetic properties of thin films are strongly influenced by their structure [5]. Small changes in the way a thin film is produced often give rise to large changes in some of the magnetic properties of the thin film [6]. This is best understood by observing how the microstructure of the film changes with processing and then correlating the microstructure directly with the properties of the thin film [6]. The behaviour of magnetic nanoparticles has fascinated materials scientists for decades [7]. Magnetic nanostructures have become a centre of great interest in the scientific community and in industry as the core technologies behind magnetic recording devices [8]. And the magnetic properties of an ultra thin multilayer can be patterned by controlled ion beam irradiation [4]. There are fundamental limits due to the atomic nature of matter which may impose ultimate physical bounds to nanofabrication and miniaturization [9]. Over the past several decades, amorphous and more recently nano-crystalline materials have been investigated for applications in magnetic devices [10]. The benefit found in the nano-crystalline alloys stem from their chemical and structural variations on a nano-scale which are important for optimizing magnetic recording devices [10].

2 Irradiation Process and Results

Several irradiation experiments carried out on the Co/Pt multi-layers samples (A1,A2, and A3 see Tables 1) cause changes in the magnetic properties of the thin films [4, 1]. High aspect ratio silica masks on Co/Pt multi-layers were obtained by e-beam lithography and reactive ion etching with feature sizes down to 30 nm for lines and 20 nm for dots [3]. He⁺ ion irradiation of the magnetic layers through these masks was used to pattern the magnetic properties [3] (with fluences between 2.10^{14} and 2.10^{16} ions/cm² [4]). After mask removal, high resolution and high density, planar magnetic nano-structures were obtained [3]. The results of the irradiation show perfectly square hysteresis loops at room temperature, the coercive field decreasing progressively to zero [4]. The high perpendicular anisotropy of Pt/Co multi-layers originates from the

interfaces between the layers [11]. Other experiments carried out on YCo₂ samples (thin polycrystalline film targets of polycrystalline with thicknesses of approximately 1μm [12]) have shown that fluences in range of 10¹² U ions/cm² cause changes in magnetic properties of the samples [1]. The result of these experiments were changes of the anisotropy perpendicular to the film plane [1], and change of spontaneous magnetisation, coercivity and initial susceptibility [13].

2.1 Equations and Calculation

The energetic model (EM) [14] is used to calculate the dependence of the shape of the hysteresis loop on M_s . The parameters of the model are calculated directly from measurements of special points of the hysteresis loop. The identification of the parameters is done at reference conditions (index 0) at a temperature $T = T_0$ without any applied mechanical stress σ , and at given M_s and N_e (N_e is the effective demagnetizing factor which is the sum of the geometric demagnetizing factor N_d and the inner demagnetizing factor N_i). The following equations show how to determine the parameter of the model from spontaneous magnetization M_s , coercivity H_c , and from the effective demagnetization factor N_e .

$$k_0 = \frac{\mu_0 M_s H_c}{1 - 2 \exp[-q_0]} \quad (1)$$

k in J/m³ related to static hysteresis loss (irreversible processes), and

$$q_0 = \frac{\mu_0 M_s^2}{k_0} \frac{1 - N_e \chi_0}{\chi_0} \quad (2)$$

q (dimensionless) is related to pinning site density (irreversible processes). Using Eqs. (1) and (2) with the approximation $\exp[-q_0] \ll 1$, we find the dependencies

$$H_c = \frac{k_0}{\mu_0 M_s} \quad (3)$$

and

$$\chi_0 = \frac{\mu_0 M_s^2}{k_0 q_0 + \mu_0 M_s^2 N_e} \quad (4)$$

which strongly affects the shape of the hysteresis. Figure 1 shows the initial magnetization curves calculated and measured major hysteresis loops in dependence of the measured value of M_s . No other change of the parameter values has been made. Table 1 shows the result of the evaluation of the equations above. Figure 2 shows the initial magnetization curves calculated with the parameters depending on M_s due to irradiation, compared to measurements.

3 Anisotropy energy after irradiation

The anisotropy energy k_u is essential for evaluation of the thermal stability condition on a given bit. For the three irradiated samples (A1,A2,A3), k_u were calculated (Equation 5).

$$k_u = \frac{H_k \mu_0 M_s}{2} \quad (5)$$

4 Nano bits stability factor and its relaxation time calculation

Assuming a factor f_{BS} a simple abbreviation for "bit stability factor", which represents the information stability of stored data on a given nano-bit, where: $f_{BS} = k_u V_{nano} / k_B T$, V_{nano} is the nano magnetic

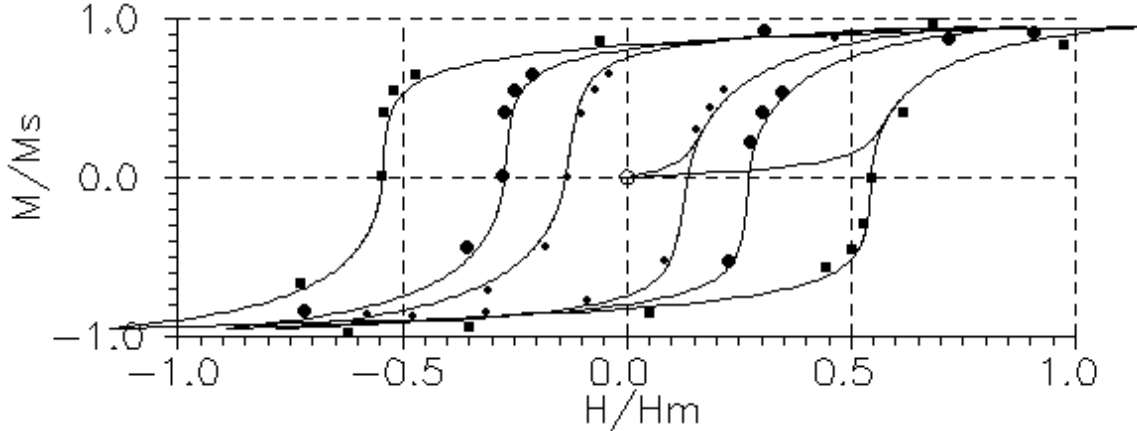


Figure 1: Calculated hysteresis loops for thin Films after different ion irradiation fluences perpendicular to the film plane and measured points. The Hvalues are related to the maximum field $H_m = 160$ kA/m. The Mvalues are related to the respective saturation values of $M_s = 20$ kA/m, $M_s = 40$ kA/m, and $M_s = 60$ kA/m 1. Only these values have been changed to calculate the different major hysteresis loops

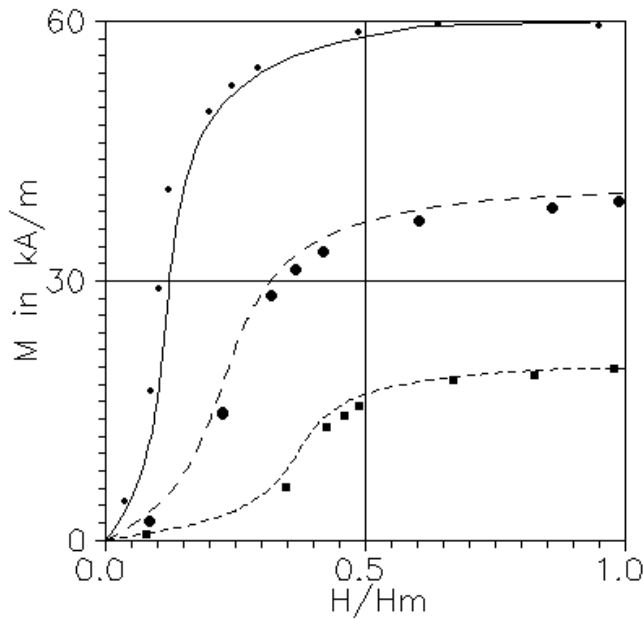


Figure 2: Calculated initial hysteresis curves loops for thin films after different ion irradiation fluences perpendicular (Table 1) to the film plane and measured points. The Hvalues are related to the maximum field $H_m = 160$ kA/m. The calculation has been done by varying the value of M_s , only

structure volume, $k_u V_{nano}$ is the energy barrier (ΔE), and $k_B = 1.38 \times 10^{-23}$ J/deg Boltzmann constant. The magnetic stored information on a nano dot is then stable: if only the condition ($f_{BS} > 40$) is satisfied [16]. The relaxation time (time duration of stored information) or switching time of stored information τ can be obtained from the Arrhenius relation as:

$$\tau = \frac{1}{f_0} \exp f_{BS} \quad (6)$$

Φ	[ions/cm ²]	A1, 10 ¹²	A2, 5 · 10 ¹²	A3, 2 · 10 ¹³
M_s	[kA/m]	20	40	60
χ_0	[1]	0.157	0.199	0.536
H_c	[kA/m]	43.6	21.8	14.5

Tabelle 1: Macroscopic hysteresis features depending on M_s [14]

samples	k_u [J/m ³]	τ [Years]
A ₁	592.51	20.3 × 10 ²
A ₂	1017.67	23.6 × 10 ¹⁶
A ₃	1975.46	11.8 × 10 ³⁸

Tabelle 2: Relation between k_u , and relaxation time τ at dot-width $D_w = 22$ nm and T=10 K, as a result of irradiation, where f_{BS} condition is satisfied

Where f_0 is the thermal attempt frequency [17], which is usually assumed to be 10⁹ s⁻¹. The irradiation of the samples (A₁,A₂,A₃) with different fluences as shown in Table 1, caused changes of the calculated values of k_u for each sample. Hence different values of f_{BS} and τ were calculated (see Table 2).

5 Conclusion

Magnetic nano-structures are subject of growing interest because of their potential applications in high density magnetic recording media and their original magnetic properties [11],[14]-[16]. The rapid development of magnetic recording leads to a large increase of the bit density. Multilayer thin films with perpendicular magnetic anisotropy devices may play an active role in the development and establishment of future storage technologies. Patterning magnetic media is a potential solution for ultrahigh density magnetic recording [3]. The shape of hysteresis loops depends strongly on M_s , where H_c is inversely proportional to M_s , and χ_0 is proportional to M_s^2 . Thermal stability is one of the serious issues for developing high density recording, and thus much effort has been made to overcome this issue [18]. The idea to use a regular array of physically isolated grains/dots promises an improvement in thermal stability of the recorded bits [19]. The anisotropy energy k_u is essential for evaluation of the thermal stability condition on a given bit, because k_u value is used in calculation of bit stability factor f_{BS} . A given nano bit is then thermaly stable: if only the condition ($f_{BS} > 40$) is satisfied.

References

- [1] M. Solzi, M. Ghidini, G. Asti, Magnetic Nanostructures **4**, 123 (2002).
- [2] A. Lapicki, K. Kang, T. Suzuki, IEEE Trans. Magn. **38**, 589 (2002).
- [3] T. Devolder, C. Chappert, Y. Chen, E. Cambril, H. Launois,H. Bernas, J. Ferre, J. P. Jamet, J. Vac. Sci. Technol. **B 17**, 3177 (1999).
- [4] J. Ferre, C. Chappert, H. Bernas, J.-P. Jamet, P. Meyer, O. Kaitasov, S. Lemerle, V. Mathet, F. Rousseaux, H. Launois, J. Magn. Magn. Mater. **198**, 191 (1999).
- [5] D. J. Sellmyer, C.P. Luo, Y.Qiang, Handbook of Thin Film Devices Magnetic, Nanomaterials And Magnetic Thin Films, Academic Press **5**, 337 2000.

- [6] D. E. Laughlin, Bin Lu, Seagate Research Center, Materials Science and Engineering Department and Data Storage Systems Center, Carnegie Mellon University, Pittsburgh, 2 (2001).
- [7] C. Binns, M. J. Maher, New Journal of Physics **4**, 85.1 (2002).
- [8] Diarmaid MacMathuna, **Surface studies of nanomagnetic systems**, A thesis submitted to the University of Dublin, Trinity College, Physics Department, 3 2002.
- [9] Dennis E. Speliotis, Presented at the THIC Meeting at the Naval Surface Warfare Center Center Carderock Bethesda, Digital Measurement Systems/ADE Technologies, 4 (2000)
- [10] Michael E. McHenry, Matthew A. Willard, David E. Laughlin, Progress in Materials Science **44**, 291 (1999).
- [11] M. Jamet, W. Wernsdorfer, C. Thirion, D. Mailly, V. Dupuis, P. Mélinon, A. Pérez, Phys. Rev. Lett. **86**, 4676 (2001).
- [12] J. P. Noziéres, M. Ghidini, N. M. Dempsey, B. Gervais, D. Givord, G. Suran, J. M. D. Coey, Nucl. Instr. and Meth. in Phys. Res. **B 146**, 250 (1998).
- [13] D. Givord, J. P. Noziéres, M. Ghidini, B. Gervais, Y. Otani, J. Magn. Magn. Mater. **148**, 253 (1995).
- [14] D. Bajalan, H. Hauser, P. L. Fulmek, Physica **B 343**, 384 (2004).
- [15] D. Bajalan, H. Hauser, P. L. Fulmek, 4th Int. Symposium on HMM, University of Salamanca, **8**, 78 (2003).
- [16] H. Hauser, D. Bajalan, P. L. Fulmek, Progress in Electromagnetic Research Symposium (March 28 to 31), 2004, Pisa, Italy: Extended paper (ISBN 88 8492 268 2), 667 (2004).
- [17] L. Sun, Y. Hao, C.-L. Chien, P. C. Searson, IBM J. Res. Develop., **49**, (2005) 79.
- [18] M. Mochidaa, T. Suzuki, J. Appl. Phys. **10**, 8644 (2002).
- [19] A. Lapicki, K. Kang, T. Suzuki, IEEE Trans. Magn. **38** 2589 (2002).

Magnetic Nanostructure Hysteresis Loop Calculation for Modified Thin Film Multi-layer by Ion Irradiation

D. Bajalan

Vienna University of Technology, Austria

Abstract—The nonlinear dependence of magnetization on direction of the applied magnetic field and history is described by statistical domain behavior using phenomenological adaptive parameters (like: g [1], h [A/m], k [J/m³], and q that are related to anisotropy, saturation field, static hysteresis loss, and pinning site density). The loop simulation data could be used also as parameters for thermal stability equation to calculate the relaxation time of the stored information on any magnetic nano particles (dots) of patterned magnetic media.

1. Introduction

Magnetic nanostructures are subjects of growing interest because of their potential applications in high density magnetic recording media and their original magnetic properties [1]. Multilayer thin films (like Co/Pt) are well known for their high magnetic anisotropy, and the origin of this high magnetic anisotropy has been the subject of interest for many researchers [2]. Demands for the continuous increase in the data storage density bring the challenge to overcome physical limits for currently used magnetic recording media [3]. Patterned magnetic media could be a way of realizing ultra high density storage media. Recently, demonstrations of areal recording density over 60 Gb/in² in both longitudinal and perpendicular magnetic recordings have been successfully made [4]. Determining the properties of small magnetic structures is extremely important for the development of data storage devices [5]. Better understanding of the micromagnetic processes in magnetic recording media is essential for developing novel materials for future ultrahigh density recording [6]. Good understanding of the noise mechanism in magnetic recording is required for developing heads and media for future applications [7].

In perpendicular recording, the magnetization pattern corresponding to the bits is provided perpendicular to the plane of the medium. The information is being stored in vertical domains or other structures of uniform magnetization [8]. The magnetic properties of an ultra thin multilayer can be patterned by controlled ion beam irradiation [9]. The basic step in this technique is to control the changes in the magnetic properties induced by the irradiation process.

In magnetic materials two characteristic length scales have to be considered [10]:

- at the atomic level, nearest neighbour exchange interaction is dominating,
- at a mesoscopic level, the domain wall width is the characteristic length dominating the magnetization reversal.

When the physical dimensions of a system become comparable to the interatomic spacing, strong modifications of the intrinsic magnetic properties (ordering temperature, magnetic anisotropy, spontaneous magnetization) are expected.

Micromagnetic modeling of the behavior of a nanostructured film beautifully describes the magnetization process, but requires a high calculational effort and long computation times. Furthermore, it is difficult to predict changes of the macroscopic physical behaviour due to variation of parameters. Phenomenological models, on the other hand, are very useful to simulate the behaviour of the magnetic material under the influence of varying parameters, especially when the parameters are based on physical constants.

2. Experiments

An assembly of ferromagnetic amorphous nanoparticles has been prepared by heavy ions irradiation of paramagnetic YCo₂ thin films [11, 12]. Several irradiation experiments carried out on YCo₂ samples have shown that fluences on the order 10¹² U ions/cm² causes changes in magnetic properties of the samples [12]. Important changes are reported to take place after the irradiation:

- change of spontaneous magnetization, coercivity and initial susceptibility [12], and
- a distinct change of the anisotropy perpendicular to the film plane [11].

3. Energetic Model

The magnetic behaviour of magnetic moments is mainly described by the well known equations of Schrödinger (exchange interaction) and Landau, Lifshitz, and Gilbert (dynamics of magnetization reversal). Above this fundamental is the shell of the physical constants describing spontaneous magnetization, anisotropy, magnetostriction, etc. The energetic model (EM) is designed as an interface between this shell and the macroscopic hysteresis phenomenon, able to predict many magnetic properties due to the relation of the parameters with the physical constants. The EM has been applied for different magnetization processes and materials [13–17].

The hysteresis of the magnetization M depending on the applied field H is described by the following equations, with the spontaneous magnetization M_s , the geometrical demagnetizing factor N_d , and the following phenomenological parameters:

1. g [1] related to anisotropy, reversible processes;
2. h [A/m] related to saturation field H_s , reversible processes;
3. k [J/m³] related to static hysteresis loss, irreversible processes;
4. q [1] related to pinning site density, irreversible processes.

In the cases of large domains, the microscopic constant c_r describes the influence of reversal speed. The $\text{sgn}(x)$ function provides the correct four quadrant calculation (with the related magnetization $m = M/M_s$):

$$H = H_d + \text{sgn}(m)H_R + \text{sgn}(m - m_o)H_I. \quad (1)$$

The first term of Eq. (1) describes linear material behaviour, using the demagnetizing field

$$H_d = -N_d M_s m, \quad (2)$$

the second term represents non-linear behaviour using the reversible field

$$H_R = h \left[((1+m)^{1+m} (1-m)^{1-m})^{g/2} - 1 \right], \quad (3)$$

including saturation at a field $H_s(M_s)$, and the third term describes hysteresis effects like initial susceptibility χ_0 , remanence M_r , coercivity H_c , static losses, and accomodation, using the irreversible field

$$H_I = \left(\frac{k}{\mu_0 M_s} + c_r H_R \right) \left[1 - \kappa \exp \left(- \frac{q}{\kappa} |m - m_o| \right) \right]. \quad (4)$$

For the initial magnetization, beginning with $M = 0$, $H = 0$, we set $m_o = 0$ and $\kappa = 1$. The function κ describes the influence of the total magnetic state at points of magnetization reversal. Therefore, κ (previous value κ_o) depends on the unit magnetization reversals $s = |m - m_o|$ up to this point of field reversal (m_o is the starting value of m at the last field reversal) with the simplification $e^{-q} \ll 1$:

$$\kappa = 2 - \kappa_o \exp \left[- \frac{q}{\kappa_o} |m - m_o| \right]. \quad (5)$$

The calculation always starts with the initial magnetization curve and m is increased stepwise (the stepwidth determines the desired resolution of the calculation), which gives the corresponding field by Eq. (1). At a point of field reversal κ is calculated by Eq. (5) and m_o is set to the actual value of m at this point. Then m is decreased stepwise until the next reversal point, etc.

3.1 Identification

The identification of the EM with measurements or data sheets can be done easily. At given M_s and N_d the parameters are directly calculated from special points of the hysteresis loop. Considering reference conditions, the index 0 is to indicate that the identification is done at a temperature $T = T_0$ without applied mechanical stress σ , using the following equations:

$$k_0 = \mu_0 M_s H_c \quad (6)$$

$$q_0 = \frac{M_s}{H_c} \frac{1 - N_d \chi_0}{\chi_0} \quad (7)$$

If χ_0 is not available one can also use the total static losses $w_l = \int_{-M_s}^{+M_s} H dM + \int_{+M_s}^{-M_s} H dM$ corresponding to the area of the closed major loop (upper and lower branch of hysteresis)

$$w_l = 4k \left(1 - \frac{2}{q} \right) \quad (8)$$

and we can write the equation for q_0 as

$$q_0 = \frac{8\mu_0 M_s H_c}{4\mu_0 M_s H_c - w_l}. \quad (9)$$

These relations allow even an estimation of M_s (at $c_r \approx 0$), using Eqs. (6), (7), and (9) to

$$M_s = \frac{2\chi_0 H_c}{1 - N_d \chi_0} + \frac{w_l}{4\mu_0 H_c}. \quad (10)$$

Furthermore, q_0 can also be determined by the reduced remanence m_r of the upper branch of a loop with the measured reduced maximum magnetization m_m . Using f_q as a factor related to m_r ,

$$f_q = [(1 + m_r)^{1+m_r} (1 - M_r)^{1-m_r}]^{g_0/2} - 1, \quad (11)$$

we identify q_0 as

$$q_0 = \frac{2}{m_m - m_r} \ln \frac{2H_c}{H_c - h_0 f_q + N_d M_s m_r} \quad (12)$$

By using f_g as a factor related to m_g which is the reduced magnetization at $H = H_g$, in the knee of the lower branch of the hysteresis,

$$f_g = \frac{1}{\ln \sqrt{(1 + m_g)^{1+m_g} (1 - m_g)^{1-m_g}} - \ln 2}, \quad (13)$$

hence g_0 is

$$g_0 = f_g \ln \frac{H_g - H_c - N_d M_s m_g}{H_s - H_c - N_d M_s} \quad (14)$$

Using f_c as a factor related to m_r and m_m ,

$$f_c = 1 - 2 \exp \left[q_0 \frac{m_r - m_m}{2} \right], \quad (15)$$

the microscopic constant describing the domain (grain) geometry ratio becomes

$$c_r = \frac{f_q \frac{H_s - H_c - N_d M_s}{M_s \exp g_0 \ln 2} - f_c \frac{H_c}{M_s} + N_d m_r}{\left(f_q \frac{H_s - H_c - N_d M_s}{M_s \exp g_0 \ln 2} + f_c \frac{H_c}{M_s} \right) - N_d m_r} \quad (16)$$

Finally, the identification equation of h_0 is

$$h_0 = \frac{H_s - H_c - N_d M_s}{(c_r + 1)(\exp[g_0 \ln 2] - 1)} \quad (17)$$

If H_s is not available, one can estimate H_s from the measured maximum field H_m at m_m using the approximation $H_s \gg H_c + N_d M_s$. Using f_h as a factor related to m_g and m_m

$$f_h = \frac{\ln \sqrt{(1 + m_m)^{1+m_m} (1 - m_m)^{1-m_m}} - \ln 2}{\ln \sqrt{\frac{(1 + m_g)^{1+m_g} (1 - m_g)^{1-m_g}}{(1 + m_m)^{1+m_m} (1 - m_m)^{1-m_m}}}} \quad (18)$$

we find

$$H_s = (H_m - H_c - N_d M_s m_m) \left(\frac{H_m - H_c - N_d M_s m_m}{H_g - H_c - N_d M_s m_g} \right)^{f_h}. \quad (19)$$

If N_d of the experimental arrangement is unknown then it can be estimated roughly by the differential susceptibility χ_c at coercivity of a measured hysteresis loop:

$$N_d \approx \frac{1}{\chi_c} \Big|_{H=H_c}. \quad (20)$$

If N_d of the sample is rather large so that the magnetization curve is strongly sheared ($M_r N_d > H_c$), then it can be necessary to identify g_0 and c_r by the backsheared curve ($N_d = 0$).

3.2 Calculation

The calculations have been done as following: At a given $N_d = 0.47$, the parameters $g_0 = 5.24$, $h_0 = 2.79 \text{ kA/m}$, $k_0 = 1.10 \text{ kJ/m}^3$, and $q_0 = 8.79$ are identified for the perpendicular hysteresis at $\Phi = 5 \cdot 10^{12} \text{ ions/cm}^2$ with $M_s = 20 \text{ kA/m}$. In the next step we vary only M_s in order to calculate the hysteresis of the other irradiation cases. Using Eqs. (6) and (7), we find the dependencies

$$H_c = \frac{k_0}{\mu_0 M_s} \quad (21)$$

and

$$\chi_0 = \frac{\mu_0 M_s^2}{k_0 q_0 + \mu_0 M_s^2 N_d} \quad (22)$$

which strongly affects the shape of the hysteresis Curve.

4. Conclusions

The rapid development of magnetic recording leads to a large increase of the bit density. Multilayer thin films with a perpendicular magnetic anisotropy devices may play an active role in the development and establishment of future storage technologies. Patterning magnetic media is a potential solution for ultrahigh density magnetic recording [18]. Ion beam modification of magnetic layers may be the possible future of ultra high density magnetic recording media.

After ion irradiation of YCo₂ thin films with different fluence values, the measured magnetization curves clearly show a perpendicular anisotropy [11]. The shape of the hysteresis loops depends strongly on M_s , which is predicted by the EM. It turns out that H_c is inversely proportional to M_s and χ_0 is proportional to M_s^2 , if N_d is neglected. As the EM parameters are also related to anisotropy it will be possible also to calculate the direction dependence of these magnetization curves, which is subject to further work.

REFERENCES

1. Jamet, M., W. Wernsdorfer, C. Thirion, D. Mailly, V. Dupuis, P. Mélinon, and A. Pérez, *Phys. Rev. Lett.*, Vol. 86, 4676, 2001.
2. Yamada, Y., T. Suzuki, H. Kanazawa, and J. C. Osterman, *J. Appl. Phys.*, Vol. 85, 5094, 1999.
3. Lapicki, A., K. Kang, and T. Suzuki, *IEEE Trans. Magn.*, Vol. 38, 2589, 2002.
4. Papusoi, C. and T. Suzuki, *J. Magn. Magn. Mater.*, Vol. 240, 568, 2002.
5. Kirk, K. J., J. N. Chapman, and C. D. W. Wilkinson, *J. Appl. Phys.*, Vol. 85, 5237, 1999.
6. Kisker, H., N. Abarra, Y. Yamada, P. Glijer, and T. Suzuki, *J. Appl. Phys.*, Vol. 81, 3937, 1997.
7. Phillips, G. N., T. Suzuki, K. Takano, and M. Takahashi, *J. Magn. Magn. Mater.*, Vol. 193, 434, 1999.
8. Suzuki, T., *Magneto-Optic Recording Thin Films*, in: I. M. H. Francombe (Ed.), *Handbook of Thin Film Devices Magnetic*, Vol. 4, *Magnetic Thin Film Devices*, Academic Press, 2000.
9. Ferre, J., C. Chappert, H. Bernas, J.-P. Jamet, P. Meyer, O. Kaitasov, S. Lemerle, V. Mathet, F. Rousseaux, and H. Launois, *J. Magn. Magn. Mater.*, Vol. 198, 191, 1999.
10. Nozières, J. P., M. Ghidini, N. M. Dempsey, B. Gervais, D. Givord, G. Suran, and J. M. D. Coey, *Nucl. Instr. and Meth. in Phys. Res. B*, Vol. 146, 250–259, 1998.
11. Givord, D., J. P. Nozières, M. Ghidini, B. Gervais, and Y. Otani, *J. Magn. Magn. Mater.*, Vol. 148, 253–259, 1995.
12. Solzi, M., M. Ghidini, and G. Asti, *Magnetic Nanostructures*, Vol. 4, 123, 2002.
13. Hauser, H. and P. L. Fulmek, *J. Magn. Magn. Mater.*, Vol. 133, 32, 1994.
14. Fulmek, P. L. and H. Hauser, *J. Magn. Magn. Mater.*, Vol. 157, 361, 1996.
15. Hauser, H. and R. Grössinger, *J. Appl. Phys.*, Vol. 85, 5133, 1999.
16. Andrei, P., L. Stoleriu, and H. Hauser, *J. Appl. Phys.*, Vol. 87, 6555, 2000.
17. Grössinger, R., H. Hauser, M. Dahlgren, and J. Fidler, *Physica B*, Vol. 275, 248, 2000.
18. Devolder, T., C. Chappert, Y. Chen, E. Cambril, H. Launois, H. Bernas, J. Ferre, and J. P. Jamet, *J. Vac. Sci. Technol. B*, Vol. 17, 3177, 1999.

Innovation Use of Nano Technology in Magnetic Storage Devices and Nano Computers

D. Bajalan

Vienna University of Technology, Austria

J. A. Aziz

University Sains, Malaysia

Abstract—The fluence of ion irradiation on polycrystalline thin films affects both anisotropy and spontaneous magnetisation M_s . The dependence of coercivity and initial susceptibility on M_s is predicted by a hysteresis model considering the balance of energy with good qualitative agreement.

1. Introduction

Demands for the continuous increase in the data storage density bring the challenge to overcome physical limits for currently used magnetic recording media [1, 2]. Ferromagnetic nano-particles of different polycrystalline thin films have been formed by heavy or light ion irradiation [2–4]. Although this modification technique may be a way to produce nano-magnetic particles, there are some critical size limits of nanomagnetic structures like the superparamagnetic limit (SPML) which faces magnetic nanotechnology. The magnetic properties of thin films are strongly influenced by their structure [5]. Small changes in the way a thin film is produced often give rise to large changes in some of the magnetic properties of the thin film [6]. This is best understood by observing how the microstructure of the film changes with processing and then correlating the microstructure directly with the properties of the thin film [6]. The behaviour of magnetic nanoparticles has fascinated materials scientists for decades [7]. Magnetic nanostructures have become a centre of great interest in the scientific community and in industry as the core technologies behind magnetic recording devices [8]. And the magnetic properties of an ultra thin multilayer can be patterned by controlled ion beam irradiation [4]. There are fundamental limits due to the atomic nature of matter which may impose ultimate physical bounds to nanofabrication and miniaturization [9]. Over the past several decades, amorphous and more recently nano-crystalline materials have been investigated for applications in magnetic devices [10]. The benefit found in the nanocrystalline alloys stem from their chemical and structural variations on a nano-scale which are important for optimizing magnetic recording devices [10].

2. Irradiation Process and Results

Several irradiation experiments carried out on the Co/Pt multi-layers samples (A1, A2, and A3 see Table 1) cause changes in the magnetic properties of the thin films [1, 4]. High aspect ratio silica masks on Co/Pt multi-layers were obtained by e-beam lithography and reactive ion etching with feature sizes down to 30 nm for lines and 20 nm for dots [3]. He⁺ ion irradiation of the magnetic layers through these masks was used to pattern the magnetic properties [3] (with fluences between 2.10^{14} and 2.10^{16} ions/cm² [4]). After mask removal, high resolution and high density, planar magnetic nano-structures were obtained [3]. The results of the irradiation show perfectly square hysteresis loops at room temperature, the coercive field decreasing progressively to zero [4]. The high perpendicular anisotropy of Pt/Co multi-layers originates from the interfaces between the layers [11]. Other experiments carried out on YCo₂ samples (thin polycrystalline film targets of polycrystalline with thicknesses of approximately 1 μm [[12]]) have shown that fluences in range of 10^{12} U ions/cm² cause changes in magnetic properties of the samples [1]. The result of these experiments were changes of the anisotropy perpendicular to the film plane [1], and change of spontaneous magnetisation, coercivity and initial susceptibility [13].

2.1. Equations and Calculation

The energetic model (EM) [14] is used to calculate the dependence of the shape of the hysteresis loop on M_s . The parameters of the model are calculated directly from measurements of special points of the hysteresis loop. The identification of the parameters is done at reference conditions (index 0) at a temperature $T = T_0$ without

any applied mechanical stress σ , and at given M_s and N_e (N_e is the effective demagnetizing factor which is the sum of the geometric demagnetizing factor N_d and the inner demagnetizing factor N_i). The following equations show how to determine the parameter of the model from spontaneous magnetization M_s , coercivity H_c , and from the effective demagnetization factor N_e .

$$k_0 = \frac{\mu_0 M_s H_c}{1 - 2 \exp(-q_0)} \quad (1)$$

k in J/m^3 related to static hysteresis loss (irreversible processes), and

$$q_0 = \frac{\mu_0 M_s^2}{k_0} \frac{1 - N_e \chi_0}{\chi_0} \quad (2)$$

q (dimensionless) is related to pinning site density (irreversible processes). Using Eqs. (1) and (2) with the approximation $\exp[-q_0] \ll 1$, we find the dependencies

$$H_c = \frac{k_0}{\mu_0 M_s} \quad (3)$$

and

$$\chi_0 = \frac{\mu_0 M_s^2}{k_0 q_0 + \mu_0 M_s^2 N_e} \quad (4)$$

which strongly affects the shape of the hysteresis. Figure 1 shows the initial magnetization curves calculated and measured major hysteresis loops in dependence of the measured value of M_s . No other change of the parameter values has been made. Table 1 shows the result of the evaluation of the equations above. Figure 2 shows the initial magnetization curves calculated with the parameters depending on M_s due to irradiation, compared to measurements.

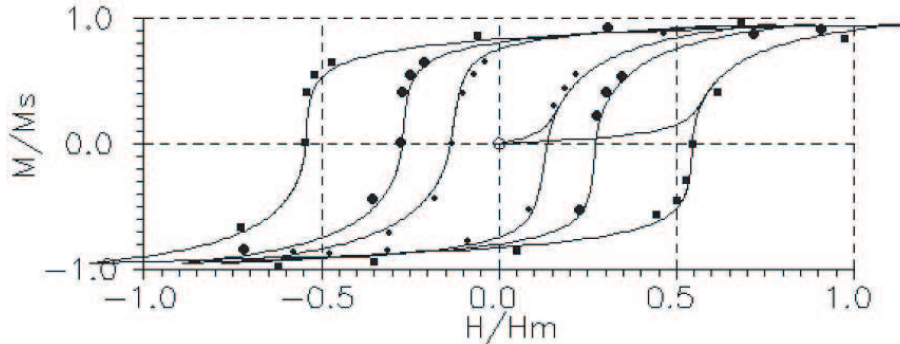


Figure 1: Calculated hysteresis loops for thin Films after different ion irradiation fluences perpendicular to the film plane and measured points. The H -values are related to the maximum field $H_m = 160 \text{ kA/m}$. The M -values are related to the respective saturation values of $M_s = 20 \text{ kA/m}$, $M_s = 40 \text{ kA/m}$, and $M_s = 60 \text{ kA/m}$. Only these values have been changed to calculate the different major hysteresis loops.

3. Anisotropy Energy after Irradiation

The anisotropy energy k_u is essential for evaluation of the thermal stability condition on a given bit. For the three irradiated samples (A1, A2, A3), k_u was calculated (Eq. 5).

$$k_u = \frac{H_k \mu_0 M_s}{2} \quad (5)$$

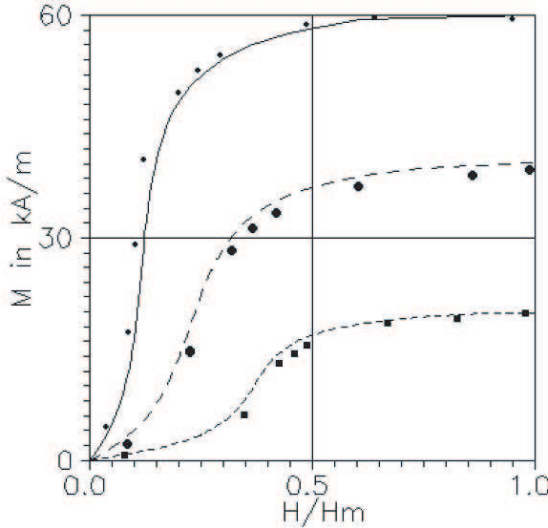


Figure 2: Calculated initial hysteresis curves loops for thin films after different ion irradiation fluences perpendicular (Tab. 1) to the film plane and measured points. The H-values are related to the maximum field $H_m = 160 \text{ kA/m}$. The calculation has been done by varying the value of M_s , only.

Table 1: Macroscopic hysteresis features depending on M_s [14].

Φ	[ions/cm ²]	A1, 10^{12}	A2, $5 \cdot 10^{12}$	A3, $2 \cdot 10^{13}$
M_s	[kA/m]	20	40	60
χ_0	[1]	0.157	0.199	0.536
H_c	[kA/m]	43.6	21.8	14.5

4. Nano Bits Stability Factor and Its Relaxation Time Calculation

Assuming a factor f_{BS} a simple abbreviation for “bit stability factor”, which represents the information stability of stored data on a given nano-bit, where: $f_{BS} = k_u V_{nano}/k_B T$, V_{nano} is the nano magnetic structure volume, $k_u V_{nano}$ is the energy barrier (ΔE), and $k_B = 1.38 \times 10^{-23} \text{ J/deg}$ Boltzmann constant. The magnetic stored information on a nano dot is then stable: if only the condition ($f_{BS} > 40$) is satisfied [16]. The relaxation time (time duration of stored information) or switching time of stored information τ can be obtained from the Arrhenius relation as:

$$\tau = \frac{1}{f_0} \exp(f_{BS}) \quad (6)$$

Where f_0 is the thermal attempt frequency [17], which is usually assumed to be 10^9 s^{-1} . The irradiation of the samples (A1, A2, A3) with different fluences as shown in Table 1, caused changes of the calculated values of k_u for each sample. Hence different values of f_{BS} and τ were calculated (see Table 2).

Table 2: Relation between k_u , and relaxation time τ at dot-width $D_w = 22 \text{ nm}$ and $T=10 \text{ K}$, as a result of irradiation, where f_{BS} condition is satisfied.

samples	k_u [J/m ³]	τ [Years]
A ₁	592.51	20.3×10^2
A ₂	1017.67	23.6×10^{16}
A ₃	1975.46	11.8×10^{38}

5. Conclusion

Magnetic nano-structures are subject of growing interest because of their potential applications in high density magnetic recording media and their original magnetic properties [11, 14–16]. The rapid development of magnetic recording leads to a large increase of the bit density. Multilayer thin films with perpendicular magnetic anisotropy devices may play an active role in the development and establishment of future storage technologies. Patterning magnetic media is a potential solution for ultrahigh density magnetic recording [3]. The shape of hysteresis loops depends strongly on M_s , where H_c is inversely proportional to M_s , and χ_0 is proportional to M_s^2 . Thermal stability is one of the serious issues for developing high density recording, and thus much effort has been made to overcome this issue [18]. The idea to use a regular array of physically isolated grains/dots promises an improvement in thermal stability of the recorded bits [19]. The anisotropy energy k_u is essential for evaluation of the thermal stability condition on a given bit, because k_u value is used in calculation of bit stability factor f_{BS} . A given nano bit is then thermally stable: if only the condition ($f_{BS} > 40$) is satisfied.

Acknowledgement

I would like to express my words of gratitude to Prof. H. Hauser, TU-WIEN.

REFERENCES

1. Solzi, M., M. Ghidini, and G. Asti, *Magnetic Nanostructures*, Vol. 4, 123, 2002.
2. Lapicki, A., K. Kang, and T. Suzuki, *IEEE Trans. Magn.*, Vol. 38, 589, 2002.
3. Devolder, T., C. Chappert, Y. Chen, E. Cambril, H. Launois, H. Bernas, J. Ferre, and J. P. Jamet, *J. Vac. Sci. Technol. B*, Vol. 17, 3177, 1999.
4. Ferre, J., C. Chappert, H. Bernas, J.-P. Jamet, P. Meyer, O. Kaitasov, S. Lemerle, V. Mathet, F. Rousseaux, and H. Launois, *J. Magn. Magn. Mater.*, Vol. 198, 191, 1999.
5. Sellmyer, D. J., C. P. Luo, and Y. Qiang, "Handbook of thin film devices magnetic, nanomaterials and magnetic thin films," *Academic Press*, Vol. 5, 337, 2000.
6. Laughlin, D. E. and B. Lu, Seagate Research Center, Materials Science and Engineering Department and Data Storage Systems Center, Carnegie Mellon University, Pittsburgh, 2, 2001.
7. Binns, C. and M. J. Maher, *New Journal of Physics*, Vol. 4, 85.1, 2002.
8. MacMathuna, D., "Surface studies of nanomagnetic systems," A thesis submitted to the University of Dublin, Trinity College, Physics Department, 3, 2002.
9. Speliotis, D. E., Presented at the THIC Meeting at the Naval Surface Warfare Center Carderock Bethesda, "Digital measurement systems/ADE technologies," 4, 2000.
10. McHenry, M. E., M. A. Willard, and D. E. Laughlin, *Progress in Materials Science*, Vol. 44, 291, 1999.
11. Jamet, M., W. Wernsdorfer, C. Thirion, D. Mailly, V. Dupuis, P. Mélinon, and A. Pérez, *Phys. Rev. Lett.*, Vol. 86, 4676, 2001.
12. Noziéres, J. P., M. Ghidini, N. M. Dempsey, B. Gervais, D. Givord, G. Suran, and J. M. D. Coey, *Nucl. Instr. and Meth. in Phys. Res. B*, Vol. 146, 250, 1998.
13. Givord, D., J. P. Noziéres, M. Ghidini, B. Gervais, and Y. Otani, *J. Magn. Magn. Mater.*, Vol. 148, 253, 1995.
14. Bajalan, D., H. Hauser, and P. L. Fulmek, *Physica B*, Vol. 343, 384, 2004.
15. Bajalan, D., H. Hauser, and P. L. Fulmek, *4th Int. Symposium on HMM*, Vol. 8, 78, University of Salamanca, 2003.
16. Hauser, H., D. Bajalan, and P. L. Fulmek, *Progress in Electromagnetic Research Symposium (March 28 to 31), 2004*, Pisa, Italy, Extended paper (ISBN 88 8492 268 2), 667, 2004.
17. Sun, L., Y. Hao, C.-L. Chien, and P. C. Searson, *IBM J. Res. Develop.*, Vol. 49, 79, 2005.
18. Mochidaa, M. and T. Suzuki, *J. Appl. Phys.*, Vol. 10, 8644, 2002.
19. Lapicki, A., K. Kang, and T. Suzuki, *IEEE Trans. Magn.*, Vol. 38, 2589, 2002.

Interpolating Wavelets on the Interval for Time-Domain Electromagnetics

C. Represa¹, J. Muñoz², and S. Amat³

¹Dpt. Ingeniería Electromecánica. Universidad de Burgos. Burgos. Spain.

²Dpt. Física. Universidad de Murcia. Murcia. Spain.

³Dpt. Matemática Aplicada y Estadística. Universidad Politécnica de Cartagena. Murcia. Spain.

Abstract—The aim of this work is to investigate a new MRTD scheme for the time domain solution of Maxwell equations. A wavelet-type approach based on interpolating wavelets on the interval is described. On this scheme, Maxwell curl equations are discretized both in space and time following a leapfrog algorithm and written in matrix form. Following Harten's framework, a derivative operator written in standard form is applied to the multiresolution decomposition of the electromagnetic field. This decomposition is obtained using Deslauriers-Dubuc interpolating wavelets on the interval. The simplest case of a TEM plane wave propagating is analyzed in order to show its capability to divide it into low resolution and high resolution details.

1. Introduction

Orthogonal wavelet bases have been presented as a powerful tool to perform the approximation and the numerical resolution of partial differential equations. Therefore, wavelets have been also applied to the solution of Maxwell's equations in time domain. This has given rise to the techniques known as Multi Resolution in Time Domain (MRTD) [1]. Otherwise, orthogonal wavelets have some inconveniences, such as a large support and a very oscillatory behaviour. In [2], multiresolution theory is presented from a different point of view, based on interpolatory schemes. New algorithms based on multiresolution analysis are devised. These algorithms are broad enough to include not only orthogonal wavelets as special case, but also non orthogonal wavelets. The freedom to choose the interpolatory functions makes it possible to keep advantages of multiresolution, while eliminating inconveniences of orthogonal wavelets. Another advantage to be considered in this interpolatory multiresolution setting is the possibility of analyzing nonlinear interpolation schemes in a natural way.

In this work, we propose to investigate a new MRTD scheme for the time domain solution of Maxwell equations. We adopt an interpolatory stencil which is symmetric around a given interval and was considered by Deslauriers and Dubuc [3]. A point-value interpolation scheme is used, where no integrals have to be solved, with one-sided stencils at intervals where the centred-stencil choice would require function values that are not available. Hence, boundary conditions receive a simplified treatment. Maxwell's curl equations are discretized both in space and time following a leap-frog algorithm and written in matrix form. Following Harten's framework [4], an Interpolatory Wavelet Transform (IWT) is defined and a derivative operator written in standard form is applied to the multiresolution decomposition of the electromagnetic field.

2. Formulation

As a starting point, the simplest case of a TEM plane wave propagating in a homogeneous, linear, isotropic and non-dispersive media, with fields E_x and H_y is analyzed. Hence, the equations to solve are:

$$\begin{aligned} \frac{\partial E_x}{\partial z} &= -\mu \frac{\partial H_y}{\partial t} \\ \frac{\partial H_y}{\partial z} &= -\epsilon \frac{\partial E_x}{\partial t} \end{aligned} \quad (1)$$

In the proposed scheme, we follow Yee's notation [5] in order to discretize equations (1) both in space and time. Therefore, centred finite differences are used for the time and space derivatives, computing the field values in discrete positions at the Yee's mesh points. In this way, knowing the initial conditions (boundary and excitation), the fields on the nodal points of the space-time mesh can be calculated in a leapfrog time marching manner. The discretized equations can be written in matrix form as follows:

$$\begin{aligned} \left[{}_{n+\frac{1}{2}}^{\frac{n+1}{2}} H_i \right] &= \left[{}_{n-\frac{1}{2}}^{\frac{n-1}{2}} H_i \right] - \frac{1}{\mu \Delta z} \frac{\Delta t}{\Delta z} \mathbf{D} \left[{}_n^n E_i \right] \\ \left[{}_{n+1}^{n+1} E_i \right] &= \left[{}_n^n E_i \right] - \frac{1}{\epsilon \Delta z} \frac{\Delta t}{\Delta z} \mathbf{D} \left[{}_{n+\frac{1}{2}}^{\frac{n+1}{2}} H_i \right] \end{aligned} \quad (2)$$

where Δt and Δz are the time and space steps respectively, which are related by the Courant stability factor [6], and \mathbf{D} represents the space derivative operator. In that way, ${}^n F_i$ means a field value at position $z = i\Delta z$ and at time $t = n\Delta t$. The space discretization is achieved by dividing the domain in N_0 cells of size Δz , as a starting point, then getting N_0+1 sampling points. This is what we call resolution level 0 ($k = 0$). Following the multiresolution analysis stated in [4], [7], we can now divide the spatial domain in $N_k = 2^k N_0$ cells or intervals, until a maximum level of desired resolution L ($k = L$) is reached, and the simulation domain having now $2^L N_0 + 1$ sampling points. Therefore, if we consider normalized simulation domain of length unity, a set of nested grid is defined as follows and depicted in figure 1:

$$Z^k = \{z_i^k\}_{i=0}^{N_k}, \quad z_i^k = i\Delta z_k, \quad \Delta z_k = 2^{-k}/N_0, \quad N_k = 2^k N_0.$$

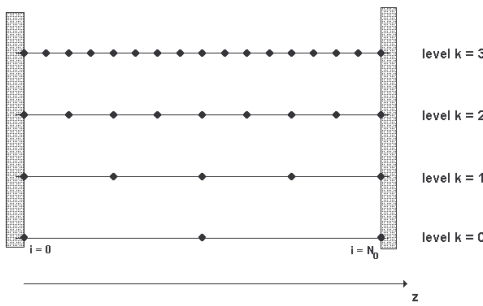


Figure 1: Simulation domain bounded by perfect electric or magnetic walls decomposed in a set of nested grids. Each level k has $N_k = 2^k N_0$ cells or intervals, and a total of $2^k N_0 + 1$ grid points.

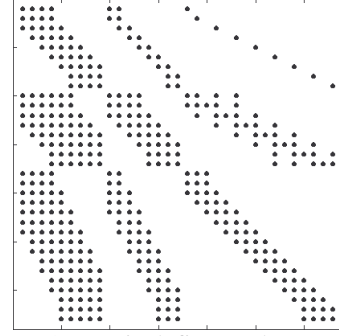


Figure 2: Typical finger shape of the derivative matrix written on its standard form.

We consider the point-value discretization at level k

$${}^n F^k = \left({}^n F_i^k \right)_{i=0}^{N_k} = \left({}^n F(z_i^k) \right)_{i=0}^{N_k}. \quad (3)$$

This is a real sequence of length N_k+1 corresponding to actual values of the sampled field F at time $t = n\Delta t$. Following [7] one can define an Interpolatory Wavelet Transform (IWT); thus, we can define the so-called direct (4) and inverse (5) multiresolution transform as

$$F^L \rightarrow M F^L \begin{cases} \text{do } k = L, \dots, 1 \\ F_i^{k-1} = F_{2i}^k, & 0 \leq i \leq N_{k-1} \\ d_i^k = F_{2i-1}^k - I_{k-1}(z_{2i-1}^k; F^{k-1}), & 1 \leq i \leq N_{k-1} \end{cases} \quad (4)$$

$$M F^L \rightarrow M^{-1} M F^L \begin{cases} \text{do } k = 1, \dots, L \\ F_{2i-1}^k = d_i^k + I_{k-1}(z_{2i-1}^k; F^{k-1}), & 1 \leq i \leq N_{k-1} \\ F_{2i}^k = F_i^{k-1}, & 0 \leq i \leq N_{k-1} \end{cases} \quad (5)$$

where $I_k(z; F)$ is just an interpolation of the function F at the points $\{z_i^k\}$. In the linear case, that is, where the interpolation operator I_k does not depend on the data, the multiresolution transform is a matrix M . Notice that in the point-value framework, the detail coefficients d_k are simple interpolation errors at the odd points of the grid that specifies the level of resolution. The most usual interpolatory techniques are polynomials. Hence, we can consider the Lagrange interpolation polynomials for the stencil of grid points $\{z_{i+m}^k\}$, where m belongs to the set of indexes $\xi(r,s) = \{-s, -s+1, \dots, -s+r\}$, with $r \geq s > 0$, $r \geq 1$:

$$I_k(z, F^k) = \sum_{m=-s}^{-s+r} F_{i+m}^k L_m\left(\frac{z - z_i^k}{\Delta z_k}\right), z \in [z_{i-1}^k, z_i^k] \quad (6)$$

being $L_m(z)$ the Lagrange polynomials of order r

$$L_m(y) = \prod_{l=-s, l \neq m}^{-s+r} \left(\frac{y-l}{m-l} \right), L_m(i) = \delta_i^m, i \in \xi. \quad (7)$$

The order of the reconstruction procedure, which characterize its accuracy, is $p = r + 1$. The particular situation $r = 2s + 1$ correspond to an interpolatory stencil which is symmetric around the given interval and was considered by Deslauriers-Dubuc [3]. For instance, if we choose $s = 2$ (that is, $r = 3$), from equations (4) and (5) we obtain the following multiresolution transform,

$$\begin{cases} \text{do } k = L, \dots, 1 \\ F_i^{k-1} = F_{2i}^k, & 0 \leq i \leq N_{k-1} \\ d_i^k = F_{2i-1}^k - \frac{1}{16} (-F_{i-2}^{k-1} + 9F_{i-1}^{k-1} + 9F_i^{k-1} - F_{i+1}^{k-1}), & 1 \leq i \leq N_{k-1} \end{cases} \quad (8)$$

$$\begin{cases} \text{do } k = 1, \dots, L \\ F_{2i-1}^k = d_i^k + \frac{1}{16} (-F_{i-2}^{k-1} + 9F_{i-1}^{k-1} + 9F_i^{k-1} - F_{i+1}^{k-1}), & 1 \leq i \leq N_{k-1} \\ F_{2i}^k = F_i^{k-1}, & 0 \leq i \leq N_{k-1} \end{cases} \quad (9)$$

where equation (8) are the direct transform (decomposition) and equation (9) states for the inverse transform (reconstruction). At the boundary, we choose one-sided stencils of $r + 1 = 2s$ points at intervals where the centred stencil choice would require function values which are not available. For instance, if $s = 2$, at the left boundary we get

$$d_1^k = F_1^k - \frac{1}{16} (5F_0^{k-1} + 15F_1^{k-1} - 5F_2^{k-1} + F_3^{k-1}), \quad (10)$$

and modifications at the right boundary can be found by symmetry. The advantage of Deslauriers-Dubuc interpolating wavelets is that their expansion coefficients represent actual values of the field. Consequently, it is no necessary to reconstruct the values of the fields by taking a weighted sum of neighbouring coefficients, resulting in a complicated algorithm and large computational overhead. Equation (8) refers to the direct multiresolution transform and it can be written in matrix form denoted as M . On the other side, equation (9) refers to the inverse multiresolution transform and its corresponding matrix form is M^{-1} . Once we have defined the multiresolution transform M , we can apply it to equations (2). Therefore, we obtain a multiresolution scheme for Maxwell's curl equations written in standard form:

$$\begin{aligned} \left[{}_{n+\frac{1}{2}} H_i \right]^L &= \left[{}_{n-\frac{1}{2}} H_i \right]^L - \frac{1}{\mu \Delta z} D^S \left[{}^n E_i \right]^L \\ \left[{}^{n+1} E_i \right]^L &= \left[{}^n E_i \right]^L - \frac{1}{\epsilon \Delta z} D^S \left[{}_{n+\frac{1}{2}} H_i \right]^L \end{aligned} \quad (11)$$

With this algorithm, a discrete sequence F^L is encoded to produce a multi-scale representation of its information contents, $(F^0, d^1, d^2, \dots, d^L)$. The standard form of the derivative matrix D is [7]:

$$D^S = MDM^{-1}. \quad (12)$$

The standard form also satisfies $M(DF) = D^S M(F)$, for every vector F . Both M and M^{-1} are continuous transformations. Then, if a matrix D represent a piecewise smooth operator, the matrix D^S will have significant coefficients in the typical *finger shape* as it is shown in figure 2.

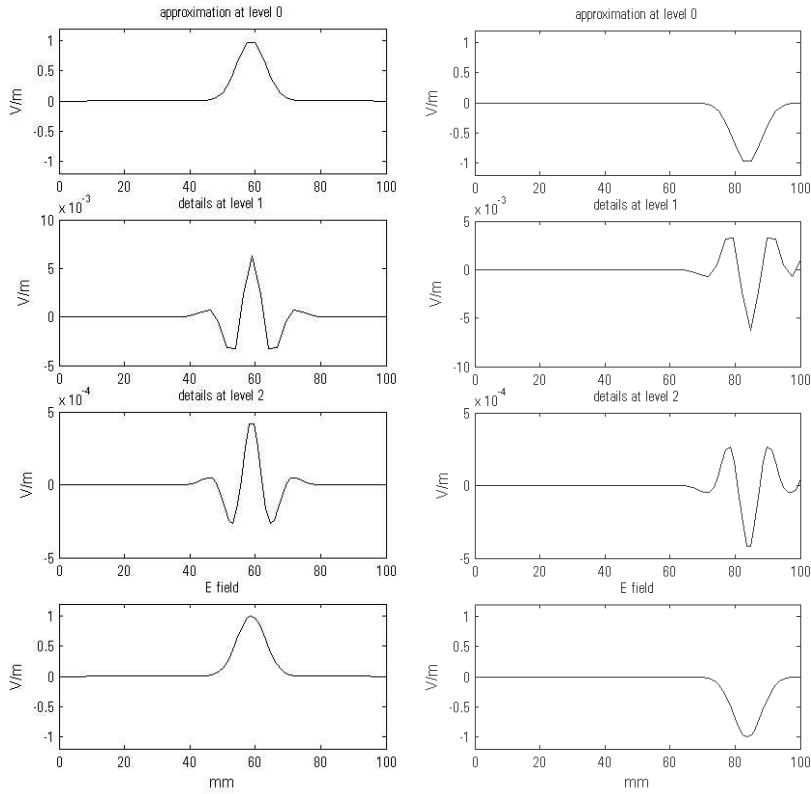


Figure 3: Snapshots of a gaussian pulse propagating along z axis before (left) and after (right) reflection on a electric wall.

Three levels of decomposition are depicted, that is, approximation at level 0, details at level 1 and details at level 2.

Notice the change on the scale of the vertical axis

3. Results

In order to show the capability of this scheme to separate approximations from details, a TEM plane wave propagating in a homogeneous, linear, isotropic and non-dispersive media is analyzed. Hence, a gaussian pulse is excited between electric walls (PEC) separate 100 mm. The simulation has been done dividing our domain into $N_0 = 20$ cells (coarse grid) and with a resolution of $L = 3$, that is, $20 \times 2^3 + 1 = 161$ sample points (fine grid). Therefore, a spatial resolution $\Delta z = 0.625$ mm is achieved. Following Yee's mesh, the electric and magnetic fields are specified at $t = 0$ and at $t = 1/2\Delta t$ respectively, where the width of the pulse is $i_w = 10$ and its centre is $i_c = 80$ in terms of the index of the spatial mesh. We have chosen a stability factor $s = 1$, thus the time discretization is $\Delta t = 2.08$ ps. Perfect electric and magnetic walls are modelled utilizing the symmetry conditions for the tangential fields, which are taken into account for the construction of the derivative operators. Figure 3 shows two snapshots of the gaussian pulse propagating from left to right. Three levels of decomposition are depicted, that is, approximation at level 0, details at level 1 and details at level 2. We can appreciate how it reflects on the electric wall and notice the change on the scale of the vertical axis. This feature shows us that details are negligible and this simulation could be done using the coarse grid with an acceptable error.

An additional simulation of a TEM plane wave propagating in a heterogeneous medium has been done. Here, a gaussian pulse is excited between electric walls (PEC) separate 100 mm and filled with two media of different permittivities, that is, $\epsilon_r = 1$ and $\epsilon_r = 5$. Two snapshots of the gaussian pulse going through one medium to another are depicted in figure 4. We notice how details become bigger as the gaussian pulse penetrates into the second medium. This feature tells us that in this situation details are not negligible and must use the finest grid to reduce the error.

4. Conclusion

A new MRTD scheme for the time domain solution of Maxwell equations has been investigated. A multiresolution transform has been derived using Lagrange interpolation polynomials which are symmetric around a given interval, leading us to a wavelet-type approach based on Deslauriers-Dubuc interpolating wavelets on the interval. The advantage of Deslauriers-Dubuc interpolating wavelets is that their expansion coefficients represent direct physical values of the

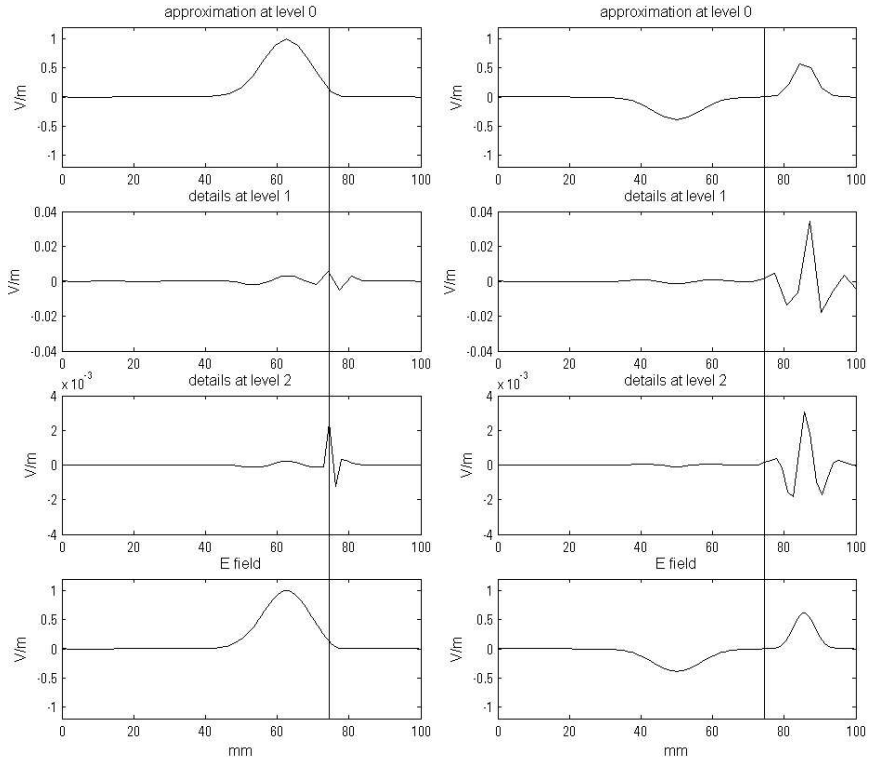


Figure 4: Snapshots of a gaussian pulse propagating along z axis through two media with different permittivity: vacuum, $\epsilon_r = 1$ (left) and $\epsilon_r = 5$ (right). Three levels of decomposition are depicted, that is, approximation at level 0, details at level 1 and details at level 2. Notice the change on the scale of the vertical axis.

field, and consequently it is no necessary to reconstruct actual values of the fields by taking a weighted sum of neighbouring coefficients. The wavelet decomposition, dividing a field component into approximations and details, allows us to decide if a coarse grid or a fine one is needed to achieve some fixed error. Therefore, another feature which makes this scheme attractive is that regarding to a scale adaptative time discretization, that will lead to a reduction of the numerical effort.

Acknowledgment

The authors acknowledge the support from Junta de Castilla y León, reference code UB 13/05.

REFERENCES

1. M. Krumpholz and L.P.B. Katehi, "MRTD: New Time-Domain schemes based on multiresolution analysis," *IEEE Trans. Microwave Theory Tech.*, Vol. 44, No. 4, 555-571, 1996.
2. A. Harten, "Discrete multiresolution analysis and generalized wavelets," *J. Applied Num. Math.*, Vol. 12, 153-193, 1993.
3. G. Delauries, S. Dubuc, "Symmetric iterative interpolation scheme," *Constr. Approx.*, Vol. 5, 49-68, 1989.
4. F. Aràndiga, V.F.Candela, "Multiresolution standard form of a matrix," *SIAM J. Numer. Anal.*, Vol. 33, No. 2, 417-434, 1996.
5. K. S. Yee, "Numerical solution of initial boundary value problems involving Maxwell's equations in isotropic media," *IEEE Trans. Antennas Propagat.*, Vol. AP-14, 302-307, 1966.
6. A. Taflove, *Computational Electrodynamics: The Finite-Difference Time-Domain Method*, Artech House, 1995.
7. S. Amat, S. Busquier, J.M. Gutiérrez, "An adaptive version of a fourth-order iterative method for quadratic equations," *Journal of Computational and Applied Mathematics*, in press.

Computation of the scattering of arbitrary shape bodies modeled by parametric surfaces using the multilevel fast multipole method.

I. González, O. Gutiérrez, F. Saez de Adana, M.F. Catedra
 Dpto. de Ciencias de la Computación. Universidad de Alcalá
 Escuela Politécnica, Campus Universitario, Universidad de Alcalá
 28806 Alcalá de Henares (MADRID), SPAIN
 Fax: + 34 91 885 66 46, email: felipe.catedra@uah.es

Abstract.

An application of the MLFMA to the electromagnetic analysis of realistic bodies modeled by NURBS surfaces is presented. The discretization of the geometry is carried out using also NURBS surfaces that permit an exact representation of the body under analysis. The basis and test functions are also conformed to the geometry to take advantage of the exact representation. A dual mesh is used to improve the convergence of the method and to allow analyzing non conducting bodies.

1. Introduction.

The application of the Method of Moments (MoM) to the analysis of large and arbitrarily shaped bodies has been a very important challenge in the last years [1]. A very fast and reliable technique to reduce the memory and time requirements using MoM is the Multilevel Fast Multipole Method (MLFMA) [1]. This method has become very popular due to the considerable reduction of computer resources derived from its application in the analysis of large scatterers, obtaining very good results in the analysis of complex bodies of arbitrary shape.

However, a very important problem when MoM is applied to the analysis of complex bodies is the discretization of the geometry to represent, as exactly as possible, the shape of the body. Classical representations are given by means of plane or quadratic patches with triangular or quadrangular shapes. The size of the patches and therefore, the number of unknowns in this case are given, not only, by the variations in the current phase, but also by the representation error derived by the approximation of the complex geometry by means of triangular or quadrangular patches.

An application of the MLFMA to the analysis of realistic bodies modelled by NURBS surfaces is presented. The discretization is carried out using quadrangular patches that are also pieces of NURBS surfaces completely conformed to the real shape of the object. Therefore, the electromagnetic method works directly over a model collected from the designing process (aeronautical, civil engineering) of the structure and no conversion programs are required. This fact implies that no representation error would be added since the geometry is analysed as it is.

2. Discretization of the geometry.

The main advantage of the presented scheme, as mentioned above, is the use of a discretization of the geometry totally conformed to the exact shape of the body under analysis. Each NURBS surface is divided in quadrangular patches, obtaining a lower number of subdomains by comparison of the discretization using triangular patches. Moreover, being the patches completely conformed to the real NURBS, there is an exact correspondence between the geometrical and the electrical representations of the body under analysis, allowing the treatment of complex bodies without any kind of approximation in the electrical representation.

There is an important difference between the discretization presented here and the one presented in [2], which is also NURBS conformed. While in [2], the discretization is accomplished in the parametric space, here it is done in the real space. The problem of the first one is that if you select an equally spaced step in the parametric space, this results on a non-equally spaced step in the real space. This produces two problems for some geometries: a higher number of subdomains and the presence of very small subdomains with low distance between them that can penalize the convergence of the method. Figure 1 shows the discretization accomplished in the parametric space (a) compared with the one in the real space (b) for a quarter of sphere. It can be seen that, meshing in the parametric space results on a high number of small patches close to the pole of the sphere, producing a higher amount of unknowns than in case (b) and making the convergence of the method worse.

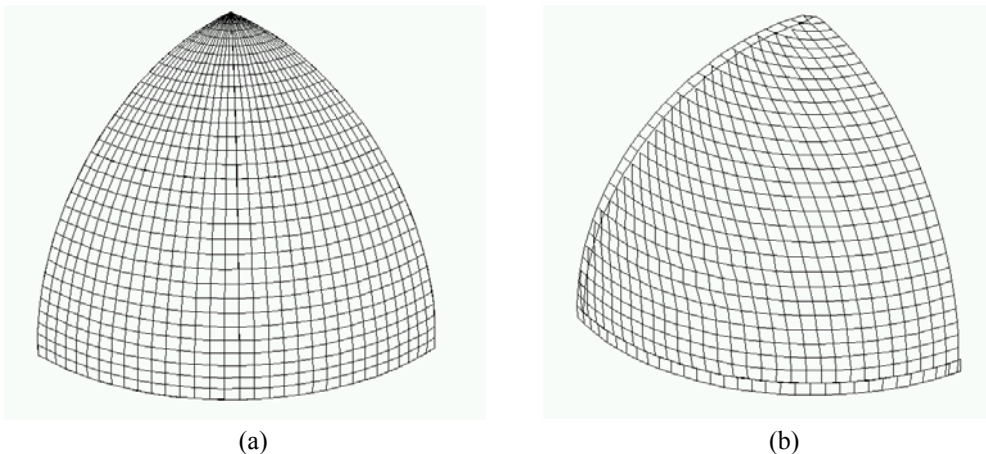


Figure 1. Comparison between the geometrical discretization in the parametric space (a) and in the real space (b).

The procedure of the creation of the conformed mesh is as follows: each NURBS surface of the geometry is divided in quadrangular subpatches of a size equal to the number of unknowns per wavelength considered for the electromagnetic analysis. Each subpatch is totally conformed to the NURBS surface. Therefore, there is not error in the electromagnetic modelling of the geometry. The division is performed in the real space, following the isoparametric lines of the surfaces. Quadrangular subpatches of the same size are built controlling the dimensions of one of their sides.

Using this new method for the division of the geometry, two kind of subpatches can be defined: the inner and the boundary subpatches. The boundary subpatches introduce the missing subpatches at each boundary to fully cover the NURBS surface. Figure 2 shows in black the inner subpatches to the surface in a sphere and in red the boundary subpatches.

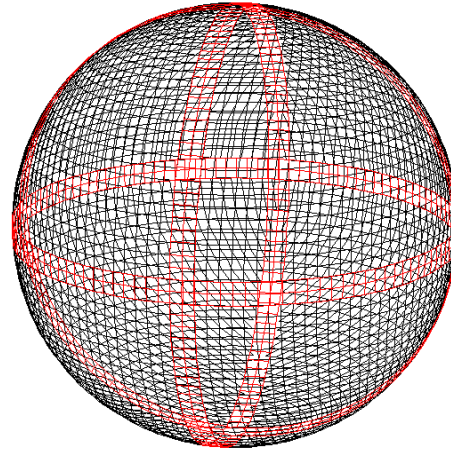
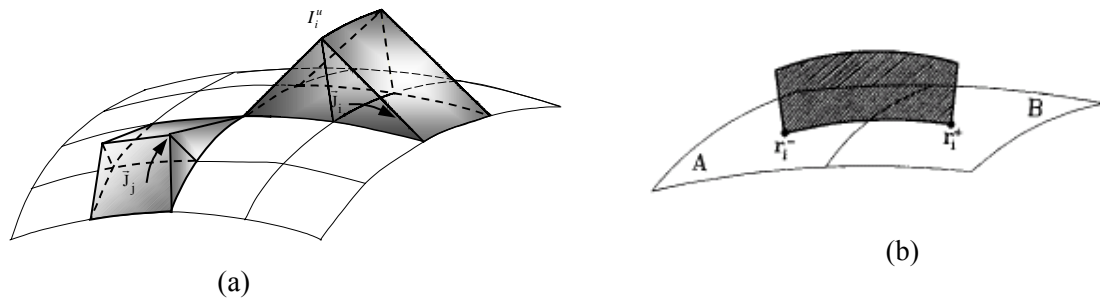


Figure 2. Example the mesh at a sphere.

3. Electromagnetic treatment.

Multilevel Fast Multipole Method (MLFMA) [1] has been implemented over the geometrical discretization described above. The method is implemented in such way, that the number of levels of the multilevel approach can be as high as desired, and it is a parameter that can be chosen by the user. The aggregation and dis-aggregation terms are obtained by the Fast Multipole Method (FMM) formulation [1], at the lowest level following an interpolation-interpolation procedure to accomplish the matrix-vector product at the highest levels.

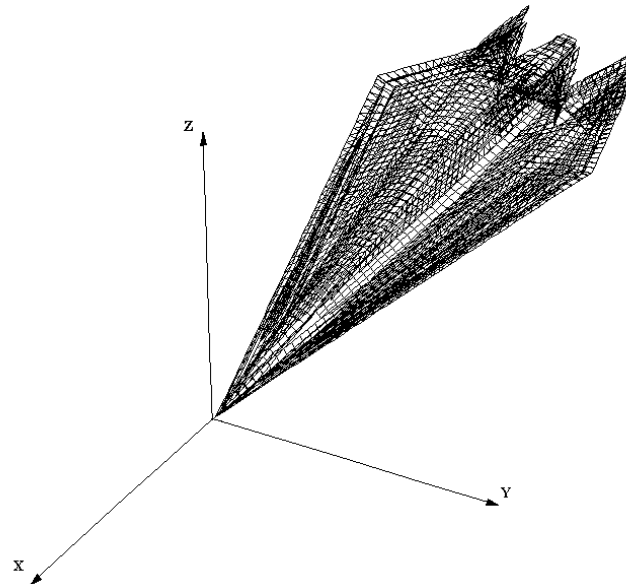
The basis functions are the Rao-Wilton-Glisson rooftops [3] and the test functions are the razor-blade functions [3]. Both functions have been modified in the implemented approach to be adapted to the conformed mesh described in Section 2 as can be seen in Figure 3.

**Figure 3.** Conformed basis and test functions.

A new approach to solve the problem is used. The approach can be an alternative to the Combined-Field Integral Equation (CFIE) formulation and shows better features than the CFIE to calculate the scattering from conducting bodies for ill conditioned problems. The scheme is also useful to analyze, using the Impedance Boundary Condition (IBC) approximation, the scattering from conducting bodies that can be totally or partially coated by dielectric materials. The scheme uses a dual mesh to represent the currents: one mesh represents the electric currents, and its dual mesh represents the magnetic currents [4].

4. Results.

Results of a scaled model of stealth airborne target, called FLAMME are shown. The CAD model of the FLAMME is depicted in Figure 4. The dimensions of the model are 240x595x 60 mm. The conformed mesh obtained from the discretization is shown in the Figure for a frequency of 3 GHz, illustrating the capability of the method to analyze complex bodies directly from the CAD model, without approximations. The number of unknowns is only 4490 due to the reduction accomplished with the conformed mesh. A comparison between the bistatic RCS obtained from measurements and from our approach can be seen in Figure 5 for 3 GHz. The incidence angle is $\theta=90^\circ$ and $\phi=200^\circ$ and the RCS is obtained for a cut with $\theta=90^\circ$ with ϕ varying from 206° to 360° . The results shown correspond to the HH polarization.

**Figure 4.** Discretized FLAMME model.

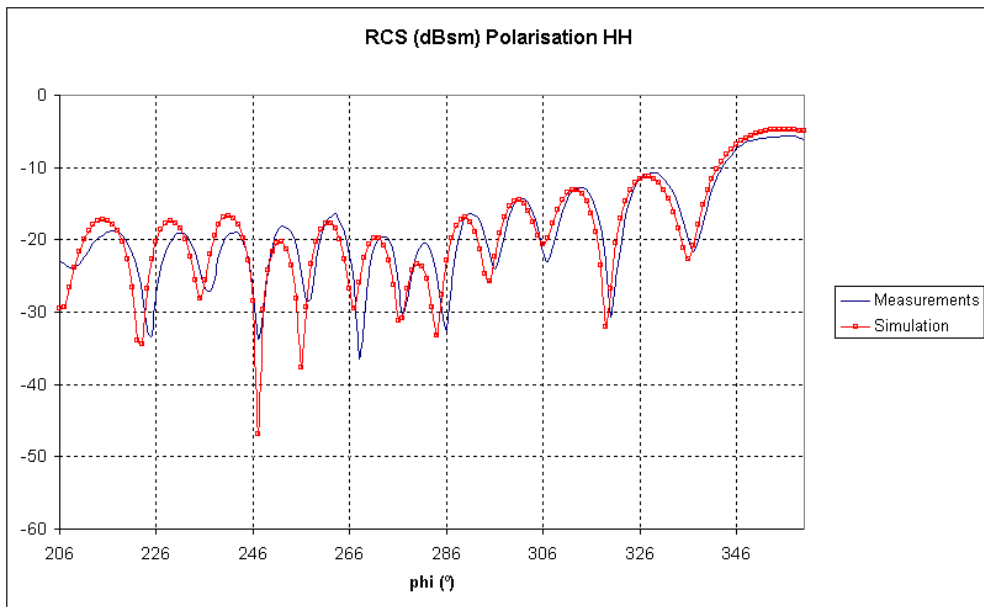


Figure 5. Bistatic RCS for a cut with $\theta=90^\circ$ (frequency 3 GHz).

A comparison between the measurements and the results of the proposed approach for an onboard antenna the Jason-I satellite mock-up are shown in Figure 7. The dimensions of the mock-up are 2.220x1.158x1.507 m and its geometrical model is shown in Figure 6. The frequency of analysis is 2.2 GHz and the results shown correspond to the cut $\phi=67.5^\circ$. Given the dimensions of the satellite the number of unknowns in this case is 152867, and the analysis is performed in 2h28m14s in an AMD Opteron at 2.4 GHz, thanks to the application of the MLFMA combined with the conformed mesh.

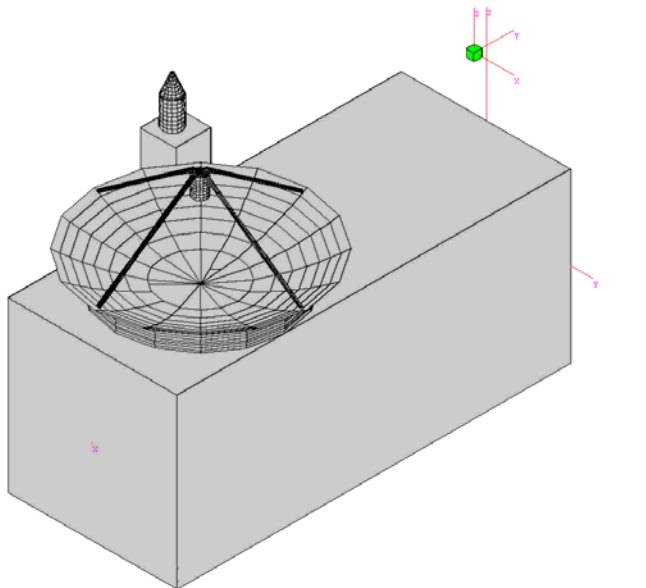


Fig. 6. Modelo del satélite Jason-I junto con la posición de la antena.

Eph Phi=67.5°

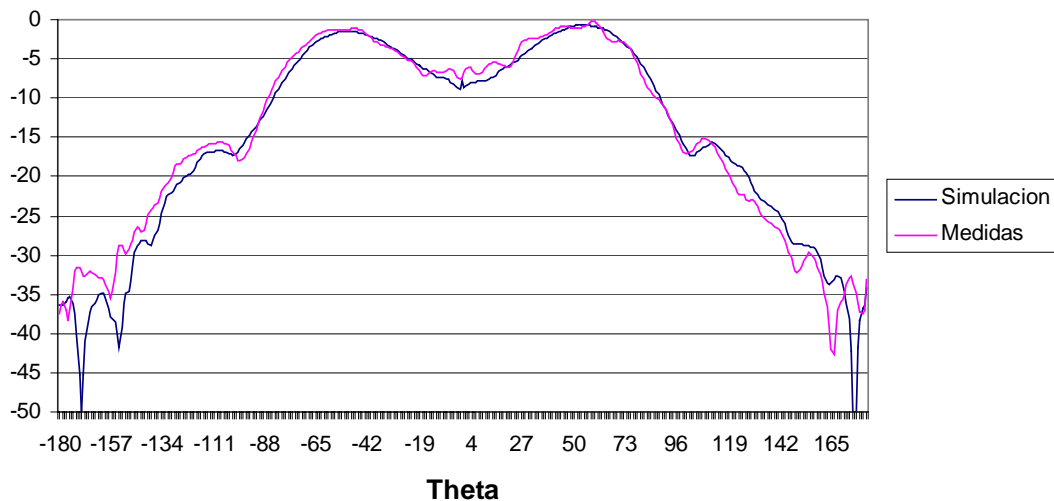


Fig. 7. Comparación entre las medidas y la simulación utilizando la aproximación presentada para el diagrama de radiación de la antena piramidal embarcada en el satélite Jason-I.

Acknowledgements.

The authors would like to thank to the Electromagnetism and Radar Department of ONERA(France) and FGAN-FHR(Germany) for the geometrical models and measurements of the FLAMME test case and to the CNES (France) for the measurements of the Jason-I mock-up.

This work has been supported, in part by the Spanish Department of Education and Science, Project TEC 2004-03187 and by Comunidad de Madrid and Universidad de Alcalá, projects PI2005/069 and CAM-UAH 2005/005.

References.

- [1] W. C. Chew, J. Jin, E. Michielssen, J. Song, Editors: "Fast and Efficient Algorithms in Computational Electromagnetics". Artech House Inc. 2001.
- [2] L. Valle, F. Rivas, M.F. Cátedra, "Combining the Moment Method with Geometrical Modelling by NURBS Surfaces and Bézier Patches", IEEE Transactions on Antennas and Propagation, vol. AP-42, No.3, pp.373-381, March 1994.
- [3] S.M. Rao, D.R. Wilton, A.W. Glisson. "Electromagnetic Scattering by Surfaces of Arbitrary Shape". IEEE Transactions on Antennas and Propagation, pp. 409-418, 1982.
- [4] O. Gutiérrez, F.J. Bueno, I. González, M.F. Cátedra. "An Improvement of the Method of Moments Combining EFIE and MFIE Formulations for Coated Conducting Bodies". 2005 USNC/URSI National Radio Science Meeting, Washington, USA, 3-8 July 2005.

Statistical Representative Volume Element for Predicting the Dielectric Permittivity of Random Media

Dominique Jeulin, Maxime Moreaud

Ecole des Mines de Paris

Centre de Morphologie Mathématique

35, rue Saint Honoré 77300 FONTAINEBLEAU

Abstract - When using numerical simulations, it is of primary importance to know the precision of the effective property estimated on a bounded domain of a microstructure, and the size of a so-called Representative Volume Element RVE. To solve this problem, a statistical approach was developed, based on the experimental determination of the integral range from numerical simulations. It enables us to relate the variance of the effective permittivity as a function of the volume V of the simulation, or equivalently of the number of small size unbiased simulations.

1. Introduction

An efficient way to solve the problem of homogenization of physical properties, for instance to predict the dielectric permittivity of heterogeneous media, makes use of numerical solutions of the corresponding partial differential solutions, before estimating the effective properties by spatial averaging of the solution. When working on realizations of a random medium, a natural question arises [1]: what is the representativity of the effective property estimated on a bounded domain of a microstructure? In other words, what is the size of a so-called "Representative Volume Element" RVE. We address the problem by means of a probabilistic approach, which is illustrated for two models of random media: A 2D autodual random set, and a 3D Boolean model of spheres, which can be used to model some nanocomposite materials.

2. Estimation of the Dielectric Permittivity by Homogenization

We use a method derived from [2], [3] and [4]. It estimates the equivalent macroscopic dielectric constant ϵ^* from the structure of a material and the properties of its constituents. For this, we determine the polarization field $P(x)$ inside the material knowing the local dielectric permittivity $\epsilon(x)$, by application of a constant electric field E_0 , and of periodic boundary conditions. An iterative scheme in the Fourier space is used to estimate $P(x)$, giving ϵ^* by means of a spatial average $\langle \rangle$. We have $\epsilon^* = \frac{\langle D \rangle}{\langle E \rangle} = \frac{\langle (\epsilon(x) - \epsilon_0)^{-1} \epsilon(x) P(x) \rangle}{\langle (\epsilon(x) - \epsilon_0)^{-1} P(x) \rangle}$, ϵ_0 being the dielectric permittivity of a reference medium.

3. Integral Range and Representative Volume Element

We consider different realizations of a model of stationary ergodic random functions $Z(x)$ on a volume V. We focus on fluctuations of the average measure obtained inside a volume V. The variance $\sigma_Z^2(V)$ of this average property depends on the volume and on the integral range of $Z(x)$ [5] [6] [7]:

$\sigma_Z^2(V) = \sigma_Z^2 \frac{A}{V}$ with σ_Z^2 the point variance of $Z(x)$, and A the integral range of the random function $Z(x)$. In the 3D case, the integral range A_3 is expressed as a function of the centered correlation function $W_2(h)$ by : $A_3 = \frac{1}{\sigma_Z^2} \int_{R^3} \overline{W}_2(h) dh$. Now, a representative volume element is defined for a physical property (in our case the dielectric permittivity), a given contrast between phases, and for a given precision for the estimation of the effective property [1]. In statistics, the absolute statistical error ϵ_{abs} and the relative error ϵ_{rela} on the mean value obtained with n independent realizations of the volume V are given by: $\epsilon_{abs} = \frac{2\sigma_Z(V)}{\sqrt{n}}$ and $\epsilon_{rela} = \frac{2\sigma_Z(V)}{Z\sqrt{n}}$. Using the integral range, we have:

$\varepsilon_{\text{abs}}^2 = \frac{4A\sigma_z^2}{nV}$ and $\varepsilon_{\text{rela}}^2 = \frac{4A\sigma_z^2}{Z^2 nV}$. The RVE can be defined as the minimal volume to estimate the property Z with a single realization and a given relative error $\varepsilon_{\text{rela}}$. Alternatively, it can be useful to reduce the computational costs, to operate on many small volumes. Therefore it becomes necessary to define a minimal volume V_{\min} providing no bias on the average effective property measure, and a number of realizations n_{\min} giving $\varepsilon_{\text{rela}}$. It is obtained from $n_{\min} V_{\min} = \frac{4A\sigma_z^2}{Z^2 \varepsilon_{\text{rela}}^2}$.

4. 2D application: Autodual dead leaves model

Dead leaves models [8] [9] [10] allow to simulate in any dimension sequential random images with a covering process. These random models are used to reproduce perspective views, as powders observed by scanning electronic microscopy, or sequences of multicomponent textures. Here we use a 2D autodual dead leaves model (with the area fraction $p = 0.5$) with white and black discs having a constant diameter of 10 pixels (cf. *Figure 1*). For this model ε^* is known exactly ($\varepsilon^* = \sqrt{\varepsilon_1 \varepsilon_2}$, ε_1 and ε_2 being the dielectric permittivity of the two phases), as well as the theoretical values of the point variance of $E(x)$ and $D(x)$ fields. We simulated several realizations of this model for different sizes of images (cf. *Table 1*).

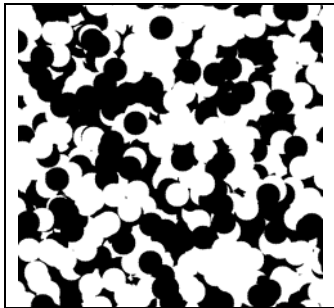


Figure 1: autodual dead leaves model of discs.

Size of image	Number of realizations
32^2	5000
64^2	2000
128^2	800
256^2	400
512^2	200
1024^2	100
2048^2	60

Table 1: number and size of realizations.

4.1. Integral Range of the area fraction

With the simulated images, the integral range A_2 for the surface area is estimated by means of a linear fit of the expression $A_2 = \sigma_{\text{Aa}}^2 (\sigma^2 / S)^{-1}$ with $\sigma^2 = 0.5^2$. We obtain $A_2 = 54.24 \text{ pixels}^2$, very close to its theoretical value (52.234 pixels^2).

4.2. Integral Range of the Effective Dielectric Permittivity for an increasing contrast of permittivity

To estimate the integral range for ε^* for an increasing contrast of permittivity, we use the previous realizations of autodual dead leaves models with $\varepsilon_1 = 1$ and $\varepsilon_2 = 2, 10, 100, 1000$ or 10000 . For each realization and for each contrast, ε^* is estimated by means of the homogenization method, applying a uniform unit field E_0 along axis x. Figure 2 shows the estimations of ε^* and the intervals of confidence, as a function of the size of the images for two contrasts. The larger the contrast is, the larger are the bias on estimations of ε^* and the interval of confidence, for small size domains.

The integral range for ε^* can be estimated by means of a linear fit of the expression $A = \sigma_{\varepsilon^*}^2 (\sigma^2 / S)^{-1}$. For the autodual model, the theoretical point variance for $D(x)$ is given by the expression:

$\sigma_D^2 = \frac{E_0^2}{2} \sqrt{\varepsilon_1 \varepsilon_2} (\sqrt{\varepsilon_1} - \sqrt{\varepsilon_2})$. Consequently, the theoretical point variance for ε^* is given by $\sigma_{\varepsilon^*}^2 = \frac{1}{2} \sqrt{\varepsilon_1 \varepsilon_2} (\sqrt{\varepsilon_1} - \sqrt{\varepsilon_2})$. In addition, by means of maps of $D(x)$, $\sigma_{\varepsilon^*}^2$ can be estimated. We have

$\sigma^2 = \sigma^2(., S) \left(1 - \frac{A}{S}\right)^{-1}$, $\sigma^2(., S)$ being the point variance for a finite area S. From large size maps (2048^2

for instance), we get a good estimation of the point variance for all contrasts (cf. *Table 2*). Estimations of the integral range as a function of the contrast are given in *Table 2*.

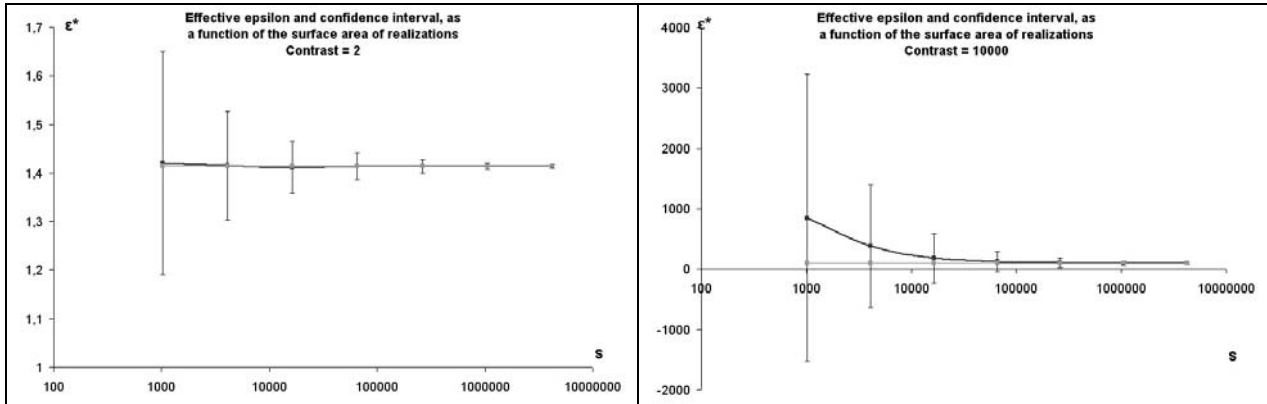


Figure 2 : Effective Dielectric Permittivity and interval of confidence for two contrasts (2 and 10000). In dark grey, estimation using homogenization method; in light grey, expected theoretical value.

Contrast	2	10	100	1000	10000
$\sigma_{\epsilon^*}^2$ theoretical	0.12	7.39	405	14827.2	490050
$\sigma_{\epsilon^*}^2$ estimated from the D(x) field	0.12	7.39	404	14781	490355
Integral range of ϵ^* (pixels ²)	111	145	213	470	848

Table 2: Estimations of the point variance and of the integral range of effective dielectric permittivity for several contrasts.

The higher the contrast is, the higher is the integral range of ϵ^* . This is explained by the covariance of D(x) maps: for a low contrast, the covariance curve goes under its asymptotic level, due to a short distance negative correlation along the axis y (cf. *Figure 3*), which lowers the integral range. This phenomenon is not present for a high contrast of permittivity.

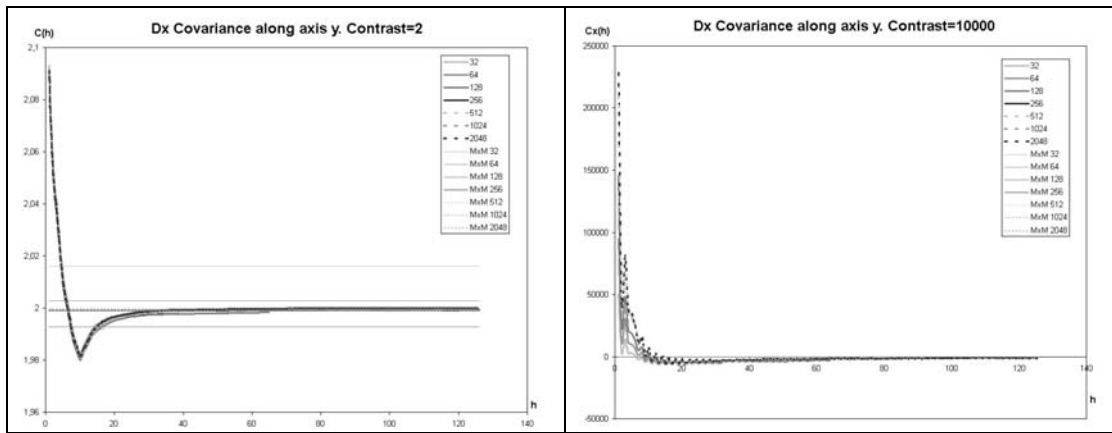


Figure 3: Covariance of electric displacement field D(x) according to axis y.

4.3. Representative Volume Element for the effective dielectric permittivity

For a given contrast, we can determine, by means of curves like in Figure 1, a minimal area for which the bias on the estimation of ϵ^* is lower than a given relative error. The minimum number n_{min} of realizations allowing an estimation of ϵ^* with a precision equal to the fixed relative error is given by the expression: $n_{min} S_{min} = \frac{4A\sigma^2}{\epsilon^{*2} \epsilon_{rela}^2}$. For instance, for a 5% relative error, and a contrast of 10, 42 realizations of size 64^2 are required; for a 10000 contrast, 63 realizations of size 1024^2 are required.

5. 3D application: Boolean Model of spheres

The Boolean model of spheres can be used to simulate some nanocomposite materials with carbon black [11]. It is obtained by implantation of random grains (here spheres with a constant diameter of

10 voxels) on germs of a Poisson point process [12]. The percolation threshold of this model is known from simulations (about 0.2895) [13]. Simulations were generated according to Table 3, with average volume fractions surrounding the percolation threshold (0.2, 0.3, 0.5).

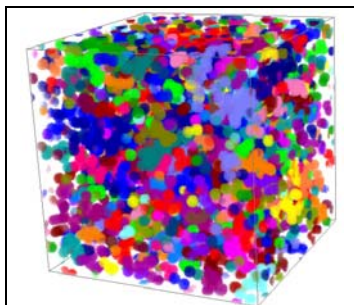


Figure 4: Boolean Model of spheres.

Size of image	Number of realizations
32^3	200
64^3	50
128^3	20
256^3	10

Table 3: number and size of realizations.

5.1. Integral Range of volume fraction

Using the simulation, the integral range is estimated for the volume fraction by means of a linear fit of the expression $A_3 = \sigma_{vv}^2 (\sigma^2/V)^{-1}$ with $\sigma^2 = p(1-p)$ (p : volume fraction of spheres). We obtain $A_3 = 425$, 423 and 351 voxels 3 , for respectively $p = 0.2$, 0.3 and 0.5 . These estimations are in a good agreement (within 10-15%) with the corresponding theoretical values (484, 462, and 408 voxels 3).

5.2. Integral Range and Representative Volume Element of the Effective Dielectric Permittivity for an increasing contrast of permittivity

For the Boolean model the same approach as previously was used, with $\epsilon_1 = 1$ (for the matrix) and $\epsilon_2 = 10, 100$ or 1000 (for the spheres). In Figure 5 are shown the estimations of ϵ^* and the intervals of confidence as a function of the size of the 3D images for three volume fractions and for two contrasts. As for the dead leaves model, higher the contrast is, higher the bias on estimations of ϵ^* and the intervals of confidence are. For $p = 0.3$ and for contrasts of 10 and 1000 , the estimated integral ranges of ϵ^* are respectively 558 and 1663 voxels 3 . The integral range increases with the contrast, since the covariance curve goes below its asymptotic level for a low contrasts (cf. Figure 6), as for the dead leaves model.

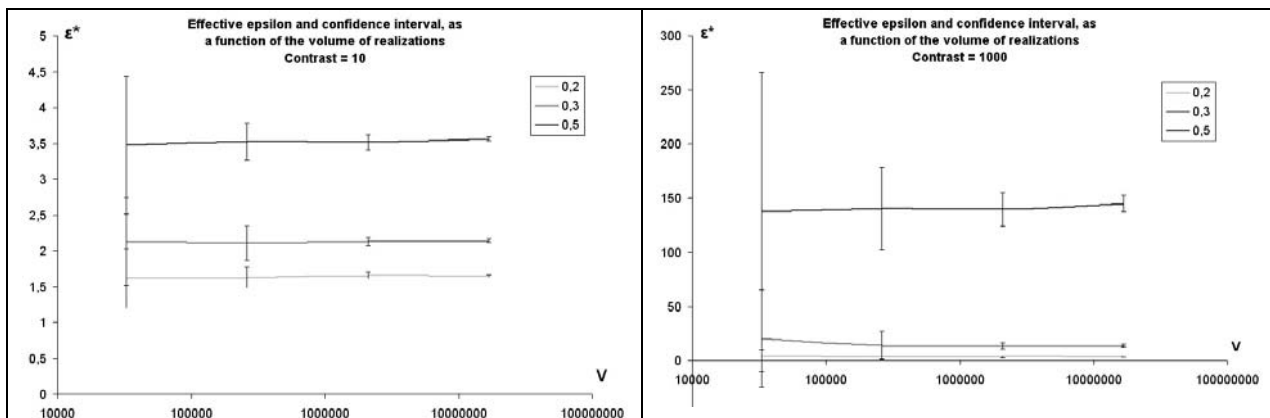


Figure 5: Effective Dielectric Permittivity and interval of confidence for two contrasts (10 and 1000) and for several volume fractions.

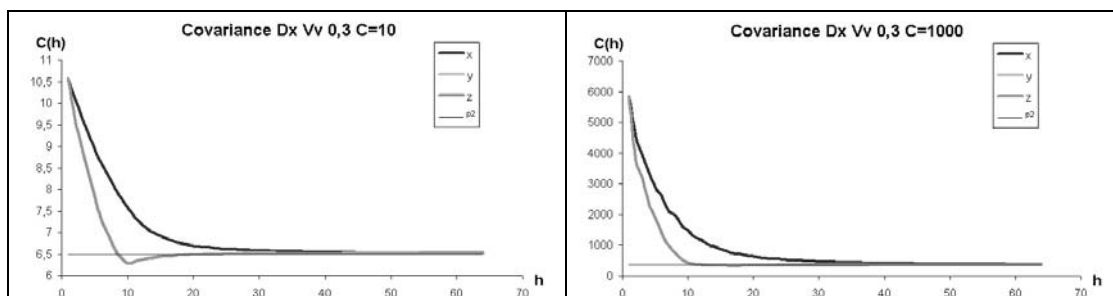


Figure 6: Covariance of the electric displacement field Dx for contrasts 10 and 1000.

Now the size of a RVE is obtained. For instance, for a 5% relative error, $p = 0.3$ and for a contrast of 10, 33 realizations of size 32^3 are needed; for a 1000 contrast, 542 realizations of size 64^3 are required.

6. Conclusion

The proposed methodology enables us to give an interval of confidence for the prediction of the effective properties of a random medium from finite size simulations. It was first validated by integral ranges obtained from the estimation of the dielectric permittivity of 2D autodual random sets (a two phase symmetrical dead leaves model [10], for which the exact effective permittivity is known), and then applied to 3D Boolean models of spheres. The effective permittivity ϵ^* and the corresponding RVE were estimated on images of $D(x)$ with increasing sizes and for an increasing contrast of properties. More complex models of 3D multiscale random nanocomposites reproducing the non homogeneous distribution of carbon black or of carbon nanotubes in a matrix [13] [14] are now studied by the same method.

Acknowledgment: This work was made possible thanks to a DGA-CNRS grant for Maxime Moreaud.

REFERENCES

- [1] Jeulin D., Kanit T., Forest S. "Representative volume element: a statistical point of view", Bergman D. et al (eds.) 2004, *Continuum Models and Discrete Systems*, 21-36.
- [2] Moulinec H., Suquet P. "A numerical method for computing the overall response of nonlinear composites with complex microstructure", *Comp. Meth. in appl. Mech. and Eng.* 157 (1998) 69-94.
- [3] Eyre D.J., Milton G.W. "A fast numerical scheme for computing the response of composites using grid refinement", *Eur. Phys. J. Appl. Phys.* 6 (1999) 41-47.
- [4] Delarue A. *Prévision du comportement électromagnétique de matériaux composites à partir de leur mode d'élaboration et de leur morphologie*, Thesis, Paris School of Mines, 26 september 2001, 139-144.
- [5] Matheron G. *The theory of regionalized variables and its applications*, Paris School of Mines publications 1971.
- [6] Matheron G. *Estimating and Choosing*, Springer-Verlag 1989, Berlin.
- [7] Lantuejoul Ch. "Ergodicity and integral range", *Journal of Microscopy* 1991, 161:387-403.
- [8] Matheron G. « Schéma booléen séquentiel de partition aléatoire», N-83, CMM, *Paris School of Mines publication*, 1968.
- [9] Jeulin D. *Morphologie Mathématique et Propriétés Physiques des agglomérés de minérais de fer et du coke métallurgique*, Thesis, Paris School of Mines, 23 november 1979.
- [10] Jeulin D. "Dead leaves models: from space tessellation to random functions", *Advances in Theory and Applications of Random sets*. Jeulin D. (ed.). World Scientific Publishing Company, 1997, pp. 137-156.
- [11] Savary L., Jeulin D., Thorel A. "Morphological analysis of carbon-polymer composite materials from thick sections", *Acta Stereologica*, vol. 18 (1999), No.3, 297-303.
- [12] Matheron G. *Random sets and Integral Geometry*, Wiley, 1975.
- [13] Jeulin D., Moreaud M. "Multi-scale simulation of random spheres aggregates – application to nanocomposites", *Proc. 9th European Congress on Stereology and Image Analysis*, Zakopane, Poland, May 10-13 2005, Vol. I p. 341-348.
- [14] Jeulin D., Moreaud M. "Percolation of multi-scale fiber aggregates", *Proc. 6th International Conference on Stereology, Spatial Statistics and Stochastic Geometry*, Czech Republic, June 26-26 2006.

Right Angle-Shaped Slot Antenna for IEEE 802.11b/g/j Applications

P. Rakluea

Dept. of Electronic and Telecommunication Engineering
Rajamangala University of Technology Thanyaburi,
Pathumtane, Thailand
E-mail : paitoon_r@rit.ac.th

T. Wakabayashi

School of Information Technology and Electronics
Tokai University
Hirasuka, Kanagawa, 259-1292 Japan
E-mail : wakaba@dt.u-tokai.ac.jp

P. Wiriacosol and N. Anantrasirichai

ReCCIT and Faculty of Engineering
King Mongkut's Institute of Technology Ladkrabang
Ladkrabang, Bangkok, 10520, Thailand
E-mail : kanoppin@kmitl.ac.th

Abstract—A microstrip-fed right angle-shaped slot antenna is enhanced to support user demands on wireless LAN applications. This paper presents procedure details on designing a right angle-shaped slot antenna for the conventional IEEE 802.11b/g, Wi-Fi standard, and extensional IEEE 802.11j operating in Japan. Some matching techniques to control the dual-frequency range characteristics are revealed. Effects of the ratio of the right angle-shaped slot arm length, the position and length of the feed line were evaluated. Method of moment (MoM) was adopted to analyze the characteristic of the proposed antenna. Antenna characteristics including return loss, VSWR and input impedance are shown. The simulation results show a remarkable microstrip-fed right angle-shaped slot antenna that can be utilized in 2.4 to 2.4835 GHz and 4.9 to 5.091 GHz bands. The return losses, at the center resonant frequencies, 2.43 GHz and 4.95 GHz, are lower than -35 dB with properly match with 50-ohm transmission line.

1. Introduction

A right angle-shaped slot antenna is one of the simple structures developed from a right angle antenna, as referred in [1-2]. The advantages of the proposed right angle-shaped antenna are lightweight, thin profile and the ease of fabrication. The antenna was designed at the perimeter of 0.44 of the guided wavelength. The IE3D software as referred in [3] was used to analyze the proposed antenna.

In this study, a microstrip-fed right angle-shaped slot antenna is presented. The design objective is to satisfy IEEE 802.11b/g and IEEE 802.11j standards covering 2.4 to 2.4835 GHz and 4.9 to 5.091 GHz bands. Method of moment was applied to evaluate the characteristic of the proposed antenna.

Although many researchers have studied the right angle-shaped antenna, the controlling of dual matching resonant frequency was rarely investigated. In this paper, the effects on varying the length of microstrip feed line was investigated and then the effects on positioning of microstrip feed line were studied. After a proper adjusting, the ratio of the vertical slot length to the horizontal slot length was 1:1.7. The simulation result showed that the antenna could be applied to serve 2.4 to 2.4835 GHz and 4.9 to 5.091 GHz bands.

2. Antenna Design

This antenna was designed on RT/Duroid 5880 with 1.575 mm of thickness, h , and 2.2 of dielectric constant, ϵ_r . The right angle structure was selected as the simple structure to be simulated, as shown in Fig. 1a, whereas the concerned parameter was shown in Fig. 1b.

The microstrip width, W_m , of the proposed antenna was determined by (1), as referred in [4], and then was truncated to 4.5 mm.

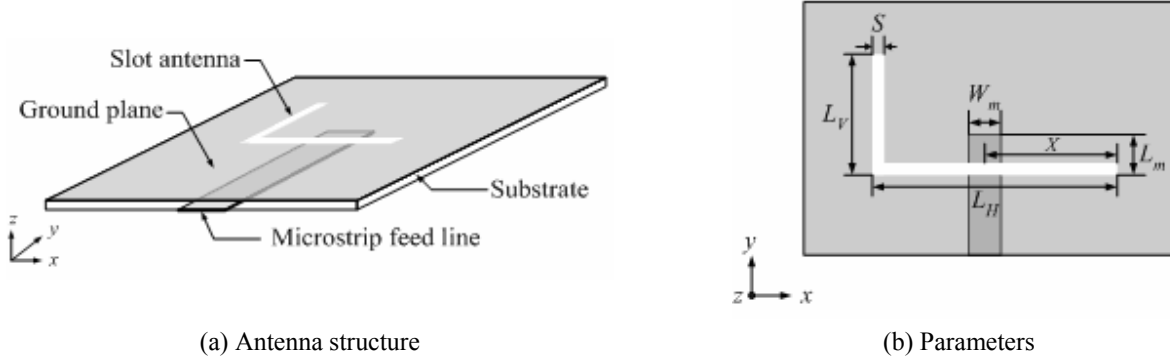


Figure 1: Antenna configuration

$$Z_0 = A(C - B) \quad (1)$$

Where; Z_0 = transmission line impedance.

$$A = \frac{119.9}{\left[2(\epsilon_r + 1)\right]^{\frac{1}{2}}}, \quad B = \left[\ln\left(\frac{\pi}{2}\right) + \frac{\ln\left(\frac{4}{\pi}\right)}{\epsilon_r} \right] \frac{\epsilon_r - 1}{2(\epsilon_r + 1)} \quad \text{and} \quad C = \ln\left\{ \frac{4h}{W_m} + \left[\left(\frac{4h}{W_m} \right)^2 + 2 \right]^{\frac{1}{2}} \right\}$$

Equation (2) was used determine a λ_g at 2.44 GHz, which is the center frequency of operating band in IEEE 802.11 b/g. The guided wavelength, λ_g , about 97 mm was obtained.

$$\lambda_g = \frac{c/f}{\sqrt{\epsilon_{eff}}} \quad \text{Where; } \epsilon_{eff} = \frac{\epsilon_r + 1}{2} \quad (2)$$

In this design, the slot width was set at 1.0 mm. The vertical and horizontal slot was orthogonal to each other. The total length of vertical and horizontal slot, measured on the inner edge was 46 mm.

3. Effects of Varying the Length of Microstrip Feed Line for Dual-frequency Operation

In this study, the effect of varying the length of microstrip feed line, L_m , with the objective to get dual frequency characteristic to support dual-frequency range. It was hoped that the two ranges had equal return loss. The expected dual-frequency ranges were the bands that possessed lower order resonant frequency centered at 2.44 GHz, and the higher order resonant frequency centered at 5.0 GHz.

The total sum length of the vertical and the horizontal slot was arbitrarily kept constant at 46 mm. The length of vertical slot was allowed to increase while the length of the horizontal slot decreased. As a result, the lower order resonant frequency shifted up, while higher order resonant frequency shifted down. On the other hand, decreasing the length of vertical slot and increasing the length of horizontal slot caused the lower order resonant frequency to shift down and the higher order resonant frequency to shift up.

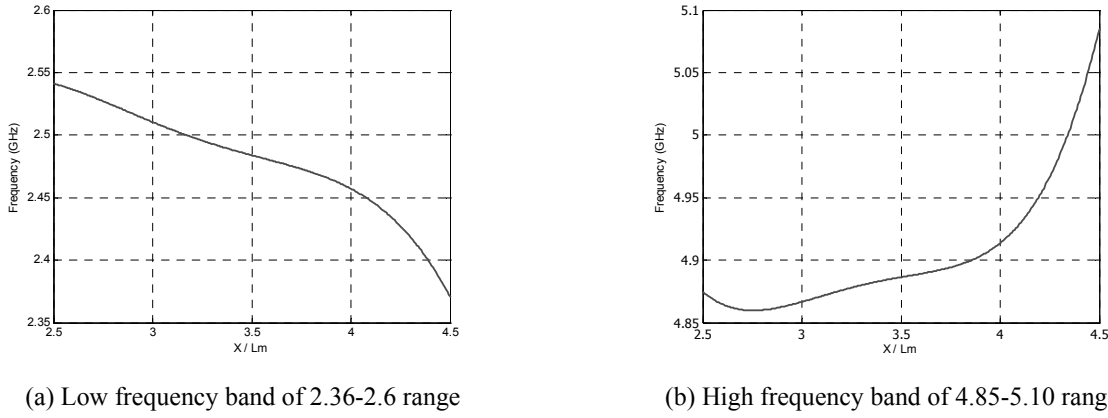
4. Effects of Positioning of Microstrip Feed Line

The effect of positioning of microstrip feed line along the length of the horizontal slot was investigated. The microstrip feed line was moved away from the center to one side along the horizontal slot. At the same time, the length L_m was adjusted such that both the lower and the higher frequency matched the impedance and yielded even return losses. As the position of the microstrip line moved closer to the vertical slot, the lower resonant frequency shifted down while the higher resonant frequency shifted up. On the contrary, when the microstrip line moved away further from the vertical slot, the lower resonant frequency shifted up while the higher resonant frequency shifted down.

L_m was adjusted in relation to the positioning of microstrip feed line. When the microstrip feed line moved away from the vertical slot, L_m should be increased. On the contrary, as microstrip feed line moved toward the vertical slot, L_m should be decreased. From this method of matching, the ratio X/L_m was calculated and represented by a graph over a wide range of frequency as shown in Fig. 2a and Fig. 2b.

For designing purposes, in the beginning, the length of microstrip feed line should be determined to achieve dual frequency close to the desired frequency according to IEEE 802.11 b/g/j with even return loss. In the following stage, the microstrip feed line was moved along the horizontal slot for fine-tuning to achieve the requirements of the standard.

In designing process, varying the length of microstrip feed line for dual-frequency operation technique was suggested to be apply first to obtain an even return loss, then technique of positioning of microstrip feed line around the length of horizontal slot would be used to fine tuning for dual-frequency followed desired standards.



(a) Low frequency band of 2.36-2.6 range

(b) High frequency band of 4.85-5.10 range

Figure 2. Simulation results of an operating band as a function of distance ratio X/L_m

5. Results

The desired antenna with dual frequency range between 2.4 -2.4835 GHz (IEEE802.11 b/g) and 4.9 – 5.0 GHz, 5.03 – 5.091 GHz (IEEE 802.11j) could be achieved by using the ratio of the inner edge length of the slot vertically to horizontally at 1:1.7. The position of the microstrip feed was such that the vertical slot length, L_V , was 17 mm ($0.176\lambda_g$), and the horizontal slot length, L_H , was 29 mm ($0.3\lambda_g$). The result return loss in dB is shown in Fig. 3. Some of the results are shown in Table 1.

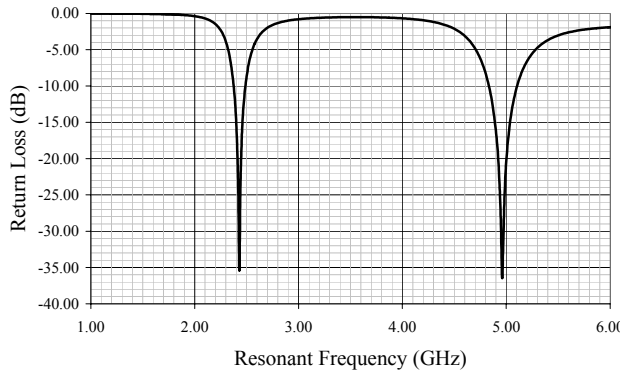


Figure 3. Return loss

Table 1: Result antenna dimension and characteristic

	Design frequency (GHz)	2.44	5.00
L_H (mm)		29.00	
L_V (mm)		17.00	
W_m (mm)		4.50	
L_m (mm)		3.36	
S (mm)		1.00	
X (mm)		14.20	
Return loss (dB)		-35.39	-36.41
-10 dB Bandwidth (%)		4.65	5.32
Input impedance	Real (Ω)	51.29	50.31
	Imaginary (Ω)	-1.141	-1.484
Resonant frequency (GHz)		2.43	4.96
VSWR		1.04	1.03

6. Conclusion

The lengths of vertical and horizontal slot and position of the microstrip feed line have obvious effects on the dual-frequency characteristics of a microstrip-fed right angle-shaped slot antenna.

The effects were studied and an antenna was designed to achieve dual frequency that could be used in the frequency range between 2.4 -2.4835 GHz (IEEE802.11 b/g) and 4.9 – 5.0 GHz, 5.03 – 5.091 GHz (IEEE 802.11j).

REFERENCES

1. Rakluea, P., "Analysis of Right Angle Microstrip Slot Antenna", Tenccon 2005 – IEEE Region10, 21-24 November, 2005.
2. Jamjank C., P. Rakluea, N. Anantrasirichai, and T. Wakabayashi, "Right Angle Microstrip Slot Antenna for Dual Frequency Operation", ISIC-2004, 8-10 September, 2004.
3. IE3D User's Manual Release 9, Zeland Software, Inc., U.S.A., 2002
4. Benson, F. A. and T. M. Benson, Fields Waves and Transmission Lines, Chapman & Hall, 1991.

Particle Swarm Optimization of Dual-band CPW-fed Antenna for WLAN Operation

W. C. Liu and C. M. Wu

National Formosa University, Taiwan, R. O. C.

Abstract - A design of a coplanar waveguide (CPW)-fed monopole antenna with wide dual-band operation simultaneously suitable for use in the WLAN application is presented in this paper. The evolutionary design process of using a particle swarm optimization (PSO) algorithm in conjunction with the method of moments (MoM) is employed to determine the dimensions of the antenna for optimum dual-band operation. The two impedance bandwidths of the proposed antenna could reach 30% and 56.7% , in 10 dB return loss, at bands of 2.43 and 5.33 GHz, respectively, and cover the 2.4/5.2/5.7 GHz WLAN requirements. Also, radiation characteristics are also studied and discussed.

1. Introduction

The growth of IEEE 802.11 wireless local area network (WLAN) communication systems has generated significant interest in the development of various antenna designs with low-profile, lightweight, flush mounted and single-feed to fit the limited equipment space of the WLAN devices, and dual- or multi-band capabilities to satisfy the WLAN standards in the 2.4/5.2/5.7 GHz operating bands. So far, many related antenna designs including the planar inverted-F antennas (PIFAs) [1,2], the meander-line chip antennas [3, 4], the planar monopole antennas [5-7], and the coplanar waveguide (CPW)-fed antennas [8-10] have been presented. Among these antennas, the CPW-fed monopole antenna has especially received much more attention owing to its attractive features such as wide bandwidth, good impedance matching, simple structure of a single metallic layer, no soldering point, and easy integration with active devices etc. However, design of an antenna with dual-band or multiband operation function usually involves many geometry parameters and the improvement of one characteristic for such kind a design normally results in the degradation of another. To optimize such antennas to closely approximate the set objective is similar to searching the global solution from a multidimensional solution space. For this, recently, one heuristic optimization algorithm, the particle swarm optimization (PSO), has been proposed. The PSO is based on the simulation of a simplified sociological behavior associated with swarm such as bees, bird flocking, and fish schooling and first proposed by Kennedy and Eberhart in 1995 for solving multidimensional discontinuous problems [11]. This technique is simpler than the GA and has been successfully applied to a variety of fields. Especially, the PSO, used in conjunction with the numerical electromagnetic solver, is found to be a revolutionary new approach to antenna design and optimisation [12-14]. Based on the iterative optimisation processes of “movement” and “intelligence” in an evolutionary system, the PSO can lead quickly and ultimately to the closest approximation to the antenna specification with minimal foresight or pre-conditioning on the part of the designer. The immense power of the technique is its ability to satisfy a performance criterion without any *a priori* knowledge of candidate configurations, and the facility for finding the global optimum result.

In this paper, we examine the use of a PSO to search a CPW-fed planar monopole antenna with optimal dual-band operation simultaneously suitable for use in the WLAN system. A pair of short strips is introduced to the coplanar waveguide (CPW) feeding line to achieve good dual-band resonance and reduce the antenna size. During the approach, the geometry parameters including the dimensions of the planar monopole patch and the additional strips, the sizes of the coplanar ground planes, and the spaces between the ground plane to either the patch or the CPW feeding line are all left as the design variables for manipulation by the PSO. In addition, the IE3D™ (method of moments based software by Zeland) was used to predict the performance of each antenna designed by the PSO. Details of the antenna design are described, and prototypes of the PSO-optimised antenna for dual-band operation have been constructed and tested. Also, comparison between the theoretical and experimental results of the optimal antenna is presented and discussed.

2. Synthesis procedure

Figure 1 shows the examined geometrical configuration of the candidate CPW-fed planar monopole antenna for achieving dual-band operation. As shown, the antenna including the ground plane is printed on only one side of an FR4 dielectric microwave substrate (thickness 1.6 mm and dielectric constant 4.4). The

basis of the antenna structure is a rectangle patch element with dimensions of width W and length L , and with a vertical spacing of d away from the ground plane. A conventional $50\ \Omega$ CPW-fed line designed with a fixed signal strip thickness w_f and a gap distance of S_w between the single strip and the coplanar ground plane is used for exciting the radiating patch element. Two finite ground planes with the same size of width W_g and length L_g , are situated symmetrically on each side of the CPW feeding line. In this study, for trying to obtain good dual-band impedance matching by adjusting the current paths and controlling the compensation between the capacitive and inductive effects caused from the electromagnetic coupling effects of the finite ground planes and the modified feeding line at the desired two operating frequencies, two short strips, each with dimensions of $l_s \times w_s$, were horizontally and symmetrically embedded from the left and right sides into the feeding line with a distance of h_1 away from the feeding point. The additional two stripes resemble the feeding line in a cross shape.

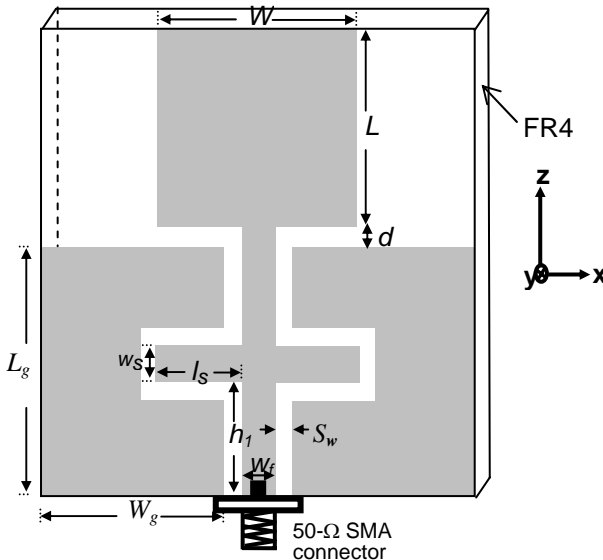


Figure 1: Geometrical configuration of proposed dual-band CPW-fed antenna.

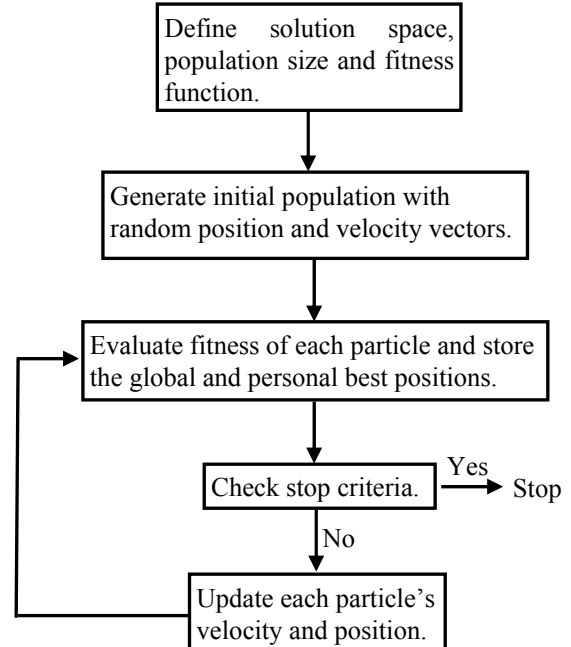


Figure 2: Optimization procedure of a PSO algorithm.

Table 1: Ranges of the design parameters for the dual-band CPW-fed antenna.

Parameter	W	L	d	w_f	S_w	W_g	L_g	w_s	l_s	h_1
Range (mm)	2~25	2~25	0.5~10	1~5	0.2~5	10~25	10~30	0.5~10	0~15	2~20

Thus we defined ten geometry parameters to compose a possible antenna design and thereupon each of them was given appropriate minimum and maximum values as shown in Table I. These parameters define a ten-dimensional solution space in which the PSO searches for the optimal dual-band CPW-fed antenna. Each particle (i.e. each possible antenna design) therefore is represented by ten position variables of ($W, L, d, w_f, S_w, W_g, L_g, w_s, l_s, h_1$) for used in the PSO optimization procedure as shown in Figure 2. A population size of 30 particles is used in this study case. This number is suggested for most engineering problems [12] and has also been shown to result in a very fast convergence for our problem. On commencement of the iterations the so-called *fitness function* reflects the design goals is set to evaluate the fitness of each created particle for assessing its leadership among the swarm. The particle yielding the best objective function value will act as the swarm leader. Since the goal here is to achieve good impedance matching at the 2.4, and 5.25 GHz operating bands for suitable use in 2.4/5.2 GHz WLAN applications, and in view of the wide variation of initial values obtained, the return loss S_{11} calculated by IE3D at the above two operating frequencies were both normalized by an objective factor of -35 dB, which is considered to be good enough for impedance matching. As expected in such a multidimensional problem, numerical experiments showed that the two normalized terms made different contributions to the value of the fitness function. To prevent either of them from dominating the iteration process, each of the two terms was weighted by an associated

constant. In this example, we have found that the improvement of return loss at 5.25 GHz changed much more quickly than did the return loss at 2.4 GHz, so it must be less weighted. Thus weighting values of 0.6 and 0.4 were selected for 2.4 and 5.25 GHz terms, respectively, after a number of preliminary runs. This weighting technique effectively quickens the improvement of return loss at 2.4 GHz but slows that at 5.25 GHz. In addition, to ensure the algorithm quickly reaches to a solution of dual-band operation a threshold of -10 dB return loss for each band was also set in the fitness function. The resulting fitness function was then:

$$\text{fitness function} = 0.6 \frac{S_{11}(2.4 \text{ GHz})}{-35} + 0.4 \frac{S_{11}(5.25 \text{ GHz})}{-35} + \sum_{i=1}^2 G_i \quad (1)$$

$$G_i = \begin{cases} 1, & \text{if } S_{11}(f_i) \leq -10 \text{ dB}, \\ 0, & \text{if } S_{11}(f_i) > -10 \text{ dB}. \end{cases} \quad i = 1 \text{ and } 2 \text{ for } 2.4 \text{ and } 5.25 \text{ GHz, respectively} \quad (2)$$

In addition, another scheme we applied to avoid the solution's becoming stuck in a local pool is that once a return loss of less than -35 dB is achieved for any frequency, only -35 dB will be put in the fitness function to evaluate the fitness. The other PSO parameters were selected the same as those used in [11]. Finally, a stop criterion was set arbitrarily to operate once the fitness function became asymptotic to its maximum value and remained so for at least 30 iterations. If the procedure does not stop, the modified velocity and position of each particle can be calculated using the current velocity and the distance from the stored individual's and global best positions. The algorithm runs through these processes iteratively until it converges.

3 Optimized and Measured Results

The optimal dual-band CPW-fed antenna with geometry parameters of $W=13.64 \text{ mm}$, $L=20 \text{ mm}$, $d=1.24 \text{ mm}$, $w_f=3.64 \text{ mm}$, $s_w=0.35 \text{ mm}$, $W_g=18.95 \text{ mm}$, $L_g=18.42 \text{ mm}$, $w_s=5 \text{ mm}$, $l_s=10 \text{ mm}$, and $h_1=7.63 \text{ mm}$ has been obtained and then it was constructed and experimentally studied. Figure 3 shows the measurement and simulation frequency response of the return loss for the proposed antenna. Obviously, the simulation results show that except the dual resonant bands at frequencies of 2.4 and 5.25 GHz, which are exactly the same as those we put in the fitness function of the PSO process, an additional resonant band is also excited at frequency about 7.25 GHz. As for the measured results, also, three resonant modes at frequencies of 2.43, 5.33, and 7.09 GHz were obtained. The measured -10 dB impedance bandwidth at 2.43 GHz band is about 730 MHz (2.23-2.96 GHz), while the measured bandwidths across the two excited resonant bands at 5.33 and 7.09 GHz are sufficient to produce a much broad continuous bandwidth of about 3.02 GHz ranged from 4.6 to 7.62 GHz. The two continuous bandwidths are corresponding to an impedance bandwidth of 30 % and 56.7 % with respective to the appropriate resonant frequencies of 2.43 and 5.33 GHz, respectively. Reasonable agreement between the measurement and the simulation is observed. Obviously, the obtained measured bandwidths can cover the WLAN standards in the 2.4 GHz (2.4-2.484GHz), 5.2 GHz (5.15-5.35 GHz), and 5.7 GHz (5.725-5.825 GHz) bands.

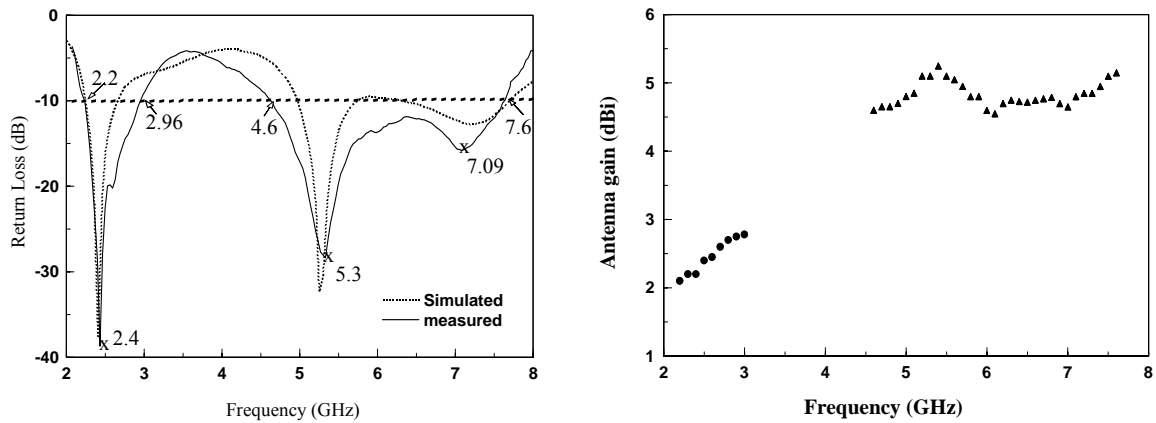


Figure 3: Measured and simulated return loss for the proposed dual-band CPW-fed antenna.

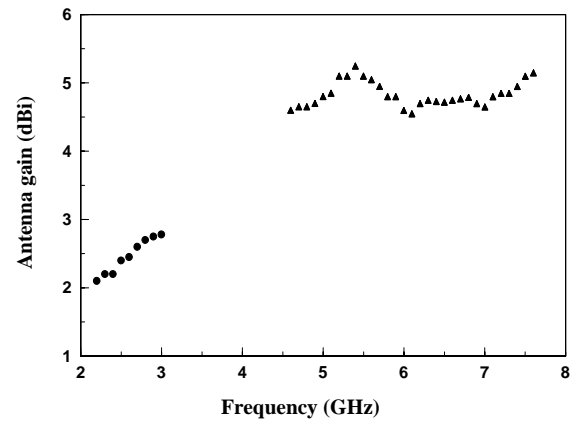


Figure 4: Measured peak antenna gain for frequencies across the lower and upper bands for the proposed antenna.

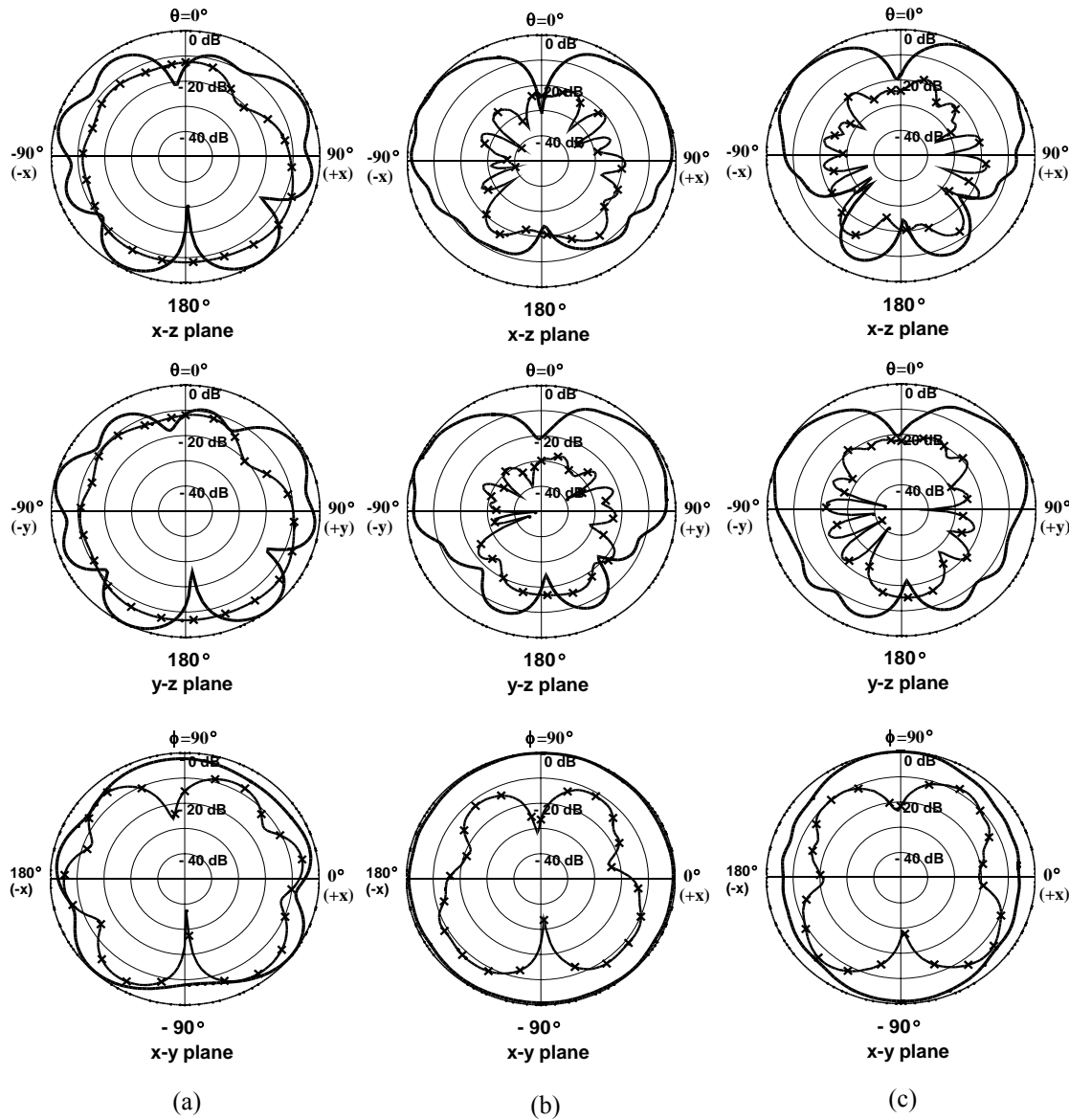


Figure 5: Measured radiation patterns for the proposed antenna at a) $f=2.45$ GHz, b) $f=5.25$ GHz, and c) $f=5.75$ GHz. (— E_θ ; ×—× E_ϕ)

Figure 4 shows the measured peak antenna gain for frequencies across the lower and higher bands. The ranges of antenna gain are about 2.1-2.8 dBi and 4.5-5.3 dBi across the 2.43 and 5.33 GHz bands, respectively, and the gain variations are both less than 1 dBi. Figure 5 plots the measured radiation patterns including the vertical (E_θ) and the horizontal (E_ϕ) polarization patterns in the elevation cuts (x-z and y-z planes) and azimuthal cut (x-y plane) at 2.45, 5.25 and 5.75 GHz for the WLAN application. Due to the symmetry in structure, rather symmetrical radiation patterns are seen in the x-z and y-z planes as depicted in the plots. The radiation patterns of the proposed antenna are observed to be in general very monopole-like for each measured frequency as the pattern in the azimuthal direction is nearly omnidirectional, and those in the horizontal direction are both very conical. In addition, it is also found that the E_θ and E_ϕ components of the patterns in both x-z and y-z planes for operating at 2.45 GHz are seemed to be more comparable than those operating at 5.25 and 5.75 GHz. The stable radiation patterns similar to those plotted here have been obtained for the proposed antenna across the bandwidth of each band.

4. Conclusion

A CPW-fed planar monopole antenna, which makes use of a cross-shaped feeding line to enhance the dual-band wide impedance matching on the patch element, has been developed. The design process used the particle swarm optimization to optimize the performance of the antenna by choosing the most appropriate configuration parameters. The constructed prototype of the PSO-resulted antenna has two

broaden operation bands at 2.43 and 5.33 GHz, which satisfy the bandwidth requirements of the 2.4, 5.2 and 5.7 GHz WLAN systems. Also, good antenna performances have been obtained and shown to match well with the numerical prediction.

Acknowledgement

This work was supported by the National Science Council of the Republic of China under grant NSC 94-2213-E150-009-

REFERENCES

1. Dou, W. P. and Y. W. M. Chia, "Novel meandered planar inverted-F antenna for triple-frequency operation," *Microwave Opt. Technol. Lett.*, Vol. 27, No. 2, 58-60, 2000.
2. Song, C. T. P., P. S. Hall, H. Ghafouri-Shiraz, and D. Wake, "Triple band planar inverted F antennas for handheld devices," *Electron. Lett.*, Vol. 36, No. 2, 112-114, 2002.
3. Choi, W., S. Kwon, and B. Lee, "Ceramic chip antenna using meander conductor lines," *Electron. Lett.*, Vol. 37, No. 15, 933-934, 2001.
4. Dakeya, Y., T. Suesada, K. Asakura, N. Nakajima, and H. Mandai, "Chip multiplayer antenna for 2.45 GHz-band application using LTCC technology," *IEEE MTT-S Int. Microwave Symp. Dig.*, 2000, 1693-1696.
5. Lee, L. S., P. S. Hall, and P. Gardner, "Compact wideband planar monopole antenna," *Electron. Lett.*, Vol. 35, No. 25, 2157-2158, 1999.
6. Kuo, Y. L. and K. L. Wong, "Printed double-T monopole antenna for 2.4/5.2 GHz dual-band WLAN operations," *IEEE Trans. Antennas Propagat.*, Vol. 51, No. 9, 2187-2192, 2003.
7. Wong, K. L., G. Y. Lee, and T. W. Chiou, "A low-profile planar monopole antenna for multiband operation of mobile handsets," *IEEE Trans. Antennas Propagat.*, Vol. 51, No. 1, 121-124, 2003.
8. Laheurte, J. M., "Switchable CPW-fed slot antenna for multifrequency operation," *Electron. Lett.*, Vol. 37, No. 25, 1498-1499, 2001.
9. Angelopoulos, E. S., Y. E. Stratakos, A. I. Kostaridis, D. I. Kaklamani, and N. K. Uzunoglu, "Multiband miniature coplanar waveguide slot antennas for GSM-802.11b and 802.11b-802.11a wireless applications," *IEEE Wireless Commun. and Network.*, Vol. 1, 103-108, 2003.
10. Liu, W. C. and C. M. Wu, "Broadband dual-frequency cpw-fed planar monopole antenna with rectangular notch," *Electron. Lett.*, Vol. 40, No. 11, 642-643, 2004.
11. Kennedy, J. and R. C. Eberhart, "Particle swarm optimization," *Proc. IEEE Conf. Neural Networks IV*, Piscataway, NJ, 1995.
12. Robinson, J. and Y. Rahmat-Samii, "Particle swarm optimization in electromagnetics," *IEEE Trans. Antennas Propagat.*, Vol. 52, No. 2, 397-407, 2004.
13. Boeringer, D. W. and D. H. Werner, "Particle swarm optimization versus genetic algorithms for phased array synthesis," *IEEE Trans. Antennas Propagat.*, Vol. 52, No. 3, 771-779, 2004.
14. Boeringer, D. W. and D. H. Werner, "Efficiency-constrained particle swarm optimization of a modified bernstein polynomial for conformal array excitation amplitude synthesis," *IEEE Trans. Antennas Propagat.*, Vol. 53, No. 8, 2662-2673, 2005.